MOUNTAIN-PLAINS CONSORTIUM

MPC 22-451 | T. Sjurseth, E. Greeneway, K. Hart, M. LaVoy, M. Tazarv, and N. Wehbe

MECHANICALLY SPLICED PRECAST BRIDGE COLUMNS

A University Transportation Center sponsored by the U.S. Department of Transportation serving the Mountain-Plains Region. Consortium members:

Colorado State University
North Dakota State University
South Dakota State University
University of Colorado Denver
University of Denver
University of Utah
Utah State University
University of Wyoming

Mechanically Spliced Precast Bridge Columns

Theodore Sjurseth
Evan Greeneway
Kallan Hart
Mathew LaVoy
Mostafa Tazarv
Nadim Wehbe
Department of Civil and Environmental Engineering
South Dakota State University
Brookings, South Dakota

March 2022

Technical Report Documentation Page

1. Report No.	2. Government Accession No.	3. Recipient's Catalog No.
MPC-595		

4. Title and Subtitle	5. Report Date
Mechanically Spliced Precast Bridge Columns	March 2022
	6. Performing Organization Code
7. Author(s) T. Sjurseth E. Greeneway K. Hart M. LaVoy M. Tazarv N. Wehbe	8. Performing Organization Report No. MPC 22-451
9. Performing Organization Name and Address South Dakota State University Brookings, SD, 57007	10. Work Unit No. (TRAIS) 11. Contract or Grant No.
12. Sponsoring Agency Name and Address Mountain-Plains Consortium North Dakota State University PO Box 6050, Fargo, ND 58108	13. Type of Report and Period Covered Final Report 14. Sponsoring Agency Code

15. Supplementary Notes

Supported by a grant from the US DOT, University Transportation Centers Program

16. Abstract

A mechanical bar splice is an alternative to the traditional lap splicing to connect bars in reinforced concrete (RC) structures. Even though mechanical bar splices can be used as new precast column connections to accelerate bridge construction (ABC), the use of bar couplers in the plastic hinge region of bridge columns is prohibited in current US codes. The literature lacks a systematic performance database on mechanically spliced bridge columns. An experimental investigation was performed to determine the seismic performance of mechanically spliced bridge columns and to develop the first-of-its-kind mechanically spliced column performance database. Eight half-scale bridge columns were constructed and tested. One column was cast-in-place (CIP) and seven were precast incorporating different coupler products at the column base. One of the precast columns included a repairable detailing that allowed replacement of steel bars through detachable couplers. All columns were tested under the same slow cyclic displacement-controlled lateral loading. The test results showed that seismic couplers can reduce the precast column displacement capacities from 3% to 45% compared with CIP. Nevertheless, all precast columns tested in this project met the current code seismic requirements thus they are recommended for use in all 50 states of the nation. The repair through replacement of BRR was feasible but difficult at 5% drift ratio due to a Z-shape buckling of the exposed bars. Three design methods for mechanically spliced bridge columns were evaluated and were found viable for practice.

17. Key Word	18. Distribution Statement
bridge construction, bridge design, columns, couplers, earthquake resistant design, feasibility analysis, precast concrete, splicing, structural connection	Public distribution

19. Security Classif. (of this report)	20. Security Classif. (of this page)	21. No. of Pages	22. Price
Unclassified	Unclassified	357	n/a

Form DOT F 1700.7 (8-72) Reproduction of completed page authorized

Acknowledgements

The work presented in this report conducted with support from South Dakota State University, the Mountain-Plains Consortium (MPC), which is a University Transportation Center (UTC) funded by the U.S. Department of Transportation, and industry partners. Their support and feedback are greatly appreciated. The contents of this paper reflect the views of the authors, who are responsible for the facts and accuracy of the information presented.

The project objectives could not be accomplished without the support of several industry partners. The authors are indebted to Dayton Superior Corp., Dextra America, Inc., nVent LENTON Corp., Headed Reinforcement Corp., Splice Sleeve North America, Inc., Contractors Materials Company, and Gage Brothers for sponsoring the project, in-kind material donation, and/or technical feedback throughout the project. The authors would like to thank Mr. Zach Gutzmer, manager of the Lohr Structures Laboratory, and undergraduate student Aric Jensen for their efforts during this project.

ABSTRACT

A mechanical bar splice, also known as bar coupler, is an alternative to the traditional lap splicing to connect bars in reinforced concrete (RC) structures. Even though mechanical bar splices can be used as new precast column connections to accelerate bridge construction (ABC), the use of bar couplers in the plastic hinge region of bridge columns is prohibited in current U.S. codes. This is mainly because the coupler performance and the effects of couplers on the seismic behavior of columns have not been fully investigated. A recent study at South Dakota State University (SDSU) attacked the first problem by testing more than 160 bar couplers, established a comprehensive database of the coupler behavior, and proposed standard test methods and acceptance criteria for seismic couplers. Nevertheless, test data regarding the performance of mechanically spliced bridge columns is scarce, and the available data is for columns with different geometries, confinement levels, and testing procedures. The literature lacks a systematic performance database on mechanically spliced bridge columns. An experimental investigation was performed at the SDSU Lohr Structures Laboratory to determine the seismic performance of mechanically spliced bridge columns and to develop the first-of-its-kind mechanically spliced column performance database. Eight half-scale bridge columns were constructed and tested. One column was cast-in-place (CIP) to serve as the reference model and seven were precast, incorporating different coupler products at the column base. One of the precast columns included a repairable detailing that allowed replacement of steel bars through detachable couplers. All columns were tested under the same slow cyclic displacement-controlled lateral loading. The test results showed that seismic couplers can reduce the precast column displacement capacities from 3% to 45% compared with CIP. Nevertheless, all precast columns tested in this project met the current code seismic requirements, thus they are recommended for use in all 50 U.S. states. The drift capacity of the repairable column was 9.8%, which was higher than the CIP drift capacity of 8.96%. The stiffness of the repairable column was lower than that for CIP due to the nature of the new connection and the damage of concrete at the rocking face. The repair through replacement of BRR was feasible but difficult at 5% drift ratio due to a Z-shape buckling of the exposed bars. Furthermore, a post-test analytical study was performed to evaluate current modeling methods for bridge columns, specifically mechanically spliced columns, followed by a parametric study including 400 pushover and 540 nonlinear dynamic analyses. The models were able to successfully reproduce the force-displacement relationship of the test columns. The results from the pushover analyses showed that columns with couplers may reduce the displacement ductility capacity up to 45% when compared with conventional CIP columns, which agreed well with the new column experimental data. Furthermore, the results from the nonlinear dynamic analyses, the first of its kind on mechanically spliced columns, showed that couplers have minimal effect on the precast column seismic drift demands. A maximum of 7% deviation was found when spliced column dynamic response was compared with that of the CIP column. Three design methods for mechanically spliced bridge columns were evaluated and found viable for practice.

TABLE OF CONTENTS

Abbreviations & Notations

AASHTO	American Association of State Highway and Transportation Officials
ASTM	American Society of Testing and Materials
ABC	Accelerated Bridge Construction
ACI	American Concrete Institute
AR	Column Aspect Ratio, the ratio of the column length to the column diameter
ALI	Column Axial Load Index, the ratio of the column axial load to the product of the column cross-section area and the concrete strength
ALR	Column Axial Load Ratio, the same as ALI
CIP	Cast-in-Place
DOT	Department of Transportation
DOF	Degrees of Freedom
Drift	The ratio of the column lateral displacement to the column length
Ductility	the ratio of the column lateral displacement to the column idealized yield displacement
ft	Feet
GS	Grouted Sleeve Coupler
HR	Headed Reinforcement Coupler
HY	Hybrid Coupler
in.	Inch
kip	1000 pounds
ksi	kip per square inch
LVDT	Linear Variable Displacement Transducer
RC	Reinforced Concrete
SDSU	South Dakota State University
SH	Shear Screw Coupler
SW	Swaged Coupler
TH	Threaded Coupler
UHPC	Ultra-High Performance Concrete

LIST OF TABLES

LIST OF FIGURES

EXECUTIVE SUMMARY

ES.1 Introduction

Bars must be spliced in reinforced concrete (RC) structures for a successful load transfer between joints and elements. Lap splicing is the conventional method to provide continuity in RC members, which is achieved through bond mechanism between concrete and the overlapping bars with sufficient length. The lap splicing is generally an adequate method for connecting bars; however, it can lead to constructability issues in heavily reinforced and/or precast members.

An alternative to lap splicing is the use of mechanical bar splices, which are also referred to as bar couplers. A bar coupler connects two ends of reinforcing bars through various mechanisms such as grouting, threading, pressing, and/or other techniques. Bar couplers may reduce the reinforcement congestion and lower the material cost since a lower amount of reinforcement is used. Further, for precast members, couplers may reduce construction time due to member prefabrication and improve the quality of the product.

Bar couplers are currently used in accelerated bridge construction (ABC) for capacity protected members but are prohibited in bridge columns located in high seismic regions. This is mainly because (1) the coupler performance has not been fully established, and (2) the effects of the couplers on the column seismic behavior have not been completely understood. Recent studies have tried to fill these knowledge gaps, but the literature lacks unified experimental data to determine how the various coupler types/products and column properties, such as geometry, aspect ratio, and axial loads, affect the capacity and demand of spliced bridge columns.

The main objectives of the present study were to: (1) establish a comprehensive performance database for mechanically spliced precast bridge columns through large-scale testing, and (2) verify or update current state-of-the-art design methods for mechanically spliced precast bridge columns. To achieve these goals, several tasks were completed. A summary of the tasks and the key findings are discussed in this chapter.

ES.2 Literature Review

A review was carried out to synthesize the literature on the performance of various coupler types and the performance of columns incorporating bar couplers.

More than 60 mechanical bar splices are commercially available in several configurations and models produced by different manufacturers, but they are usually classified based on the mechanism utilized to transfer load between two bars: shear screw (SS), headed (HC), swaged (SW), threaded (TH), grouted (GC), or a combination of these mechanisms named hybrid (HY). Therefore, couplers can generally be categorized into six types.

Couplers vary in their shapes, sizes, lengths, thicknesses, and anchoring mechanisms, making them difficult to simulate in engineering analyses. A few studies have proposed models to estimate coupler material behavior (Haber et al., 2015; Tazarv and Saiidi, 2016; Ameli et al., 2016). The coupler stress-strain material model developed by Tazarv and Saiidi (2016) was adopted in this study (Fig. ES.1). When a spliced bar is in tension, only a portion of the coupler is considered to contribute to the overall elongation while the remaining portion is assumed to be rigid. The rigid portion of the coupler (βL_{sp}) is due to the coupler anchoring mechanism. The coupler rigid length factor (β) estimates what length of the coupler does not contribute to the splice total elongation. The rigid length factor can be different for different couplers and should be determined through experiment. The length of the coupler region (L_{cr}) is the physical length of the coupler (L_{sp}) plus a distance (α times the bar diameters, αd_b) from each end of the coupler. Subjected to the same tensile force, the unspliced reference bar will elongate more than a spliced bar due to the coupler rigidity. Therefore, the strain of the unspliced bar (ε_s) will be greater than the strain of the corresponding spliced bar (ε_{sp}). Equation ES.1 can be used to relate the coupler strains to the reference bar strains.

$$\frac{\varepsilon_{sp}}{\varepsilon_s} = \frac{L_{cr} - \beta L_{sp}}{L_{cr}} \quad \text{(Eq. ES.1)}$$

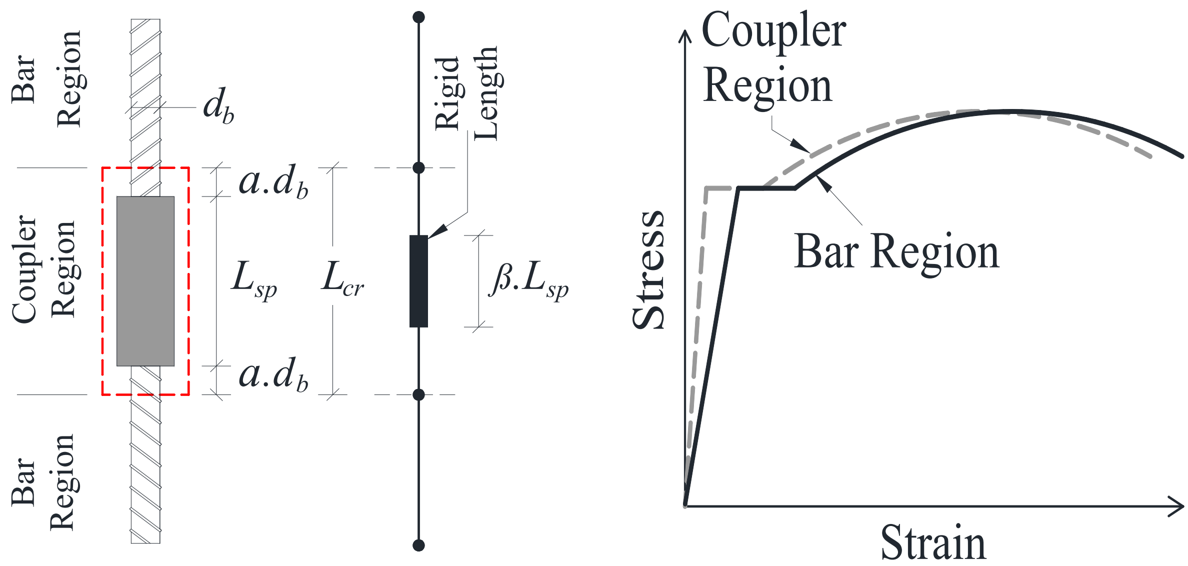

a) Regions of a Mechanical Bar Splice b) Stress-Strain Model

Figure ES.1 Stress-Strain Model for Mechanical Bar Splices by Tazarv and Saiidi (2016)

Dahal and Tazarv (2020) tested more than 160 mechanical bar splices, including No. 5 (Ø16-mm), No. 8 (Ø25-mm), and No. 10 (Ø32-mm) bars, and developed the first database for coupler performance and quantified the coupler properties in accordance with the modeling method proposed by Tazarv and Saiidi (2016). The splices were tested to failure using both uniaxial monotonic and cyclic tensile loading. Table ES.1 presents the recommended coupler rigid length factors for different coupler types and sizes (Fig. ES.2) based on a statistical analysis of the coupler test data. Coupler connections may fail by bar pullout from the coupler, coupler failure, bar fracture within the coupler region, or bar fracture outside the coupler region. A coupler is only considered a “seismic coupler” if it consistently fails by the bar fracture outside the coupler region.

A few large-scale tests have been performed to understand the effects of couplers on the performance of RC bridge columns (e.g., Haber at al., 2013; Tazarv and Saiidi, 2014; Ameli et al., 2014; Wang et al., 2018; Bompa and Elghazouli, 2019). These studies tested columns with different geometries, setup, loading, and/or coupler types. The general experimental trend was that the column displacement capacities were adversely affected by some couplers (up to 40%) but the column strength was not significantly changed when couplers were used.

Table ES.1 Coupler Rigid Length Factors (β) Recommended by Dahal and Tazarv (2020)

Coupler Type	No. 5 (16 mm)	No. 8 (25 mm)	No. 10 (32 mm)
Headed Reinforcement	0.80	0.75	0.55
Threaded (Dextra-Type A)	1.70	1.5	1.60
Threaded (Dextra-Type B)	1.60	1.5	1.65
Threaded (Erico or nVent)	0.95	1.10	1.05
Swaged	0.90	0.90	0.95
Grouted Sleeve (NMB)	0.95	0.65	0.85
Grouted Sleeve (Dayton)	0.70	0.70	0.65
Hybrid (Dextra)	0.80	0.90	0.85
Hybrid (Erico or nVent)	0.80	0.80	0.80

Figure ES.2 Different Mechanical Bar Splice Products Tested by Dahal and Tazarv (2020)

ES.3 Experimental Investigation

A total of eight columns, including one reference cast-in-place (CIP) column and seven precast columns, have been designed, built, and tested in this project. The column test variable was the coupler type (different types have different geometries and mechanical properties) through the most feasible detailing per type. Table ES.2 presents the test matrix for the eight columns included in this study. The specimens were identified by two broad classifications, CIP and precast with a three-letter naming system starting with "P." The second letter in the precast column name identifies the coupler type: "G" for grouted, "T" for threaded, and "H" for a hybrid combination of coupling mechanisms. The last letter of the precast column name identifies the coupler manufacturer: "D" either for Dayton Superior or Dextra America, "S" for Splice Sleeve North America, "H" for Headed Reinforcement, and "V" for nVent Lenton. Four feasible connection detailing alternatives shown in Figure ES.3 were proposed for the precast specimens. Each specimen was detailed according to the alternative deemed most feasible. The last column in the test matrix, RPH, was a new column with repairable detailing based on the work by Boudaqa et al. (2017) and Tazarv et al. (2020). The main goal of this pilot testing was to investigate the feasibility of such details for a quick repair through replacement of the column damaged bars after a severe event.

Table ES.2 Column Test Matrix

SP ID	Coupler Type	Manufacturer, Model	Coupler Properties, in. (mm)	Coupler Rigid Length Factor, β	Remark
CIP	N/A	N/A	N/A	N/A	Reference cast-in-place
PGD	Grouted	Dayton Superior Corp., Sleeve Lock	Length: 16.5 (419) Diameter: 2.89 (73)	0.70	Use ALT1 detailing
PGS	Grouted	Splice Sleeve North America, Inc., NMB	Length: 14.57 (370) Diameter: 2.52 (64)	0.70	Use ALT1 detailing
PHD	Hybrid (Grouted-Threaded)	Dextra America, Inc., Groutec S with Bartec	Length: 9.45 (240) Diameter: 2.17 (55)	0.79	Use ALT1 detailing (Fig. 3.1)
PHV	Hybrid (Grouted-Threaded)	nVent LENTON Corp., Interlock	Length: 8.63 (219) Diameter: 2.67 (68)	0.82	Use ALT1 detailing
PTV	Threaded	nVent LENTON Corp., Ultimate PT15 Position	Length: 9.0 (228.6) Diameter: 1.5 (38)	0.4	Use ALT2 detailing, column dowels tapered (MT12)
PHH	Hybrid (Grouted-Headed)	Headed Reinforcement Corp., HRC560	Length: 7.75 (196.9) Diameter: 2.625 (67)	0.80	Use ALT1 detailing
RPH	Headed	Headed Reinforcement Corp., HRC510XL	Length: 3.13 (80) Diameter: 2.13 (54)	0.75	Repairable column with BRR, ALT4

Note: Coupler properties are for No. 8 (25-mm) bars. All couplers except HRC510 were tested in this project. Data for HRC510 coupler were from Dahal and Tazarv (2020).

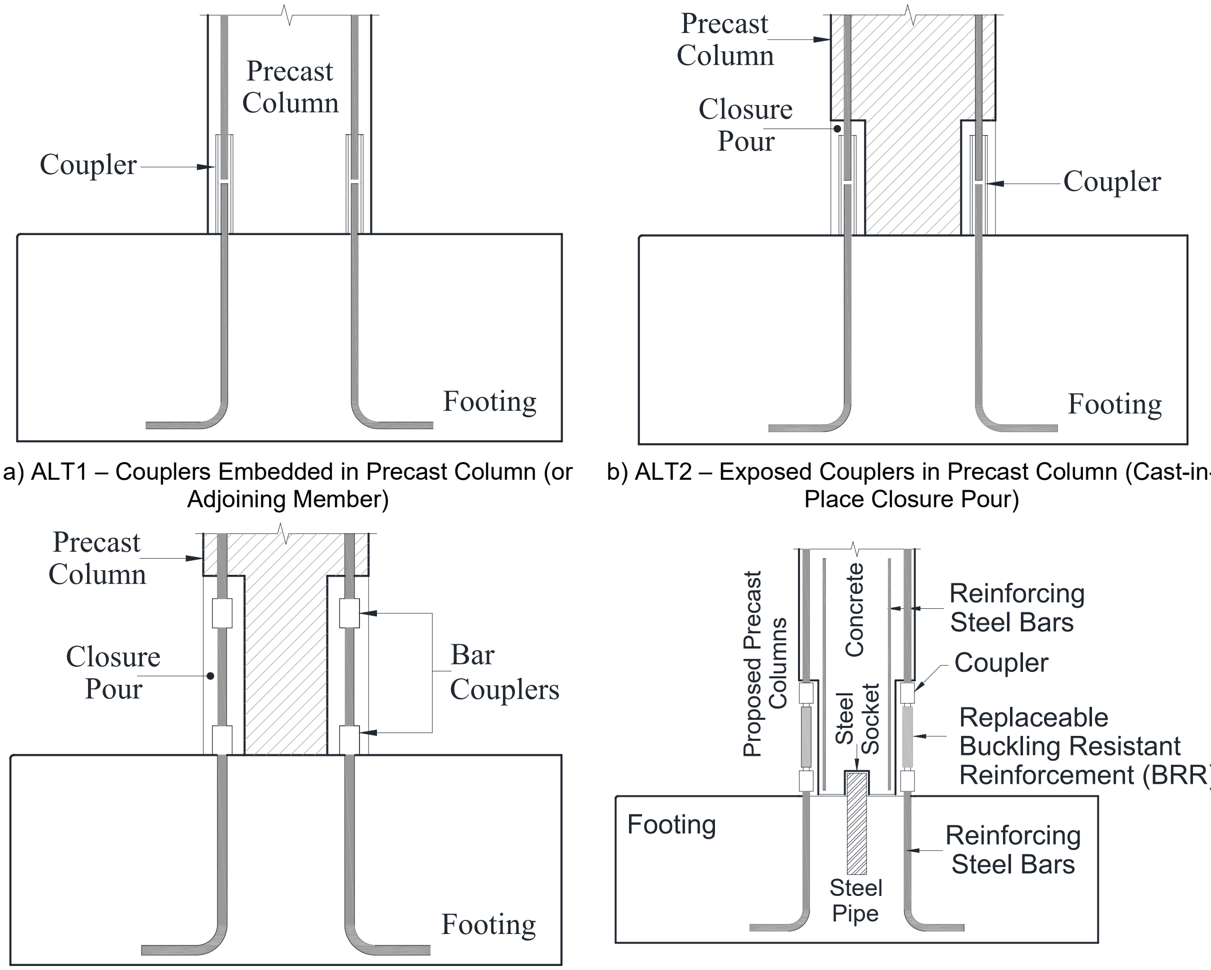

a) ALT1 – Couplers Embedded in Precast Column (or Adjoining Member)

b) ALT2 – Exposed Couplers in Precast Column (Cast-in-Place Closure Pour)

c) ALT3 – Exposed Two-Level Couplers in Precast Column (Cast-in-Place Closure Pour)

d) ALT4 – Repairable Precast Columns

Figure ES.3 Feasible Connection Details for Mechanically Spliced Precast Bridge Columns

ES.3.1 Observed Damage for all Columns

Figure ES.4 shows the plastic hinge damage of columns after the second pull of the 2% drift cycle. CIP had numerous cracks in the plastic hinge region at this drift. However, the general trend for the precast columns was that they had less damage, especially cracking compared with CIP. This is because seismic couplers tend to make the coupler region stronger, thus shifting the damage to the ends of the coupler. For example, the coupler used in PGD was the longest among all couplers used in the precast specimens. As a result, PGD showed the least number of cracks within the plastic hinge region.

Figure ES.5 shows the plastic hinge damage for CIP and all mechanically spliced columns at their failure drift. As a general trend, CIP showed higher damage compared with precast columns. Those spliced columns with the bar fracture mode of failure, e.g., PGS, showed similar damage as the CIP column. However, those precast columns with other modes of failure, such as bar pullout from the coupler, showed the minimal visible damage compared with CIP. Examples of this behavior are PGD and PHD.

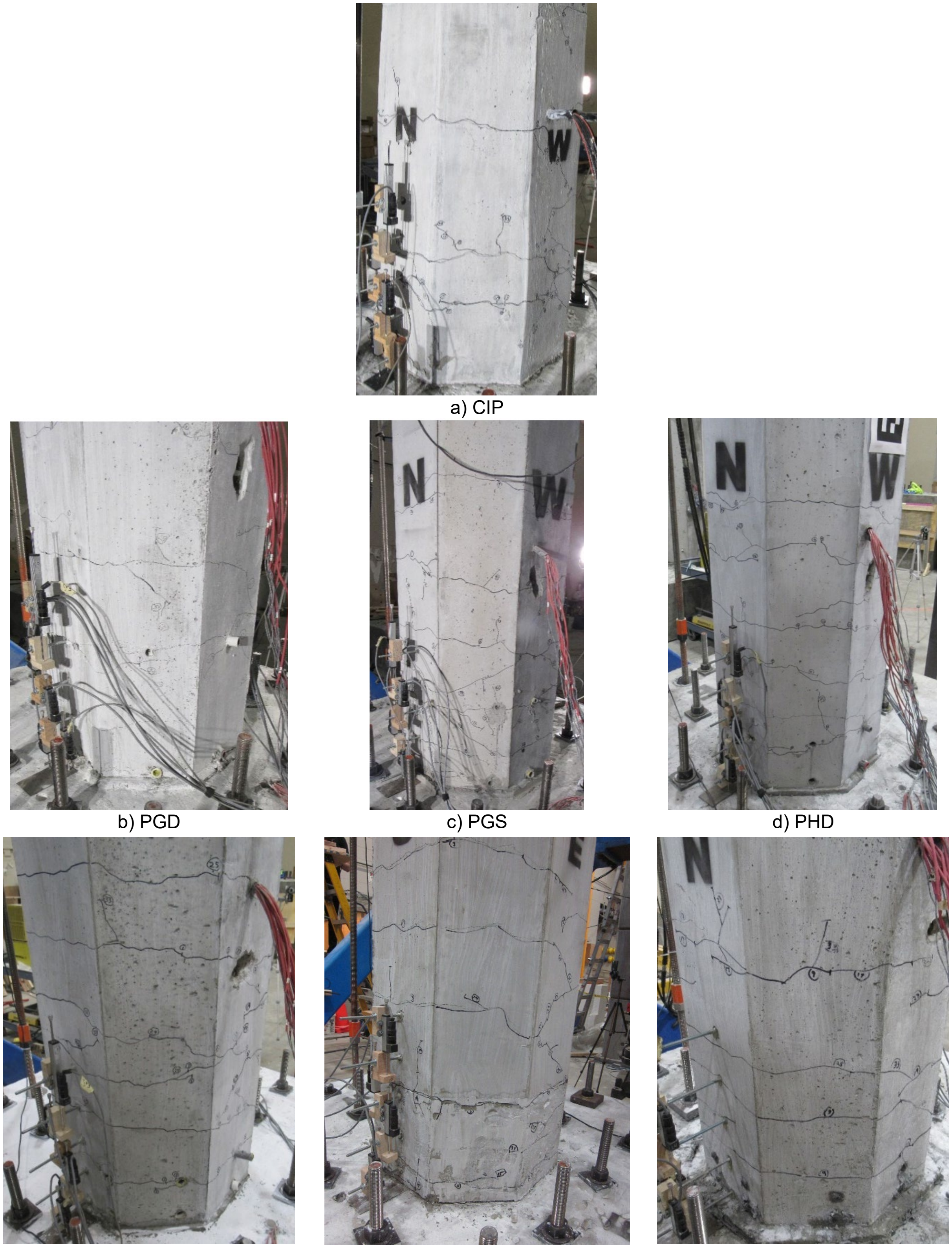

a) CIP

b) PGD

c) PGS

d) PHD

e) PHV

f) PTV

g) PHH

Figure ES.4 CIP, PGD, PGS, PHD, PHV, PTV, and PHH Plastic Hinge Damage at 2% Drift Ratio

a) CIP at 10%

b) PGD at 6%

c) PGS at 9%

d) PHD at 4%

e) PHV at 10%

f) PTV at 7%

g) PHH at 10%

Figure ES.5 CIP, PGD, PGS, PHD, PHV, and PTV Plastic Hinge Damage at Failure Drift Ratio

ES.3.2 Force-Displacement Relationship for all Columns

Figure ES.6 shows the measured lateral force-drift hysteretic response for CIP and all mechanically spliced precast columns. The precast columns exhibited similar behavior compared with that of CIP up to their failure point. All columns showed a wide and stable hysteretic behavior. The precast column with the HRC hybrid grouted-headed couplers showed a pinching starting at 4% drift ratio during unloading due to a gap between the head of the bar and the head seating area within the coupler. All precast columns showed a slightly higher stiffness and a higher lateral strength compared with CIP due to the coupler rigidity and a higher concrete compressive strength.

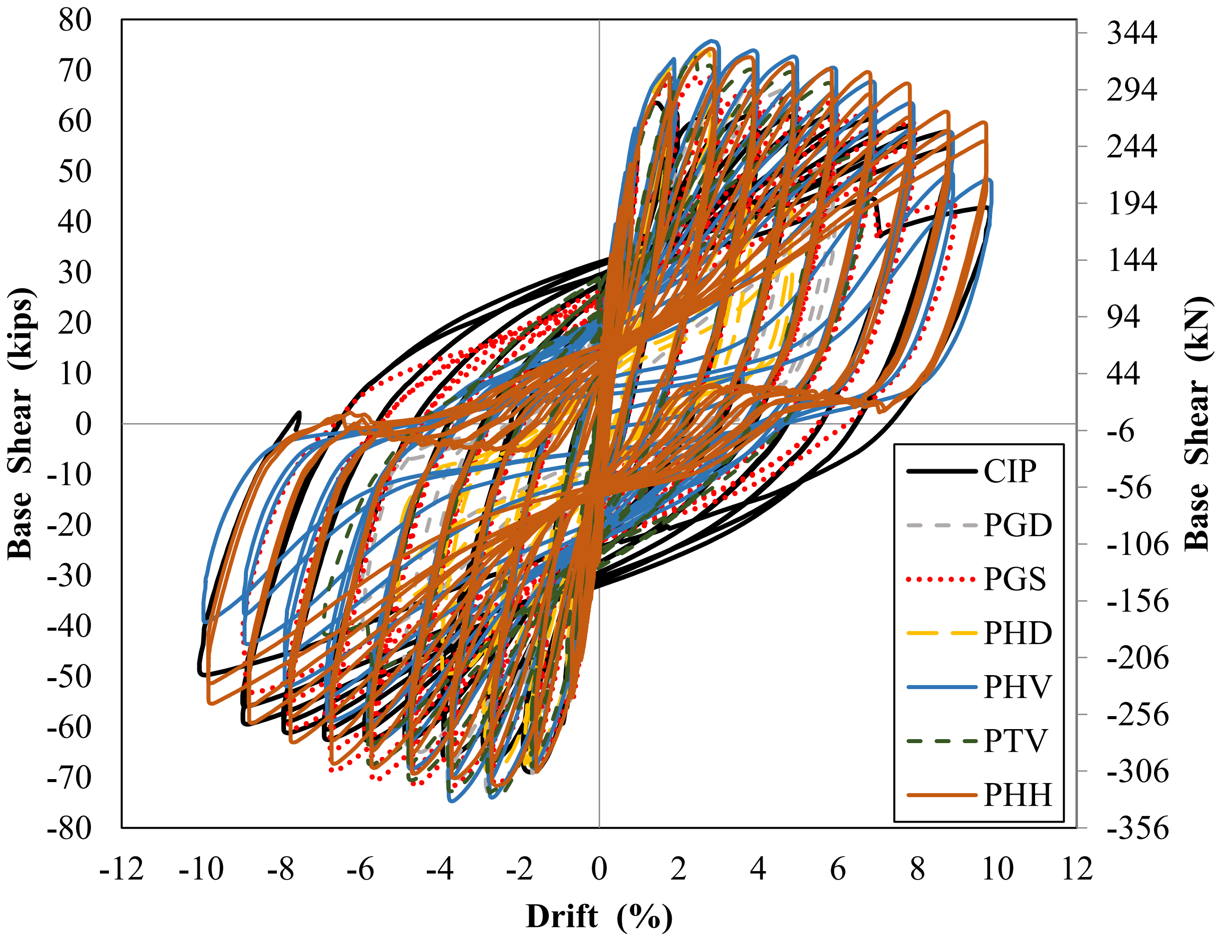

Figure ES.6 Measured CIP, PGD, PGS, PHD, PHV, PTV, and PHH Column Force-Drift Hysteretic Responses

Figure ES.7 shows the measured average push and pull lateral force-drift (pushover) envelopes for CIP and all spliced columns tested in this project. All mechanically spliced columns showed a similar initial stiffness but a higher lateral strength than the CIP column, approximately 6% to 14% higher. The higher strength can be due to the higher stiffness of the couplers shifting the plastic hinge and making the column shear span slightly shorter. Furthermore, the precast column had stronger concrete than CIP. The displacement capacity of PGD, PGS, PHD, PHV, PTV, and PHH was 45%, 14%, 63%, 24%, 33%, and 3.3% less than CIP, respectively. Furthermore, the displacement ductility capacity of PGD, PGS, PHD, PHV, PTV, and PHH was 53%, 27%, 71%, 17%, 37%, and 7% less than CIP, respectively. Both PGD and PHD failed due to the longitudinal bar pullout from the coupler base, thus exhibited the lowest ductility. PGS failed by longitudinal bar rupture, therefore showed the highest displacement ductility capacity. PHV, PTV, and PHH failed by a strength loss (mainly due to the concrete failure) and showed an intermediate ductility. Also included in the figure is the design level drift demand based on the AASHTO spectrum for downtown Los Angeles, CA, which is a high seismic area. It can be seen that all columns met the current seismic design requirements (AASHTO SGS, 2011) since (1) they had a displacement ductility capacity that was higher than the minimum required displacement ductility capacity of 3, (2) they showed a displacement capacity that exceeded the design displacement demand (e.g., for Los Angeles), and (3) their displacement ductility demand was less than 5. Overall, even though some precast columns performed better than others, they are all acceptable and can be used in all seismic regions of the nation.

A tensile test was performed on all coupler products used in the columns, including five samples of No. 8 (25-mm) Dextra Groutec S couplers. Bar pullout from coupler was observed in four specimens and the anchored bar fractured in one specimen but inside the coupler. Overall, this coupler type was rated as a "non-seismic coupler," thus they are not suitable to be used in bridge columns, including PHD. Nevertheless, the failure mode observed in the present project was not consistent with the previous coupler testing reported by the manufacturer. After communicating the issue with the manufacturer, the reason for bar pullout could not be determined for PHD. As the result of this inferior performance at the coupler level, the PHD column also showed the least displacement capacity among all precast columns. The research team recommends that the manufacturer provides a specific grout type for field applications not a commercial off-the-shelf product, which was used in this project. In summary, a better grout product with some quality control measures should be specified/provided by the manufacturer for bridge column applications to achieve a consistent performance of "seismic couplers." Note that PHD also met all the AASHTO requirements discussed above, but an improvement of the coupler performance will improve the column performance for seismic applications.

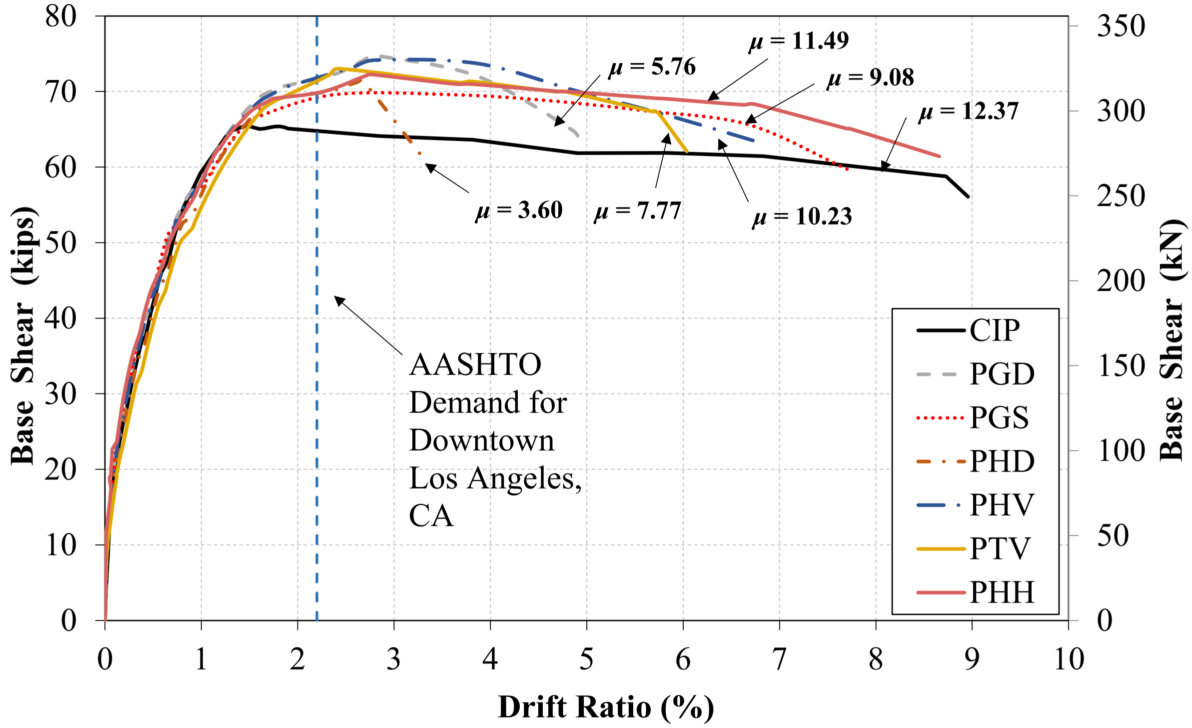

Figure ES.7 Measured CIP, PGD, PGS, PHD, PHV, PTV, and PHH Column Pushover Envelopes

ES.3.3 Strain Profile for all Columns

Figure ES.8 shows the peak tensile strain profiles at various levels for CIP, PGD, PGS, PHD, PHV, PTV, and PHH. Note that strain gauges were not placed on the couplers, thus strain data is not available at some levels of the precast columns. All columns generally had higher strains at their base. The strain profile for CIP was typical in which the strain was the highest at the base and gradually decreased above and below the column-footing interface (solid black lines). However, at larger drift ratios, the mechanically spliced precast columns exhibited higher strains below and above the coupler levels compared with CIP. This is because the coupler region is much stiffer, shifting the nonlinearity outside of the coupler and causing higher strains on the longitudinal bars immediately beyond the coupler ends.

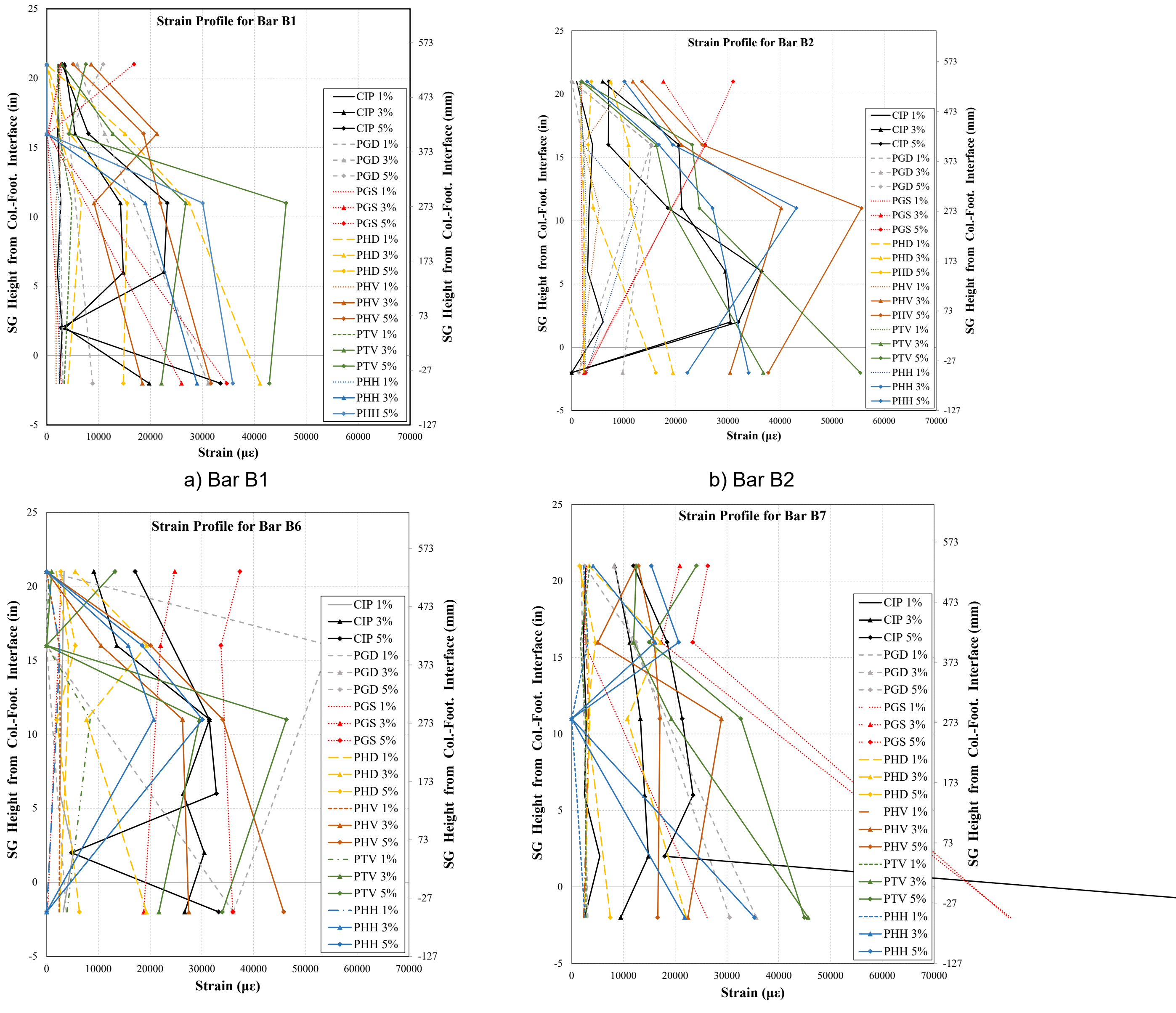

a) Bar B1

b) Bar B2

c) Bar B6

d) Bar B7

Figure ES.8 Measured CIP, PGD, PGS, PHD, PHV, PTV, and PHH Column Strain Profiles

ES.3.4 Energy Dissipation for all Columns

Figure ES.9 shows the cumulative energy dissipation of the CIP and all mechanically spliced columns tested in this project. The precast columns had a lower energy dissipation than CIP. This is because the longitudinal bars within the couplers do not yield or experience minimal yielding, thus some portion of the mechanically spliced column plastic hinge does not contribute to the column overall displacement. As a result, the dissipated energy, or the strain energy, in mechanically spliced columns are generally smaller than CIP. For small couplers, the dissipated energy of the precast column is expected to be close to that of CIP. For example, the energy dissipation of PTV, in which a threaded coupler was used, is close to that of CIP.

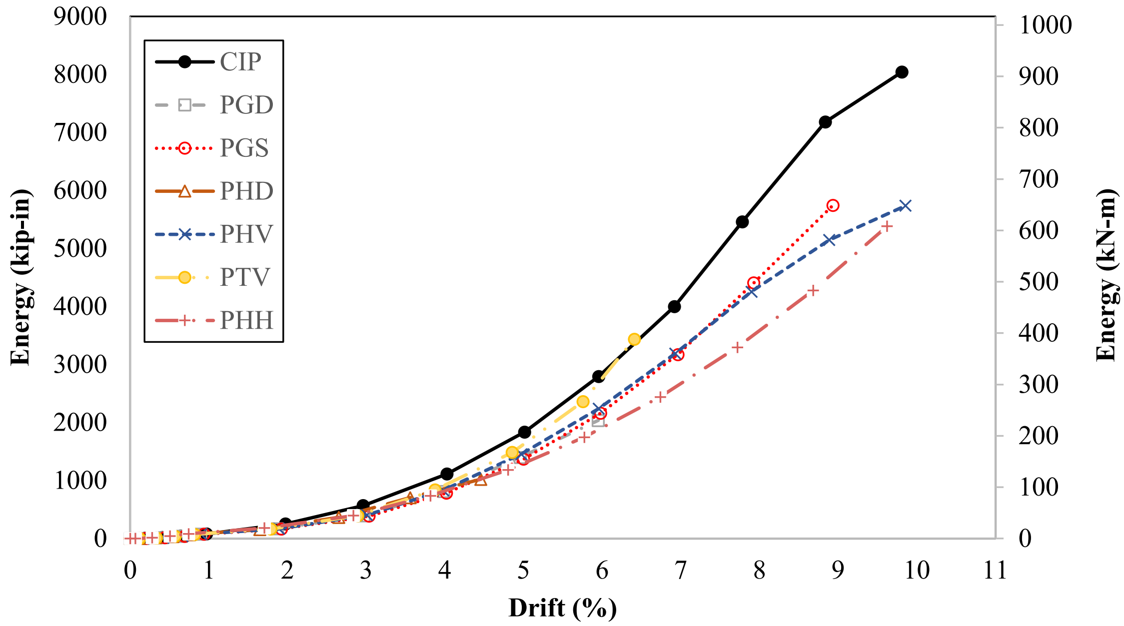

Figure ES.9 Energy Dissipation for CIP, PGD, PGS, PHD, PHV, PTV, and PHH Columns

ES.4 Analytical Investigation of Column Test Specimens

Analytical modeling methods were developed, and pushover analyses were performed for the CIP and mechanically spliced precast bridge columns tested in this project. Figure ES.10 schematically shows the analytical model for the coupler columns. A 3D fiber-section finite element model with six degrees of freedom was used to simulate the precast column behavior in OpenSees (2016). However, three elements were needed to successfully include the sectional changes. Element 1 was a “zeroLength” element to monitor the stress-strain behavior of unspliced reinforcing steel bars (the same as that obtained from the tensile testing) and concrete fibers. In this element, the bond-slip effects can also be included by modifying the longitudinal steel reinforcement properties. Elements 2 and 3 were “forceBeamColumn” elements, each with five integration points. Element 2 was used to include the coupler effects by modifying the steel bar properties based on the coupler model (Fig. ES.1). The coupler rigid length factor was based on the measured properties. The stress-strain data was monitored for the extreme concrete and steel fibers at the column base (Element 1). Furthermore, the column tip displacements and lateral forces were recorded. The column analytical failure point was the displacement at which one of the following limit states first occurred: (1) the extreme steel fiber reached its ultimate tensile strain, (2) the extreme concrete core fiber reached the ultimate compressive strain, and (3) the column lateral load carrying capacity reduced by 15% compared with the peak lateral strength.

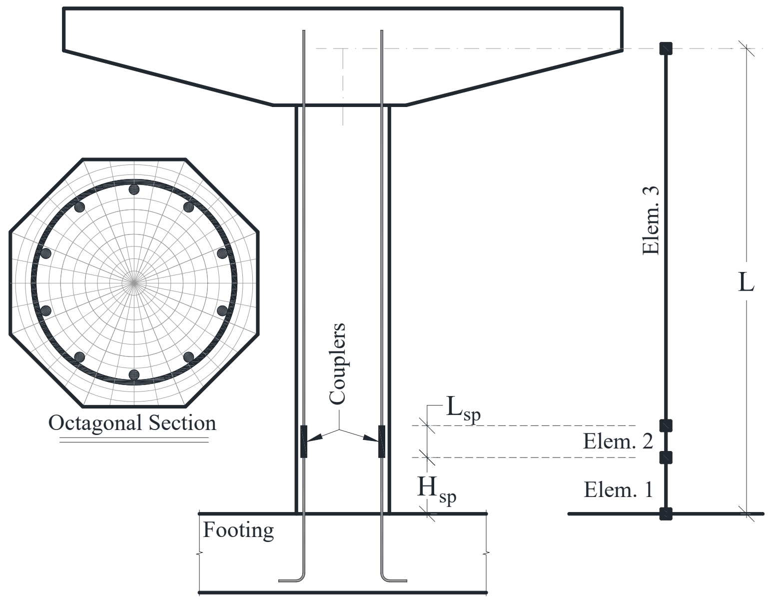

Figure ES.10 Analytical Modeling Method for Mechanically Spliced Columns

Table ES.3 Summary of Analytical Study on Column Test Specimens

SP ID	Coupler Type	Manufacturer, Model	Coupler Length, L_{sp}, in. (mm)	Coupler Rigid Length Factor, β	Measured Drift Ratio	Calculated Drift Ratio	Error (%)
CIP	N/A	N/A	N/A	N/A	8.96%	7.64%	-14.7
PGD	Grouted	Dayton Superior Corp., Sleeve Lock	16.5 (419)	0.70	4.93%	6.24%	+26.6
PGS	Grouted	Splice Sleeve North America, Inc., NMB	14.57 (370)	0.70	7.71%	6.03%	-21.8
PHD	Hybrid (Grouted-Threaded)	Dextra America, Inc., Groutec S with Bartec	9.45 (240)	0.79	3.33%	2.71%	-18.6
PHV	Hybrid (Grouted-Threaded)	nVent LENTON Corp., Interlock	8.63 (219)	0..82	6.84%	5.59%	-18.3
PTV	Threaded	nVent LENTON Corp., Ultimate PT15 Position	4.87 (124)	0.40	6.04%	6.77%	+12
PHH	Hybrid (Grouted-Headed)	Headed Reinforcement Corp., HRC560	7 (177.8)	0.80	8.66%	6.0%	-30.7

Table ES.3 presents a summary of the analytical study performed on the seven column test specimens. The error between the calculated and measured drifts is also presented in which the positive error means that the calculated displacement is higher than the measured displacement. The proposed analytical modeling method tends to underestimate the failure displacement of the CIP and the mechanically spliced precast columns, which is safe for design purposes. On average, the proposed model resulted in 8.5% lower displacement capacities for the six mechanically spliced bridge columns.

ES.5 Analytical Investigation of Mechanically Spliced Bridge Columns

A parametric study was performed to determine the effect of mechanical bar splices on the seismic performance of precast columns, especially displacement capacities and demands. Twenty-two CIP columns with circular cross sections and 23 CIP columns with square cross sections were designed as the reference models. Subsequently, eight coupler types were used at the base of the CIP columns to make them precast. A total of 405 pushover analyses were performed on unspliced and spliced columns, and the results are summarized in Figure ES. 11. Tazarv and Saiidi (2016) proposed an equation (Eq. ES.2) to predict the ductility loss for mechanically spliced columns. This equation was also included in the graphs using two marginal β factors of 0.65 and 1.0. The lower bound Beta was the lowest measured in all No. 10 (32-mm) bar couplers tested by Dahal and Tazarv (2020), and the upper bound value indicates that the full length of a coupler is rigid, thus the coupler does not contribute to the splice strains. A linear trendline was also included for each target ductility.

$$\frac{\mu_{sp}}{\mu_{CIP}} = (1 - 0.18\beta)\left(\frac{H_{sp}}{L_{sp}}\right)^{0.1\beta} \qquad \text{(Eq. ES.2)}$$

Some general trends were observed in this parametric pushover study. Couplers seem to affect the spliced column behavior in the same manner regardless of the section geometry. Columns with high axial load indices and high aspect ratios seem to be less affected by the couplers since those columns tend to fail by geometric nonlinearities rather than the coupler effects. As the coupler rigid length factor or the coupler length increases, the column displacement ductility generally decreases. Regardless of the column cross section, couplers could reduce the column displacement ductility capacity up to 45%. Most of the datapoints were above the design lines (based on Eq. ES.2), indicating that this design equation is conservative. Furthermore, the data shows that columns utilizing short couplers can exhibit a displacement capacity that is close to that of unspliced columns. For example, the AR6-ALI5-D5 square column spliced with the HR couplers showed less than 1% smaller displacement ductility capacity when compared with its corresponding CIP column.

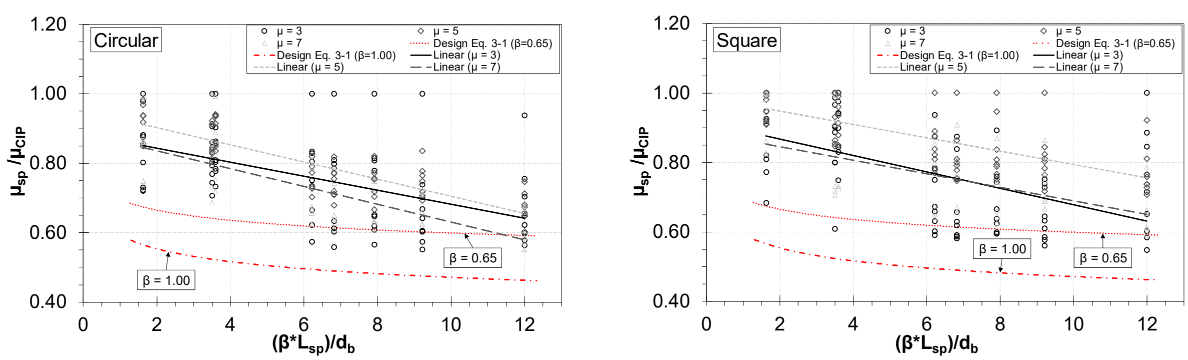

a) Circular Columns

b) Square Columns

Figure ES.11 Summary Parametric Pushover Study on Mechanically Spliced Bridge Columns

A nonlinear parametric dynamic study was performed to determine the effect of couplers on the seismic demands of bridge columns with square and circular cross sections. Six CIP columns with circular cross sections and six CIP columns with square cross sections, all with a displacement ductility capacity of seven, were included in the analysis. Subsequently, eight coupler types were used at the base of the CIP columns to make them precast. A total of 540 seismic demand analyses were performed on unspliced and spliced columns and the results were synthesized in Figure ES.12. In general, couplers did not have significant effects on the drift demands of bridge columns. Long and rigid couplers tend to make the columns slightly stiffer, thus reducing the displacement demands on columns. The dynamic behavior of columns with low aspect ratios appeared to be affected slightly more by couplers than the columns with higher aspect ratios. This is likely because the force-drift behavior of slender columns is largely controlled by the P-Δ effects and not couplers. Overall, couplers may change the seismic displacement demands of RC columns by up to 7%.

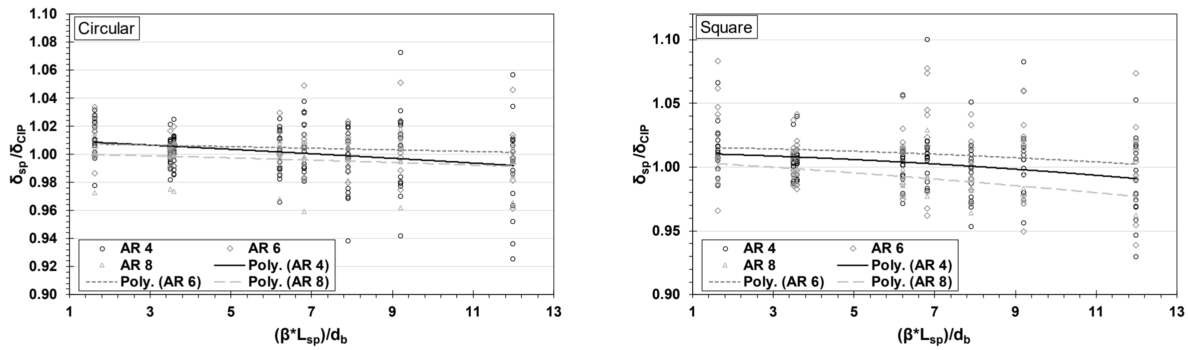

a) Circular Columns b) Square Columns

Figure ES.12 Summary Parametric Dynamic Study on Mechanically Spliced Bridge Columns

ES.6 Evaluation of Current Design Methods for Mechanically Spliced Bridge Columns

NCHRP 935 (Saiidi et al., 2020) recommends three methods to quantify the effects of bar couplers on the performance of bridge columns (Table ES.4). The methods are labeled as Method 1, Method 2, and Method 3. Method 1 is based on a simple reduction factor for the displacement ductility capacity using the coupler properties. In this method, the displacement ductility capacity of CIP is first calculated (using a moment-curvature or pushover analysis) then it is modified based on the coupler properties. Method 2 can be performed using a moment-curvature or pushover analysis, but the plastic hinge length should be modified based on the coupler properties. Method 3 is a pushover analysis using the coupler stress-strain relationship.

NCHRP 935 evaluated the accuracy of these three methods using data for four mechanically spliced bridge columns. Data for three columns were collected from the literature (GCNP and HCNP from Haber et al., 2014; and GGSS-1 from Pantelides et al., 2014) and the fourth column, GC10, was tested in the NCHRP project. Furthermore, six mechanically spliced bridge columns, PGS, PGD, PHD, PHV, PTV, and PHH, were tested in the present study. In total, a database of 10 large-scale mechanically spliced bridge columns was compiled and used to evaluate the abovementioned three design methods for coupler columns.

Table ES.5 presents the measured and calculated responses using the three methods for 10 mechanically spliced bridge columns. In the table, the error between the calculated and the measured responses is also presented in parentheses. Figure ES.13 is a graphical representation of the data in the table. A red dashed line at 1.0 was included in the figure, indicating that responses above this line are unconservative and responses below the line are conservative. All three design methods of mechanically spliced bridge columns were included. Method 3 (the pushover analysis with coupler stress-strain within the coupler region) generally resulted in the most accurate response. Nevertheless, other two methods, which are simpler and less involved, resulted in a conservative design. The large errors seen in PHD were because this column had couplers that were not seismic graded in the present study. Overall, all three methods were found viable for the analysis/design of mechanically spliced bridge columns.

Table ES.4 Three Design Methods for Mechanically Spliced Bridge Columns (NCHRP 935)

Design Method	**Analysis Type**	**Column Element in Pushover Analysis**	**Analysis Requirements**
Cast-in-place (CIP) columns	Moment-Curvature or Pushover	Usually conducted using a lumped plasticity model, which requires an analytical plastic hinge length. However, distributed plasticity model can also be utilized	AASHTO Guide Specifications for LRFD Seismic Bridge Design
Method 1. Spliced columns using a displacement ductility equation	Use CIP analysis results	Use CIP analysis results	$\frac{\mu_{sp}}{\mu_{CIP}} = (1 - 0.18\beta)(\frac{H_{sp}}{L_{sp}})^{0.1\beta}$
Method 2. Spliced columns using modified plastic hinge length equation	Moment-Curvature or Pushover	Lumped plasticity model only	Similar to CIP but with $L_p^{sp} = L_p - (1 - \frac{H_{sp}}{L_p})\beta L_{sp} \leq L_p$
Method 3. Spliced columns using proposed stress-strain model for couplers	Pushover only	Distributed plasticity model only	Coupler stress-strain model (Fig. 4.2)

Note: μ_{sp}: The mechanically spliced bent displacement ductility capacity; μ_{CIP}: The corresponding non-spliced cast-in-place bent displacement ductility capacity; β: The coupler rigid length ratio; H_{sp}: The distance from the column end to the nearest face of the coupler embedded either inside the column or inside the column adjoining member (*in.*); L_{sp}: The coupler length (*in.*); L_p^{sp}: The modified plastic hinge length for mechanically spliced bridge columns; L_p: The conventional column analytical plastic hinge length according to the current AASHTO SGS.

Table ES.5 Evaluation of Current Design Methods for Mechanically Spliced Bridge Columns

Reference	Column ID	Measured Ductility Capacity	Measured Drift Capacity (%)	Method 1 Calculated Ductility Capacity (error)	Method 2* Calculated Ductility Capacity (error)	Method 3 Calculated Drift Capacity (error)
Haber et al. (2014)	GCNP	4.52	5.95	4.56 (+0.9%)	4.49 (-0.7%)	N/A
Haber et al. (2014)	HCNP	6.49	9.85	6.33 (-2.5%)	7.0 (+7.9%)	N/A
Pantelides et al. (2014)	GGSS-1	5.4	8.38	5.52 (+2.2%)	5.46 (+1.5%)	N/A
NCHRP 935	GC10	5.07	7.78	5.00 (-1.3%)	5.17 (+2.0%)	N/A
Present Study	PGD	5.76	4.93	7.55 (+31.1%)	5.95 (+3.3%)	6.24 (+26.6%)
Present Study	PGS	9.08	7.71	7.67 (-15.5%)	6.63 (-27.0%)	6.03 (-21.8%)
Present Study	PHD	3.6	3.33	6.43 (+78.6%)	6.96 (+93.3%)	2.71 (-18.6%)
Present Study	PHV	10.23	6.84	7.30 (-28.6%)	8.17 (-20.1%)	5.59 (-18.3%)
Present Study	PTV	7.77	6.04	9.65 (+24.2%)	9.81 (+26.3%)	6.77 (+12.1%)
Present Study	PHH	11.49	8.66	7.42 (-35.4%)	8.59 (-25.2%)	6.0 (-30.7%)

* Note that moment-curvature was used in Method 2. An alternative in this method is to perform a pushover analysis using a lumped plasticity element with modified plastic hinge length including coupler effects.

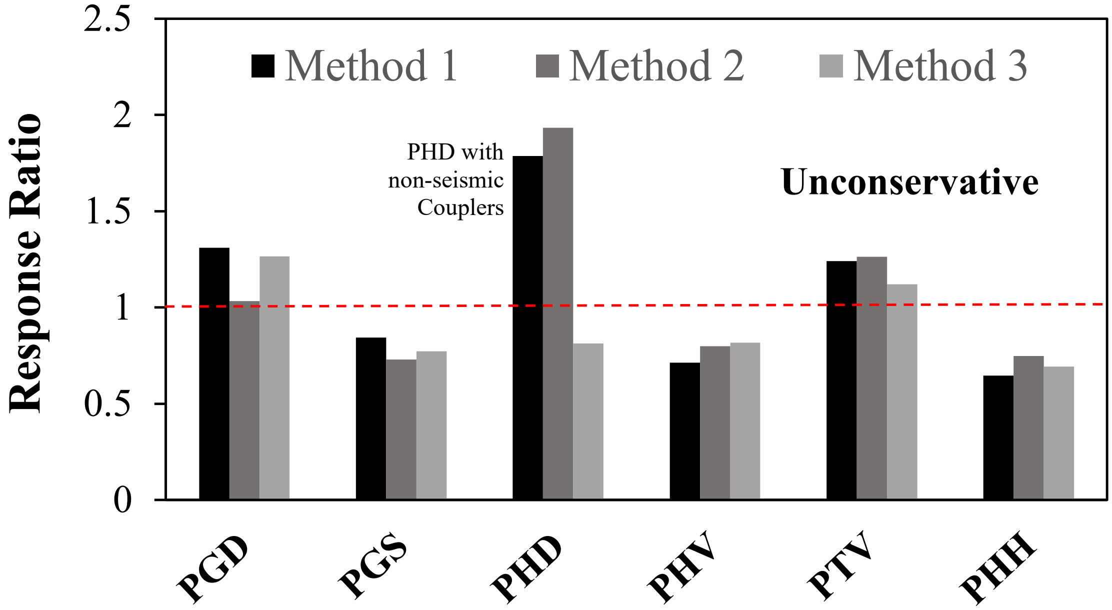

Figure ES.13 Evaluation of Three Design Methods for Mechanically Spliced Bridge Columns

ES.7 Conclusions

Based on the experimental and analytical investigations, the following conclusions were drawn from this study:

- In CIP, flexural and shear cracks developed and extended at low drifts. Spalling began at 2% drift ratio. Major spalling occurred at larger drift ratios leading to longitudinal bar buckling then bar fracture. The CIP mode of failure was the longitudinal bar fracture. The CIP lateral load capacity was 65.4 kips (291 kN), and the CIP drift capacity was 8.96%.

- In PGD, flexural and shear cracks developed and extended at low drifts. Spalling began at 3% drift ratio. PGD failed due to the longitudinal bar pullout from the coupler base; whereas, CIP failed due to the longitudinal bar fracture. The PGD peak lateral force was 74.7 kips (332 kN), and its drift capacity was 4.93%. The lateral load capacity of PGD was 14% higher than that of CIP, and the drift capacity of PGD was 45% less than that of CIP.

- PGS exhibited flexural and shear cracks at low drifts, then concrete spalled at 3% drift ratio. The spalling continued until the end of the test exposing the bars and couplers. Similar to CIP, the failure mode for PGS was the longitudinal bar rupture. The PGS lateral force capacity was 69.6 kips (310 kN), and its drift capacity was 7.71%. The lateral force capacity of PGS was 6.4% higher than that of CIP. The displacement capacity of PGS was 14% lower than that of CIP.

- PHD exhibited flexural and shear cracks throughout the test with some minor spalling occurring during the 3% drift ratio cycles. The mode of failure for PHD was the longitudinal bar pullout from the coupler base. The PHD lateral force capacity was 71.5 kips (318 kN), and its drift capacity was 3.33%. The lateral force capacity of PHD was 9% higher than that of CIP. The drift capacity of PHD was 63% less than CIP. It is recommended that the manufacturer imposes higher quality control measures to obtain consistent performance of bar fracture for this coupler type.

- In PHV, flexural and shear cracks developed and extended at low drifts. Spalling began at 3% drift ratio. PHV failed by a gradual loss of strength after the peak lateral force. The measured peak lateral strength was 74.2 kips (330 kN), which was 12.6% higher compared with CIP. The drift capacity of PHV was 6.84%, which was 26.8% lower than CIP.

- PTV experienced flexural cracking around the edges of the closure pour starting at low drifts. Spalling was observed at 1% at the top of the closure pour. PTV failed by the bar fracture, similar to CIP. The peak lateral strength of PTV was 73.0 kips (324.7 kN), an increase of 11.6% compared with CIP. PTV had a drift capacity of 6.04%, which was 32.6% lower than CIP.

- PHH experienced significant flexural and shear cracking. Spalling began at a drift ratio of 4.0% at the column base and continued throughout the test. PHH failed by a gradual loss of strength. PHH reached a peak lateral force of 72.3 kips (321kN), which was 10% higher than the CIP peak lateral force. The measured drift capacity of PHH was 8.66%, which was close to that of CIP with only 3.4% difference.

- RPH exhibited minor flexural cracks throughout the test. Significant spalling at the column base and on the south face above the neck section was initiated at 2.0% and 3.0% drift ratios, respectively. The test was stopped at 5.0% drift ratio to replace the exposed bars (BRR fuses). Limited damage was observed in the second set of testing. However, BRR exhibited a Z-shape buckling starting at 2.0% drift ratio, and this buckling worsened throughout the test. RPH-R (the repaired column) began to fail by strength degradation, but the test was halted after completing the 10% drift cycles since the displacement capacity of the CIP column, the reference column, was reached. RPH showed a peak lateral force of 69.2 kips (308 kN) when the test was stopped at 5.0% drift while RPH-R reached a lateral force of 74.7 kips (332 kN) at a drift ratio of 8.31%. The measured drift capacity of RPH-R was 9.8%, exceeding the 8.9% drift capacity of CIP. Repair and replacement of the BRR was proven to be a viable option with comparable results between the repaired and initial column. However, the initial stiffness of the two sets were not the same and must be improved in future testing. Furthermore, the Z-shape buckling of the longitudinal bars at high displacements was another point of concern, which can be eliminated with the use of tension-only members such as steel tendons.

- The pushover analysis for CIP correctly predicted the mode of failure by longitudinal bar rupture. The calculated peak lateral strength was 61.9 kips (275 kN) while the measured lateral strength was 65.4 kips (291 kN), or a 5.5% difference. The calculated failure drift for CIP was 7.64% while the CIP measured failure drift was 8.96%, or a 15.9% difference.

- The proposed pushover modeling method for the mechanically spliced bridge columns were found reasonably accurate for all spliced columns with seismic couplers. A method was devised to analyze columns with non-seismic couplers, which also successfully reproduced the column (PHD) behavior.

- Three design methods for bridge columns incorporating bar couplers were evaluated using experimental data for 10 precast columns. Method 1, a simple equation to reduce the displacement ductility capacity, resulted in an average error of -2.9 for the columns with seismic couplers. Therefore, this method was overall conservative.

- Method 2, which was based on the modified plastic hinge length, resulted in an average error of -3.5% for the columns incorporating seismic couplers. Therefore, this method was overall conservative.

- Method 3, which was based on the pushover analysis using the coupler stress-strain relationship within the spliced region, resulted in an average error of -6.4% for the columns utilizing seismic couplers. Therefore, this method was overall conservative. This method was the only technique that could reproduce the behavior of the column with non-seismic couplers, PHD, with reasonable accuracy.

Overall, all mechanically spliced precast bridge columns met the current code seismic requirements, thus they are recommended for use in all 50 states. Furthermore, the three design methods evaluated herein for mechanically spliced bridge columns were found viable. Some errors were observed, but the general trend was that the three methods usually resulted in a conservative design for mechanically spliced bridge columns.

1. INTRODUCTION

1.1 Introduction

Bars must be spliced in reinforced concrete (RC) structures for a successful load transfer between joints and elements. Lap splicing, the conventional method to provide continuity in RC members, is achieved through bond mechanism between concrete and the overlapping bars with sufficient length. The lap splicing is generally an adequate method for connecting bars; however, it can lead to constructability issues in heavily reinforced and/or precast members.

An alternative to lap splicing is the use of mechanical bar splices, which are also referred to as bar couplers. A bar coupler connects ends of two reinforcing bars through various mechanisms such as grouting, threading, pressing, and/or other techniques. Bar couplers may reduce the reinforcement congestion and lower the material cost since less reinforcement is used. Further, for precast members, couplers may reduce the construction time due to member prefabrication and improve the quality of the product.

Bar couplers are currently used in accelerated bridge construction (ABC) for capacity protected members but are prohibited in bridge columns located in high seismic regions. This is mainly because (1) the coupler performance has not been fully established, and (2) the effects of the couplers on the column seismic behavior have not been completely understood. Recent studies have tried to fill these knowledge gaps, but the literature lacks a unified experiment data to determine how varying the coupler types/products and column properties, such as geometry, aspect ratio, and axial loads, affect the capacity and demand of spliced bridge columns.

1.2 Objective and Scope

The main objectives of the present study were to: (1) establish a comprehensive performance database for mechanically spliced precast bridge columns through large-scale testing, and (2) verify or update current state-of-the-art design methods for mechanically spliced precast bridge columns. To achieve these goals, several tasks were completed. First, the literature was reviewed to synthetize the latest studies on the coupler performance and the spliced column behavior. Second, the coupler products that were suitable for bridge column applications were identified and the manufacturers were contacted for collaboration. Subsequently, eight half-scale bridge columns were designed, constructed, and tested using the same lateral loading regime simulating earthquakes. One column followed the conventional cast-in-place detailing to serve as the benchmark model and seven utilized a type of coupler product per specimen at the column base. All columns had the same geometry, reinforcement, confinement, aspect ratio, and axial load with only one target variable of the coupler connection. The test data was processed, and a new experimental coupler column performance database was formed. The current design methods for mechanically spliced bridge columns were evaluated using the new database. Finally, a comprehensive parametric study, including pushover and dynamic analyses, was performed to better understand the capacity and demand of mechanically spliced bridge columns for a wide range of practical parameters.

1.3 Document Outline

Chapter 1 presents an introduction to this study, the scope of work, and the document outline. Chapter 2 presents a literature review on coupler material models and performance, and columns with coupler connections. Chapter 3 discusses the experimental investigation conducted on the mechanically spliced bridge columns. Chapter 4 presents the post-test analytical investigation. Chapter 5 includes a summary result of the parametric study performed on mechanically spliced bridge columns. The evaluation of the current design methods for mechanically spliced bridge columns was presented in Chapter 6. Finally, Chapter 7 presents a summary of the study and the key findings from the experimental and analytical investigations.

2. LITERATURE REVIEW

2.1 Introduction

Reinforcing bars in concrete structures are conventionally spliced together using lap splices. This can lead to congestion issues in highly reinforced sections. Alternatively, reinforcing bars can be spliced together by means of a mechanical bar splice, also referred to as a bar coupler. Couplers can be used in non-seismic regions in cast-in-place and/or precast building members or capacity-protected bridge elements to reduce congestion and to improve quality control. Nevertheless, U.S. codes currently do not allow couplers to be used in the plastic hinge region of bridge columns in high seismic regions, which prevents couplers as an accelerated bridge construction (ABC) technique. This section reviews past studies on coupler behavior and coupler effects on bridge column performance.

2.2 Mechanical Bar Splices

More than 60 mechanical bar splices are commercially available with several configurations and models produced by different manufacturers. Couplers may be classified based on the mechanism utilized to transfer load between two bars as: shear screw (SS), headed (HC), swaged (SW), threaded (TH), grouted (GC), or a combination of these mechanisms named hybrid (HY) (Tazarv and Saiidi, 2016; Dahal and Tazarv, 2020).

2.2.1 Shear Screw Couplers

Shear screw couplers connect two bars together using screws along the length of the coupler as shown in Figure 2.1. The screws penetrate the bar and transfer the bar forces through friction between the screws, the steel sleeve, and the two bars. Shear screw couplers are typically long since several screws are needed to develop full strength to splice the bars.

Figure 2.1 Sample of Shear Screw Couplers (Image Courtesy: www.bar.us.com)

2.2.2 Headed Couplers

Headed couplers are made of two components that thread together as shown in Fig. 2.2. Headed couplers require the bar ends to be modified by creating an enlarged headed end. The headed end then transfers tension through the bar head bearing on the coupler, and the compression through the headed ends bearing on each other. Headed couplers are typically one of the shortest couplers available in the market.

Figure 2.2 Sample of a Headed Couplers (Dahal et al., 2019)

2.2.3 Swaged Couplers

Swaged couplers splice two bars together through friction from a sleeve that is pressed on to the bars (Fig. 2.3). Each end of the bars is inserted into the sleeve and a special tool is used to clamp the sleeve on to the bars. Swaged couplers are typically long to develop the bars.

Figure 2.3 Example of a Swaged Coupler (Dahal et al., 2019)

2.2.4 Threaded Couplers

A threaded coupler is an enlarged sleeve with internal threads in which reinforcing bars with matching threads are connected. Threads on bars can either be created by forging a threaded component onto the bar or by cutting threads into the bar. Threads may also be either parallel or tapered as shown in Figure 2.4. Threaded couplers tend to be one of the shortest type of couplers.

a) Parallel Threaded Coupler (Dahal et al., 2019)

b) Tapered Threaded Coupler (www.aleno.com)

Figure 2.4 Examples of Threaded Couplers

2.2.5 Grouted Couplers

Figure 2.5 shows a grouted coupler in which bars are connected through a bond between the sleeve and a high-strength grout that is pumped into the sleeve after bar placement. Grouted couplers are typically the longest coupler types. They provide easy installation and allow large construction tolerances compared with other coupler types.

Figure 2.5 Example of a Grouted Coupler (Dahal et al., 2019)

2.2.6 Hybrid Couplers

Hybrid couplers are mechanical bar splices that use a combination of two or more of the previously mentioned connecting mechanisms. Figure 2.6 shows a hybrid coupler that uses a threaded connection at one end and the grouted connection at the other end. Use of hybrid couplers can be advantageous by combining the benefits of various coupler types.

Figure 2.6 Example of a Threaded-Grouted Hybrid Coupler (Dahal et al., 2019)

2.3 Material Models for Couplers

Couplers vary in their shapes, sizes, lengths, thicknesses, and anchoring mechanisms, making them difficult to model and estimate their engineering behavior. A few studies have proposed models to simulate the coupler material behavior (Haber et al., 2015; Tazarv and Saiidi, 2016; Ameli et al., 2016). The coupler stress-strain material model developed by Tazarv and Saiidi (2016) was adopted in this study. A brief overview of this model is presented in the following section.

2.3.1 Material Model by Tazarv and Saiidi (2016)

Figure 2.7 shows key parameters of a mechanical bar splice per Tazarv and Saiidi (2016). When a spliced bar is in tension, only a portion of the coupler is considered to contribute to the overall elongation while the remaining portion is assumed to be rigid. The rigid portion of the coupler (βL_{sp}) is due to the coupler anchoring mechanism. The coupler rigid length factor (β) estimates what length of the coupler does not contribute to the splice total elongation. The rigid length factor can be different for different couplers and should be determined through experiment. The length of the coupler region (L_{cr}) is the physical length of the coupler (L_{sp}) plus a distance (α times the bar diameters, αd_b) from each end of the coupler. Subjected to the same tensile force, the unspliced reference bar will elongate more than a spliced bar due to the coupler rigidity. Therefore, the strain of the unspliced bar (ε_s) will be greater than the strain of the corresponding spliced bar (ε_{sp}). Equation 2.1 or 2.2 can be used to relate the coupler strains to the reference bar strains.

$$\frac{\varepsilon_{sp}}{\varepsilon_s} = \frac{L_{cr} - \beta L_{sp}}{L_{cr}} \qquad \text{(Eq. 2.1)}$$

$$\frac{\varepsilon_{sp}}{\varepsilon_s} = \frac{(1-\beta)L_{sp} + 2\alpha d_b}{L_{sp} + 2\alpha d_b} \qquad \text{(Eq. 2.2)}$$

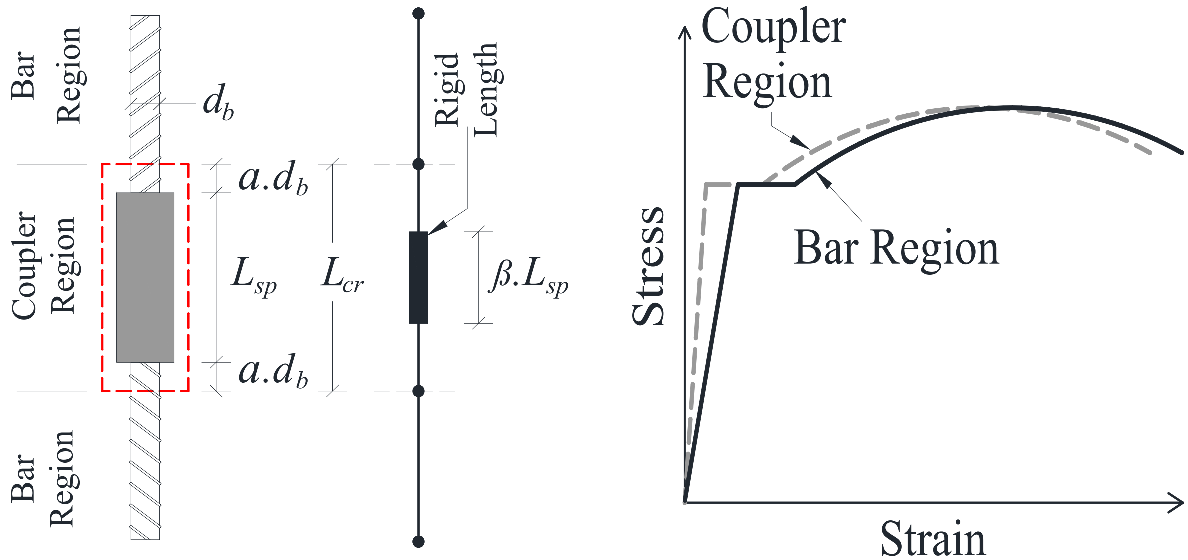

a) Regions of a Mechanical Bar Splice b) Stress-Strain Model

Figure 2.7 Stress-Strain Model for Mechanical Bar Splices by Tazarv and Saiidi (2016)

The model assumes that a tensile failure would happen outside of the coupler region (such splices were named “seismic couplers”); therefore, seismic couplers are stronger than the anchoring bars, thus the stress on couplers follows the bar stress. Nevertheless, the strain properties of a reference bar can be modified to obtain the strain properties of the coupler.

The coupler rigid length factor (β) is used to determine the stress-strain relationship of a mechanical bar splice. A spliced connection with a rigid length factor of zero would be emulative of a reference unspliced bar. As the rigid length factor increases, the strain of the spliced connection decreases.

2.3.1.1 Study by Dahal and Tazarv (2020)

Two main factors behind banning the couplers for seismic bridge applications might be the knowledge gaps on the coupler behavior and how each coupler type affects the seismic performance of mechanically spliced columns. Dahal and Tazarv (2020) aimed to establish the behavior of mechanical bar splices through an extensive experimental work. The study developed the first database for coupler performance and quantified the coupler properties in accordance with the modeling method proposed by Tazarv and Saiidi (2016). The study tested more than 160 mechanical bar splices, including No. 5 (Ø16-mm), No. 8 (Ø25-mm), and No. 10 (Ø32-mm) bars. The splices were tested to failure using both uniaxial monotonic and cyclic tensile loading. Table 2.1 presents the recommended coupler rigid length factors for different coupler types and sizes (Figure 2.8) based on a statistical analysis of the coupler test data. Note that the manufacturer Erico was purchased by nVent and will be named as nVent in the present study. Coupler connections may fail by bar pullout from the coupler, coupler failure, bar fracture within the coupler region, or bar fracture outside the coupler region. A coupler is only considered a “seismic coupler” if it consistently fails by the bar fracture outside the coupler region.

Table 2.1 Coupler Rigid Length Factors (β) Recommended by Dahal and Tazarv (2020)

Coupler Type	No. 5 (16 mm)	No. 8 (25 mm)	No. 10 (32 mm)
Headed Reinforcement	0.80	0.75	0.55
Threaded (Dextra-Type A)	1.70	1.5	1.60
Threaded (Dextra-Type B)	1.60	1.5	1.65
Threaded (Erico or nVent)	0.95	1.10	1.05
Swaged	0.90	0.90	0.95
Grouted Sleeve (NMB)	0.95	0.65	0.85
Grouted Sleeve (Dayton)	0.70	0.70	0.65
Hybrid (Dextra)	0.80	0.90	0.85
Hybrid (Erico or nVent)	0.80	0.80	0.80

Figure 2.8 Different Mechanical Bar Splice Products Tested by Dahal et al. (2019)

A parametric study was also performed in Dahal et al. (2019) to investigate the seismic performance of bridge columns incorporating different couplers using the recommended rigid length factors (Table 2.1). More than 240 pushover analyses were performed on columns with varying aspect ratios, axial loads, and ductilities. Couplers were modeled using the Tazarv's model. It was found that the coupler size, type, and length significantly affect the ductility of a bridge column. It was generally observed that columns with longer and/or higher rigid length factors showed lower displacement capacities.

2.4 Mechanically Spliced Bridge Columns

Tazarv and Saiidi (2016) and later Saiidi et al. (2020) conducted a state-of-the-art review on mechanical bar splices and mechanically spliced bridge columns. The present literature review is to discuss the key past studies and to complement the aforementioned works with new studies.

2.4.1 Study by Haber et al. (2013)

Haber et al. (2013) developed new connections using headed (HC) and grouted (GC) couplers for accelerated bridge construction in the regions of high seismicity. Figure 2.9 shows the two precast connections. The study tested five half-scale bridge columns. Two of the columns were connected to their footing with no intermediate sections labeled as “No Pedestal” (NP) and the other two columns were linked to their footing via a precast pedestal (PP). Grouted couplers were used in two models and headed couplers were used in other two precast columns. The fifth column was a conventional cast-in-place model (CIP) that served as the reference.

a) Headed Couplers with No Pedestal (HCNP) b) Grouted Couplers with No Pedestal (GCNP)

Figure 2.9 Details of Mechanically Spliced Precast Columns Tested by Haber et al. (2014)

Figure 2.10 shows the force-displacement response of the four precast columns superimposed on the reference CIP column response. The columns that used the headed couplers exhibited similar performance to the CIP column. However, the columns spliced with grouted couplers only achieved a drift capacity of 6% while the CIP column was able to reach a drift capacity of 10%. The drift is the ratio of the column lateral displacement to the column height. The study concluded that precast bridge column connections incorporating mechanical bar splices are feasible and are suitable for ABC in high seismic regions of the nation.

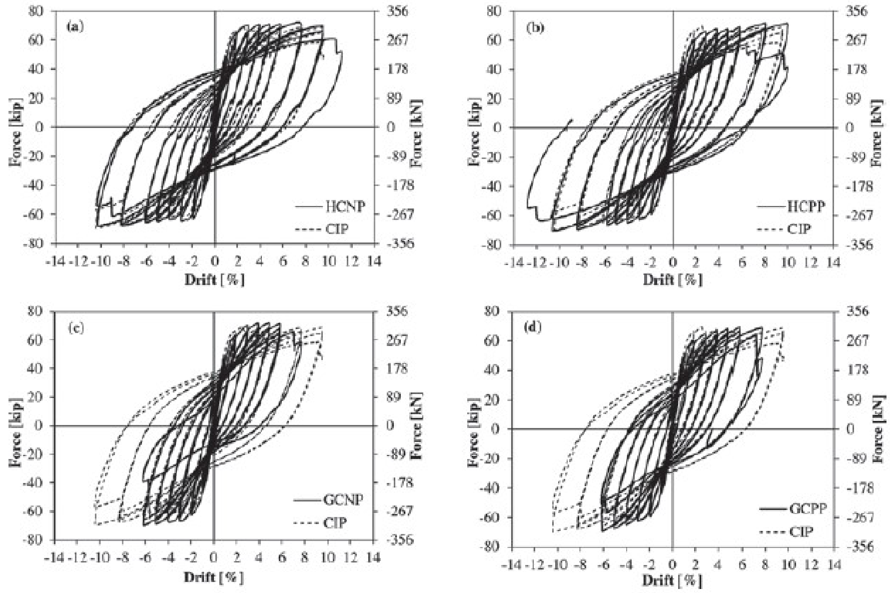

Figure 2.10 Force-Displacement Response of Mechanically Spliced Columns Tested by Haber et al. (2013)

2.4.2 Study by Tazarv and Saiidi (2014)

Following the study by Haber et al. (2013), Tazarv and Saiidi (2014) conducted a study in which three additional half-scale precast bridge columns were tested (PNC, GCDP, and HCS). PNC used a connection in which reinforcing bar dowels extended from the column base into corrugate galvanized steel ducts that were embedded in the footing. The ducts were filled with ultra-high-performance concrete (UHPC). GCDP used grouted couplers and the bars were debonded near the coupler to reduce strain concentrations. GCDP also utilized a pedestal at the column-footing connection to shift the coupler higher in the plastic hinge region. Similar to PNC, HCS also used steel ducts in the footing. However, HCS used materials, such as shape memory alloy (SMA), engineered cementitious composite (ECC), and headed bar couplers, at the base of column. Figure 2.11 shows detailing of the precast columns.

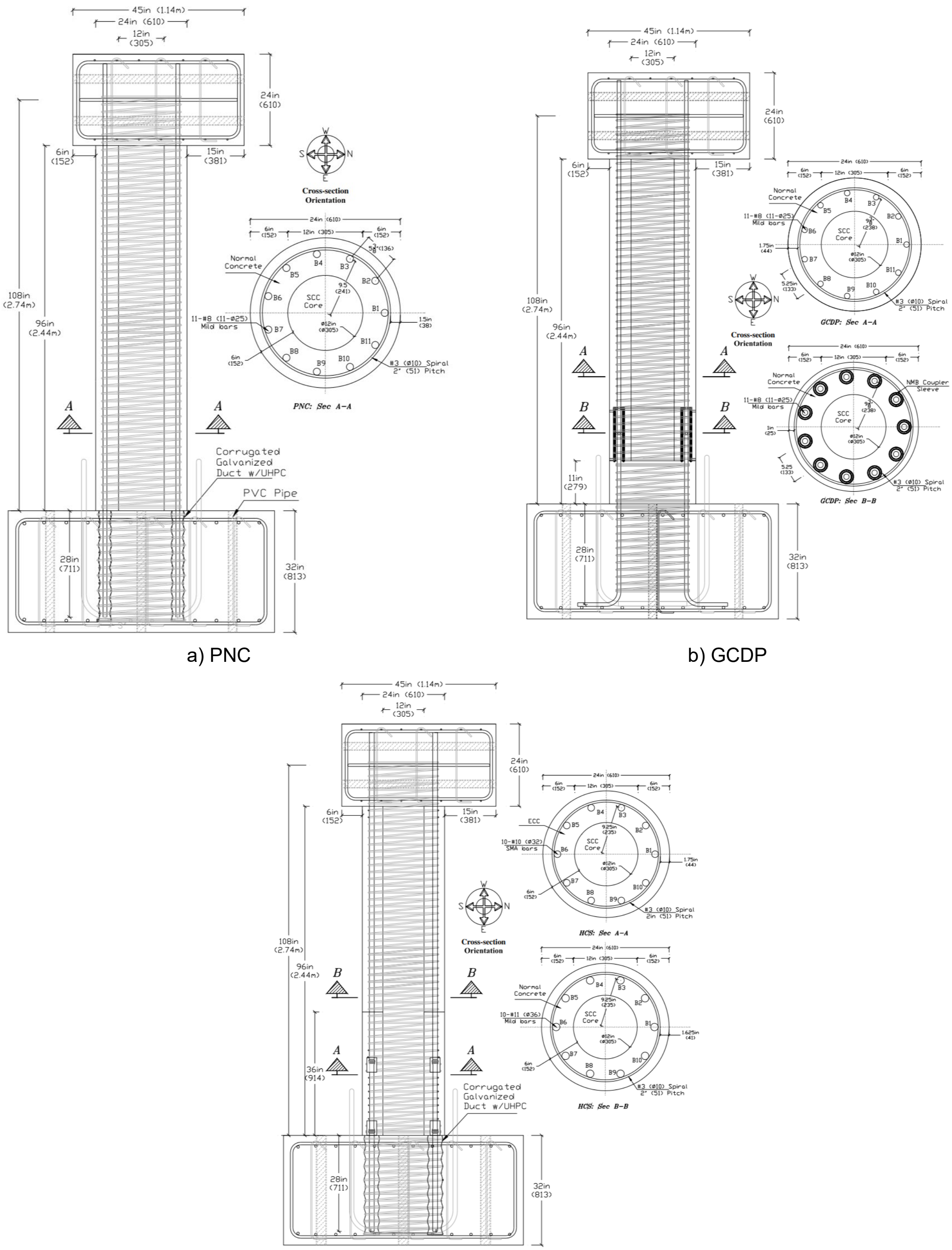

a) PNC

b) GCDP

c) HCS

Figure 2.11 Details of Precast Columns Tested by Tazarv and Saiidi (2014)

All columns failed due to longitudinal bar fracture and exhibited large displacement capacities. The drift capacities of PNC, GCDP, and HCS were 8%, 8%, and 10%, respectively (Fig. 2.12). PNC and GCDP had a 10% and 12% reduction in the displacement capacity compared with the CIP column from Haber et al. (2013). HCS showed a 5% increase in the displacement capacity compared with CIP. Overall, the force-displacement backbone of the precast models was comparable to that of CIP.

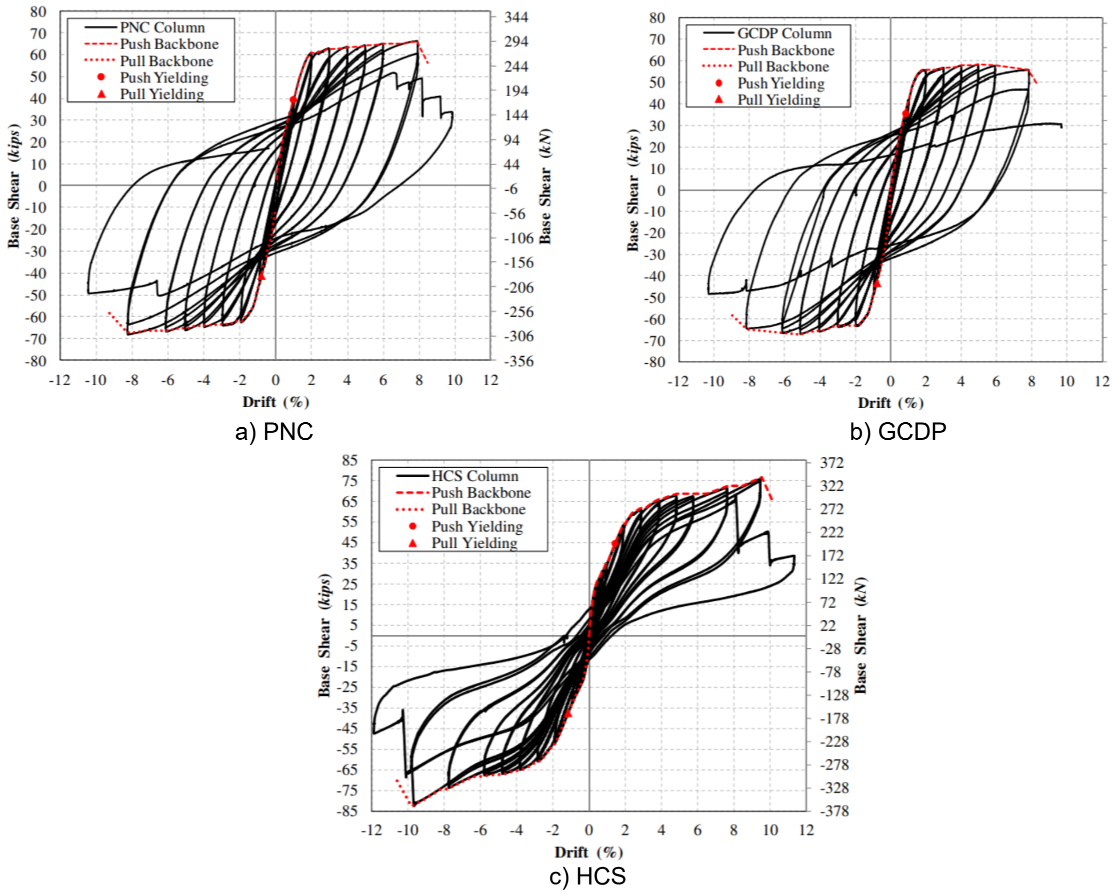

Figure 2.12 Force-Displacement Response of Precast Columns Tested by Tazarv and Saiidi (2014)

2.4.3 Study by Ameli et al. (2014)

This study was to investigate the seismic performance of precast columns connected to footings and cap beams using grouted couplers. Six half-scale precast bridge columns were tested using grouted couplers. Three of these were for a column-footing connection (GGSS) and three were for a column-cap beam connection (FGSS). A CIP column was also tested for each connection type as the reference. Figure 2.13 shows the detailing of the test specimens.

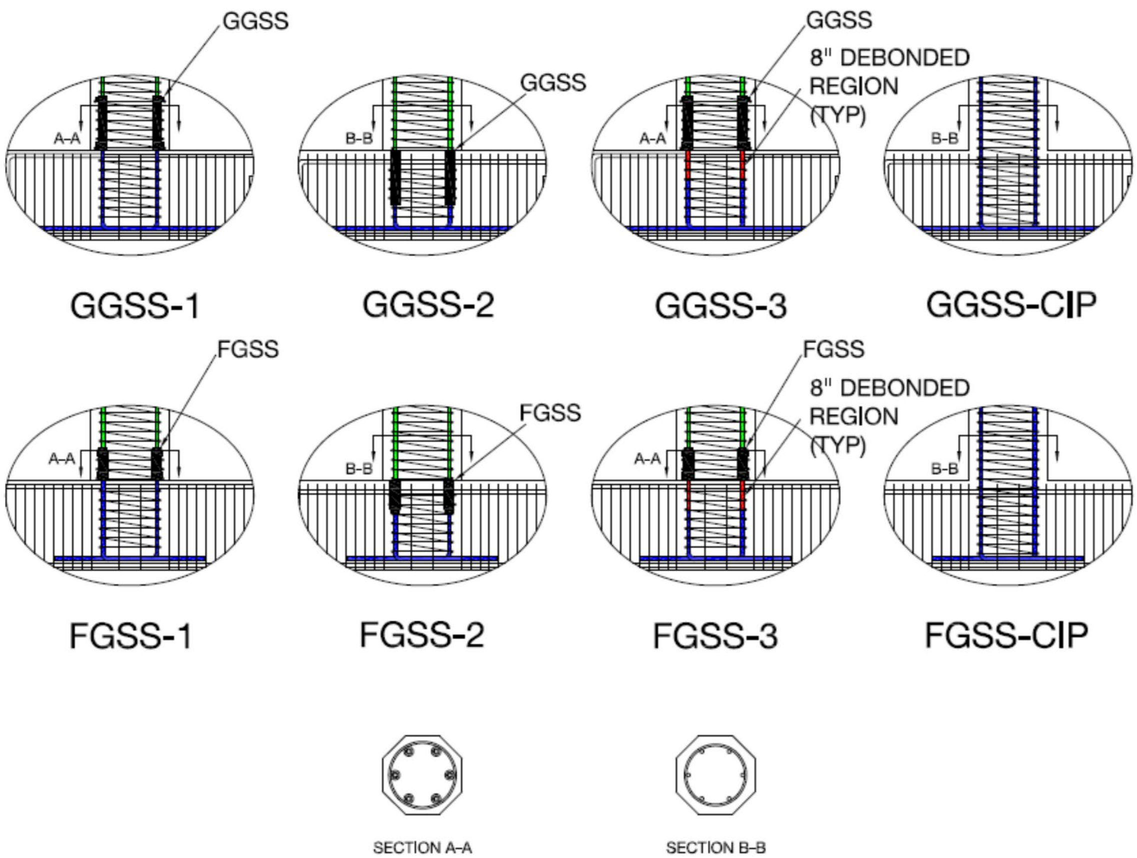

Figure 2.13 Details of Columns with Grouted Couplers Tested by Ameli et al. (2014)

The seismic performance of the precast columns was evaluated by placing the couplers at two alternative locations:

1) Couplers placed in the plastic hinge region with and without debonding
2) Couplers placed in the footing or cap beam

The columns were tested laterally under cyclic loading to failure. The columns had an axial load index of 6% (the ratio of the column axial load to the product of the column concrete compressive strength and the column cross-section area). Figure 2.14 shows the force-displacement response of each column. The study concluded that the precast details utilizing couplers are feasible and are expected to perform adequately in high seismic regions.

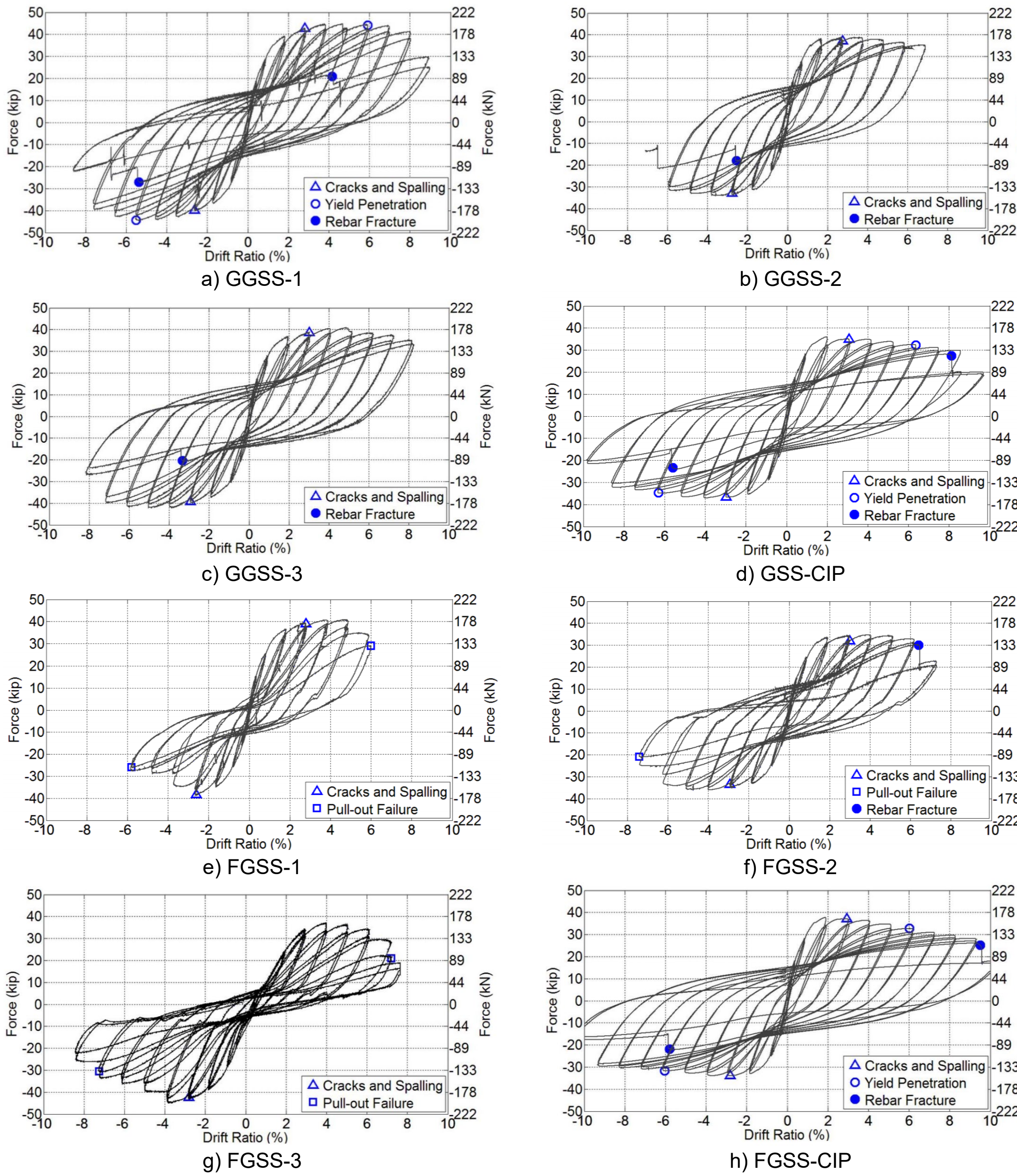

a) GGSS-1
b) GGSS-2
c) GGSS-3
d) GSS-CIP
e) FGSS-1
f) FGSS-2
g) FGSS-3
h) FGSS-CIP

Figure 2.14 Force-Displacement Response of Columns Tested by Ameli et al. (2014)

2.4.4 Study by Tazarv and Saiidi (2016)

Tazarv and Saiidi (2016) proposed acceptance criteria for couplers to be incorporated in the plastic hinge region of bridge columns as:

- The total length of a mechanical bar coupler (L_{sp}) shall be no greater than $15d_b$ where d_b is the diameter of the smallest of two spliced bars.
- A spliced bar shall fracture outside the coupler region regardless of loading scenario. The coupler region is defined as the physical length of the coupler plus $1.0d_b$ beyond each end of the coupler. Only ASTM A706 reinforcing bars shall be used in seismic regions.

Tazarv and Saiidi (2016) did not test any column. However, they performed an extensive analytical study and proposed design methods for mechanically spliced bridge columns based on the analytical findings and the experimental data from past studies.

2.4.5 Study by Wang et al. (2018)

Wang et al. tested seven square, large-scale bridge columns. Of the seven, two columns utilized grouted couplers at the column-footing interface and are relevant to the present study (Fig. 2.15). Further, one column was constructed as a conventional CIP column to serve as the reference model. The columns were subjected to unidirectional lateral cyclic loading with a displacement-controlled protocol. Figure 2.16 shows the force-displacement relationship of the three columns. The column with the couplers embedded in the footing had a 15% reduction in the displacement ductility compared with the CIP column. The column with couplers embedded at the base of the column had a 1.4% reduction in the displacement ductility compared with the reference column.

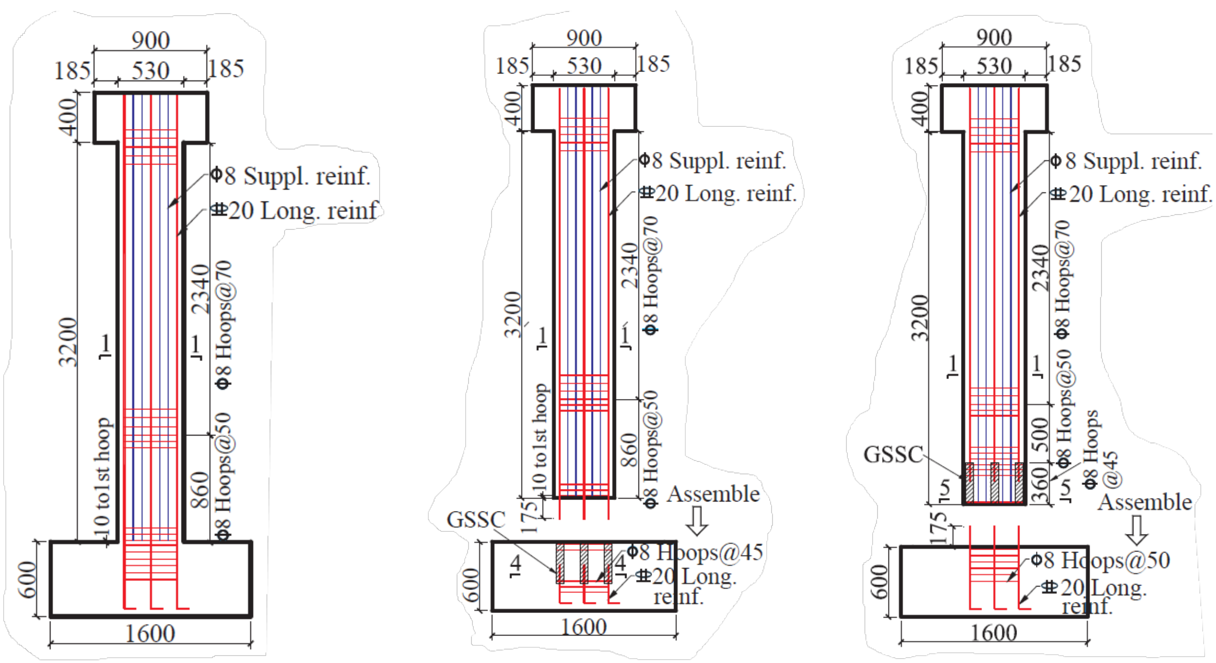

a) CIP Section b) Couplers Embedded in Footing c) Couplers at Base of Column

Figure 2.15 Details of Columns Tested by Wang et al. (2018)

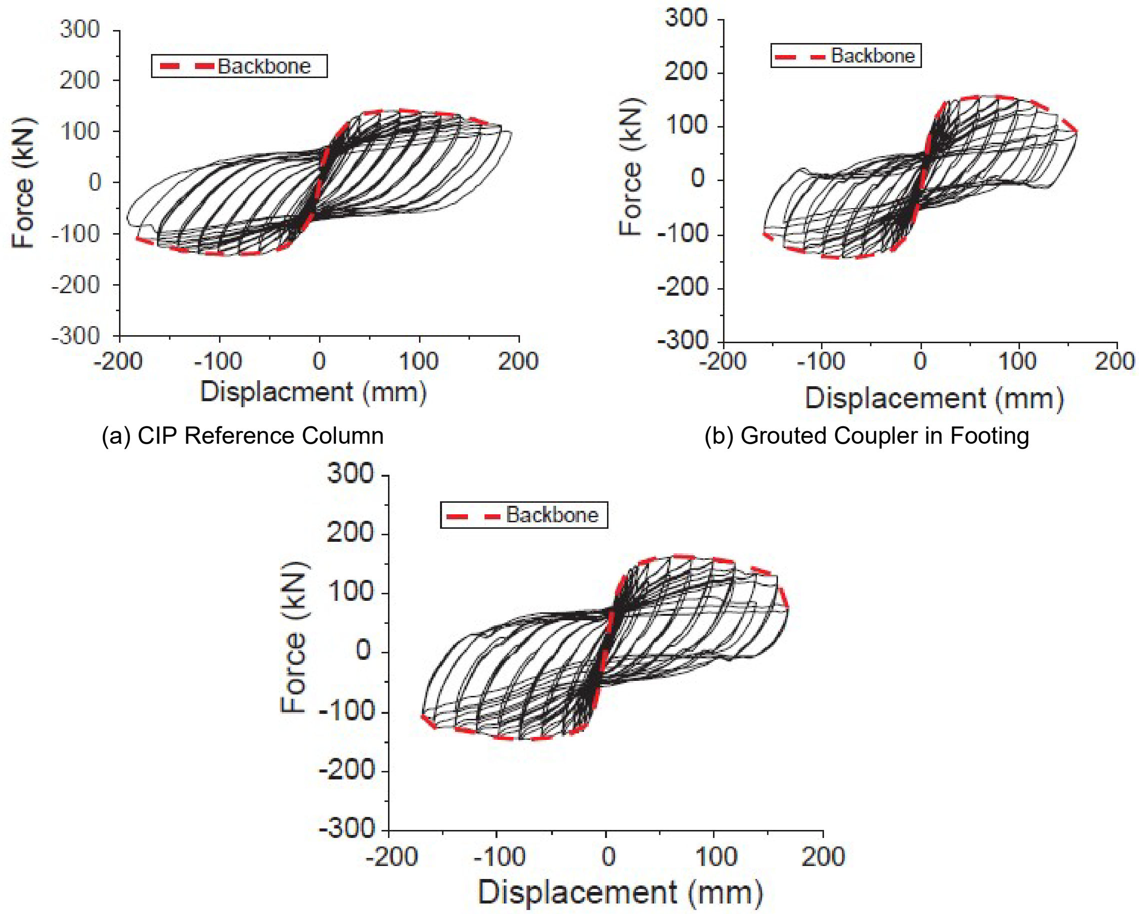

(a) CIP Reference Column
(b) Grouted Coupler in Footing
c) Grouted Coupler in Column Base

Figure 2.16 Force-Displacement Response of Columns Tested by Wang et al. (2018)

2.4.6 Study by Bompa and Elghazouli (2019)

Bompa and Elghazouli (2019) conducted an experimental investigation on the inelastic cyclic performance of RC members that incorporated threaded couplers. Four beam-column specimens were tested; one had conventional continuous reinforcement which served as the reference model while the other three used a threaded coupler embedded at the column base. Figure 2.17 shows the specimen detailing. Of the three columns with couplers, one column used a hybrid swaged-threaded coupler. The last two specimens incorporated a shorter, compact coupler. One of the columns with the compact couplers was subjected to an axial load index of 15% during testing while the other columns had no axial load. Each column was subjected to a quasi-static lateral cyclic loading until failure. The column named "C300-C0-N0" was the reference column. "C300-CC-N0" and "C300-CC-N1" were the columns that used the compact couplers and had axial load indexes of 0.0% and 15%, respectively. "C300-CS-N0" was the column that used the slender hybrid swaged-threaded couplers.

Figure 2.18 shows the full force-displacement relationship of the columns. "C300-CC-N1" exhibited a higher lateral resistance but experienced strength degradation from concrete spalling and a 36% reduction in the displacement capacity. The other specimens showed a similar performance.

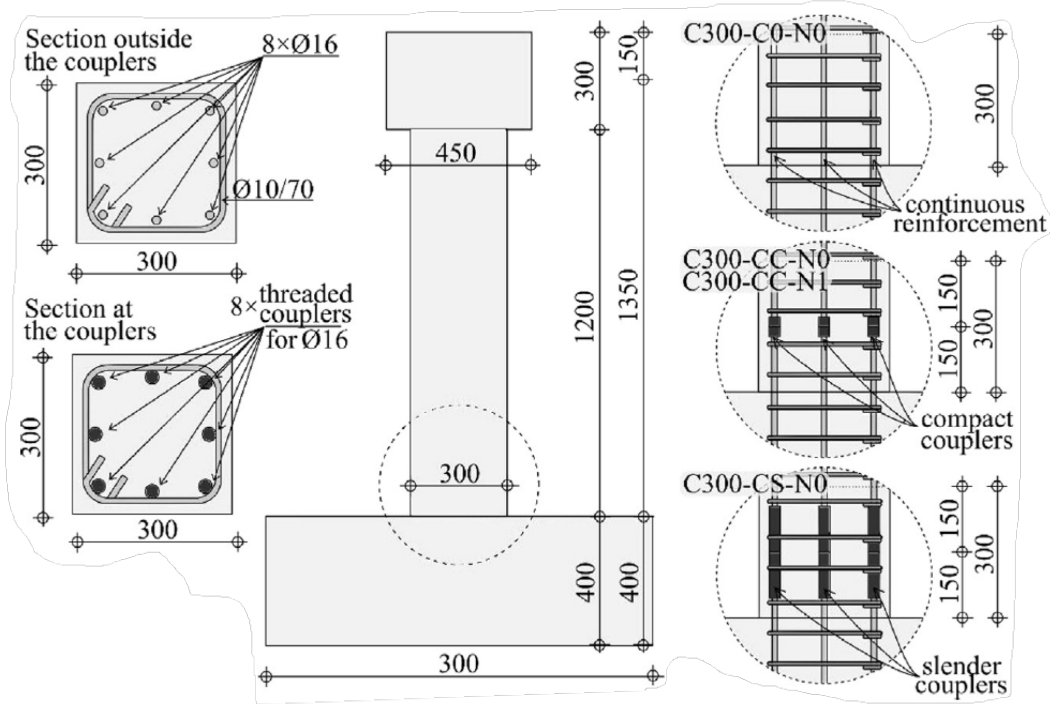

Figure 2.17 Details of Columns Tested by Bompa and Elghazouli (2019)

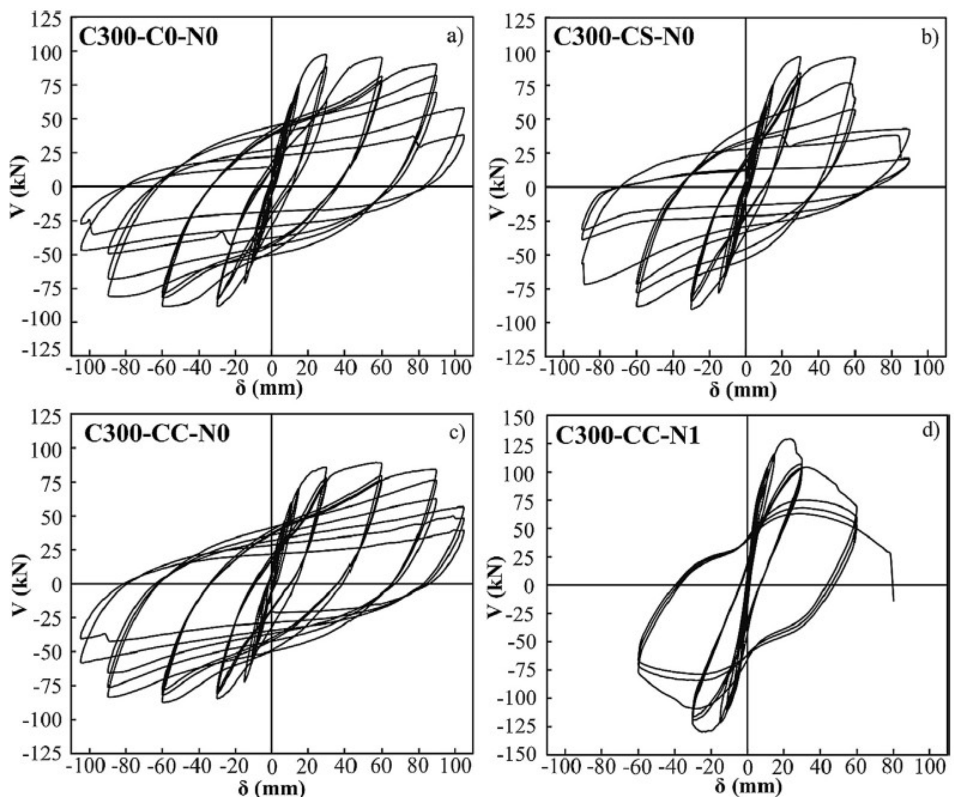

Figure 2.18 Force-Displacement Response of Columns Tested by Bompa and Elghazouli (2019)

2.5 References

Ameli, M.J., Brown, D.N., Parks, J.E., and Pantelides, C.P. (2014). “Seismic Evaluation of Grouted Splice Sleeve Connections for Precast RC Bridge Piers in ABC.” Utah Department of Transportation, Research Division, Report No. UT-14.09.

Ameli, M.J., Brown, D.N., Parks, J.E., and Pantelides, C.P. (2016). “Seismic Column-to Footing Connections Using Grouted Splice Sleeves.” *ACI Structure Journal*, Vol. 113, No. 5, pp.1021-1030.

Bompa, D.V., Elghazouli, A.Y. (2019), “Inelastic Behaviour of RC Members Incorporating Threaded Reinforcement Coupler.” *Engineering Structures*, DOI: 10.1016/j.engstruct.2018.11.053, Vol. 180, pp.468-483.

Dahal, P.K., Tazarv, M., and Wehbe, N. (2019). “Mechanical Bar Splices for Accelerated Construction of Bridge Columns,” North Dakota State University - Upper Great Plains Transportation Institute, Fargo: Mountain-Plains Consortium (MPC), MPC Report No. 19-372, 142 pp.

Dahal, P.K., and Tazarv, M. (2020). “Mechanical Bar Splices for Incorporation in Plastic Hinge Regions of RC Members,” *Construction and Building Materials*, Vol. 258, 120308, 17 pp.

Haber, ZB, Saiidi, M.S., and Sanders, D.H. (2013). “Precast Column Footing Connections for Accelerated Bridge Construction in Seismic Zones.” Rep. No. CCEER 13-08 Center for Civil Engineering Earthquake Research, Dept. of Civil and Environmental Engineering, Univ. of Nevada, Reno. NV.

Saiidi, M.S., Mehraein, M., Shrestha, G., Jordan, E., Itani, A., Tazarv, M., Sanders, D., Murphy, T.M., Reno, M.L., and Pohll, M.N. (2020). “Proposed AASHTO Seismic Specifications for ABC Column Connections,” National Academies of Sciences, Engineering, and Medicine, NCHRP Report No. 935, Washington, DC: The National Academies Press, 354 pp.

Tazarv, M., and Saiidi, M.S. (2014). “Next Generation of Bridge Columns for Accelerated Bridge Construction in High Seismic Zones,” Center For Civil Engineering Earthquake Research, Department of Civil and Environmental Engineering, University of Nevada, Reno, Nevada, Report No. CCEER-14-06, 400 pp.

Tazarv, M., and Saiidi, M.S. (2016). “Seismic Design of Bridge Columns Incorporating Mechanical Bar Splices in Plastic Hinge Regions,” *Engineering Structures*, DOI: 10.1016/j.engstruct.2016.06.041, Vol 124, pp. 507-520

Wang, Z., Qu, H., Li, T., Wei, H., Wang, H., Duan, H. (2018). “Quasi-Static Cyclic Tests of Precast Bridge Columns with Different Connection Details for High Seismic Zones,” *Engineering Structures*, DOI: 10.1016/j.engstruct.2017.12.035, Vol 158, pp. 13-27.

3. EXPERIMENTAL INVESTIGATION OF MECHANICALLY SPLICED BRIDGE COLUMNS

3.1 Introduction

A bridge column in a region with high seismic demand must be designed to handle large inelastic lateral deformations. Different accelerated bridge construction (ABC) details for RC bridge columns have been developed, and a few have been proof tested. Of which, precast columns incorporating mechanical bar splices are the focus of this study. There are several bar couplers in the market, and new ones are emerging. Furthermore, there are a few laboratory-scale tests on the seismic performance of these types of ABC columns. However, the literature is lacking a systematic testing of mechanically spliced columns using the same scaling, testing methods, and materials, and under the same loading protocol. An experimental investigation was performed in the Lohr Structures Laboratory at South Dakota State University to systematically determine the seismic performance of mechanically spliced bridge columns and develop the first-of-its-kind comprehensive experimental database. This chapter discusses the experimental study including test matrix, design and construction, test setup, instrumentation, loading protocol, and test results.

3.2 Test Matrix

A total of eight columns, including one reference cast-in-place (CIP) column and seven precast columns, have been designed, built, and tested in this project. The column test variable was the coupler type (different types have different geometry and mechanical properties) through the most feasible detailing per type.

Table 3.1 presents the test matrix for the eight columns included in this study. The specimens were identified by two broad classifications, CIP and precast with a three-letter naming system starting with "P." The second letter in the precast column name identifies the coupler type: "G" for grouted, "T" for threaded, and "H" for a hybrid combination of coupling mechanisms. The last letter of the precast column name identifies the coupler manufacturer: "D" for Dayton Superior and also Dextra America, "S" for Splice Sleeve North America, "H" for Headed Reinforcement, and "V" for nVent Lenton. Four feasible connection detailing alternatives shown in Figure 3.1 were proposed for the precast specimens. Each specimen was detailed according to the alternative deemed most feasible. The last column in the test matrix, RPH, was a new column with repairable detailing based on the work by Boudaqa et al. (2017) and Tazarv et al. (2020). The main goal of this pilot testing was to investigate the feasibility of such detailing for a quick repair through replacement of the damaged bars after the event.

Table 3.1 Column Test Matrix

SP ID	Coupler Type	Manufacturer, Model	Coupler Properties, in. (mm)	Coupler Rigid Length Factor, β	Remark
CIP	N/A	N/A	N/A	N/A	Reference cast-in-place
PGD	Grouted	Dayton Superior Corp., Sleeve Lock	Length: 16.5 (419) Diameter: 2.89 (73)	0.70	Use ALT1 detailing
PGS	Grouted	Splice Sleeve North America, Inc., NMB	Length: 14.57 (370) Diameter: 2.52 (64)	0.70	Use ALT1 detailing
PHD	Hybrid (Grouted-Threaded)	Dextra America, Inc., Groutec S with Bartec	Length: 9.45 (240) Diameter: 2.17 (55)	0.79	Use ALT1 detailing (Fig. 3.1)
PHV	Hybrid (Grouted-Threaded)	nVent LENTON Corp., Interlock	Length: 8.63 (219) Diameter: 2.67 (68)	0.82	Use ALT1 detailing
PTV	Threaded	nVent LENTON Corp., Ultimate PT15 Position	Length: 9.0 (228.6) Diameter: 1.5 (38)	0.4	Use ALT2 detailing, column dowels tapered (MT12)
PHH	Hybrid (Grouted-Headed)	Headed Reinforcement Corp., HRC560	Length: 7.75 (196.9) Diameter: 2.625 (67)	0.80	Use ALT1 detailing
RPH	Headed	Headed Reinforcement Corp., HRC510XL	Length: 3.13 (80) Diameter: 2.13 (54)	0.75	Repairable column with BRR, ALT4

Note: Coupler properties are for No. 8 (25-mm) bars. All couplers except HRC510 were tested in this project. Data for HRC510 coupler were from Dahal and Tazarv (2020).

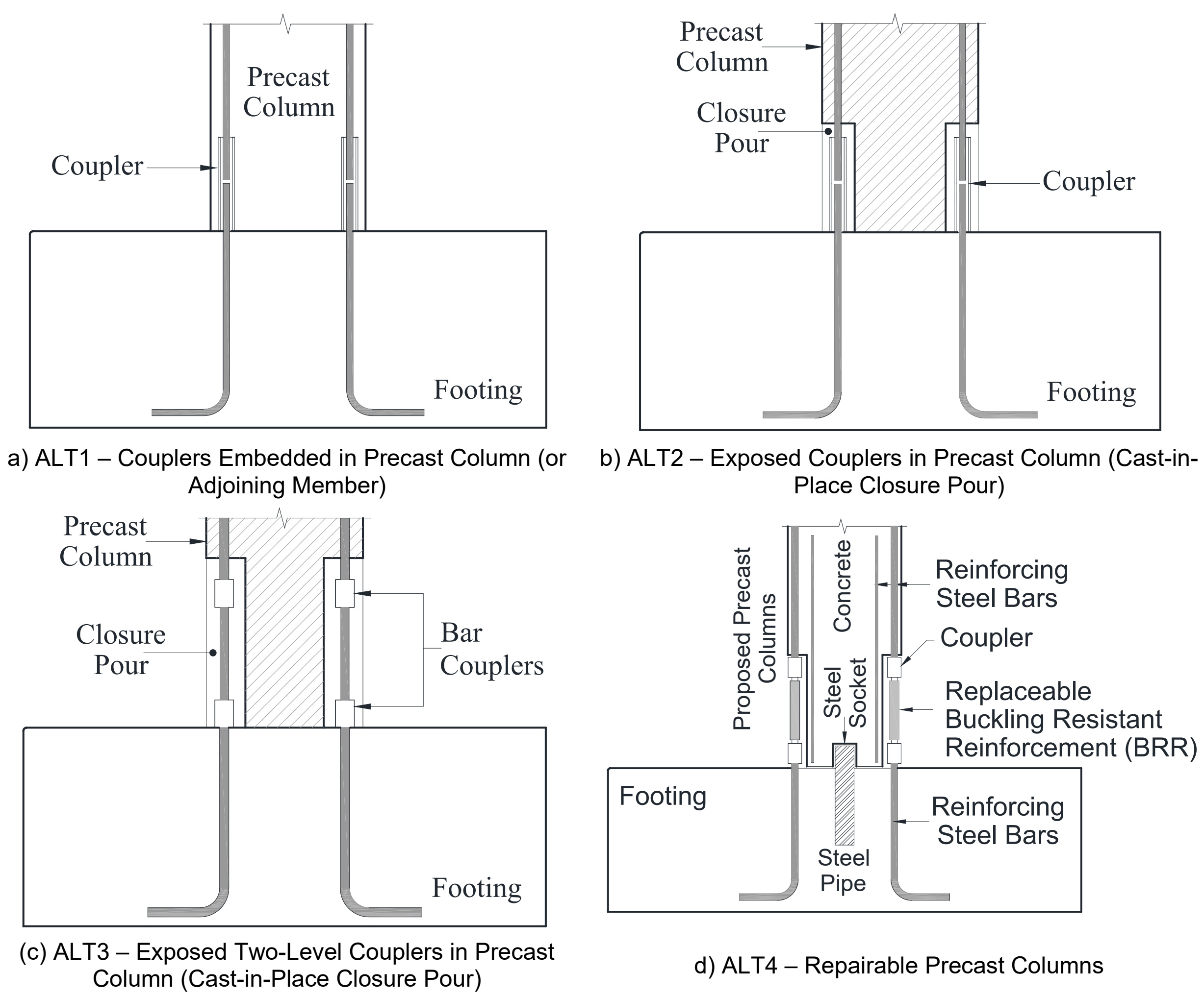

Figure 3.1 Feasible Connection Details for Mechanically Spliced Precast Bridge Columns

3.3 Design and Construction of Column Test Specimens

This section presents a summary of the design and construction of the column test specimens starting from CIP then the precast columns.

3.3.1 CIP Column Model

The test column overall geometry was determined based on an analytical study at SDSU in which it was found that coupler effects are more profound on columns with low aspect ratios, low axial loads, and a high displacement capacity. The coupler effect was the highest for a column with an aspect ratio (the column height to the column diameter) of 4, an axial load index (the ratio of the column axial load to the product of concrete strength and the column cross-sectional area) of 5%, and a displacement ductility capacity of 7.0 (LaVoy, 2020). More discussion of the findings will be presented in Chapter 5. Therefore, these properties were adopted for the design of the prototype test specimen. Furthermore, the study aims at developing new precast connections for bridge columns. Precast plants usually function in horizontal pour, and specimen preparation in the vertical direction is limited. Even though circular reinforced concrete (RC) columns are the best and the most common shape for seismic performance due to high confinement provided by hoops/spirals, a rectilinear in lieu of curvilinear cross-section is preferred for precast products (Hewes, 2013). Therefore, an octagonal cross-section with circular bar arrangement was selected in this study for testing.

The prototype conventional CIP column was designed based on AASHTO SGS (2011) (also Caltrans Seismic Design Criteria, 2019). As discussed before, CIP serves as the reference column to comment on the performance of the mechanically spliced precast columns. The CIP model was a typical bridge column but with a thicker clear cover than usual practice to account for the coupler diameter in the precast specimens. Due to the test setup limitation, a half-scale model of the prototype column was selected for testing. The column scaling was carried out following the recommendations of Krawinkler and Moncarz (1982).

Based on the abovementioned requirements and limitations, the cross section of the test specimen was selected to be octagonal with a medium diagonal of 24 in. (610 mm) and a height of 8 ft (2.44 m), from the top of the footing to the centerline of the hydraulic actuator to apply lateral loads, resulting in an aspect ratio of 4.

The reinforcement schedule for the CIP column model was 10, No. 8 (Ø25-mm) longitudinal bars and No. 4 (Ø13-mm) transverse hoops spaced at 2 in. (51 mm) resulting in a longitudinal steel ratio and a transverse volumetric steel ratio of 1.66% and 2.0%, respectively. Figure 3.2 shows the CIP column model reinforcement detailing. The axial load index was 5%. The column was designed with a concrete compressive strength of 6,000 psi (41.4 MPa), and ASTM A706 bar was used for all reinforcement. The column was designed to achieve a minimum displacement ductility capacity of 7 based on AASHTO SGS (2011).

To secure the actuator to the column, the column cross-section at the tip was changed from octagonal to square with a side dimension of 24 in. (610 mm). PVC pipes were used to make holes in two layers to fix the actuator to the column head using high strength threaded rods. To minimize test variations, only one batch of longitudinal black steel was used in all columns (expect the repairable column in which stainless steel was used). The single-batch A706 longitudinal reinforcement was purchased from a provider in Ohio, was shipped either to the coupler manufacturers for the bar end preparation or to the Lohr Structures Laboratory for direct use in the columns. CIP was constructed at SDSU. However, Gage Brothers, a leading precast company in the region located in Sioux Falls, SD, was hired to construct the precast columns. To further minimize the test variations, the Gage Brothers concrete mix design was used to prepare the CIP column concrete.

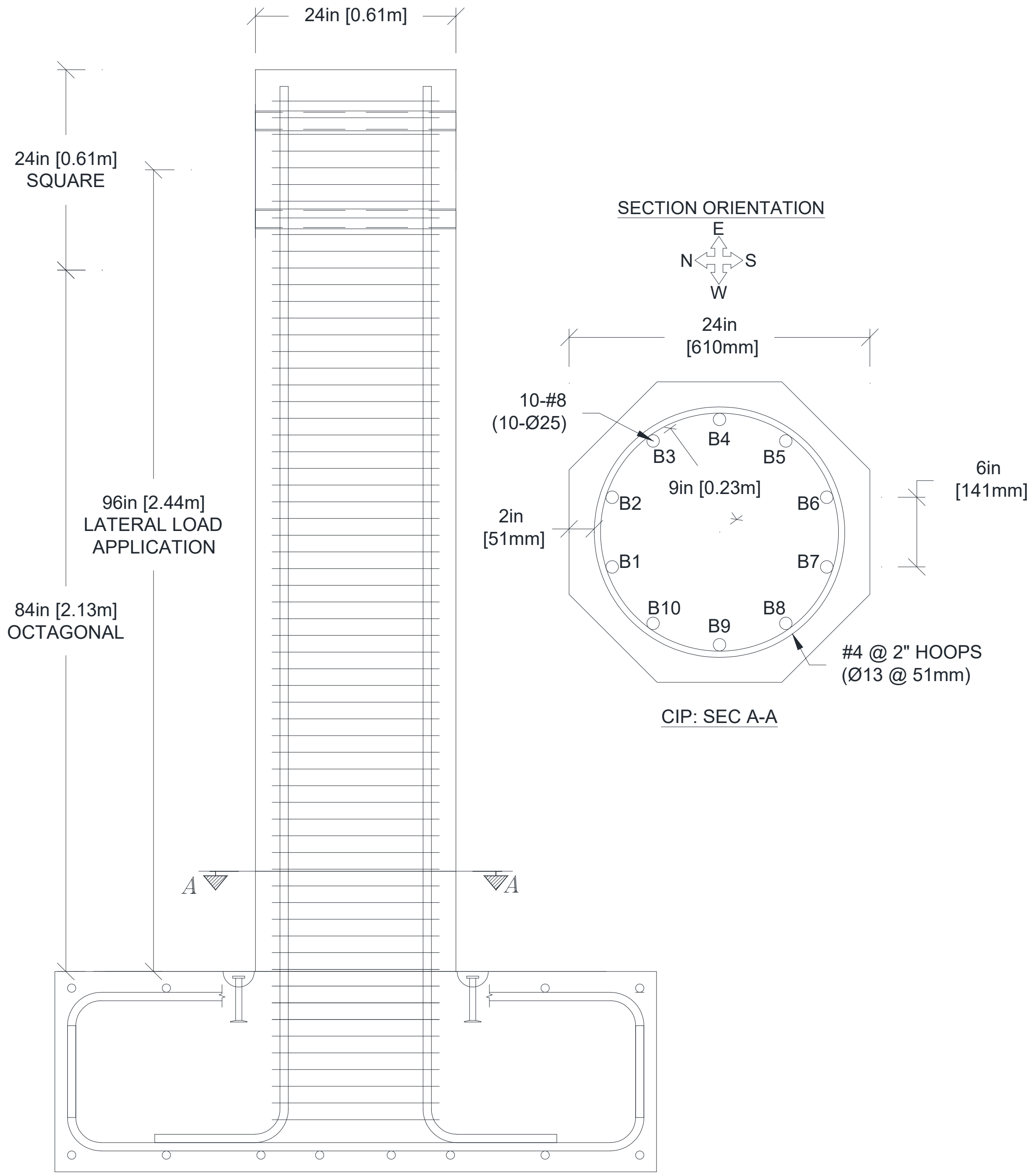

Figure 3.2 Reinforcement Detailing of CIP Column

The CIP column was constructed vertically at SDSU by first casting the footing with the column cage embedded (Fig. 3.3) followed by casting the column itself (Fig. 3.4). A ready mixed concrete company was hired to prepare the concrete for the CIP footing and column following the precast concrete mix design with a target design compressive strength of 6,000 psi (41.4 MPa). Samples were collected and slump tests were performed before placement.

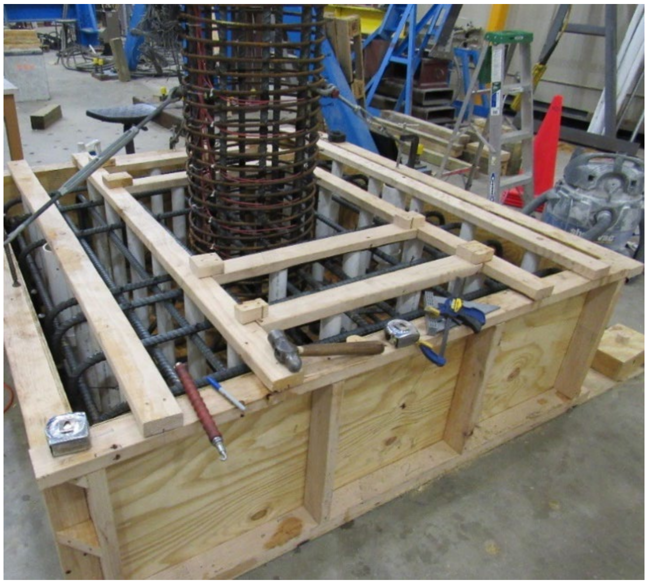

a) Before Pour

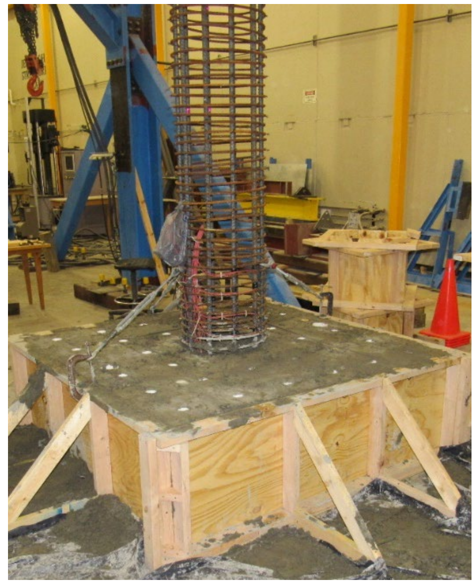

b) After Pour

Figure 3.3 Construction of CIP Footing

a) During Pour

b) After Pour

Figure 3.4 Construction of CIP Column

3.3.2 PGD Column Model

Following the CIP column model detailing, the PGD column model was detailed (Fig. 3.5) to incorporate the Dayton Superior "D410 Sleeve-Lock" grouted couplers. The reinforcement for this column was the same as the CIP except larger diameter hoops were used at the sections with couplers. The clear cover at the section with the coupler was 1.06 in. (27 mm) and the clear cover away from the coupler was 2 in. (50.8 mm). The coupler was filled with the company specified "D490 Sleeve-Lock" grout, which can achieve a compressive strength of 12,000 psi (82.7 MPa) at 28 days when mixed at the flowable consistency.

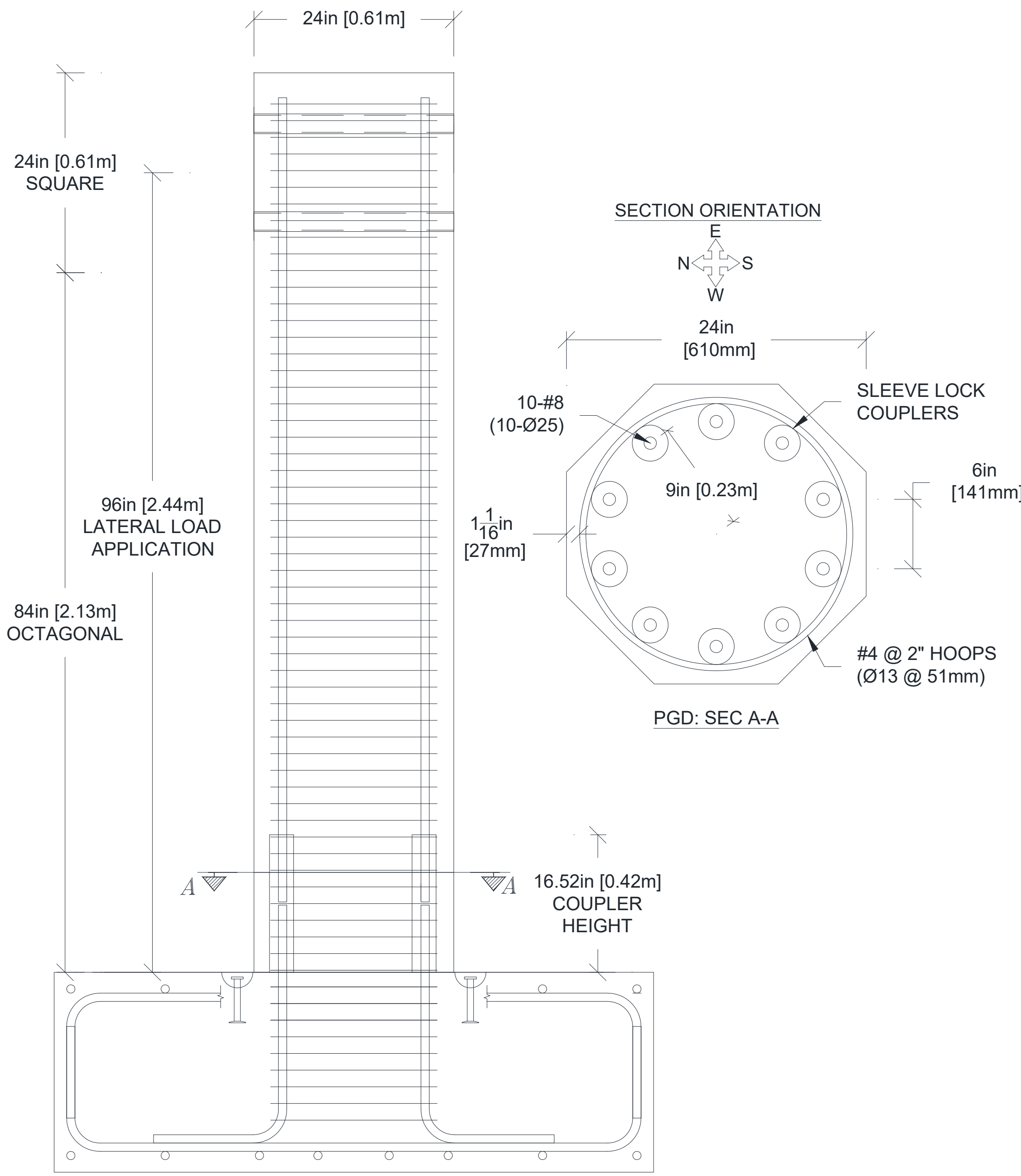

Figure 3.5 Reinforcement Detailing of PGD Column with Dayton Grouted Couplers

As mentioned earlier, all precast columns, but not the footing, were built by Gage Brothers in Sioux Falls, SD. The construction sequence for PGD was as follows:

- Cast the footing at SDSU with dowel bars extended (Fig. 3.6)
- Cast the column at the precast plant with the couplers embedded (Fig. 3.7)
- Erect and install the column at SDSU (Fig. 3.8)
- Fill the gap between the column and footing at SDSU
- Inject Sleeve-Lock grout into the couplers at SDSU (Fig. 3.9)

a) Footing Cage　　b) Concrete Pouring

Figure 3.6 Construction of PGD Footing

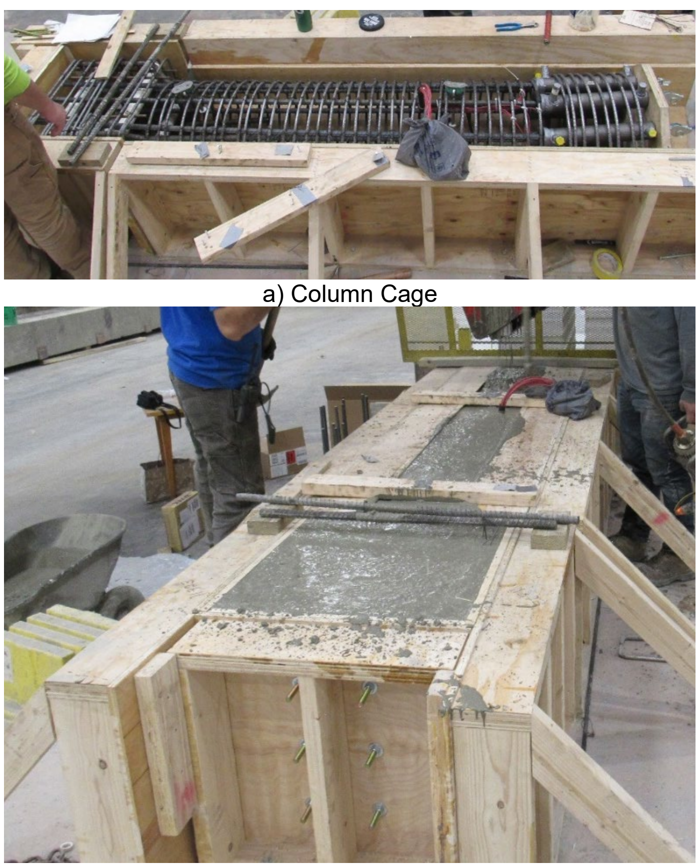

a) Column Cage

b) Column Pouring

Figure 3.7 Casting PGD Column

a) Matching Couplers and Dowel Bars

b) Column Secured

Figure 3.8 Erecting PGD Column

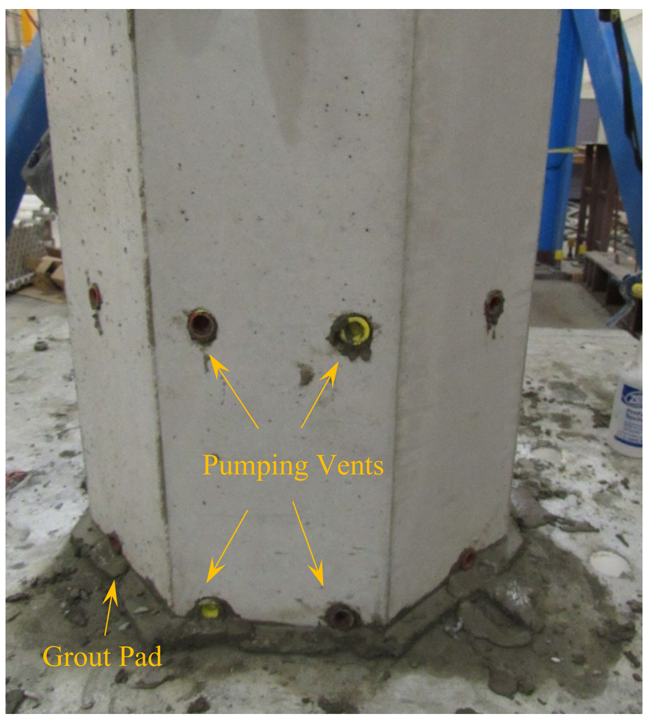

Figure 3.9 PGD Column Base After Coupler Grout Injection

The dowels extending from the footing were cut in a way that they could protrude into the coupler with the maximum embedment depth of 8.07 in. (205 mm). Once the column was secured, the minimal gap at the column-footing interface was filled using a high-strength, non-shrink grout (1428HP). The maximum gap observed in PGD was approximately 0.375 in. (9.5 mm). Finally, the couplers were injected with the "Sleeve-Lock" grout from bottom vents letting grout to push the air from the bottom-to-top vent, and the specimen was left undisturbed until the grout reached a sufficient strength (e.g., 7,500 psi or 51.7 MPa).

3.3.3 PGS Column Model

Following the CIP column model detailing, the PGS column model was detailed (Fig. 3.10) to incorporate the "NMB Splice-Sleeve" grouted couplers. The reinforcement for this column was the same as CIP except larger diameter hoops were used at the sections with couplers. The clear cover at the section with the couplers was 1.24 in. (31 mm) and the clear cover away from the couplers was 2 in. (50.8 mm). The couplers were filled with the company specified "SS Mortar" grout, a non-shrink high-early-strength grout with a minimum 28-day compressive strength of 11,000 psi (75.8 MPa).

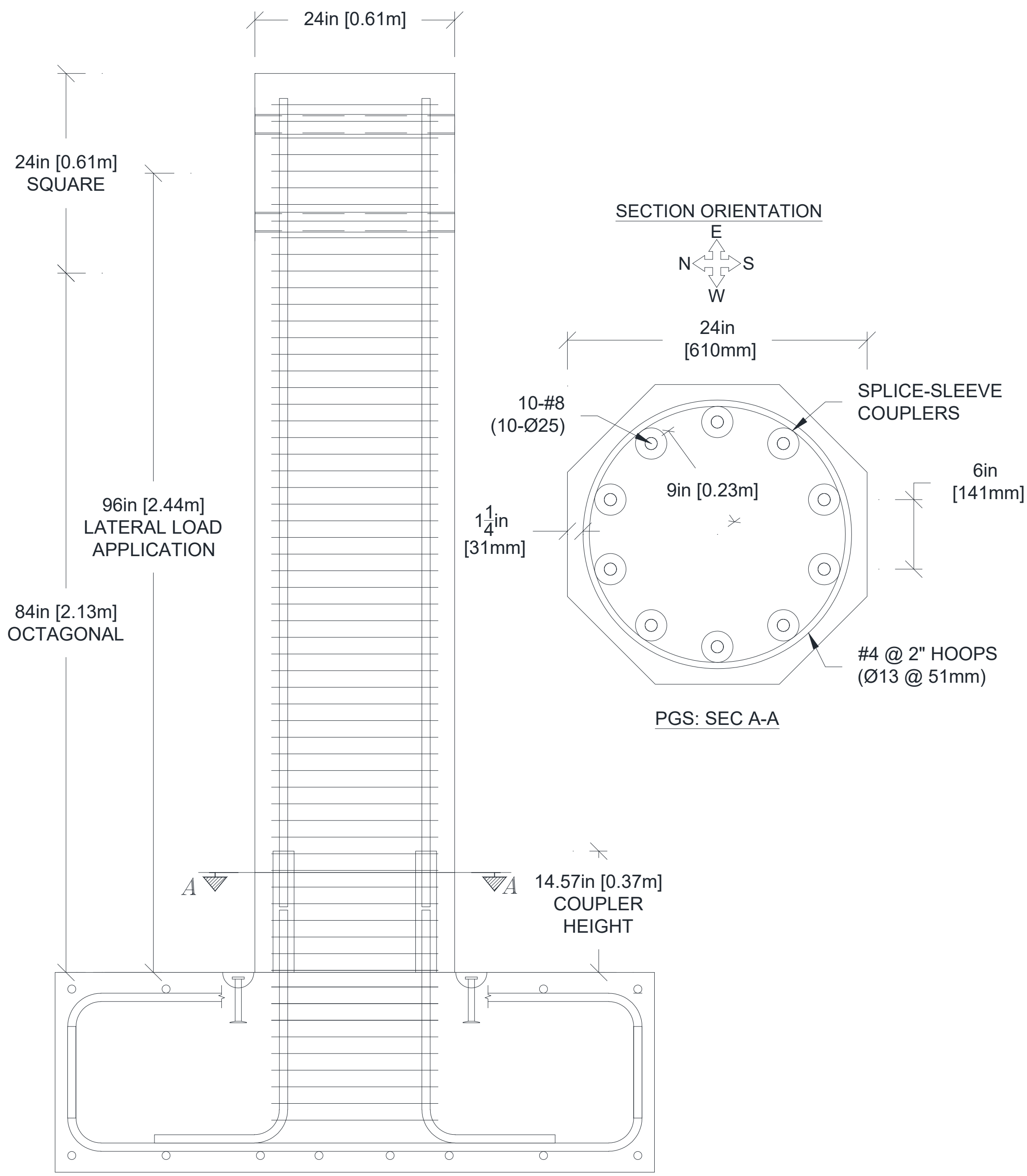

Figure 3.10 Reinforcement Detailing of PGS Column with NMB Grouted Couplers

The construction sequence for PGS was as follows:

- Cast the footing at SDSU with dowel bars extended
- Cast the column at the precast plant with the couplers embedded (Fig. 3.11)
- Erect and install the column at SDSU (Fig. 3.12)
- Fill the gap between the column and footing at SDSU
- Inject "SS Mortar" grout into the couplers at SDSU (Fig. 3.13)

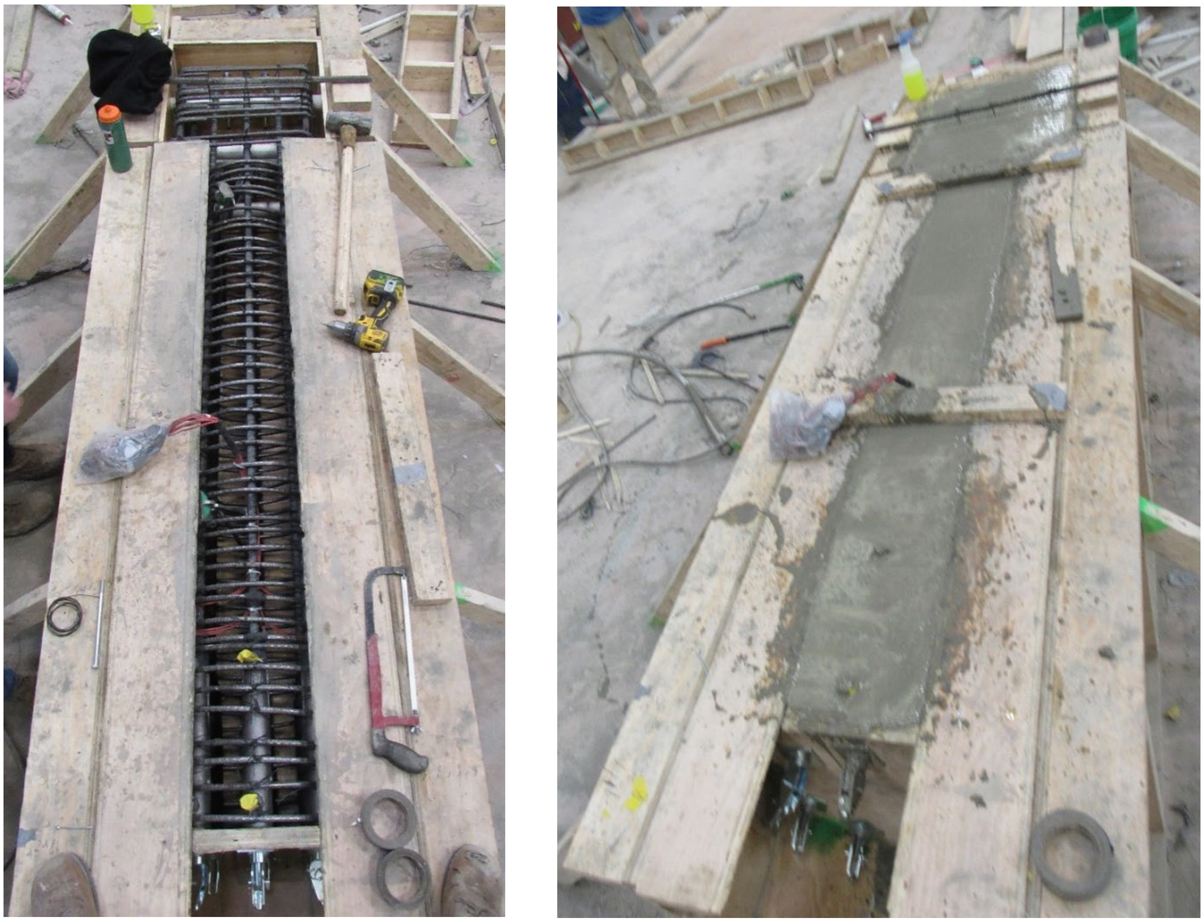

a) Column Cage　　b) Column Pouring

Figure 3.11 Casting PGS Column

a) Matching Couplers and Dowel Bars

b) Column Securing Setup

Figure 3.12 Erecting PGS Column

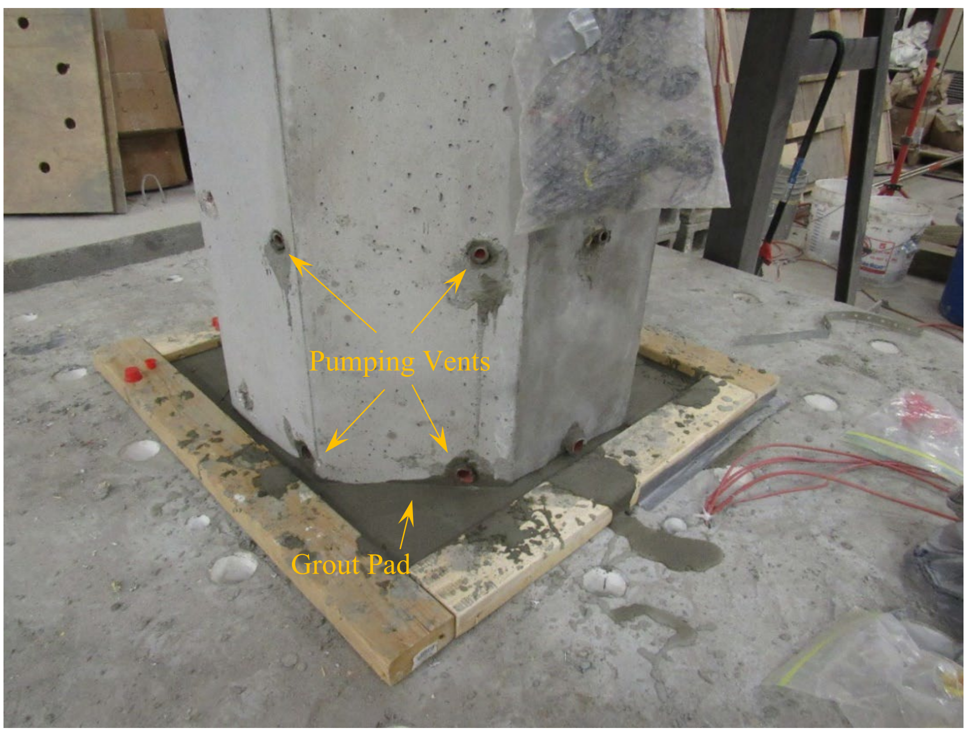

Figure 3.13 PGS Column Base After Coupler Grout Injection

The footing dowels were cut and extended into the couplers with a maximum embedment depth of 7.48 in. (190 mm). Once the column was secured, the minimal gap at the column-footing interface was filled using a high-strength, non-shrink grout (1428HP). The maximum gap observed in PGS was approximately 0.375 in. (9.5 mm). Finally, the couplers were injected with the "SS Mortar" grout from bottom vents letting grout to push the air from the top vent, and the specimen was left undisturbed until the grout reached a sufficient strength.

3.3.4 PHD Column Model

Following the CIP column model detailing, the PHD model was detailed (Fig. 3.14) to incorporate the Dextra "Groutec" grouted-threaded couplers. The reinforcement for this column was the same as CIP except larger diameter hoops were used at the sections with couplers. The clear cover at the sections with the couplers was 1.42 in. (36 mm) and the clear cover away from the couplers was 2 in. (50.8 mm). Following the company recommendation, the couplers were filled with an off-the-shelf product, "Quikrete 15800-00 Precision" grout, which can achieve a compressive strength of 12,500 psi (86.2 MPa) at 28 days when mixed at the flowable consistency.

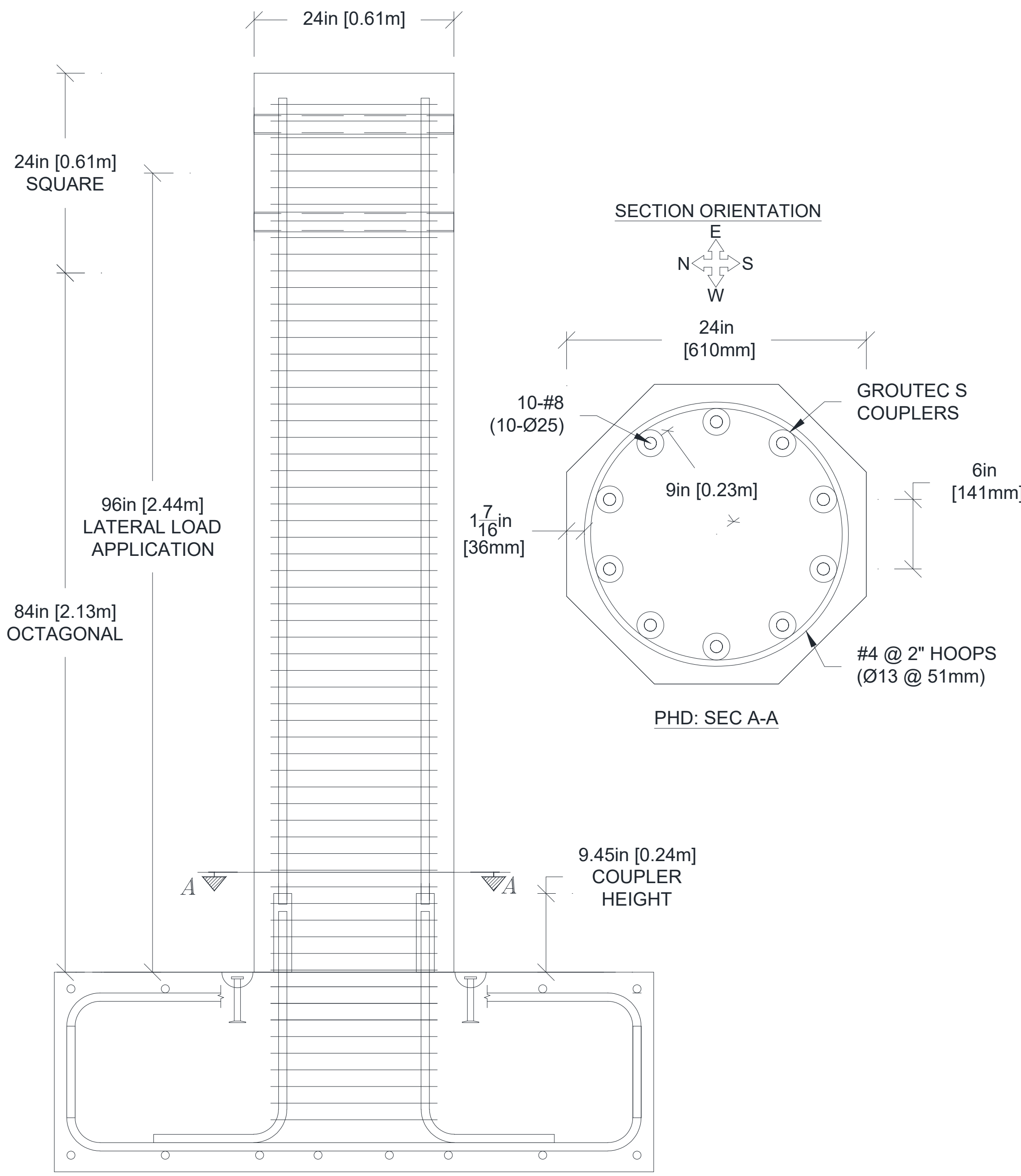

Figure 3.14 Reinforcement Detailing of PHD Column with Hybrid Grouted-Threaded Couplers

The construction sequence for PHD was as follows:

- Cast the footing at SDSU with dowel bars extended
- Cast the column at the precast plant with the couplers embedded (Fig. 3.15)
- Erect and install the column at SDSU (Fig. 3.16)
- Fill the gap between the column and footing at SDSU
- Inject "Quikrete" grout into the couplers at SDSU (Fig. 3.17)

a) Column Cage b) Column Pouring

Figure 3.15 Casting PHD Column

a) Matching Couplers and Dowel Bars b) Column Secured

Figure 3.16 Erecting PHD Column

a) Injecting Grout b) After Grouting

Figure 3.17 Injecting Grout into PHD Couplers

The footing dowels were cut and extended into the couplers with a maximum embedment depth of 7.87 in. (200 mm). Once the column was secured, the gap at the column-footing interface, which was no more than 0.375 in. (9.5 mm), was filled using a high-strength, non-shrink grout (1428HP). Finally, the couplers were injected with the "Quikrete" grout from bottom vents, and the specimen was left undisturbed until the grout reached a sufficient strength.

3.3.5 PHV Column Model

Following the CIP column model detailing, PHV was detailed to incorporate the "nVent Lenton Interlock" splice, which was a hybrid grouted-threaded coupler (Fig. 3.18). The reinforcement for this column was the same as CIP except the diameters for the hoops at sections with the couplers. The clear cover at the sections with the couplers was 1.19 in. (30.2 mm) and the clear cover outside the coupler section was 2 in. (50.8 mm). The coupler was filled with the company specified "HY10L" high strength grout, which can achieve a minimum compressive strength of 8,500 psi (58.6 MPa) at 28 days when mixed at the flowable consistency.

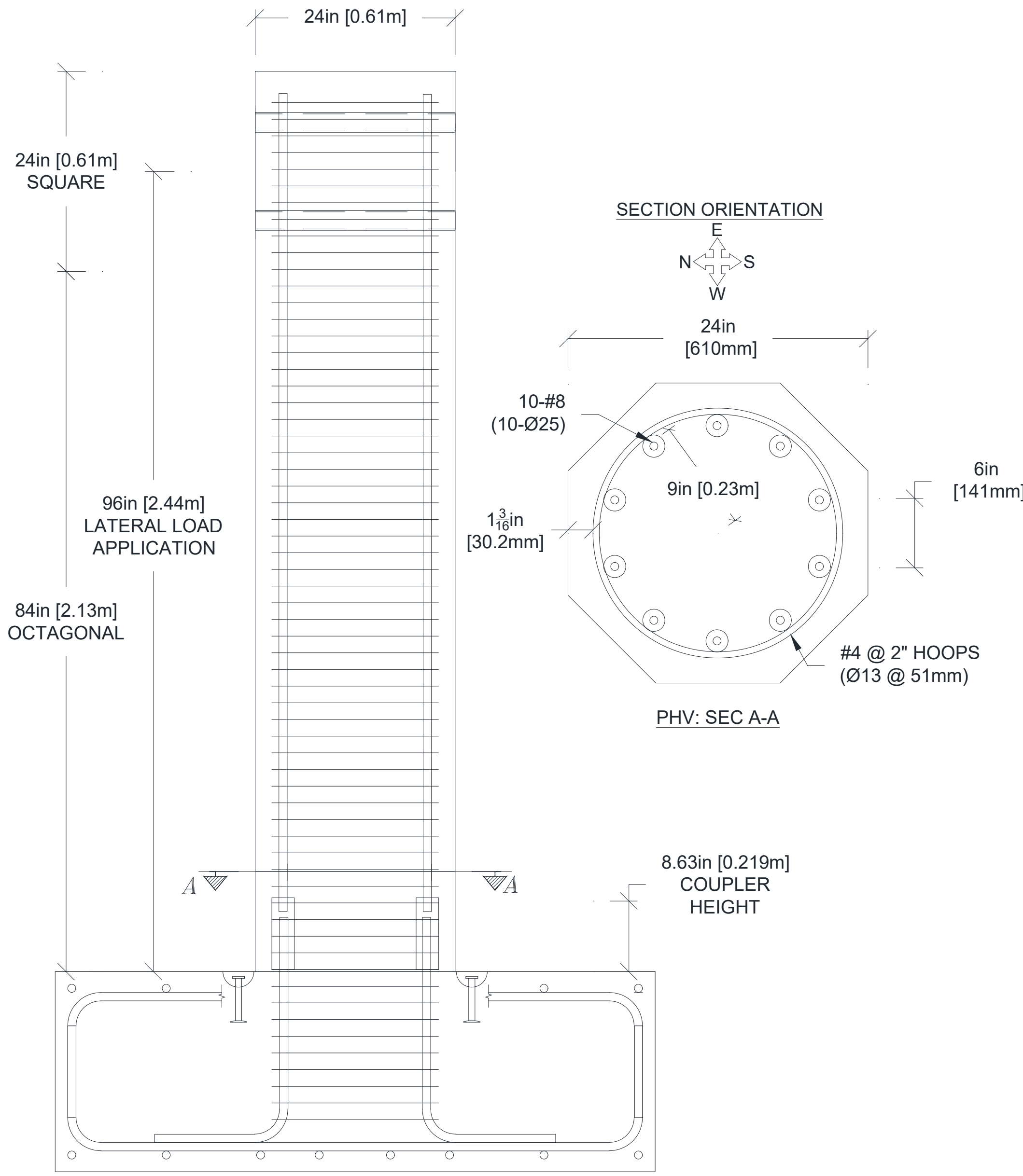

Figure 3.18 Reinforcement Detailing of PHV Column with Hybrid Grouted-Threaded Couplers

The construction sequence for PHV was:

- Cast the footing at SDSU with dowel bars extended (Fig. 3.19)
- Cast the column at the precast plant with the couplers embedded (Fig. 3.20)
- Erect and install the column at SDSU (Fig. 3.21)
- Fill the gap between the column and footing at SDSU
- Inject "HY10L" grout into the couplers at SDSU (Fig. 3.22)

a) Footing Cage

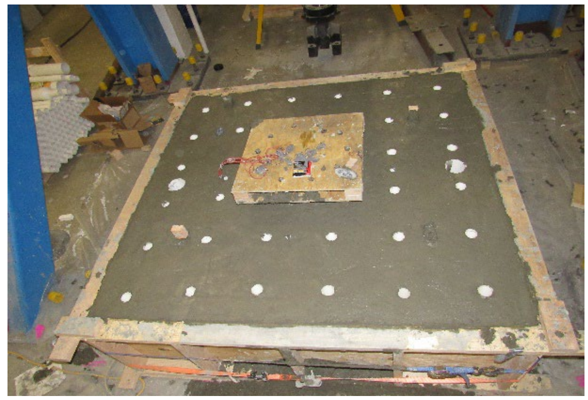

b) Concrete Pouring

Figure 3.19 Construction of PHV Footing

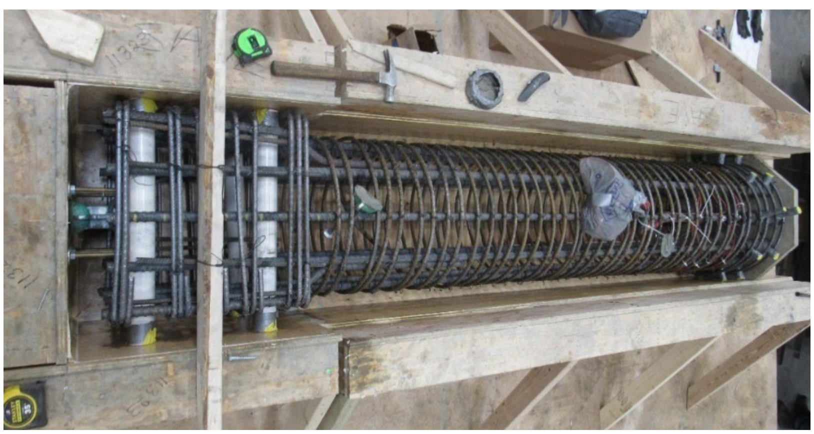

a) Column Cage

b) Column Pouring

Figure 3.20 Casting PHV Column

a) Matching Couplers and Dowel Bars

b) Column Secured

Figure 3.21 Erecting PHV Column

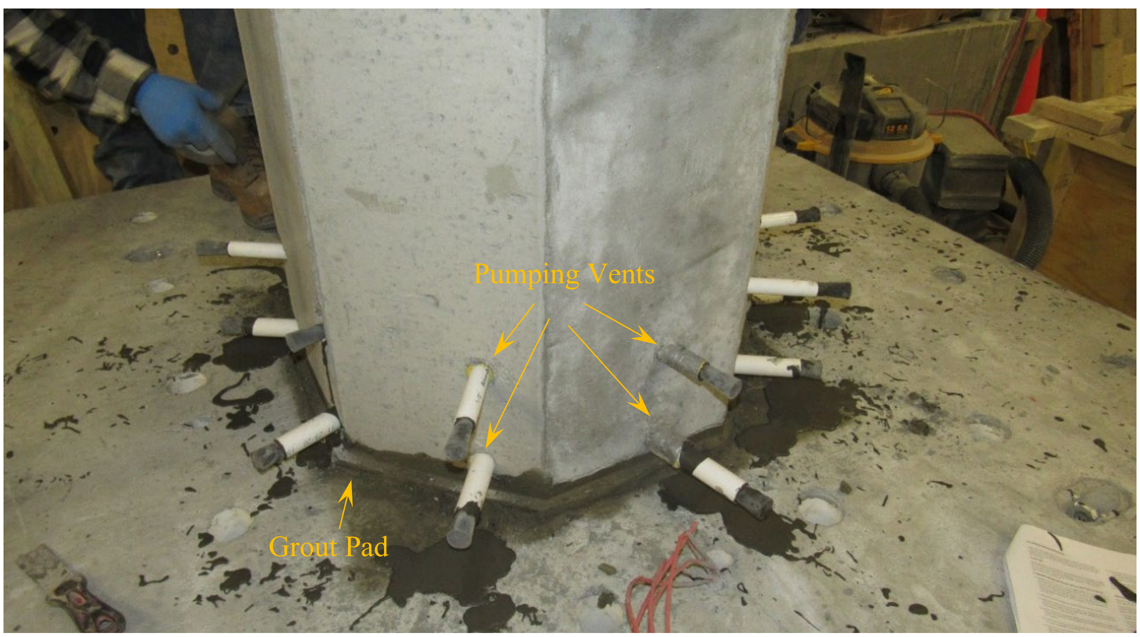

Figure 3.22 PHV Column Base After Coupler Grout Injection

The footing dowels were extended into the couplers with a maximum embedment depth of 7 in. (177.8 mm). Once the column was secured, the minimal gap at the column-footing interface was filled using a high-strength, non-shrink grout (1428HP). Finally, the couplers were injected with the “HY10L” high strength grout from bottom vents, and the specimen was left undisturbed until the grout reached a sufficient strength.

3.3.6 PTV Column Model

The PTV column model was detailed (Fig. 3.23) to incorporate the "nVent Lenton Ultimate PT15 Position" threaded couplers. The reinforcement for this column was the same as CIP. The clear cover at the section with the coupler was 1.75 in. (44.5 mm) and the clear cover away from the coupler was 2 in. (50.8 mm). To access the threaded couplers after the column casting, a closure pour detailing was devised. The coupler was spun into place and torqued once the precast column and footing were aligned. The exposed region around the coupler was then filled with a non-shrink high-strength, "1428 HP," grout.

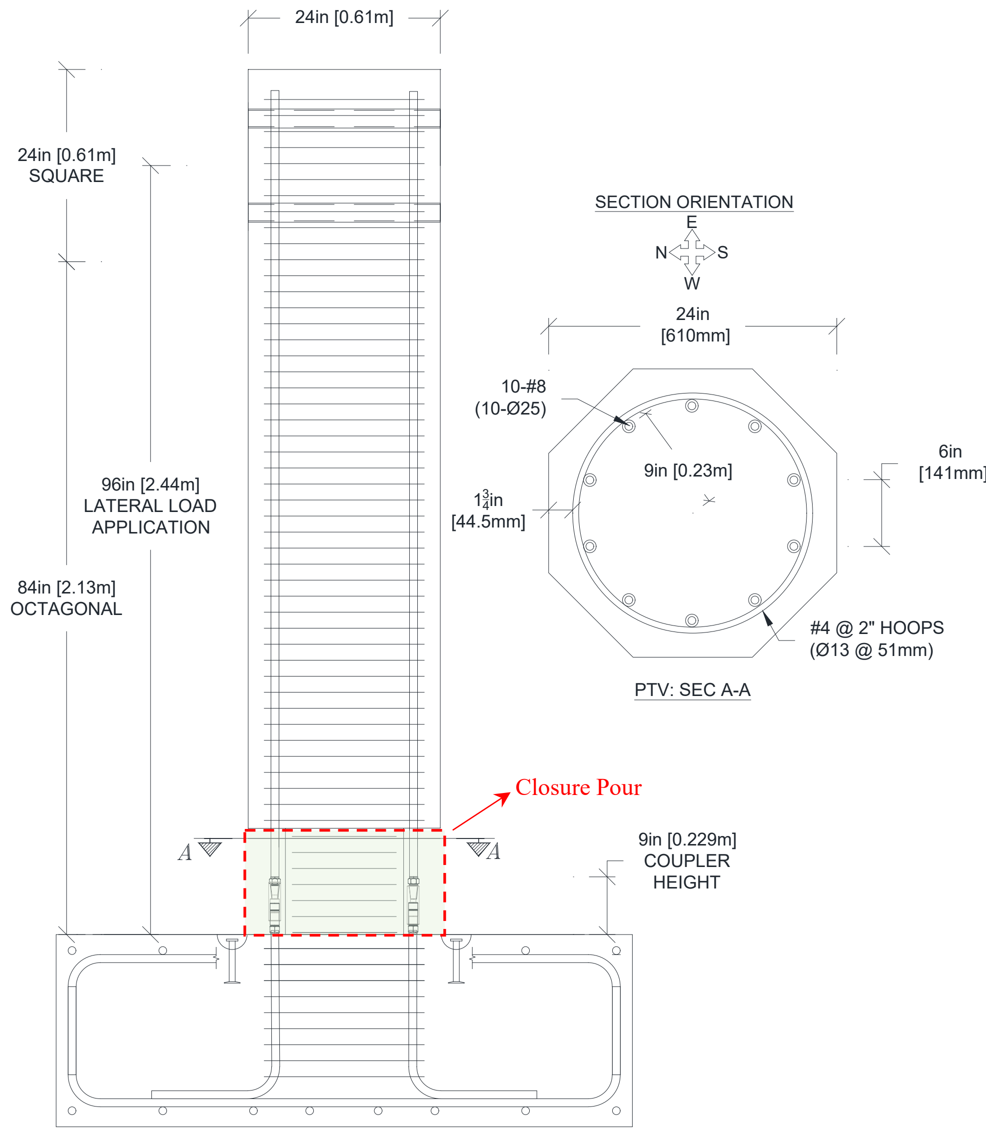

Figure 3.23 Reinforcement Detailing of PTV Column with Threaded Couplers

The construction sequence for PTV was:

- Cast the footing at SDSU with dowel threaded bars extended
- Cast the column at the precast plant with the couplers attached (Fig. 3.24)
- Position the column, torque the couplers, and tie the hoops at SDSU (Fig. 3.25)
- Closure pour using "1428 HP" grout at SDSU (Fig. 3.26)

a) Column Cage

b) Column Pouring

Figure 3.24 Casting PTV Column

a) Column in Position above Dowels

b) Coupler Torqued and Hoops Placed

Figure 3.25 Erecting PTV Column

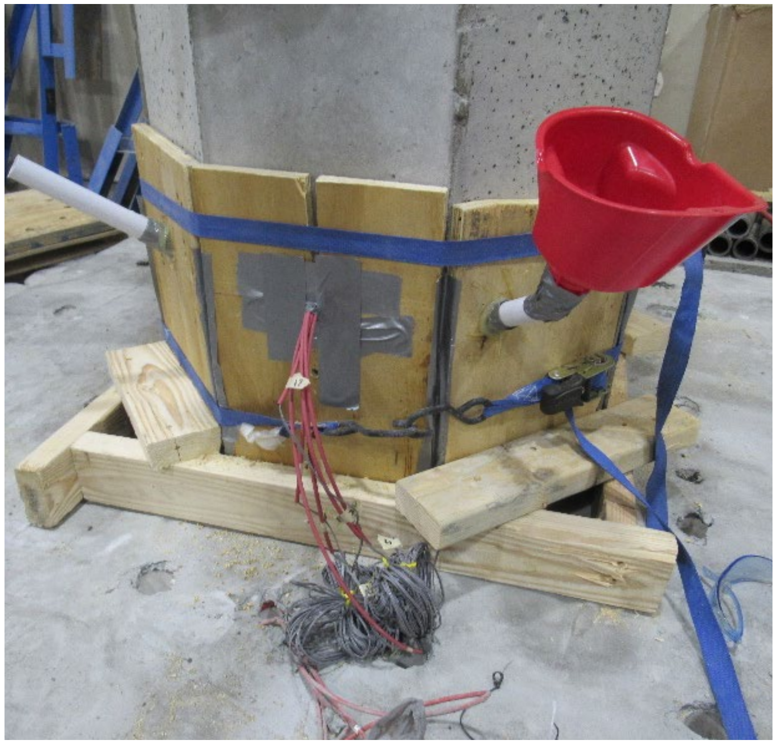

a) Closure Pour

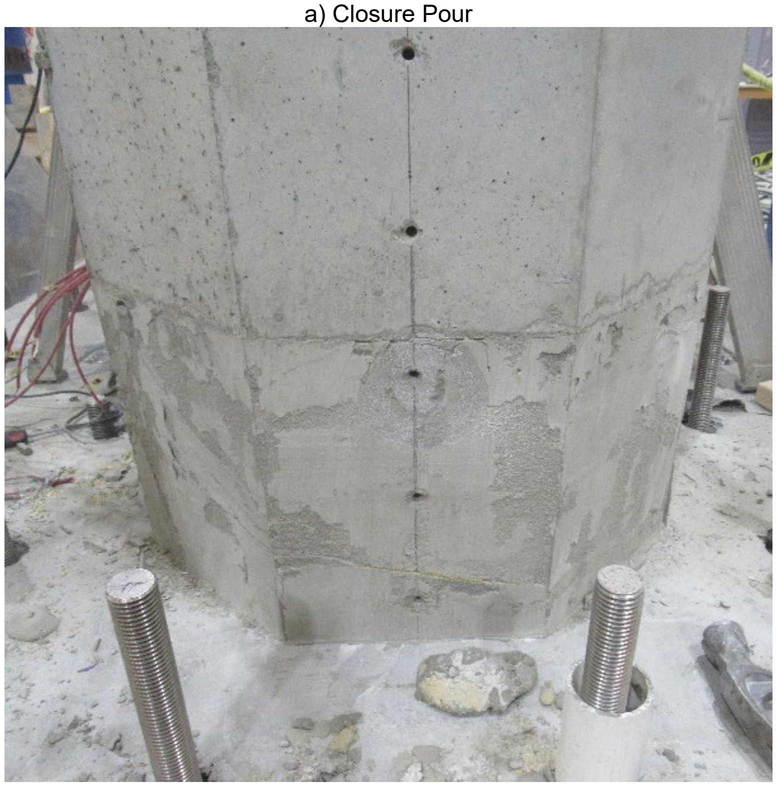

b) Column after Closure Pour

Figure 3.26 Closure Pour of PTV Column

3.3.7 PHH Column Model

The PHH model was detailed (Fig. 3.27) to incorporate HRC "HRC560" hybrid grouted-headed couplers. This product was developed during this project specifically for bridge column applications and was tested for the first time in the present study. The reinforcement for this column was the same as CIP. The clear cover at the sections with the couplers was 1.25 in. (31.75 mm) and the clear cover away from the coupler was 2 in. (50.8 mm). Following the HRC recommendation, an off-the-shelf product, "Quikrete 15800-00 Precision" grout, was used to fill the sleeves.

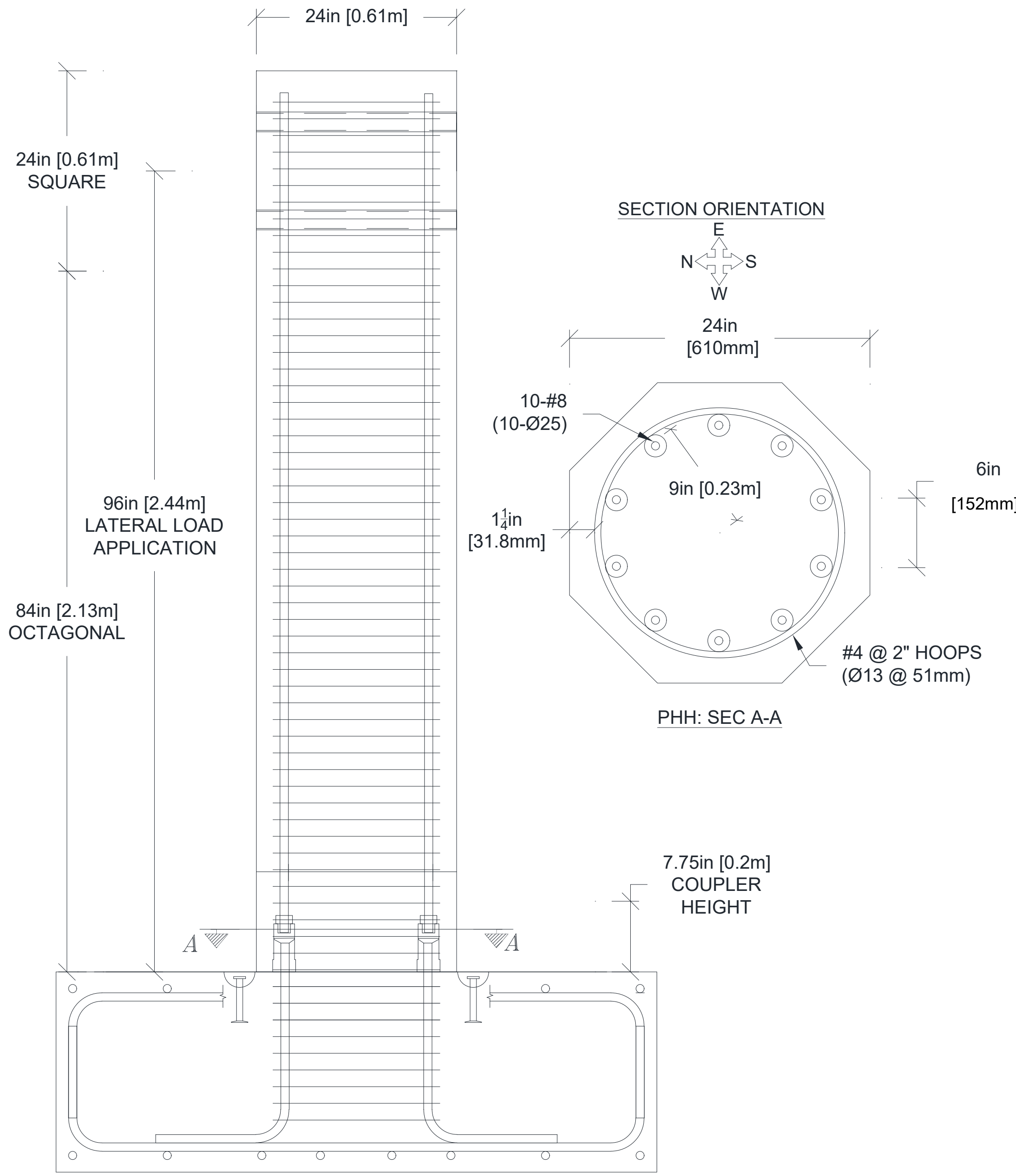

Figure 3.27 Reinforcement Detailing of PHH Column with Hybrid Grouted-Headed Couplers

The construction sequence for PHH was:

- Cast the footing at SDSU with dowel headed bars extended
- Cast the column at the precast plant with couplers embedded (Fig. 3.28)
- Erect and install the column at SDSU (Fig. 3.29)
- Fill the gap between the column and footing at SDSU
- Inject “Quikrete” grout into the couplers at SDSU (Fig. 3.30)

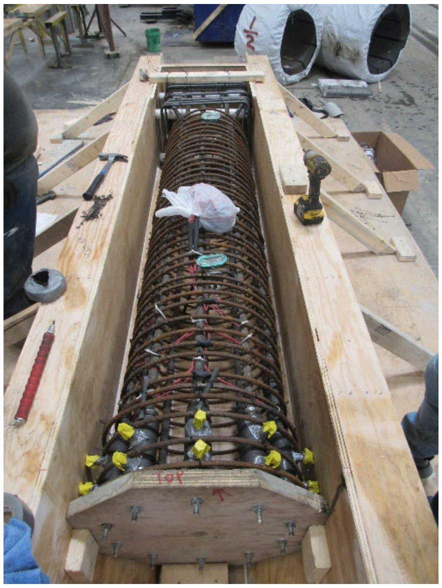

a) Column Cage

b) Column Pouring

Figure 3.28 Casting PHH Column

a) Column in Position above Headed Dowels

b) Matching Couplers and Dowel Bars

Figure 3.29 Erecting PHH Column

Note: all bars were cleaned before placement of the column.

a) Injecting Grout

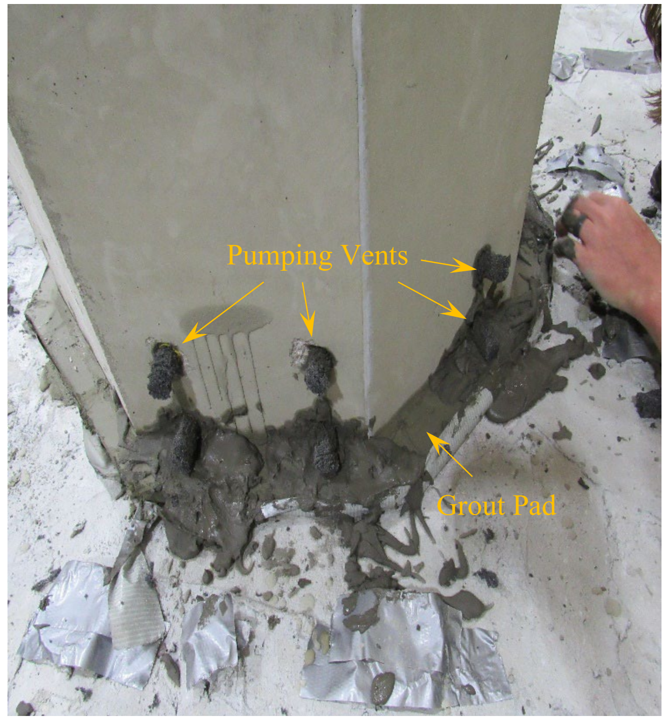

b) After Grouting

Figure 3.30 Injecting Grout into PHH Couplers

The footing dowels were extended into the couplers with a minimum embedment depth of 4.875 in. (124 mm) but not exceeding 5.75 in. (146 mm). Due to heading, this hybrid grouted coupler has the smallest length among other hybrid products available in the market. Once the column was secured, the minor gap at the column-footing interface was filled using a high-strength, non-shrink grout (1428HP). Finally, the couplers were injected with the "Quikrete 15800-00 Precision" grout from bottom vents.

3.3.8 RPH Column Model

The repairable precast column with headed couplers (RPH) (Fig. 3.31) used a similar cross section as the CIP column but incorporating a pipe-pin connection at the base to resist plastic shear forces. A circular reduced-diameter neck section was detailed to access and replace the exposed reinforcement. The exposed bars were designed to develop tensile and compressive (T&C) ultimate stresses of the bar, allowing a full moment-resisting joint. The combined use of the pipe-pin and the exposed bars with T&C mechanism was to develop a repairable moment-resisting joint for bridge columns. HRC couplers are detachable, allowing the bars to be replaced.

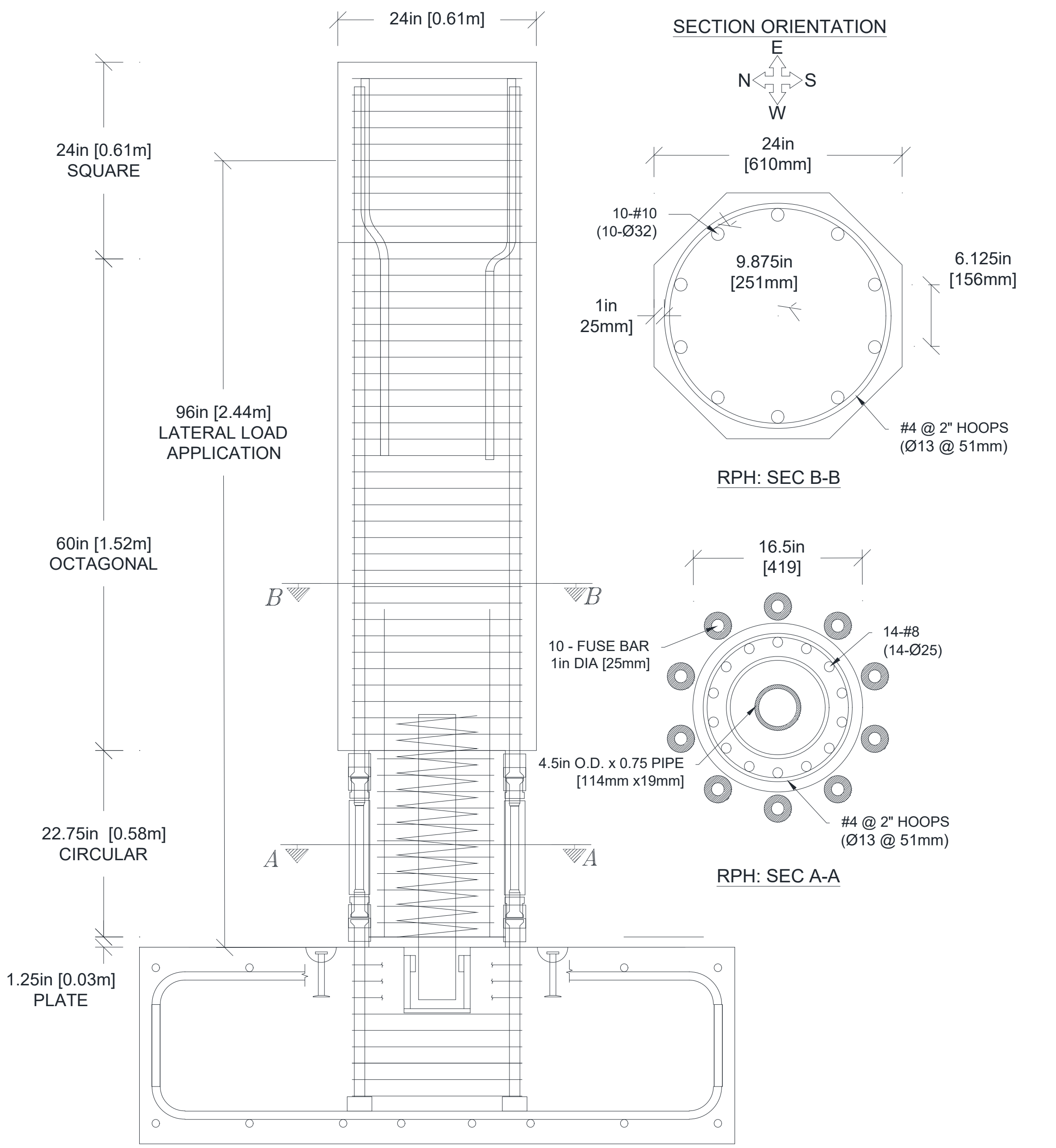

Figure 3.31 Reinforcement Detailing of RPH Column with Headed Couplers

Stainless steel bars were used instead of conventional black steel to improve the durability of the exposed elements. The bars extended out of the footing and the octagonal column section and were headed to accommodate the female portion of Headed Reinforcement Corp. (HRC) 500 Series couplers. Headed fuse bars accommodating the male portion of the couplers on either end could then be screwed into the reduced neck section of the column.

The RPH longitudinal bars were increased in size from No. 8 (Ø25 mm) to No. 10 (Ø32 mm) to ensure that the bar yielding will occur within the fuses and not elsewhere in the column. The replaceable fuse bars were machined down from No. 10 (Ø32 mm) to 1.0 in. (25 mm) in diameter (Fig. 3.32) to match the CIP longitudinal reinforcement. In an initial testing, the exposed bar (painted in yellow) had a "dog-boned" length of 10.25 in. (260 mm) while the reduced diameter length was 5.125 in. (130 mm) in the second testing, in which the column was repaired by replacing those exposed bars (painted in green). Different fuse lengths were used to investigate their effects on the column overall ductility. Larger hoops were necessary to accommodate the increased longitudinal bar diameters, which reduced the column clear cover to 1 in. (25 mm). The fuse bars were placed inside steel tubes and filled with "1428 HP" grout to prevent buckling. These exposed buckling restrained bars are hereafter referred to as BRR. BRR was designed following the recommendation by Boudaqa et al. (2017).

The neck section was designed assuming a secondary moment occurs in the opposite direction of the main column moment due to the lateral force against the pin connection. A moment-curvature analysis was performed in OpenSees (2016), assuming a 16.5-in. (419-mm) diameter neck section longitudinally reinforced with BRR outside the neck, to determine the moment capacity of the column at the BRR section (Sec. A-A in Fig. 3.31). Subsequently, the corresponding lateral force at the column base was determined by dividing the maximum moment to the column length. This peak baseshear will cause a secondary moment at the top of the neck, which was approximately 24 in. (610 mm) above the footing surface. This moment was further increased with an overstrength factor of 1.2 and was used to design the longitudinal reinforcement of the neck. This was done to ensure that the neck section of the column remains linear-elastic with minimal damage during testing. Following this design, the required longitudinal reinforcement within the neck was 14 No. 8 (14-Ø25 mm) conventional black steel bars with No. 4 (Ø13 mm) transverse hoops spaced at 2 in. (51 mm) to match the upper portion of the column. An additional 10-in. (254-mm) O.D. No. 3 (Ø10-mm) spiral was incorporated in the neck section to provide additional confinement for the steel pipe.

The pipe-pin connection was designed using the recommendations by Zaghi and Saiidi (2010). In this case, the reference lateral load capacity was taken as the lesser of the pure shear capacity of the in-filled (including the concrete within the pipe) steel pipe and the moment capacity of the pipe multiplied by its plastic hinge length. The shear capacity of the concrete in the neck, both sets of transverse reinforcement, and the pipe (determined using the ultimate moment capacity of the pipe) were also added to determine the shear capacity of the neck section. The steel cup within the footing was assumed to have a significant shear capacity due to the large amount of concrete and reinforcement within the footing. It was found that the shear capacity of the in-filled pipe governed the design.

The pipe-pin connection consisted of a 4.5 in. (114 mm) O.D. x 0.375 in. (10 mm) wall steel pipe, which protruded into the neck section by 6.625 in. (168 mm). A 0.5-in. (13-mm) plate was welded to the base of an 8-in. (203 mm) O.D. x 0.75 in. (19 mm) wall steel tube to provide a cup for the pipe to be inserted into. An additional 6.5 in. (165 mm) O.D. x 0.625 in. (16 mm) wall tube of length 2 in. (51 mm) was welded inside the upper portion of the larger cup to provide a contact surface for the pipe while still allowing the column to rotate.

A 1.25-in. (32-mm) thick steel plate with a diameter matching that of the neck section was placed between the column and footing to prevent concrete crushing during testing as the column rocked. The plate had a 6-in. (152-mm) diameter hole at the center to allow for the pipe to pass through the cup embedded in the footing.

a) Dog-boned Fuse Bars and Couplers

b) Fuse Bars and Steel Tubes

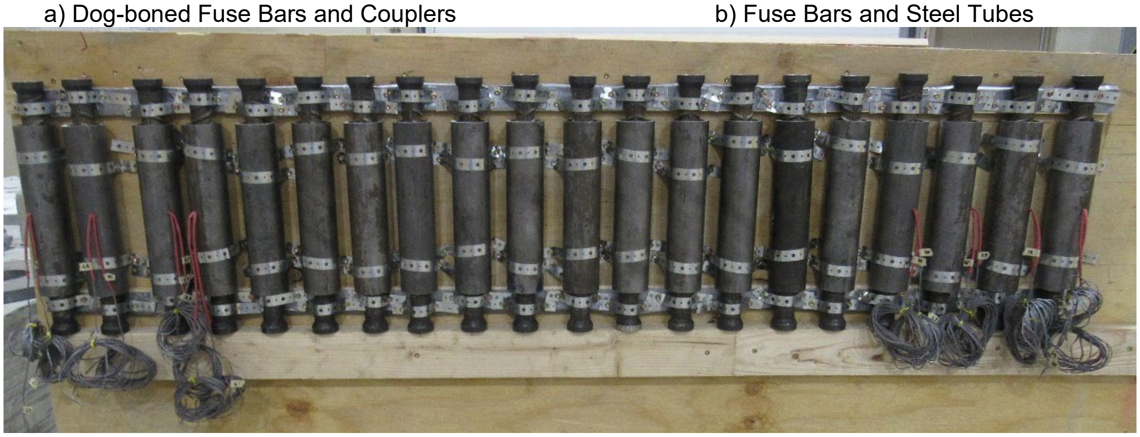

c) BRR Grout Pour Setup

Figure 3.32 Construction of RPH Fuses

Similar to other precast columns, the RPH specimen was built by Gage Brothers in Sioux Falls, SD, while the footing was constructed at SDSU to reduce costs. The construction sequence for RPH was:

- Cast the column at precast plant with female portion of the couplers on headed longitudinal bars (Fig. 3.33)
- Cast footing at SDSU with female portion of couplers on the headed longitudinal bars (Fig. 3.34)
- Construct the BRR fuses at SDSU (Fig. 3.32)
- Erect and install the column (Fig. 3.35)
- Insert the fuses, tighten the couplers, and add clamping collars to prevent buckling of the bars outside the couplers (Fig. 3.36)

a) Column Cage b) Concrete Pouring

Figure 3.33 Casting of RPH Column

a) Footing Cage b) Footing after Casting, Steel Socket at Middle

Figure 3.34 Casting of RPH Footing

a) Inserting Steel Pipe into Steel Socket   b) Lowering Column

Figure 3.35 Erecting RPH Column

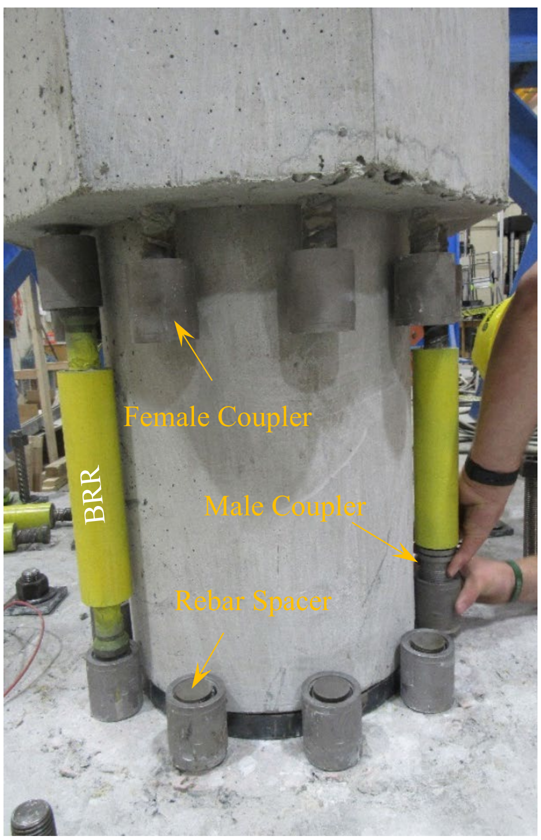

b) Tightening Couplers

a) Inserting Fuses   c) Clamping Collars and Shims

Figure 3.36 RPH BRR Fuse Installation

The longitudinal bars were extended out of both the footing and the main column cross section with a length of 3.375 in. (86 mm). After column installation, there was a head-to-head distance of 7.25 in. (184 mm), which resulted in a total gap of 0.25 in. (6 mm) between the bar heads when the 7-in. (178-mm) long fuses were inserted. This gap was closed by inserting circular 0.125-in. (3-mm) spacers between the heads of the bar. The couplers were first tightened by hand before using a pipe wrench. The remaining gap between the female portion of the couplers and the footing/main column section was closed using 1.325-in. (34-mm) bore clamping collars as well as steel washers (Fig. 3.36). A slight gap between the base of the column and the steel plate was noticeable on the southeast corner of the column and was filled by inserting rectangular 16-gauge (1.59-mm) steel shims.

3.4 Test Setup, Instrumentation, and Loading Protocol

The test setup, instrumentation, and loading protocol were designed and selected to simulate seismic actions. This section discusses these topics in detail.

3.4.1 Test Setup

The modular lateral test setup, which was designed and constructed as part of this project, provides a cantilever configuration to laterally test a column specimen (Fig. 3.37). The actuator was mounted to a series of 3 x 5 x 8-ft (0.91 x 1.52 x 2.44-m) concrete reaction blocks that were post-tensioned to the lab strong floor. A 328-kip (1460-kN) hydraulic actuator was used to apply lateral loads at the column head. The column axial load was applied using a self-reacting system with two hollow core jacks installed on a spreader beam perpendicular to the loading direction with high-strength threaded rods transferring the load from the jacks to the column footing.

3.4.2 Instrumentation

Local and global column responses were measured using multiple instruments. Bar strains were measured using strain gauges installed at different levels. Figure 3.38 shows the strain gauge plan. Strain gauges were not placed in the sections where a coupler was present. Table 3.2 shows the strain gauge schedule for all column models. Rotations and curvatures were measured within the plastic hinge of the columns using linear variable displacement transducers (LVDTs) placed on the opposite faces of the column in the direction of loading at different levels (Fig. 3.39). The lateral displacements of the column tip and its rotations were measured using three string potentiometers as shown in Fig. 3.39. The lateral load on the column was measured using the actuator load cell. Furthermore, two 100-kip (445-kN) load cells were placed above the hollow core jacks, one per jack, to measure the column axial loads during testing. In all tests, the target axial load was 155 kips (689 kN), which was slightly different in different columns and was adjusted during testing to achieve the target load at large displacements. Note that the applied axial load was equivalent to approximately 5% axial load index for a design concrete strength of 6,000 psi (41.4 MPa). However, the index varied based on the actual concrete strength at the column test day. A 128-channel data acquisition system was used to record data with a sampling rate of 10 Hz.

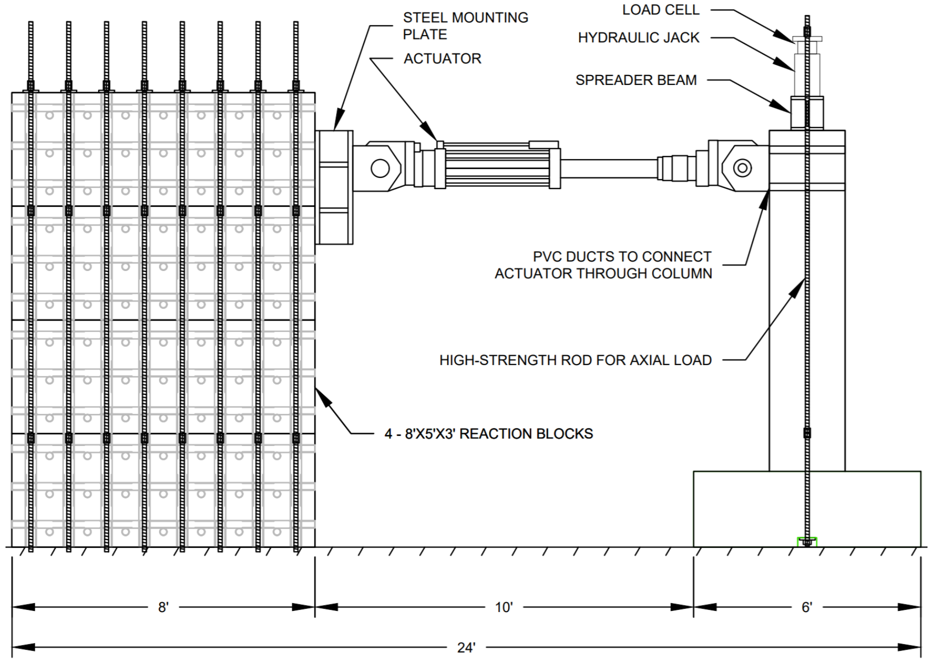

a) Column Test Setup Elevation View

b) Photograph of Column Test Setup

Figure 3.37 Column Test Setup

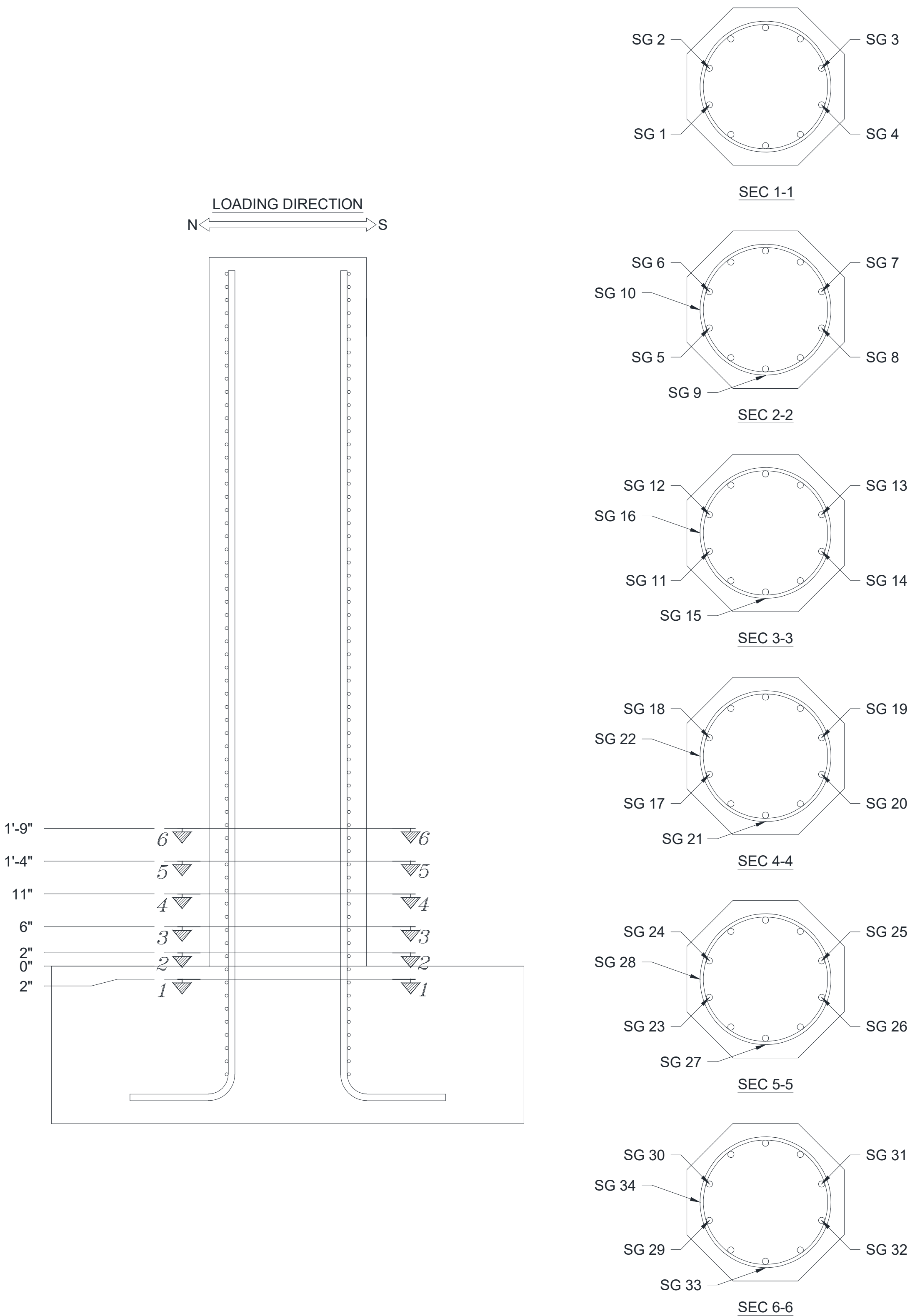

Figure 3.38 Typical Strain Gauge Sections and Elevations Used in Column Models

Table 3.2 Column Model Strain Gauge Placement Schedule

Column	Sections Where Strain Gauges Were Placed					
	SEC 1-1	SEC 2-2	SEC 3-3	SEC 4-4	SEC 5-5	SEC 6-6
CIP	X	X	X	X	X	X
PGD	X	No SG	No SG	No SG	X	X
PGS	X	No SG	No SG	No SG	X	X
PHD	X	No SG	No SG	X	X	X
PHV	X	No SG	No SG	X	X	X
PTV	X	No SG	No SG	X	X	X
PHH	X	No SG	No SG	X	X	X
RPH*	X	X	No SG	X	X	X

Note: "X" indicates that strain gauges were placed in column cross sections shown in Fig. 3.38.
* For RPH, 10 concrete strain gauges were placed at the rocking interface following the bar distribution pattern.

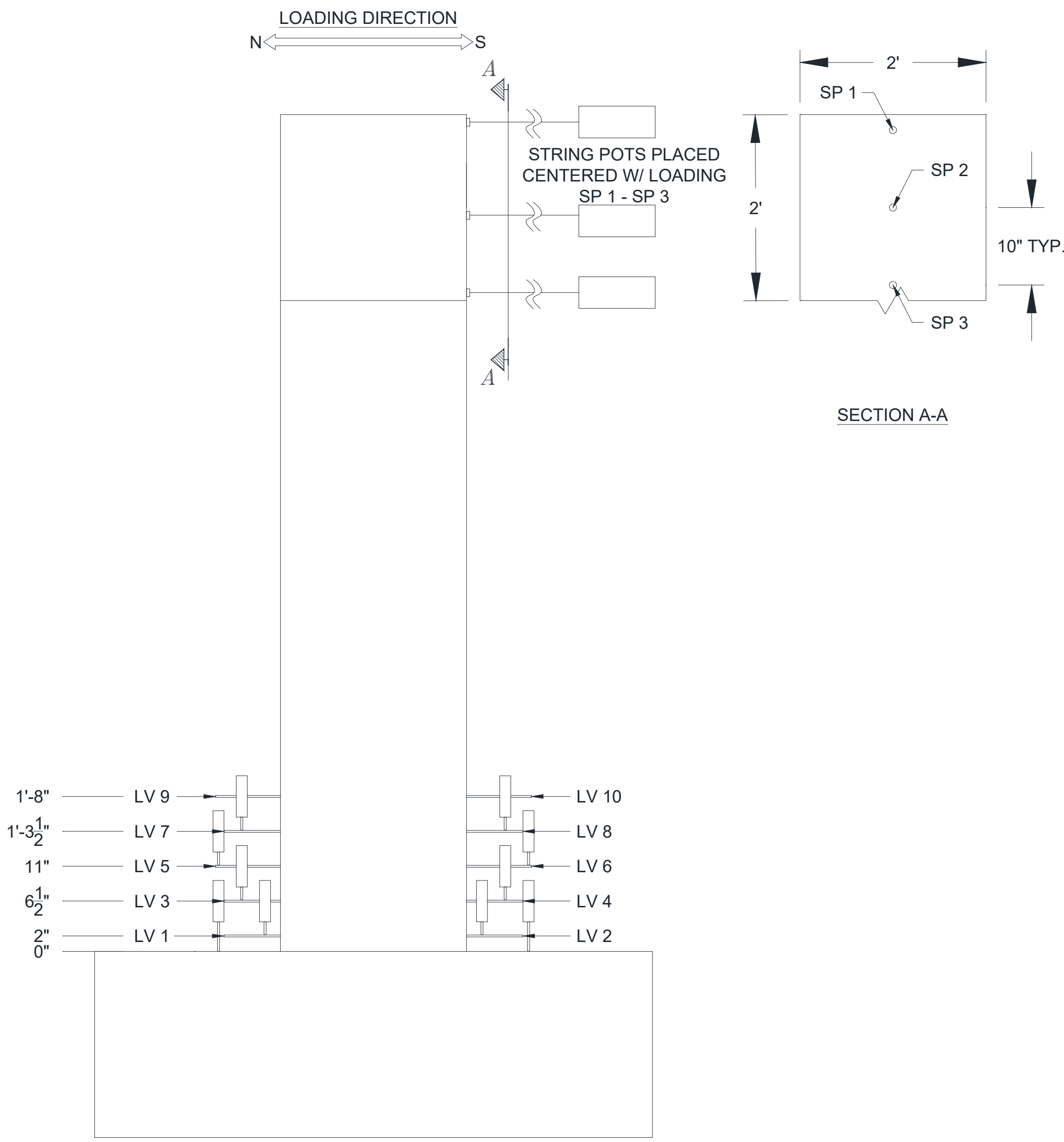

Figure 3.39 Typical LVDT & String Potentiometer Locations Used in Column Models

3.4.3 Loading Protocol

The column models were tested using a slow cyclic lateral drift-based loading following ACI 374.2R-13 (2013). The drift is the ratio of column lateral displacement to the column height. Figure 3.40 shows the loading protocol for each test. Two full cycles were completed at each drift level. A displacement rate of 3.0 in./min (76.2 mm/min) was used for drift ratios from 0.25% to 2% to capture the yield point. A 10-time faster displacement rate of 30 in./min (762 mm/min) was used for drift ratios including 3% to failure. The displacement rates were estimated based on ASTM E8 strain rate limits for steel bar tensile testing.

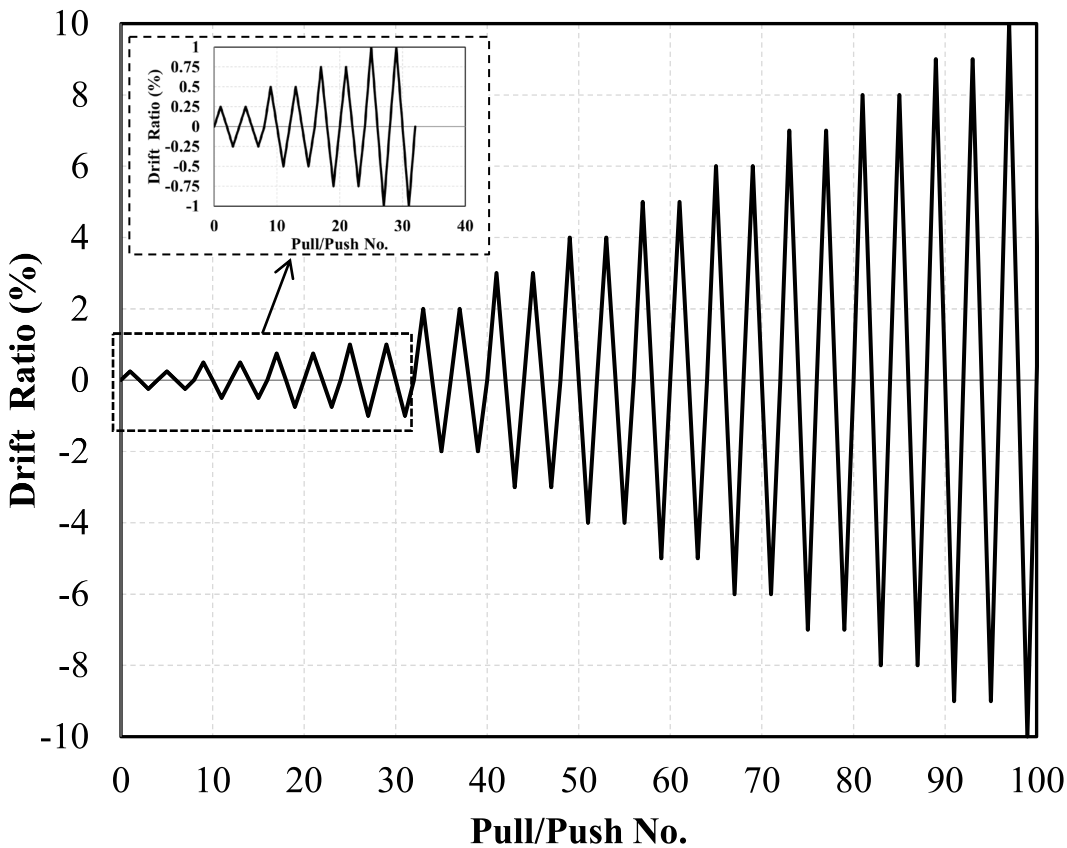

Figure 3.40 Typical Loading Protocol Used for Column Testing

3.5 Test Results

Testing of all columns was conducted in the Lohr Structures laboratory at SDSU. Each of the precast columns used a different model of mechanical bar splice at the column base. All columns were tested using the same displacement-controlled loading discussed in the previous section. The constitutive materials of each column model were also tested to determine their mechanical properties. The results of material testing and column testing are presented in this section.

3.5.1 Material Properties

Several materials were used in the construction of the columns, including conventional concrete, self-consolidating concrete (SCC), different non-shrink grout types, different reinforcing steel bars, and seven products of mechanical bar splices. The measured properties of each material, following their standard ASTM procedures, are presented herein.

3.5.1.1 Conventional Concrete

Conventional concrete was used in the footing for all models and in the CIP column. The concrete compressive strength testing was conducted according to ASTM C39/C39M in which standard concrete cylinders with a diameter of 6 in. (152 mm) and a height of 12 in. (305 mm) were used. Table 3.3 presents the measured compressive strength of cementitious materials used in each column model. The average concrete compressive strength of three samples was reported in the table at 7-day, 28-day, and the test day of each column model.

3.5.1.2 SCC

All precast columns were built with SCC. The sample sizes and testing procedure were the same as conventional concrete. The SCC measured compressive strength at 7-day, 28-day, and column test day is reported in Table 3.3.

3.5.1.3 Non-Shrink Grout

Non-shrink grout was injected into the grouted and hybrid couplers per the coupler manufacturer's requirements. "D410 Sleeve Lock," "SS Mortar," and "Quikrete 1580-00" grouts were used for the PGD, PGS, and PHD column models, respectively. "Quikrete 1580-00" and "HY10L" grouts were used for the PHH and PHV column models, respectively. For PTV, which utilized a threaded coupler, the "1428 HP" grout was used in the cast-in-place closure pour. Two-inch (51-mm) cube samples were collected according to ASTM C109/C109M and were tested according to ASTCM C109/C109M. Table 3.3 presents the measured grout compressive strength. Note many samples were tested prior to the column testing to decide when to test the column, but those intermediate tests were not reported in the table.

Table 3.3 Measured Compressive Strength of Cementitious Materials Used in Column Models

Material	Element	Measured at	Column Model							
			CIP	**PGD**	**PGS**	**PHD**	**PHV**	**PTV**	**PHH**	**RPH**
Conventional Concrete & SCC*	Footing	7-Day	3670 (25.3)	4365 (30.1)	3275 (22.6)	5435 (37.5)	3472 (23.9)	4266 (29.4)	3700 (25.5)	5954 (41.1)
		28-Day	4620 (31.9)	N/A	3900 (26.9)	6335 (43.7)	4041 (27.9)	4743 (32.7)	N/A	6894 (47.5)
		Col. Test Day	4920 (33.9)	4830 (33.3)	3980 (27.4)	6770 (46.7)	4304 (29.7)	5176 (35.7)	4523 (31.2)	7421 (51.2)
	Column	7-Day	3360 (23.2)	6980 (48.1)	7890 (54.4)	8380 (57.8)	8919 (61.5)	8826 (60.9)	9150 (63.1)	9161 (63.2)
		28-Day	4010 (27.6)	7950 (54.8)	8880 (61.2)	8875 (61.2)	9715 (67.0)	9738 (67.1)	N/A	10189 (70.3)
		Col. Test Day	4300 (29.6)	7950 (54.8)	8590 (59.2)	9640 (66.5)	10120 (69.8)	10115 (69.7)	9782 (67.4)	10699 (73.8)
Grout**	Coupler	7-Day	N/A	11160 (76.9)	13130 (90.5)	7140 (49.2)	6777 (46.7)	9210† (63.5)	8970 (61.8)	6132‡ (42.3)
		28-Day	N/A	N/A	N/A	N/A	10622 (73.2)	N/A	N/A	N/A
		Col. Test Day	N/A	12680 (87.4)	14680 (101.2)	15480 (106.7)	17895 (123.4)	10963† (75.6)	11725 (80.8)	7055‡ (48.7)

* Conventional concrete was used in the CIP column and all footings. SCC was used in the precast columns.
** "D410 Sleeve Lock," "SS Mortar," and "Quikrete 1580-00" grouts were used for the PGD, PGS, and PHD column models, respectively. "Quikrete 1580-00," "1428 HP," and "HY10L" grouts were used for the PHH, PTV, and PHV column models, respectively.
† The coupler was threaded; but the "1428 HP" grout was used in the closure pour.
‡ For RPH, "1428 HP" was used to fill BRR tubes.

3.5.1.4 Reinforcing Steel

The reinforcing steel bars used in all columns except RPH conformed to ASTM A706 Grade 60 (413.7 MPa). Stainless steel was used in RPH as the longitudinal bars. Further, ASTM A615 Grade 60 (413.7 MPa) was used in the footings of all columns. The columns, except RPH, were longitudinally reinforced with No. 8 (Ø25 mm) black steel bars and transversely reinforced with No. 4 (Ø13 mm) black steel hoops. The longitudinal bars used in all columns except RPH were from the same heat number (batch) and therefore had the same properties. This was done to minimize the column response variations. The transverse reinforcement used in the CIP model was from one heat number, while the transverse reinforcement used in the precast models came from another heat number.

Both conventional black steel conforming to ASTM A706 Grade 60 (413.7 MPa) and stainless steel conforming to ASTM A955-12 Grade 60 (413.7 MPa) were used in the RPH column. The repairable column was longitudinally reinforced using No. 10 (Ø32 mm) stainless steel bars. Furthermore, the BRR fuse bars were the dog-boned version of the same stainless steel bars but machined down to a diameter of 1 in. (25 mm) to match the CIP column longitudinal bar area. RPH was transversely reinforced with No. 4 (Ø13 mm) hoops at 2 in. (51 mm) pitch.

Tensile testing of all rebars was conducted according to ASTM E8. Table 3.4 presents the measured average tensile properties for different bars used in the columns. A sample of the longitudinal bar stress-strain behavior is presented in the following section accompanied with the coupler behavior.

Table 3.4 Measured Strength of Reinforcing Steel Used in Column Models

Bar	Column Model	Bar Size	ASTM Type	Yield Strength, f_y ksi (MPa)	Ultimate Strength, f_u ksi (MPa)	Post-Yield Stiffness, E_{sh} ksi (MPa)	Ultimate Strain*, ε_u (%)
Longitudinal	All Models Except RPH	No. 8 (Ø25)	A706 Gr. 60	69.3 (478)	97.4 (672)	853 (5880)	12.0
	RPH	No. 10 (Ø32)	A955 Gr. 60	90.4 (632)	113.4 (782)	141.1 (973)	16.6
Hoops	CIP	No. 4 (Ø13)	A706 Gr. 60	66.6 (459)	102.1 (704)	1873 (12910)	9.9
	Precast	No. 4 (Ø13)	A706 Gr. 60	65.3 (450)	100.7 (694)	2567 (17700)	9.8
	Repairable Precast	No. 4 (Ø13)	A706 Gr. 60	65.3 (450)	100.7 (694)	2567 (17700)	9.8

* Strain at the peak stress

3.5.1.5 Couplers

Monotonic tensile loading was conducted on two to five samples of each of the coupler types used in the precast column models. The test protocol followed the recommendations of Dahal and Tazarv (2020). The displacement-based loading was conducted at a rate of 0.021 in/in/min. Figure 3.41 shows the mechanical bar splice testing setup, and Figure 3.42 shows the geometry of the coupler specimens. The total specimen length (L_{tot}) depends on the bar diameter and the physical length of the splice (L_{sp}). The coupler region length (L_{cr}) is the coupler length plus α (alpha) times the bar diameter ($\alpha.d_b$) from each end of the coupler. An alpha of 1.25 in. (31.8 mm) was used for all coupler samples tested in this study. The length of bar outside of the coupler was always at least 6 in. (152.4 mm) to avoid stress concentration.

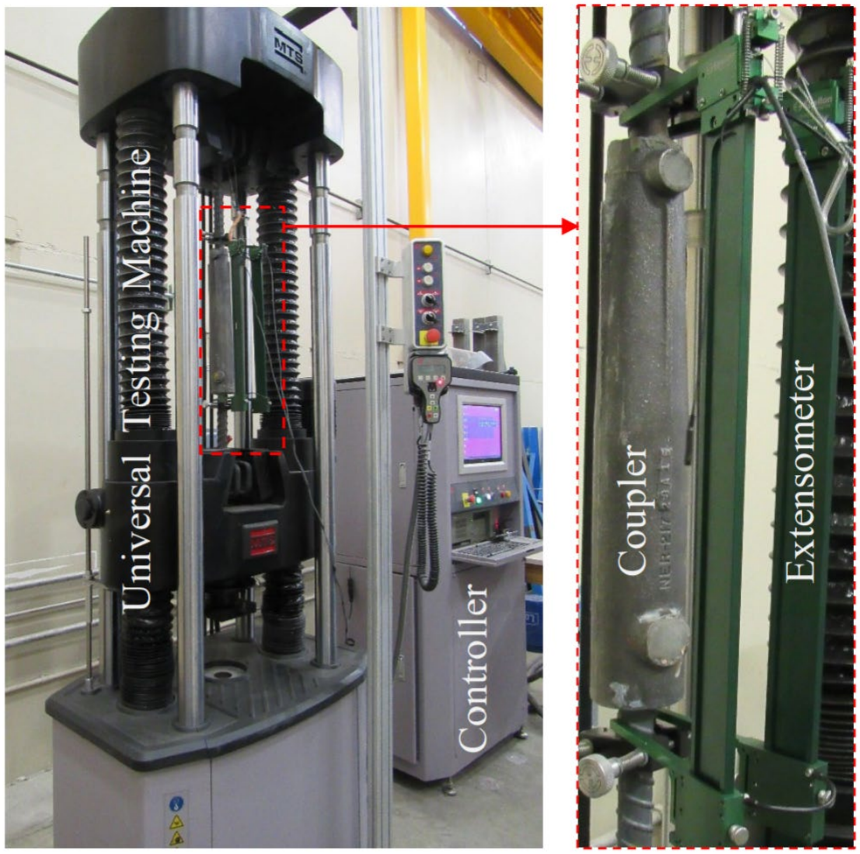

Figure 3.41 Test Setup for Mechanical Bar Splices

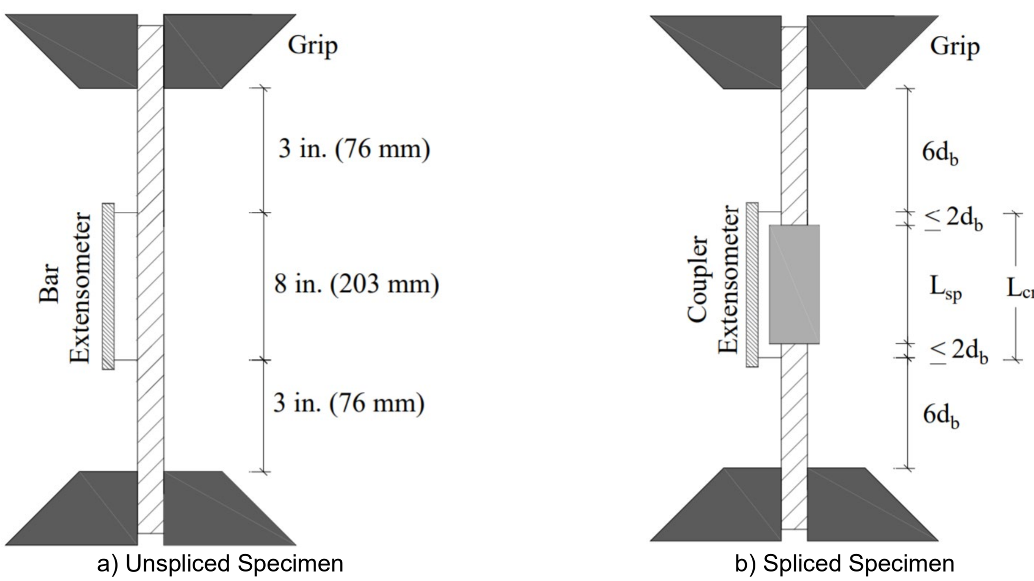

Figure 3.42 Geometry of Tensile Testing on Bar and Coupler Specimens

Figure 3.43 shows the tensile test results for the No. 8 (25-mm) Dayton Superior Sleeve-Lock couplers. The couplers, respectively, showed a reduction in the ultimate strain compared with the reference bar of 63%, 56%, 58%, 63%, and 64% in Runs 1 through 5. The average reduction in the ultimate strain compared with the unspliced reference bar was 61%. Out of five samples, bars fractured in four couplers and a bar pulled out from one sample (the first sample tested that had the lowest grout strength) at 4.4% strain. Overall, this coupler was rated as a “seismic coupler”.

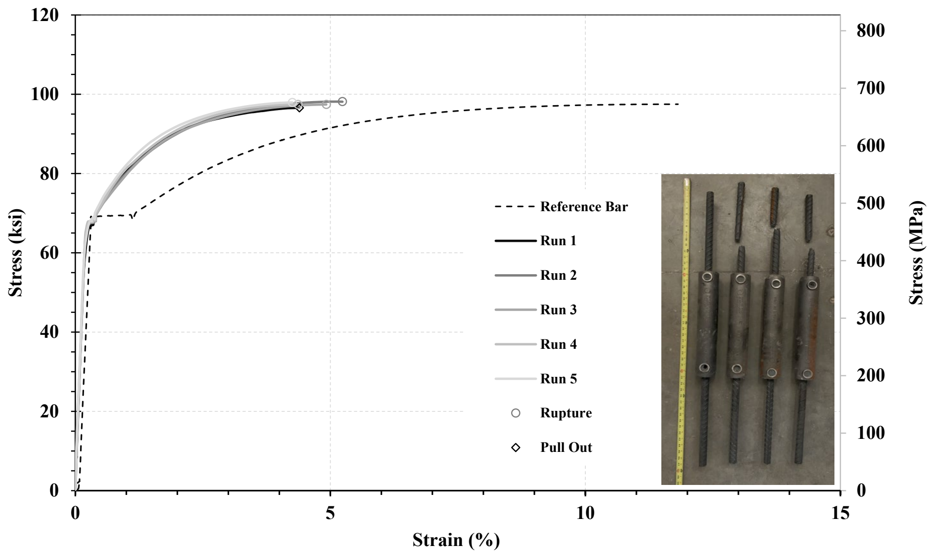

Figure 3.43 Tensile Test Results for No. 8 (25-mm) Dayton Superior Sleeve-Lock Couplers

Figure 3.44 shows the tensile test results for the No. 8 (25-mm) NMB Splice Sleeve couplers. Bars fractured in all five specimens, and the reduction in the ultimate strain compared with the reference bar was, respectively, 58%, 61%, 60%, 60%, and 65% for Runs 1 through 5. The average reduction in strain compared with the unspliced reference bar was 61%. Overall, this coupler was rated as a “seismic coupler.”

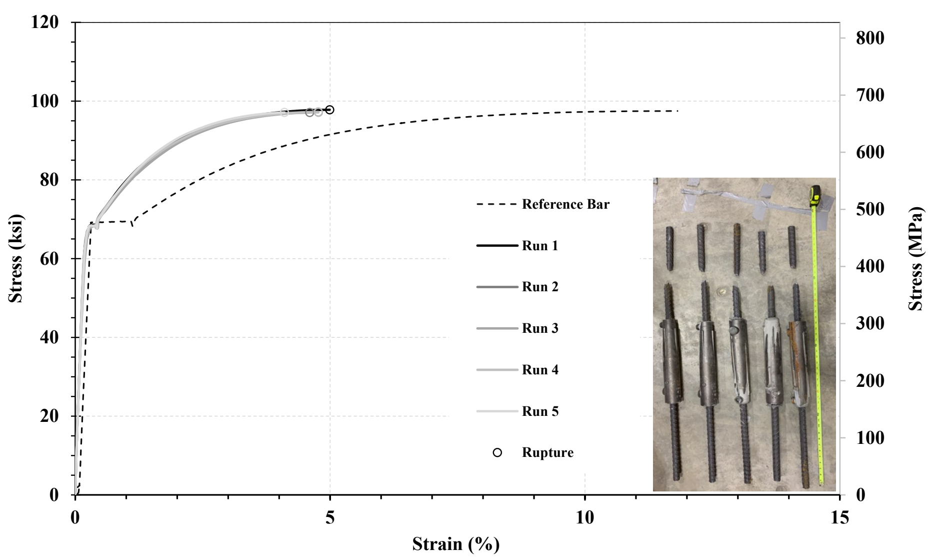

Figure 3.44 Tensile Test Results for No. 8 (25-mm) NMB Splice Sleeve Couplers

Figure 3.45 shows the tensile test results for the No. 8 (25-mm) Dextra Groutec S couplers. The couplers showed a reduction in the ultimate strain compared with the reference bar of 80%, 75%, 47%, 38%, and 74%, respectively, for Runs 1 through 5. The average reduction in the strain capacity compared with the unspliced reference bar was 63%. Bars pulled out from four couplers and a bar fractured in one specimen but inside the coupler. Overall, this coupler type was rated as a "non-seismic coupler," thus they should not be used in bridge columns with this performance. It should be noted that the failure mode observed in the present project was not consistent with the previous coupler testing reported by the manufacturer. After communicating the issue with the manufacturer, the reason for bar pullout could not be determined. The actual grout strength in our tests was higher than the required strength.

The research team recommends that the manufacturer, Dextra, provides a specific grout type for field use, not a commercial off-the-shelf product, which was used in this project per Dextra's recommendations. In summary, a better grout product with some quality control measures should be specified/provided by the manufacturer for bridge column applications to achieve a consistent performance of "seismic couplers."

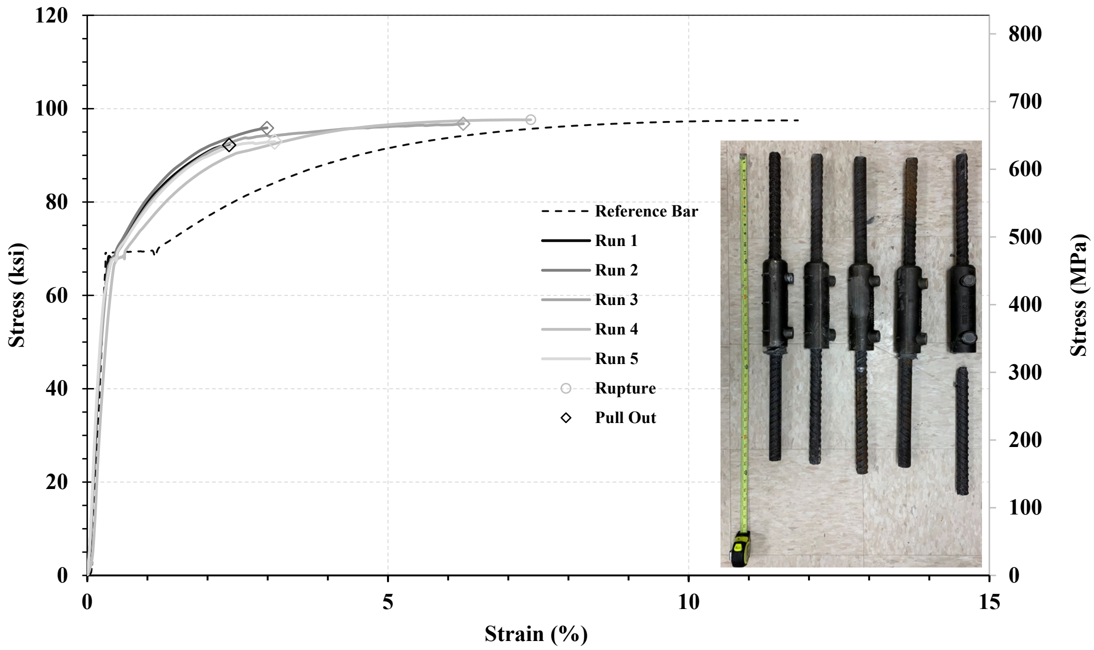

Figure 3.45 Tensile Test Results for No. 8 (25-mm) Dextra Groutec S Couplers

Figure 3.46 shows the tensile test results for the No. 8 (25-mm) nVent Lenton Interlock couplers. The couplers, respectively, showed a reduction in the ultimate strain compared with the reference bar of 63% and 64% in Runs 1 and 2. The average reduction in the ultimate strain compared with the unspliced reference bar was 63.5%. Bar fracture was observed in both coupler tests. Overall, this coupler was rated as a "seismic coupler."

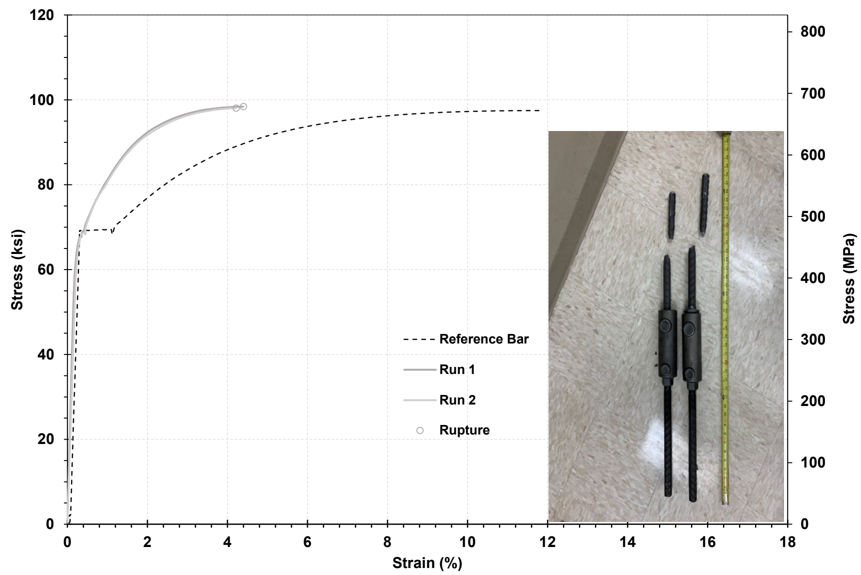

Figure 3.46 Tensile Test Results for No. 8 (25-mm) nVent Grouted-Threaded Couplers

Figure 3.47 shows the tensile test results for the No. 8 (25-mm) nVent Lenton Ultimate PT15 Position threaded couplers. The couplers showed a reduction in the ultimate strain compared with the reference bar of 30% and 20% in Runs 1 and 2, respectively. The average reduction in the ultimate strain compared with the unspliced reference bar was 25%. Bar fracture was observed in both coupler tests. Overall, this coupler was rated as a "seismic coupler."

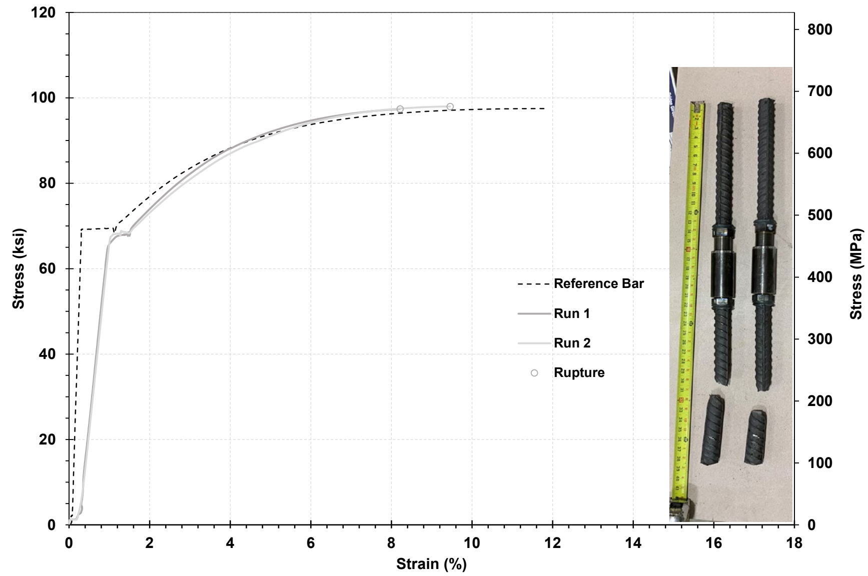

Figure 3.47 Tensile Test Results for No. 8 (25-mm) nVent Threaded Couplers

Figure 3.48 shows the tensile test results for the No. 8 (25-mm) HRC hybrid (grouted-headed) couplers. The couplers exhibited a reduction in the ultimate strain compared with the reference bar of 68% and 53% in Runs 1 and 2, respectively. The average reduction in the ultimate strain compared with the unspliced reference bar was 60.5%. The first sample, Run 1, had a full embedment length of bar into the grouting section of the coupler. However, the second sample, Run 2, had a lower embedment length compared with the first specimen to match the actual bar-into-coupler embedment length that was achieved in the column (4.875 in., or 123.8 mm). Overall, bar fractured in both tensile tests, thus this coupler was rated as a "seismic coupler."

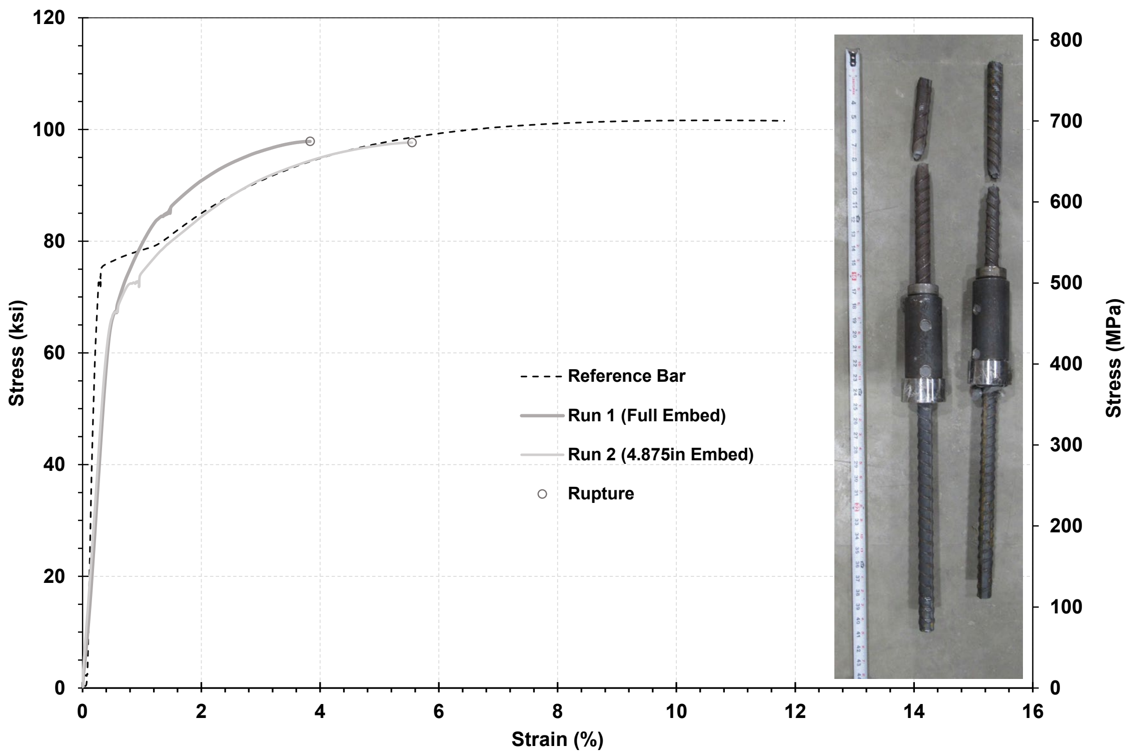

Figure 3.48 Tensile Test Results for No. 8 (25-mm) HRC Hybrid Couplers

The coupler rigid length factor, a mechanical property specific to bar couplers, based on the coupler ultimate strain (β_u) was calculated for each splice following to the method discussed in Dahal and Tazarv (2020). Table 3.5 presents the measured coupler rigid length factors for the splices used in the precast columns. The average rigid length factor for the Dayton Superior Sleeve-Lock, NMB Splice Sleeve, and Dextra Groutec S couplers was 0.70, 0.70, and 0.79, respectively. This factor for the nVent Lenton Interlock, Ultimate PT15, and HRC560 couplers was 0.82, 0.4, and 0.80, respectively. Note that the coupler rigid length factor should only be reported for the seismic couplers. However, beta for Dextra Groutec S was also reported for completeness and use in analytical studies.

Table 3.5 Measured Coupler Rigid Length Factors

No. 8 (25-mm) Bar	Sample	L_{sp} in. (mm)	α	L_{cr} in. (mm)	Mode of Failure	Coupler Strain Capacity, ε_u (%)	β_u
Dayton Superior Sleeve-Lock used in PGD Column	1	16.50 (419.1	1.25	19.00 (482.6	Bar Pullout	4.39	0.72
	2				Bar Fracture	5.24	0.64
	3				Bar Fracture	4.92	0.67
	4				Bar Fracture	4.37	0.73
	5				Bar Fracture	4.26	0.74
	Average				--	**4.63**	**0.70**
NMB Splice Sleeve used in PGS Column	1	14.57 (370)	1.25	17.07 (433.6)	Bar Fracture	5.00	0.68
	2				Bar Fracture	4.60	0.72
	3				Bar Fracture	4.77	0.70
	4				Bar Fracture	4.77	0.70
	5				Bar Fracture	4.11	0.76
	Average				--	**4.65**	**0.70**
Dextra Groutec S* used in PHD Column	1	9.45 (240)	1.25	11.95 (303.5)	Bar Pullout	2.36	1.01
	2				Bar Pullout	2.99	0.95
	3				Bar Pullout	6.26	0.60
	4				Bar Fracture	7.37	0.48
	5				Bar Pullout	3.12	0.93
	Average				--	**4.42**	**0.79**
nVent Lenton Interlock used in PHV Column	1	8.625 (219)	1.25	11.125 (282.6)	Bar Fracture	4.4	0.81
	2				Bar Fracture	4.22	0.83
	Average				--	**4.31**	**0.82**
nVent Lenton Ultimate PT15 used in PTV Column	1	9.0 (228.6)	1.25	11.5 (292.1)	Bar Fracture	8.22	0.41
	2				Bar Fracture	8.03	0.39
	Average				--	**8.13**	**0.40**
HRC 560 used in PHH Column	1	7.75 (196.9)	1.25	10.25 (260.4)	Bar Fracture	3.83	0.89
	2				Bar Fracture	5.55	0.70
	Average				--	**4.69**	**0.80**

* Beta should be calculated only for the seismic couplers. However, it is reported for this product to be used in the analytical studies of PHD column.

3.5.2 CIP Column Results

The CIP column was a reference cast-in-place model to serve as the benchmark for the precast columns. All columns were tested using the slow reversed cyclic loading protocol presented in Section 3.4. The experimental performance of the CIP column is discussed herein.

3.5.2.1 Observed Damage

The CIP cross-section orientation and the numbering of the column longitudinal bars are shown in Figure 3.2. The column was loaded in the north-south direction. The load was defined as “push” when the column was displaced from north to south and “pull” in the opposite direction (Fig. 3.37). Table 3.6 presents a summary of the damage observed for each push or pull load for the CIP column. Figures 3.49 to 3.74 show the CIP plastic hinge damage in the second cycle at different drift levels.

Flexural cracks were observed in the first cycle of 0.25% drift ratio. Shear cracks were first observed in the first cycle of 0.5% drift ratio (Fig. 3.51 & 3.52). The first tensile yielding occurred in Bar B7 (Fig. 3.2) at 0.47% drift ratio in the first push run of the 0.75% drift cycle under a lateral load of 37.53 kips (166.9 kN) (Fig. 3.53). Concrete spalling began to occur on both the north and south faces of the column during the 2% drift cycle (Fig. 3.57 & 3.58). Bars B1 and B2 were exposed during the 7% drift cycle (Fig. 3.67 & 3.68). During the first 9% drift cycle, Bars B6 and B7 were exposed and Bar B2 buckled. Bars B6 and B7 buckled during the second 9% drift cycle (Fig. 3.71 & 3.72). Finally, Bar B2 ruptured during the first 10% drift cycle leading to a major strength degradation at which the test was ended (Fig. 3.73 & 3.74).

The CIP column mode of failure was the longitudinal bar buckling followed by bar fracture above the column-footing interface during 10% drift cycles.

Table 3.6 Summary of Damage in CIP

Drift Ratio, %	Observed Damage
+0.25	• Minor flexural cracks
-0.25	• Minor flexural cracks
+0.50	• Flexural and inclined cracks
-0.50	• Flexural and inclined cracks • Cracking at column base
+0.75	• Flexural cracks • Bar yielding
-0.75	• Flexural cracks • Bar yielding
+1.00	• Vertical, flexural, and inclined cracks
-1.00	• Vertical, flexural, and inclined cracks
+2.00	• Vertical, flexural, and inclined cracks • Initiation of spalling on south face of column
-2.00	• Vertical, flexural, and inclined cracks • Initiation of spalling on north face of column
+3.00	• Widening of cracks
-3.00	• Widening of cracks
+4.00	• Extensive concrete spalling
-4.00	• Extensive concrete spalling
+5.00	• Widening of cracks
-5.00	• Transverse bars exposed on south face of column
+6.00	• Transverse bars exposed on north face of column
-6.00	• Several transverse bars exposed on south face of column
+7.00	• Several transverse bars exposed on north face of column • Longitudinal bar exposed on north face of column
-7.00	• Longitudinal bar exposed on south face of column
+8.00	• No further damage
-8.00	• No further damage
+9.00	• Longitudinal bar buckled on south face of column
-9.00	• Longitudinal bar buckled on north face of column
+10.00	• Longitudinal bar rupture on north face of column
-10.00	• No further damage

Note: Positive drifts were based on displacements away from the reaction blocks (north to south)

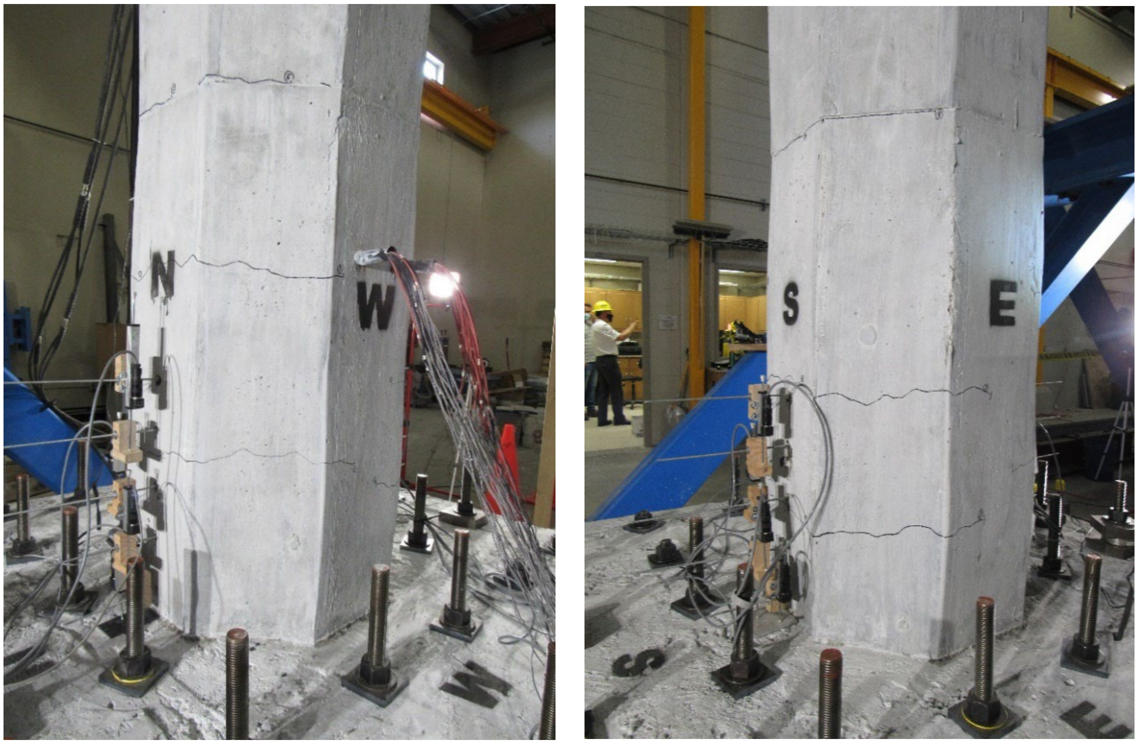

a) North-West Side b) South-East Side

Figure 3.49 CIP Column Plastic Hinge Damage, Second Push of 0.25% Drift Cycle

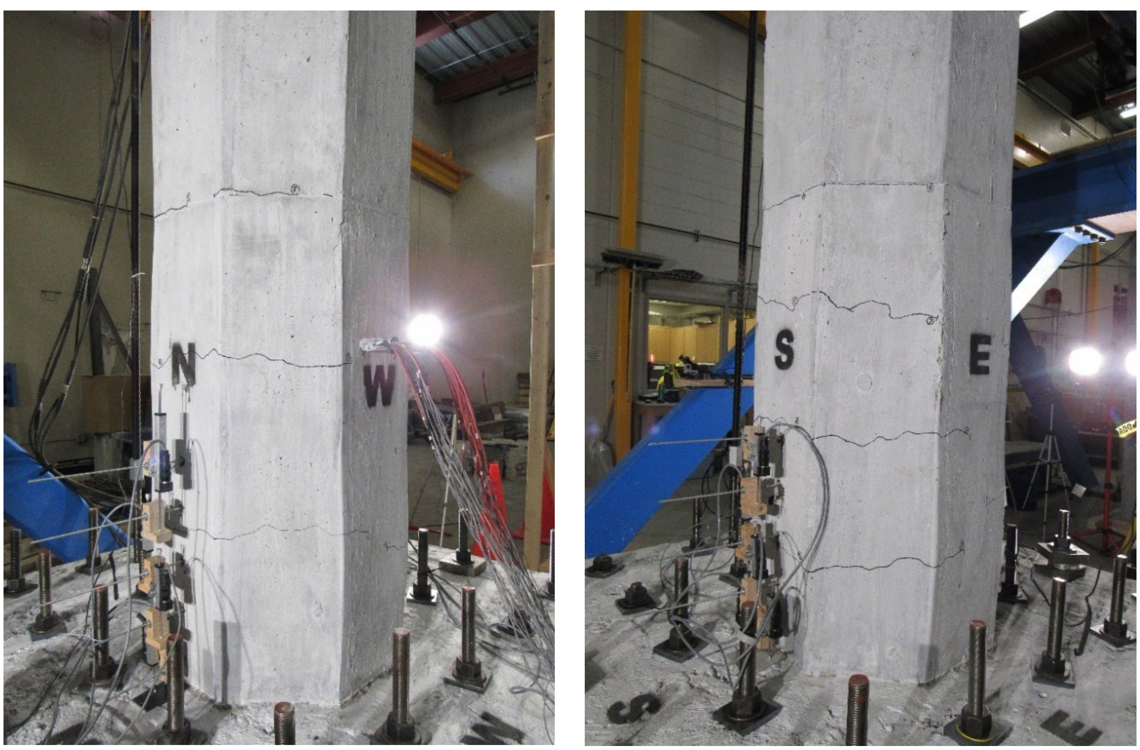

a) North-West Side b) South-East Side

Figure 3.50 CIP Column Plastic Hinge Damage, Second Pull of 0.25% Drift Cycle

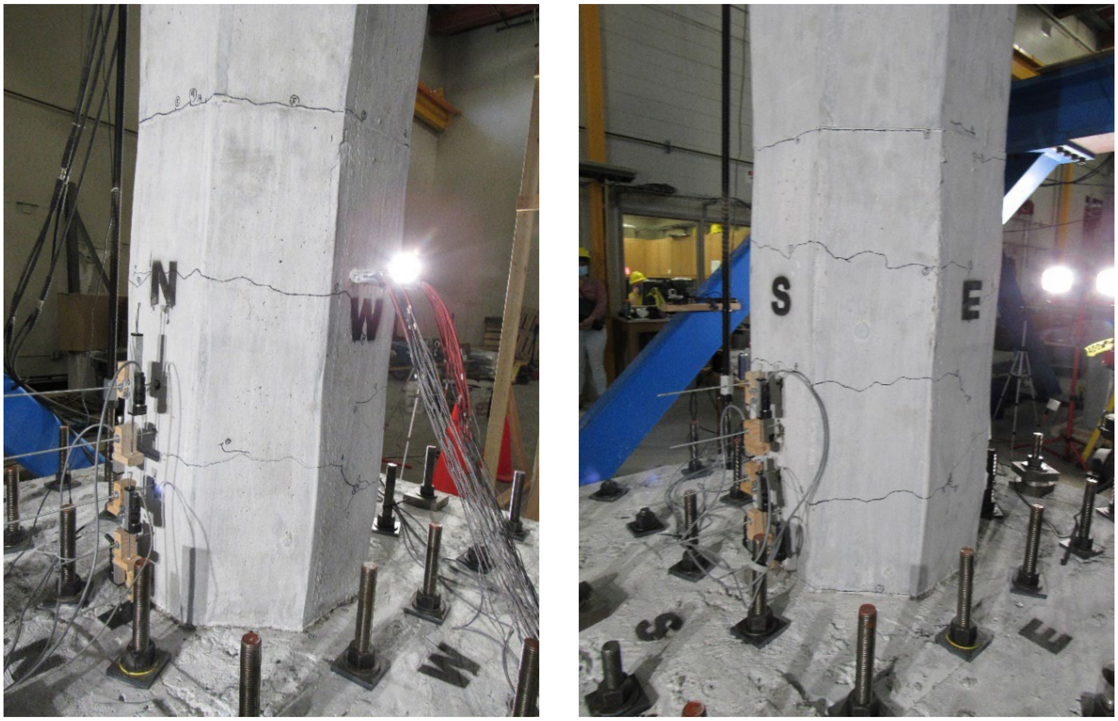

a) North-West Side b) South-East Side

Figure 3.51 CIP Column Plastic Hinge Damage, Second Push of 0.5% Drift Cycle

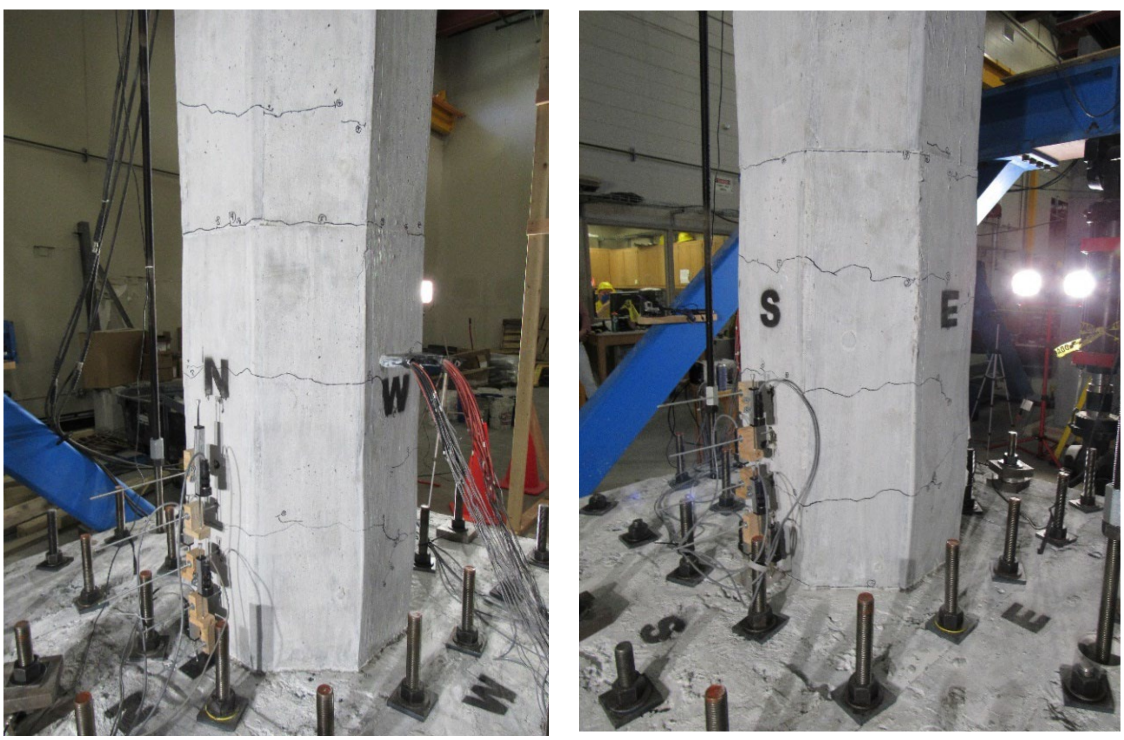

a) North-West Side b) South-East Side

Figure 3.52 CIP Column Plastic Hinge Damage, Second Pull of 0.5% Drift Cycle

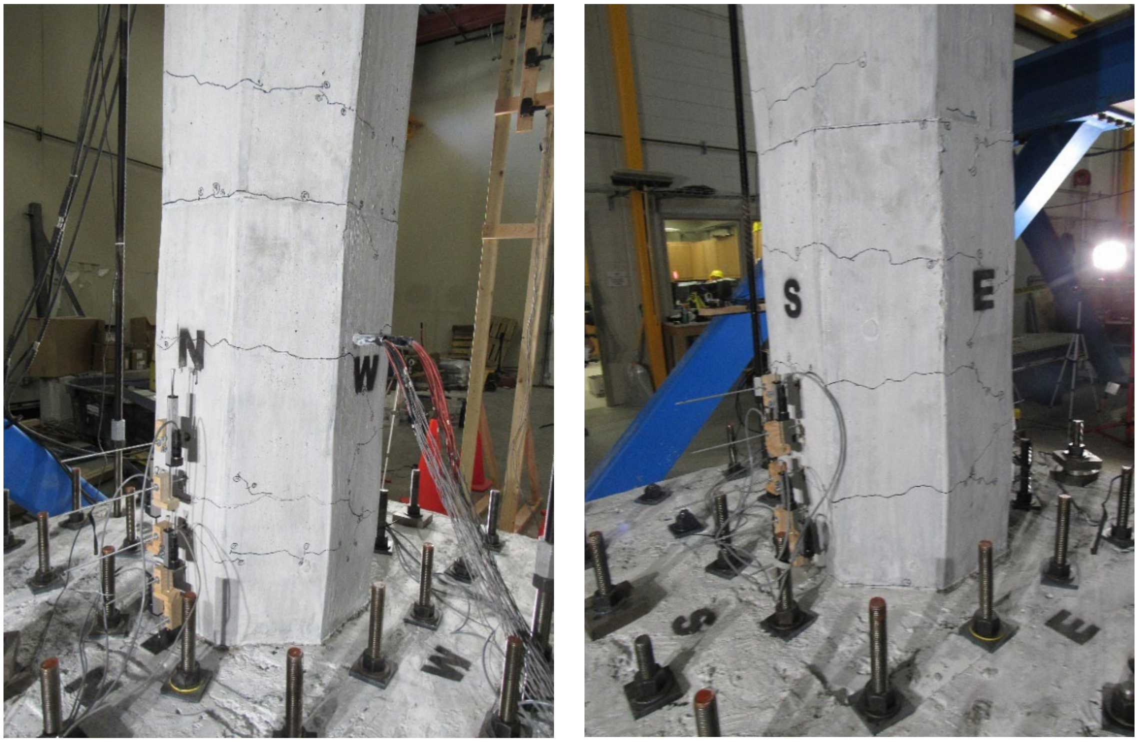

a) North-West Side b) South-East Side

Figure 3.53 CIP Column Plastic Hinge Damage, Second Push of 0.75% Drift Cycle

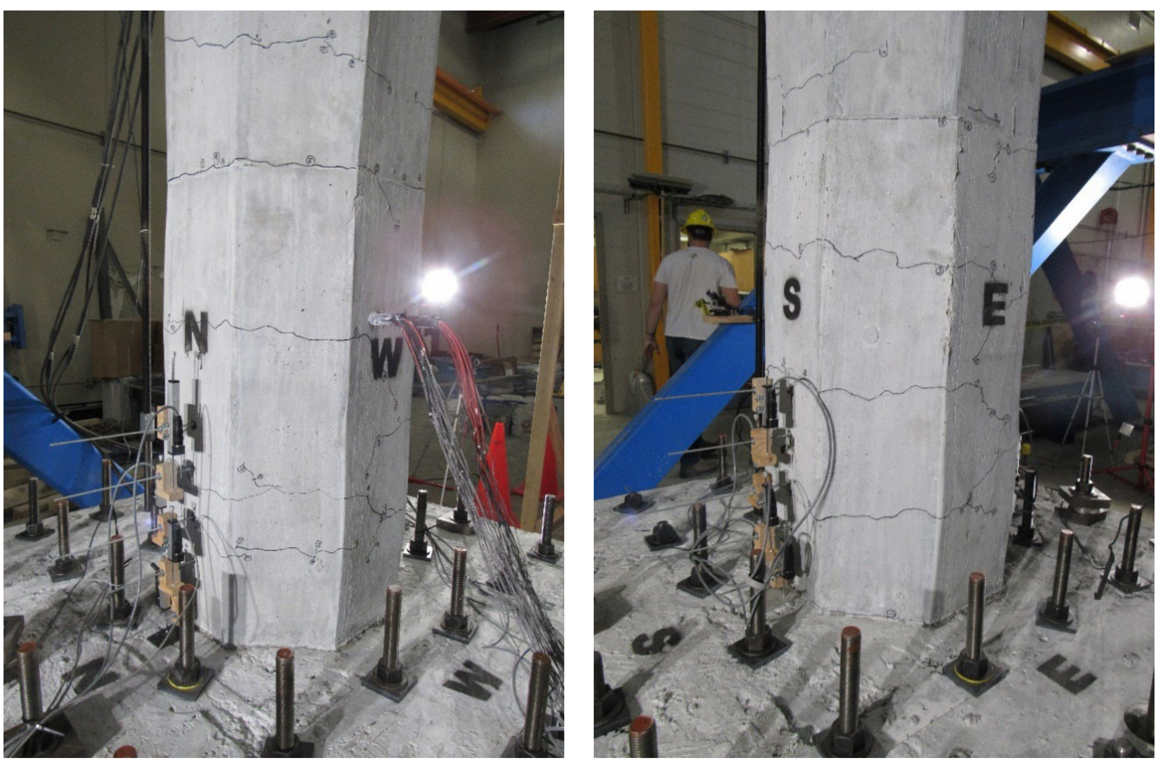

a) North-West Side b) South-East Side

Figure 3.54 CIP Column Plastic Hinge Damage, Second Pull of 0.75% Drift Cycle

a) North-West Side b) South-East Side

Figure 3.55 CIP Column Plastic Hinge Damage, Second Push of 1.00% Drift Cycle

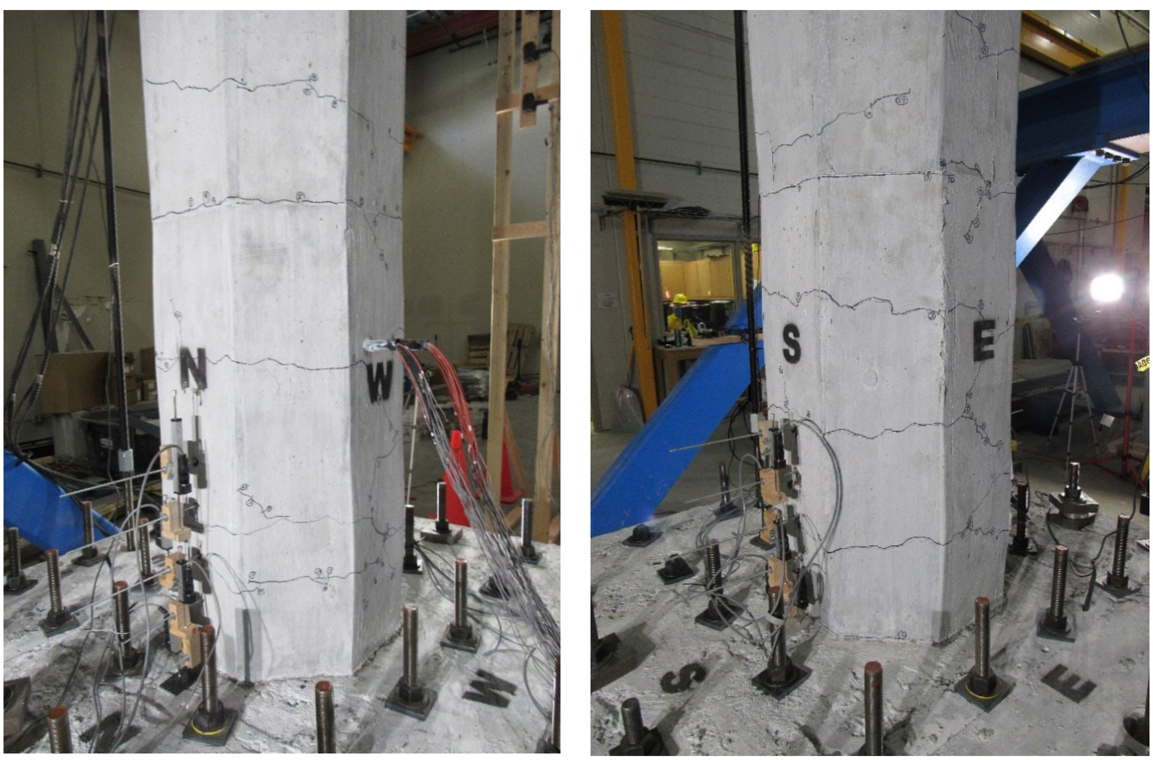

a) North-West Side b) South-East Side

Figure 3.56 CIP Column Plastic Hinge Damage, Second Pull of 1.00% Drift Cycle

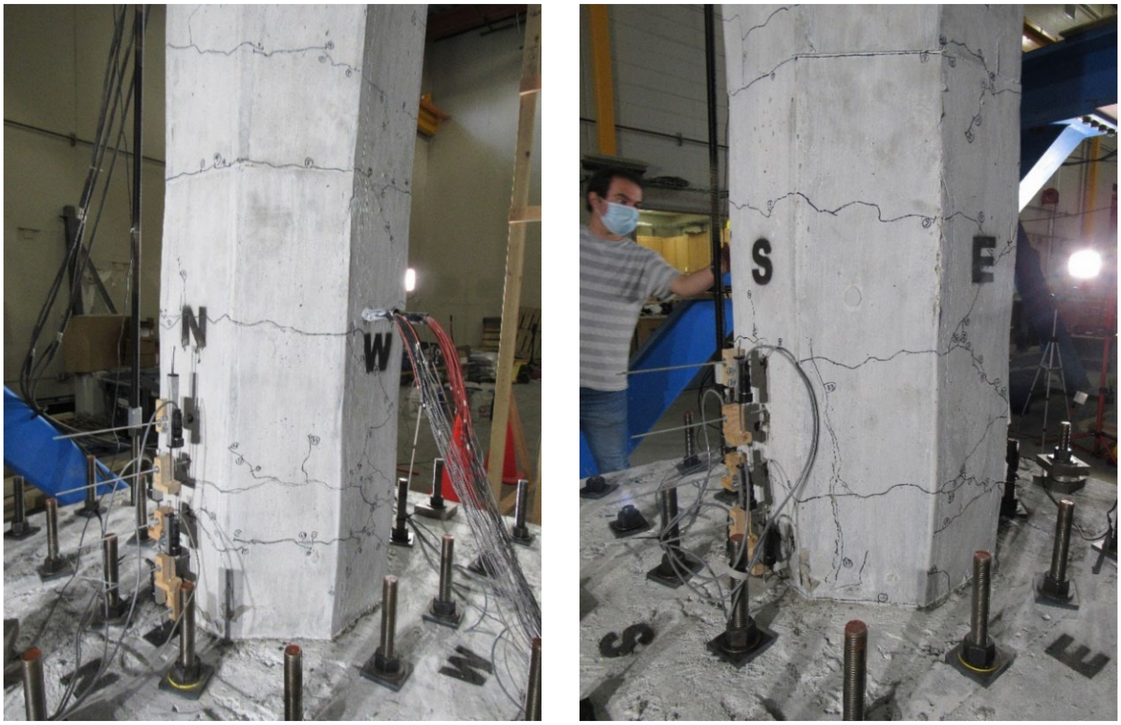

a) North-West Side b) South-East Side

Figure 3.57 CIP Column Plastic Hinge Damage, Second Push of 2.00% Drift Cycle

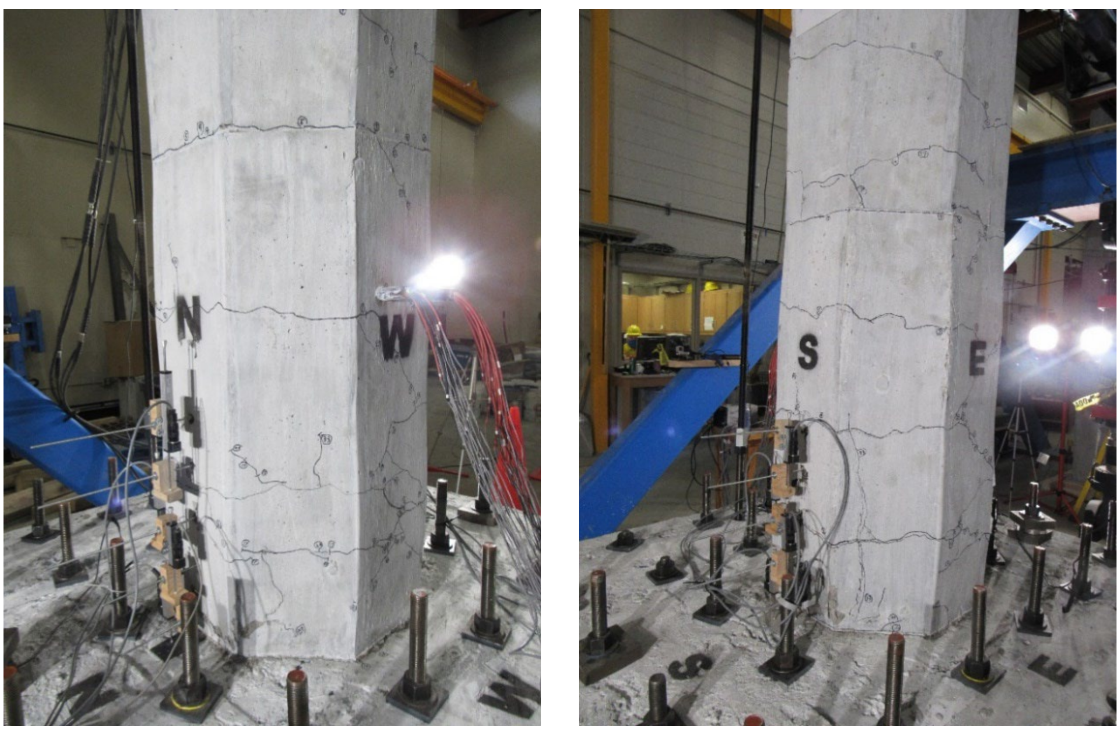

a) North-West Side b) South-East Side

Figure 3.58 CIP Column Plastic Hinge Damage, Second Pull of 2.00% Drift Cycle

a) North-West Side b) South-East Side

Figure 3.59 CIP Column Plastic Hinge Damage, Second Push of 3.00% Drift Cycle

a) North-West Side b) South-East Side

Figure 3.60 CIP Column Plastic Hinge Damage, Second Pull of 3.00% Drift Cycle

a) North-West Side b) South-East Side

Figure 3.61 CIP Column Plastic Hinge Damage, Second Push of 4.00% Drift Cycle

a) North-West Side b) South-East Side

Figure 3.62 CIP Column Plastic Hinge Damage, Second Pull of 4.00% Drift Cycle

a) North-West Side b) South-East Side

Figure 3.63 CIP Column Plastic Hinge Damage, Second Push of 5.00% Drift Cycle

a) North-West Side b) South-East Side

Figure 3.64 CIP Column Plastic Hinge Damage, Second Pull of 5.00% Drift Cycle

a) North-West Side b) South-East Side

Figure 3.65 CIP Column Plastic Hinge Damage, Second Push of 6.00% Drift Cycle

a) North-West Side b) South-East Side

Figure 3.66 CIP Column Plastic Hinge Damage, Second Pull of 6.00% Drift Cycle

a) North-West Side b) South-East Side

Figure 3.67 CIP Column Plastic Hinge Damage, Second Push of 7.00% Drift Cycle

a) North-West Side b) South-East Side

Figure 3.68 CIP Column Plastic Hinge Damage, Second Pull of 7.00% Drift Cycle

a) North-West Side b) South-East Side

Figure 3.69 CIP Column Plastic Hinge Damage, Second Push of 8.00% Drift Cycle

a) North-West Side b) South-East Side

Figure 3.70 CIP Column Plastic Hinge Damage, Second Pull of 8.00% Drift Cycle

a) North-West Side b) South-East Side

Figure 3.71 CIP Column Plastic Hinge Damage, Second Push of 9.00% Drift Cycle

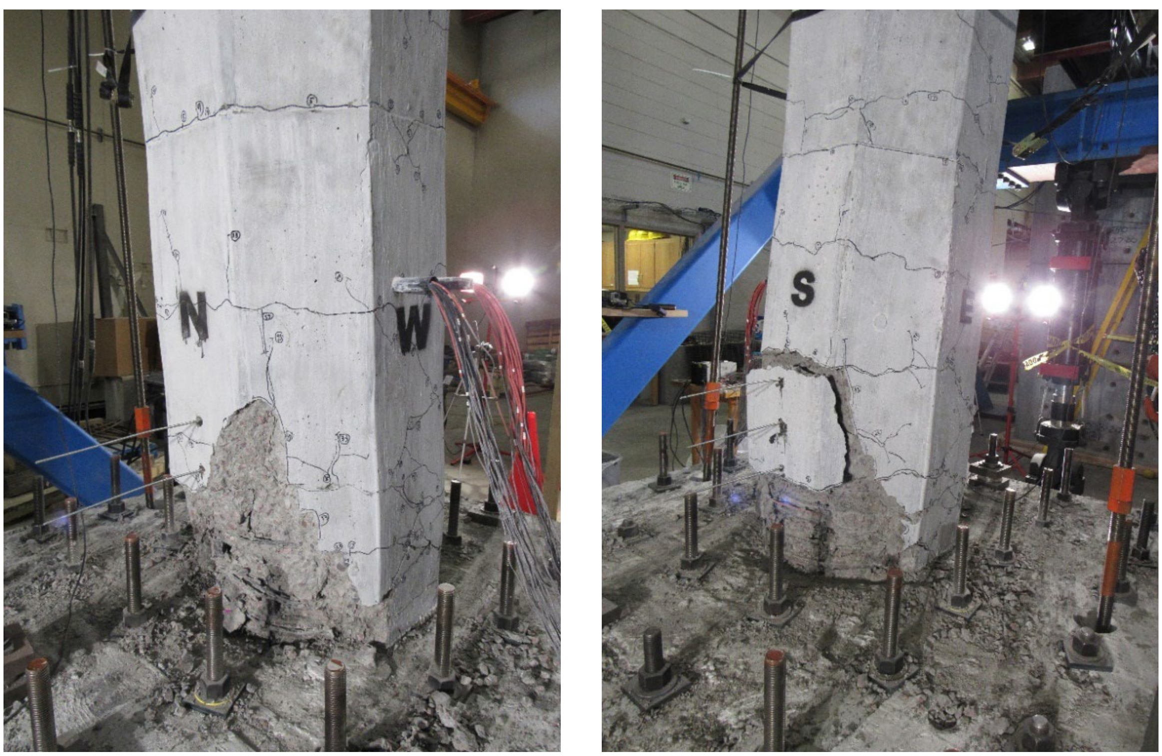

a) North-West Side b) South-East Side

Figure 3.72 CIP Column Plastic Hinge Damage, Second Pull of 9.00% Drift Cycle

a) North-West Side

b) South-East Side

Figure 3.73 CIP Column Plastic Hinge Damage, Second Push of 10.00% Drift Cycle

a) North-West Side

b) South-East Side

Figure 3.74 CIP Column Plastic Hinge Damage, Second Pull of 10.00% Drift Cycle

3.5.2.2 Force-Displacement Relationship

Figure 3.75 shows the measured lateral force-drift hysteretic and envelope responses of CIP. The envelope was extended up to the 85% of the column base shear capacity after the peak strength. The CIP column exhibited a peak lateral force capacity at 2% drift ratio and exhibited a minor strength degradation from 2% to 9% drifts. A significant strength and stiffness degradation was observed after 9% drift ratio due to the bar fracture. The column was slightly stronger in the pull direction. The CIP longitudinal bars yielded at 0.47% drift ratio in the push direction under a lateral load of 37.5 kips (166.9 kN), and at -0.44% drift ratio in the pull direction at a lateral load of -38.8 kips (172.6 kN).

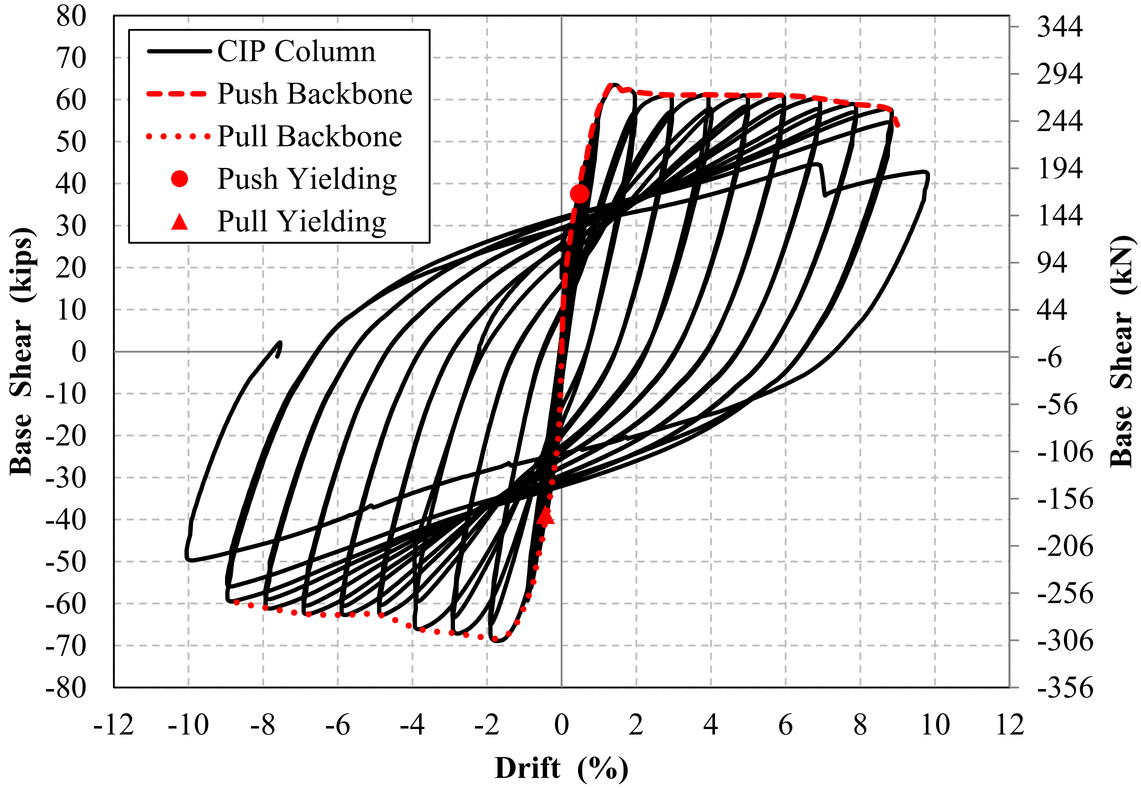

Figure 3.75 Measured CIP Column Force-Drift Hysteretic and Envelope Responses

Figure 3.76 shows the average envelope for the push and pull directions. The average yield drift ratio was 0.45% and occurred at a lateral force of 38.2 kips (169.9 kN). The column failure was the point at which the lateral load resistance drops below 85% of the peak resistance due to either bar fracture or core concrete crushing. Therefore, the drift capacity of the CIP column was 8.96%. The displacement ductility is defined as the ratio of the ultimate displacement to the effective yield displacement per AASHTO SGS (2011). The effective yield displacement is found using an idealized bilinear force-displacement curve for the column. The bilinear curve is idealized by making the area under idealized and measured curves equal from the effective yield point to the ultimate drift. Figure 3.76 shows the idealized curve for the average CIP envelope. The effective yield drift ratio was 0.72% at the effective yield lateral force of 61.9 kips (275.3 kN). Therefore, the displacement ductility capacity (μ) for the CIP column was 12.37.

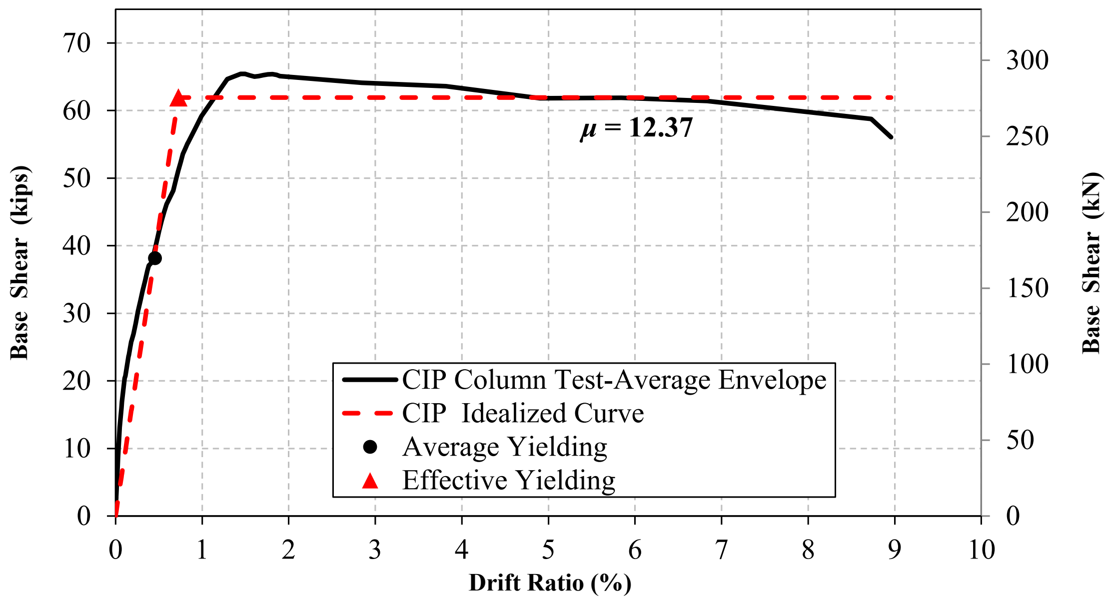

Figure 3.76 Measured CIP Column Average Push/Pull Force-Drift Envelope and Idealized Curve

3.5.2.3 Strain Profiles

Thirty-four strain gauges were installed on the CIP reinforcing steel bars at six levels of the column. Figures 3.77 to 3.80 show the maximum measured tensile strains versus the column height for Bars B1, B2, B6, and B7.

The strain profile was uniform up to the bar yield. The bar strains were generally higher closer to the column-footing interface and decreased along the height of the column, especially at the heights exceeding the column analytical plastic hinge length (approximately 20 in. or 500 mm for CIP). Overall, strains were well distributed, representing a well-designed modern RC bridge column performance.

The strain of the hoops was also monitored. The yield strain for the hoops in CIP was 0.23%. Several hoops in CIP yielded, indicating a typical performance expected for a conventional column. The maximum measured hoop strain was 2.96%, which occurred in the hoop below the column-footing interface.

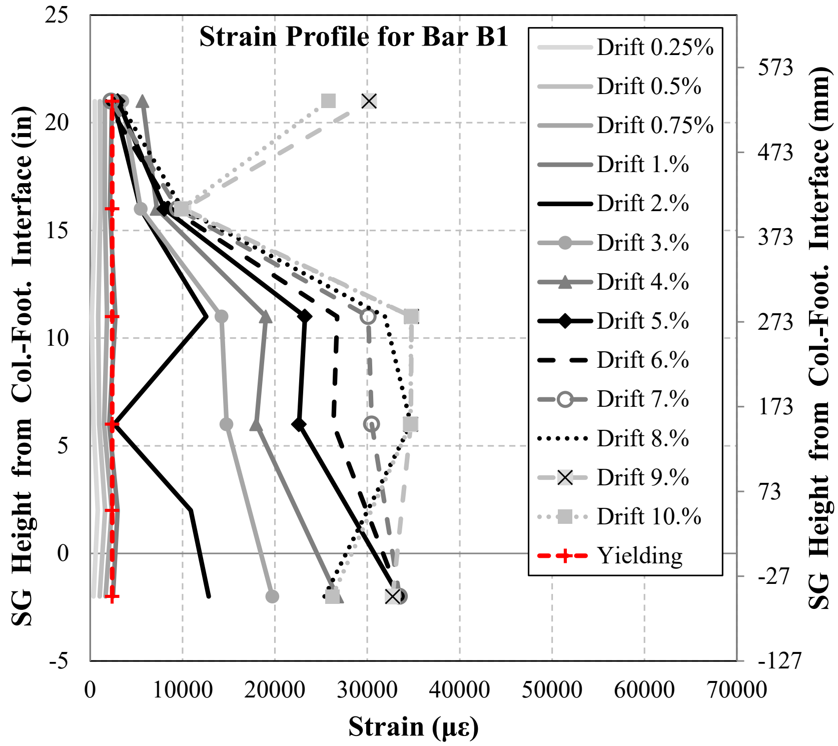

Figure 3.77 Measured Strain Profile for CIP Column Bar B1

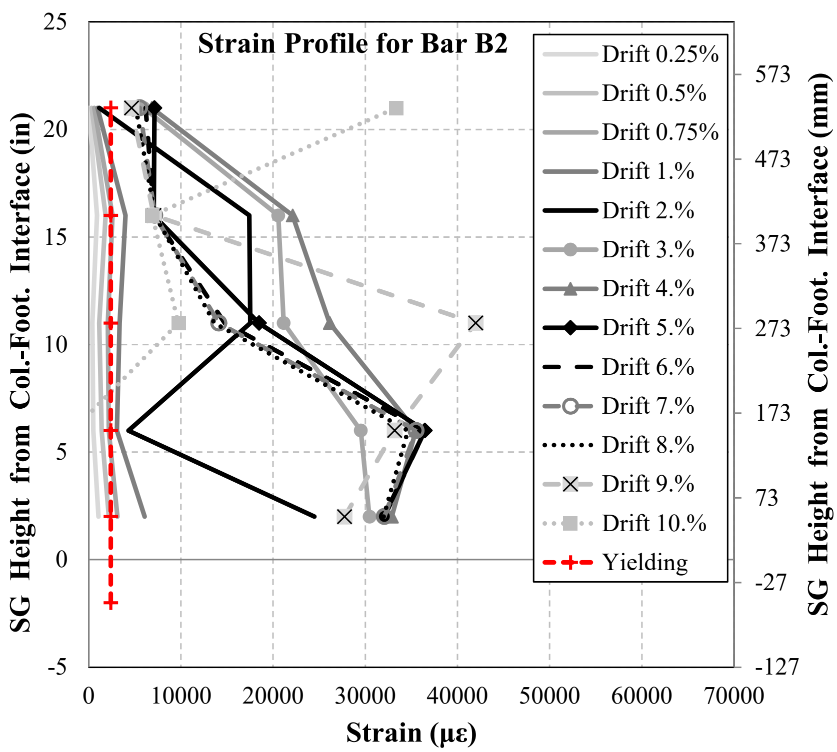

Figure 3.78 Measured Strain Profile for CIP Column Bar B2

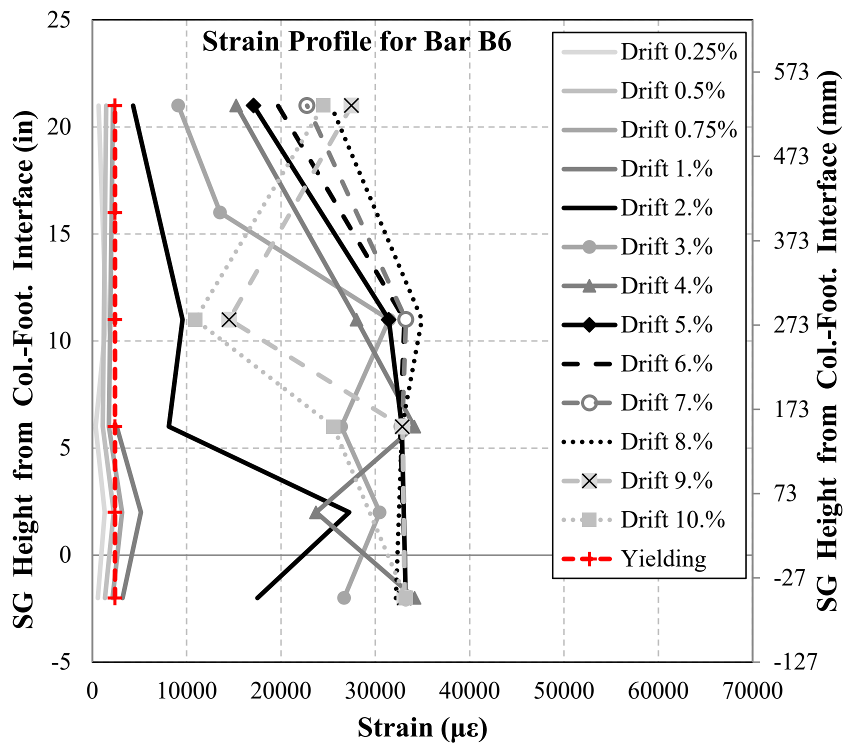

Figure 3.79 Measured Strain Profile for CIP Column Bar B6

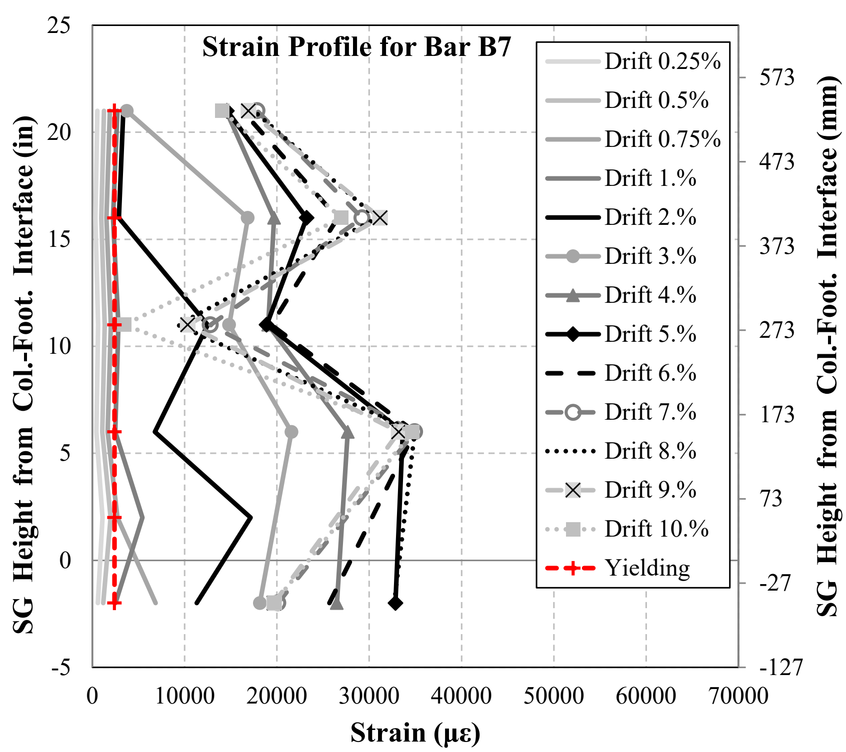

Figure 3.80 Measured Strain Profile for CIP Column Bar B7

3.5.2.4 Measured Rotation and Curvature

LVDTs were installed in the loading plane on the north and south faces of the column. The measured displacements were used to calculate rotations and curvatures in the plastic hinge region. Figure 3.39 shows the LVDT instrumentation schedule for the CIP column. Rotation (θ) and curvature (φ) were calculated as:

$$\theta = \frac{\Delta L_L - \Delta L_R}{D + d_L + d_R} \tag{4-1}$$

$$\varphi = \frac{\theta}{h} \tag{4-2}$$

where ΔL_L and ΔL_R (in. or mm) are, respectively, the measured relative displacements at the left (or north) and right (south) sides of the column in the loading direction; D (in. or mm) is the diameter of the column, d_L and d_R (in. or mm) are the distances of the left and right LVDTs from the column faces, respectively; and h is the height above the footing that the pair of LVDTs was placed. The rotations and curvatures were measured at five levels in the plastic hinge region.

Figure 3.81 shows the measured curvature profile along the height of the CIP column for drift ratios of 0.25% to 4.0%. The highest curvature always occurred at the base mainly due to strain penetration effects.

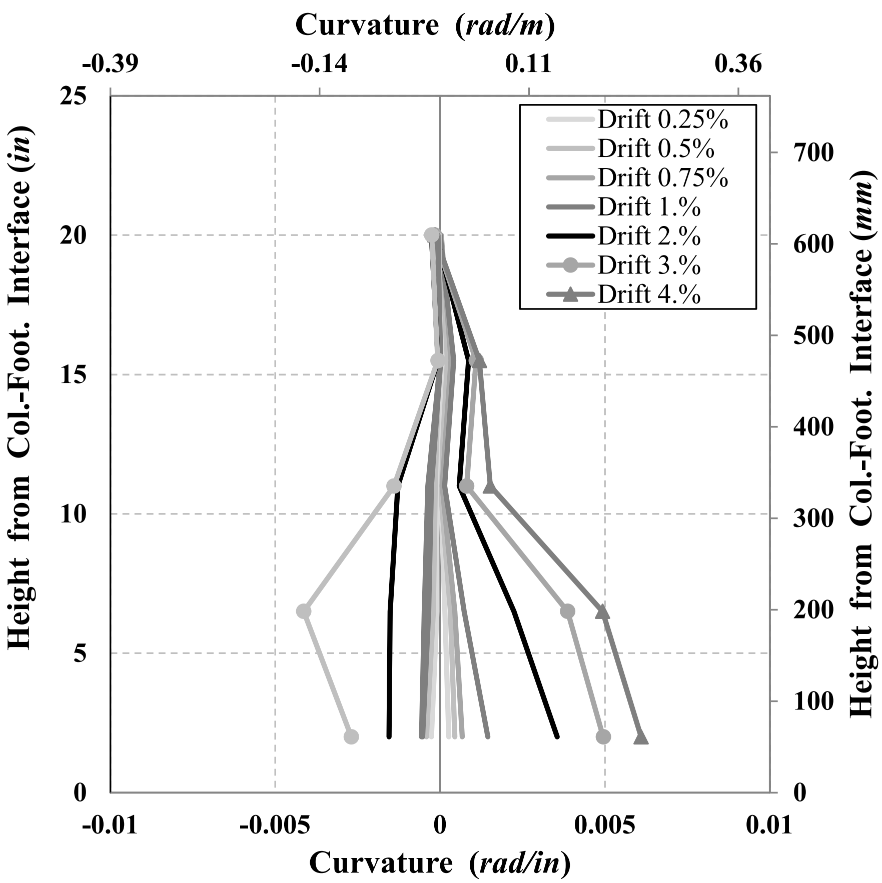

Figure 3.81 Measured Curvature Profile for CIP Column

3.5.2.5 Energy Dissipation

The dissipated energy is defined as the cumulative area under the force-displacement hysteretic loops. Figure 3.82 shows the measured cumulative energy dissipation of the CIP column at different drift ratios. The dissipated energy is negligible up to 1% drift ratio, where bar yielding was minimal. At higher drift levels, the hysteretic loops began to widen, which led to a higher dissipated energy. CIP dissipated 8,041 kip-in. (908.5 kN-m) of energy prior to the failure.

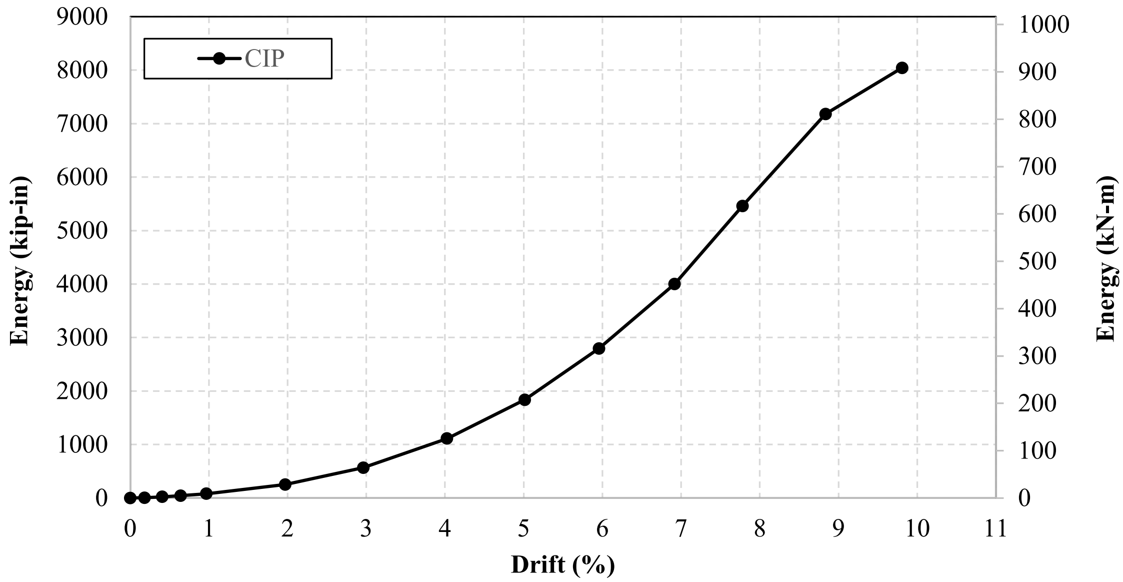

Figure 3.82 Measured Energy Dissipation for CIP Column

3.5.3 PGD Column Results

The seismic performance of the precast column incorporating the Dayton Superior Sleeve-Lock couplers, PGD, is discussed in this section.

3.5.3.1 Observed Damage

The PGD column followed the same testing procedure as the CIP column. Table 3.7 presents a summary of the damage observed for each push or pull load for the PGD column. Figures 3.83 to 3.100 show the PGD plastic hinge damage in the second cycle of the push or pull for each drift level.

Flexural cracks were observed in the first cycle of 0.25% drift ratio (Fig. 3.83 & 3.84). Shear cracks were first observed in the first cycle of 0.5% drift ratio (Fig. 3.85 & 3.86). The first yielding occurred in Bar B1 at 0.58% drift in the first push run of the 0.75% drift cycle under a lateral load of 45.9 kips (204.3 kN) (Fig. 3.87). Concrete spalled on both the north and south faces of the column during the 3% drift cycles (Fig. 3.93 to 3.94). Cracks near the top of the couplers and the base of the column began to spread during the 4% drift cycle. The lateral strength also began to degrade during the 4% drift cycle (Fig. 3.95 & 3.96). Finally, the PGD longitudinal bars pulled out from the couplers at 6% drift cycle, leading to a major strength reduction and ending the test (Fig. 3.99 & Fig. 3.100). A significant gap at the column base was observed at large displacements, indicating bar pullout from the coupler base (e.g., 1.5-in. or 38-mm gap at 6% drift ratio). Thus, the PGD column mode of failure was longitudinal bar pullout during the 6% drift cycles.

Table 3.7 Summary of Damage in PGD

Drift Ratio, %	Observed Damage
+0.25	• Minor flexural cracks • Flexural cracks at top of coupler
-0.25	• Minor flexural cracks • Flexural cracks at top of coupler
+0.50	• Flexural and inclined cracks
-0.50	• Flexural and inclined cracks • Cracking at column base
+0.75	• Flexural cracks • Bar yielding
-0.75	• Flexural cracks • Bar yielding
+1.00	• No further damage
-1.00	• Vertical crack appears on southeast column face
+2.00	• Vertical, flexural, and inclined cracks
-2.00	• Vertical, flexural, and inclined cracks
+3.00	• Widening of cracks • Initiation of spalling on south face of column
-3.00	• Widening of cracks • Initiation of spalling on north face of column
+4.00	• Beginning of strength degradation
-4.00	• Beginning of strength degradation
+5.00	• Large strength loss
-5.00	• Large strength loss
+6.00	• Longitudinal bar pulled out from coupler
-6.00	• Longitudinal bar pulled out from coupler

Note: Positive drifts were based on displacements away from the reaction blocks (north to south)

a) North-West Side b) South-East Side

Figure 3.83 PGD Column Plastic Hinge Damage, Second Push of 0.25% Drift Cycle

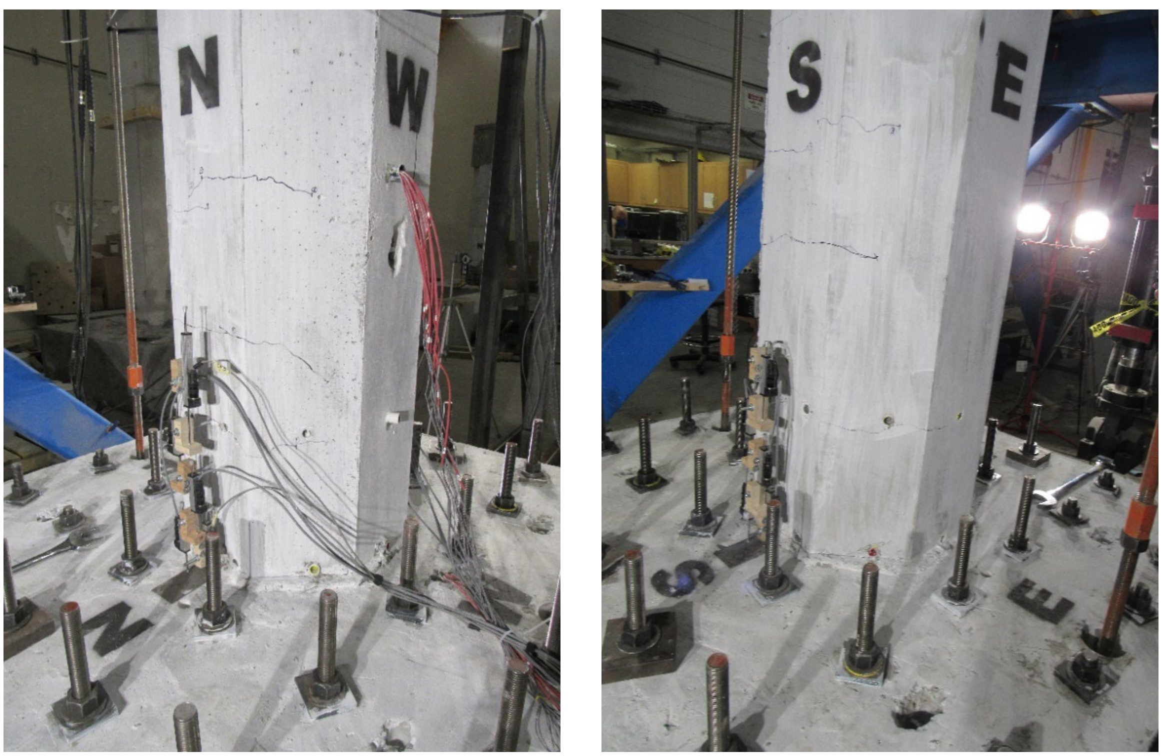

a) North-West Side b) South-East Side

Figure 3.84 PGD Column Plastic Hinge Damage, Second Pull of 0.25% Drift Cycle

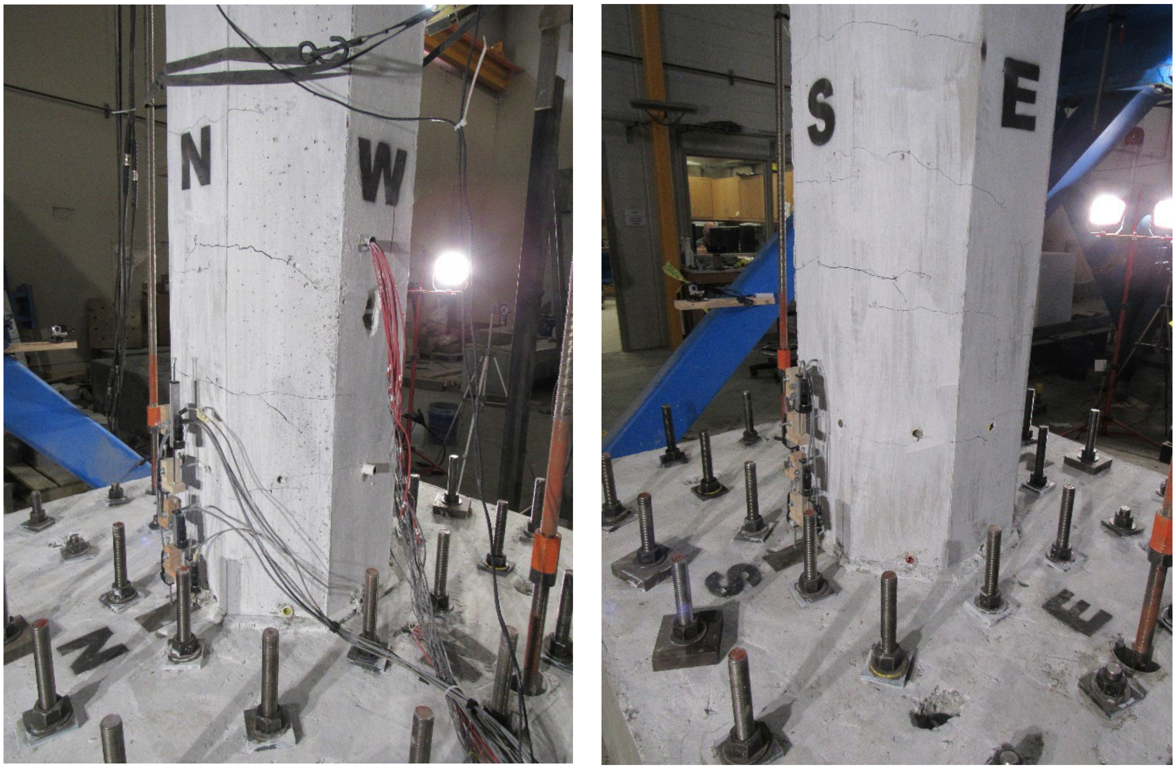

a) North-West Side b) South-East Side

Figure 3.85 PGD Column Plastic Hinge Damage, Second Push of 0.50% Drift Cycle

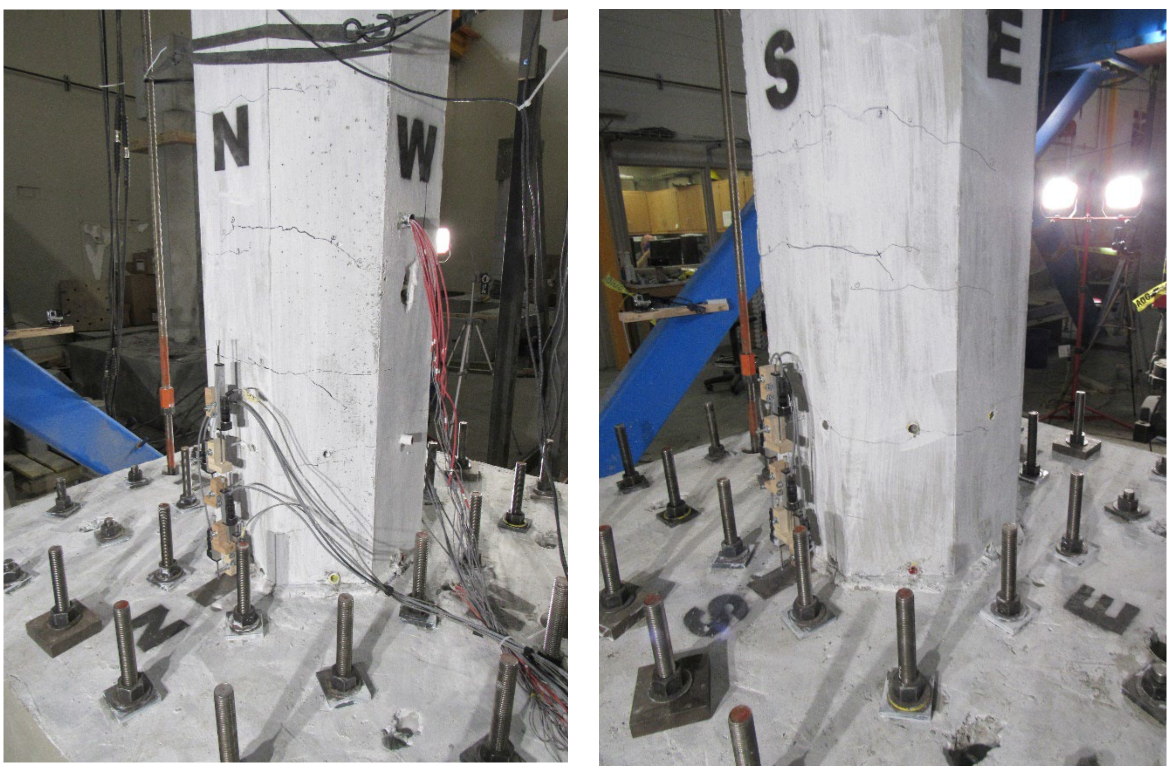

a) North-West Side b) South-East Side

Figure 3.86 PGD Column Plastic Hinge Damage, Second Pull of 0.50% Drift Cycle

a) North-West Side b) South-East Side

Figure 3.87 PGD Column Plastic Hinge Damage, Second Push of 0.75% Drift Cycle

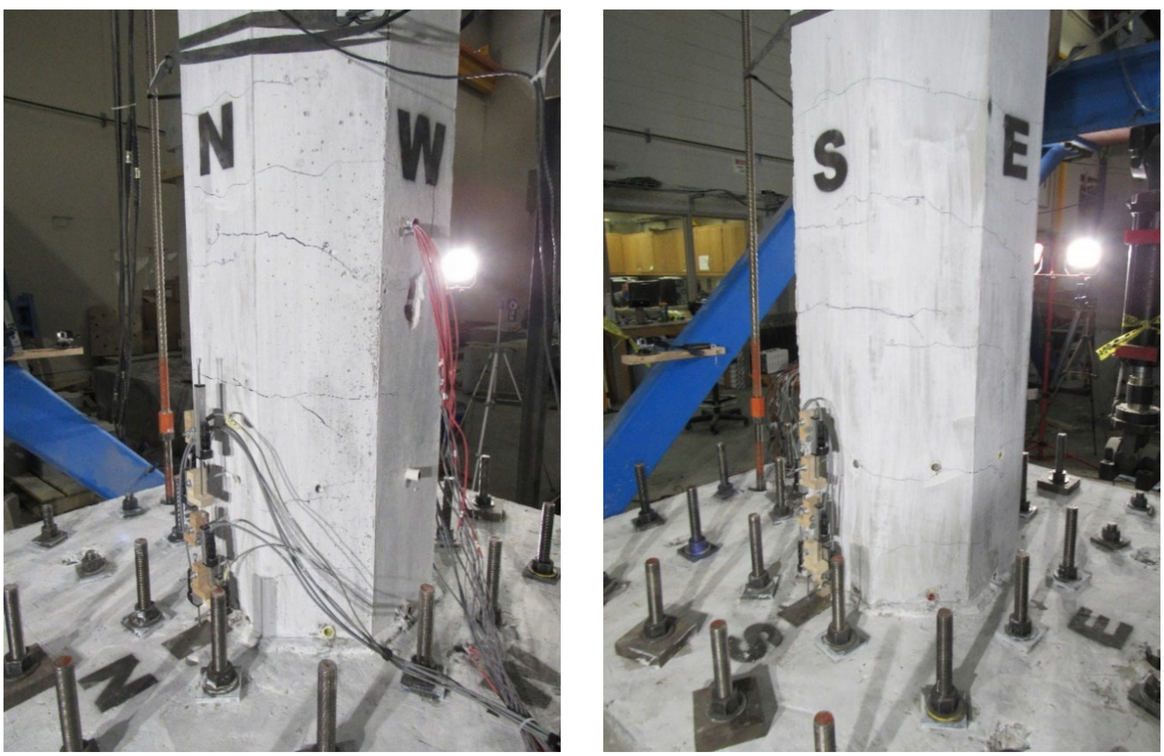

a) North-West Side b) South-East Side

Figure 3.88 PGD Column Plastic Hinge Damage, Second Pull of 0.75% Drift Cycle

a) North-West Side b) South-East Side

Figure 3.89 PGD Column Plastic Hinge Damage, Second Push of 1.00% Drift Cycle

a) North-West Side b) South-East Side

Figure 3.90 PGD Column Plastic Hinge Damage, Second Pull of 1.00% Drift Cycle

a) North-West Side b) South-East Side

Figure 3.91 PGD Column Plastic Hinge Damage, Second Push of 2.00% Drift Cycle

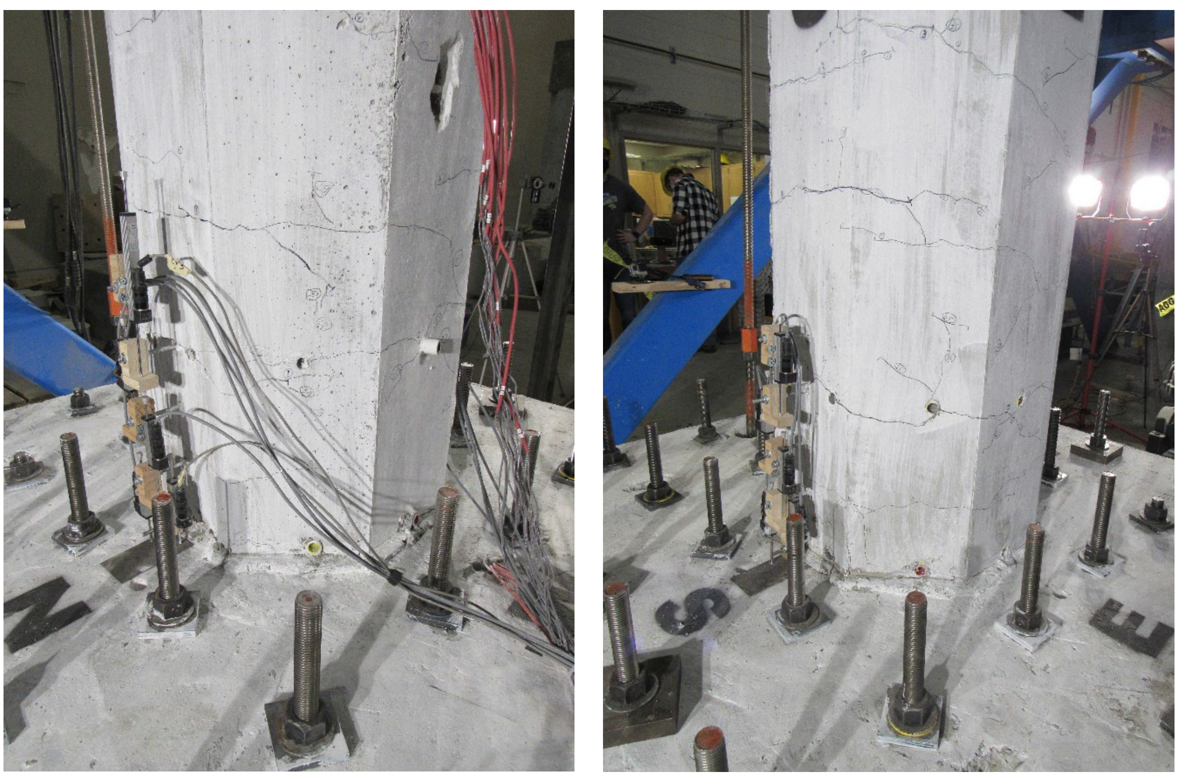

a) North-West Side b) South-East Side

Figure 3.92 PGD Column Plastic Hinge Damage, Second Pull of 2.00% Drift Cycle

a) North-West Side b) South-East Side

Figure 3.93 PGD Column Plastic Hinge Damage, Second Push of 3.00% Drift Cycle

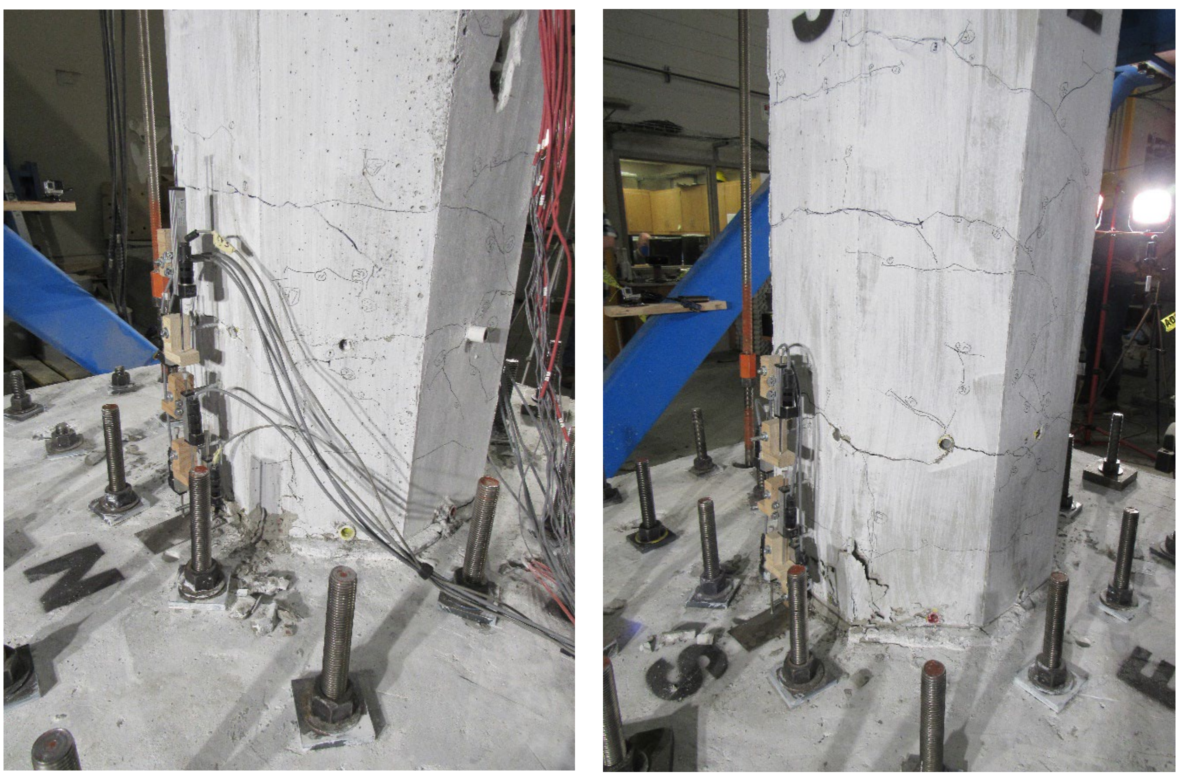

a) North-West Side b) South-East Side

Figure 3.94 PGD Column Plastic Hinge Damage, Second Pull of 3.00% Drift Cycle

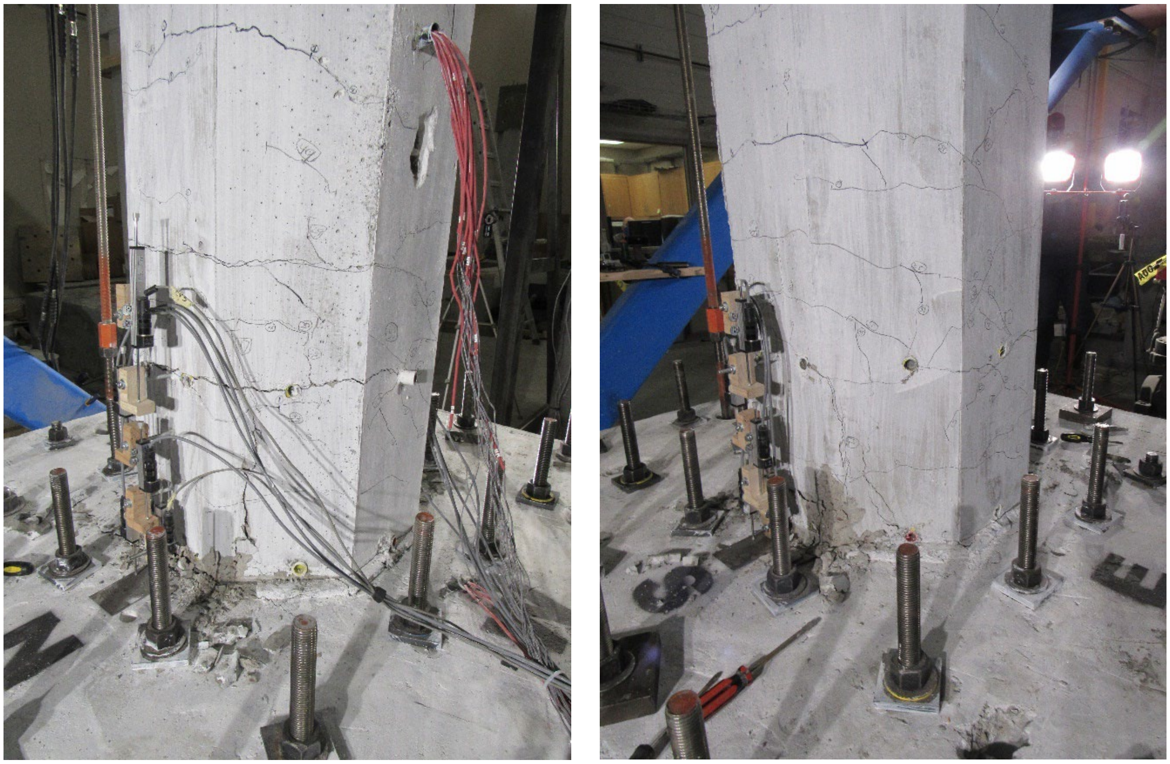

a) North-West Side b) South-East Side

Figure 3.95 PGD Column Plastic Hinge Damage, Second Push of 4.00% Drift Cycle

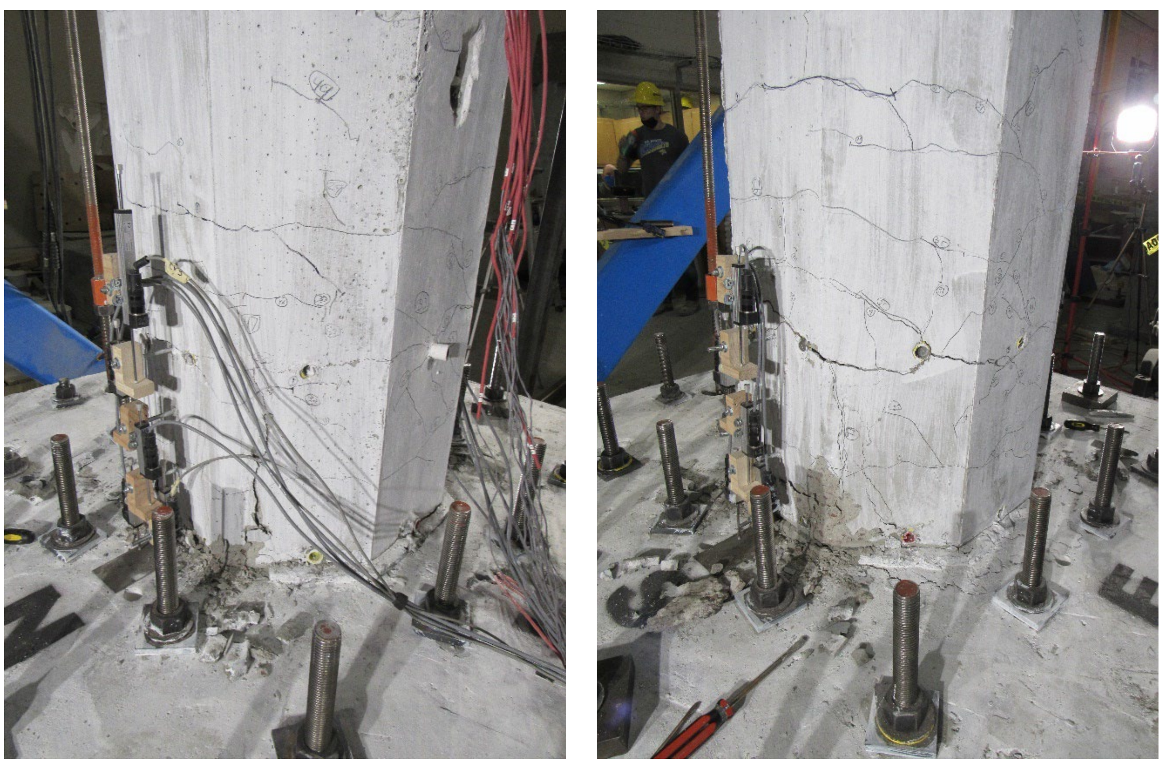

a) North-West Side b) South-East Side

Figure 3.96 PGD Column Plastic Hinge Damage, Second Pull of 4.00% Drift Cycle

a) North-West Side b) South-East Side

Figure 3.97 PGD Column Plastic Hinge Damage, Second Push of 5.00% Drift Cycle

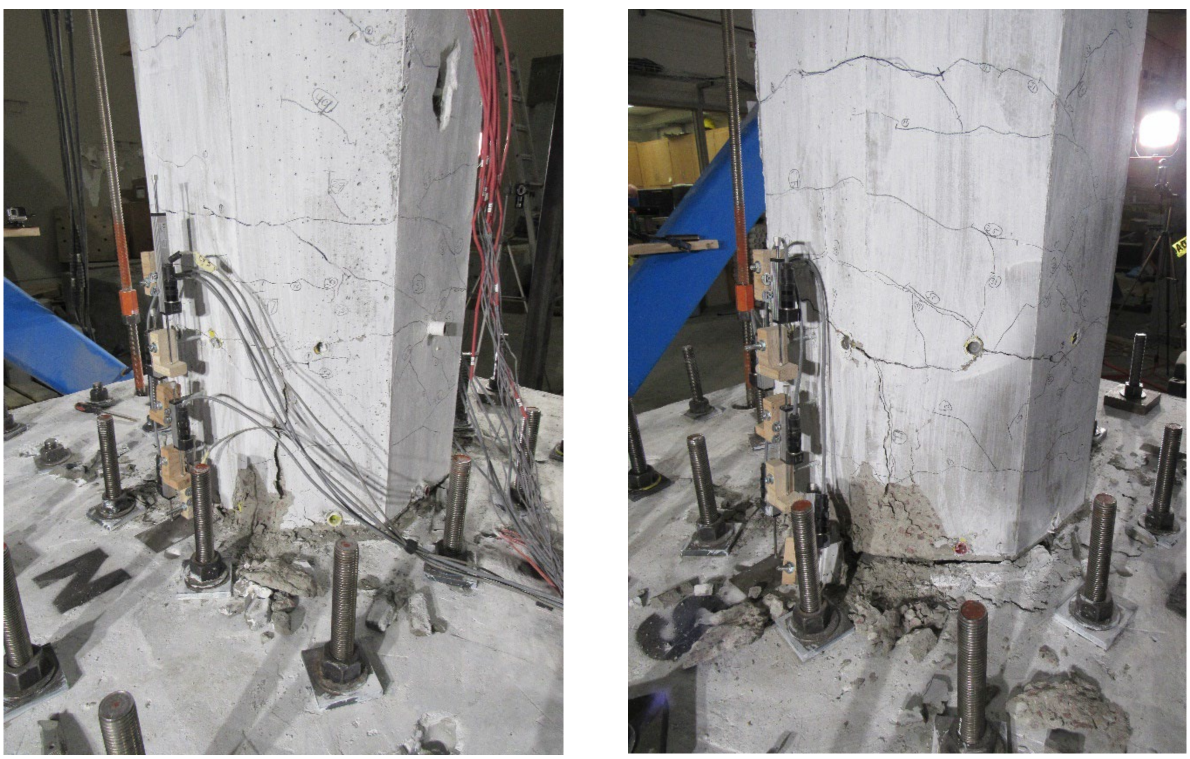

a) North-West Side b) South-East Side

Figure 3.98 PGD Column Plastic Hinge Damage, Second Pull of 5.00% Drift Cycle

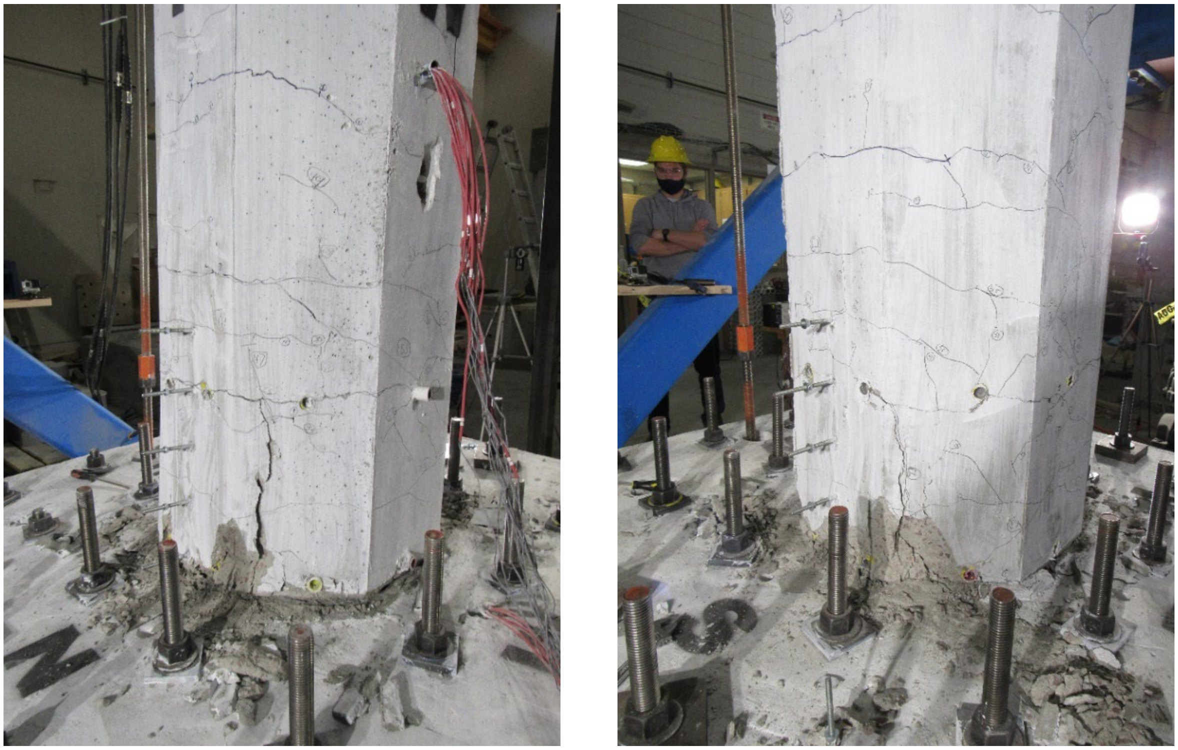

a) North-West Side b) South-East Side

Figure 3.99 PGD Column Plastic Hinge Damage, Second Push of 6.00% Drift Cycle

a) North-West Side b) South-East Side

Figure 3.100 PGD Column Plastic Hinge Damage, Second Pull of 6.00% Drift Cycle

3.5.3.2 Force-Displacement Relationship

Figure 3.101 shows the measured lateral force-drift hysteretic and envelope responses of PGD. The envelope is shown until 85% of the base shear capacity. The PGD column exhibited a maximum lateral load of 74.7 kips (332 kN) at 3% drift ratio and exhibited a steady strength degradation afterwards. A significant strength and stiffness degradation was observed after 5% drift ratio due to bar pullout from the coupler base. The column was slightly stronger in the push direction. The PGD longitudinal bars yielded at 0.58% drift ratio in the push direction under a lateral load of 45.9 kips (204.3 kN), and at -0.52% drift ratio in the pull direction at a lateral load of -46.4 kips (206.3 kN).

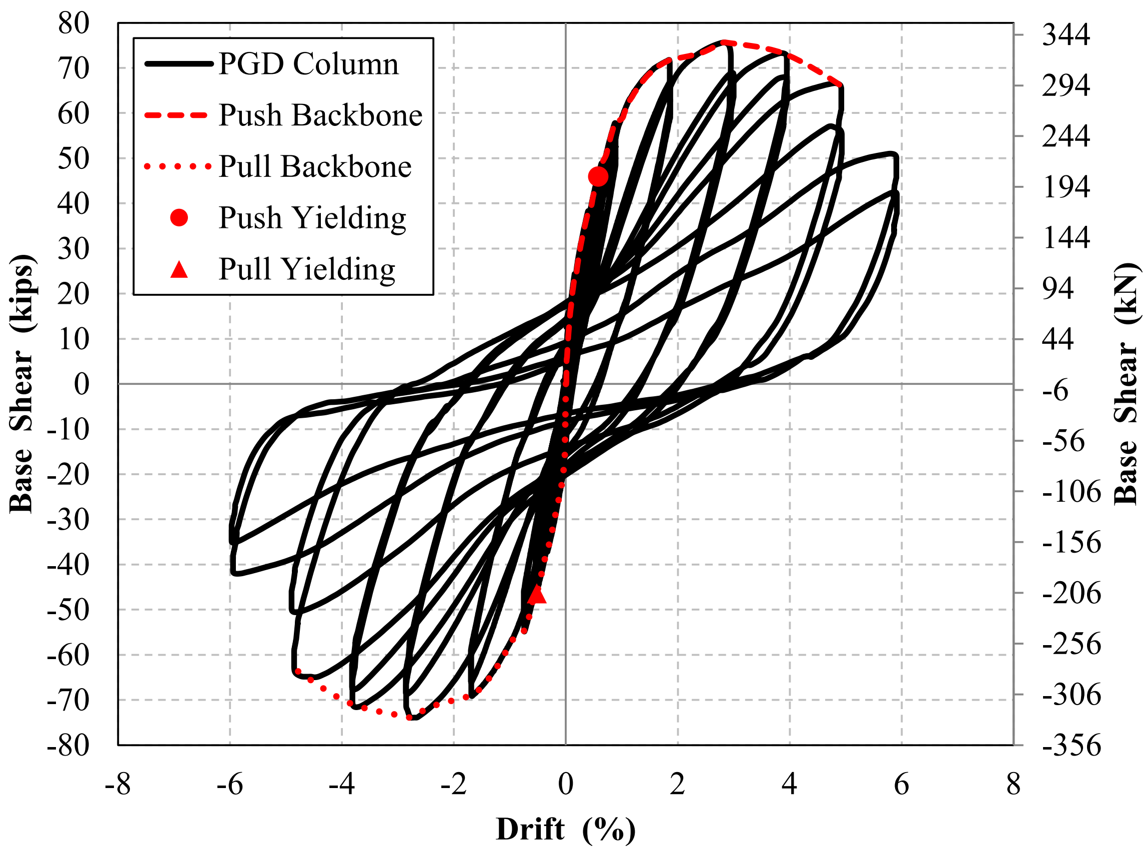

Figure 3.101 Measured PGD Column Force-Drift Hysteretic and Envelope Responses

Figure 3.102 shows the average envelope for the push and pull directions of PGD. The average yield drift ratio was 0.55% occurred at a lateral force of 46.2 kips (205.5 kN). Based on the 15% load drop discussed before as the column failure point, the drift capacity of the PGD column was estimated as 4.93%. Furthermore, Figure 3.102 shows the idealized curve for the average PGD envelope. The effective yield drift ratio was 0.86% at the effective yield lateral force of 70.4 kips (313.2 kN), resulting in a displacement ductility capacity of 5.76 for the PGD column.

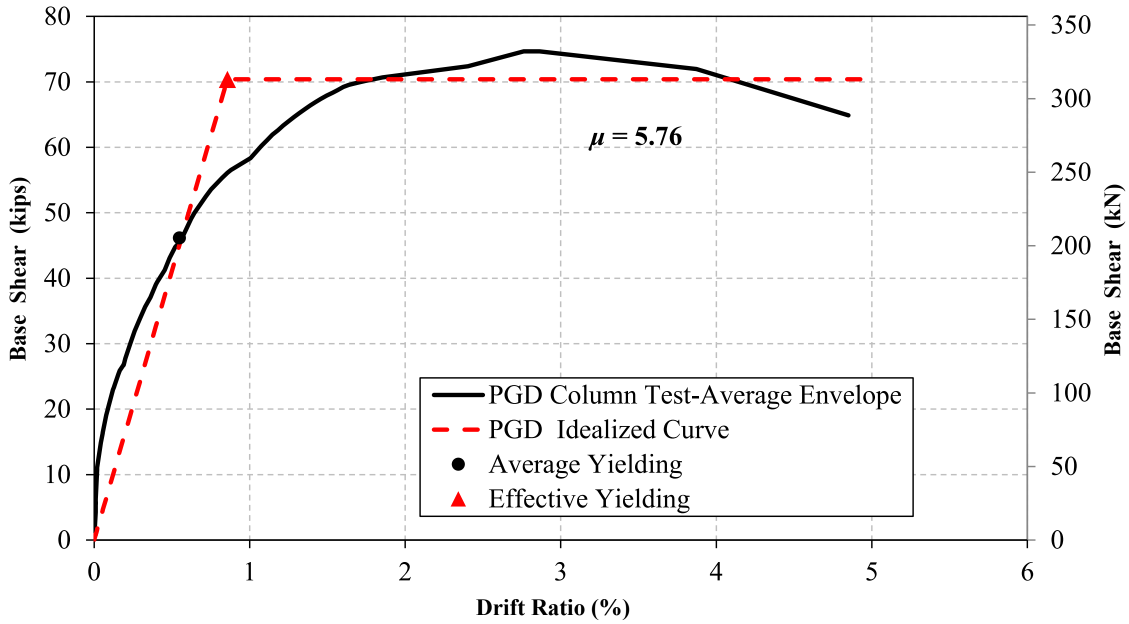

Figure 3.102 Measured PGD Column Average Push/Pull Force-Drift Envelope and Idealized Curve

3.5.3.3 Strain Profiles

Seventeen strain gauges were installed on the PGD reinforcing steel bars at three levels. Figures 3.103 to 3.106 show the measured strain profiles of the column for Bars B1, B2, B6, and B7.

The strain profile was uniform prior to the bar yielding. The strain was generally higher closer to the column-footing-interface and decreased along the height of the column once the bars yielded. The bar strains decreased significantly along the height of the column as the height exceeded the column analytical plastic hinge length (approximately 20 in. or 500 mm). It should be noted that the strain profiles for a mechanically spliced column do not follow those of CIP because couplers are stiff and strong, shifting the nonlinearity away from the coupler regions. Thus, the column longitudinal bar strains are higher at the coupler ends. This observation will be discussed further in Section 3.6.

The strain on the reinforcing hoops was also monitored. The yield strain for the hoops in the precast columns was 0.23%. The maximum measured strain in all PGD hoops was slightly higher (0.38%) than the yield strain.

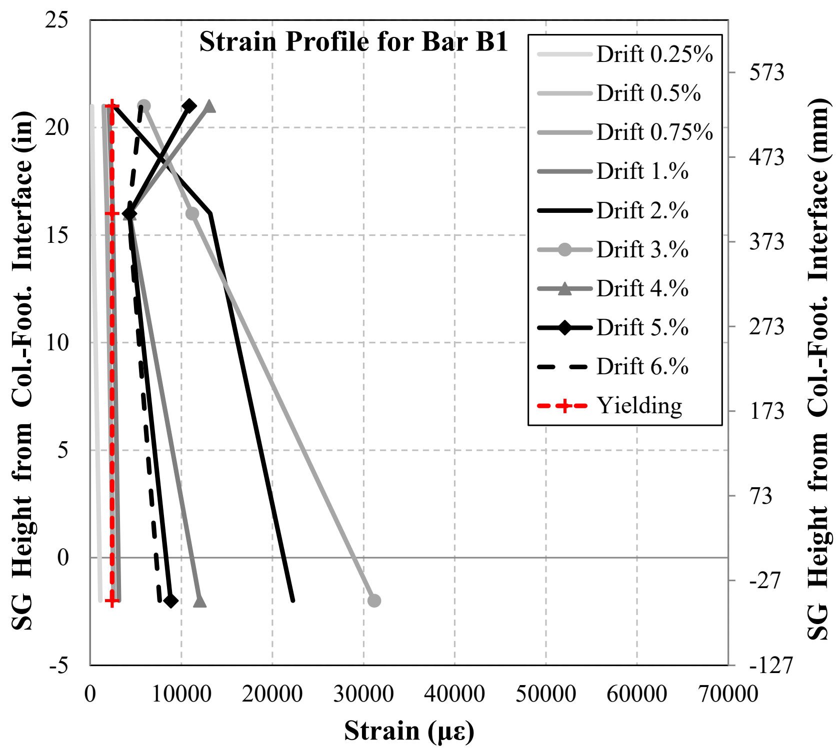

Figure 3.103 Measured Strain Profile for PGD Column Bar B1

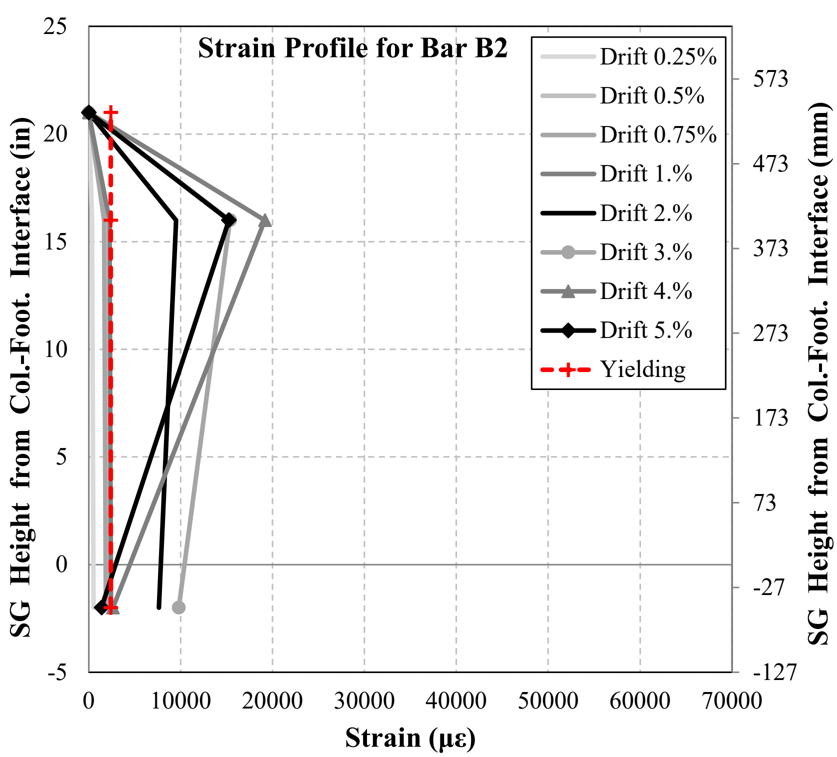

Figure 3.104 Measured Strain Profile for PGD Column Bar B2

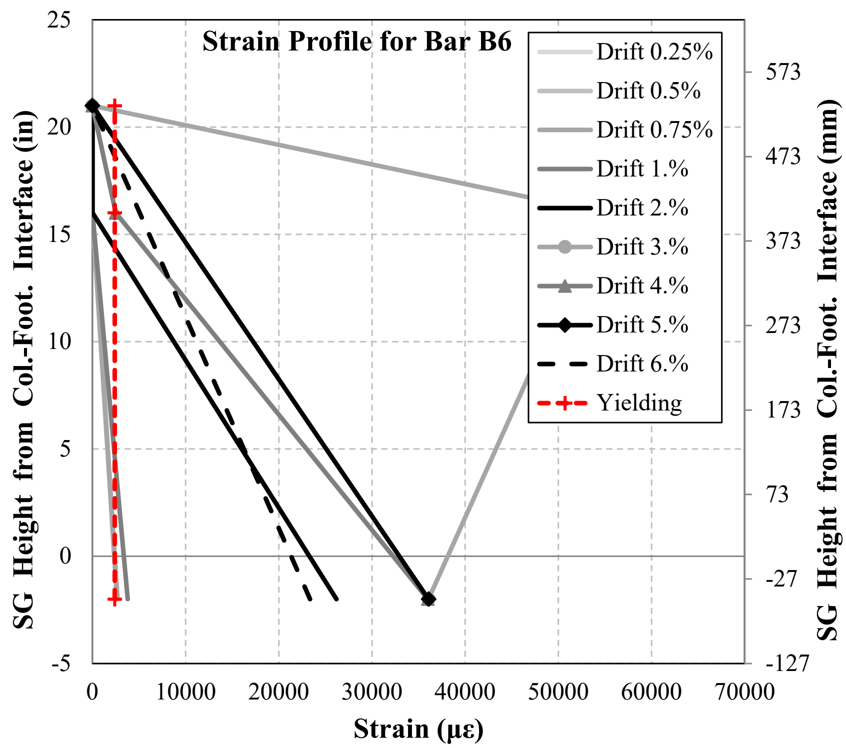

Figure 3.105 Measured Strain Profile for PGD Column Bar B6

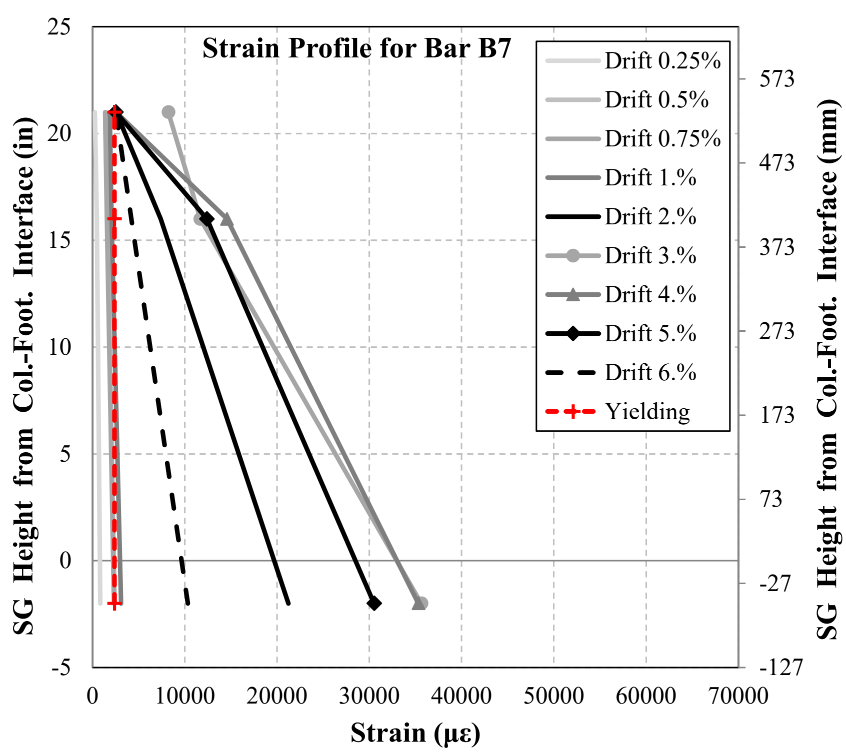

Figure 3.106 Measured Strain Profile for PGD Column Bar B7

3.5.3.4 Measured Rotation and Curvature

Rotations and curvatures were determined in the same manner as CIP. Figure 3.107 shows the measured curvature profile for the PGD column at drift ratios of 0.25% to 4.0%. The highest curvature always occurred at the base due to concentrated concrete cracking and bar-slip near the column-footing interface. The grouted couplers used in PGD increased the column stiffness in the coupler region, leading to a shift of nonlinearity outside of the coupler. The figure confirms this observation in which the curvature was relatively high near the column base, minimal along the coupler region, and high above the coupler levels.

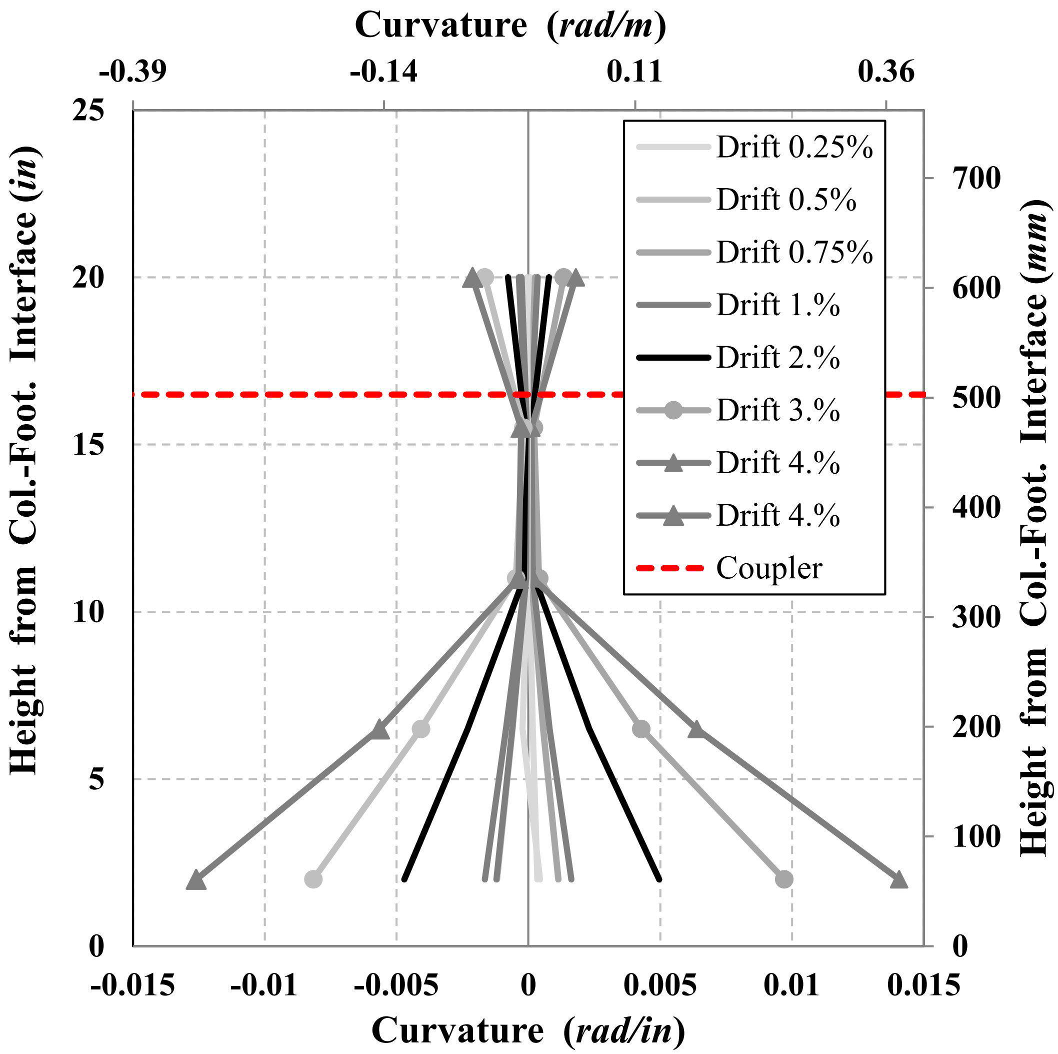

Figure 3.107 Measured Curvature Profile for PGD Column

3.5.3.5 Energy Dissipation

Figure 3.108 shows the measured cumulative energy dissipation of the PGD column at different drift ratios. The dissipated energy is negligible until 1% drift ratio, where bar yielding was minimal. At higher drift ratios, the hysteretic loops began to widen, which led to a higher dissipated energy. PGD dissipated 2,036 kip-in. (230 kN-m) of energy prior to the failure.

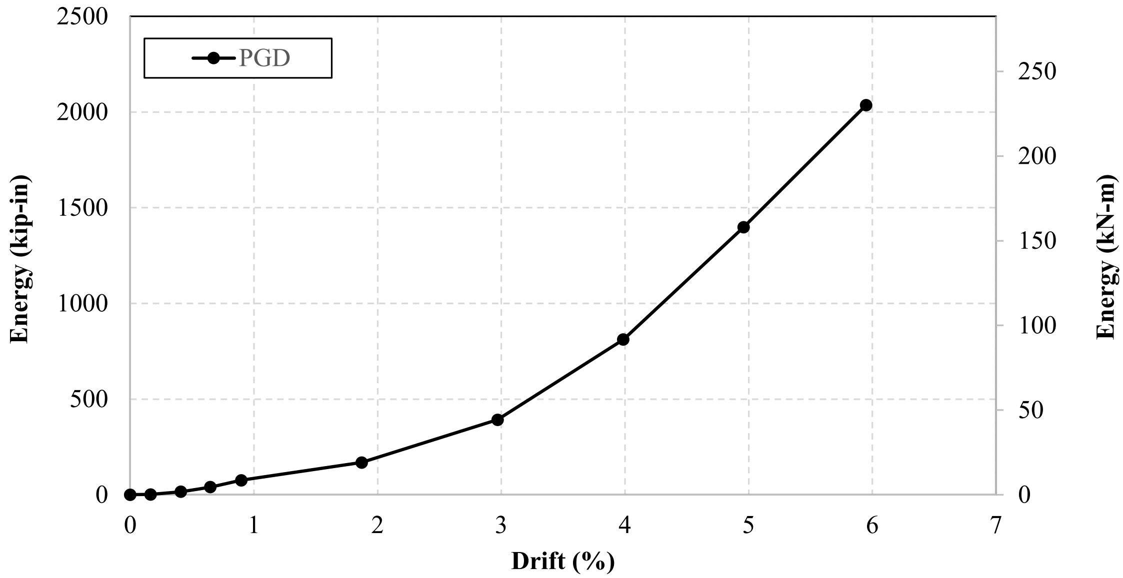

Figure 3.108 Measured Energy Dissipation for PGD Column

3.5.4 PGS Column Results

The seismic performance of the precast column using the NMB Splice Sleeve grouted coupler, PGS, is presented in this section.

3.5.4.1 Observed Damage

PGS followed the same testing procedure as CIP. Table 3.8 presents a summary of the damage observed for each push or pull load of PGS. Figures 3.109 to 3.132 show the PGS plastic hinge damage in the second cycle of the push or pull for each drift level. Flexural cracks were observed in the first cycle of 0.25% drift ratio (Fig. 3.109 & 3.110). Shear cracks were first observed in the first cycle of 0.5% drift ratio (Fig. 3.111 & 3.112). The first yielding occurred in bar B1 at 0.66% drift in the first push run of the 0.75% drift cycle under a lateral load of 48.4 kips (215.9 kN) (Fig. 3.113). Concrete spalling began to occur on both the north and south faces of the column during the 3% drift cycles (Fig. 3.119 & 3.120). Transverse bars became exposed on the north face of the column during the 4% drift cycle (Fig. 3.121 & 3.122). The longitudinal bars on the north face of the column were exposed during the 7% drift cycle (Fig. 3.127 & 3.128). Portions of the coupler and more longitudinal bars became exposed on the north face of the column during the 8% drift cycle (Fig. 3.129 & 3.130). Finally, longitudinal bars ruptured on the south face of the column during the 9% drift cycle, leading to a major strength reduction ending the test (Fig. 3.131 & 3.132). Therefore, the PGS column mode of failure was longitudinal bar rupture during the 9% drift cycles.

Table 3.8 Summary of Damage in PGS

Drift Ratio, %	Observed Damage
+0.25	• Minor flexural cracks
-0.25	• Minor flexural cracks
+0.50	• Flexural and inclined cracks
-0.50	• Flexural and inclined cracks • Cracking at column base
+0.75	• Flexural cracks • Bar yielding
-0.75	• Flexural cracks • Bar yielding
+1.00	• Widening of cracks
-1.00	• Widening of cracks
+2.00	• Vertical, flexural, and inclined cracks
-2.00	• Vertical, flexural, and inclined cracks
+3.00	• Widening of cracks • Initiation of spalling on south face of column
-3.00	• Widening of cracks • Initiation of spalling on north face of column
+4.00	• Widening of cracks
-4.00	• Widening of cracks • Transverse bars exposed on the north face of column
+5.00	• Increased spalling
-5.00	• Increased spalling
+6.00	• Several transverse bars exposed on north face of column
-6.00	• Increased spalling
+7.00	• All plastic hinge transverse bars exposed on north face of column • Longitudinal bar exposed on north face of column
-7.00	• Transverse bars exposed on south face of column
+8.00	• Coupler and longitudinal bar exposed on north face of column
-8.00	• No further damage
+9.00	• Strength reduction due to longitudinal bar pull out on north face of column
-9.00	• Longitudinal bar rupture on south face of column

Note: Positive drifts were based on displacements away from the reaction blocks (north to south)

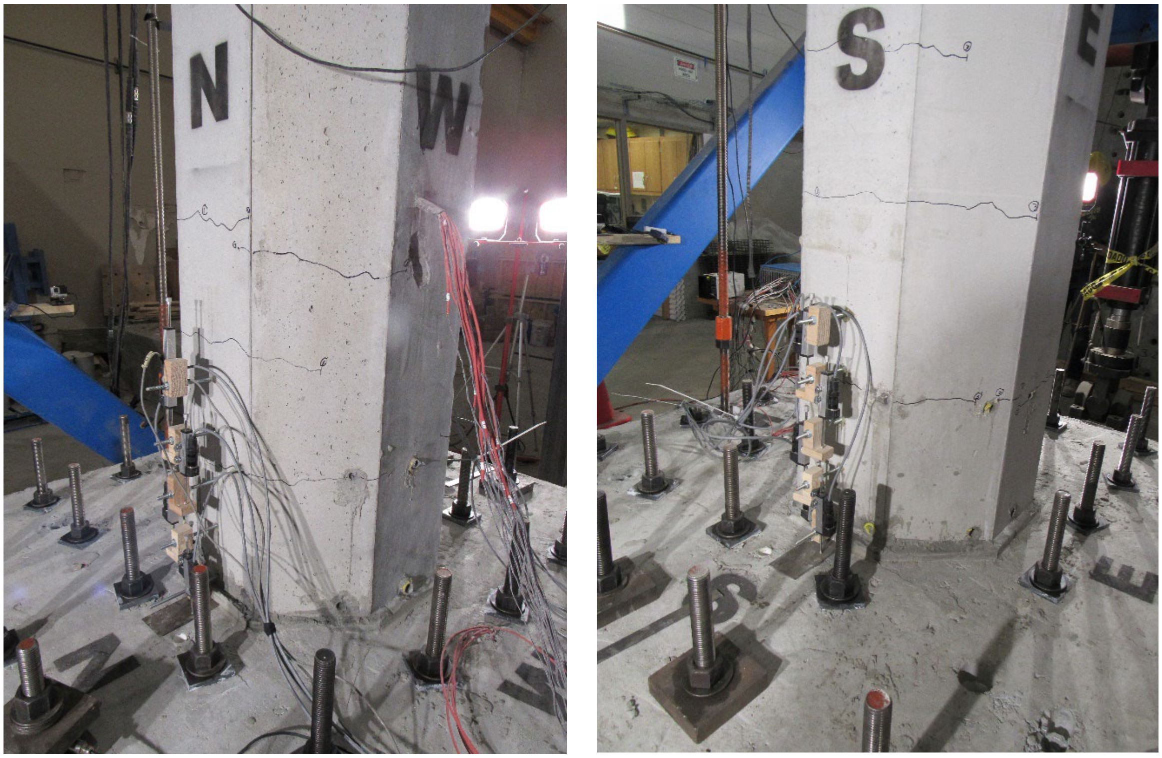

a) North-West Side b) South-East Side

Figure 3.109 PGS Column Plastic Hinge Damage, Second Push of 0.25% Drift Cycle

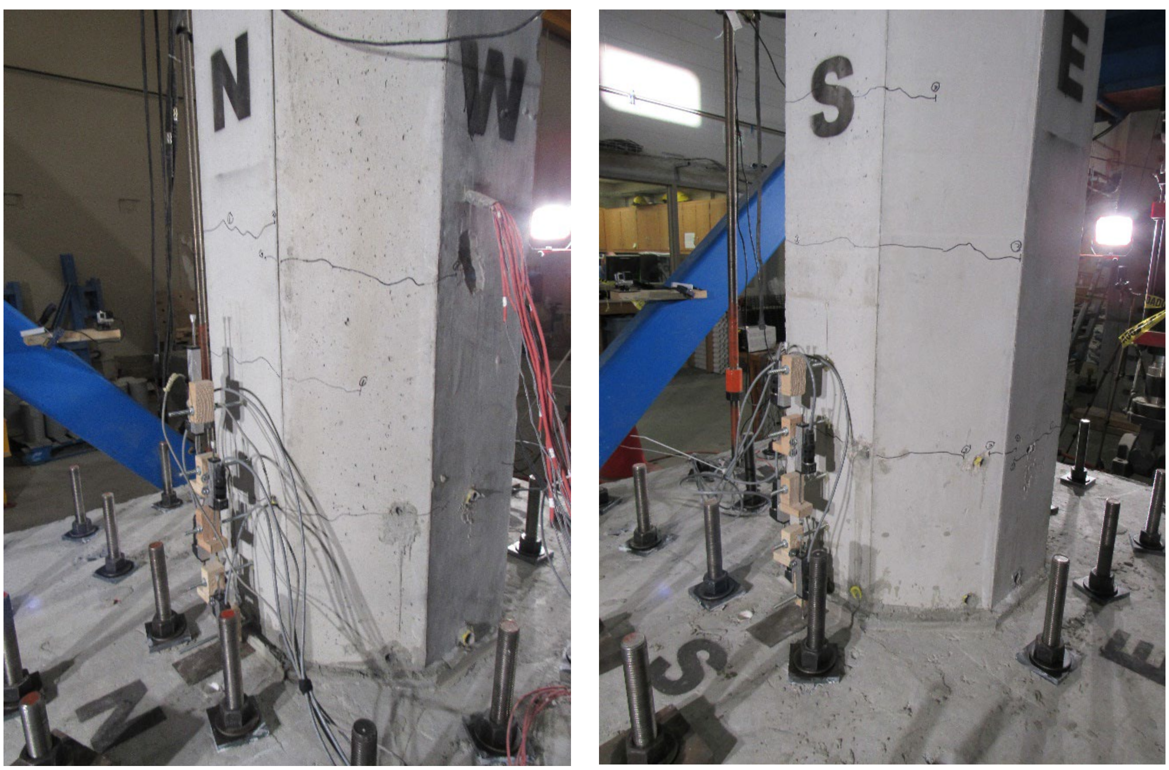

a) North-West Side b) South-East Side

Figure 3.110 PGS Column Plastic Hinge Damage, Second Pull of 0.25% Drift Cycle

a) North-West Side b) South-East Side

Figure 3.111 PGS Column Plastic Hinge Damage, Second Push of 0.50% Drift Cycle

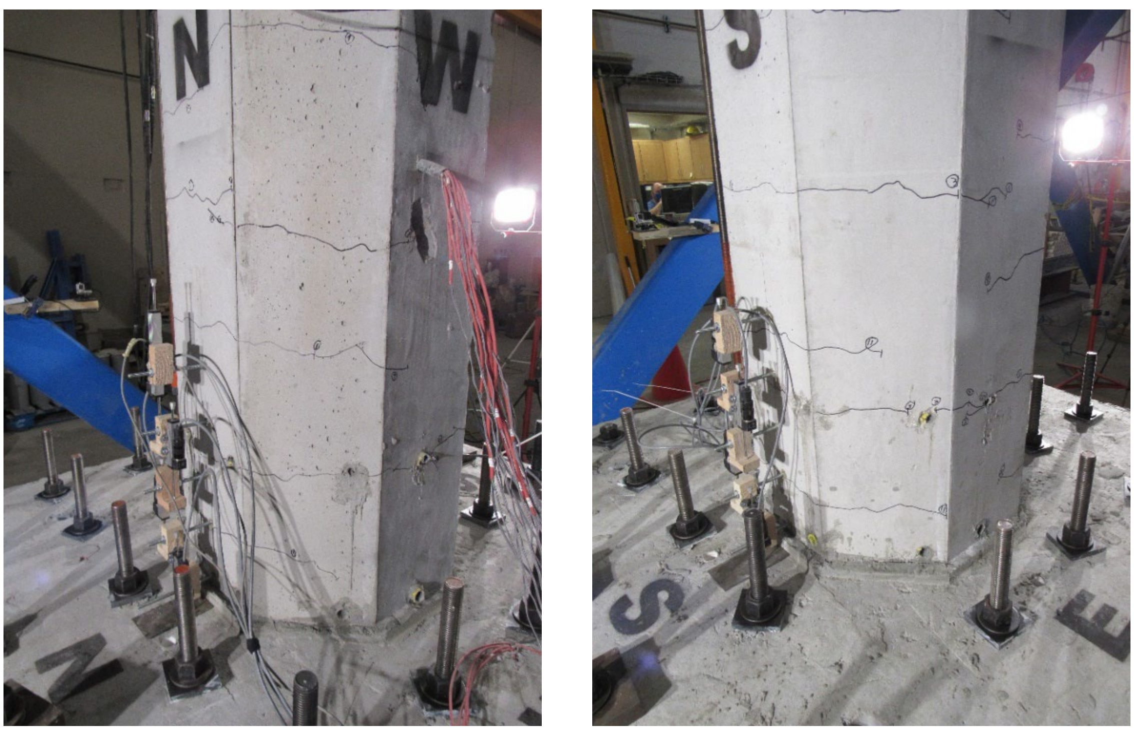

a) North-West Side b) South-East Side

Figure 3.112 PGS Column Plastic Hinge Damage, Second Pull of 0.50% Drift Cycle

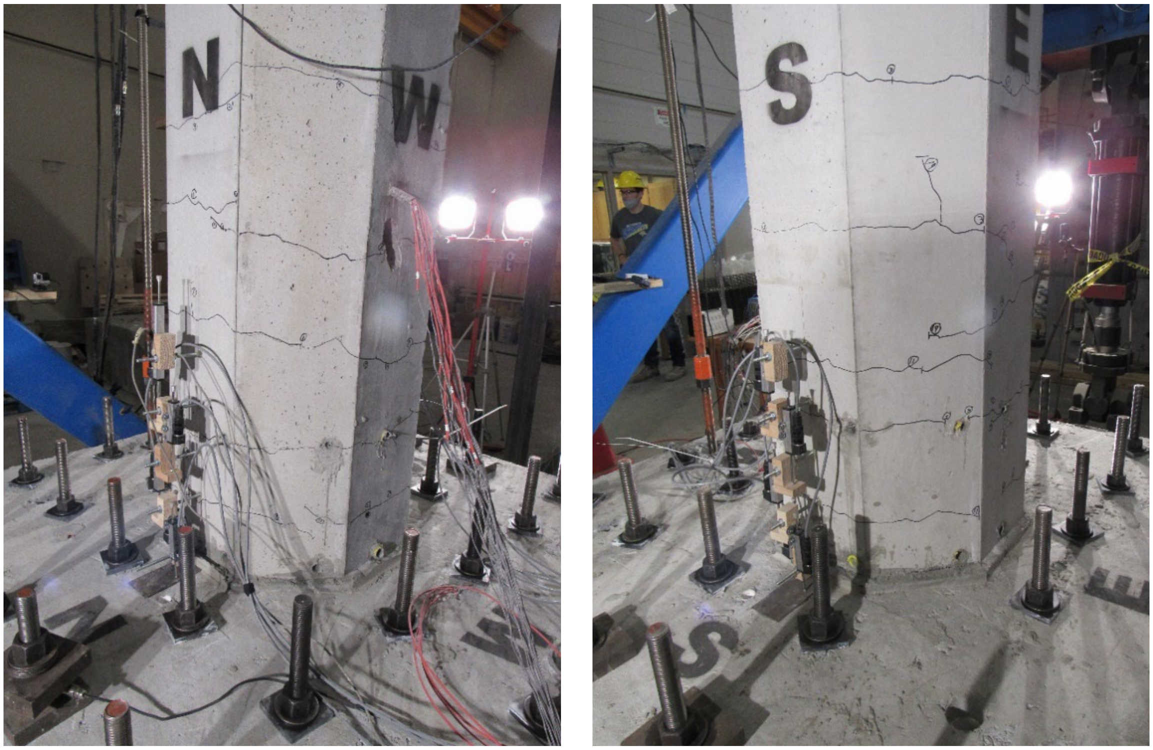

a) North-West Side b) South-East Side

Figure 3.113 PGS Column Plastic Hinge Damage, Second Push of 0.75% Drift Cycle

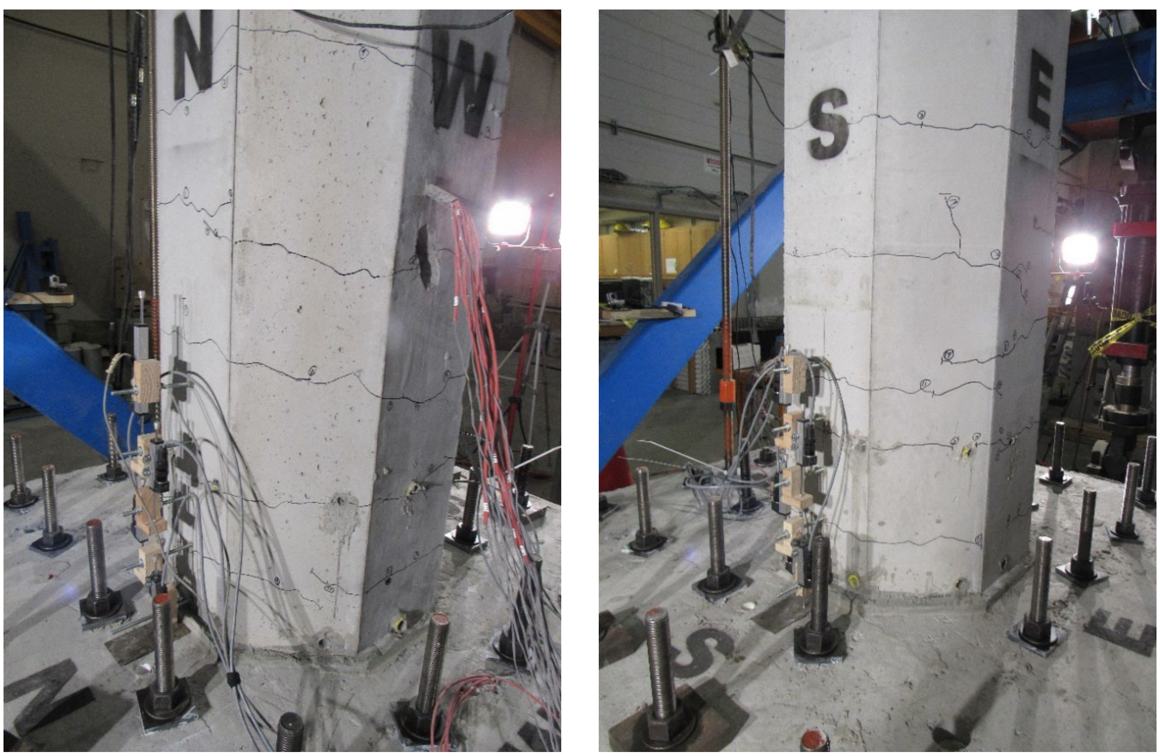

a) North-West Side b) South-East Side

Figure 3.114 PGS Column Plastic Hinge Damage, Second Pull of 0.75% Drift Cycle

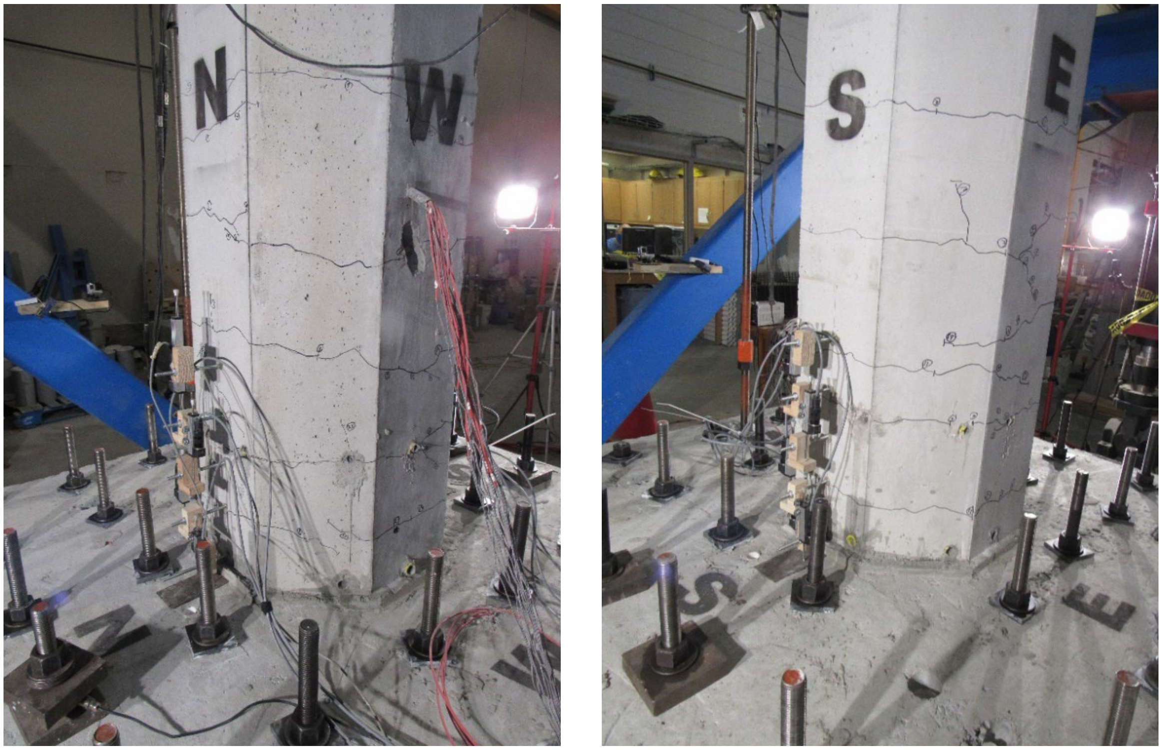

a) North-West Side b) South-East Side

Figure 3.115 PGS Column Plastic Hinge Damage, Second Push of 1.00% Drift Cycle

a) North-West Side b) South-East Side

Figure 3.116 PGS Column Plastic Hinge Damage, Second Pull of 1.00% Drift Cycle

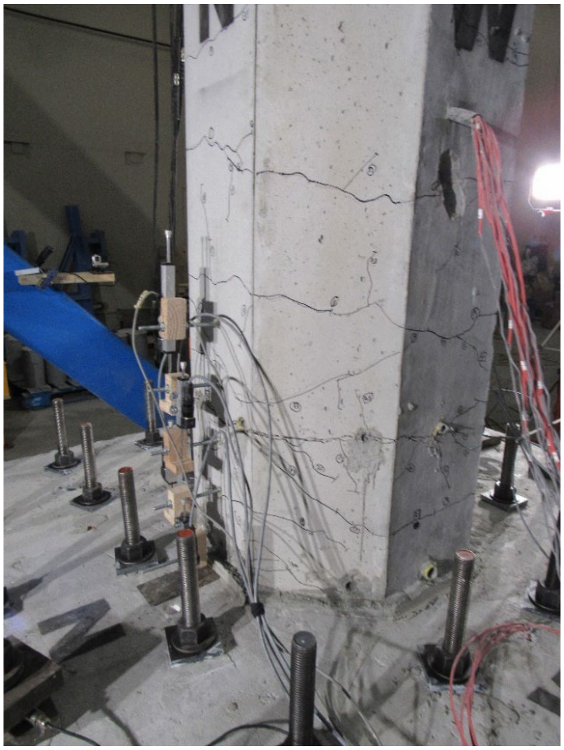

a) North-West Side

b) South-East Side

Figure 3.117 PGS Column Plastic Hinge Damage, Second Push of 2.00% Drift Cycle

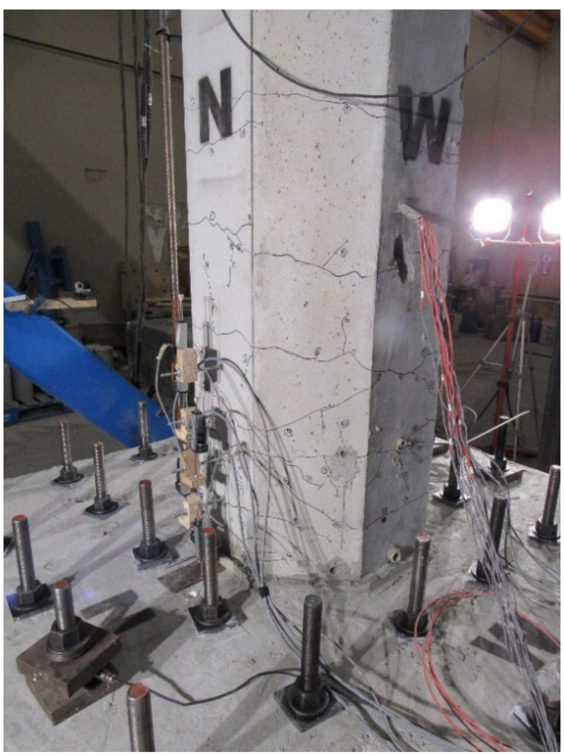

a) North-West Side

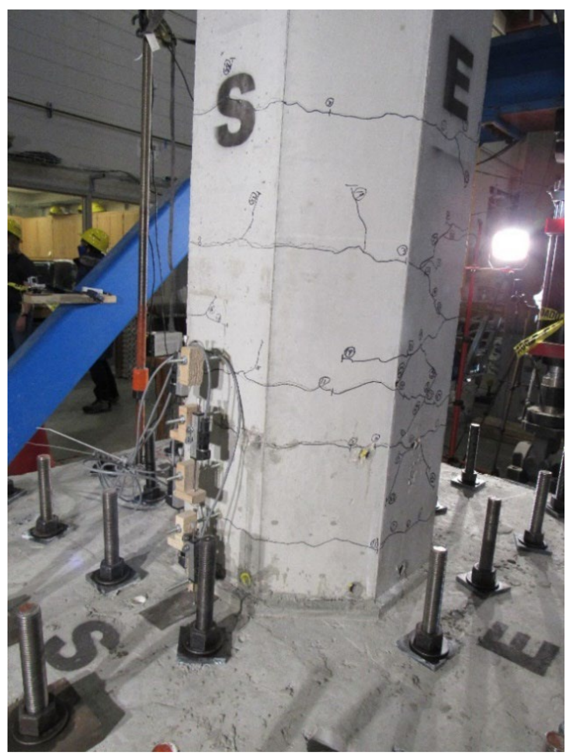

b) South-East Side

Figure 3.118 PGS Column Plastic Hinge Damage, Second Pull of 2.00% Drift Cycle

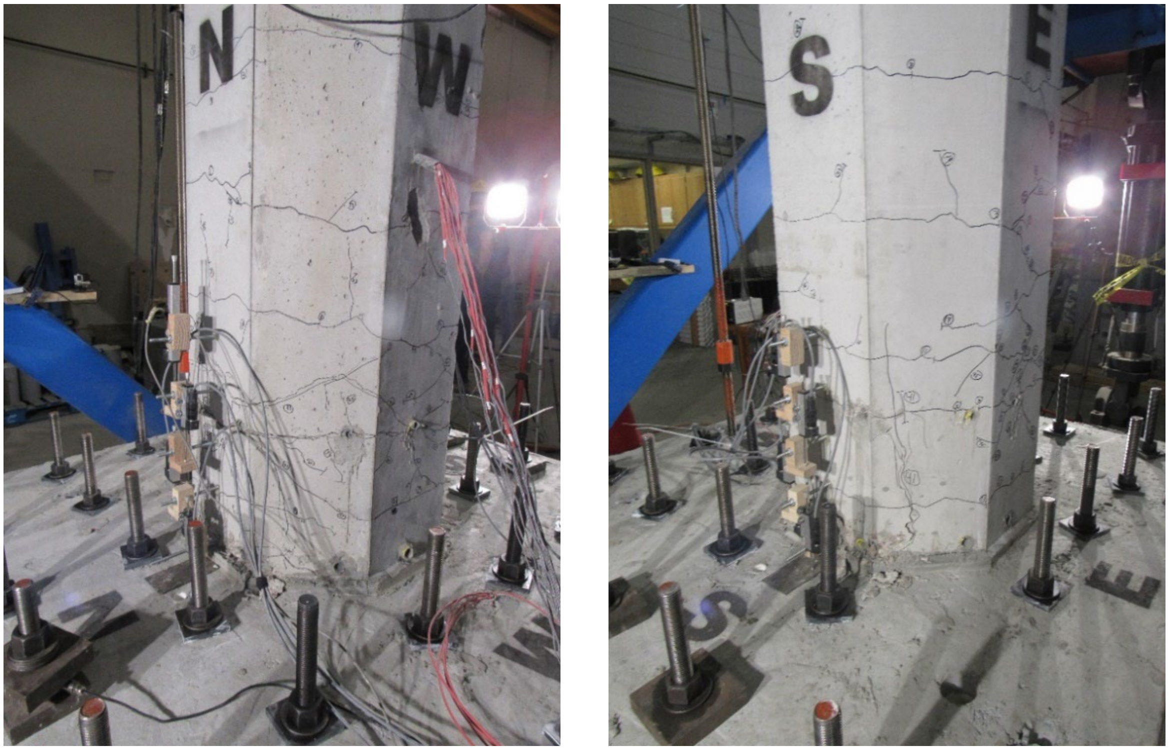

a) North-West Side b) South-East Side

Figure 3.119 PGS Column Plastic Hinge Damage, Second Push of 3.00% Drift Cycle

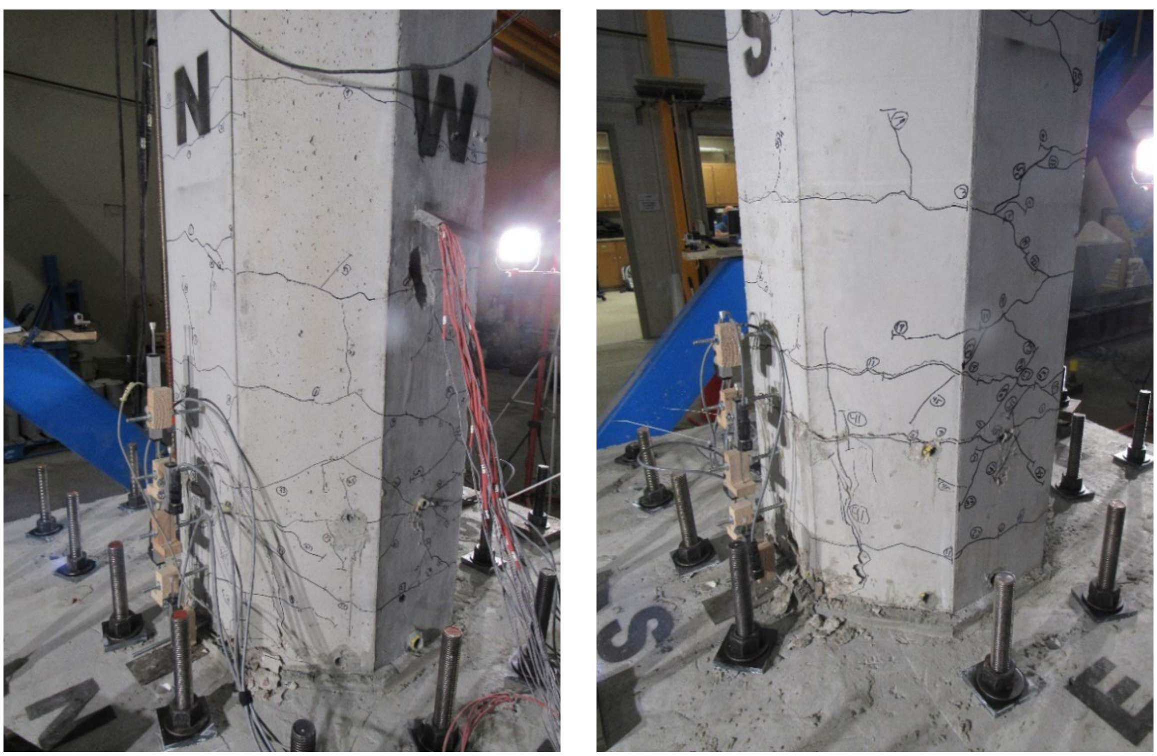

a) North-West Side b) South-East Side

Figure 3.120 PGS Column Plastic Hinge Damage, Second Pull of 3.00% Drift Cycle

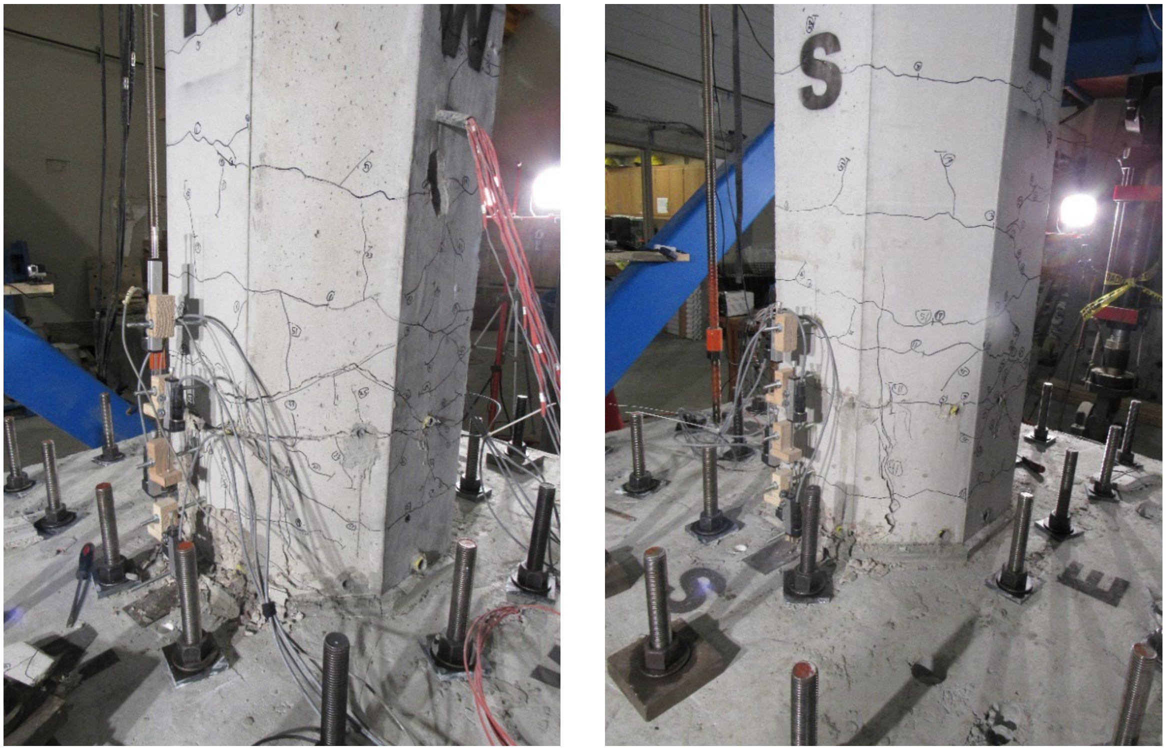

a) North-West Side　　　b) South-East Side

Figure 3.121 PGS Column Plastic Hinge Damage, Second Push of 4.00% Drift Cycle

a) North-West Side　　　b) South-East Side

Figure 3.122 PGS Column Plastic Hinge Damage, Second Pull of 4.00% Drift Cycle

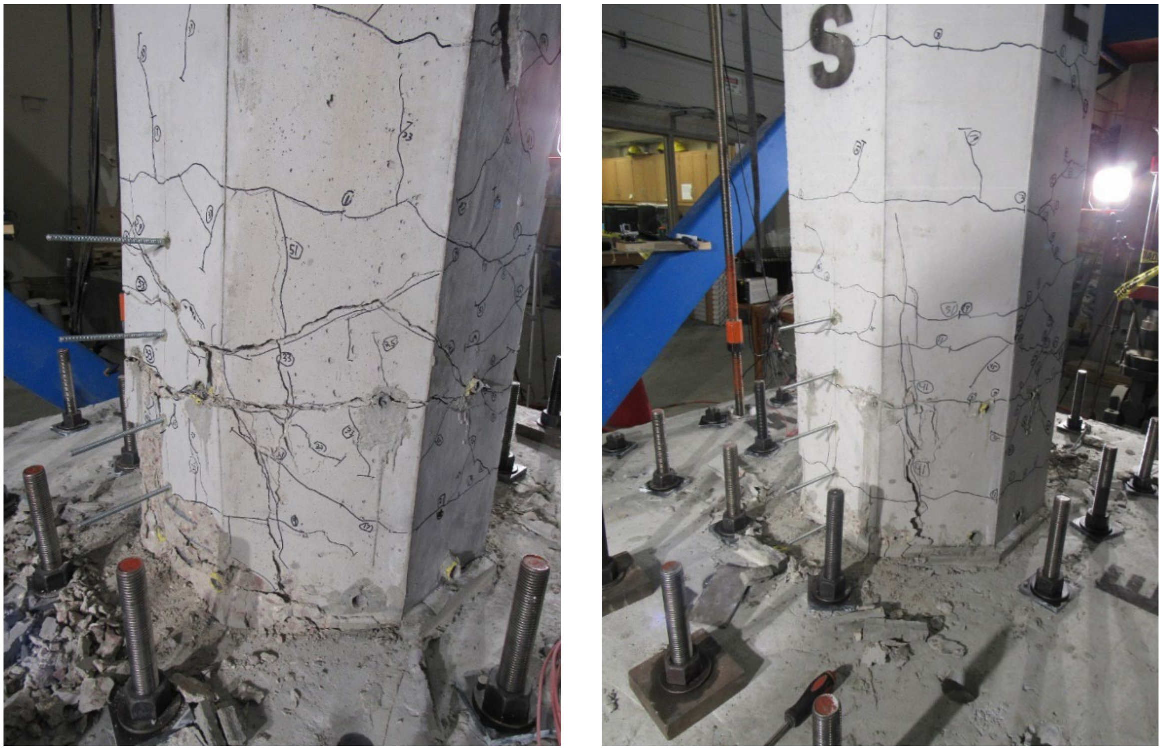

a) North-West Side　　　　b) South-East Side

Figure 3.123 PGS Column Plastic Hinge Damage, Second Push of 5.00% Drift Cycle

a) North-West Side　　　　b) South-East Side

Figure 3.124 PGS Column Plastic Hinge Damage, Second Pull of 5.00% Drift Cycle

a) North-West Side b) South-East Side

Figure 3.125 PGS Column Plastic Hinge Damage, Second Push of 6.00% Drift Cycle

a) North-West Side b) South-East Side

Figure 3.126 PGS Column Plastic Hinge Damage, Second Pull of 6.00% Drift Cycle

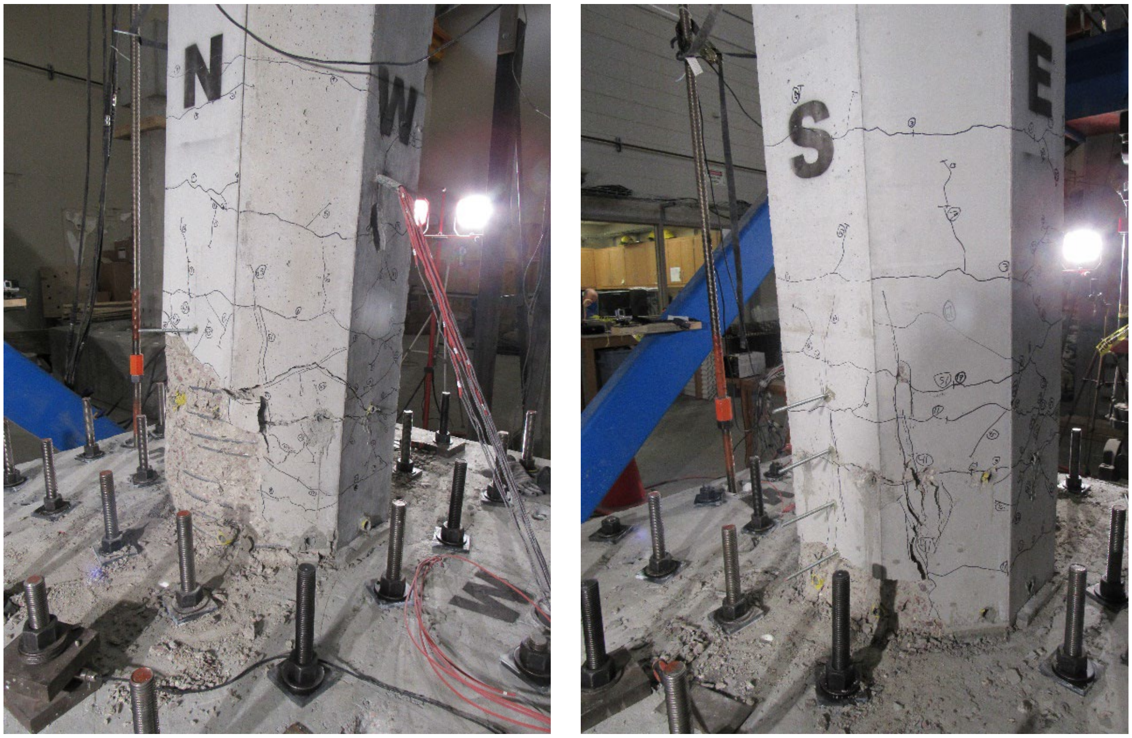

a) North-West Side b) South-East Side

Figure 3.127 PGS Column Plastic Hinge Damage, Second Push of 7.00% Drift Cycle

a) North-West Side b) South-East Side

Figure 3.128 PGS Column Plastic Hinge Damage, Second Pull of 7.00% Drift Cycle

a) North-West Side b) South-East Side

Figure 3.129 PGS Column Plastic Hinge Damage, Second Push of 8.00% Drift Cycle

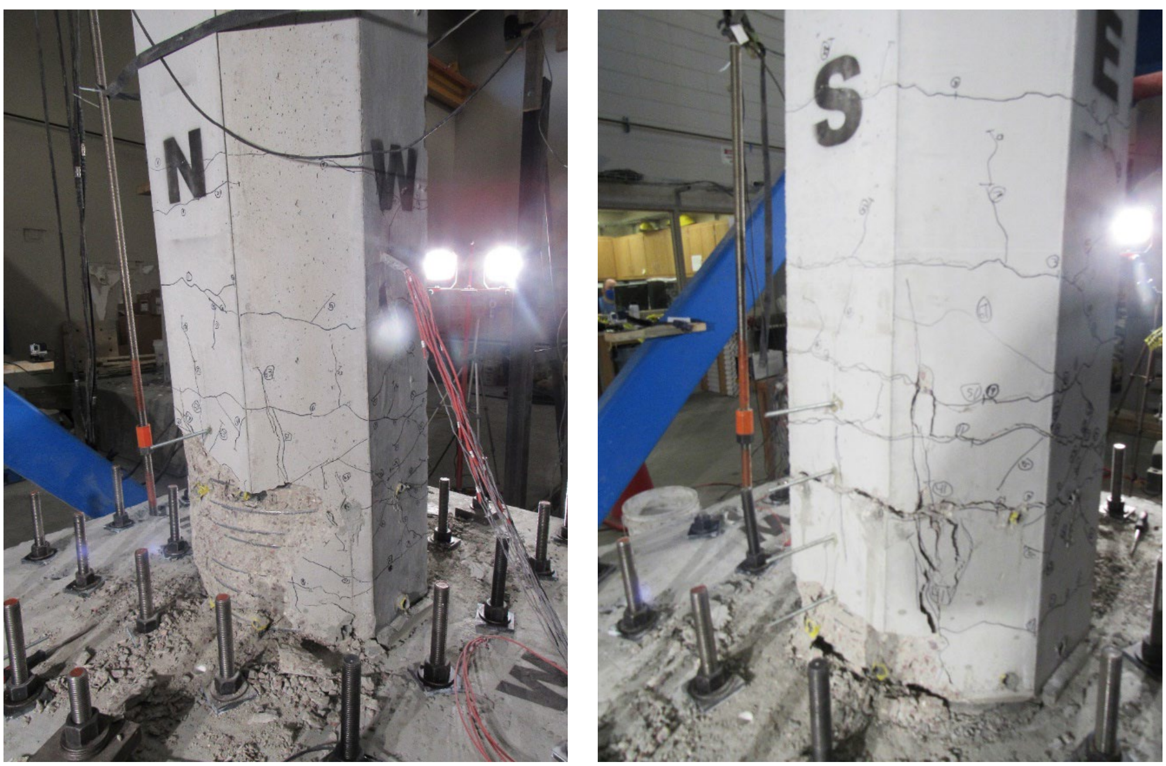

a) North-West Side b) South-East Side

Figure 3.130 PGS Column Plastic Hinge Damage, Second Pull of 8.00% Drift Cycle

a) North-West Side b) South-East Side

Figure 3.131 PGS Column Plastic Hinge Damage, First Push of 9.00% Drift Cycle

a) North-West Side b) South-East Side

Figure 3.132 PGS Column Plastic Hinge Damage, First Pull of 9.00% Drift Cycle

3.5.4.2 Force-Displacement Relationship

Figure 3.133 shows the measured lateral force-drift hysteretic and envelope responses of PGS. The PGS column exhibited a maximum lateral load of 69.6 kips (310 kN) at 2% drift ratio and exhibited a steady strength degradation afterwards. A significant strength and stiffness degradation was observed after 9% drift ratio due to the longitudinal bar fracture at the column base. The column was slightly stronger in the pull direction. The PGS longitudinal bars yielded at 0.66% drift ratio in the push direction under a lateral load of 48.4 kips (215.3 kN), and at -0.66% drift ratio in the pull direction at a lateral load of -54.0 kips (240.2 kN).

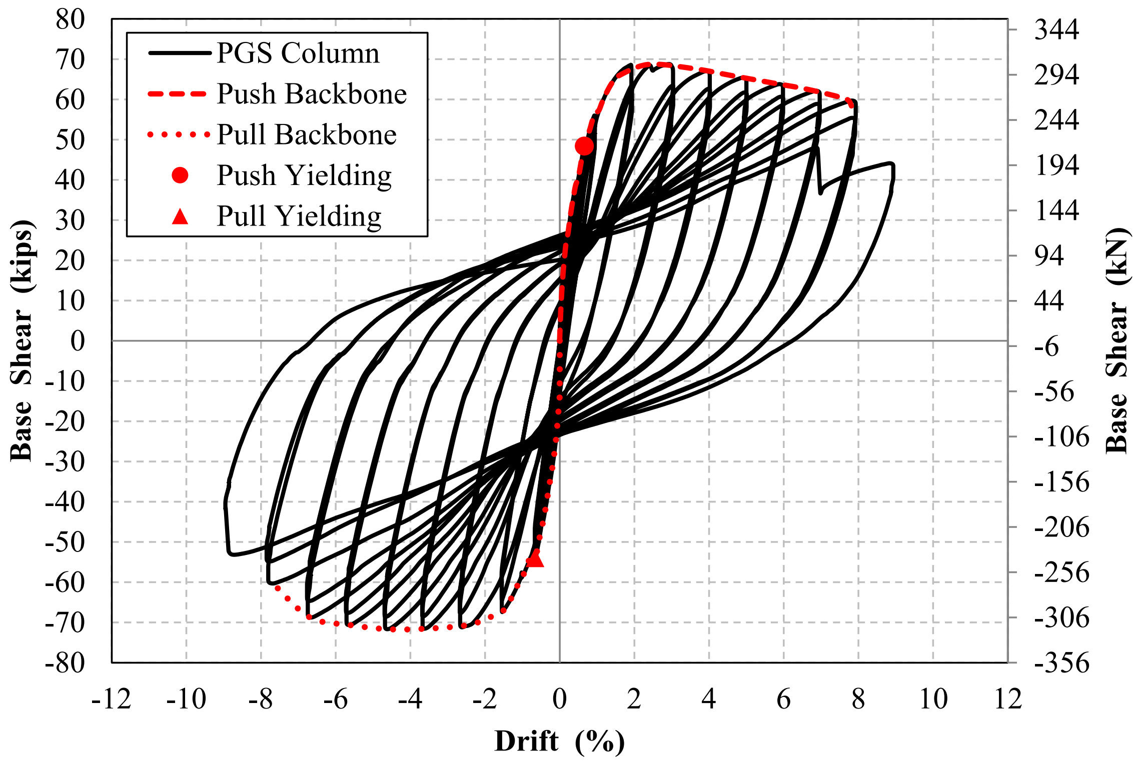

Figure 3.133 PGS Column Force-Drift Hysteretic and Envelope Responses

Figure 3.134 shows the average envelope for the push and pull directions of PGS. The average yield drift ratio of 0.66% occurred at a lateral force of 51.2 kips (227.8 kN). Based on the 15% load drop as the column failure point, the drift capacity of the PGS column was 7.71%. Furthermore, Figure 3.134 shows the idealized curve for the average PGS envelope. The effective yield drift ratio was 0.85% at the effective yield lateral force of 66.1 kip (294.0 kN) resulting in a displacement ductility capacity of 9.08 for the PGS column.

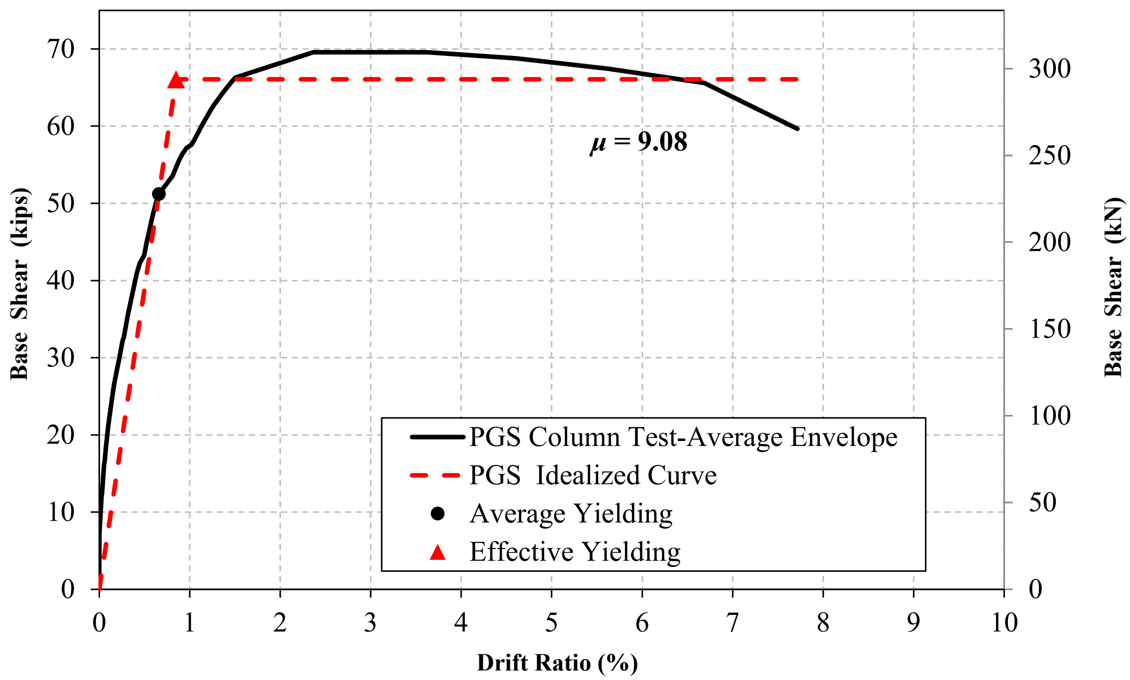

Figure 3.134 PGS Column Average Push/Pull Force-Drift Envelope and Idealized Curve

3.5.4.3 Strain Profile

Seventeen strain gauges were installed on the PGS reinforcing steel bars at three levels. Figures 3.135 to 3.138 show the measured strain profiles of the column for Bars B1, B2, B6, and B7.

The strain profile was uniform prior to the bar yielding. The strain was generally higher closer to the column-footing-interface and decreased along the height of the column once the bars yielded. As discussed before, the strain profiles for a mechanically spliced column do not follow those of CIP because couplers are stiff and strong, shifting the nonlinearity away from the coupler regions. Thus, the column longitudinal bar strains are higher at the coupler ends.

The strain on the reinforcing hoops was also monitored. The yield strain for the hoops in the precast columns was 0.23%. The maximum measured strain in the hoops was 3.1% and occurred in a hoop immediately above the top of the coupler, indicating a significant yielding of the PGS hoops.

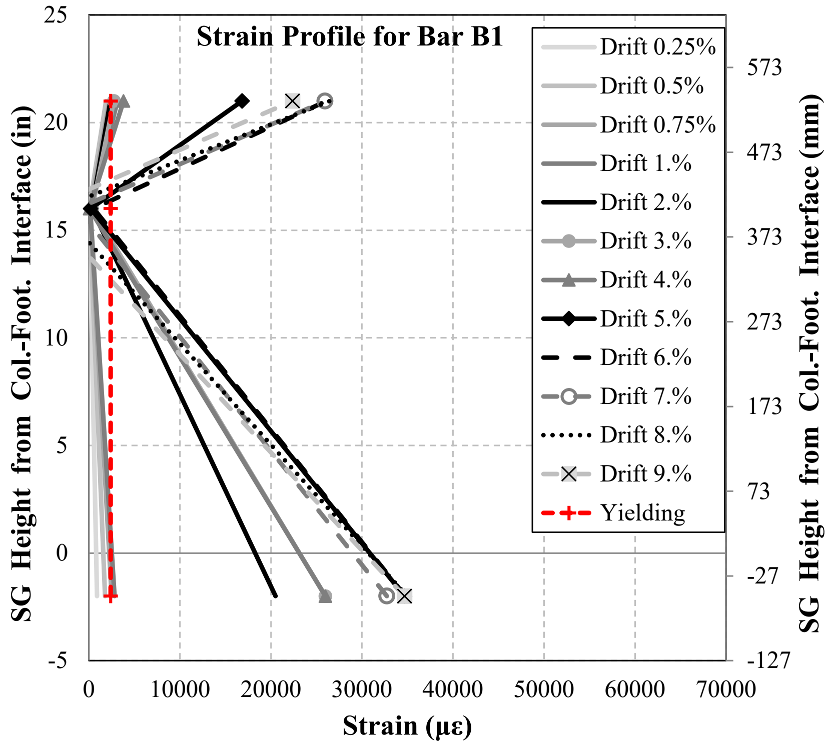

Figure 3.135 Strain Profile for PGS Column Bar B1

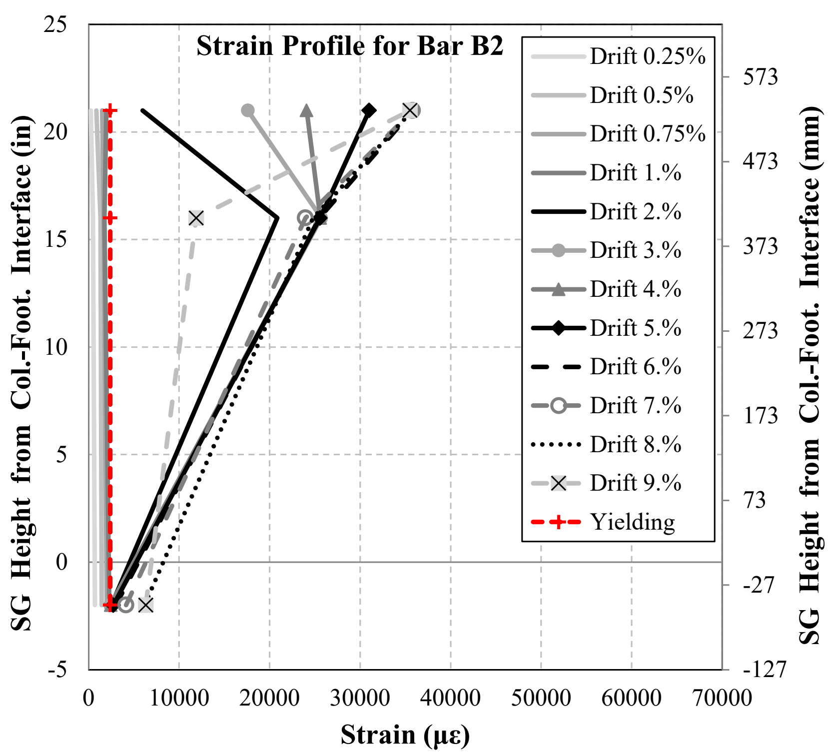

Figure 3.136 Strain Profile for PGS Column Bar B2

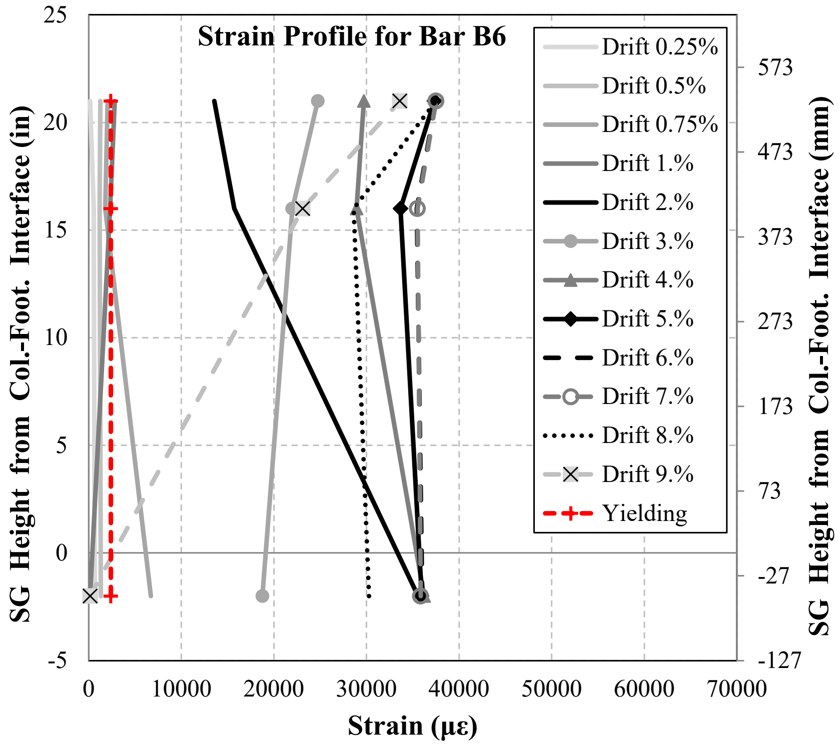

Figure 3.137 Strain Profile for PGS Column Bar B6

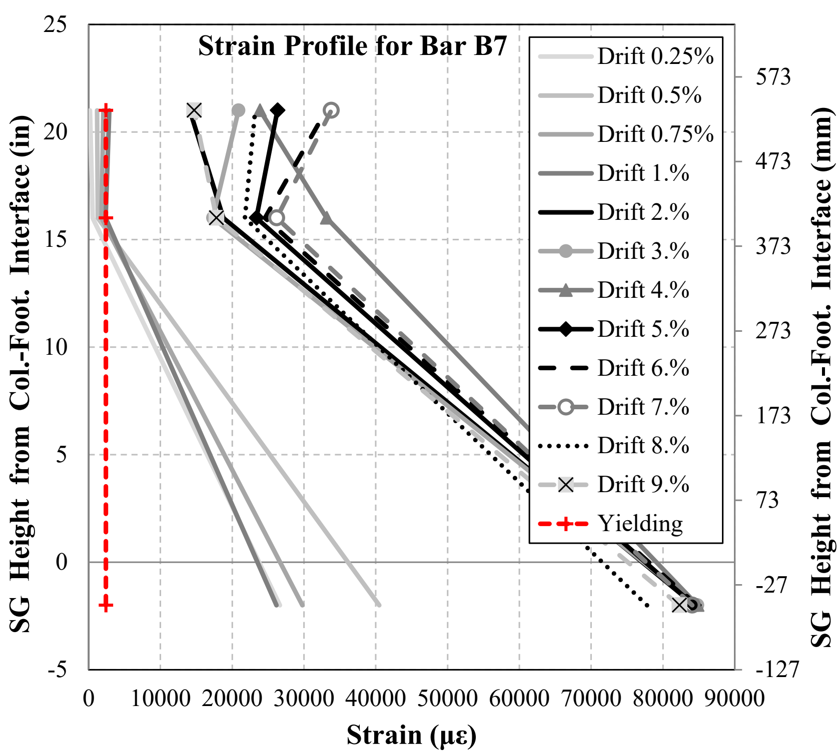

Figure 3.138 Strain Profile for PGS Column Bar B7

3.5.4.4 Measured Rotation and Curvature

Rotations and curvatures were determined in the same manner as CIP. Figure 3.139 shows the measured curvature profile for the PGS column at drift ratios of 0.25% to 4.0%. The highest curvature always occurred at the base due to concentrated concrete cracking and bar-slip near the column-footing interface. The grouted couplers used in PGS increased the column stiffness in the coupler region, leading to a shift of nonlinearity outside of the coupler. The figure confirms this observation in which the curvature was relatively high near the column base, minimal along the coupler region, and high above the coupler levels.

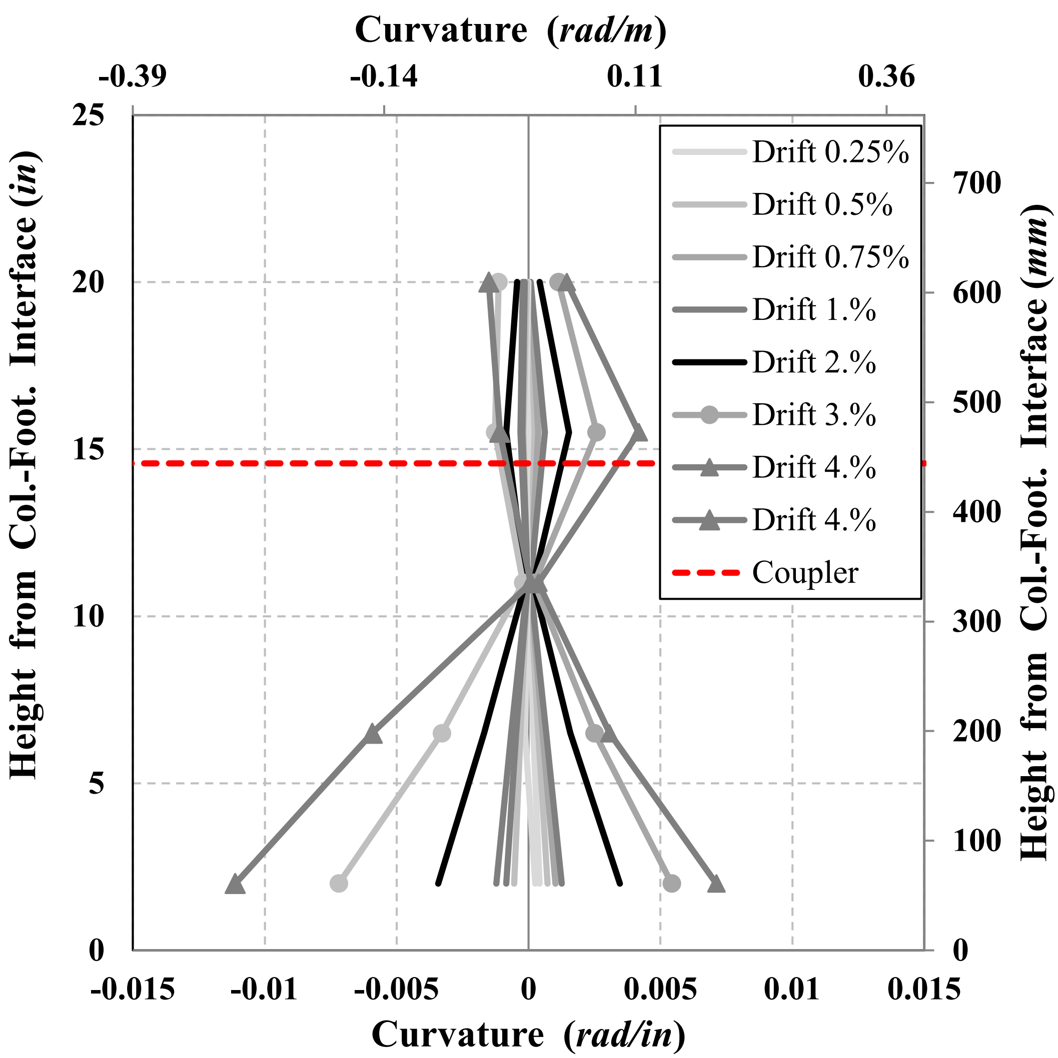

Figure 3.139 Curvature Profile for PGS Column

3.5.4.5 Energy Dissipation

Figure 3.140 shows the measured cumulative energy dissipation of the PGS column at different drift ratios. The dissipated energy is negligible until 1% drift ratio, where bar yielding was minimal. At higher drift ratios, the hysteretic loops began to widen, which led to a higher dissipated energy. PGS dissipated 5,744 kip-in. (653 kN-m) of energy prior to the failure.

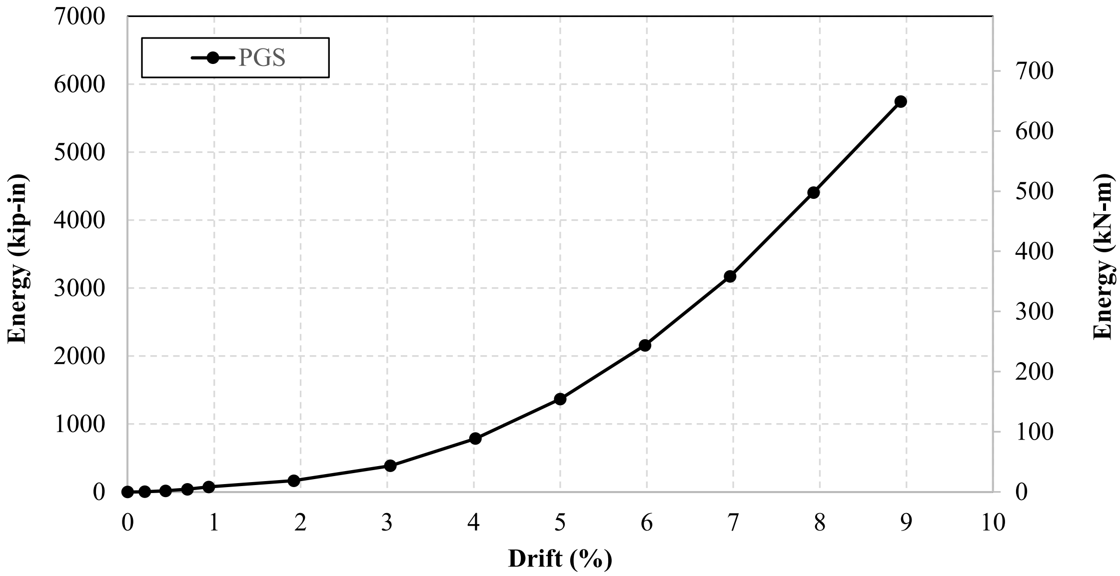

Figure 3.140 Energy Dissipation for PGS Column

3.5.5 PHD Column Results

The seismic performance of the precast column using the Dextra Groutec-S grouted-threaded hybrid coupler, PHD, is presented in this section.

3.5.5.1 Observed Damage

The PHD column followed the same testing procedure as the CIP column. Table 3.9 presents the damage observed for each push or pull loads of PHD. Figures 3.141 to 3.154 show the PHD plastic hinge damage in the second cycle of the push or pull for each drift level.

Flexural cracks were observed in the first cycle of 0.25% drift ratio (Fig. 3.141 & 3.142). Shear cracks were first observed in the first cycle of 0.5% drift ratio (Fig. 3.143 & 3.144). The first yielding occurred in Bar B1 at 0.58% drift in the first push run of the 0.75% drift cycle under a lateral load of 45.9 kips (204.3 kN) (Fig. 3.145). Concrete spalling began to occur on both the north and south faces of the column during the 3% drift cycles (Fig. 3.151 & 3.152). Finally, longitudinal bars pulled out from the bottom end of the couplers at the 4% drift cycle, leading to a major strength degradation ending the test (Figure 3.153 & 3.154). Therefore, the PHD column mode of failure was longitudinal bar pullout during the 4% drift cycles.

Table 3.9 Summary of Damage in PHD

Drift Ratio, %	Observed Damage
+0.25	• Minor flexural cracks • Flexural cracks at top of coupler
-0.25	• Minor flexural cracks • Flexural cracks at top of coupler
+0.50	• Flexural and inclined cracks
-0.50	• Flexural and inclined cracks • Cracking at column base
+0.75	• Flexural cracks • Bar yielding
-0.75	• Flexural cracks • Bar yielding
+1.00	• Flexural cracks • Vertical cracks
-1.00	• Flexural cracks
+2.00	• Vertical, flexural, and inclined cracks
-2.00	• Vertical, flexural, and inclined cracks
+3.00	• Flexural cracks • Initiation of spalling on south face of column
-3.00	• Flexural cracks • Initiation of spalling on north face of column
+4.00	• Longitudinal reinforcement pullout from coupler on north face
-4.00	• Longitudinal reinforcement pullout from coupler on south face

Note: Positive drifts were based on displacements away from the reaction blocks (north to south)

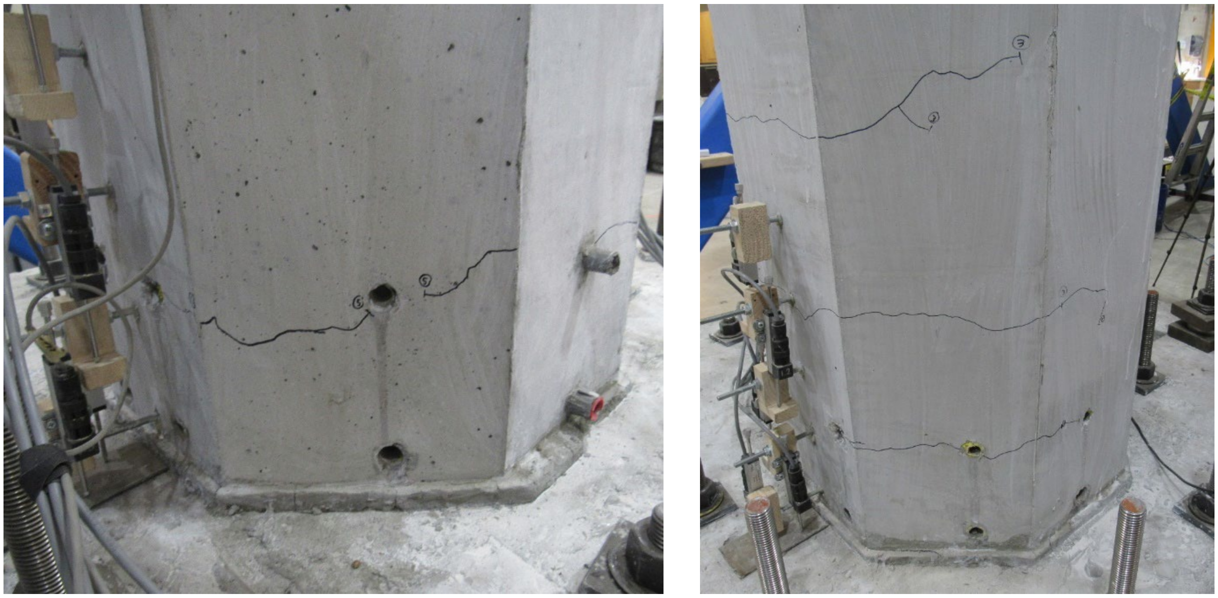

a) North-West Side b) South-East Side

Figure 3.141 PHD Column Plastic Hinge Damage, Second Push of 0.25% Drift Cycle

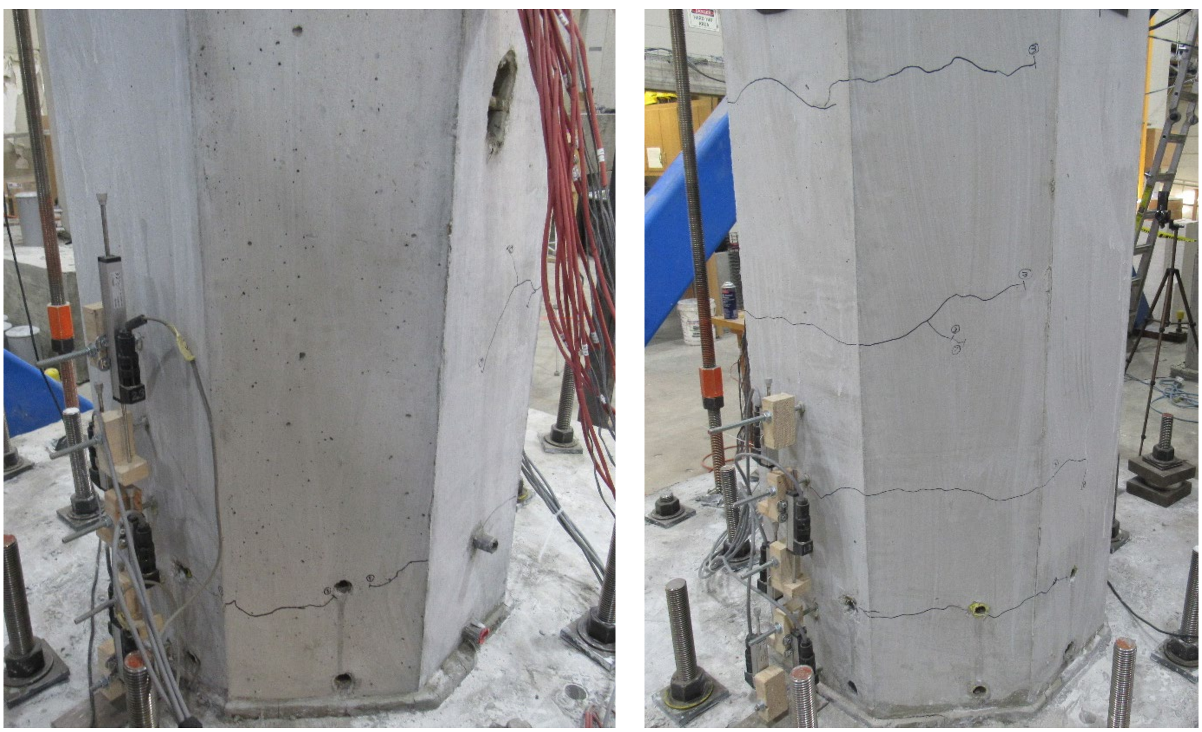

a) North-West Side b) South-East Side

Figure 3.142 PHD Column Plastic Hinge Damage, Second Pull of 0.25% Drift Cycle

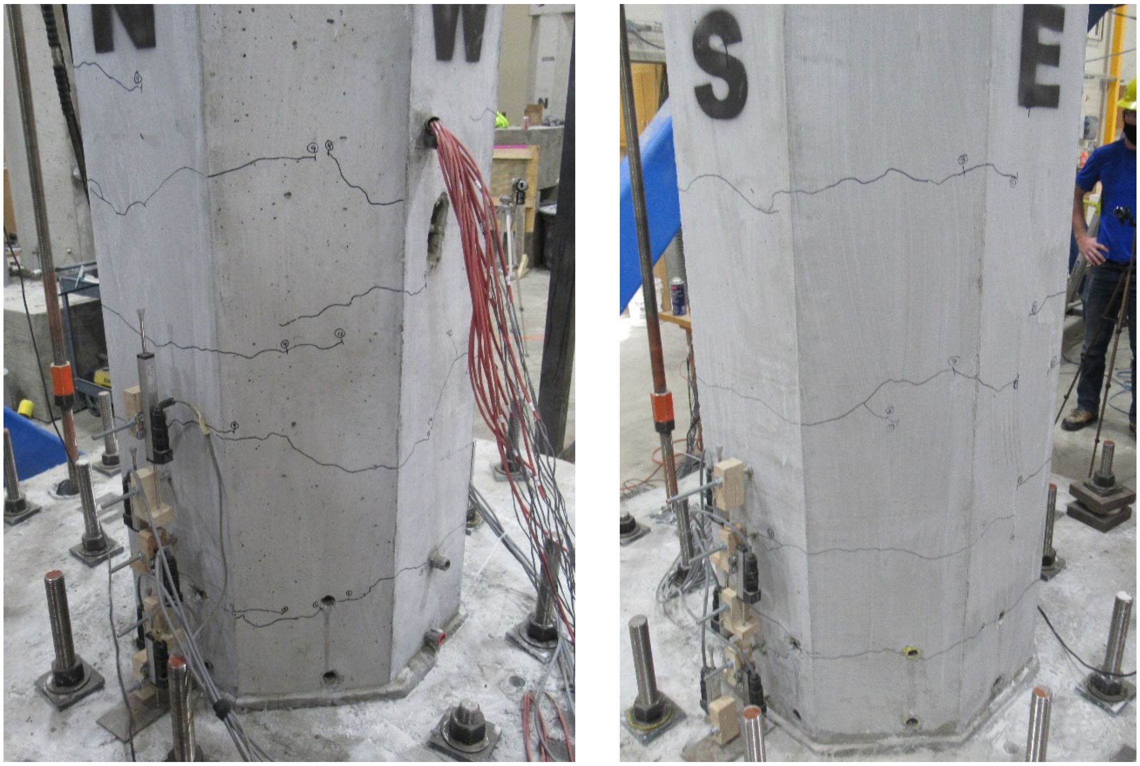

a) North-West Side b) South-East Side

Figure 3.143 PHD Column Plastic Hinge Damage, Second Push of 0.50% Drift Cycle

a) North-West Side b) South-East Side

Figure 3.144 PHD Column Plastic Hinge Damage, Second Pull of 0.50% Drift Cycle

a) North-West Side b) South-East Side

Figure 3.145 PHD Column Plastic Hinge Damage, Second Push of 0.75% Drift Cycle

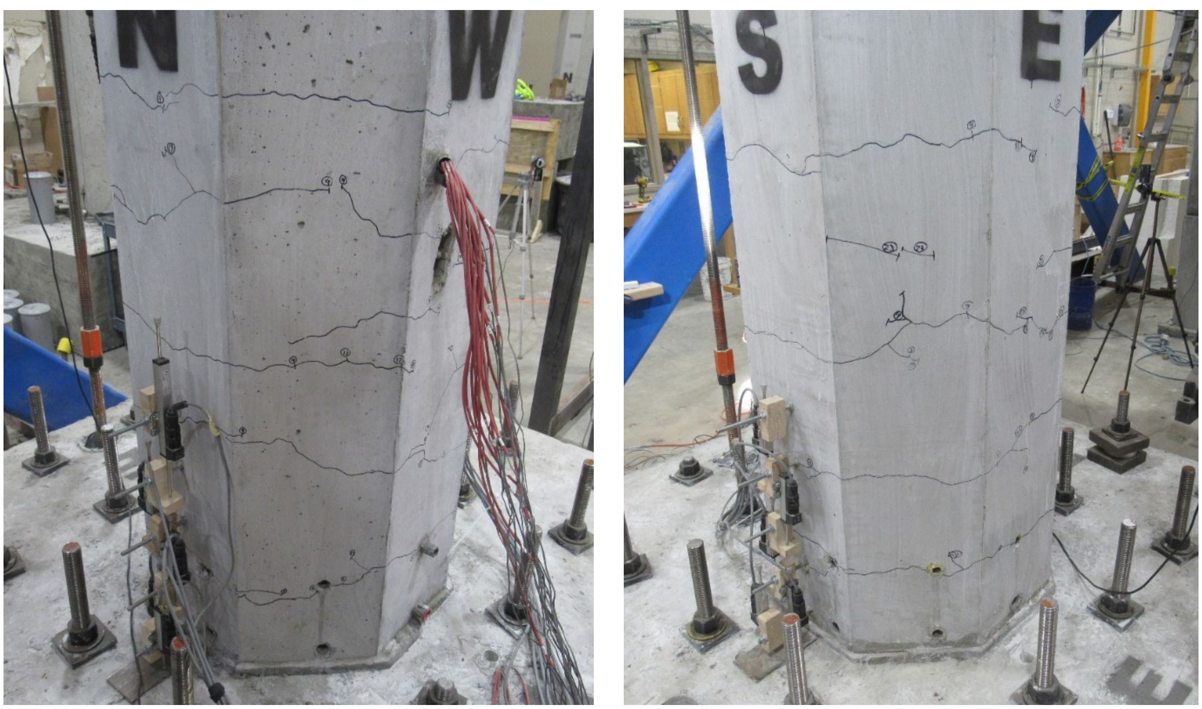

a) North-West Side b) South-East Side

Figure 3.146 PHD Column Plastic Hinge Damage, Second Pull of 0.75% Drift Cycle

a) North-West Side b) South-East Side

Figure 3.147 PHD Column Plastic Hinge Damage, Second Push of 1.00% Drift Cycle

a) North-West Side b) South-East Side

Figure 3.148 PHD Column Plastic Hinge Damage, Second Pull of 1.00% Drift Cycle

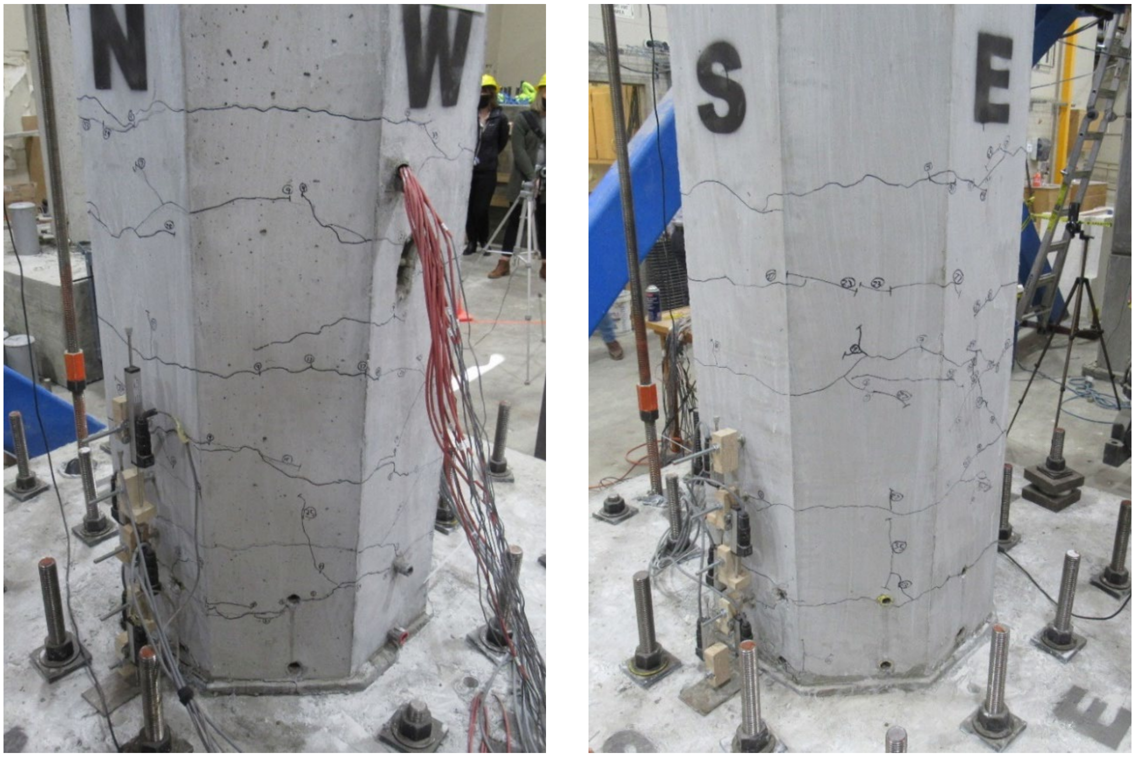

a) North-West Side b) South-East Side

Figure 3.149 PHD Column Plastic Hinge Damage, Second Push of 2.00% Drift Cycle

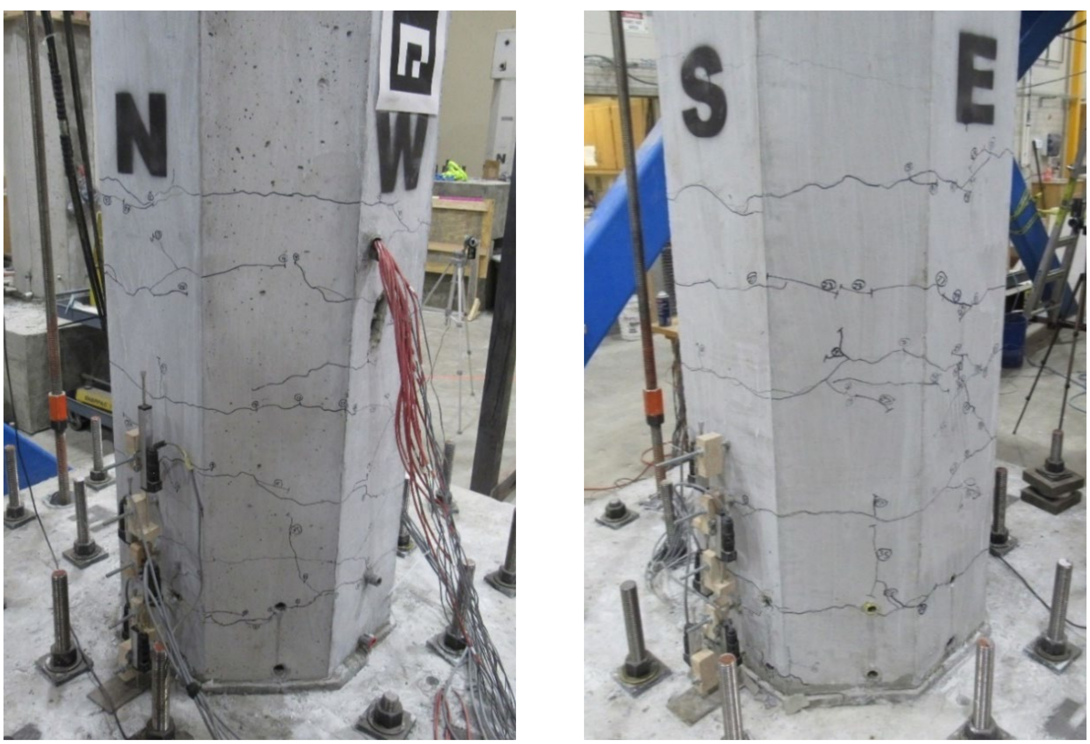

a) North-West Side b) South-East Side

Figure 3.150 PHD Column Plastic Hinge Damage, Second Pull of 2.00% Drift Cycle

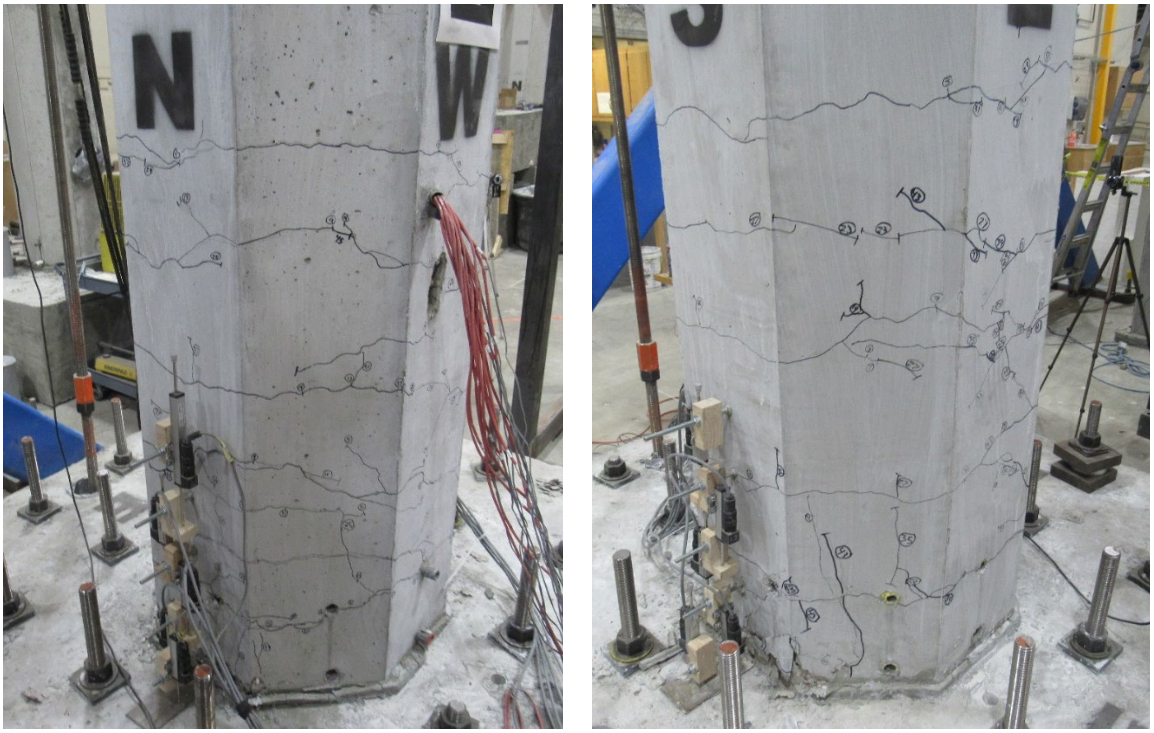

a) North-West Side b) South-East Side

Figure 3.151 PHD Column Plastic Hinge Damage, Second Push of 3.00% Drift Cycle

a) North-West Side b) South-East Side

Figure 3.152 PHD Column Plastic Hinge Damage, Second Pull of 3.00% Drift Cycle

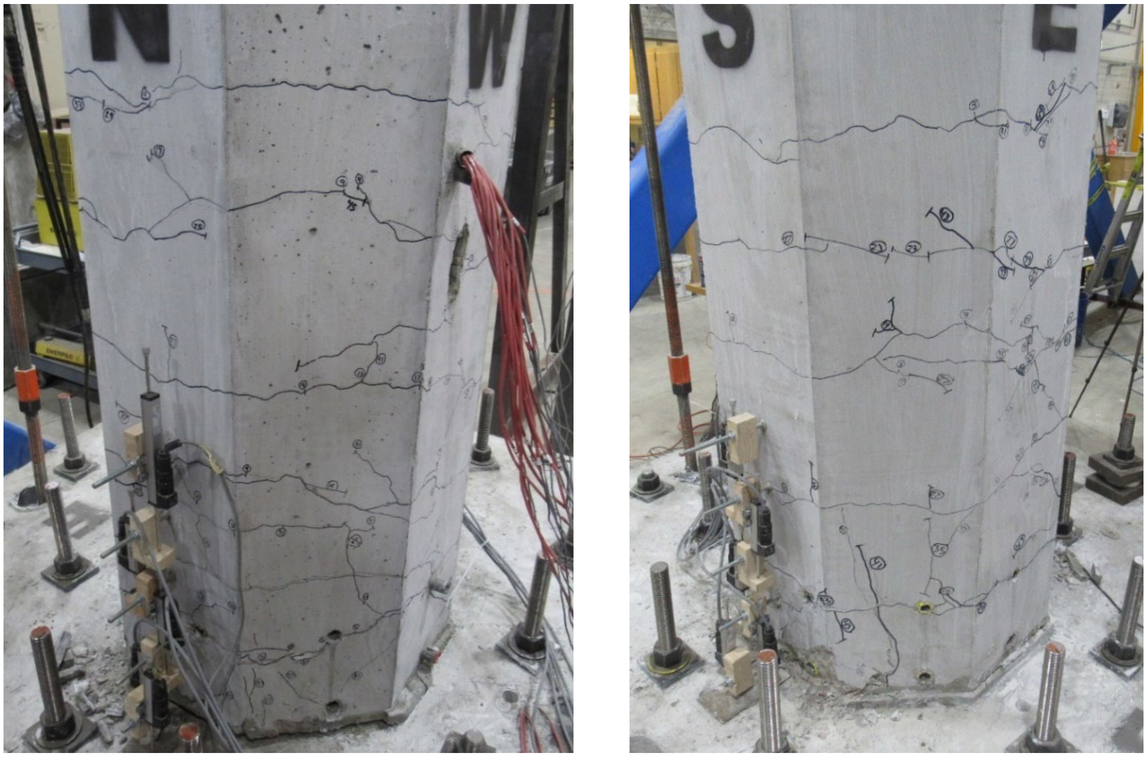

a) North-West Side b) South-East Side

Figure 3.153 PHD Column Plastic Hinge Damage, Second Push of 4.00% Drift Cycle

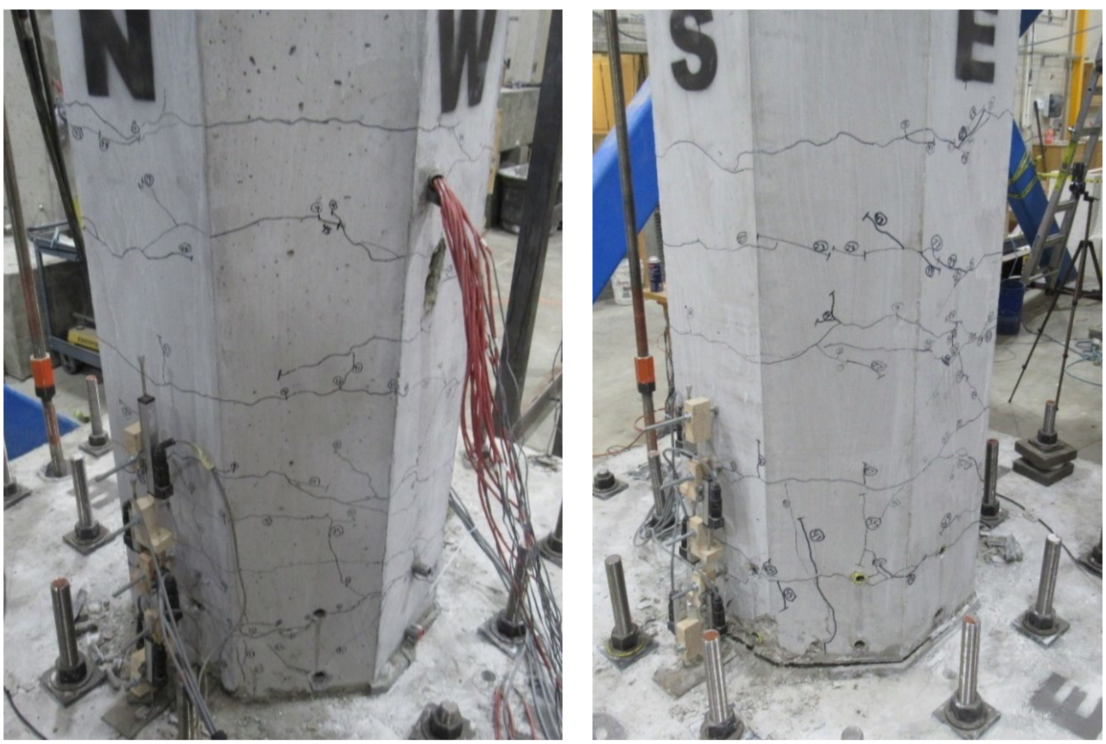

a) North-West Side b) South-East Side

Figure 3.154 PHD Column Plastic Hinge Damage, Second Pull of 4.00% Drift Cycle

3.5.5.2 Force-Displacement Relationship

Figure 3.155 shows the measured lateral force-drift hysteretic and envelope responses of PHD. The envelope is shown up to 15% drop of force beyond the peak base shear. The PHD column exhibited a maximum lateral load of 71.5 kips (318 kN) at 3% drift ratio and exhibited a rapid strength degradation afterwards. A significant strength and stiffness degradation was observed due to bar pullout from the coupler base. The column was slightly stronger in the push direction. The PHD longitudinal bars yielded at 0.54% drift ratio in the push direction under a lateral load of 41.4 kip (184.2 kN), and at -0.78% drift ratio in the pull direction at a lateral load of -52.8 kip (234.9 kN).

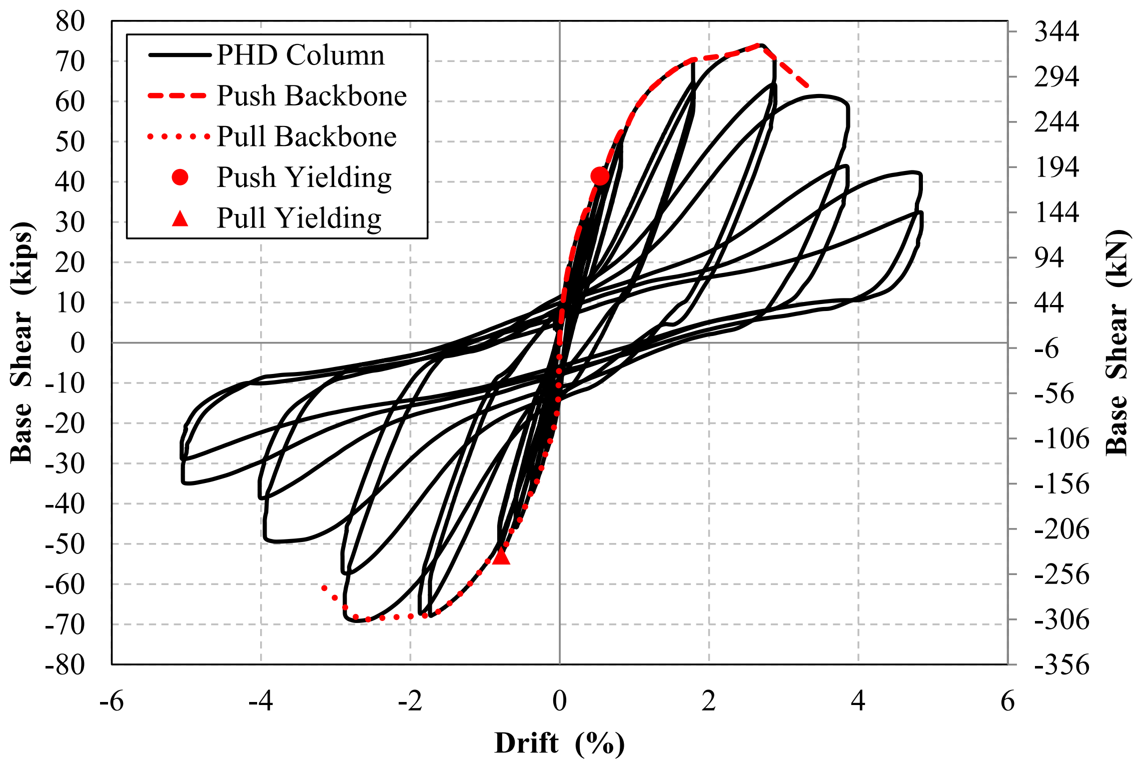

Figure 3.155 PHD Column Force-Drift Hysteretic and Envelope Responses

Figure 3.156 shows the average envelope for the push and pull directions of PHD. The average yield drift ratio of 0.66% occurred at a lateral force of 47.1 kips (209.5 kN). Based on the 15% load drop discussed before as the column failure point, the drift capacity of the PHD column was estimated as 3.33%. Furthermore, Figure 3.156 shows the idealized curve for the average PHD envelope. The effective yield drift ratio was 0.93% at the effective yield lateral force of 65.2 kip (290.0 kN), resulting in a displacement ductility capacity of 3.60 for the PHD column.

It was discussed that the couplers used in PHD showed bar pullout in tensile tests performed in the present study while they showed bar fracture in other studies/tests. The reason for this inferior performance could not be determined. However, the research team recommends that the manufacturer improves the quality measures for this coupler, especially the grout performance, for a consistent result. Only seismic couplers with the mode of failure of bar fracture in tensile testing should be used in precast bridge columns.

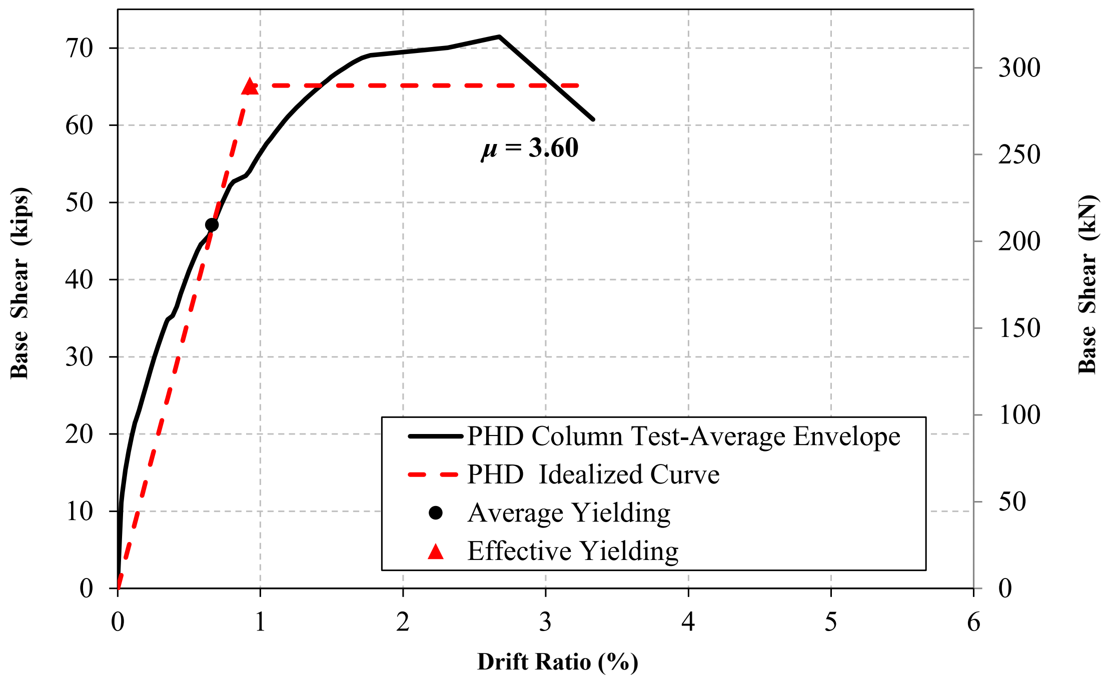

Figure 3.156 PHD Column Average Push/Pull Force-Drift Envelope and Idealized Curve

3.5.5.3 Strain Profile

Twenty-three strain gauges were installed on the PHD reinforcing steel bars at three levels of the column. Figures 3.157 to 3.160 show the measured strain profiles of the column for Bars B1, B2, B6, and B7.

The strain profile was uniform prior to the bar yielding. The strain was generally higher closer to the column-footing-interface and decreased along the height of the column once the bars yielded. As discussed before, the strain profiles for a mechanically spliced column do not follow those of CIP because couplers are stiff and strong, shifting the nonlinearity away from the coupler regions. Thus, the column longitudinal bar strains are higher at the coupler ends.

The strain on the reinforcing hoops was also monitored. The yield strain for the hoops in the precast columns was 0.23%. The maximum measured strain in the PHD hoops was 0.36% and occurred in a hoop immediately above the top of the coupler.

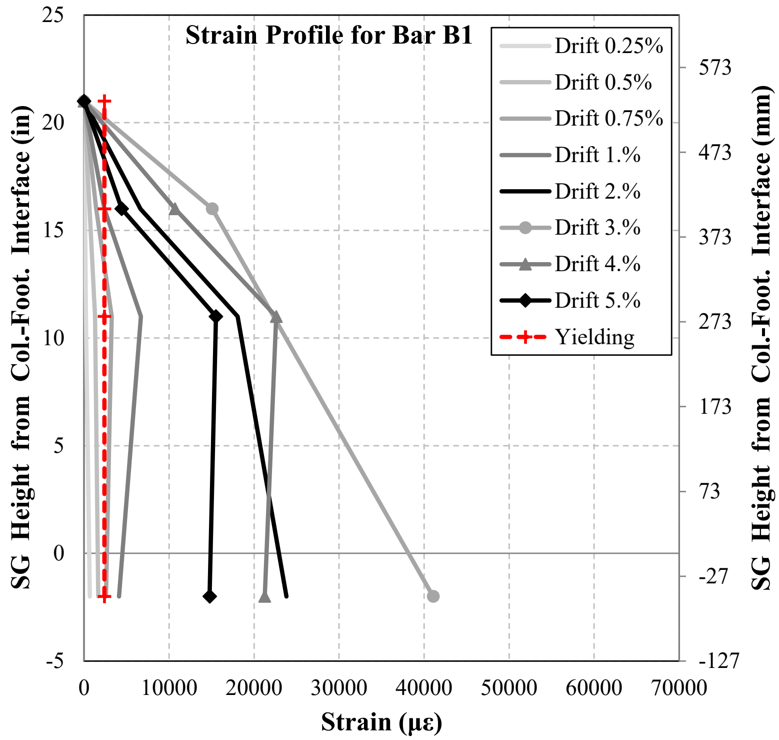

Figure 3.157 Strain Profile for PHD Column Bar B1

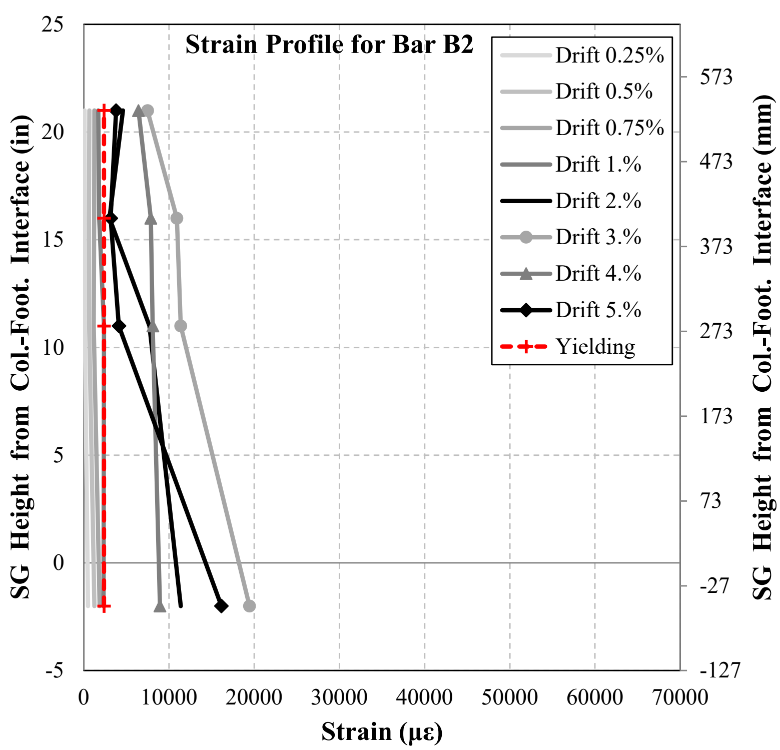

Figure 3.158 Strain Profile for PHD Column Bar B2

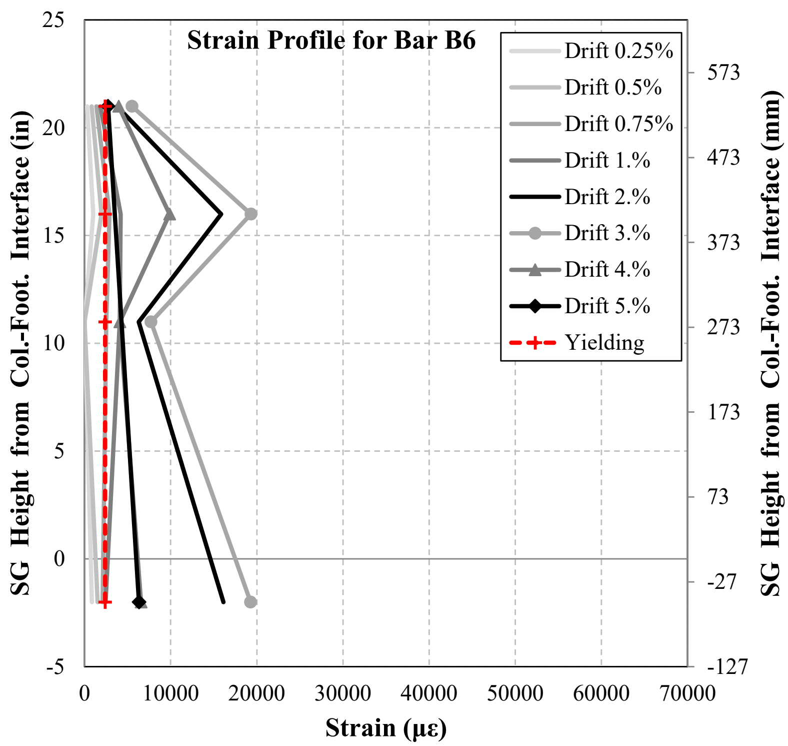

Figure 3.159 Strain Profile for PHD Column Bar B6

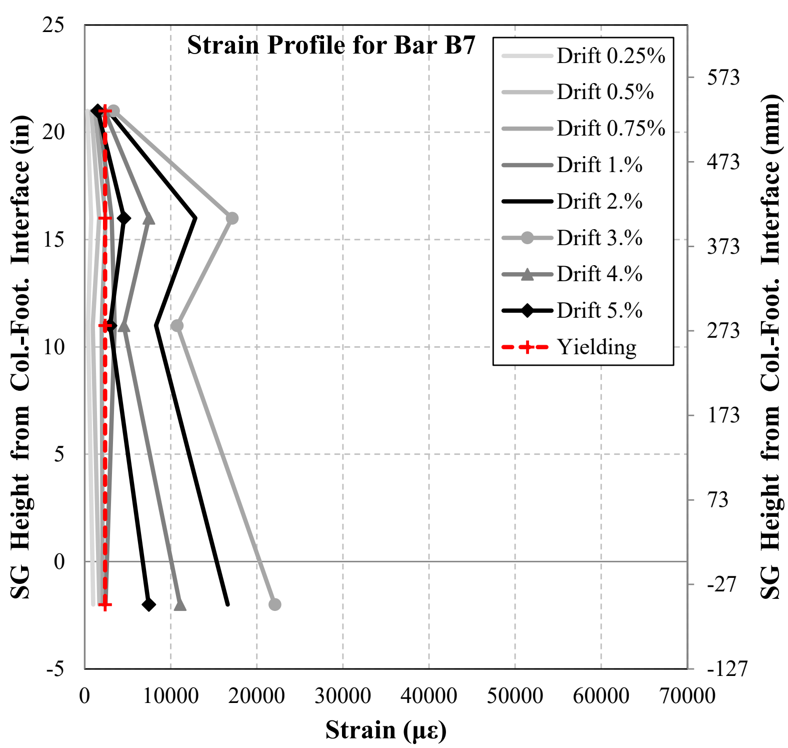

Figure 3.160 Strain Profile for PHD Column Bar B7

3.5.5.4 Measured Rotation and Curvature

Rotations and curvatures were determined in the same manner as CIP and other precast columns. Figure 3.161 shows the measured curvature profile for the PHD column at drift ratios of 0.25% to 4.0%. The highest curvature always occurred at the base due to the concentrated concrete cracking and bar-slip near the column-footing interface. Seismic and long couplers, such as grouted coupler, tend to increase the column stiffness in the coupler region, leading to a shift of nonlinearity outside of the coupler. For such seismic couplers, the curvature is generally high near the column base, minimal along the coupler region, and high above the coupler levels. However, this was not seen in the PHD column mainly because the hybrid grouted-threaded couplers used in PHD did not perform as a seismic coupler. Bars pulled out from the coupler in the in-air tensile testing and the same was observed in the column testing. Therefore, the bar pullout at the coupler bottom end resulted in a higher curvature at the PHD column base.

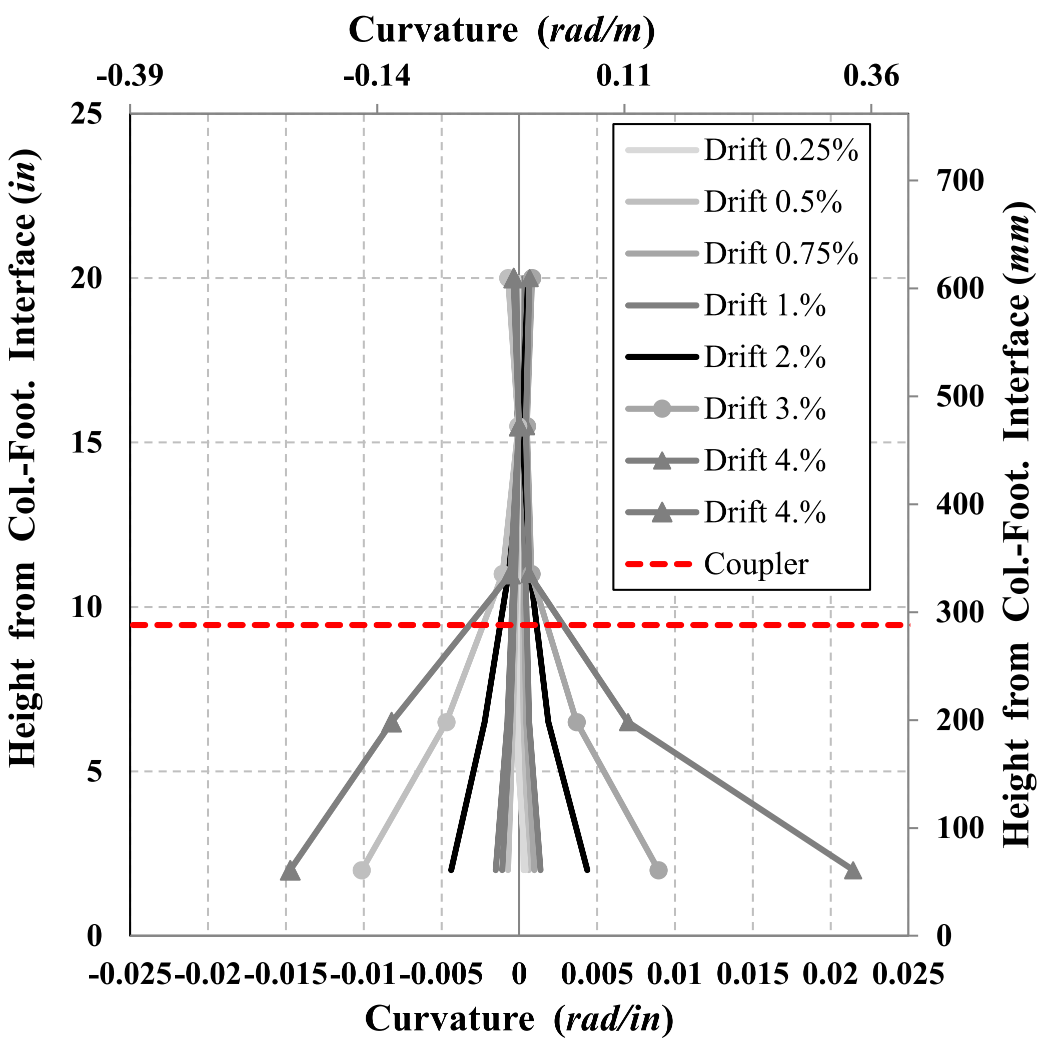

Figure 3.161 Curvature Profile for PHD Column

3.5.5.5 Energy Dissipation

Figure 3.162 shows the measured cumulative energy dissipation of the PHD column at different drift ratios. The dissipated energy was negligible up to 1% drift ratio, where the bar yielding was minimal. At higher drift ratios, the hysteretic loops began to widen, which led to a higher dissipated energy. PHD dissipated 1,021 kip-in. (115 kN-m) of energy prior to the failure.

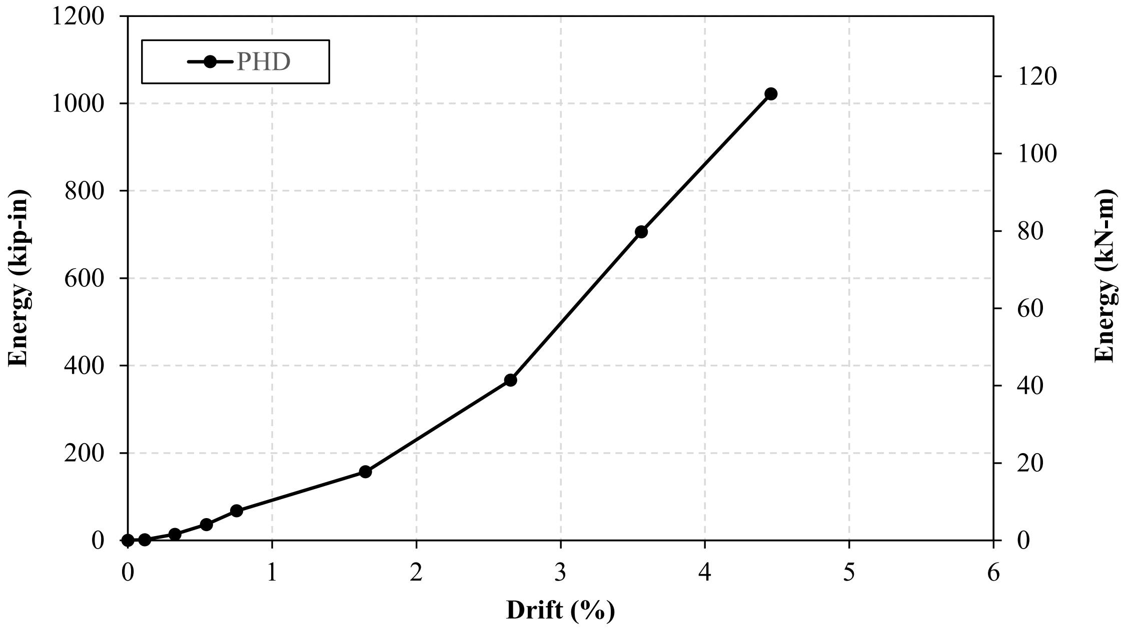

Figure 3.162 Energy Dissipation for PHD Column

3.5.6 PHV Column Results

The seismic performance of the precast column incorporating the nVent Lenton "Interlock" hybrid grouted-threaded coupler, PHV, is discussed in this section.

3.5.6.1 Observed Damage

The PHV column followed the same testing procedure as the CIP column. Table 3.10 presents a summary of the damage observed for each push or pull load for PHV. Figures 3.163 to 3.180 show the PHV plastic hinge damage in the second cycle of push or pull for each drift level.

Flexural cracks were observed in the first cycle of 0.25% drift ratio (Fig. 3.163 & 3.164). Shear cracks were first observed in the first cycle of 0.5% drift ratio (Fig. 3.167 & 3.168). The first yielding occurred in Bar B1 at 0.335% drift in the first push run of the 0.5% drift cycle under a lateral load of 35.6 kips (158.4 kN) (Fig. 3.167). Concrete spalled on the south face at 3% drift cycles (Fig. 3.173 to 3.174) and later on the north face of the column during the 5% drift cycles (Fig. 3.177 to 3.178). Cracks near the top of couplers and the base of the column began to spread during the 3% drift cycle. The lateral strength also began to degrade during the 3% drift cycle (Fig. 3.173 & 3.174). Finally, the PHV column failed by a steady loss of strength after the peak lateral force until 10% drift ratio, where the test was stopped. The strength degradation was attributed to the concrete damage.

Table 3.10 Summary of Damage in PHV

Drift Ratio, %	Observed Damage
+0.25	• Minor flexural cracks • Flexural cracks at top of coupler
-0.25	• Minor flexural cracks • Flexural cracks at top of coupler
+0.50	• Flexural and inclined cracks • Bar yielding
-0.50	• Flexural and inclined cracks • Bar yielding
+0.75	• Flexural cracking
-0.75	• Flexural and incline cracking
+1.00	• Flexural and incline cracking
-1.00	• Cracking at column base
+2.00	• Cracking at column base • Flexural, vertical, and incline cracking
-2.00	• Flexural, vertical and incline cracking
+3.00	• Flexural, vertical, and incline cracking
-3.00	• Flexural, vertical, and incline cracking • Spalling at column base • Beginning of strength degradation
+4.00	• Flexural, vertical, and incline cracking • Beginning of strength degradation
-4.00	• Vertical cracking • Widening of cracks • Increased spalling • Continued strength loss
+5.00	• Vertical and inclined cracking • Spalling at column base • Continued strength loss
-5.00	• Increased spalling • Vertical cracking
+6.00	• Flexural cracks • Crack widening
-6.00	• Crack widening • 15% loss in strength
+7.00	• Continued strength loss
-7.00	• Continued strength loss
+8.00	• Continued strength loss • 15% loss in strength
-8.00	• Continued strength loss
+9.00	• Continued strength loss
-9.00	• Continued strength loss
+10.0	• Continued strength loss
-10.0	• Continued strength loss

Note: Positive drifts were based on displacements away from the reaction blocks (north to south)

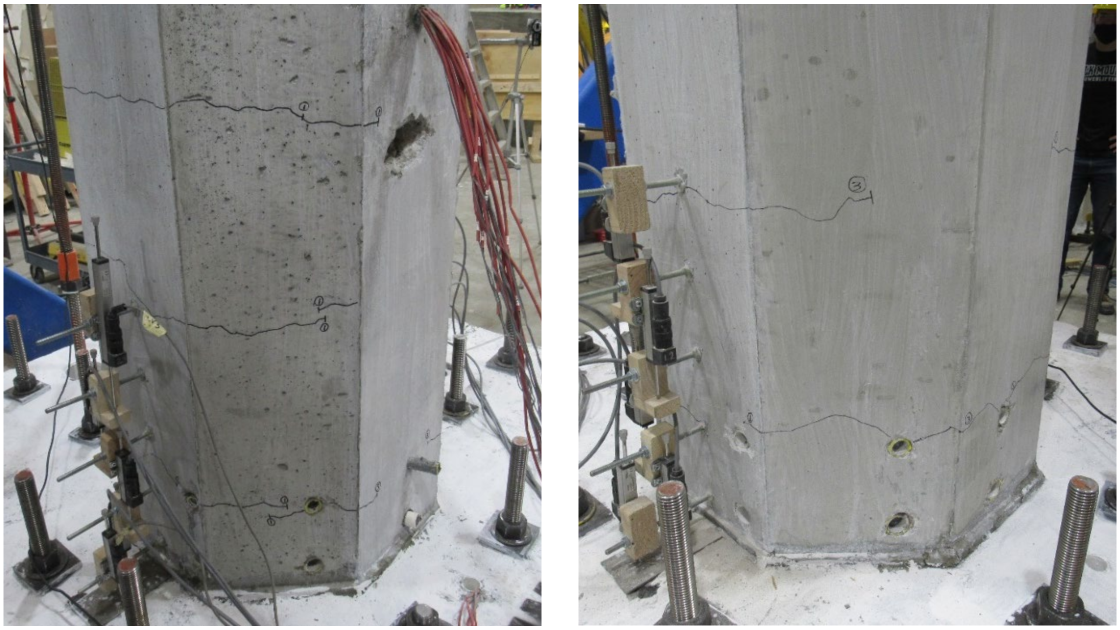

a) North-West Side b) South-East Side

Figure 3.163 PHV Column Plastic Hinge Damage, Second Push of 0.25% Drift Cycle

a) North-West Side b) South-East Side

Figure 3.164 PHV Column Plastic Hinge Damage, Second Pull of 0.25% Drift Cycle

a) North-West Side b) South-East Side

Figure 3.165 PHV Column Plastic Hinge Damage, Second Push of 0.50% Drift Cycle

a) North-West Side b) South-East Side

Figure 3.166 PHV Column Plastic Hinge Damage, Second Pull of 0.50% Drift Cycle

a) North-West Side b) South-East Side

Figure 3.167 PHV Column Plastic Hinge Damage, Second Push of 0.75% Drift Cycle

a) North-West Side b) South-East Side

Figure 3.168 PHV Column Plastic Hinge Damage, Second Pull of 0.75% Drift Cycle

a) North-West Side b) South-East Side

Figure 3.169 PHV Column Plastic Hinge Damage, Second Push of 1.00% Drift Cycle

a) North-West Side b) South-East Side

Figure 3.170 PHV Column Plastic Hinge Damage, Second Pull of 1.00% Drift Cycle

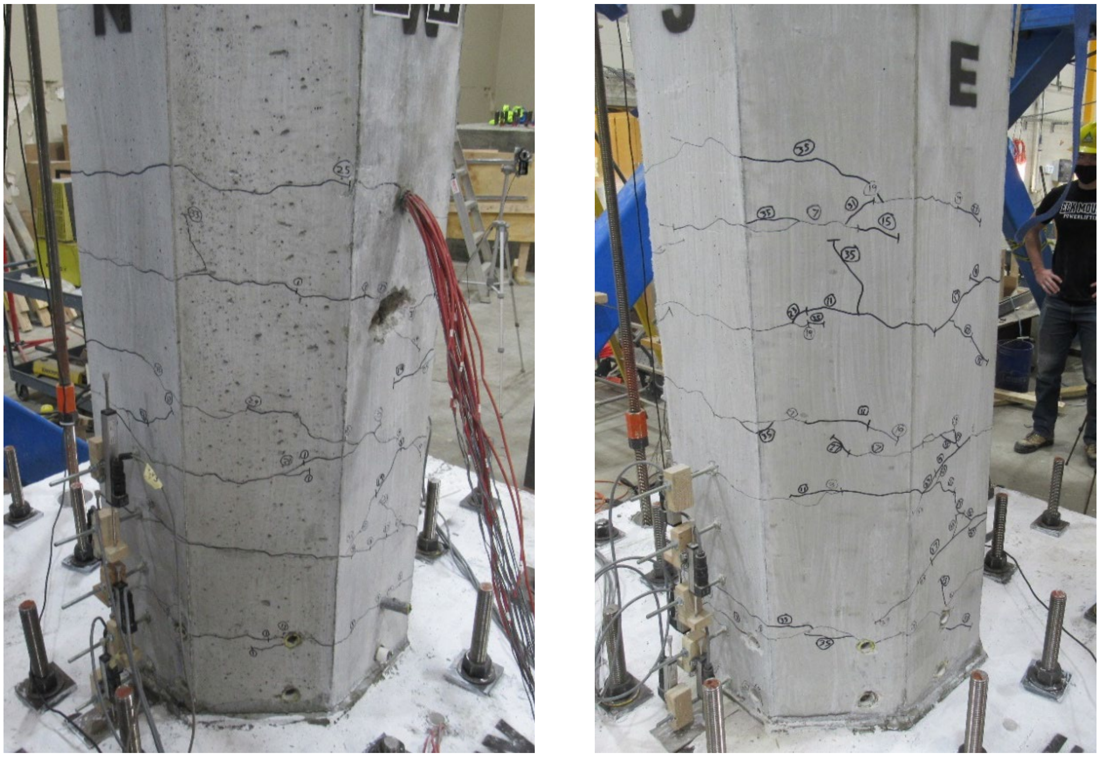

a) North-West Side b) South-East Side

Figure 3.171 PHV Column Plastic Hinge Damage, Second Push of 2.00% Drift Cycle

a) North-West Side b) South-East Side

Figure 3.172 PHV Column Plastic Hinge Damage, Second Pull of 2.00% Drift Cycle

a) North-West Side b) South-East Side

Figure 3.173 PHV Column Plastic Hinge Damage, Second Push of 3.00% Drift Cycle

a) North-West Side b) South-East Side

Figure 3.174 PHV Column Plastic Hinge Damage, Second Pull of 3.00% Drift Cycle

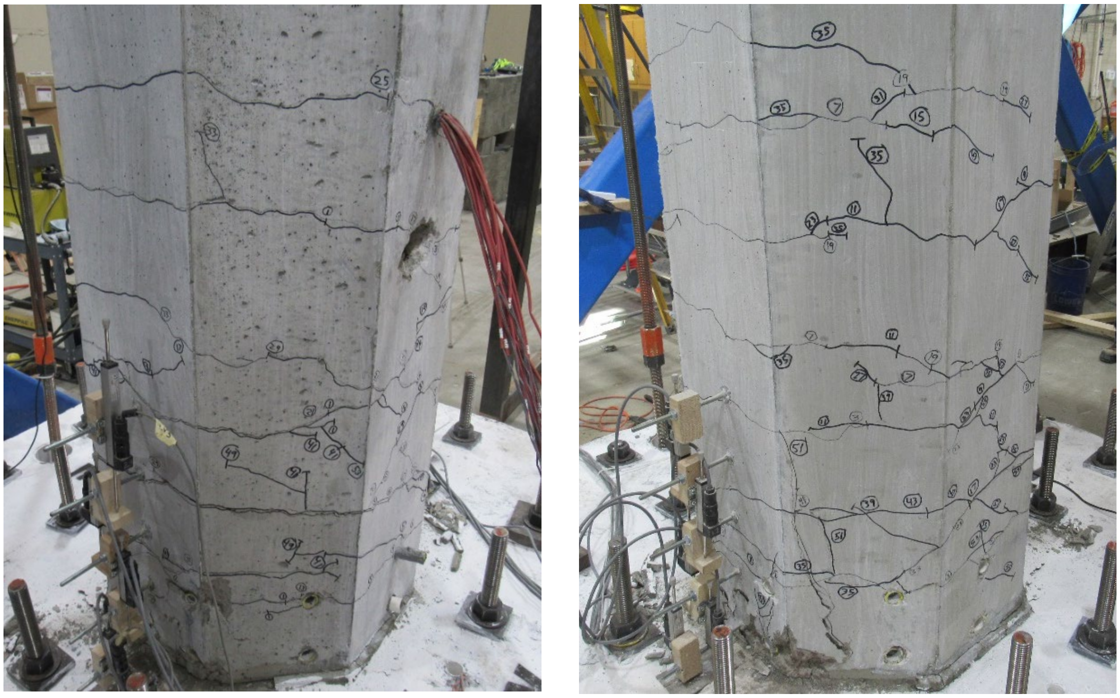

a) North-West Side b) South-East Side

Figure 3.175 PHV Column Plastic Hinge Damage, Second Push of 4.00% Drift Cycle

a) North-West Side b) South-East Side

Figure 3.176 PHV Column Plastic Hinge Damage, Second Pull of 4.00% Drift Cycle


a) North-West Side

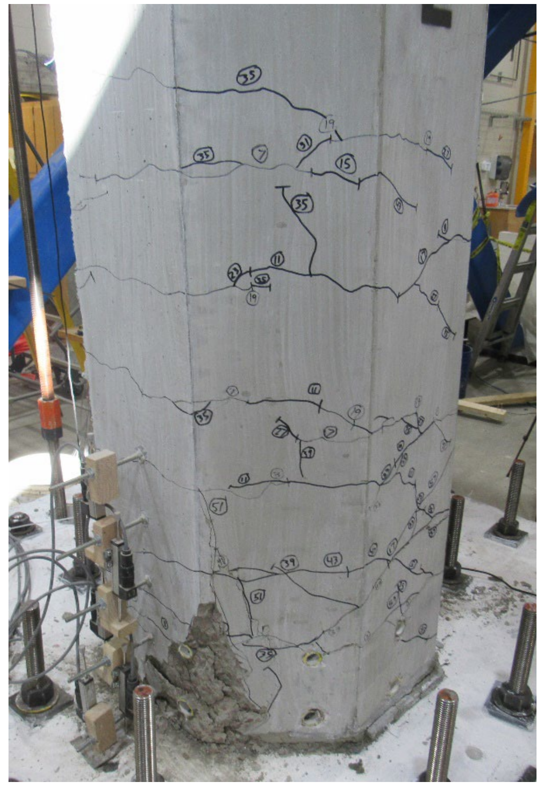
b) South-East Side

Figure 3.177 PHV Column Plastic Hinge Damage, Second Push of 5.00% Drift Cycle

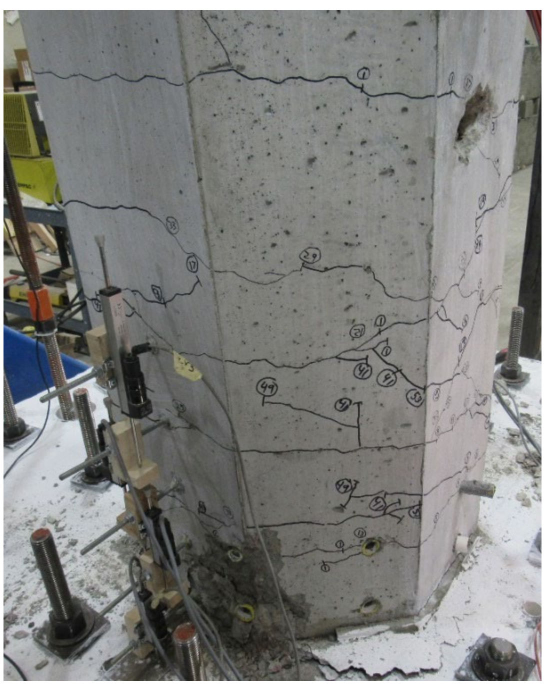
a) North-West Side

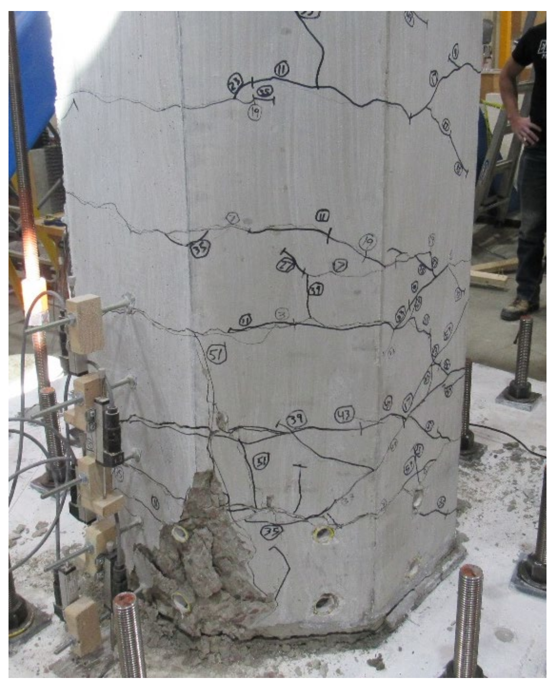
b) South-East Side

Figure 3.178 PHV Column Plastic Hinge Damage, Second Pull of 5.00% Drift Cycle

a) North Side b) South-East Side

Figure 3.179 PHV Column Plastic Hinge Damage, Second Push of 6.00% Drift Cycle

a) North-West Side b) South-East Side

Figure 3.180 PHV Column Plastic Hinge Damage, Second Pull of 6.00% Drift Cycle

a) North-West Side b) South-East Side

Figure 3.181 PHV Column Plastic Hinge Damage, Second Push of 7.00% Drift Cycle

a) North-West Side b) South-East Side

Figure 3.182 PHV Column Plastic Hinge Damage, Second Pull of 7.00% Drift Cycle

a) North-West Side b) South-East Side

Figure 3.183 PHV Column Plastic Hinge Damage, Second Push of 8.00% Drift Cycle

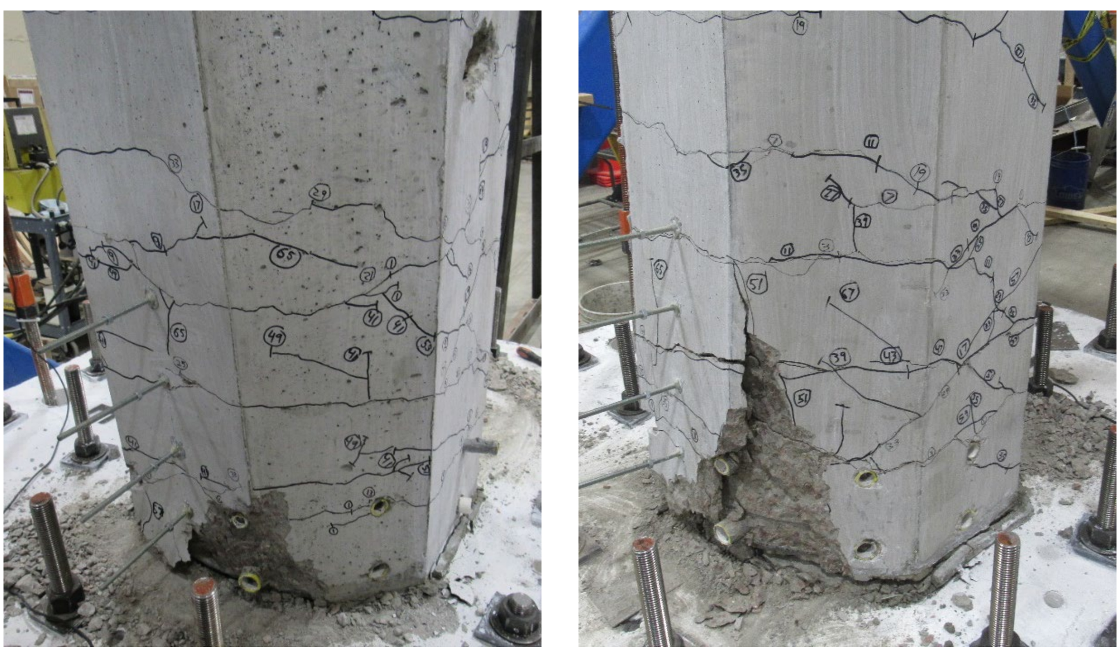

a) North-West Side b) South-East Side

Figure 3.184 PHV Column Plastic Hinge Damage, Second Pull of 8.00% Drift Cycle

a) North-West Side b) South-East Side

Figure 3.185 PHV Column Plastic Hinge Damage, Second Push of 9.00% Drift Cycle

a) North-West Side b) South-East Side

Figure 3.186 PHV Column Plastic Hinge Damage, Second Pull of 9.00% Drift Cycle

a) North Side b) South-East Side

Figure 3.187 PHV Column Plastic Hinge Damage, First Push of 10.00% Drift Cycle

a) North-West Side b) South-East Side

Figure 3.188 PHV Column Plastic Hinge Damage, First Pull of 10.00% Drift Cycle

3.5.6.2 Force-Displacement Relationship

Figure 3.189 shows the measured push and pull envelope responses and the lateral force-drift hysteretic of PHV. Note that the envelope is shown up to 15% drop of force beyond the peak base shear. In the push direction, PHV exhibited a maximum lateral load of 74.2 kips (330 kN) at 3% drift ratio and exhibited a steady strength degradation afterwards. The column was slightly stronger in the push direction than pull. The PHV longitudinal bars yielded at 0.34% drift ratio in the push direction under a lateral load of 35.6 kips (158.4 kN), and at -0.46% drift ratio in the pull direction at a lateral load of -42.1 kips (187.3 kN).

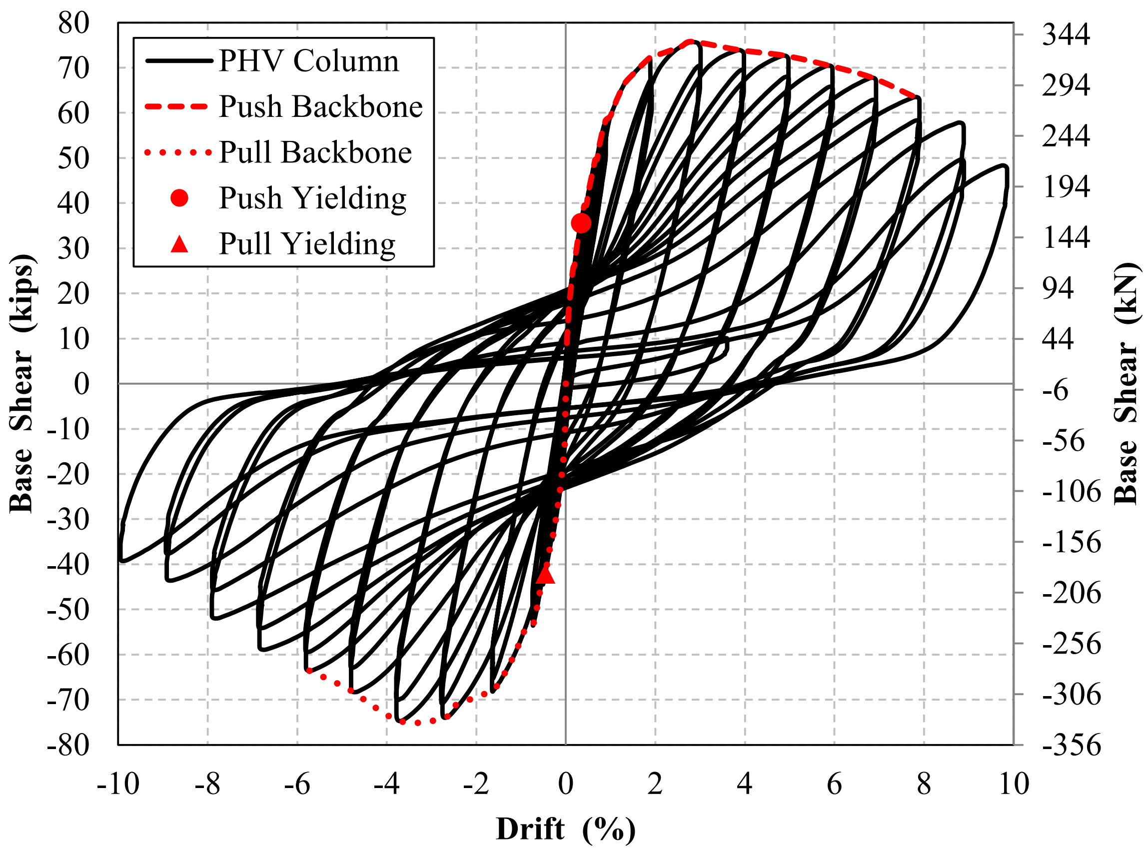

Figure 3.189 Measured PHV Column Force-Drift Hysteretic and Envelope Responses

Figure 3.190 shows the average envelope for the push and pull directions of PHV. The average yield drift ratio of 0.4% occurred at a lateral force of 38.9 kips (173 kN). Based on the 15% load drop criterion as the column failure, the drift capacity of the PHV column was estimated as 6.84%. Furthermore, Figure 3.190 shows the idealized curve for the average PHV envelope. The effective yield drift ratio was 0.669% at the effective yield lateral force of 66.67 kips (296.6 kN), resulting in a displacement ductility capacity of 10.23 for the PHV column.

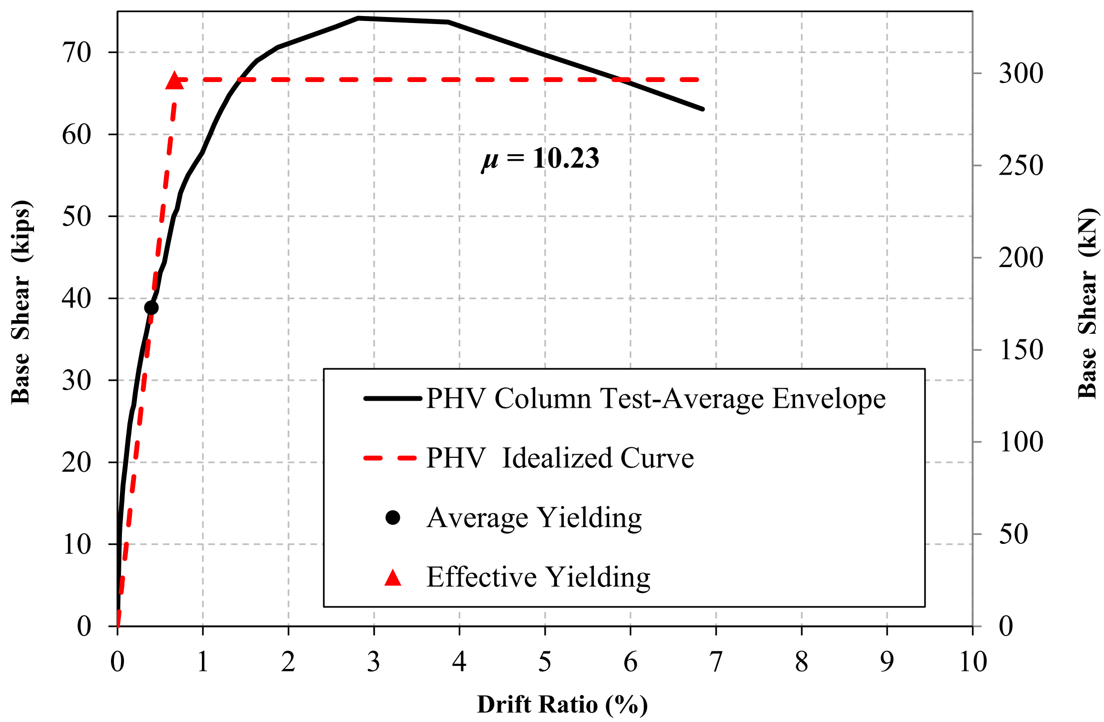

Figure 3.190 Measured PHV Column Average Push/Pull Force-Drift Envelope and Idealized Curve

3.5.6.3 Strain Profiles

Twenty-three strain gauges were installed on the PHV reinforcing steel bars at four levels. Figures 3.191 to 3.194 show the measured strain profiles of the column for Bars B1, B2, B6, and B7.

Prior to the bar yielding, the strain profile was uniform. The strain of the bars was higher near the column-footing-interface and decreased higher up the column beyond the bars yielding. Outside the plastic hinge length (about 20 in. or 500 mm) of the bars, the strains decreased drastically. The addition of the couplers is the reason for the shift in strain values due to the increased strength and stiffness in the coupler region. The strains for the longitudinal bars of the column are higher at the coupler bottom end.

Furthermore, the PHV column hoops did not yield throughout the testing. The maximum hoop strain was 0.13% while the hoop yield strain was 0.23%.

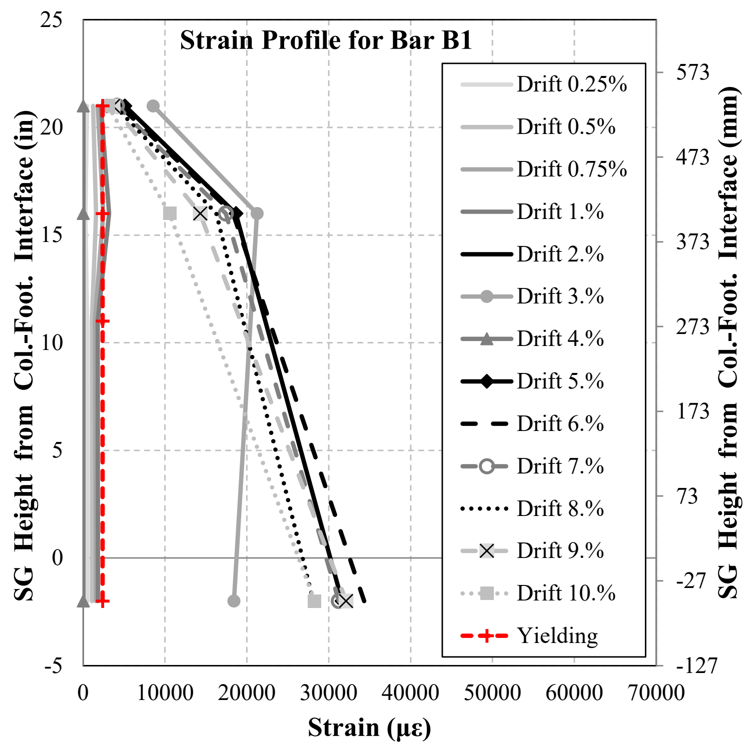

Figure 3.191 Measured Strain Profile for PHV Column Bar B1

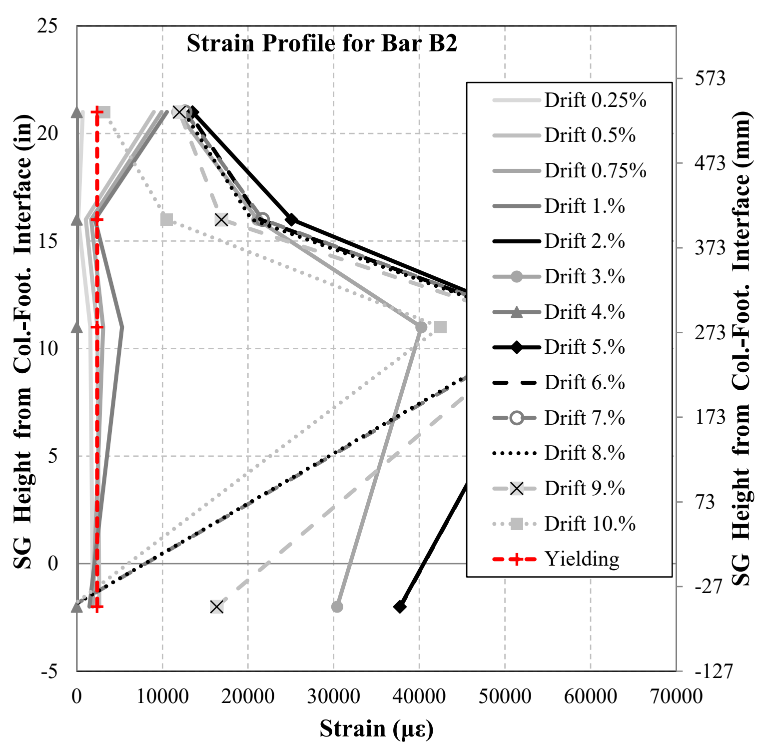

Figure 3.192 Measured Strain Profile for PHV Column Bar B2

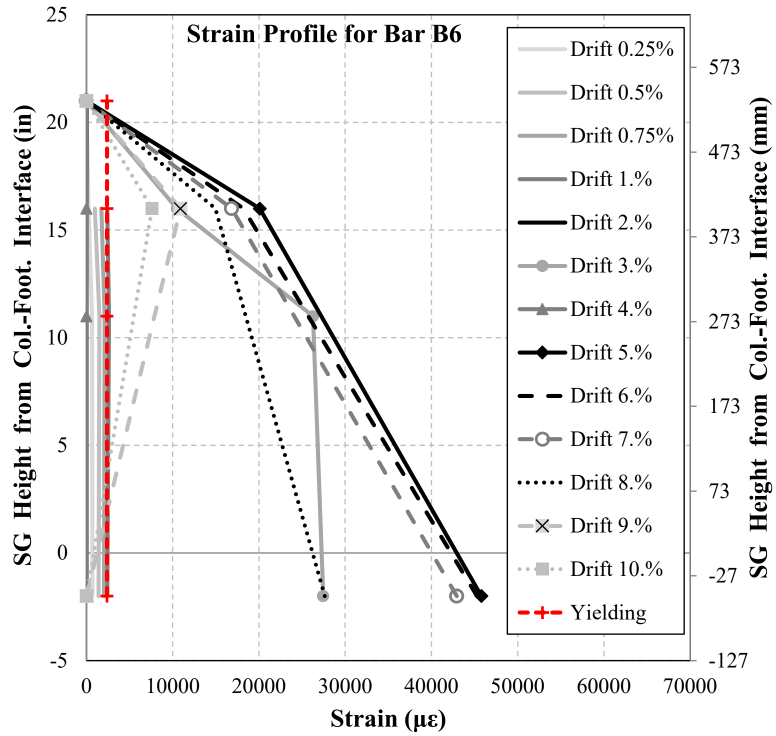

Figure 3.193 Measured Strain Profile for PHV Column Bar B6

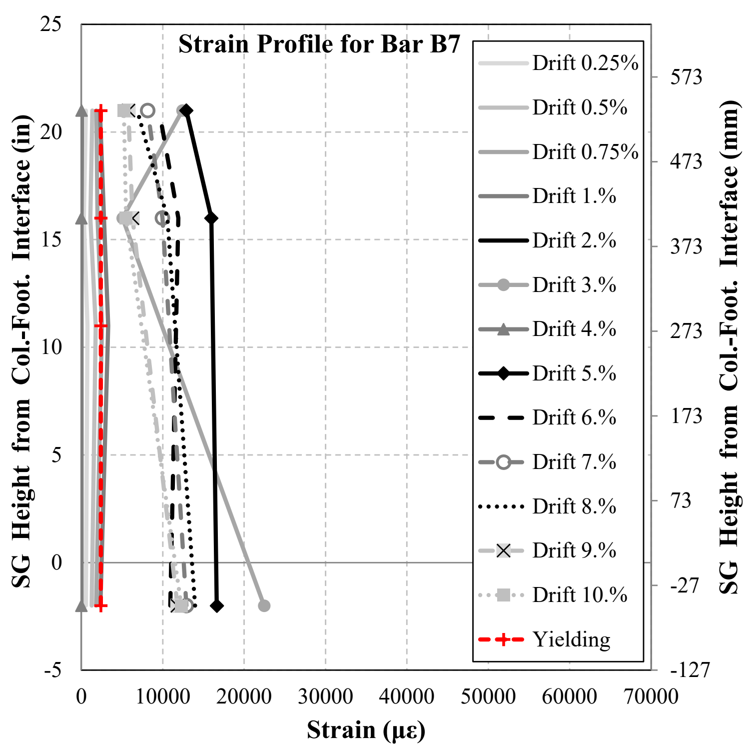

Figure 3.194 Measured Strain Profile for PHV Column Bar B7

3.5.6.4 Measured Rotation and Curvature

Rotations and curvatures were determined in the same manner as CIP. Figure 3.195 shows the measured curvature profile for the PHV column at drift ratios of 0.25% to 4.0%. The highest curvature always occurred at the base due to the concentrated concrete cracking and bar-slip near the column-footing interface. The grouted couplers used in PHV increased the column stiffness in the coupler region, leading to a shift of nonlinearity outside of the coupler. The figure confirms this observation in which the curvature was relatively high near the column base and minimal along the coupler region.

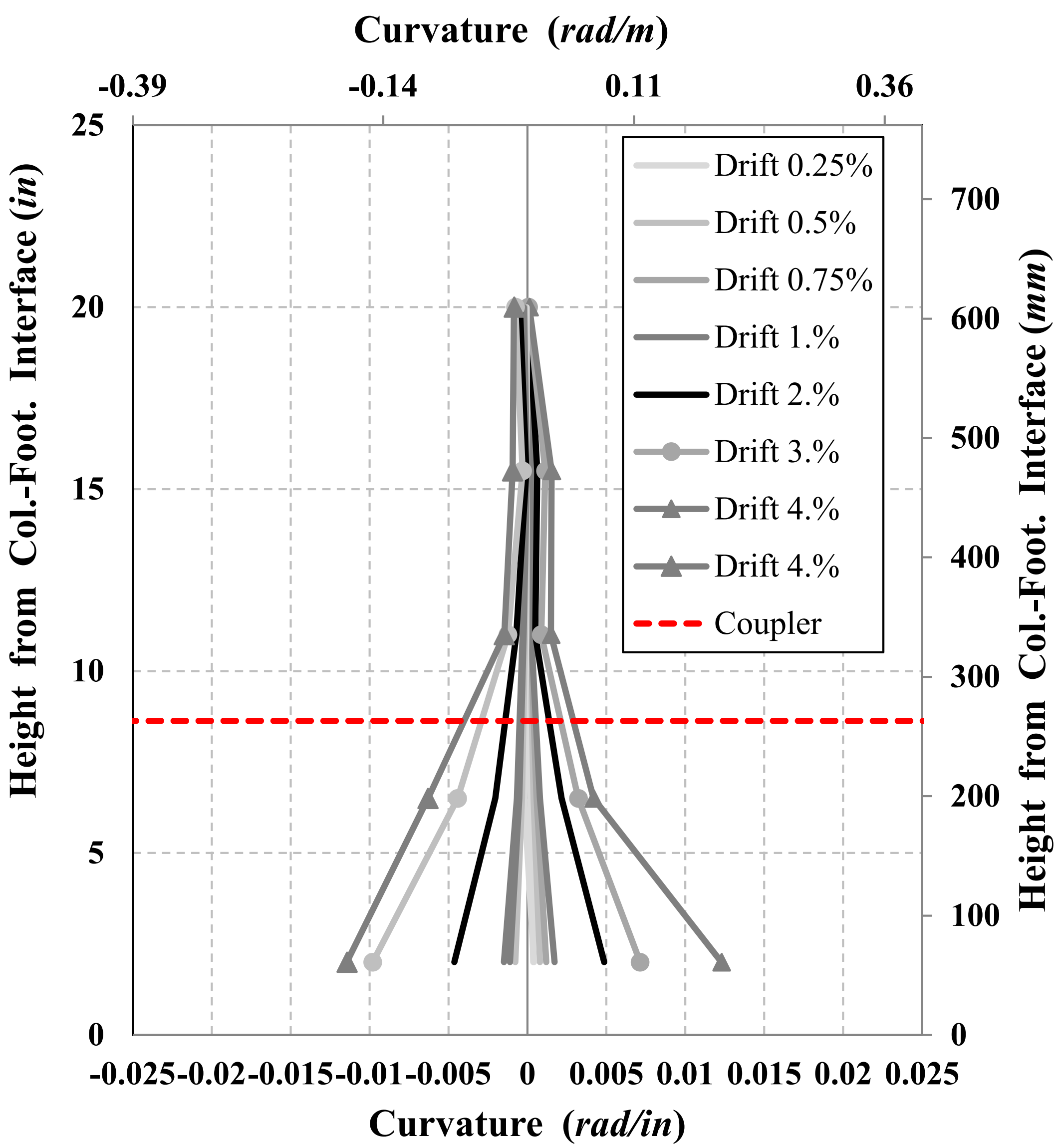

Figure 3.195 Measured Curvature Profile for PHV Column

3.5.6.5 Energy Dissipation

Figure 3.196 shows the measured cumulative energy dissipation of the PHV column at different drift ratios. The dissipated energy is negligible until 1% drift ratio, where bar yielding was minimal. The curve shows a steady increase of energy from 3.0% drift until when the test was concluded at 10.0% drift. At high drift ratios, the hysteretic loops began to widen, which led to a higher dissipated energy. PHV dissipated 5,736.5 kip-in. (648 kN-m) of energy prior to the failure.

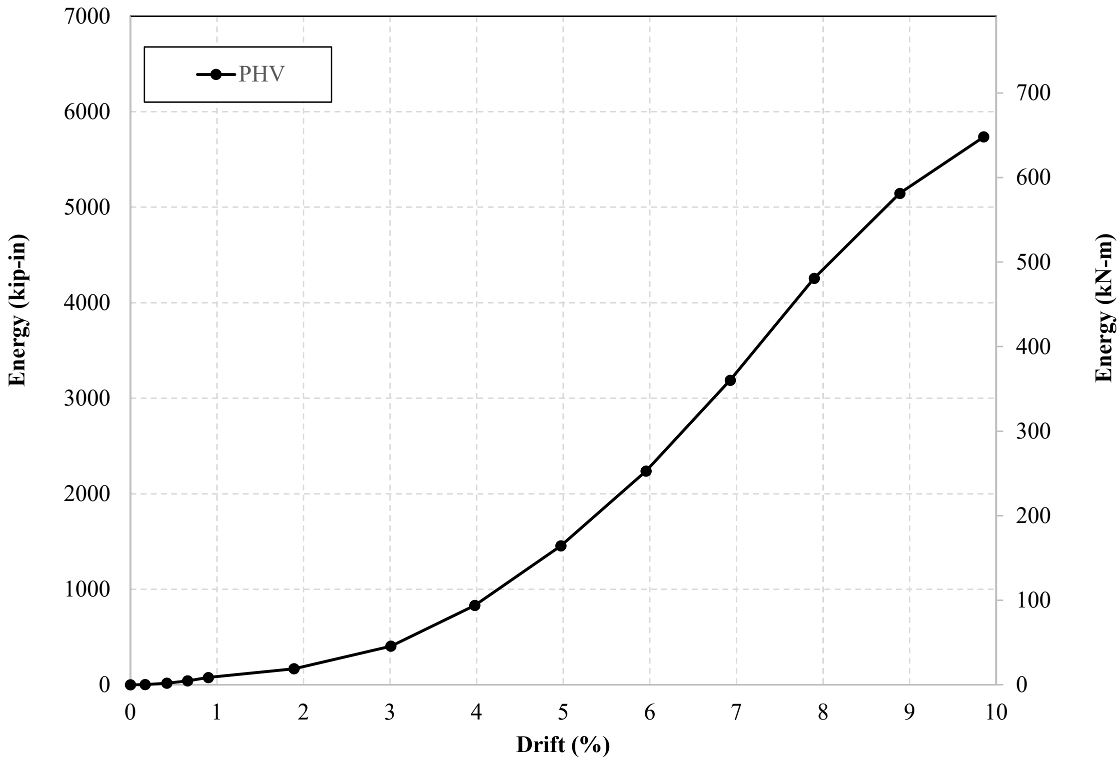

Figure 3.196 Measured Energy Dissipation for PHV Column

3.5.7 PTV Column Results

The seismic performance of the precast column incorporating the nVent Lenton "Ultimate PT15 Position" threaded coupler, PTV, is discussed in this section.

3.5.7.1 Observed Damage

The PTV column followed the same testing procedure as CIP. Table 3.11 presents a summary of the damage observed for each push or pull load for the PTV column. Figures 3.197 to 3.216 show the PTV plastic hinge damage in the second cycle of push or pull for each drift level.

Flexural cracks were observed in the first cycle of 0.25% drift ratio (Fig. 3.197 & 3.198). Shear cracks were first observed in the first cycle of 0.5% drift ratio (Fig. 3.199 & 3.200). The first yielding occurred in Bar B1 at 0.367% drift in the first push run of the 0.5% drift cycle under a lateral load of 32.77 kips (145.8 kN) (Fig. 3.199). Concrete spalled on both the north and south faces of the column during the 1% and 2% drift cycles, respectively (Fig. 3.203 to 3.204 & Fig. 205-206). Cracks developed near the top of the coupler, at the top of the closure pour, during the first cycle of 0.25% in each direction. Note there was a closure pour after installing the couplers in PTV. Extensive cracking in the plastic region of the column began to spread during the 4% drift cycle. The lateral strength also began to degrade during the 4% drift cycle (Fig. 3.209 & 3.210). Finally, three PTV longitudinal bars failed during the 7% drift cycles (Fig. 3.213 & Fig. 3.214). Therefore, PTV failed by bar fracture.

Table 3.11 Summary of Damage in PTV

Drift Ratio, %	Observed Damage
+0.25	• Minor flexural cracks • Flexural cracks at top of coupler (closure pour connection)
-0.25	• Minor flexural cracks • Flexural cracks at top of coupler (closure pour connection) • Vertical cracking
+0.50	• Flexural and inclined cracks • Bar yielding
-0.50	• Flexural and inclined cracks • Bar yielding
+0.75	• Vertical cracking • Cracking around column base
-0.75	• Vertical cracking • Cracking around column base
+1.00	• Spalling at upper closure pour connection • Crack widening • Flexural cracking
-1.00	• Cracking at column base
+2.00	• Flexural cracking
-2.00	• Flexural and incline cracking
+3.00	• Flexural, vertical, and incline cracking
-3.00	• Flexural, vertical, and incline cracking • Spalling at column base
+4.00	• Flexural, vertical, and incline cracking • Increased spalling • Widening of cracks • Beginning of force degradation
-4.00	• Flexural, vertical, and incline cracking • Widening of cracks • Increased spalling • Continued strength loss • Beginning of force degradation
+5.00	• Increased spalling at column base • Continued strength loss
-5.00	• Increased spalling • Transverse reinforcement exposed
+6.00	• Crack widening • Increased spalling • Transverse reinforcement exposed
-6.00	• Crack widening • Increased spalling
+7.00	• One bar ruptured on north side
-7.00	• Two bars ruptured on south side

Note: Positive drifts were based on displacements away from the reaction blocks (north to south)

a) North-West Side b) South-East Side

Figure 3.197 PTV Column Plastic Hinge Damage, Second Push of 0.25% Drift Cycle

a) North-West Side b) South-East Side

Figure 3.198 PTV Column Plastic Hinge Damage, Second Pull of 0.25% Drift Cycle

a) North-West Side b) South-East Side

Figure 3.199 PTV Column Plastic Hinge Damage, Second Push of 0.50% Drift Cycle

a) North-West Side b) South-East Side

Figure 3.200 PTV Column Plastic Hinge Damage, Second Pull of 0.50% Drift Cycle

a) North-West Side b) South-East Side

Figure 3.201 PTV Column Plastic Hinge Damage, Second Push of 0.75% Drift Cycle

a) North-West Side b) South-East Side

Figure 3.202 PTV Column Plastic Hinge Damage, Second Pull of 0.75% Drift Cycle

a) North-West Side b) South-East Side

Figure 3.203 PTV Column Plastic Hinge Damage, Second Push of 1.00% Drift Cycle

a) North-West Side b) South-East Side

Figure 3.204 PTV Column Plastic Hinge Damage, Second Pull of 1.00% Drift Cycle

a) North-West Side b) South-East Side

Figure 3.205 PTV Column Plastic Hinge Damage, Second Push of 2.00% Drift Cycle

a) North-West Side b) South-East Side

Figure 3.206 PTV Column Plastic Hinge Damage, Second Pull of 2.00% Drift Cycle

a) North-West Side b) South-East Side

Figure 3.207 PTV Column Plastic Hinge Damage, Second Push of 3.00% Drift Cycle

a) North-West Side b) South-East Side

Figure 3.208 PTV Column Plastic Hinge Damage, Second Pull of 3.00% Drift Cycle

a) North-West Side b) South-East Side

Figure 3.209 PTV Column Plastic Hinge Damage, Second Push of 4.00% Drift Cycle

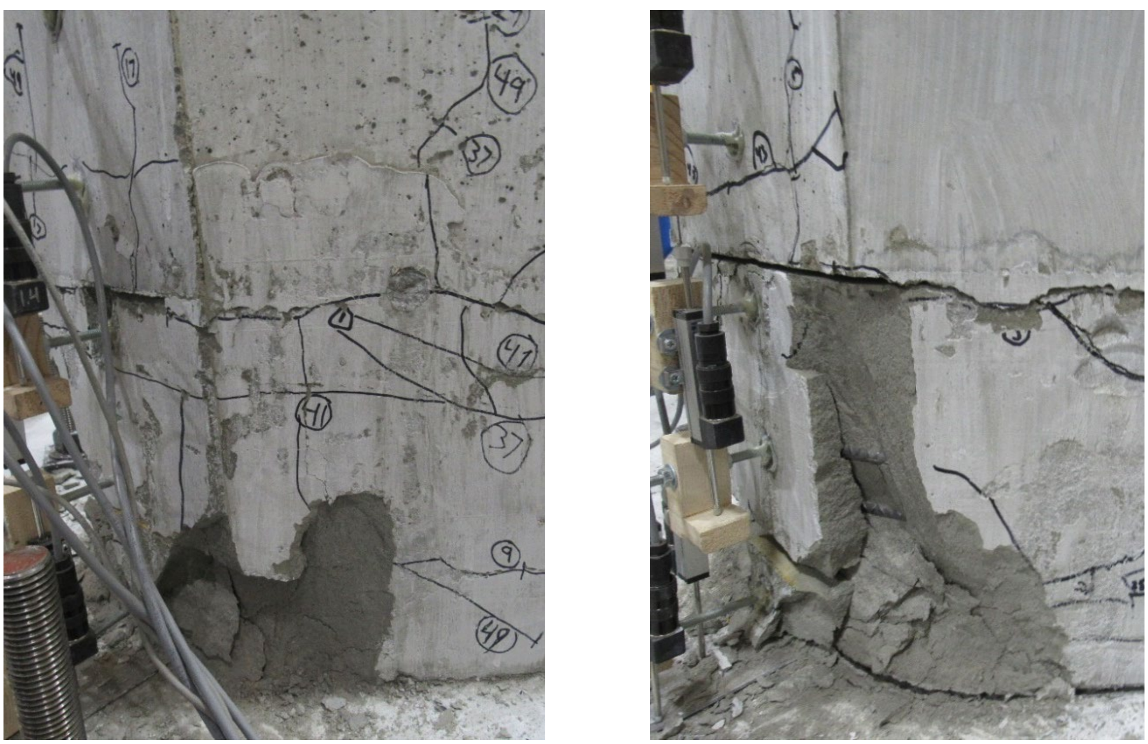

a) North-West Side b) South-East Side

Figure 3.210 PTV Column Plastic Hinge Damage, Second Pull of 4.00% Drift Cycle

a) North-West Side b) South-East Side

Figure 3.211 PTV Column Plastic Hinge Damage, Second Push of 5.00% Drift Cycle

a) North-West Side b) South-East Side

Figure 3.212 PTV Column Plastic Hinge Damage, Second Pull of 5.00% Drift Cycle

a) North-West Side b) South-East Side

Figure 3.213 PTV Column Plastic Hinge Damage, Second Push of 6.00% Drift Cycle

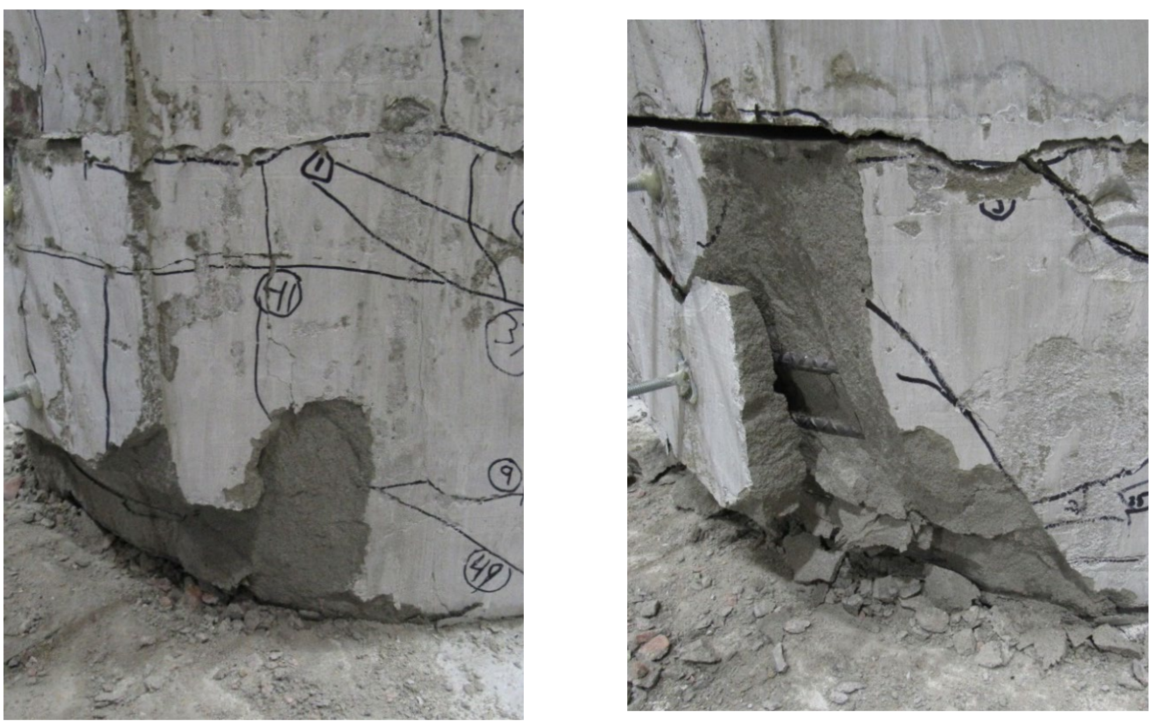

a) North-West Side b) South-East Side

Figure 3.214 PTV Column Plastic Hinge Damage, Second Pull of 6.00% Drift Cycle

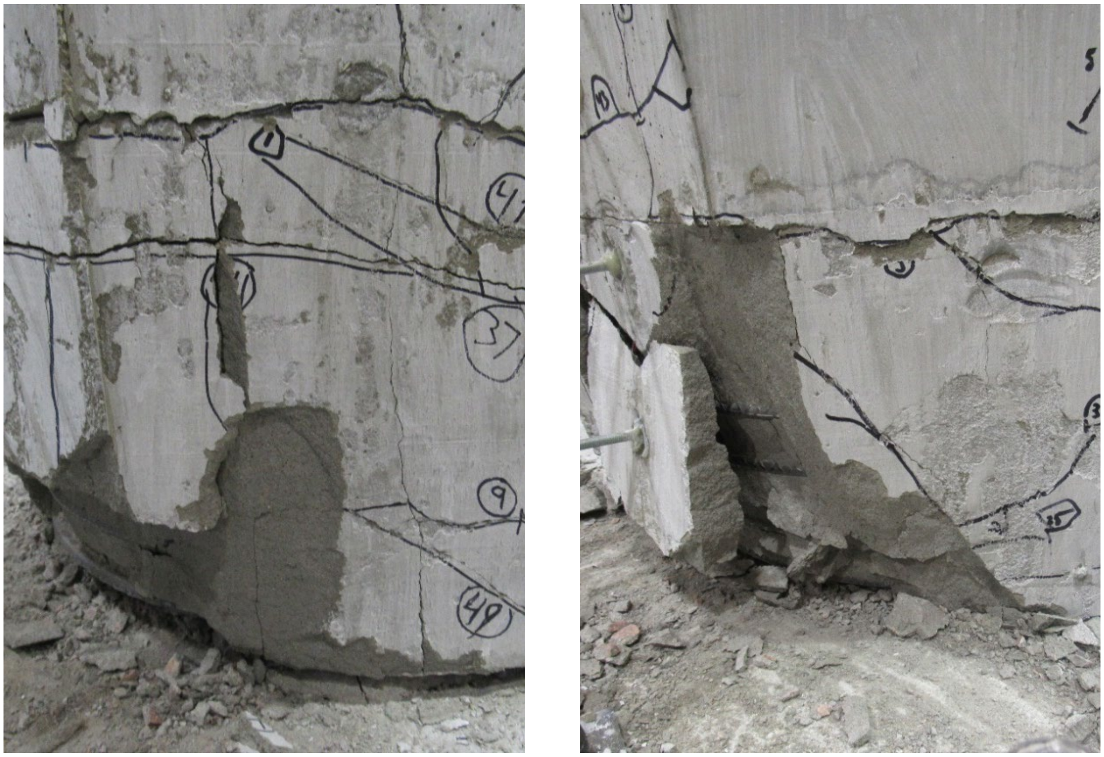

a) North-West Side b) South-East Side

Figure 3.215 PTV Column Plastic Hinge Damage, First Push of 7.00% Drift Cycle

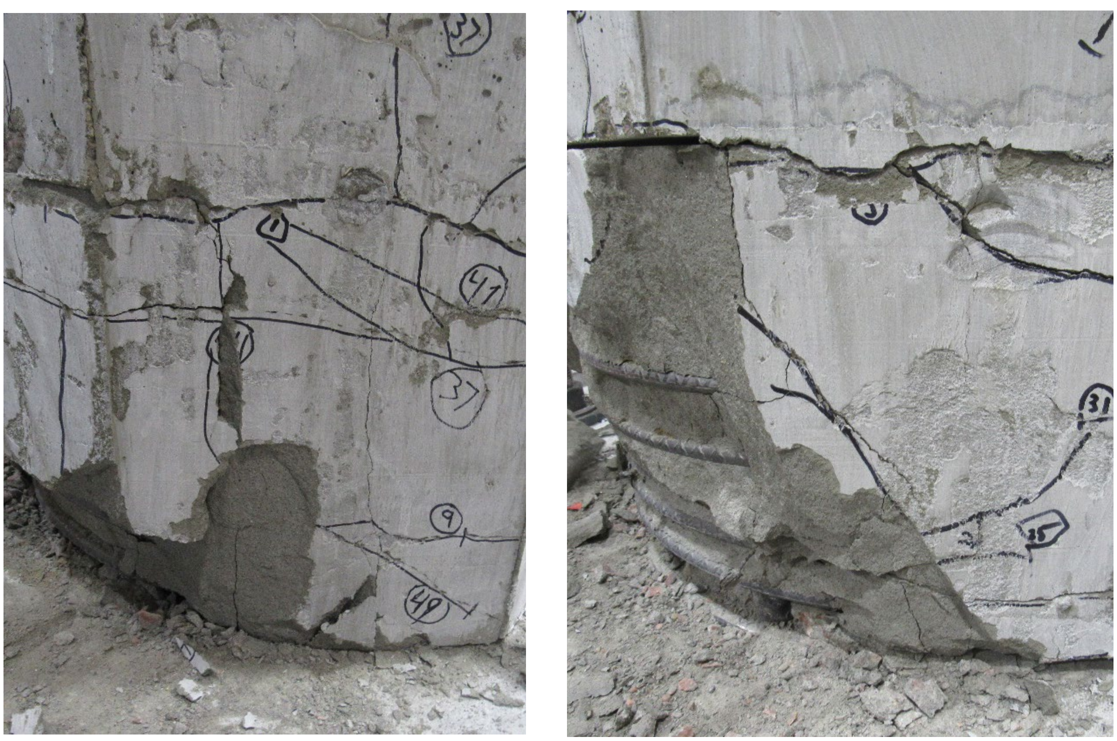

a) North-West Side b) South-East Side

Figure 3.216 PTV Column Plastic Hinge Damage, First Pull of 7.00% Drift Cycle

3.5.7.2 Force-Displacement Relationship

The measured envelope responses and lateral force-drift hysteretic of PTV are shown in Figure 3.217. The PTV column exhibited a maximum lateral load of 73.0 kips (324.7 kN) at 3% drift ratio and exhibited a slight strength degradation afterwards until 6%, then a sudden loss in force was observed due to the bar fracture. PTV was slightly stronger in the pull direction than push. The PTV longitudinal bars yielded at 0.45% drift ratio in the push direction under a lateral load of 36.6 kips (162.8 kN), and at -0.37% drift ratio in the pull direction at a lateral load of -32.8 kips (145.9 kN).

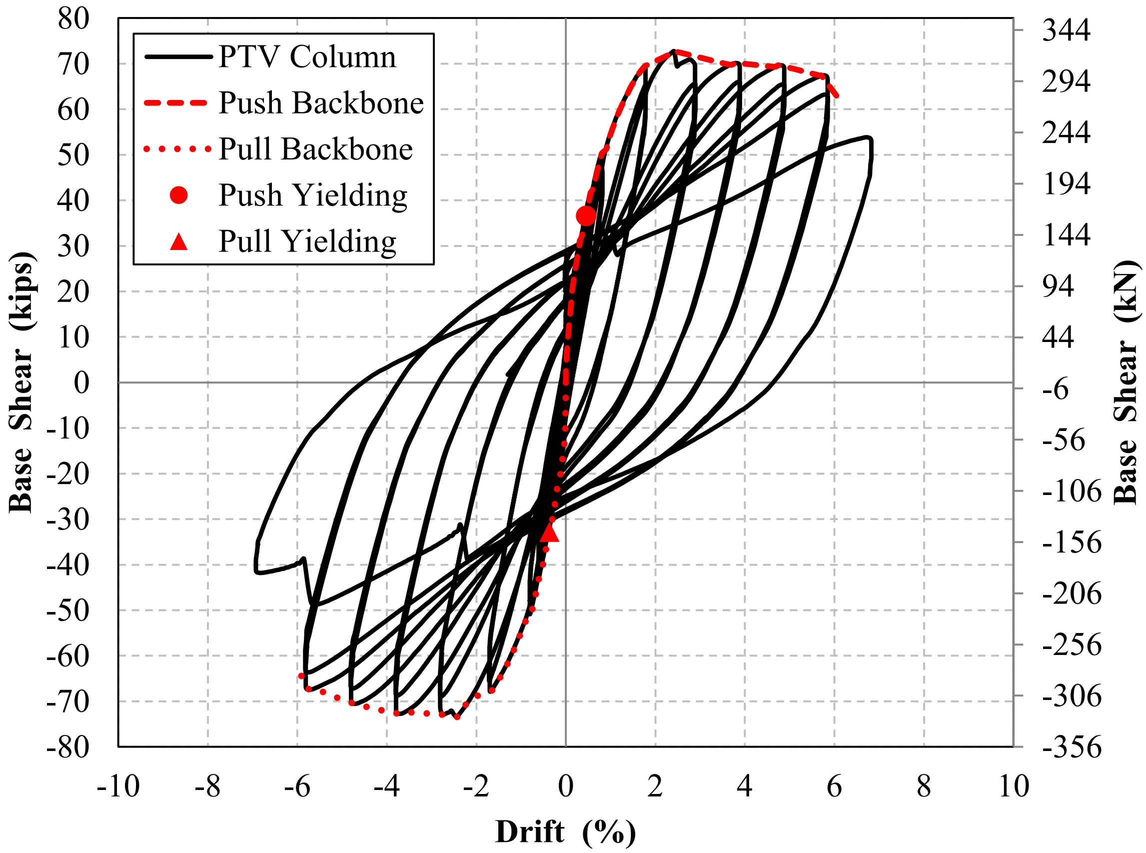

Figure 3.217 Measured PTV Column Force-Drift Hysteretic and Envelope Responses

Figure 3.218 shows the average envelope for the push and pull directions of PTV. The average yield drift ratio of 0.41% occurred at a lateral force of 34.7 kips (154.4 kN). Based on the 15% load criterion as the column failure, the drift capacity of the PTV column was estimated as 6.04%. Furthermore, Figure 3.218 shows the idealized curve for the average PTV envelope. The effective yield drift ratio was 0.778% at the effective yield lateral force of 67.41 kips (299.9 kN), resulting in a displacement ductility capacity of 7.77 for the PHV column.

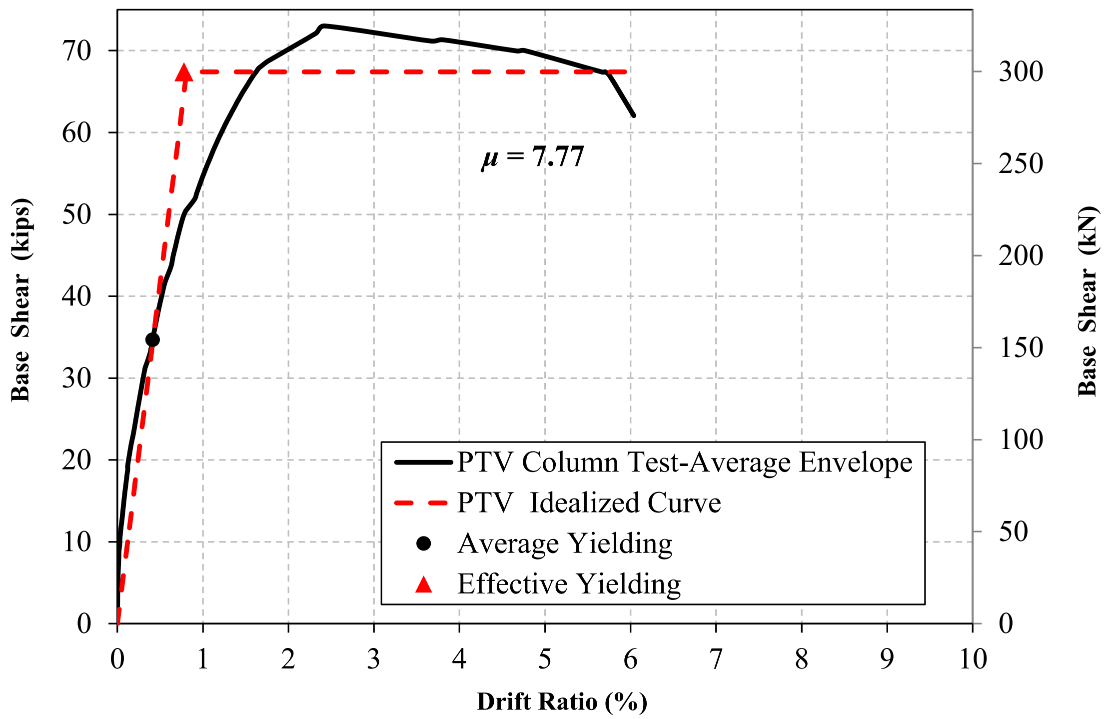

Figure 3.218 Measured PTV Column Average Push/Pull Force-Drift Envelope and Idealized Curve

3.5.7.3 Strain Profiles

Twenty-three strain gauges were installed on the PTV reinforcing steel bars at four levels of the column. Figures 3.219 to 3.222 show the measured strain profiles of PTV for Bars B1, B2, B6, and B7.

Prior to the bar yielding, the strain profile was uniform. The strain of the bars was higher near the column-footing interface and decreased at higher lengths of the column. Couplers tend to shift the nonlinearity away from the coupler region. The strain profiles show large strains at the ends of the threaded couplers used in PTV.

Furthermore, the PTV column hoops slightly yielded in the testing. The maximum hoop strain was 0.88% and the hoop yield strain was 0.23%.

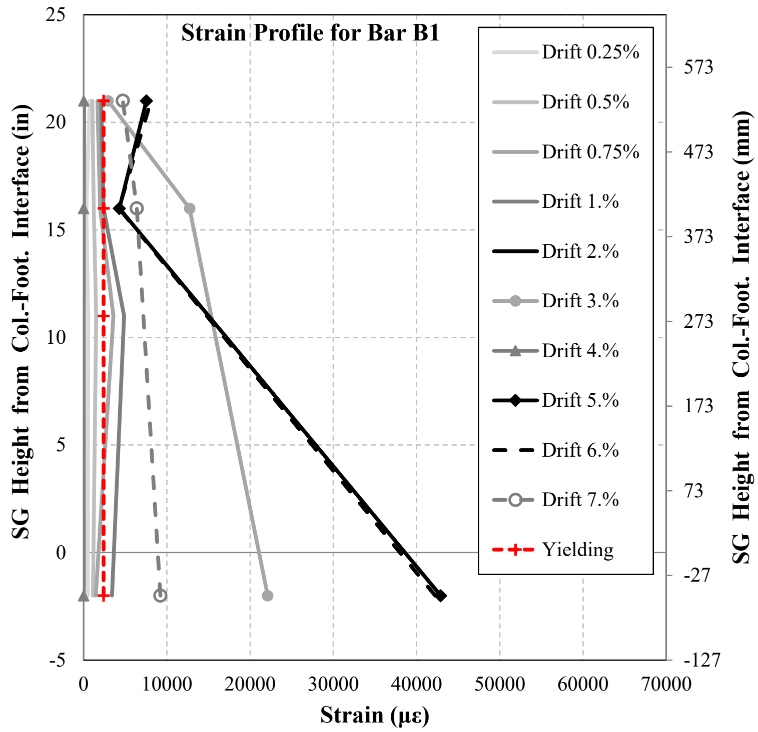

Figure 3.219 Measured Strain Profile for PTV Column Bar B1

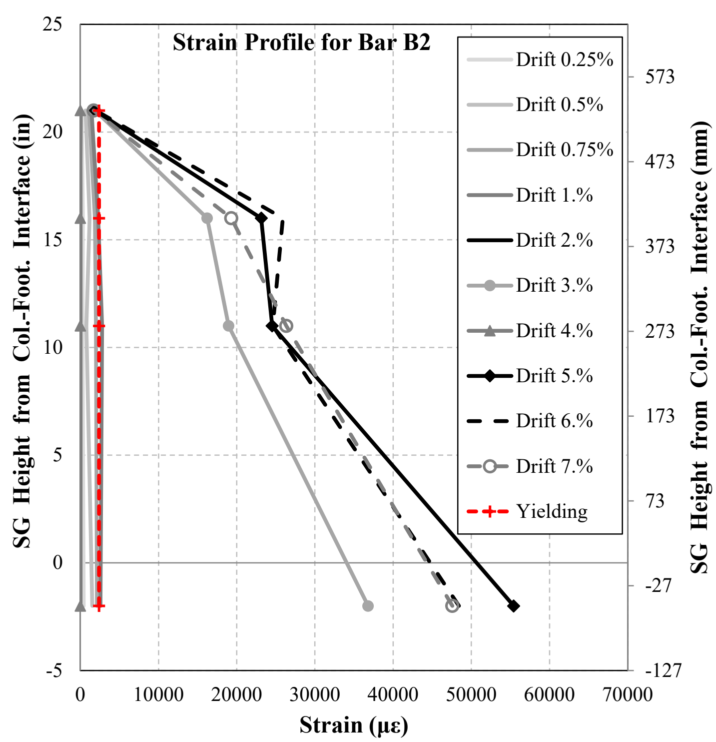

Figure 3.220 Measured Strain Profile for PTV Column Bar B2

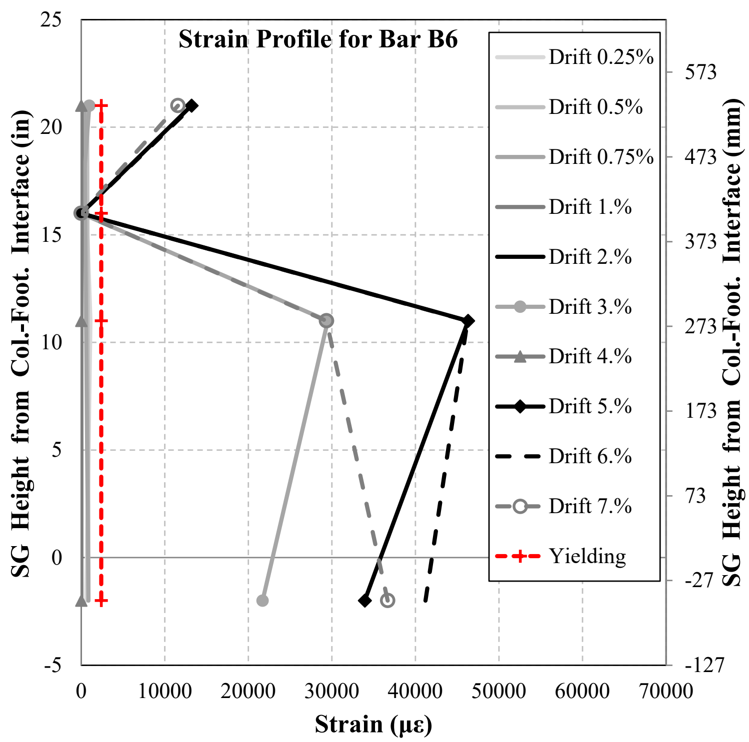

Figure 3.221 Measured Strain Profile for PHV Column Bar B6

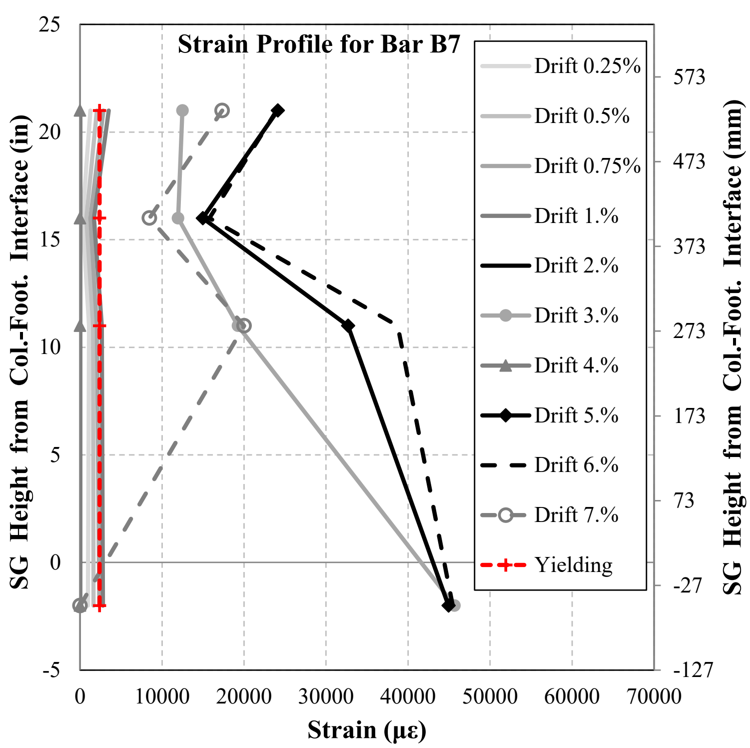

Figure 3.222 Measured Strain Profile for PTV Column Bar B7

3.5.7.4 Measured Rotation and Curvature

Rotations and curvatures were determined in the same manner as CIP. Figure 3.223 shows the measured curvature profile for the PTV column at drift ratios of 0.25% to 4.0%. The highest curvature always occurred at the base due the strain penetration into the footing. The threaded couplers used in PTV increased the column stiffness in the coupler region, resulting in an increased nonlinearity at the coupler ends. The figure confirms this behavior in which the curvature was relatively high near the column base, minimal along the coupler region, and slightly higher above the coupler.

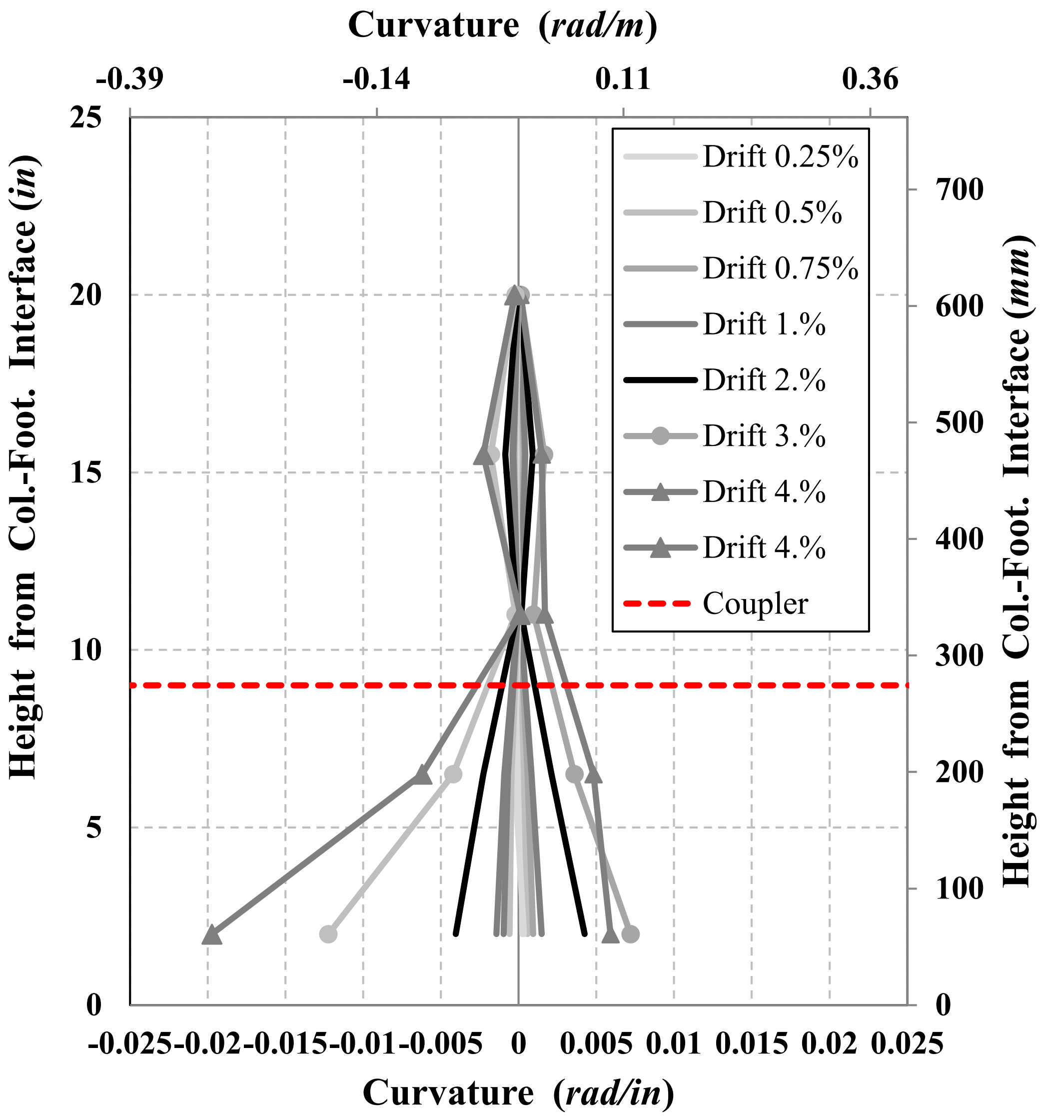

Figure 3.223 Measured Curvature Profile for PTV Column

3.5.7.5 Energy Dissipation

Figure 3.224 shows the measured cumulative energy dissipation of the PTV column at different drift ratios. The dissipated energy is negligible until 1% drift ratio, where bar yielding was minimal. The dissipated energy increased exponentially from about 3.0% drift until the test was concluded at 7.0% drift. At high drift ratios, the hysteretic loops began to widen, which led to a higher dissipated energy. PTV dissipated 3,435.8 kip-in. (388.2 kN-m) energy prior to the failure.

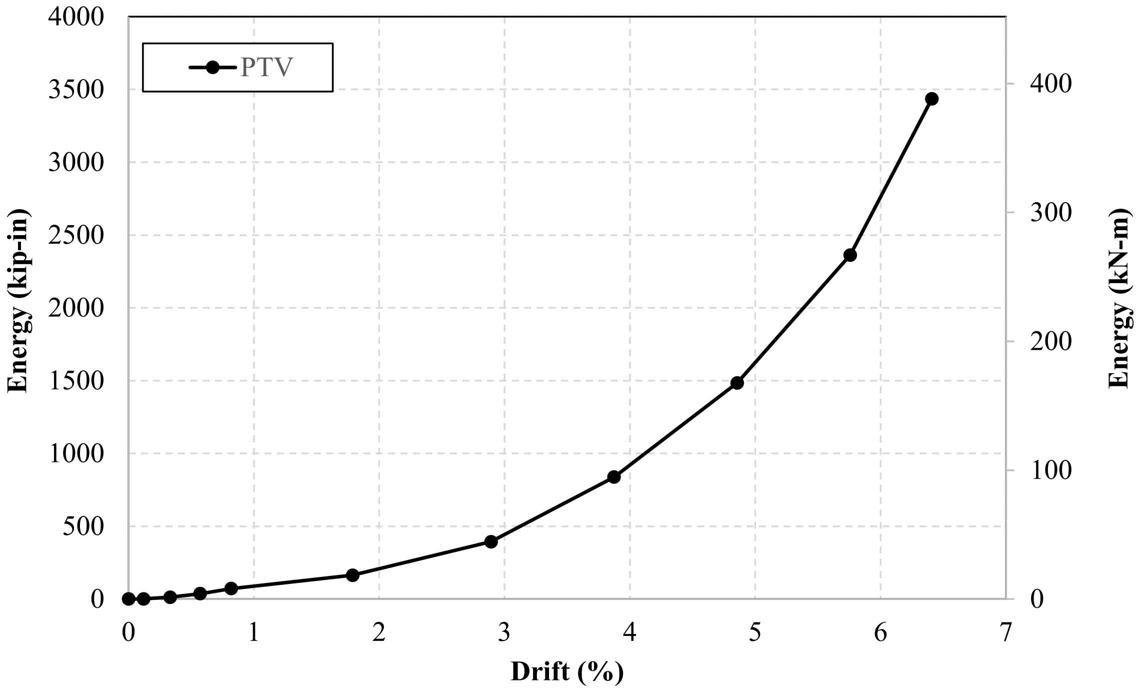

Figure 3.224 Measured Energy Dissipation for PTV Column

3.5.8 PHH Column Results

The seismic performance of the precast column incorporating the "HRC560" hybrid grouted-headed coupler, PHH, is discussed in this section.

3.5.8.1 Observed Damage

The PHH column followed the same testing procedure of the CIP column. Table 3.12 presents a summary of the damage observed during the PHH column testing, and Figures 3.225 to 3.250 show the PHH plastic hinge damage in the second cycle of each drift level.

Flexural cracks were observed in the first cycle of 0.25% drift ratio (Fig. 3.225 & 3.226). Cracks developed near the top of the coupler during the first cycle of 0.25% on the south face and the first cycle of the 0.5% drift on the north side. Shear cracks were first observed in the first cycle of 1.0% drift ratio (Fig. 3.231 & 3.232). The first yielding occurred in Bar B1 at 0.588% drift in the first push run of the 0.75% drift cycle under a lateral load of 45.18 kips (201 kN) (Fig. 3.229). Concrete spalled on both north and south faces of the column during the 4% drift cycles (Fig. 3.237 to 3.238). The lateral strength also began to degrade at the 4% drift (Fig. 3.237 & 3.238). Finally, the PHH column failed by a loss of strength toward the end of testing (10.0% drift). The source of the strength degradation could not be visually determined.

Table 3.12 Summary of Damage in PHH

Drift Ratio, %	Observed Damage
+0.25	• No observed damage
-0.25	• Minor flexural cracking
+0.50	• Flexural and inclined cracking
-0.50	• Flexural and inclined cracking
+0.75	• Flexural and inclined cracking • Cracking around column base • Bar yielding
-0.75	• Flexural cracking • Cracking around column base • Bar yielding
+1.00	• Flexural and incline cracking
-1.00	• No further damage observed
+2.00	• Flexural, incline, and vertical cracking
-2.00	• Flexural, incline, and vertical cracking
+3.00	• Flexural and vertical cracking
-3.00	• Flexural, vertical, and incline cracking
+4.00	• Flexural, vertical, and incline cracking • Spalling at column base • Beginning of force degradation
-4.00	• Flexural, vertical, and incline cracking • Beginning of force degradation • Spalling at column base
+5.00	• Increased spalling at column base • Vertical cracking • Continued strength loss
-5.00	• Increased spalling • Vertical and inclined cracking • Crack widening at top of coupler region
+6.00	• Crack widening • Increased spalling
-6.00	• Crack widening • Increased spalling
+7.00	• Significant spalling • Continued force degradation
-7.00	• Significant spalling • Continued force degradation
+8.00	• Continued force degradation
-8.00	• Continued force degradation
+9.00	• Significant strength degradation
-9.00	• Significant strength degradation
+10.0	• Continued strength degradation
-10.0	• Continued strength degradation

Note: Positive drifts were based on displacements away from the reaction blocks (north to south)

a) North-West Side b) South-East Side

Figure 3.225 PHH Column Plastic Hinge Damage, Second Push of 0.25% Drift Cycle

a) North-West Side b) South-East Side

Figure 3.226 PHH Column Plastic Hinge Damage, Second Pull of 0.25% Drift Cycle

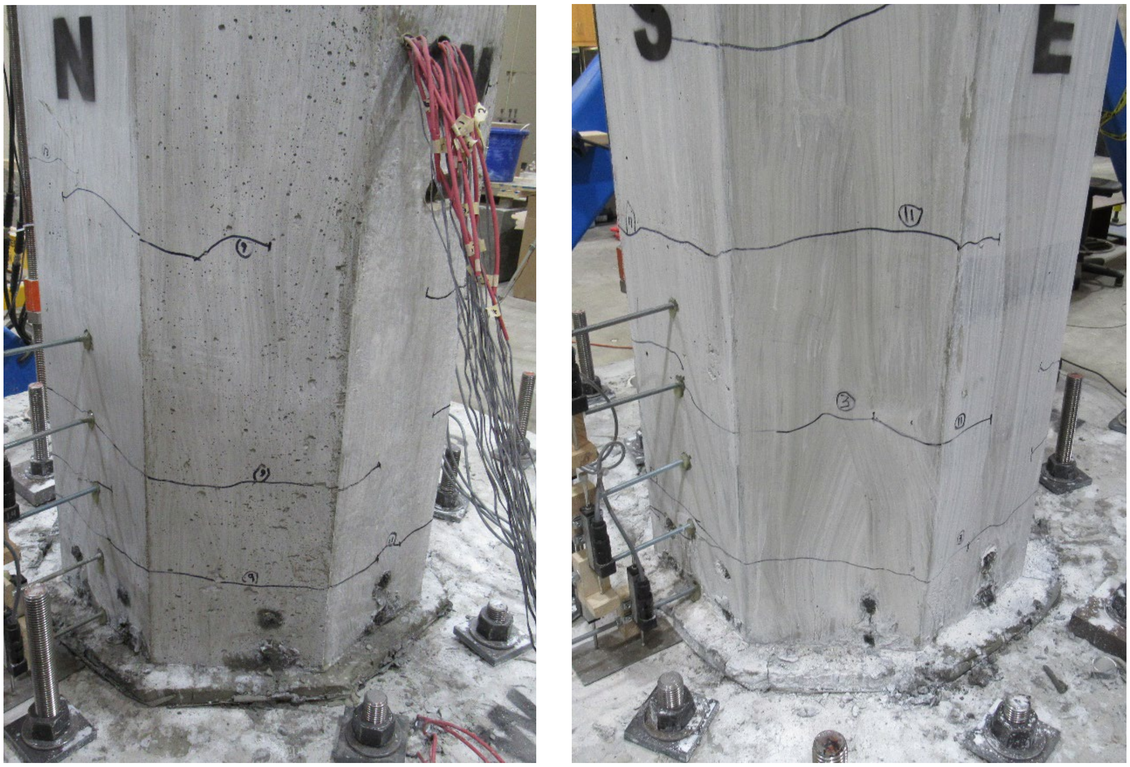

a) North-West Side   b) South-East Side

Figure 3.227 PHH Column Plastic Hinge Damage, Second Push of 0.50% Drift Cycle

a) North-West Side   b) South-East Side

Figure 3.228 PHH Column Plastic Hinge Damage, Second Pull of 0.50% Drift Cycle

a) North-West Side b) South-East Side

Figure 3.229 PHH Column Plastic Hinge Damage, Second Push of 0.75% Drift Cycle

a) North-West Side b) South-East Side

Figure 3.230 PHH Column Plastic Hinge Damage, Second Pull of 0.75% Drift Cycle

a) North-West Side b) South-East Side

Figure 3.231 PHH Column Plastic Hinge Damage, Second Push of 1.00% Drift Cycle

a) North-West Side b) South-East Side

Figure 3.232 PHH Column Plastic Hinge Damage, Second Pull of 1.00% Drift Cycle

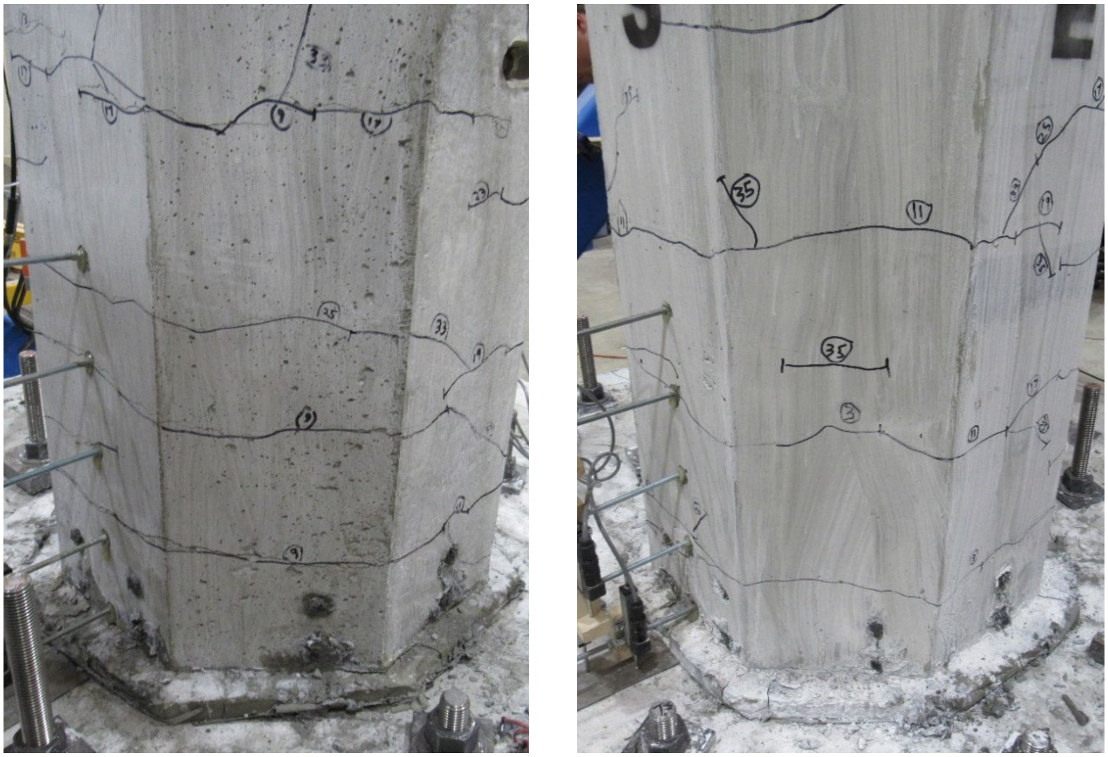

a) North-West Side b) South-East Side

Figure 3.233 PHH Column Plastic Hinge Damage, Second Push of 2.00% Drift Cycle

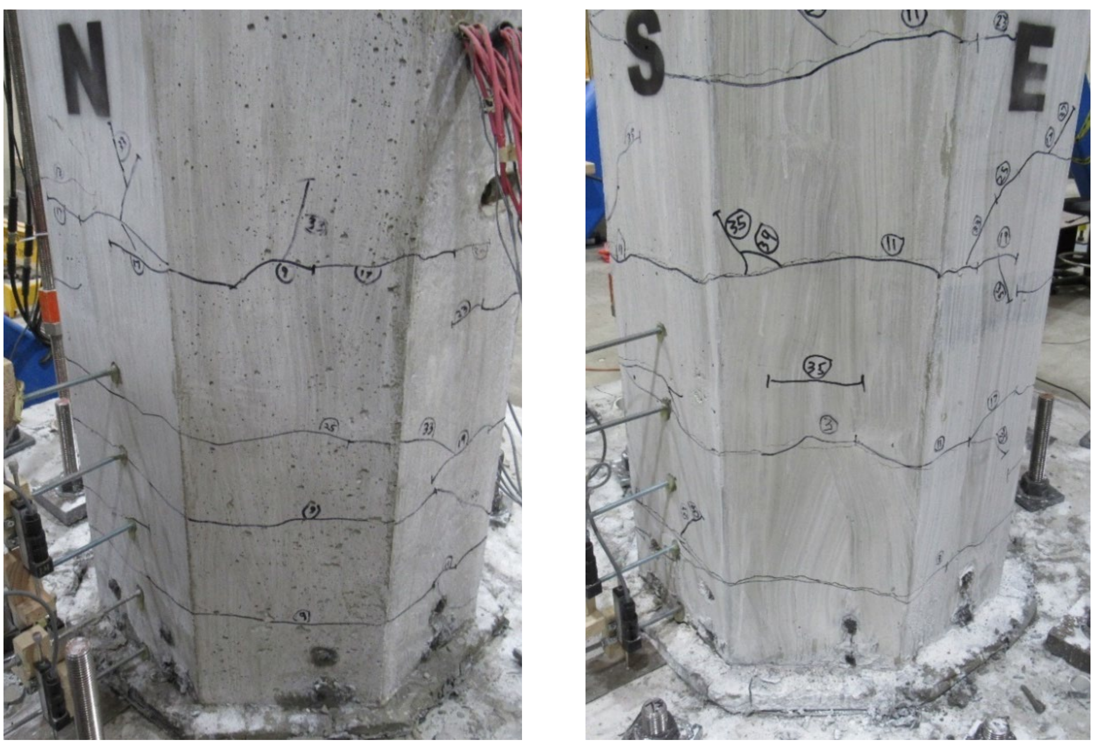

a) North-West Side b) South-East Side

Figure 3.234 PHH Column Plastic Hinge Damage, Second Pull of 2.00% Drift Cycle

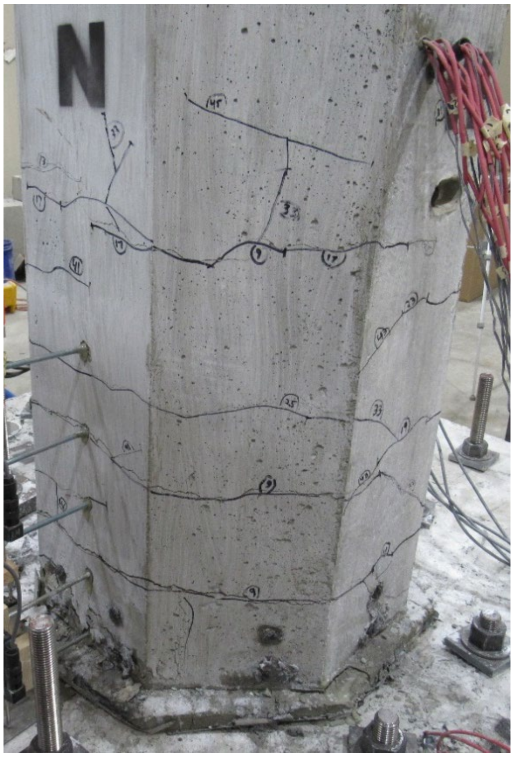

a) North-West Side

b) South-East Side

Figure 3.235 PHH Column Plastic Hinge Damage, Second Push of 3.00% Drift Cycle

a) North-West Side

b) South-East Side

Figure 3.236 PHH Column Plastic Hinge Damage, Second Pull of 3.00% Drift Cycle

a) North-West Side b) South-East Side

Figure 3.237 PHH Column Plastic Hinge Damage, Second Push of 4.00% Drift Cycle

a) North-West Side b) South-East Side

Figure 3.238 PHH Column Plastic Hinge Damage, Second Pull of 4.00% Drift Cycle

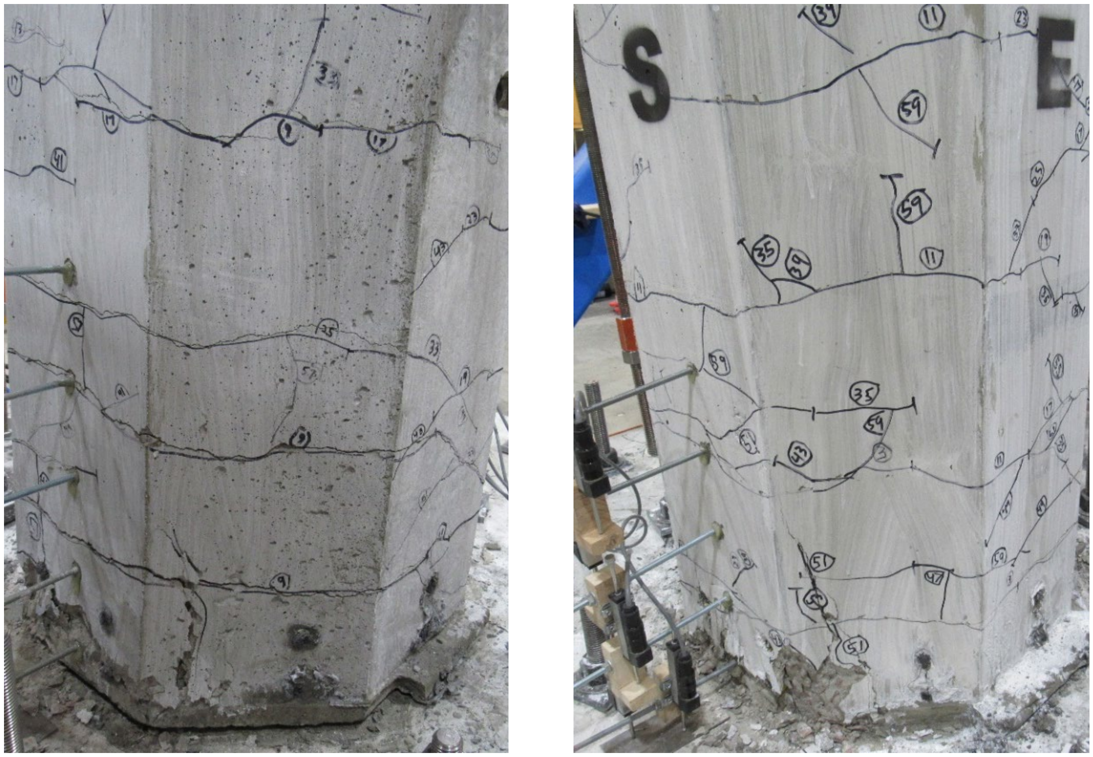

a) North-West Side

b) South-East Side

Figure 3.239 PHH Column Plastic Hinge Damage, Second Push of 5.00% Drift Cycle

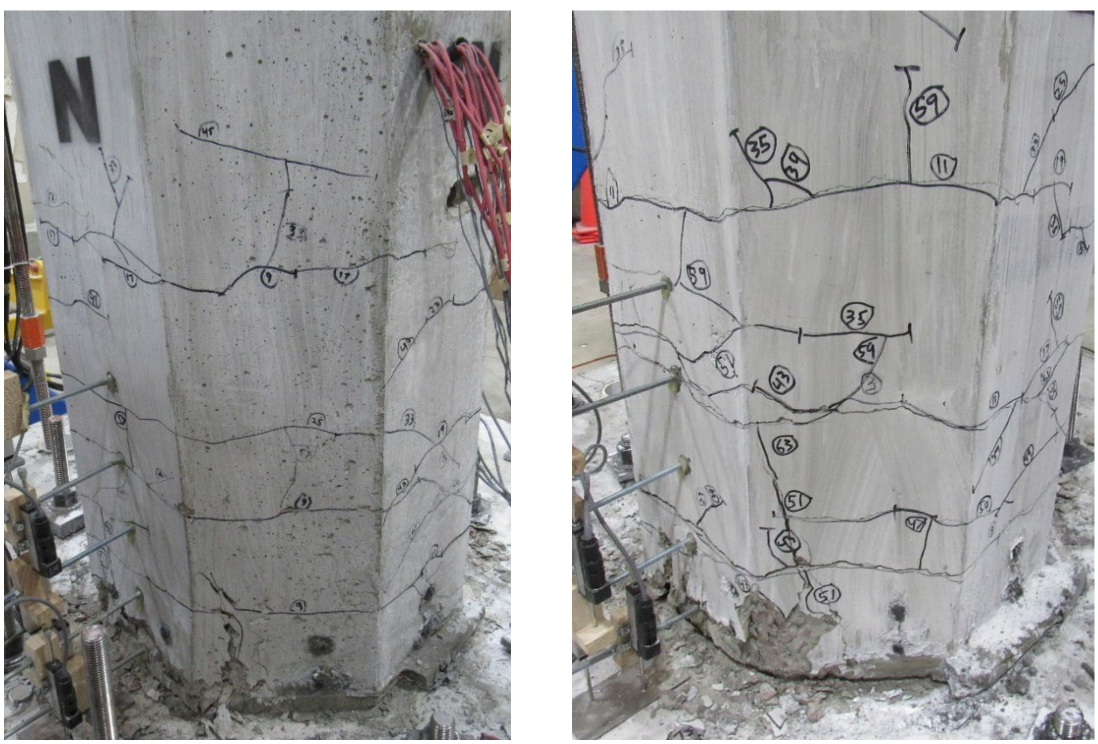

a) North-West Side

b) South-East Side

Figure 3.240 PHH Column Plastic Hinge Damage, Second Pull of 5.00% Drift Cycle

a) North-West Side b) South-East Side

Figure 3.241 PHH Column Plastic Hinge Damage, Second Push of 6.00% Drift Cycle

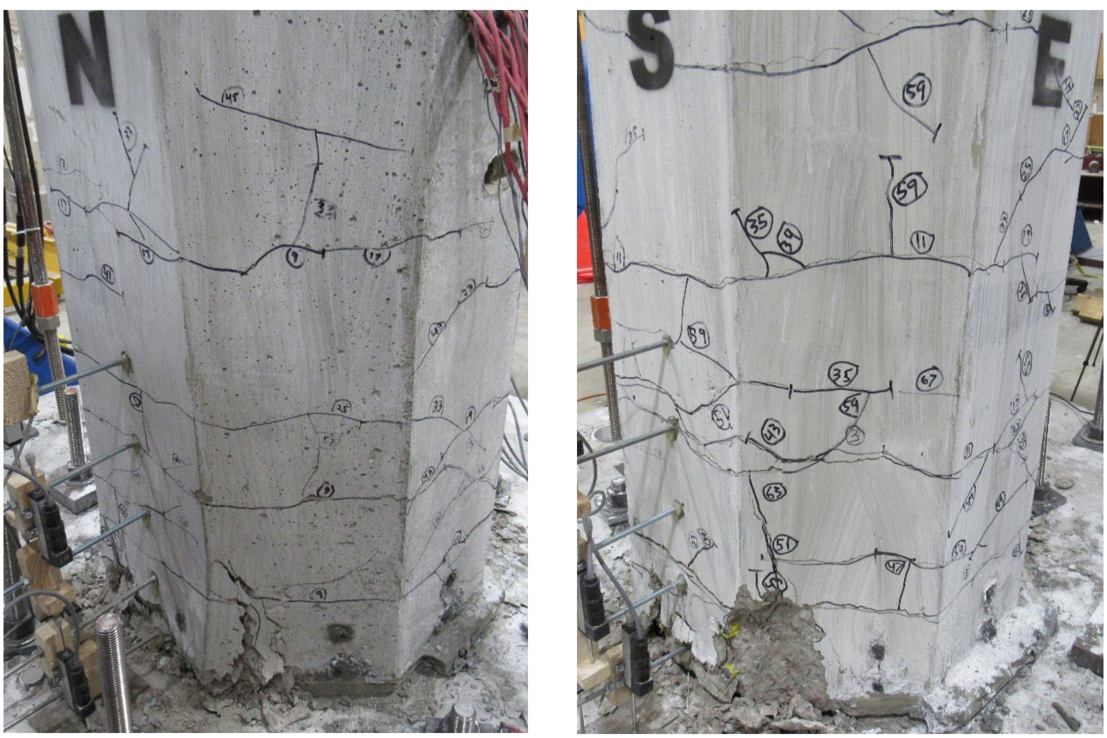

a) North-West Side b) South-East Side

Figure 3.242 PHH Column Plastic Hinge Damage, Second Pull of 6.00% Drift Cycle

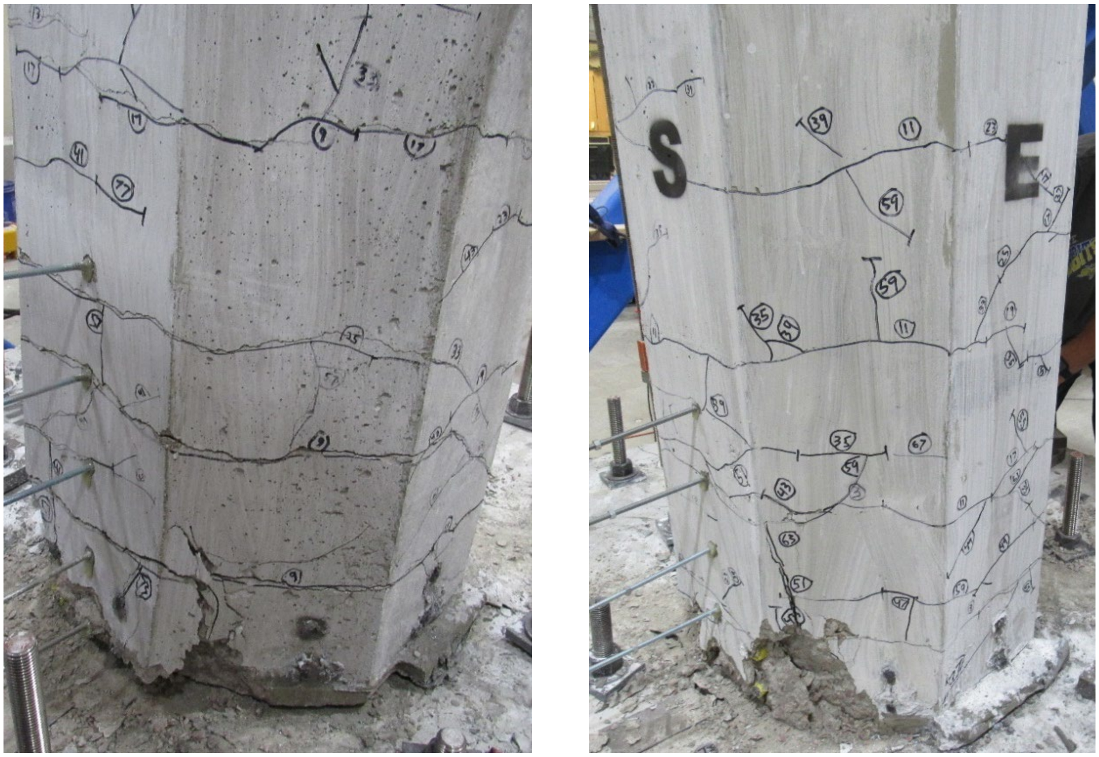

a) North-West Side b) South-East Side

Figure 3.243 PHH Column Plastic Hinge Damage, Second Push of 7.00% Drift Cycle

a) North-West Side b) South-East Side

Figure 3.244 PHH Column Plastic Hinge Damage, Second Pull of 7.00% Drift Cycle

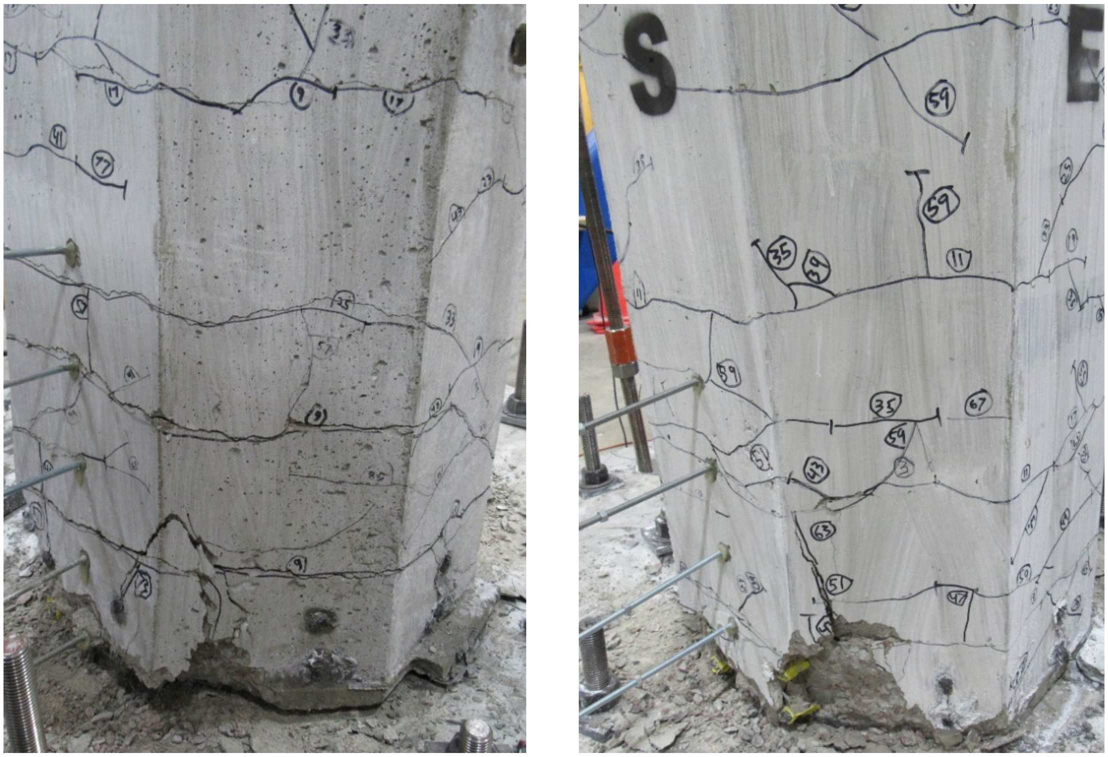

a) North-West Side b) South-East Side

Figure 3.245 PHH Column Plastic Hinge Damage, Second Push of 8.00% Drift Cycle

a) North-West Side b) South-East Side

Figure 3.246 PHH Column Plastic Hinge Damage, Second Pull of 8.00% Drift Cycle

a) North-West Side b) South-East Side

Figure 3.247 PHH Column Plastic Hinge Damage, Second Push of 9.00% Drift Cycle

a) North-West Side b) South-East Side

Figure 3.248 PHH Column Plastic Hinge Damage, Second Pull of 9.00% Drift Cycle

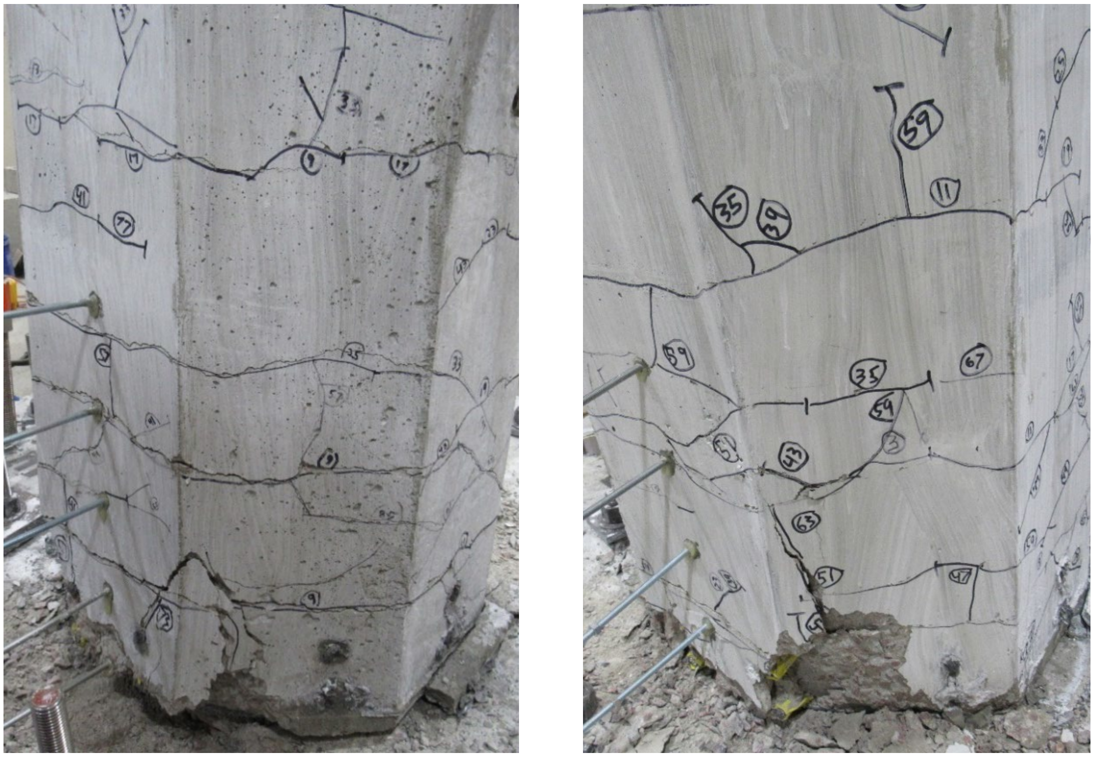

a) North-West Side b) South-East Side

Figure 3.249 PHH Column Plastic Hinge Damage, Second Push of 10.0% Drift Cycle

a) North-West Side b) South-East Side

Figure 3.250 PHH Column Plastic Hinge Damage, Second Pull of 10.0% Drift Cycle

3.5.8.2 Force-Displacement Relationship

Figure 3.251 shows the measured lateral force-drift hysteretic response and the push/pull envelopes for PHH. The envelopes are shown up to the failure points. The PHH column exhibited a maximum lateral load of 72.3 kips (321 kN) at 3% drift ratio and exhibited a minor strength degradation afterwards until the testing was concluded at 10.0%. The column was slightly stronger in the push direction than the pull direction. The PHH longitudinal bars yielded at 0.588% drift ratio in the push direction under a lateral load of 45.2 kips (201.1 kN), and at -0.587% drift ratio in the pull direction at a lateral load of -48.1 kips (214 kN). The hysteretic response shows a flag-shape behavior (or pinching) during unloading. This is because the headed bar at the top of the hybrid coupler had a gap that was opened/extended during loading and was needed to be closed during uploading (before engaging in the other direction).

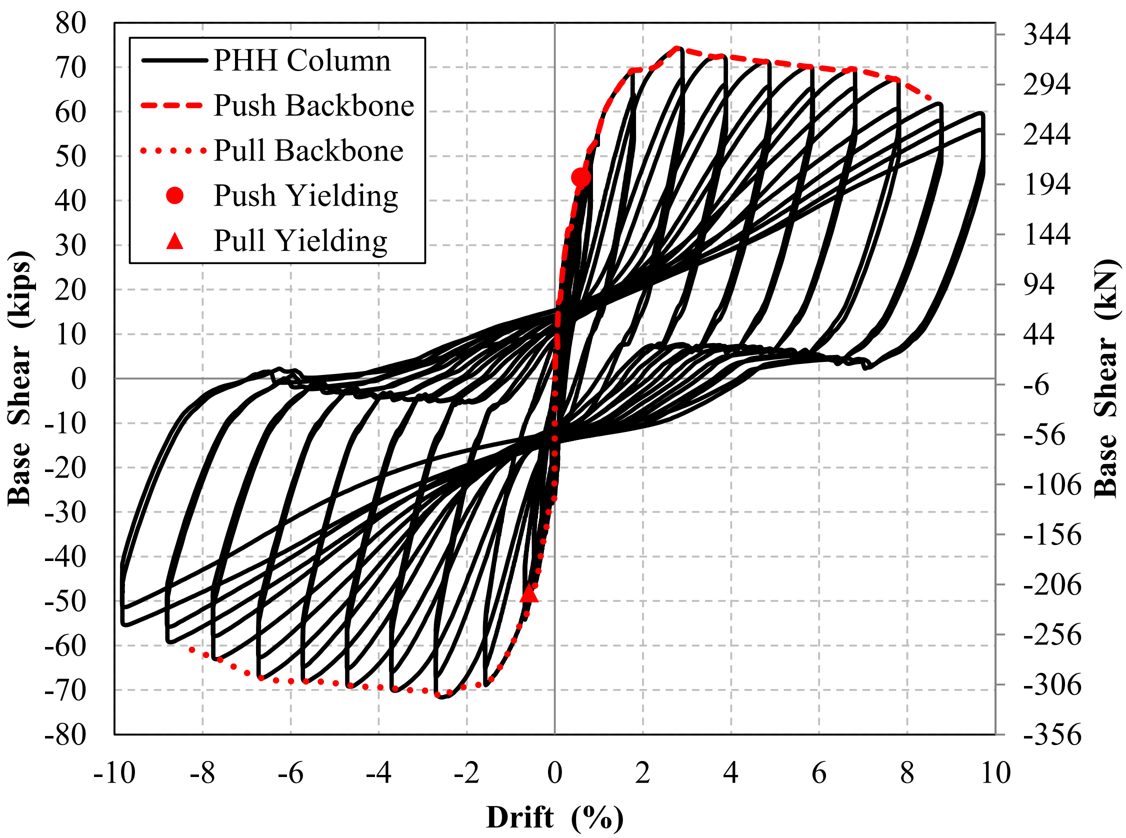

Figure 3.251 Measured PHH Column Force-Drift Hysteretic and Envelope Responses

Figure 3.252 shows the average envelope for the push and pull directions of PHH. The average yield drift ratio was 0.587% and occurred at a lateral force of 46.6 kips (207.3 kN). Based on the 15% load drop criterion as the column failure, the drift capacity of the PHH column was estimated as 8.66%. Furthermore, Figure 3.252 shows the idealized curve for the average PHH envelope. The effective yield drift ratio was 0.75% at the effective yield lateral force of 65.26 kips (290.3 kN) resulting in a displacement ductility capacity of 11.49 for the PHH column.

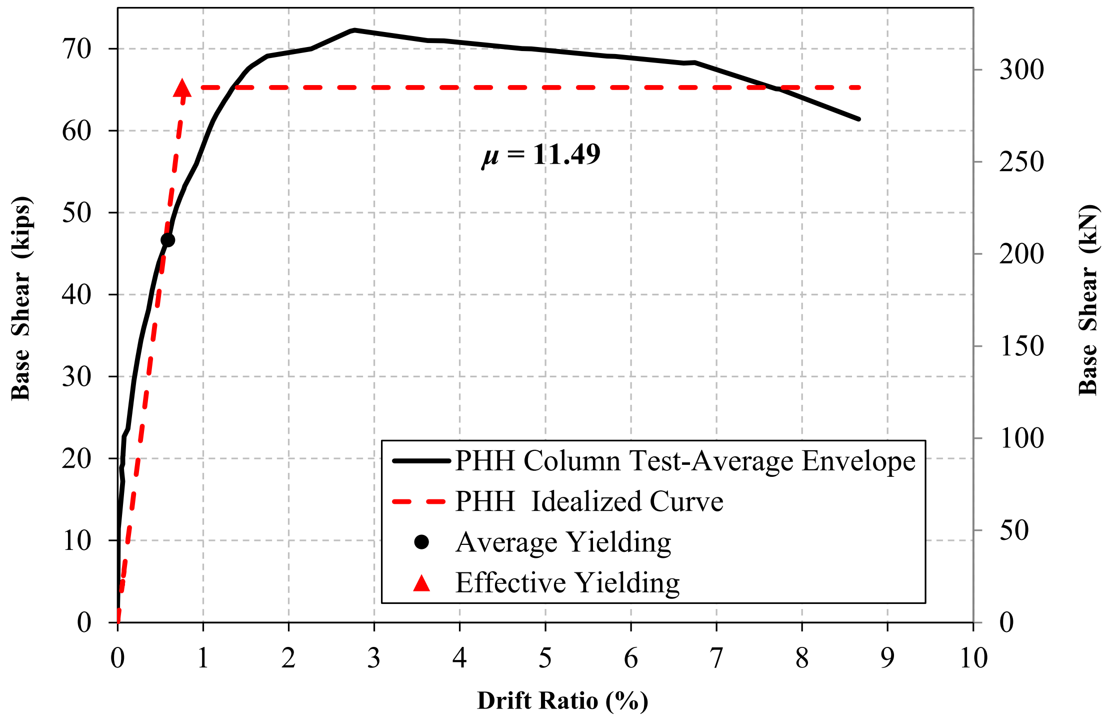

Figure 3.252 Measured PHH Column Average Push/Pull Force-Drift Envelope and Idealized Curve

3.5.8.3 Strain Profiles

Twenty-three strain gauges were installed on the PHH reinforcing steel bars at four levels of the column height. Figures 3.253 to 3.256 show the measured strain profiles of PHH for Bars B1, B2, B6, and B7.

Prior to the bar yielding, the strain profile was uniform. Note that the strain profiles for PHH was revised by removing bad strain data of a few sensors. The general trend shows an increase in the strain outside the coupler region, which is consistent with other coupler columns. This is because the coupler tends to shift the yielding away.

Furthermore, the PHH column hoops did not yield throughout the testing. The maximum hoop strain was 0.12% while the hoop yield strain was 0.23%.

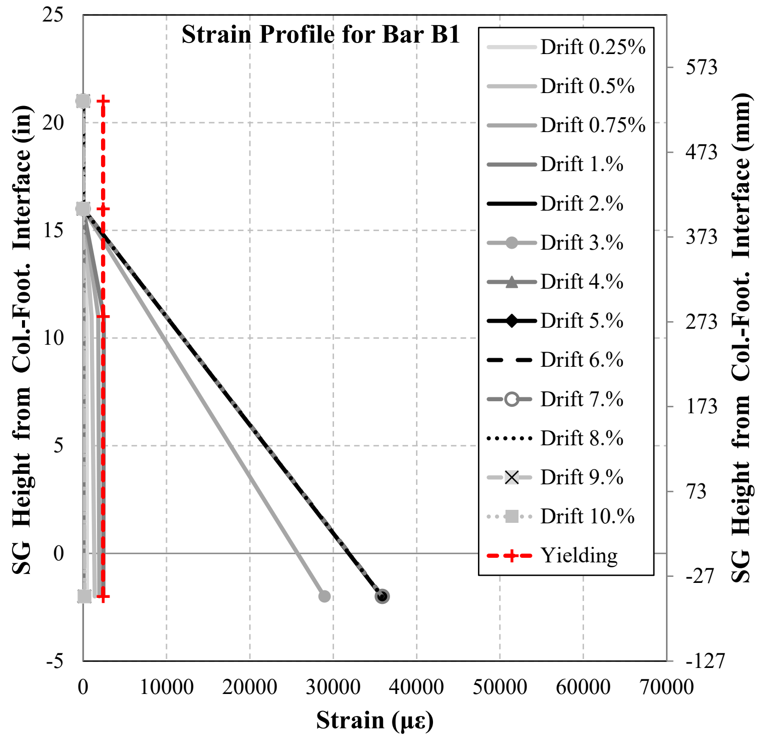

Figure 3.253 Measured Strain Profile for PHH Column Bar B1

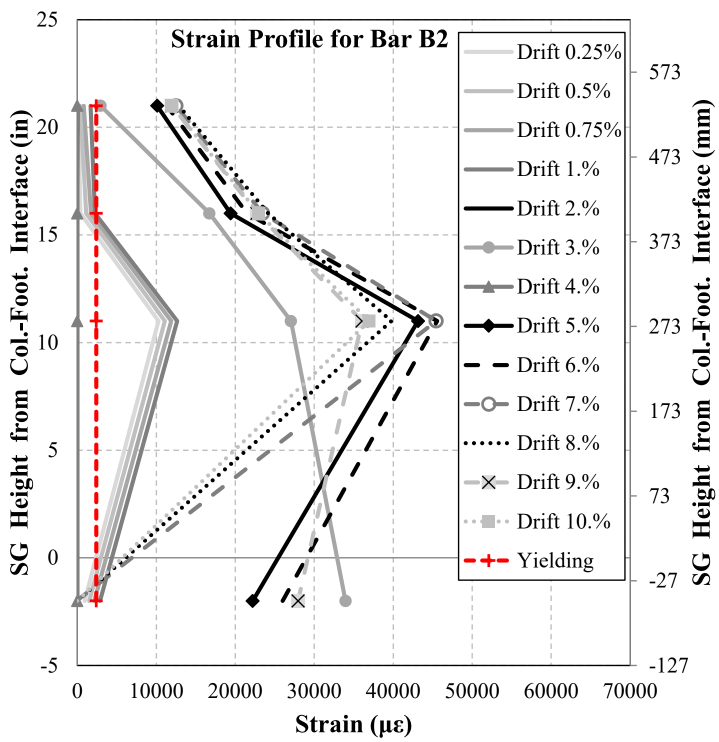

Figure 3.254 Measured Strain Profile for PHH Column Bar B2

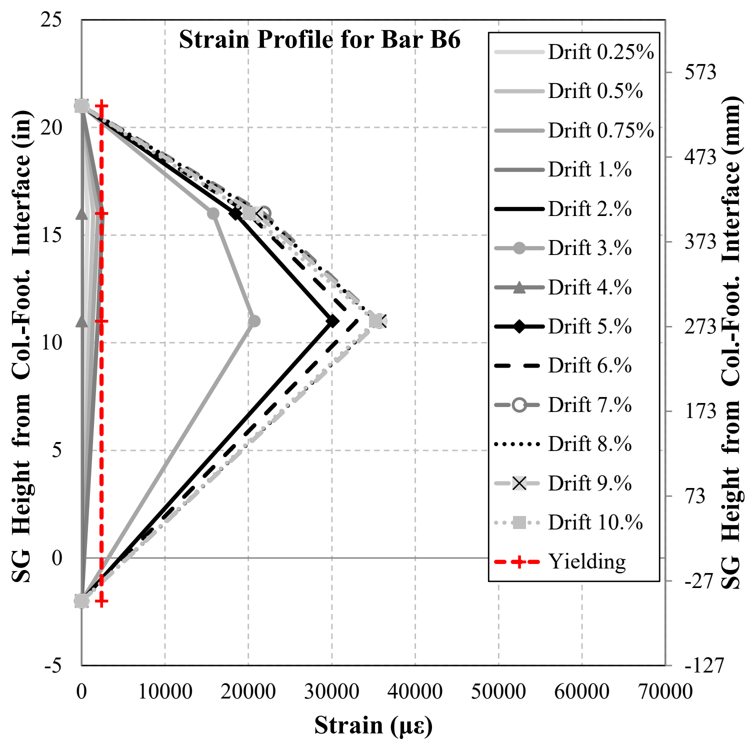

Figure 3.255 Measured Strain Profile for PHH Column Bar B6

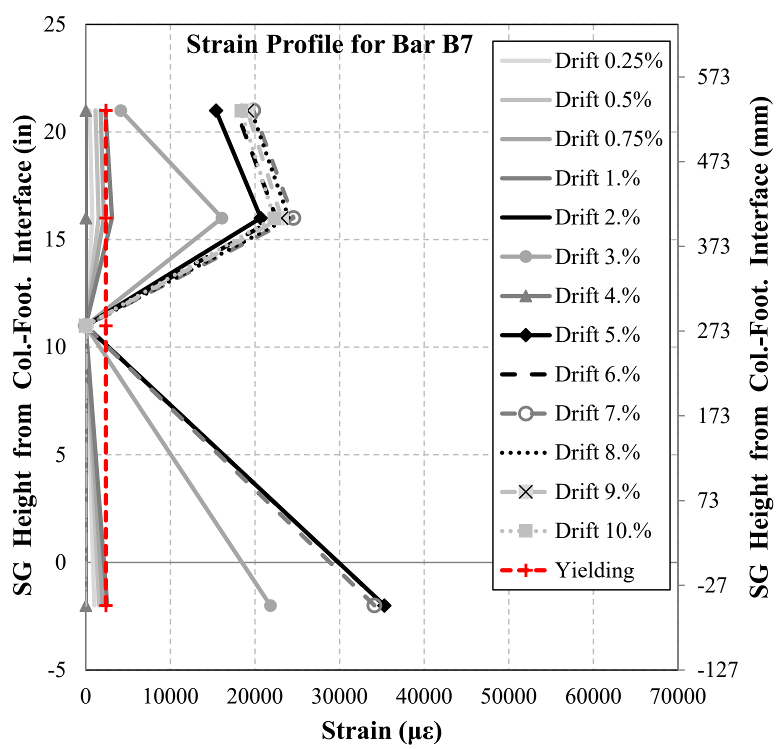

Figure 3.256 Measured Strain Profile for PHH Column Bar B7

3.5.8.4 Measured Rotation and Curvature

Rotations and curvatures were determined in the same manner as CIP. Figure 3.257 shows the measured curvature profile for the PHH column at drift ratios of 0.25% to 4.0%. The highest curvature always occurred at the base due to concentrated concrete cracking and bar-slip near the column-footing interface. The grouted-headed couplers used in PHH increased the column stiffness in the coupler region, which was relatively short compared with other grouted or hybrid couplers, thus shifting the nonlinearity away from the coupler region.

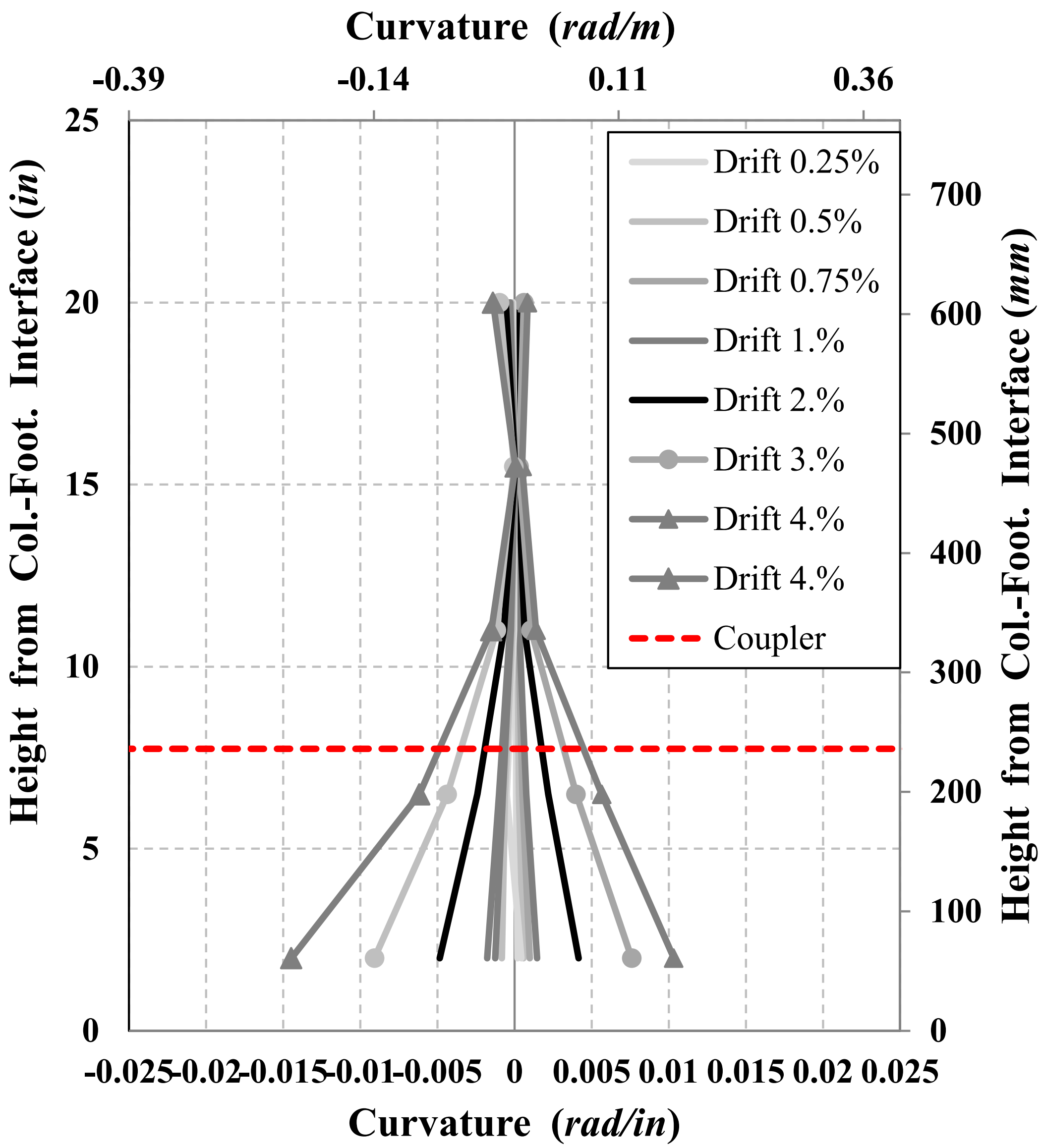

Figure 3.257 Measured Curvature Profile for PHH Column

3.5.8.5 Energy Dissipation

Figure 3.258 shows the measured cumulative energy dissipation of the PHH column at different drift ratios. The dissipated energy is negligible until 1% drift ratio, where bar yielding was minimal. At higher drift ratios, the hysteretic loops began to widen, which led to a higher dissipated energy. PHH dissipated 5383.4 kip-in. (608.2 kN-m) of energy prior to the failure.

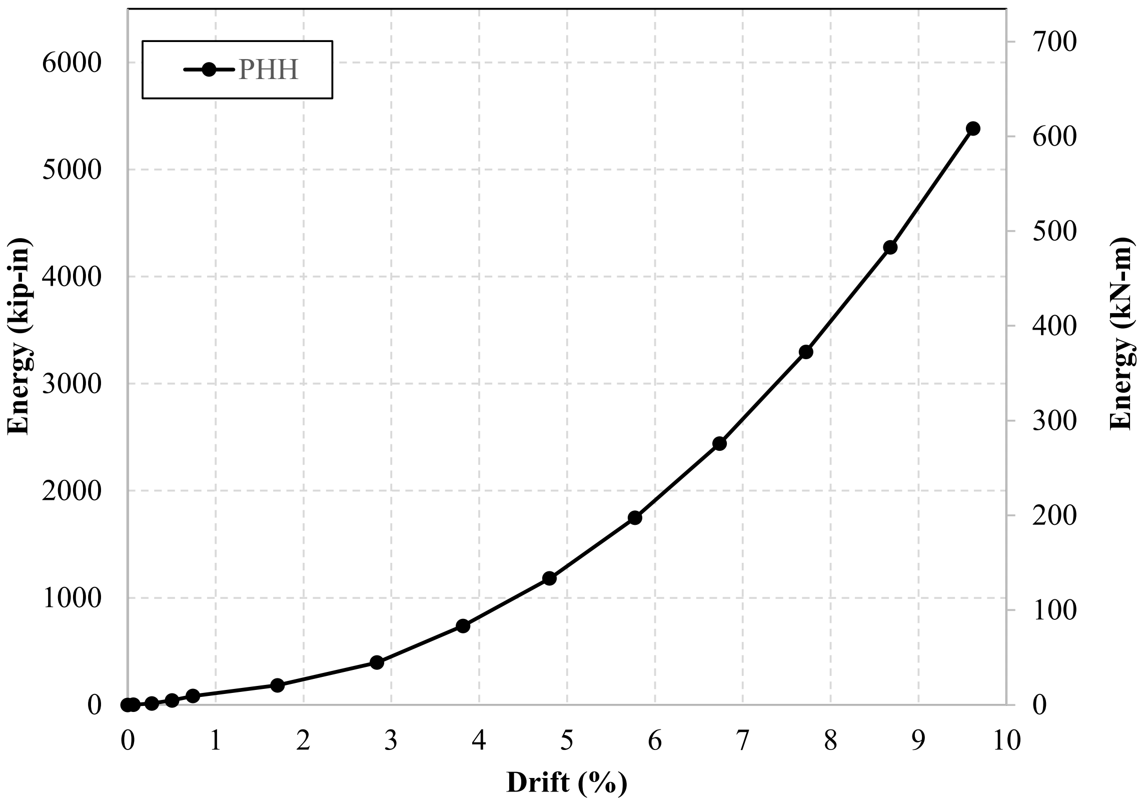

Figure 3.258 Measured Energy Dissipation for PHH Column

3.5.9 RPH Column Results

The performance of the repairable precast column, RPH, is presented in this section. RPH was tested twice, once using a long buckling restrained reinforcement (BRR, painted in yellow), and once using another set of BRR but with a shorter dog-bone length (this BRR was green colored). The second test was to prove that the column repair through replacement of exposed BRR is feasible. To differentiate the results of two tests on the same column, the precast column specimen in the first test is named "RPH" and the repaired column is labeled as "RPH-R." The fuse length, the dog-boned length of the device, in RPH was 10.25 in. (260 mm) and in RPH-R was 5.13 in. (130 mm).

3.5.9.1 RPH Observed Damage

The same testing procedure used for the CIP column was followed for RPH. Nevertheless, the test was stopped at 5% drift ratio to replace BRR. After the repair, RPH-R was tested to failure, which is discussed in the following sections. A summary of the observed damage is presented in Table 3.13 while Figure 3.259 to 3.274 show the observed damage of RPH at each drift cycle.

In RPH testing, only one minor flexural crack was observed during the first cycle of 0.25% drift ratio (Fig. 3.259 & 3.260). Additional minor flexural cracks were noticed in the neck section during the first cycle of 0.5% drift ratio (Fig. 3.261). Flexural cracks continued to form during the cycles at 0.75% and 1.0% drift ratios as well as some minor vertical cracks at the location of the inserted shims near the base of the column (Fig. 3.263). Yielding of the longitudinal rebar within the BRR fuses did not occur until the first cycle of 2.0% drift ratio, at which both bars B1 and B2 yielded in the push direction and both bars B6 and B7 yielded in the pull direction. Cover spalling at the base of the column was also initiated in both directions during the 2% drift ratio cycles while minor buckling of the BRR fuses between the couplers and steel tubes was observed (Fig. 3.267). During the first push at 3% drift ratio, cover concrete began to spall above the neck region at the point where the longitudinal bars enter the octagonal cross section due to compressive stresses as the concrete pressed against the clamping collars used to prevent buckling in the exposed portion of the rebar (Fig. 3.269). Cone-shaped failure of the grout inside the BRR steel tubes was also observed at 3% drift ratio. A Z-shape buckling of the BRR fuses (not the fuse itself but bending of the exposed bars at the ends) continued to worsen during the 4% and 5% drift ratio cycles (Fig. 3.271). The RPH column test was stopped at 5% drift ratio to replace the BRR fuses and perform the repair, which was replacement of the BRR only.

Table 3.13 Summary of Damage in RPH

Drift Ratio, %	Observed Damage
+0.25	• One minor flexural crack above neck section
-0.25	• No further damage
+0.50	• Minor flexural cracks in neck section
-0.50	• No further damage
+0.75	• Large flexural crack above neck section
-0.75	• Short vertical cracks at column base above shims
+1.00	• Flexural cracks, vertical cracks above shims
-1.00	• Flexural cracks, vertical cracks above shims
+2.00	• Bar yielding in BRR fuses • Flexural and inclined cracks, vertical cracks at base • Initiation of spalling at column base on south face • Minor buckling of BRR between coupler and steel tube on south side
-2.00	• Bar yielding in BRR fuses • Flexural and inclined cracks, vertical cracks at base • Initiation of spalling at column base on north face • Minor buckling of BRR between coupler and steel tube on north side
+3.00	• Crushing of grout inside BRR • Flexural, inclined, vertical cracks • Initiation of spalling above neck region on south face
-3.00	• Crushing of grout inside BRR • Flexural, inclined, vertical cracks
+4.00	• Large spalling above neck region on south face • Large buckling of BRR
-4.00	• Large buckling of BRR
+5.00	• Very large buckling of BRR on south side
-5.00	• Large buckling of BRR on north side

Note: Positive drifts were based on displacements away from the reaction blocks (north to south)

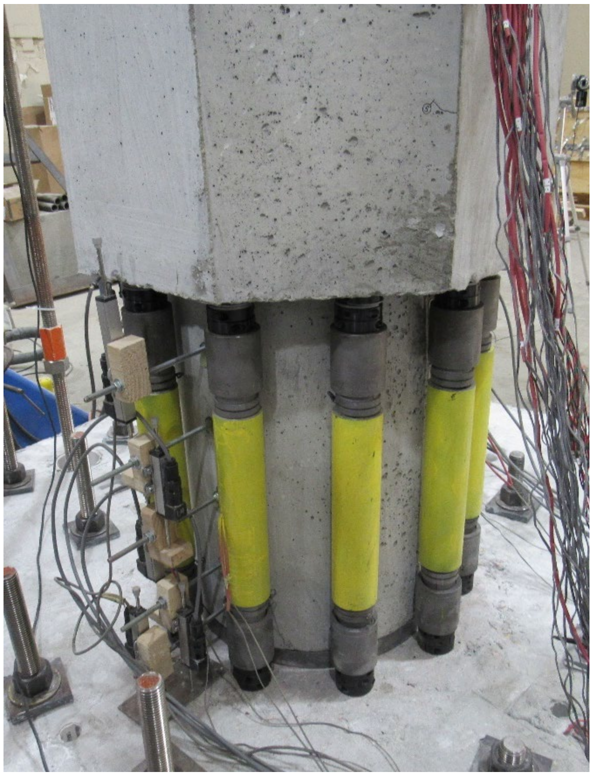

a) North-West Side

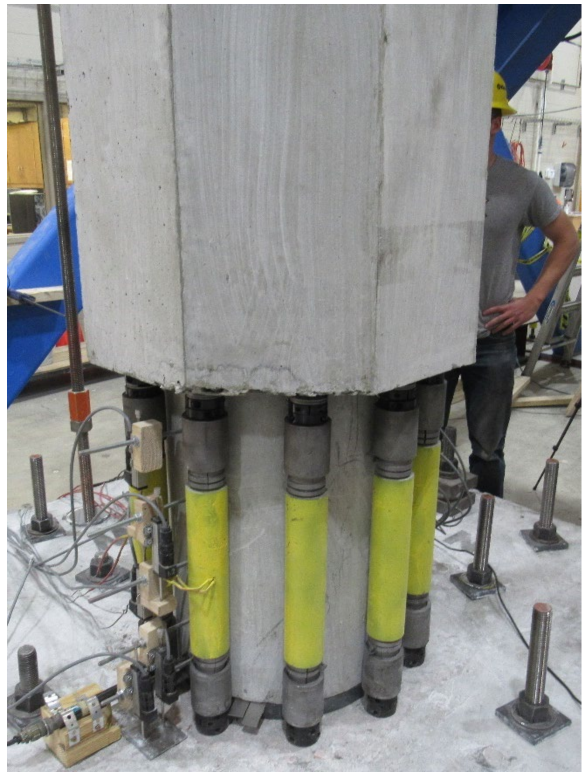

b) South-East Side

Figure 3.259 RPH Column Plastic Hinge Damage, Second Push of 0.25% Drift Cycle

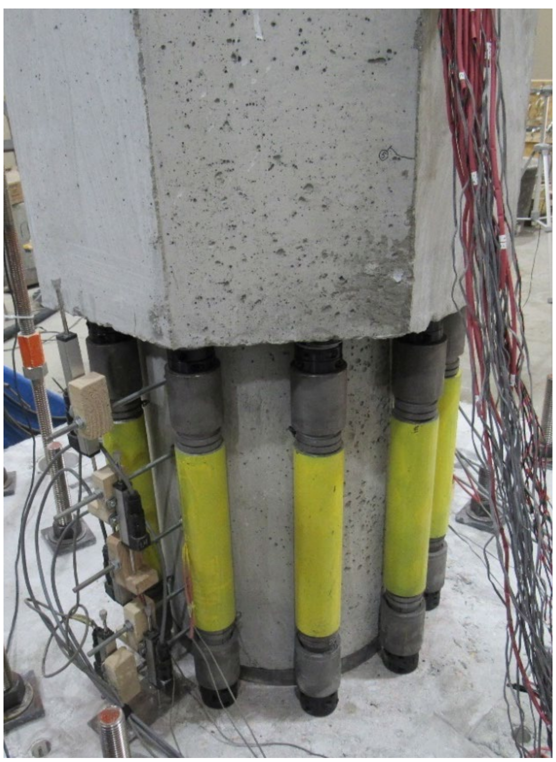

a) North-West Side

b) South-East Side

Figure 3.260 RPH Column Plastic Hinge Damage, Second Pull of 0.25% Drift Cycle

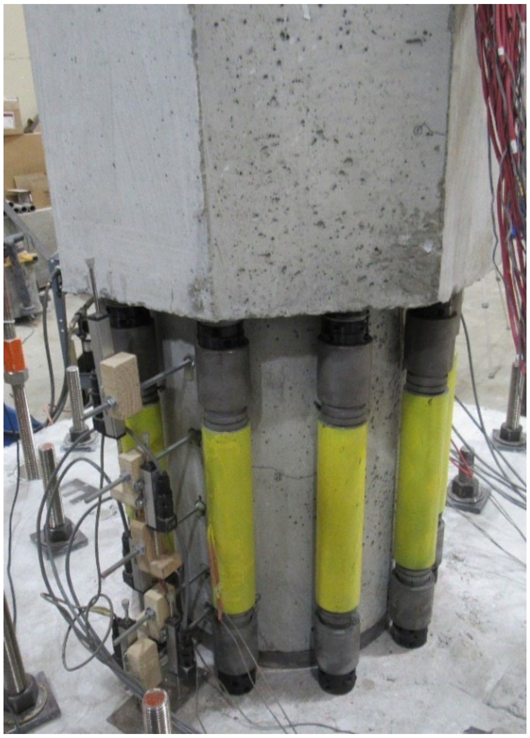

a) North-West Side

b) South-East Side

Figure 3.261 RPH Column Plastic Hinge Damage, Second Push of 0.50% Drift Cycle

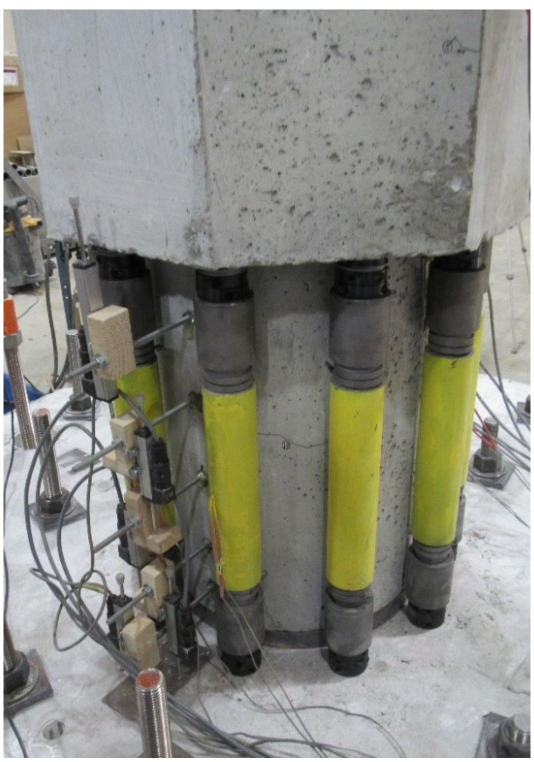

a) North-West Side

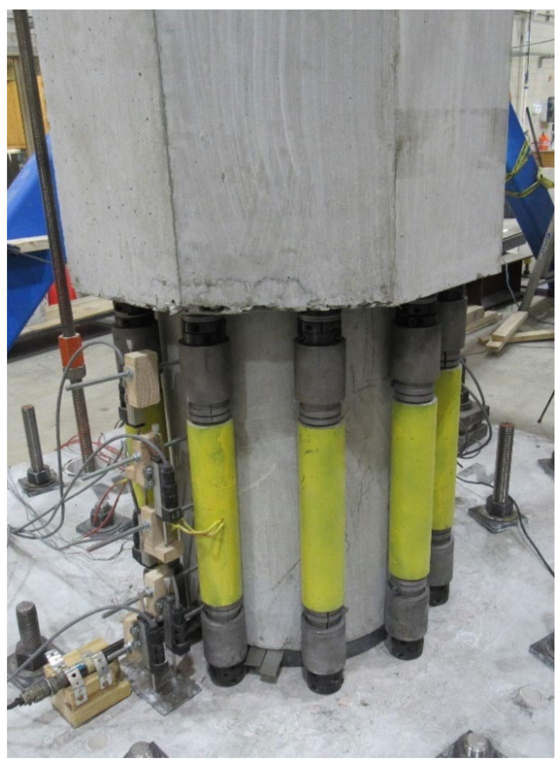

b) South-East Side

Figure 3.262 RPH Column Plastic Hinge Damage, Second Pull of 0.50% Drift Cycle

a) North-West Side b) South-East Side

Figure 3.263 RPH Column Plastic Hinge Damage, Second Push of 0.75% Drift Cycle

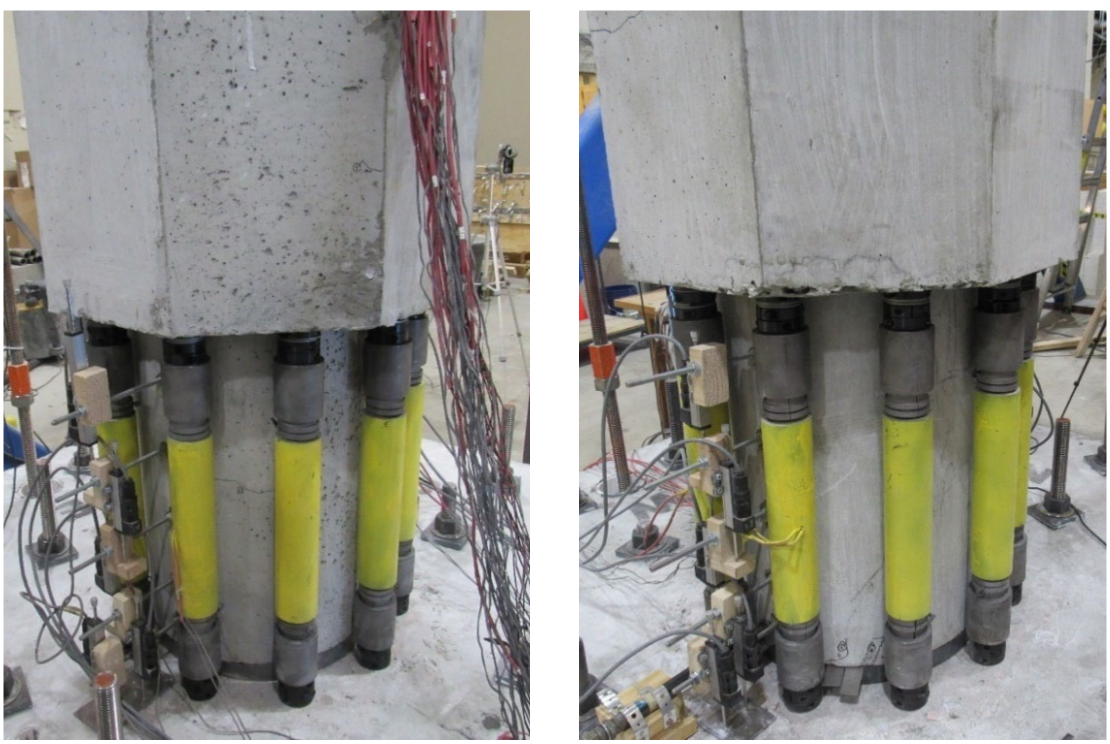

a) North-West Side b) South-East Side

Figure 3.264 RPH Column Plastic Hinge Damage, Second Pull of 0.75% Drift Cycle

a) North-West Side b) South-East Side

Figure 3.265 RPH Column Plastic Hinge Damage, Second Push of 1.00% Drift Cycle

a) North-West Side b) South-East Side

Figure 3.266 RPH Column Plastic Hinge Damage, Second Pull of 1.00% Drift Cycle

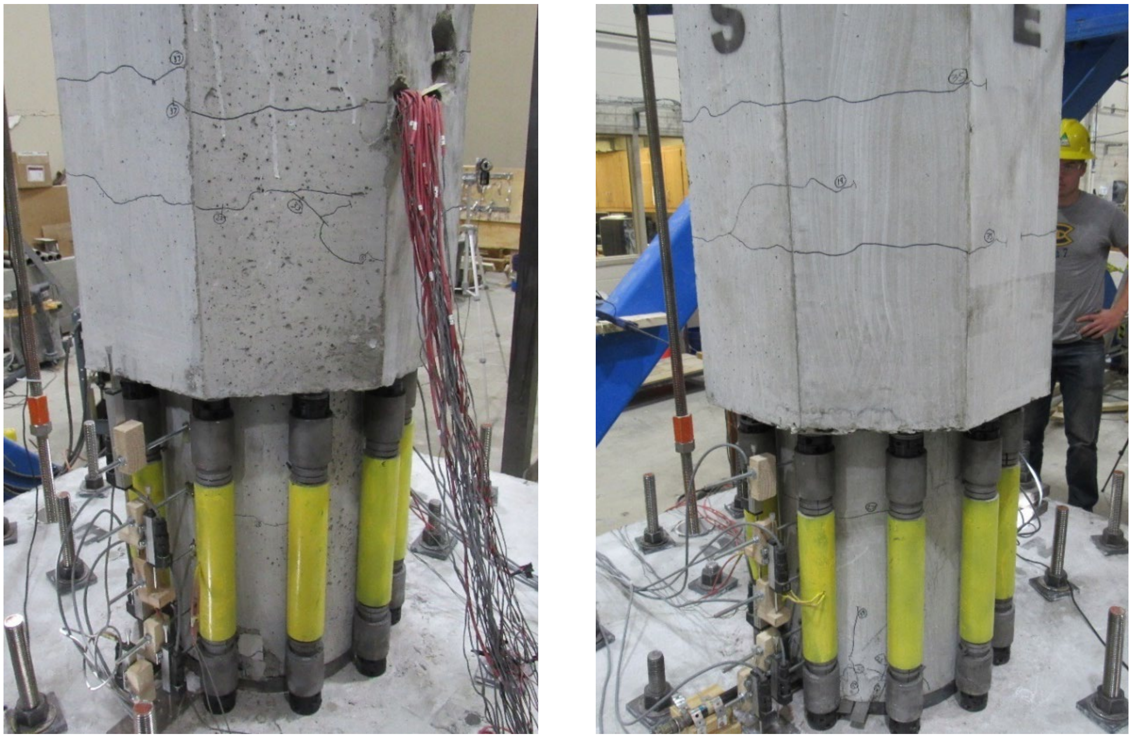

a) North-West Side b) South-East Side

Figure 3.267 RPH Column Plastic Hinge Damage, Second Push of 2.00% Drift Cycle

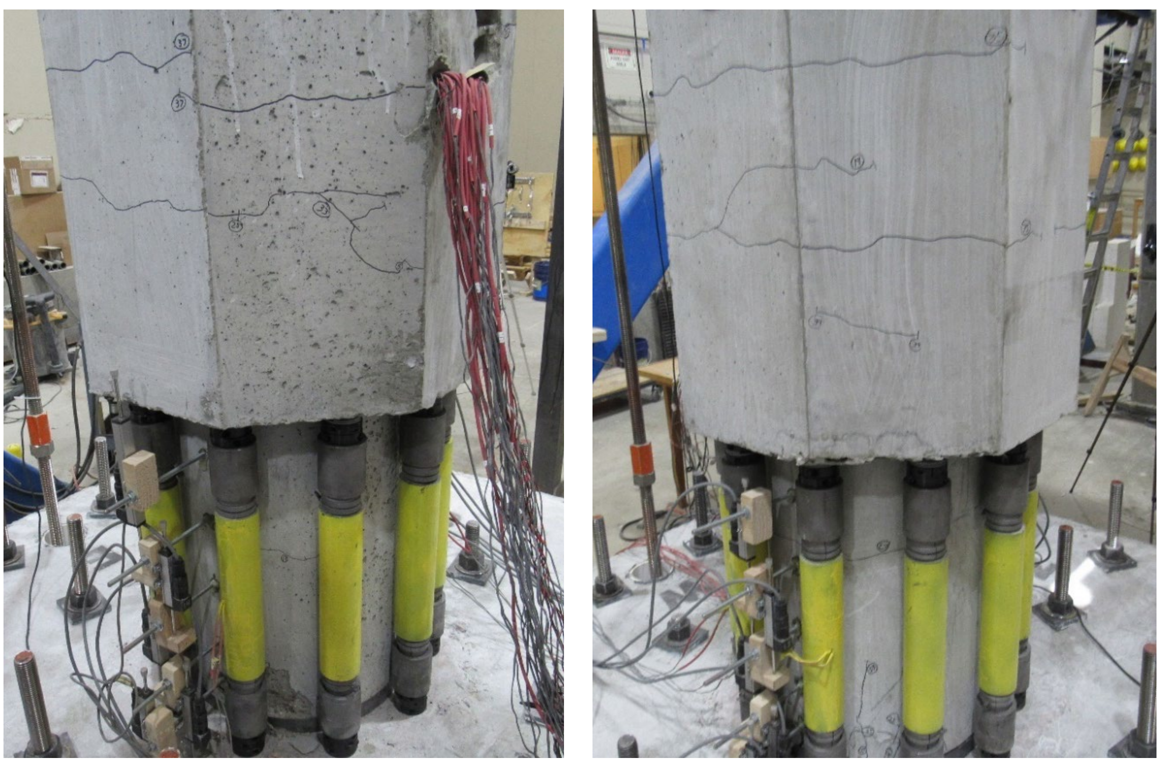

a) North-West Side b) South-East Side

Figure 3.268 RPH Column Plastic Hinge Damage, Second Pull of 2.00% Drift Cycle

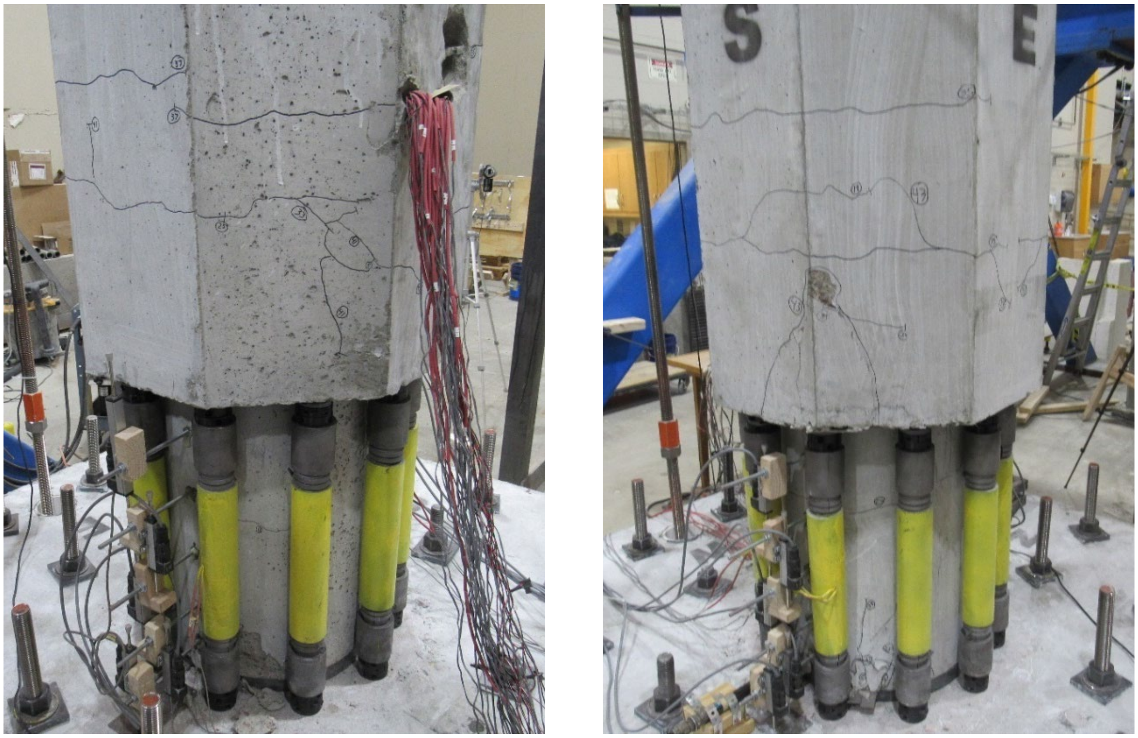

a) North-West Side b) South-East Side

Figure 3.269 RPH Column Plastic Hinge Damage, Second Push of 3.00% Drift Cycle

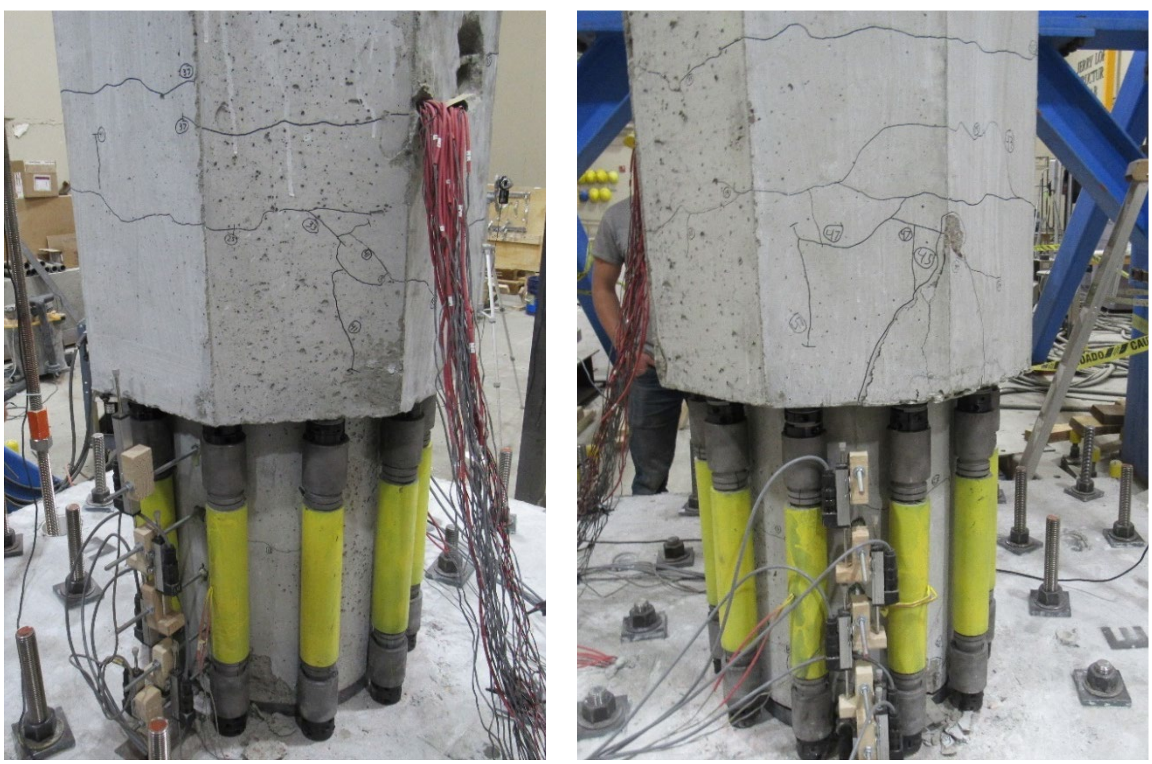

a) North-West Side b) South Side

Figure 3.270 RPH Column Plastic Hinge Damage, Second Pull of 3.00% Drift Cycle

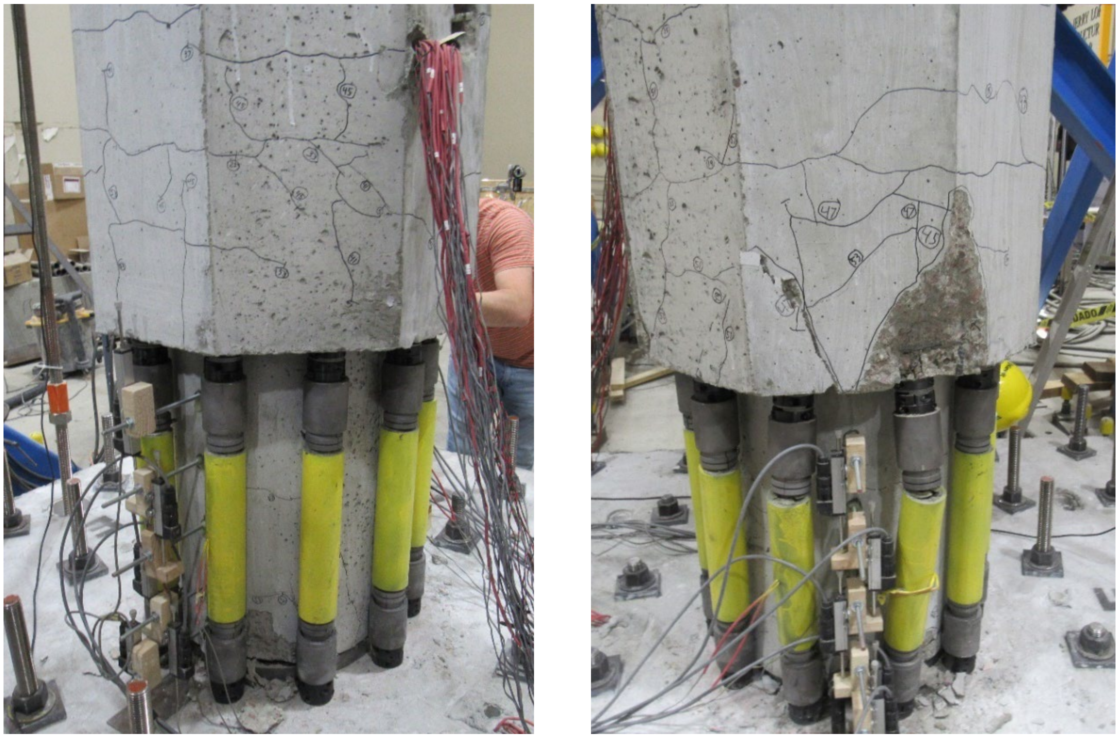

a) North-West Side b) South Side

Figure 3.271 RPH Column Plastic Hinge Damage, Second Push of 4.00% Drift Cycle

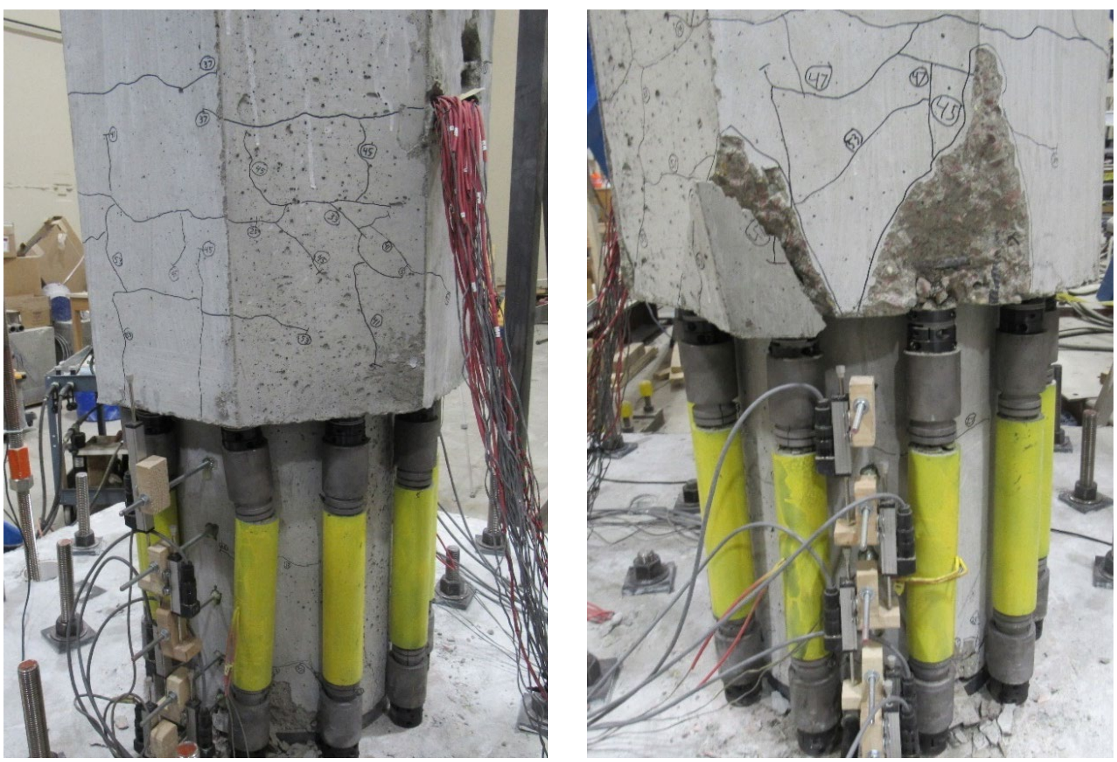

a) North-West Side b) South Side

Figure 3.272 RPH Column Plastic Hinge Damage, Second Pull of 4.00% Drift Cycle

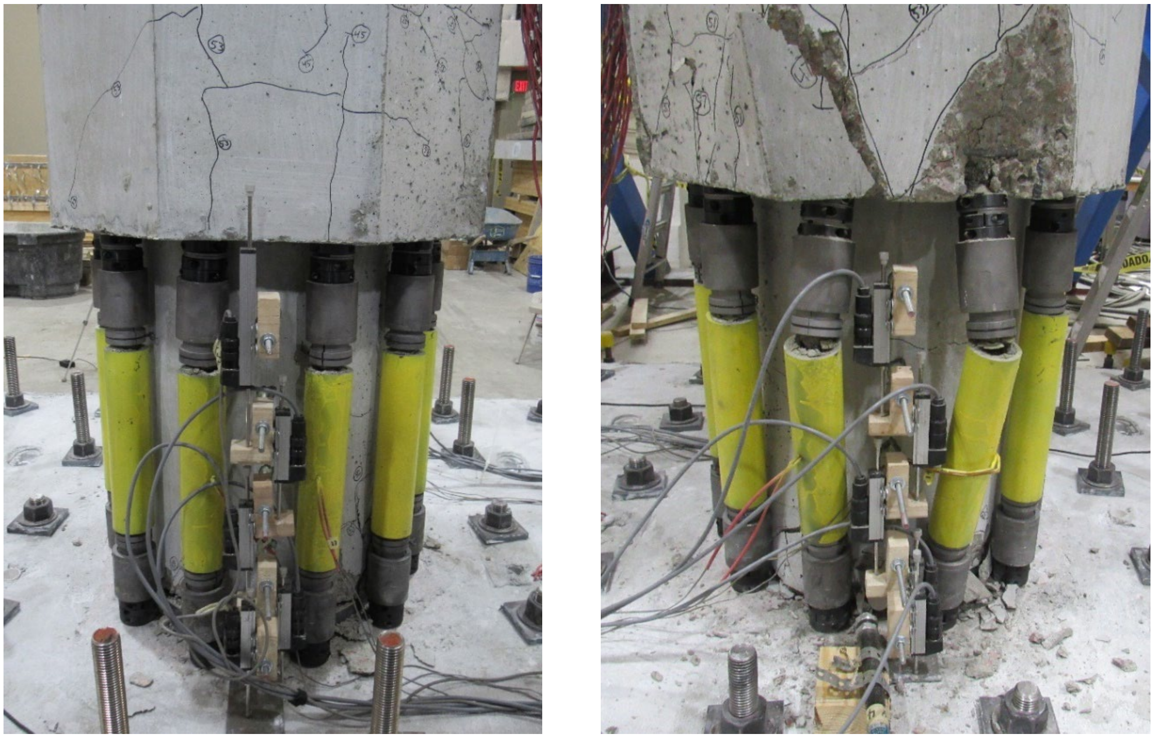

a) North Side b) South Side

Figure 3.273 RPH Column Plastic Hinge Damage, Second Push of 5.00% Drift Cycle

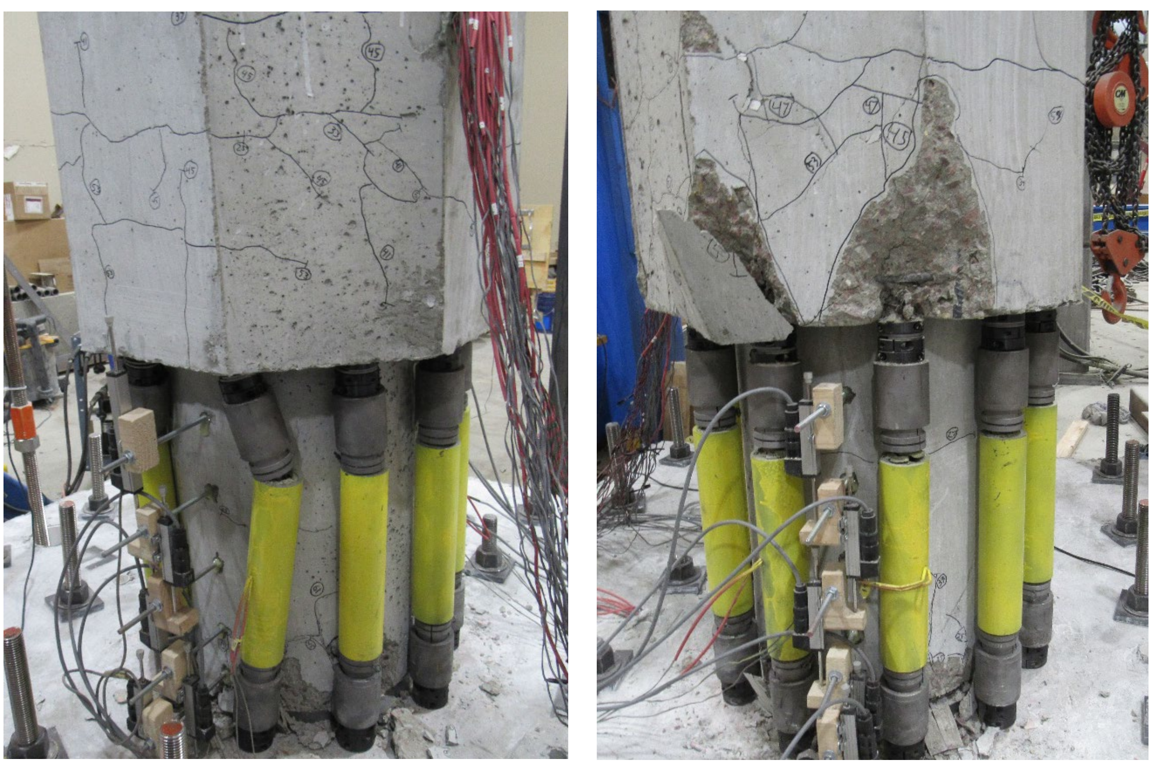

a) North-West Side b) South-East Side

Figure 3.274 RPH Column Plastic Hinge Damage, Second Pull of 5.00% Drift Cycle

3.5.9.2 Repair of RPH Column

Testing of RPH was ended after two cycles of 5% drift ratio and then the column was repaired and labeled as RPH-R. To repair the column, the clamping collars and steel washers were removed. The couplers were then unscrewed and the BRR fuses were removed. As the portion of the longitudinal bars protruding from the footing and octagonal cross section had also buckled significantly, the new fuses could not be torqued in place until the bars were straightened. This was performed by first removing the fuses on the south side of the column before using the hydraulic actuator to push the column and straighten out the bars on the north side. The process was repeated by removing the fuses on the north side and reinserting the old fuses on the south side before the actuator pulled the column to straighten out the bars on the south side. It is understood that this method is not practical in the field. A method for straightening the bars or preventing the protruded portions from buckling must be devised for future testing/applications. One option is to use steel tendons since they are tension-only members. Another option is to use recentering materials such as shape memory alloys (SMA).

After the bars were straightened, new fuses with a shorter dog-boned length of 5.128 in. (130 mm) were inserted and tightened into place using standard pipe wrenches. The clamping collars were replaced but a small gap was left between the uppermost clamping collar on each bar and the lower concrete face of the octagonal cross section to prevent the large spalling that was observed during the first set of testing on the south face of the column above the neck section (Fig. 3.274). The shims that had been placed in the gap between the bottom of the column and steel plate were not utilized in RPH-R as they had only accelerated the damage at the rocking interface of RPH. The spalled concrete was removed, and dust was vacuumed from the footing and column before testing the repaired specimen. Figure 3.275 shows the damage after cleanup and before testing RPH-R.

a) North Side

b) South Side

Figure 3.275 RPH-R Column Plastic Hinge Damage before Testing

3.5.9.3 RHP-R Observed Damage

The second set of testing of the RPH column, RPH-R, was performed by following the same testing protocol as the original test but was continued to failure. Table 3.14 presents a summary of the observed damage of RPH-R and Figures 3.276 to 3.301 show the observed damage of RPH-R. New cracks were marked in red in RPH-R for the ease of damage identification.

No additional damage was observed in RPH-R until the first cycle of 1.0% drift ratio when a small, vertical crack was spotted above the neck section on the north face (Fig. 3.382-3.383). Minor Z-shape buckling of BRR between the couplers and steel tubes became noticeable during the cycles at 2.0% drift ratio (Fig. 3.384-3.385). Bar yielding within the new BRR fuses occurred during the first cycles of 3.0% drift ratio when bar B1 yielded in the push direction and Bar B6 yielded in the pull direction (Fig. 3.386-3.387). Buckling of BRR continued to worsen, and a shallow conical failure of the grout at the ends of the BRR steel tubes was observed during the 5% drift cycles (Fig. 3.390-3.391). Spalling at the column base and above the column neck section worsened at the 6% and 7% drift cycles (Fig. 3.392-3.395). The Z-shape buckling of the BRR and spalling at the column base continued at higher drifts. RPH-R did not fail; however, the test was stopped at 10% drift ratio, at which CIP failed.

After column disassembly, no sign of damage to the pipe-pin connection (neither the pipe nor the housing socket) was observed. This indicates that the design of pipe-pin connection discussed in Section 3.3.8 was successful. Furthermore, no significant damage of the neck beside the spalling at the rocking face was observed. The neck design was overall acceptable but the damage at the rocking face should be minimized in future testing. One option is to use UHPC.

Table 3.14 Summary of Damage in RPH-R

Drift Ratio, %	Observed Damage
Beginning of Test	• Significant concrete spalling at column base on north and south faces • Significant spalling above neck region on south face
+0.25	• No further damage
-0.25	• No further damage
+0.50	• No further damage
-0.50	• No further damage
+0.75	• No further damage
-0.75	• No further damage
+1.00	• Small, inclined crack above neck section on north face
-1.00	• No further damage
+2.00	• Minor buckling of BRR between coupler and steel tube on south side • Vertical crack at column base on east face
-2.00	• Minor buckling of BRR between coupler and steel tube on north side • Vertical crack at column base on west face
+3.00	• Bar yielding in BRR fuses on north side • Vertical cracking on north face
-3.00	• Bar yielding in BRR fuses on south side
+4.00	• Buckling of BRR on south side worsens
-4.00	• Buckling of BRR on north side worsens
+5.00	• Grout crushing inside BRR tubes on south side
-5.00	• Grout crushing inside BRR tubes on north side
+6.00	• Further spalling above neck region on south face
-6.00	• No further damage
+7.00	• Further spalling above neck region and at column base on south face
-7.00	• Spalling above neck region on north face
+8.00	• Further buckling of BRR on south side
-8.00	• Further buckling of BRR on north side
+9.00	• Extreme buckling of BRR and spalling at column base on south side • Initiation of strength reduction in push direction
-9.00	• Extreme buckling of BRR and spalling at column base on north side
+10.00	• No further damage
-10.00	• No further damage

Note: Positive drifts were based on displacements away from the reaction blocks (north to south)

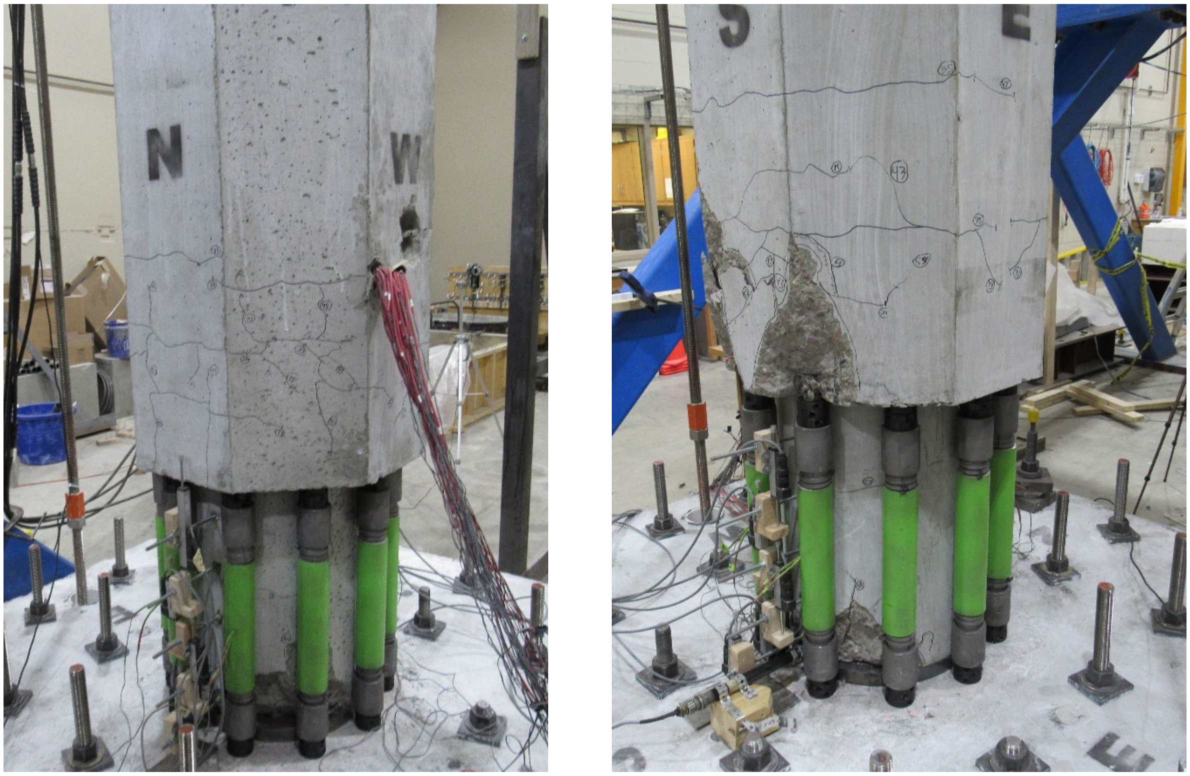

a) North-West Side b) South-East Side

Figure 3.276 RPH-R Column Plastic Hinge Damage, Second Push of 0.25% Drift Cycle

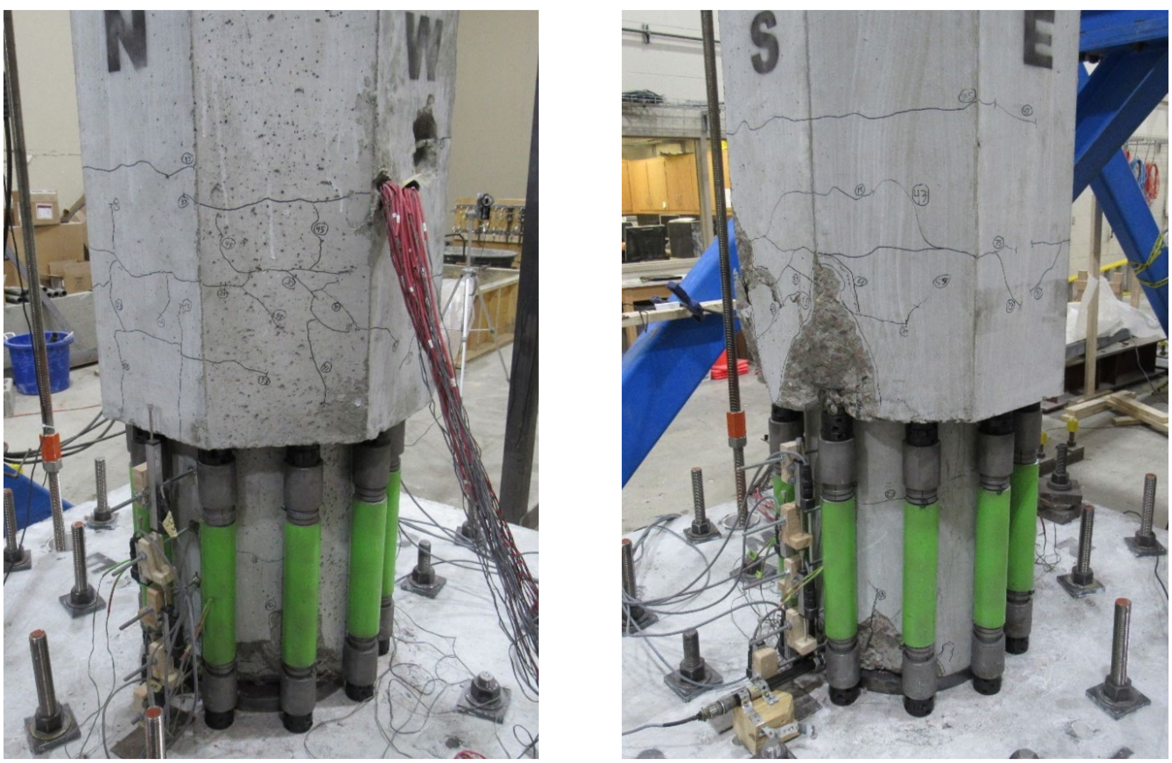

a) North-West Side b) South-East Side

Figure 3.277 RPH-R Column Plastic Hinge Damage, Second Pull of 0.25% Drift Cycle

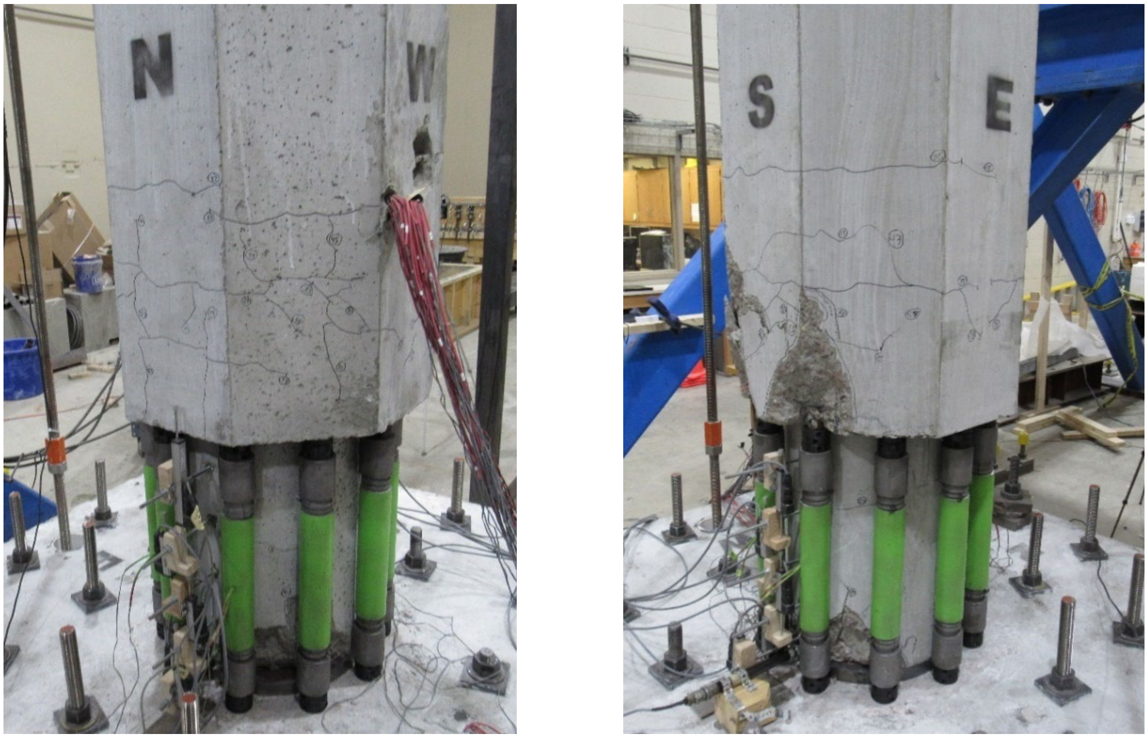

a) North-West Side b) South-East Side

Figure 3.278 RPH-R Column Plastic Hinge Damage, Second Push of 0.50% Drift Cycle

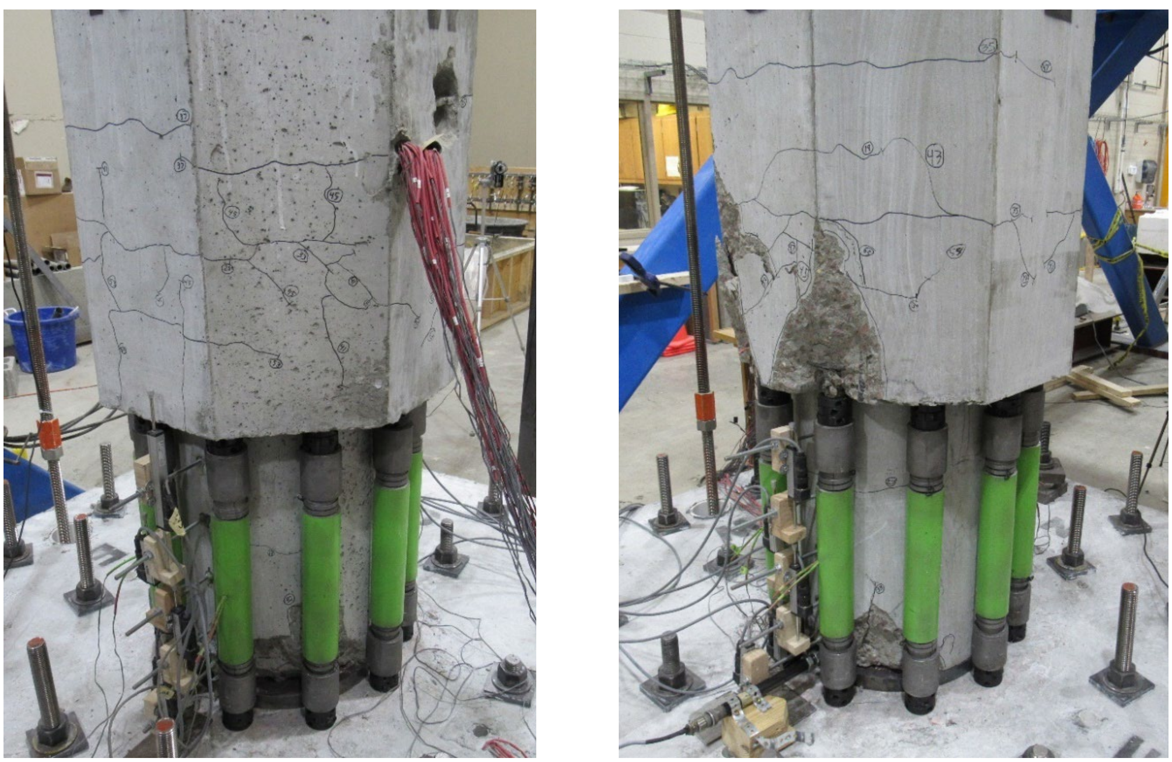

a) North-West Side b) South-East Side

Figure 3.279 RPH-R Column Plastic Hinge Damage, Second Pull of 0.50% Drift Cycle

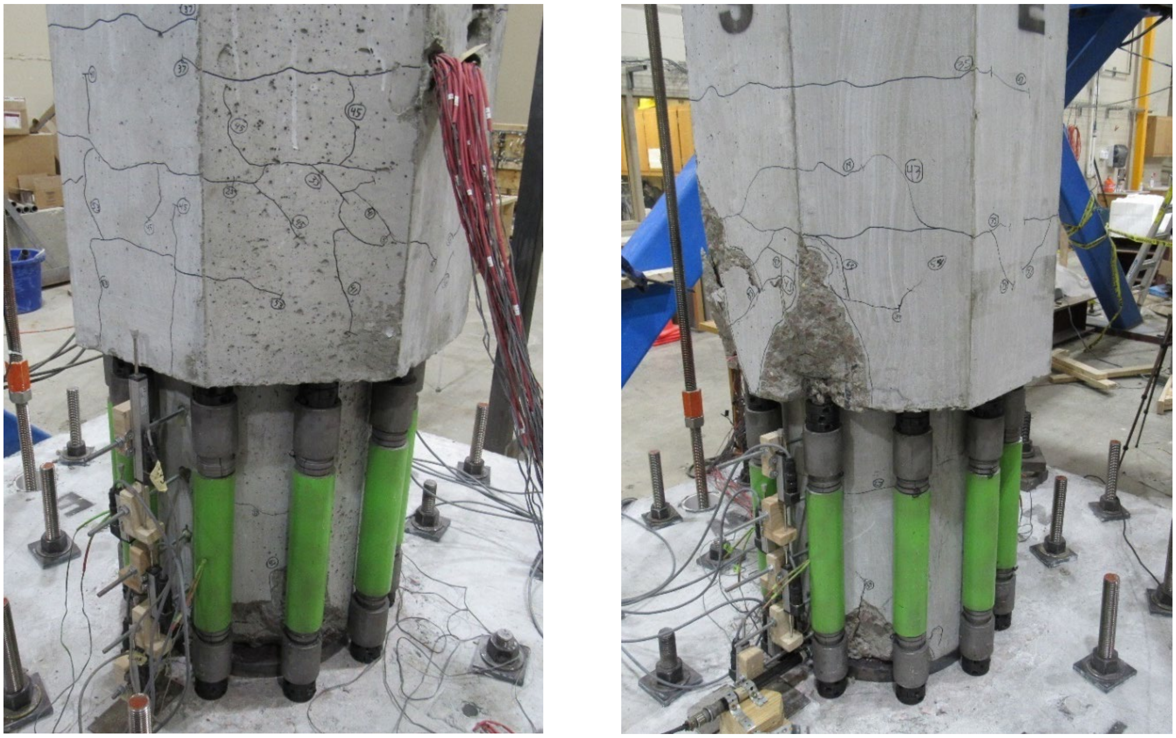

a) North-West Side b) South-East Side

Figure 3.280 RPH-R Column Plastic Hinge Damage, Second Push of 0.75% Drift Cycle

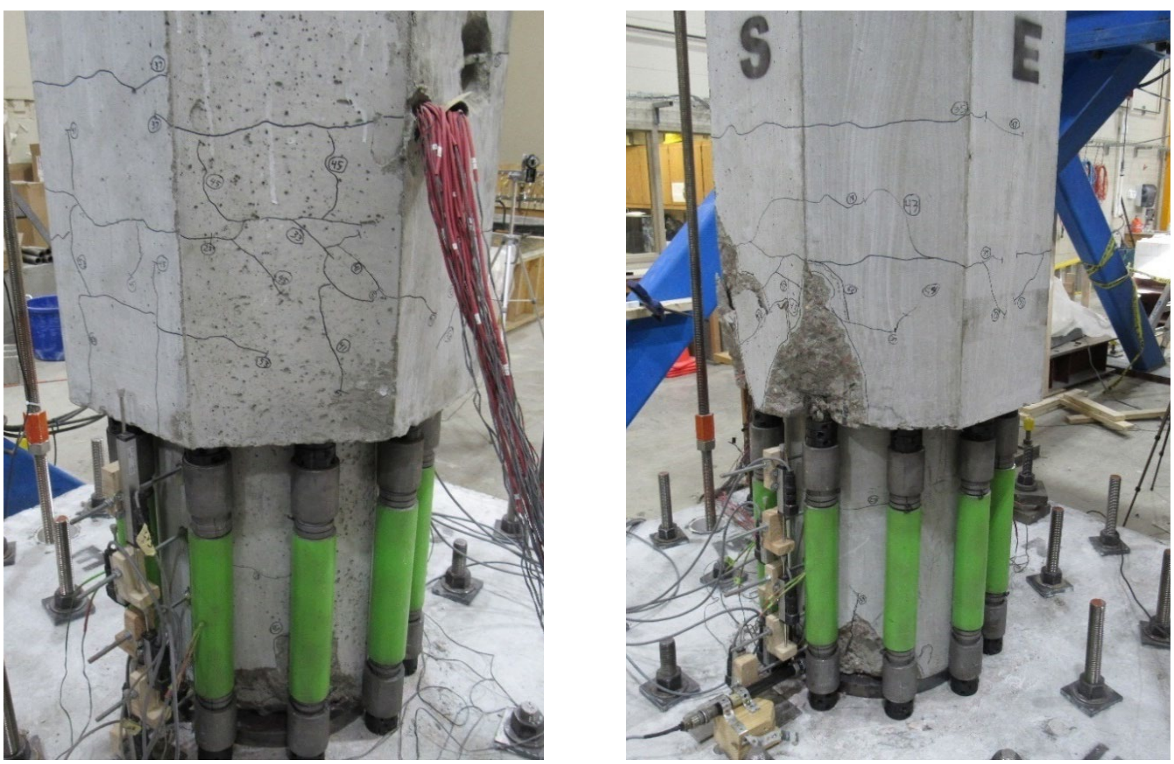

a) North-West Side b) South-East Side

Figure 3.281 RPH-R Column Plastic Hinge Damage, Second Pull of 0.75% Drift Cycle

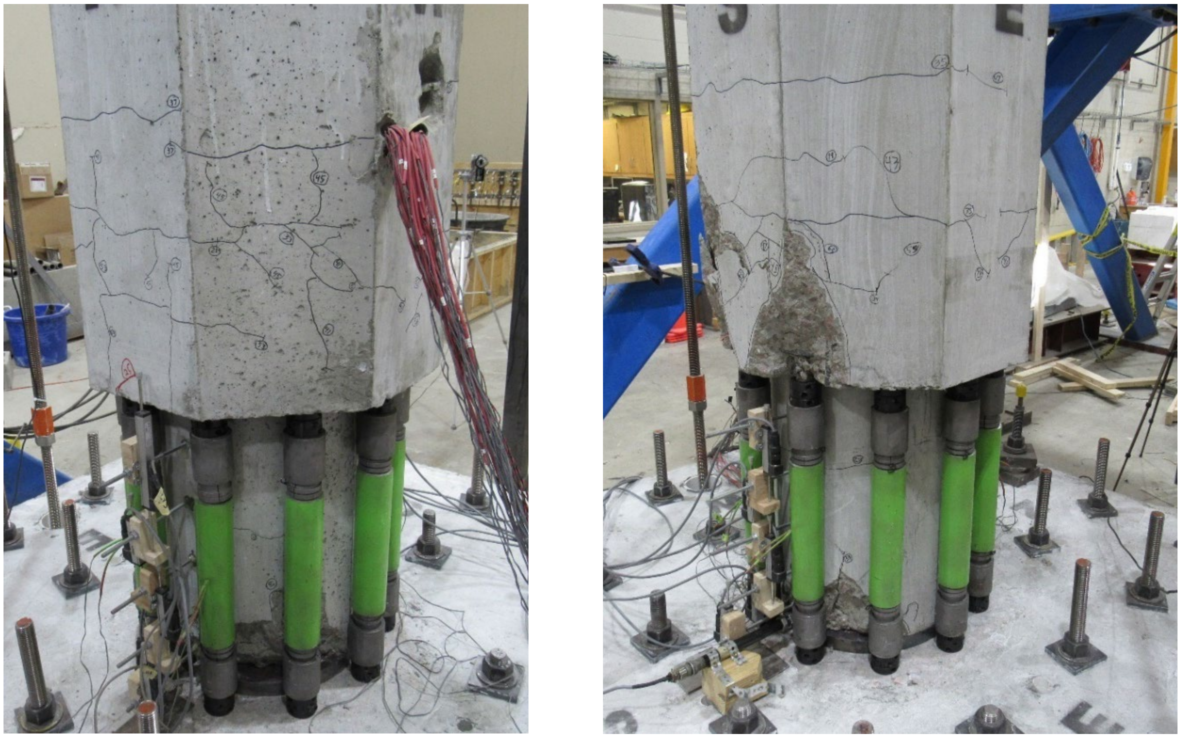

a) North-West Side b) South-East Side

Figure 3.282 RPH-R Column Plastic Hinge Damage, Second Push of 1.00% Drift Cycle

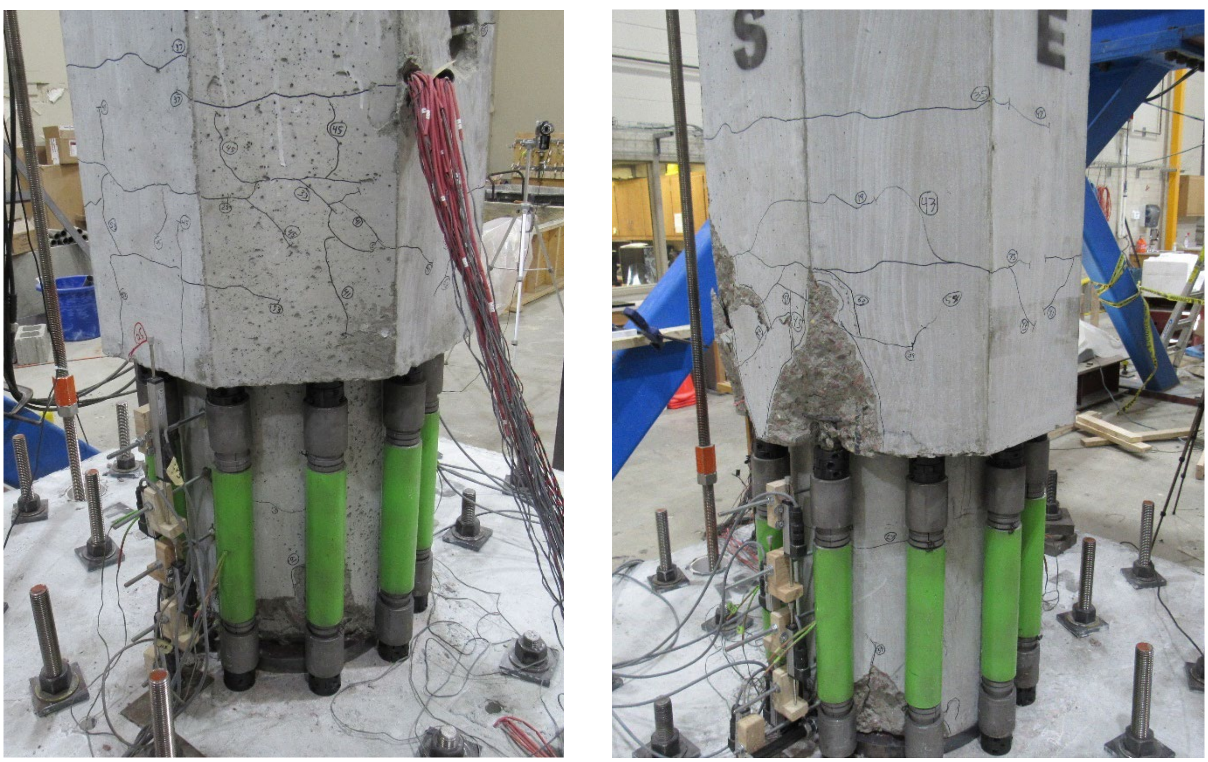

a) North-West Side b) South-East Side

Figure 3.283 RPH-R Column Plastic Hinge Damage, Second Pull of 1.00% Drift Cycle

a) North-West Side b) South-East Side

Figure 3.284 RPH-R Column Plastic Hinge Damage, Second Push of 2.00% Drift Cycle

a) North-West Side b) South-East Side

Figure 3.285 RPH-R Column Plastic Hinge Damage, Second Pull of 2.00% Drift Cycle

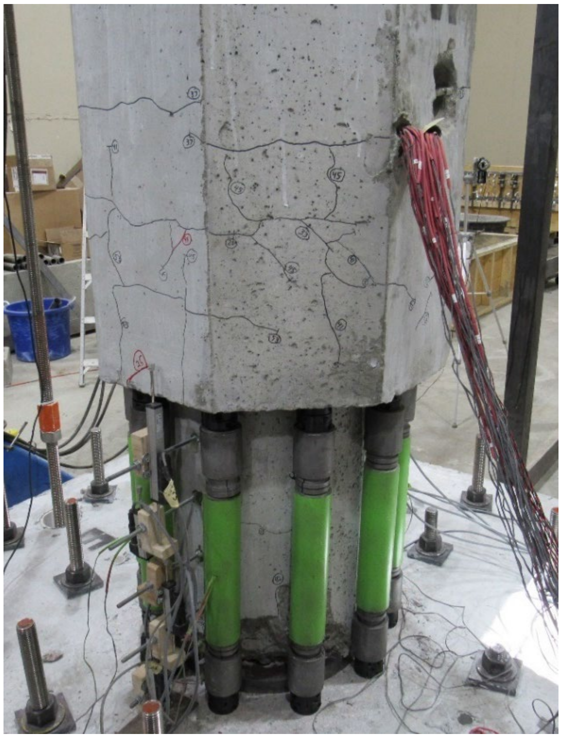
a) North-West Side


b) South-East Side

Figure 3.286 RPH-R Column Plastic Hinge Damage, Second Push of 3.00% Drift Cycle

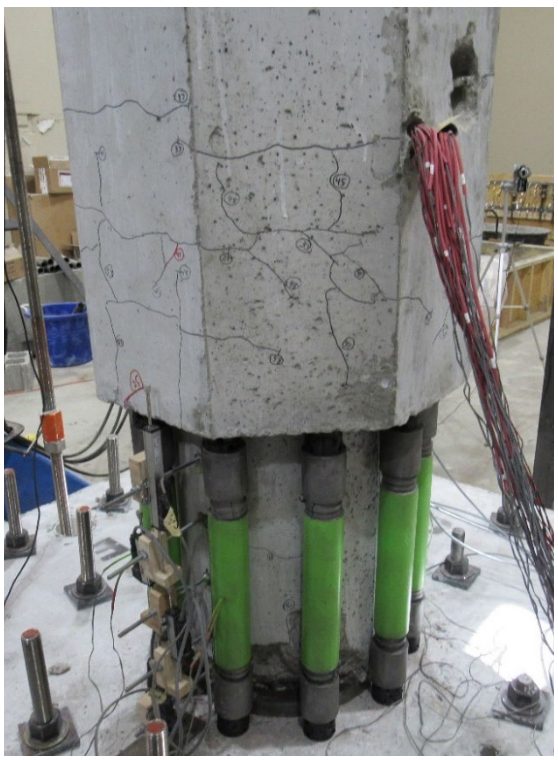
a) North-West Side

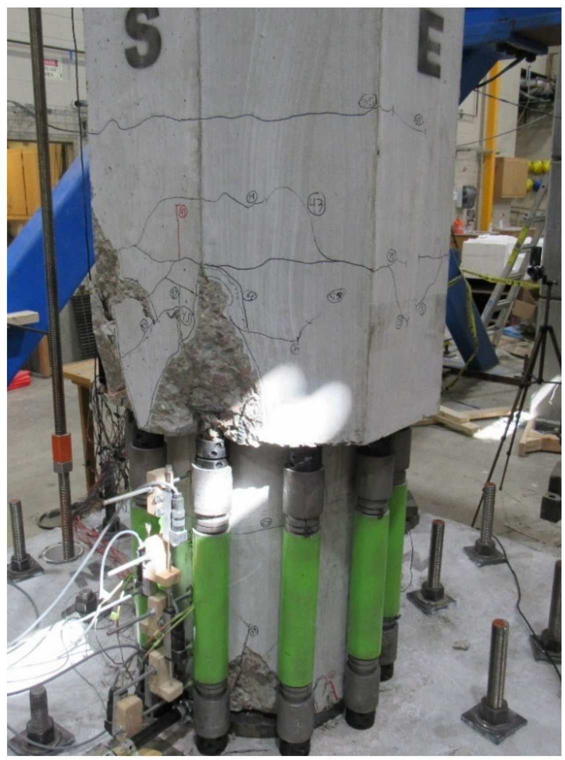
b) South-East Side

Figure 3.287 RPH-R Column Plastic Hinge Damage, Second Pull of 3.00% Drift Cycle

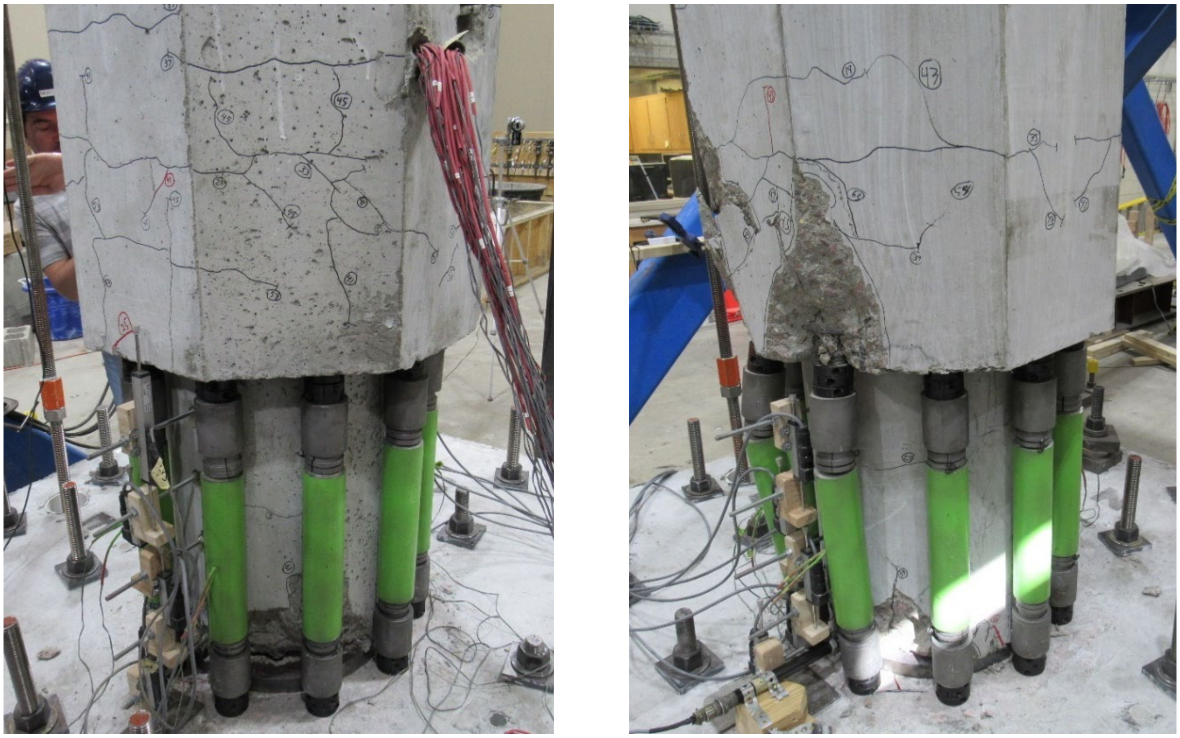

a) North-West Side b) South-East Side

Figure 3.288 RPH-R Column Plastic Hinge Damage, Second Push of 4.00% Drift Cycle

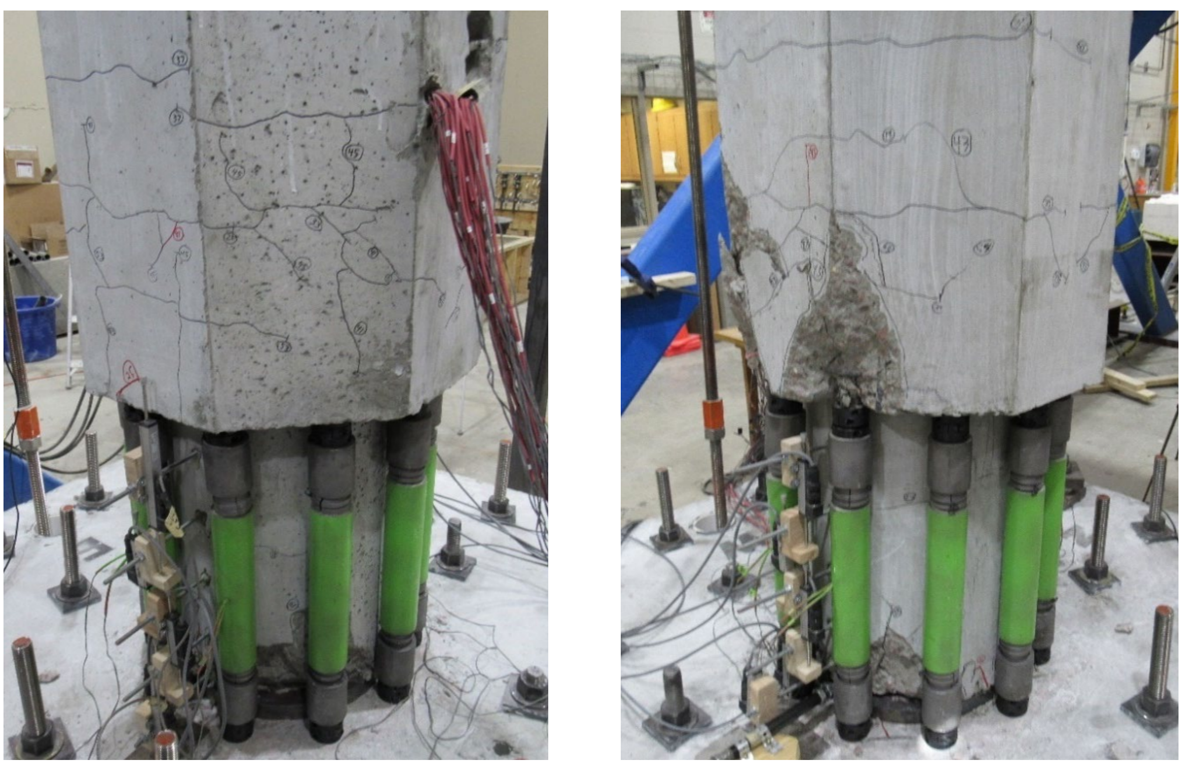

a) North-West Side b) South-East Side

Figure 3.289 RPH-R Column Plastic Hinge Damage, Second Pull of 4.00% Drift Cycle

a) North-West Side b) South-East Side

Figure 3.290 RPH-R Column Plastic Hinge Damage, Second Push of 5.00% Drift Cycle

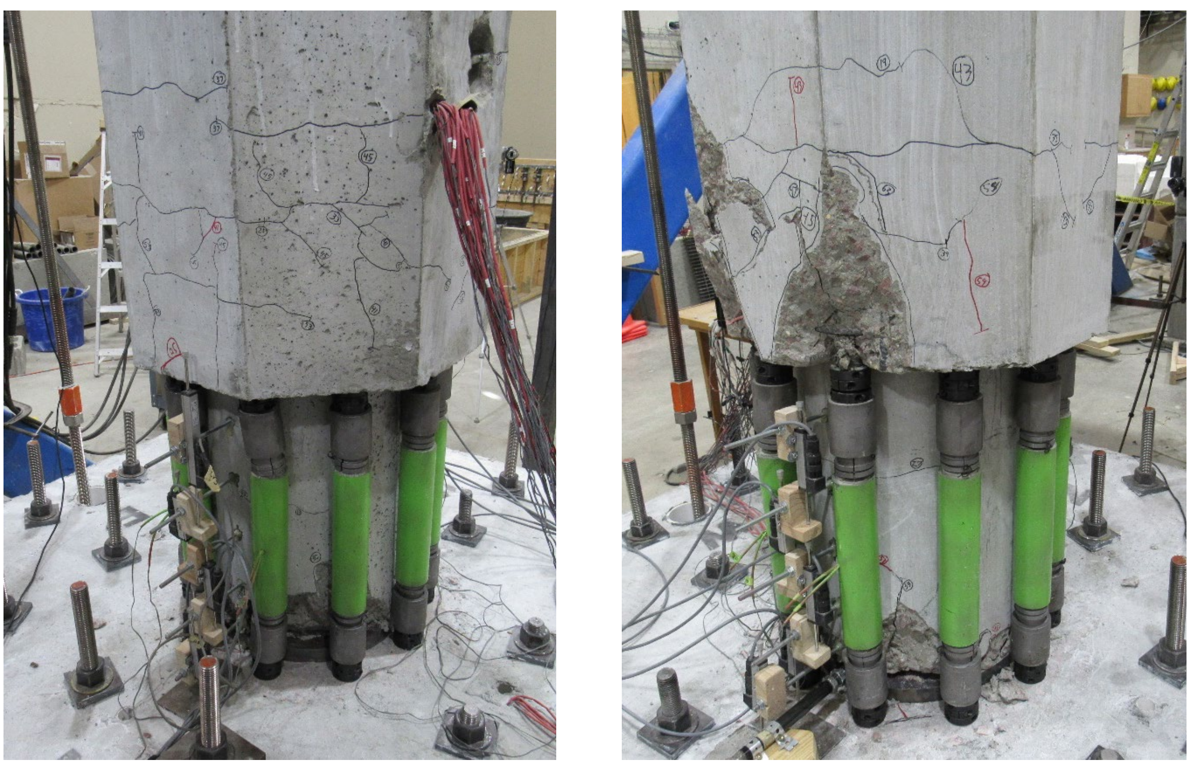

a) North-West Side b) South-East Side

Figure 3.291 RPH-R Column Plastic Hinge Damage, Second Pull of 5.00% Drift Cycle

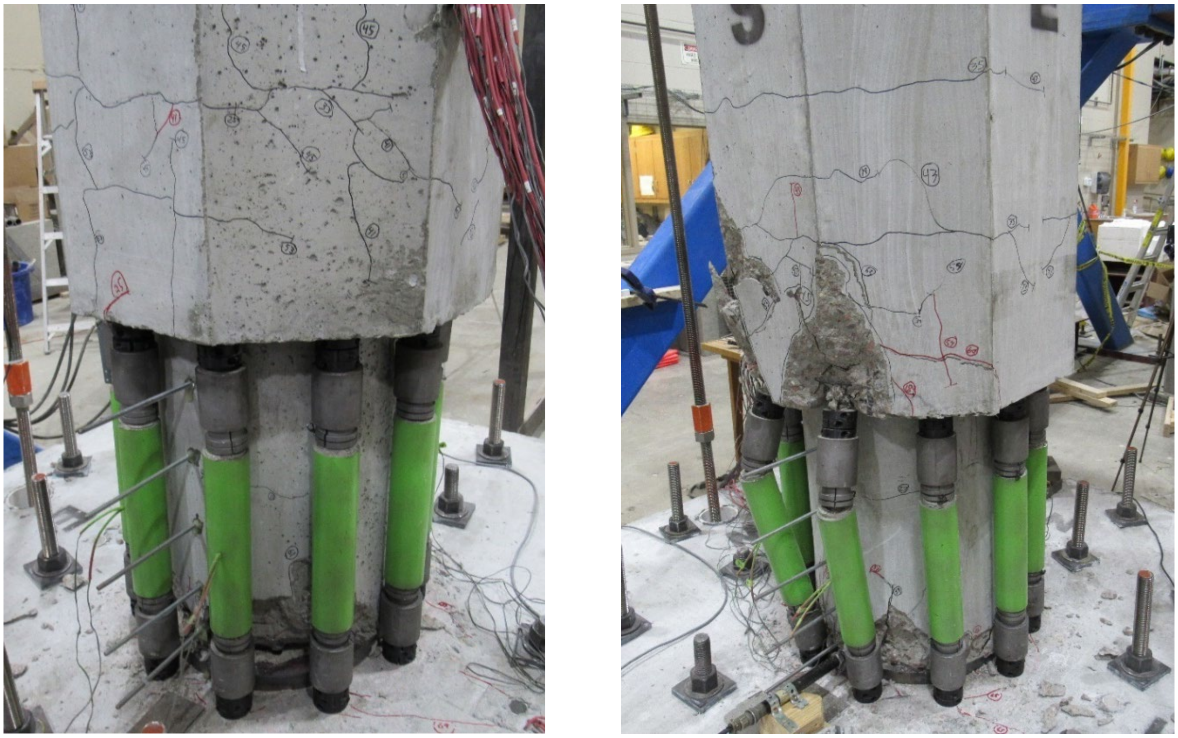

a) North-West Side b) South-East Side

Figure 3.292 RPH-R Column Plastic Hinge Damage, Second Push of 6.00% Drift Cycle

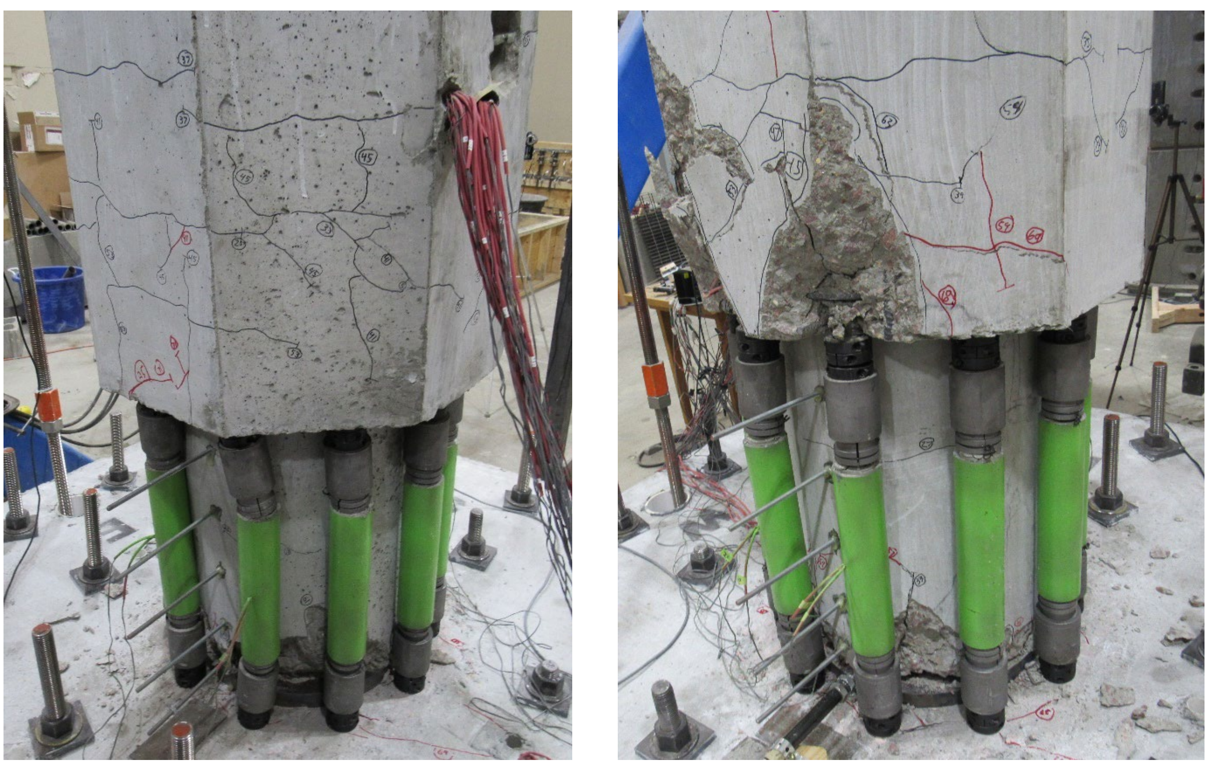

a) North-West Side b) South-East Side

Figure 3.293 RPH-R Column Plastic Hinge Damage, Second Pull of 6.00% Drift Cycle

a) North-West Side b) South-East Side

Figure 3.294 RPH-R Column Plastic Hinge Damage, Second Push of 7.00% Drift Cycle

a) North-West Side b) South-East Side

Figure 3.295 RPH-R Column Plastic Hinge Damage, Second Pull of 7.00% Drift Cycle

a) North-West Side b) South-East Side

Figure 3.296 RPH-R Column Plastic Hinge Damage, Second Push of 8.00% Drift Cycle

a) North-West Side b) South-East Side

Figure 3.297 RPH-R Column Plastic Hinge Damage, Second Pull of 8.00% Drift Cycle

a) North-West Side b) South-East Side

Figure 3.298 RPH-R Column Plastic Hinge Damage, Second Push of 9.00% Drift Cycle

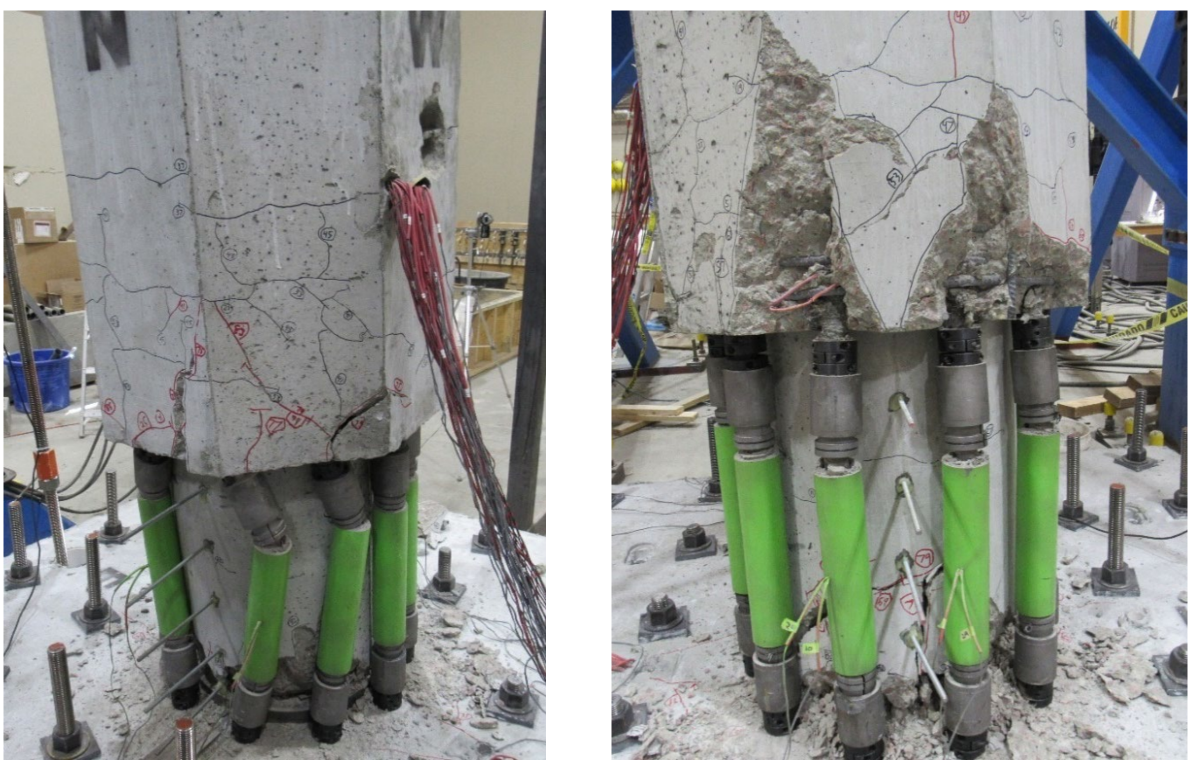

a) North-West Side b) South Side

Figure 3.299 RPH-R Column Plastic Hinge Damage, Second Pull of 9.00% Drift Cycle

a) North-West Side b) South-East Side

Figure 3.300 RPH-R Column Plastic Hinge Damage, Second Push of 10.00% Drift Cycle

a) North-West Side b) South-East Side

Figure 3.301 RPH-R Column Plastic Hinge Damage, Second Pull of 10.00% Drift Cycle

3.5.9.4 RPH Force-Displacement Relationship

Figure 3.302 shows the measured force-drift hysteretic and envelope responses of RPH. Note that this test was stopped at 5% drift ratio to replace the BRR fuses. The maximum lateral load of 69.2 kips (308 kN) occurred in the pull direction when the test was stopped at 5% drift. The column had a slightly higher stiffness and lateral load in the pull direction. The longitudinal bars yielded within the BRR fuses in the push direction at a drift ratio of 1.60% and a corresponding lateral load of 40.1 kips (178.44 kN), and in the pull direction at a drift ratio of 1.35% and a lateral load of 46.6 kips (207.3 kN).

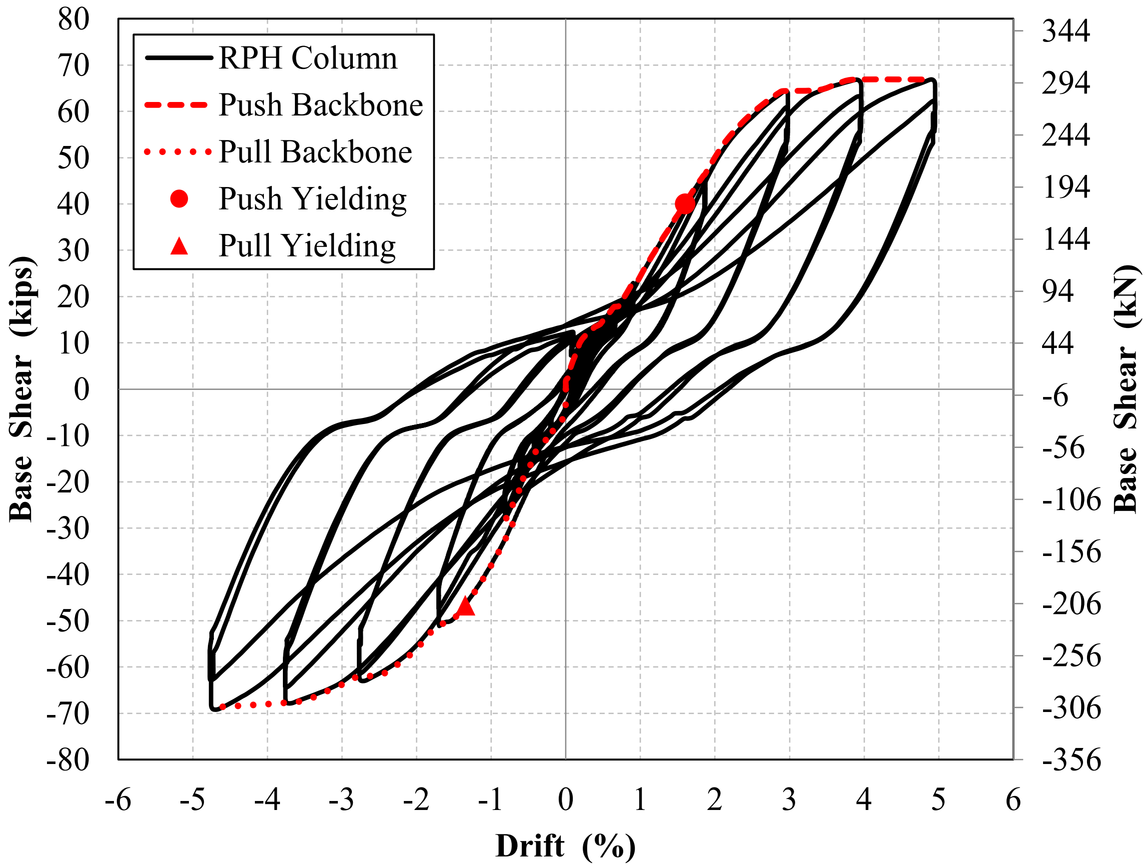

Figure 3.302 Measured RPH Column Force-Drift Hysteretic and Envelope Responses

Figure 3.303 shows the average envelope of the push and pull directions for RPH. The average yield drift ratio was 1.47%, corresponding to a lateral force of 43.0 kips (191.3 kN). No sign of failure was observed at 5% drift where the test was stopped for the repair, thus no idealization of the response was carried out for RPH.

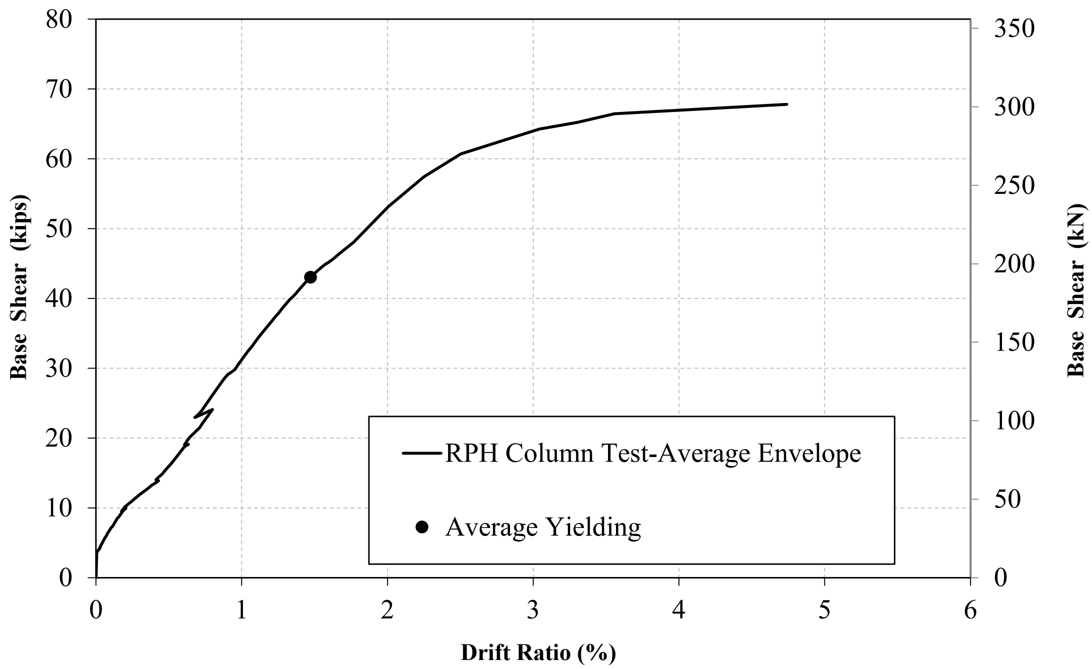

Figure 3.303 Measured RPH Column Average Push/Pull Force-Drift Envelope

3.5.9.5 RPH-R Force-Displacement Relationship

Figure 3.304 shows the measured lateral force-drift hysteretic and envelope responses from the repaired RPH, or RHP-R, up to 10% drift ratio. Even though a strength degradation can be seen after 8% drift ratio in the push direction, the force drop did not meed the 15% criterion as the column failure. Nevertheless, the test was stopped at 10% drift ratio to avoid any setup damage. Furthermore, the CIP column failed at 10% drift ratio, thus it was not necessary to exceed this drift limit.

The maximum lateral load of 74.7 kips (332.3 kN) occurred in the pull direction at a drift ratio of 8.31%. The column was softer in the push direction mainly due to the spalling above the neck region on the south face of the column. The longitudinal bars within the BRR fuses yielded in the push direction at a drift ratio and load of 3.06% and 43.8 kips (195.8 kN), respectively, and in the pull direction during the first 3% drift cycle but at a drift ratio of 2.0% and a lateral load of 44.0 kips (195.7 kN).

Figure 3.305 includes the average envelope of the push and pull directions for the RPH-R column. The average yield drift ratio was 2.53% at a lateral load of 43.7 kips (194.3 kN). The idealized curve is also included in the figure. The effective yield was at 4.0% drift ratio with a lateral load of 69.3 kips (308.3 kN). The drift capacity of the column was 9.80% (where the test was stopped). The resulting displacement ductility capacity is 2.45 for the RPH-R column. It should be noted that for novel columns, the displacement ductility is not a good indicator for the displacement capacity since the yield displacement is not a typical value. Drift ratio is a better alternative. It is evident that RPH-R column exhibited a higher drift ratio capacity compared with the CIP column (9.80% vs 8.96%).

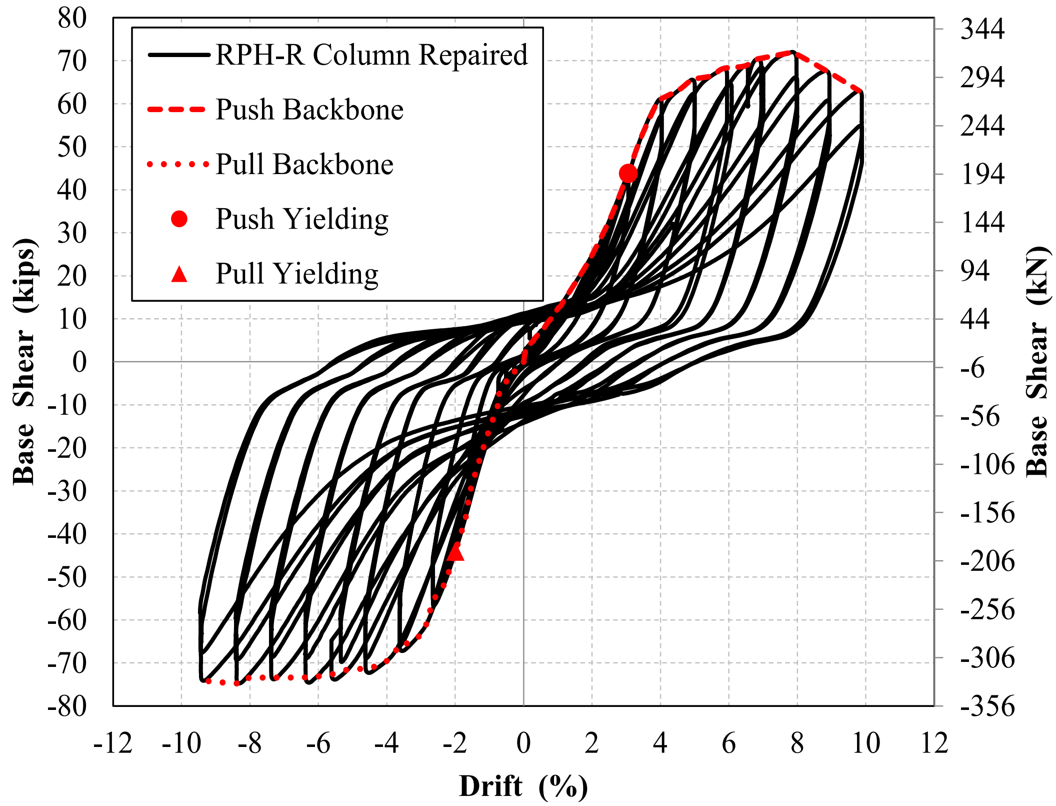

Figure 3.304 Measured RPH-R Column Force-Drift Hysteretic and Envelope Responses

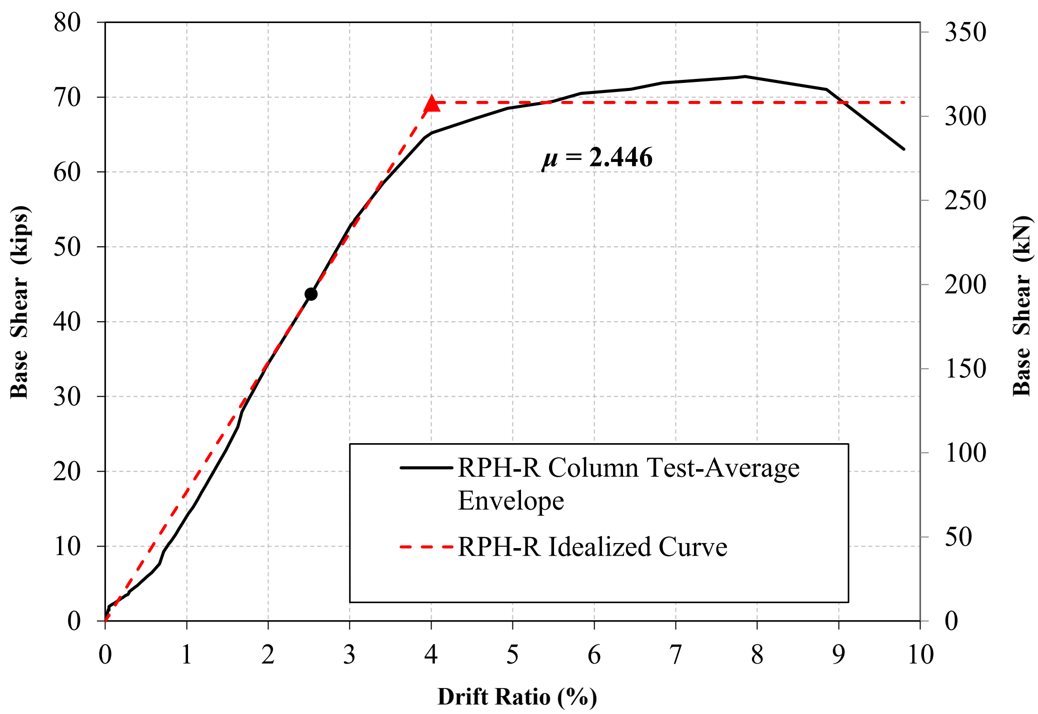

Figure 3.305 Measured RPH-R Column Average Push/Pull Force-Drift Envelope and Idealized Curve

Figure 3.306 compares the average backbones of RPH, RPH-R, and CIP. The initial stiffness of both RPH and RPH-R were significantly lower than CIP since the repairable columns had a smaller neck section and a modular bar connection. The initial stiffness of RPH-R was the lowest. The “dog-boned” length of BRR in RPH was 10.25 in. (260 mm) while the length was shortened to 5.125 in. (130 mm) in RPH-R. This would be expected to result in a higher stiffness for the repaired column; however, the initial stiffness of RPH-R decreased between the first and second testing mainly due to the concrete spalling at the column base and above the neck region. The best performance for a repairable column is that the stiffness of the column should remain the same before and after the repair. To achieve this performance in future testing, the concrete damage should be minimized. Some options are to use UHPC and tension-only fuses to avoid concrete and rebar damages.

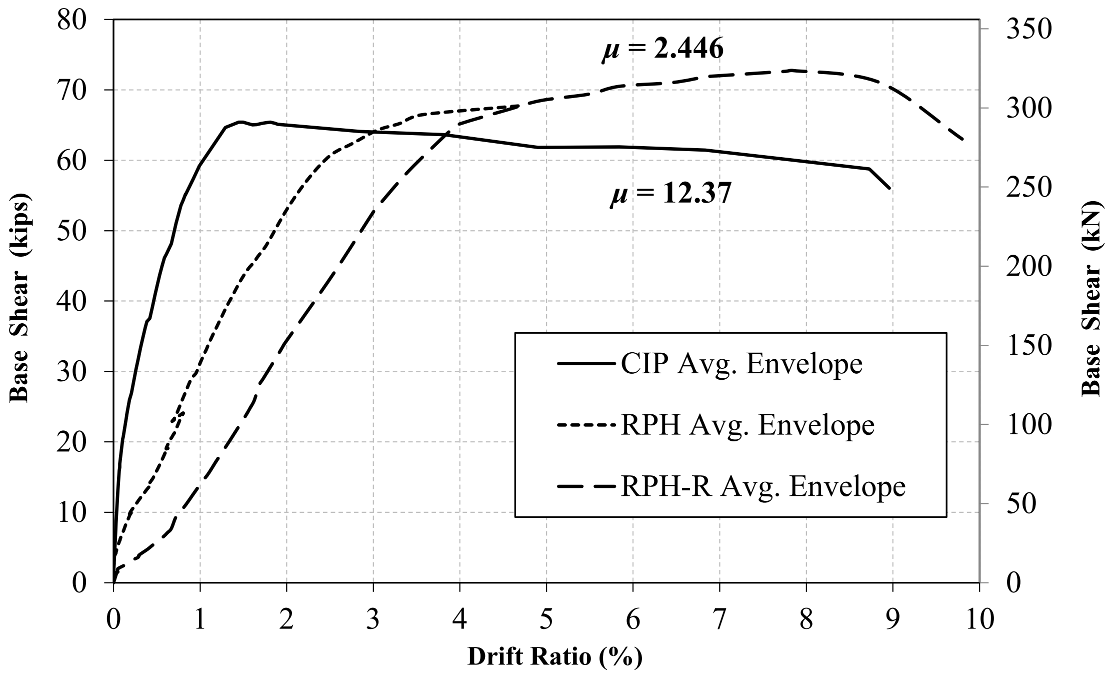

Figure 3.306 Comparison of Measured Average Force-Drift Envelopes for CIP, RPH, and RPH-R

3.5.9.6 RPH Strain Profiles

Thirty-six steel strain gauges were installed on RPH at four levels along the column. Three of these levels included strain gauges on the longitudinal bars within the neck section. Figures 3.307 to 3.310 show the measured strain profiles for Bars B1, B2, B6, and B7. The middle two levels of strain gauges were placed along the dog-boned region of the stainless-steel bars within BRR.

The strain profiles of the four bars were relatively uniform up to the yielding of the BRR bars, after which the profiles show higher strains at the middle of BRR. The longitudinal bars outside BRR (column and footing dowels) yielded later or not at all due to the higher cross-sectional area outside of the dog-boned region (dowels were No. 10 (Ø32 mm) while dog-boned fuses where machined down to No. 8 or Ø25 mm). Strains of the transverse reinforcement were also monitored. The yield strain for the hoops in RPH was 0.23% while the maximum measured strain was 0.04% recorded at a hoop in the center of the neck section. Furthermore, the strain data shows that the steel bars used to reinforce the neck in the longitudinal direction remained linear elastic during the entire test, indicating a successful design for the neck itself.

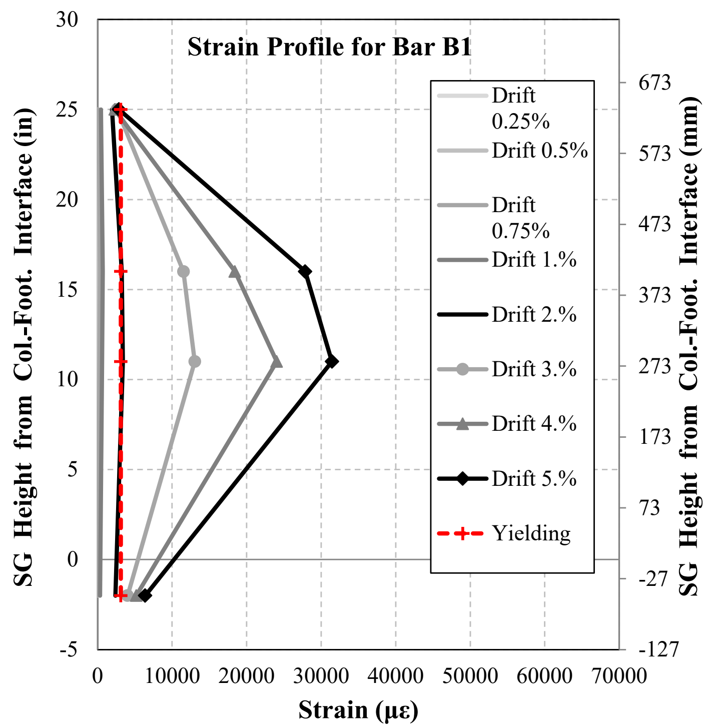

Figure 3.307 Measured Strain Profile for RPH Column Bar B1

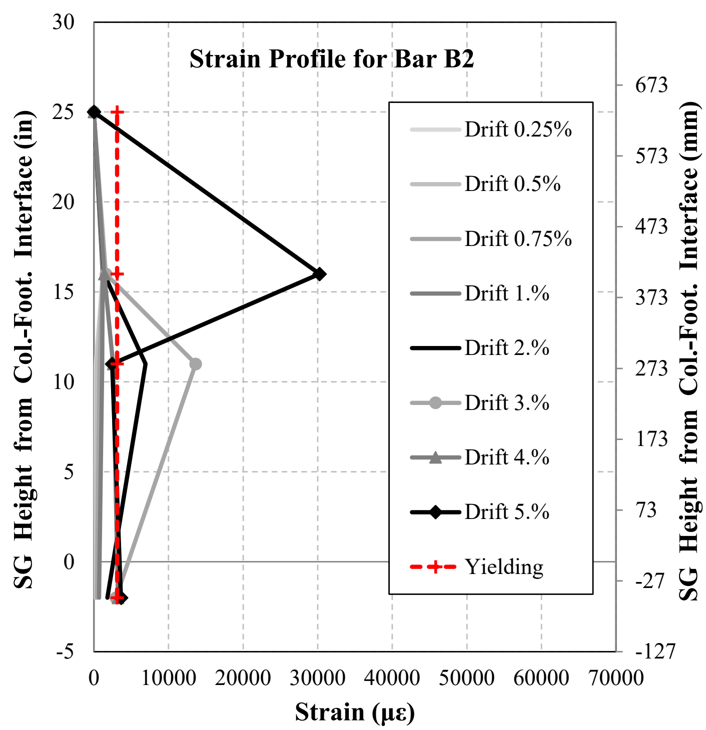

Figure 3.308 Measured Strain Profile for RPH Column Bar B2

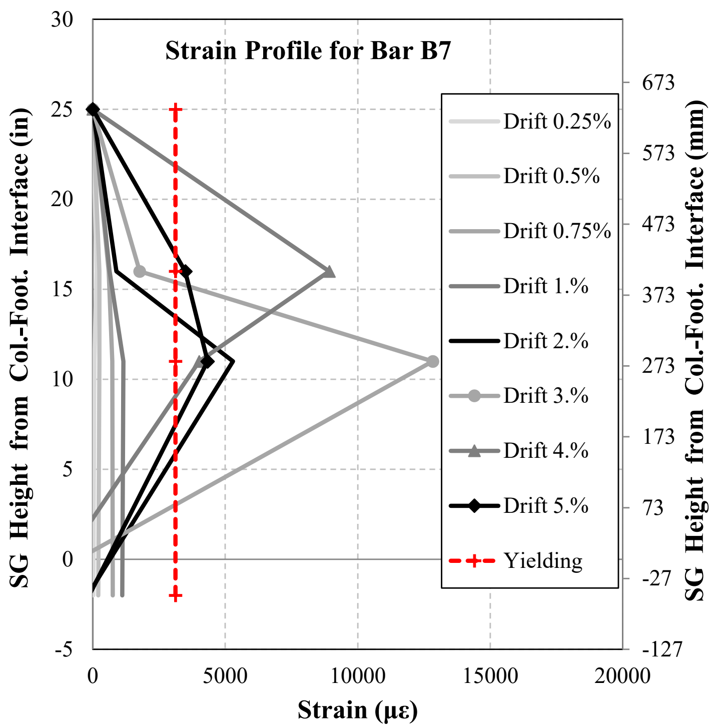

Figure 3.309 Measured Strain Profile for RPH Column Bar B6

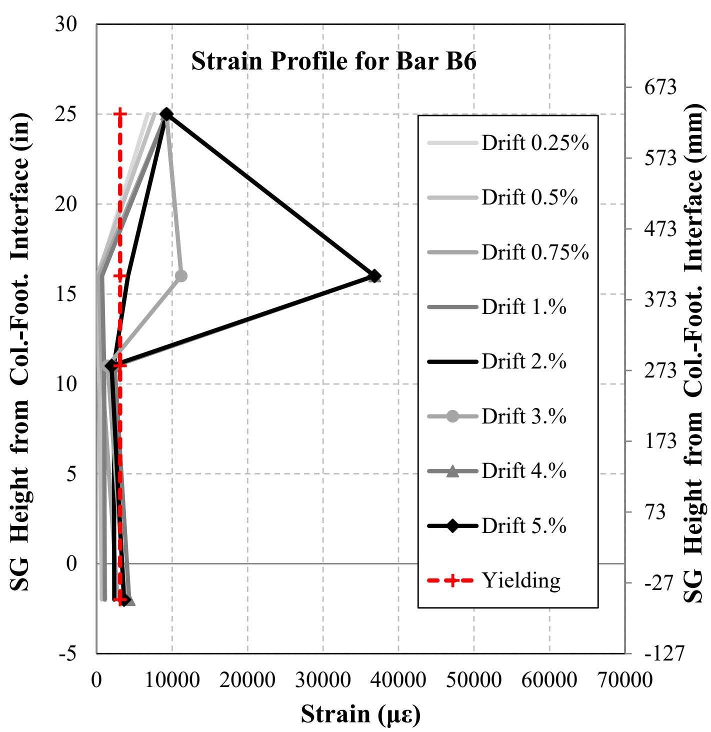

Figure 3.310 Measured Strain Profile for RPH Column Bar B7

3.5.9.7 RPH-R Strain Profiles

Figures 3.311 to 3.344 show the measured strain profiles for Bars B1, B2, B6, and B7 in RPH-R. Strain at the middle two levels was recorded with new strain gauges since BRR were replaced between the two tests. The strain profiles of the four bars for the repaired testing once again showed that most of the strain was concentrated within BRR (the center two levels of strain gauges). The maximum measured strain for the transverse reinforcement was 0.08% recorded at a hoop in the center of the neck section.

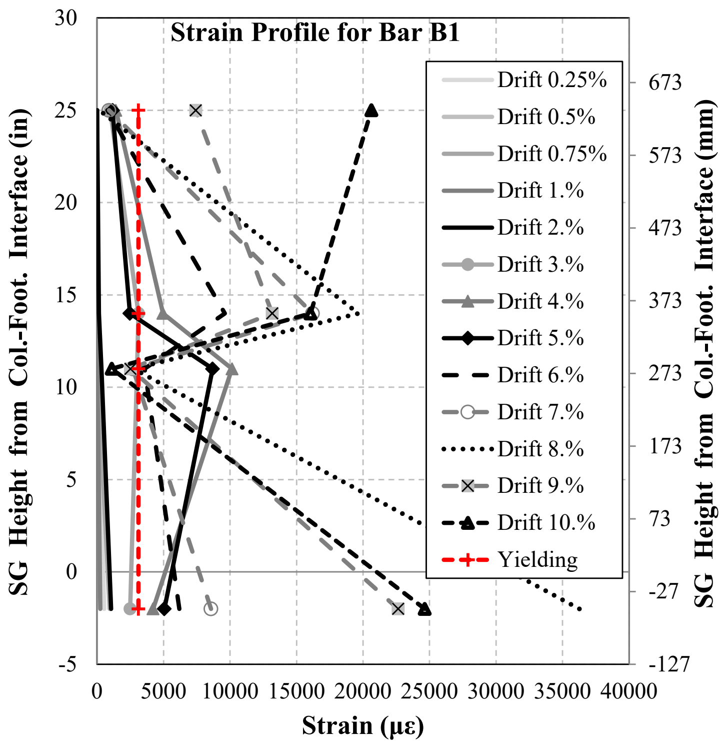

Figure 3.311 Measured Strain Profile for RPH Repaired Column Bar B1

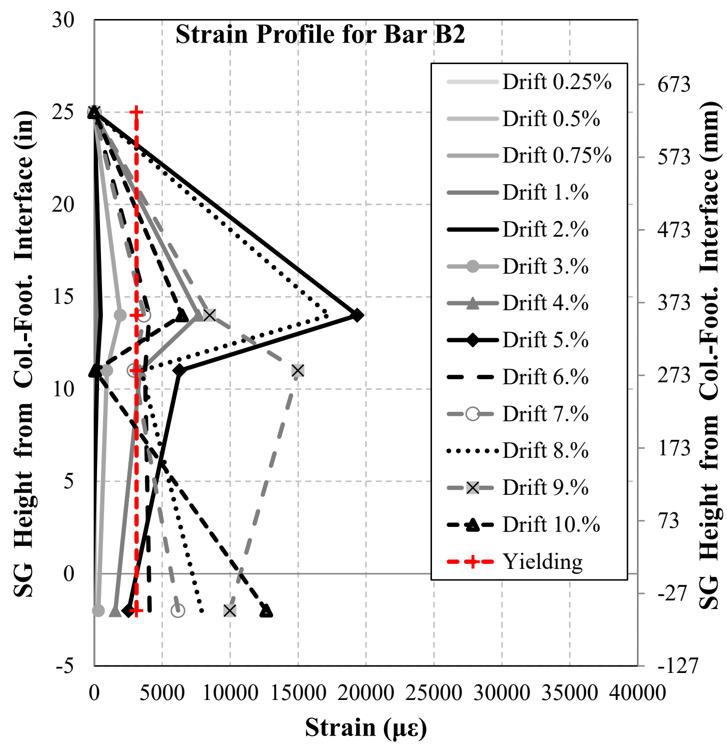

Figure 3.312 Measured Strain Profile for RPH Repaired Column Bar B2

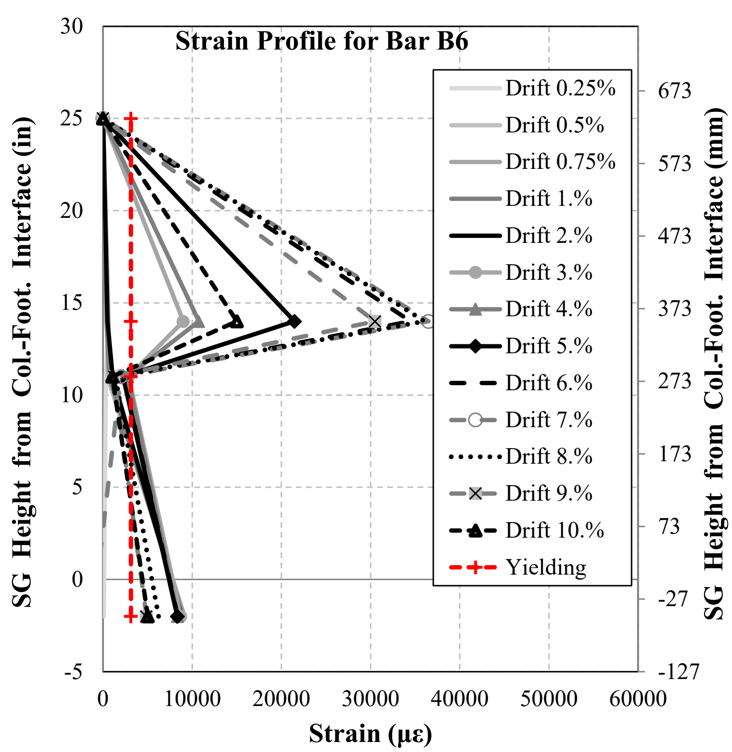

Figure 3.313 Measured Strain Profile for RPH Repaired Column Bar B6

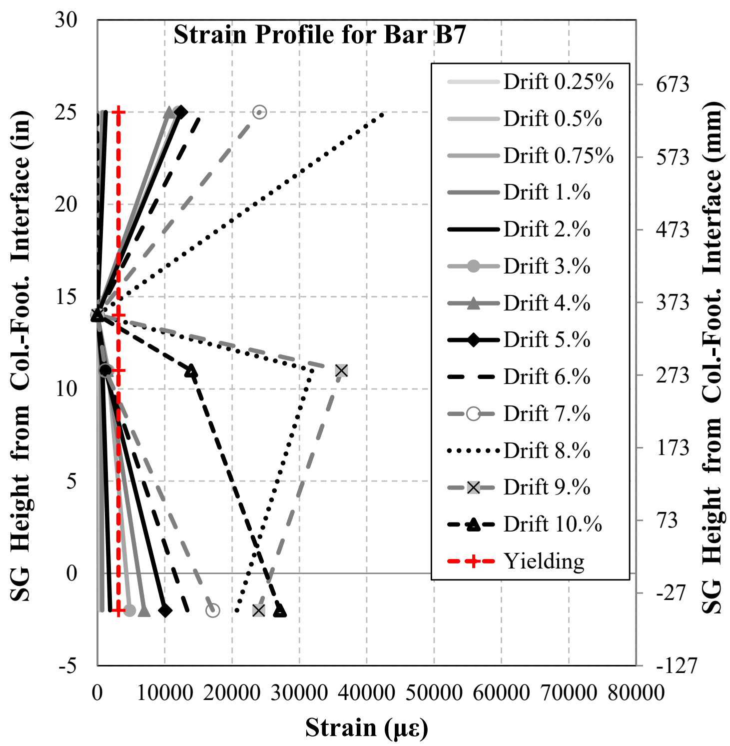

Figure 3.314 Measured Strain Profile for RPH Repaired Column Bar B7

3.5.9.8 RPH Measured Rotation and Curvature

Rotations and curvatures were recorded and determined in the same manner as CIP. Figure 3.315 shows the measured curvature profile for RPH from drift ratios of 0.25% to 4.0%. The highest curvature was concentrated at the base of the column due to the rocking allowed by the pipe-pin connection. Curvature at the second level was shown to be slightly higher than at the first.

3.5.9.9 RPH-R Measured Rotation and Curvature

Figure 3.316 shows the measured curvature profile for the RPH-R column from drift ratios of 0.25% to 4.0%. The highest curvature was concentrated at the base of the column while the first level showed higher strains. Overall, RPH and RPH-R showed a similar curvature profile.

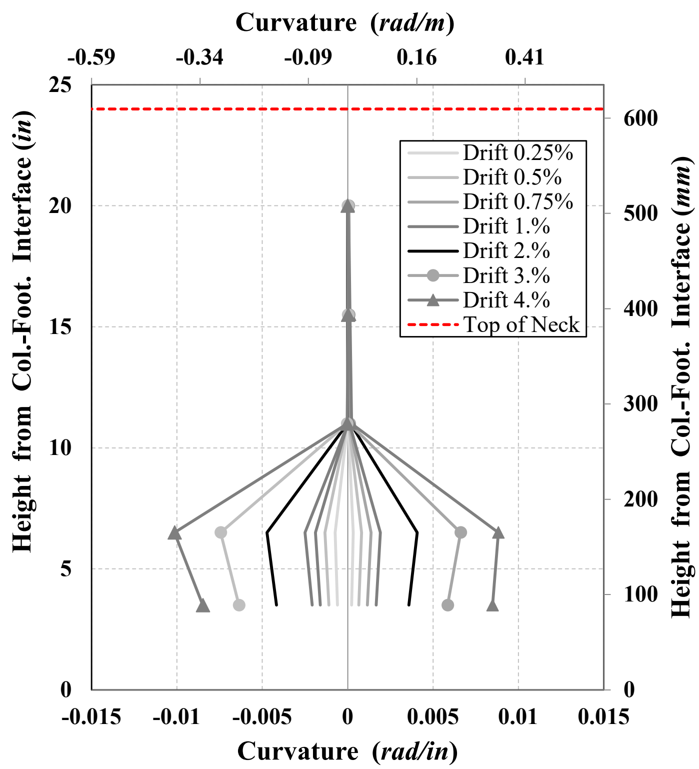

Figure 3.315 Measured Curvature Profile for RPH Column

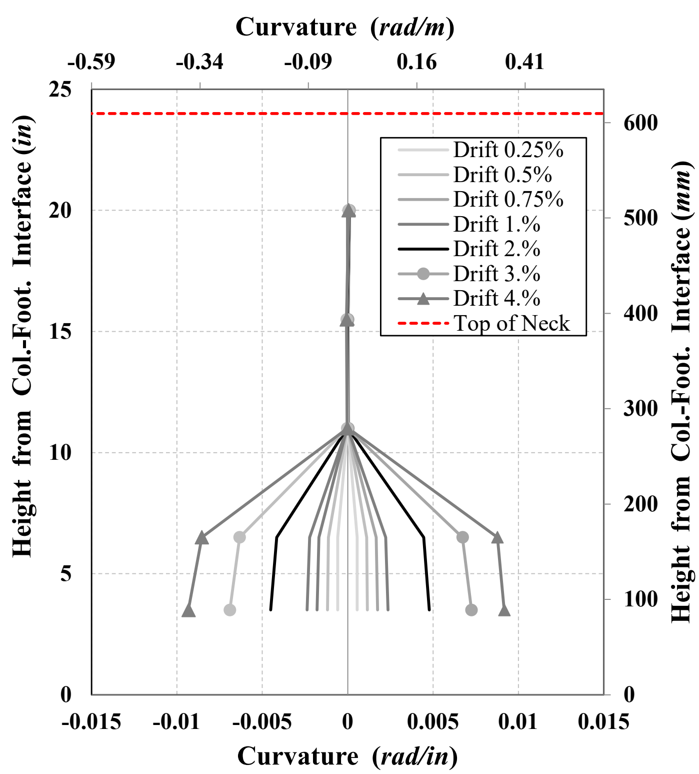

Figure 3.316 Measured Curvature Profile for RPH Repaired Column

3.5.9.10 RHP Energy Dissipation

The cumulative energy dissipation for RPH is shown in Figure 3.317 for drift ratios of 0.25% until 5.0% where the test was stopped. The dissipated energy is negligible until 1.0% drift ratio. After bars yielding during the 2.0% drift, the width of the hysteretic loops slowly began to increase, resulting in higher dissipated energy. RPH dissipated a total of 1,024 kip-in. (116 kN-m) at 5.0% drift ratio.

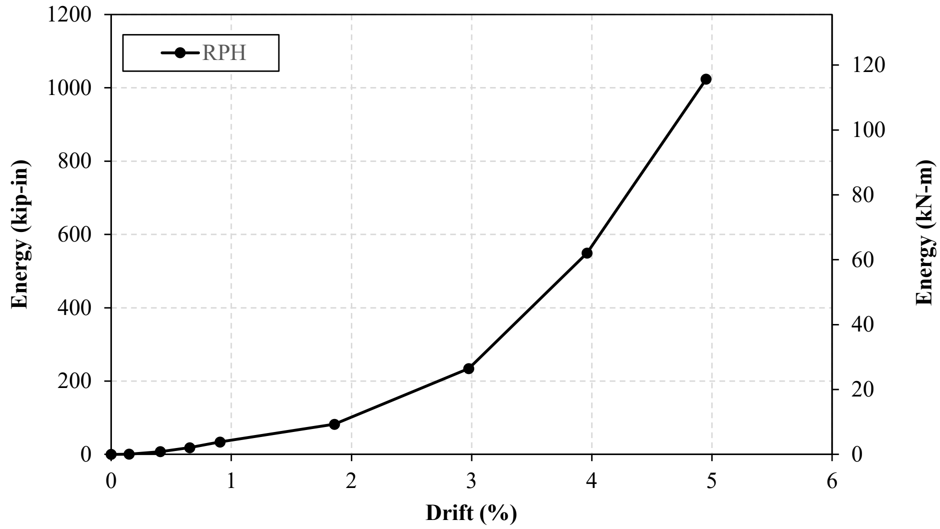

Figure 3.317 Measured Energy Dissipation for RPH Column

3.5.9.11 RPH-R Energy Dissipation

The cumulative energy dissipation for the RPH-R column is shown in Figure 3.318. The dissipated energy is low up to 3.0% drift ratio where BRR yielded. RPH-R dissipated a total of 4,171 kip-in. (471 kN-m) energy at 10.0% drift ratio.

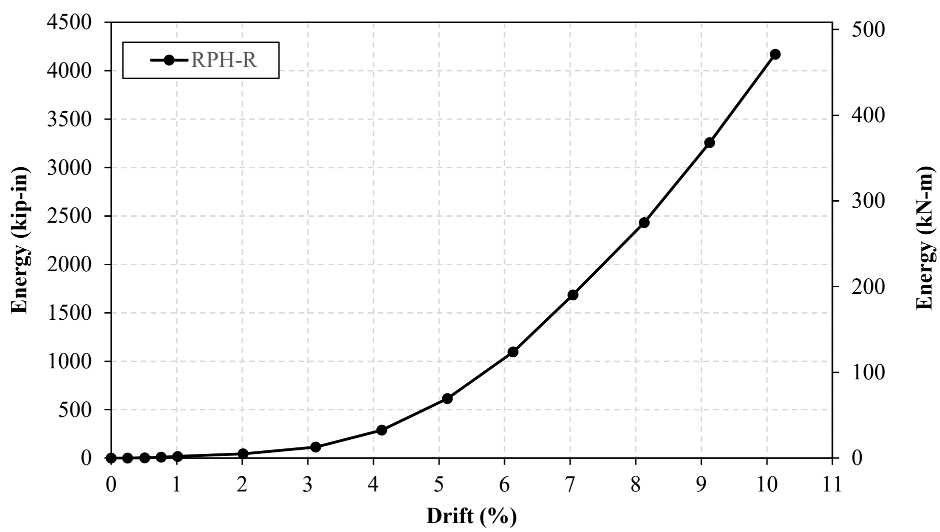

Figure 3.318 Measured Energy Dissipation for RPH Repaired Column

3.6 Mechanically Spliced Precast Column Experimental Evaluation

The main goal of this project was to assess the seismic performance of mechanically spliced bridge columns in a systematic manner. The test results for each column were individually presented in the previous sections. This section compares the performance of all mechanically spliced precast columns tested in this project with respect to the reference CIP column. The force-displacement relationship, strain profiles, and energy dissipation of the columns are compared. Note that RPH was not included herein since it is not a typical mechanically spliced bridge column.

3.6.1 Observed Damage for all Columns

Figure 3.319 shows the plastic hinge damage of columns after the second pull of the 2% drift cycle. CIP had numerous cracks in the plastic hinge region at this drift. However, the general trend for the precast columns was that they had less damage, especially cracking compared with CIP. This is because seismic couplers tend to make the coupler region stronger, thus shifting the damage to the ends of the coupler. For example, the coupler used in PGD was the longest of all couplers used in the precast specimens. As a result, PGD showed the least number of cracks within the plastic hinge region.

Figure 3.320 shows the damage of the plastic hinge for CIP and all mechanically spliced columns at their failure drift. As a general trend, CIP showed higher damage compared with precast columns. Those spliced columns with the bar fracture mode of failure, e.g., PGS, showed a similar damage as the CIP column. However, those precast columns with other modes of failure, such as bar pullout from coupler, showed the minimal visible damage compared with CIP. Examples of this behavior are PGD and PHD.

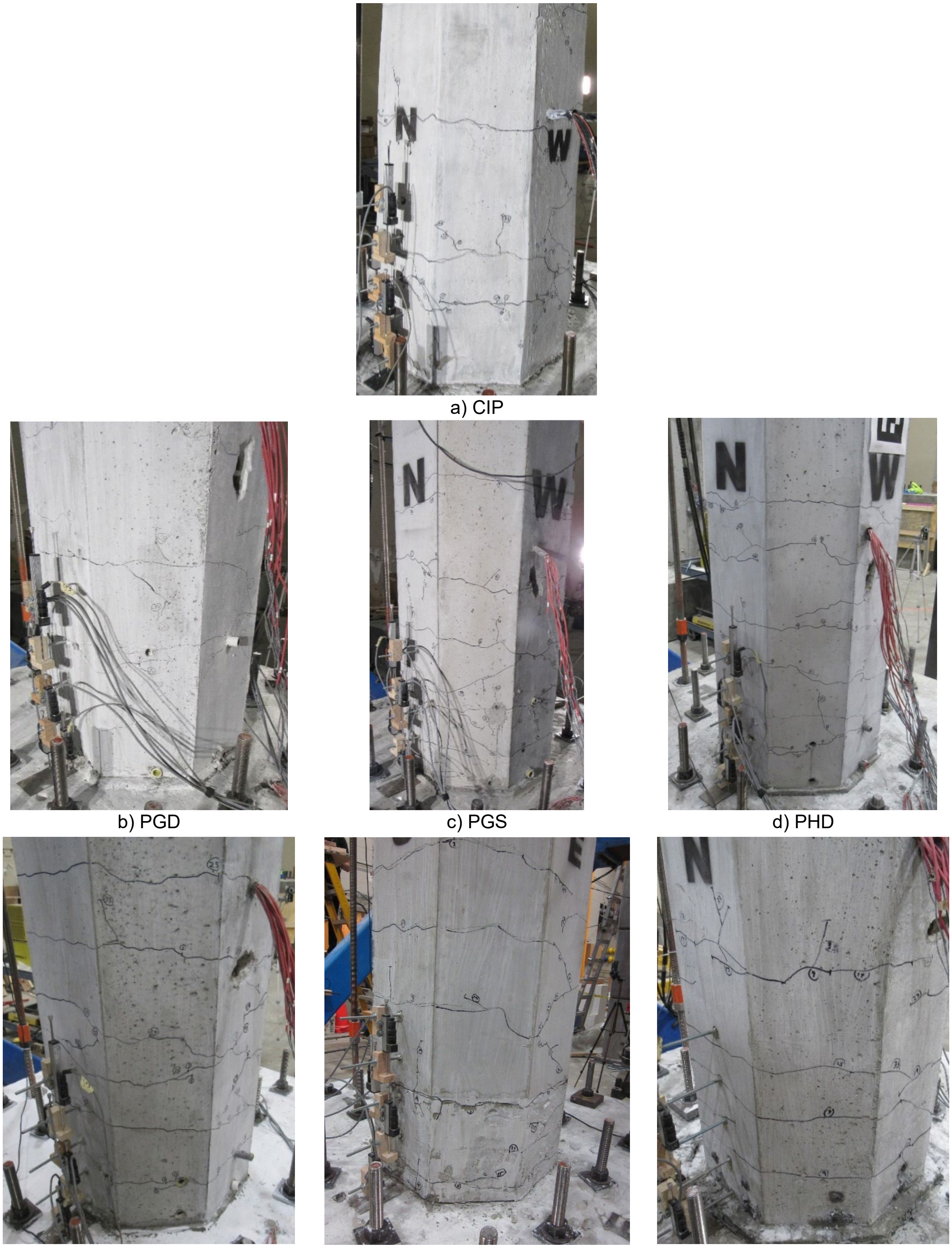

a) CIP

b) PGD

c) PGS

d) PHD

e) PHV

f) PTV

g) PHH

Figure 3.319 CIP, PGD, PGS, PHD, PHV, PTV, and PHH Plastic Hinge Damage at 2% Drift Ratio

a) CIP at 10%

b) PGD at 6%

c) PGS at 9%

d) PHD at 4%

e) PHV at 10%

f) PTV at 7%

g) PHH at 10%

Figure 3.320 CIP, PGD, PGS, PHD, PHV, and PTV Plastic Hinge Damage at Failure Drift Ratio

3.6.2 Force-Displacement Relationship for all Columns

Figure 3.321 shows the measured lateral force-drift hysteretic response for the CIP and all mechanically spliced precast columns. The precast columns exhibited similar behavior compared with that of CIP up to their failure point. All columns showed a wide and stable hysteretic behavior. The precast column with the HRC hybrid grouted-headed couplers showed a pinching starting at 4% drift ratio during unloading due to a gap between the head of the bar and the head seating area within the coupler. All precast columns showed a slightly higher stiffness and a higher lateral strength compared with CIP due to the coupler rigidity, and a higher concrete compressive strength.

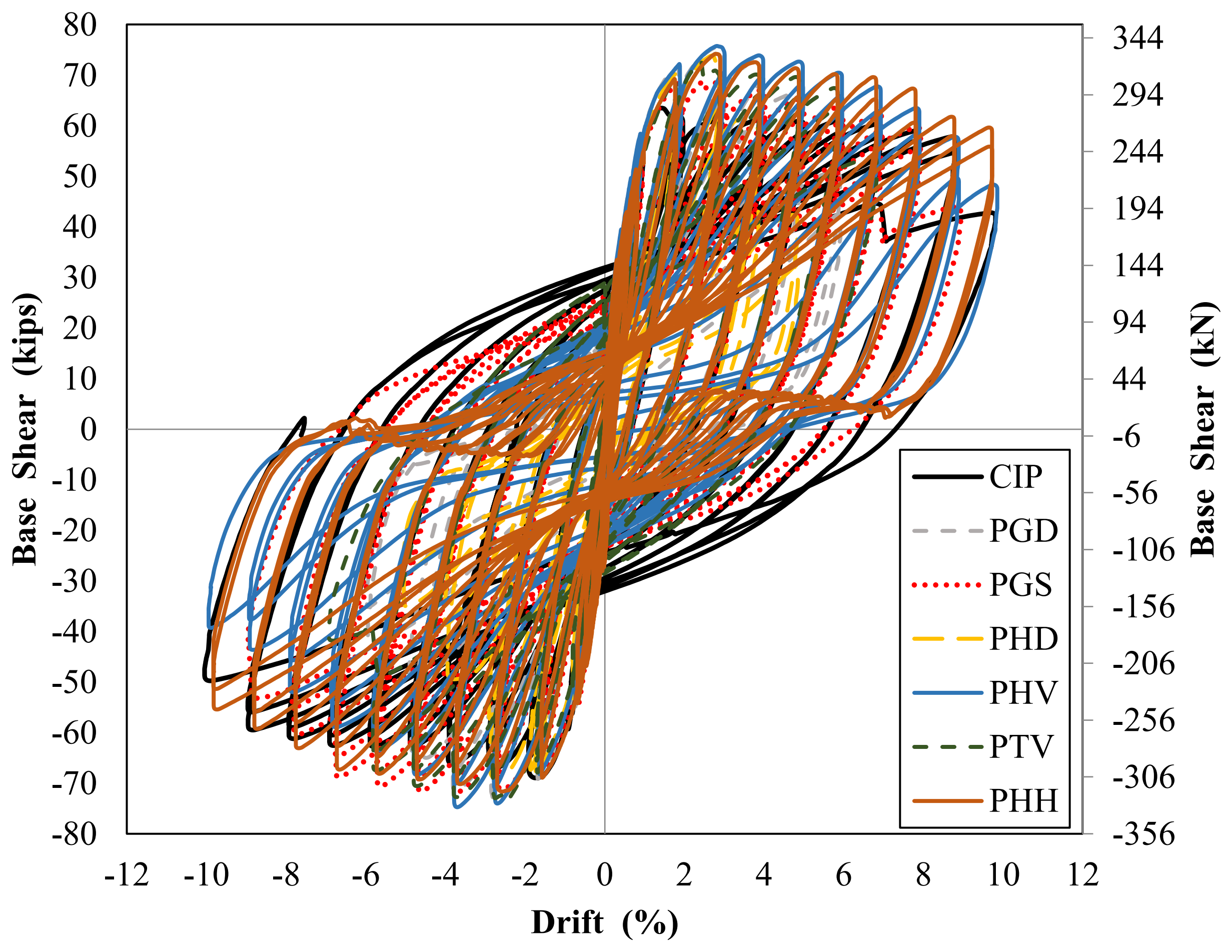

Figure 3.321 Measured CIP, PGD, PGS, PHD, PHV, PTV, and PHH Column Force-Drift Hysteretic Responses

Figure 3.322 shows the measured average push and pull lateral force-drift (pushover) envelopes for CIP and all spliced columns tested in this project. All mechanically spliced columns showed a similar initial stiffness but a higher lateral strength than the CIP column, approximately 6% to 14% higher. The higher strength can be due to the higher stiffness of the couplers shifting the plastic hinge and making the column shear span slightly shorter. Furthermore, the precast column had stronger concrete than CIP.

The displacement capacity of PGD, PGS, PHD, PHV, PTV, and PHH was 45%, 14%, 63%, 24%, 33%, and 3.3% less than CIP, respectively. Furthermore, the displacement ductility capacity of PGD, PGS, PHD, PHV, PTV, and PHH was 53%, 27%, 71%, 17%, 37%, and 7% less than CIP, respectively. Both PGD and PHD failed due to the longitudinal bar pullout from the coupler base, thus exhibited the lowest ductility. PGS failed by longitudinal bar rupture, and therefore showed the highest displacement ductility capacity. PHV, PTV, and PHH failed by a strength loss (mainly due to concrete failure) and showed an intermediate ductility.

Also included in the figure is the design level drift demand based on the AASHTO spectrum for downtown Los Angeles, CA, which is a high seismic area. We can see that all columns met the current seismic design requirements (AASHTO SGS, 2011) since (1) they had a displacement ductility capacity that was higher than the minimum required displacement ductility capacity of 3, (2) they showed a displacement capacity that exceeded the design displacement demand (e.g., for LA), and (3) their displacement ductility demand was less than 5.

Overall, even though some precast columns performed better than others, they are all acceptable and can be used in all seismic regions of the nation. As discussed before, the study recommends that the manufacturer of the hybrid couplers used in PHD specifies a grout type that can achieve a consistent performance of bar fracture in tensile testing.

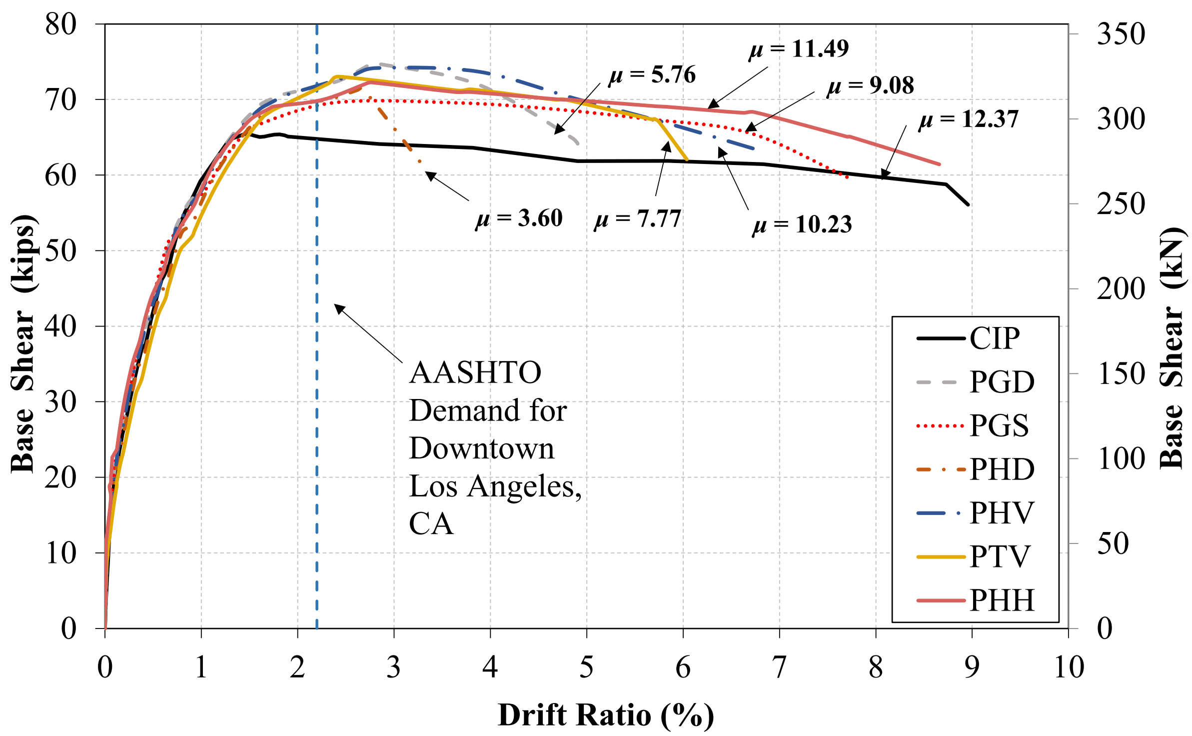

Figure 3.322 Measured CIP, PGD, PGS, PHD, PHV, PTV, and PHH Column Pushover Envelopes

3.6.3 Strain Profile for all Columns

Figures 3.323 to 3.326 show the peak tensile strain profiles at various levels for CIP, PGD, PGS, PHD, PHV, PTV, and PHH. Note that strain gauges were not placed on the couplers. Therefore, strain data is not available at some levels for the precast columns. All columns generally had higher strains at the column base. The strain profile for CIP was typical in which the strain was the highest at the base and gradually reduced above and below the column-footing interface (solid black lines). However, at larger drift ratios, the mechanically spliced precast columns exhibited higher strains below and above the coupler levels compared with CIP. This is because the coupler region is much stiffer shifting the nonlinearity outside of the coupler region, causing higher strains on the longitudinal bars immediately beyond the coupler ends.

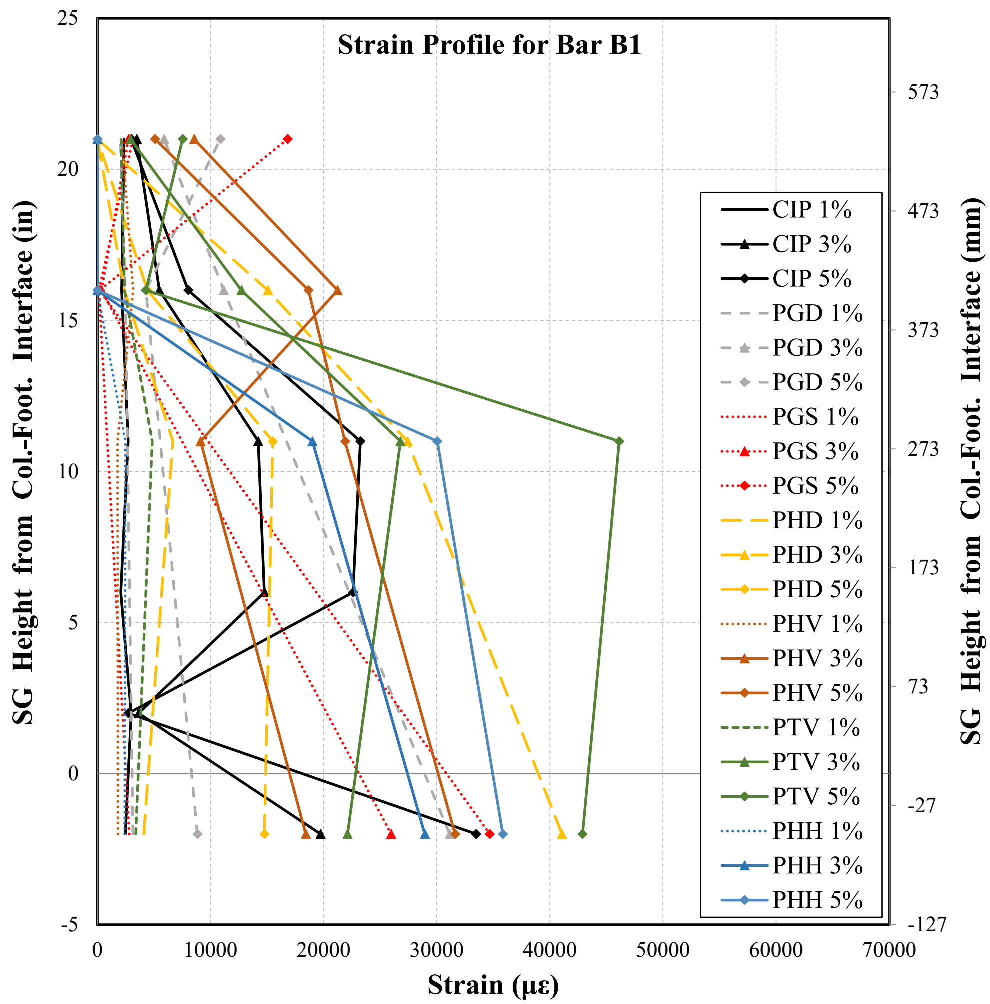

Figure 3.323 Measured CIP, PGD, PGS, PHD, PHV, PTV, and PHH Column Strain Profiles for Bar B1

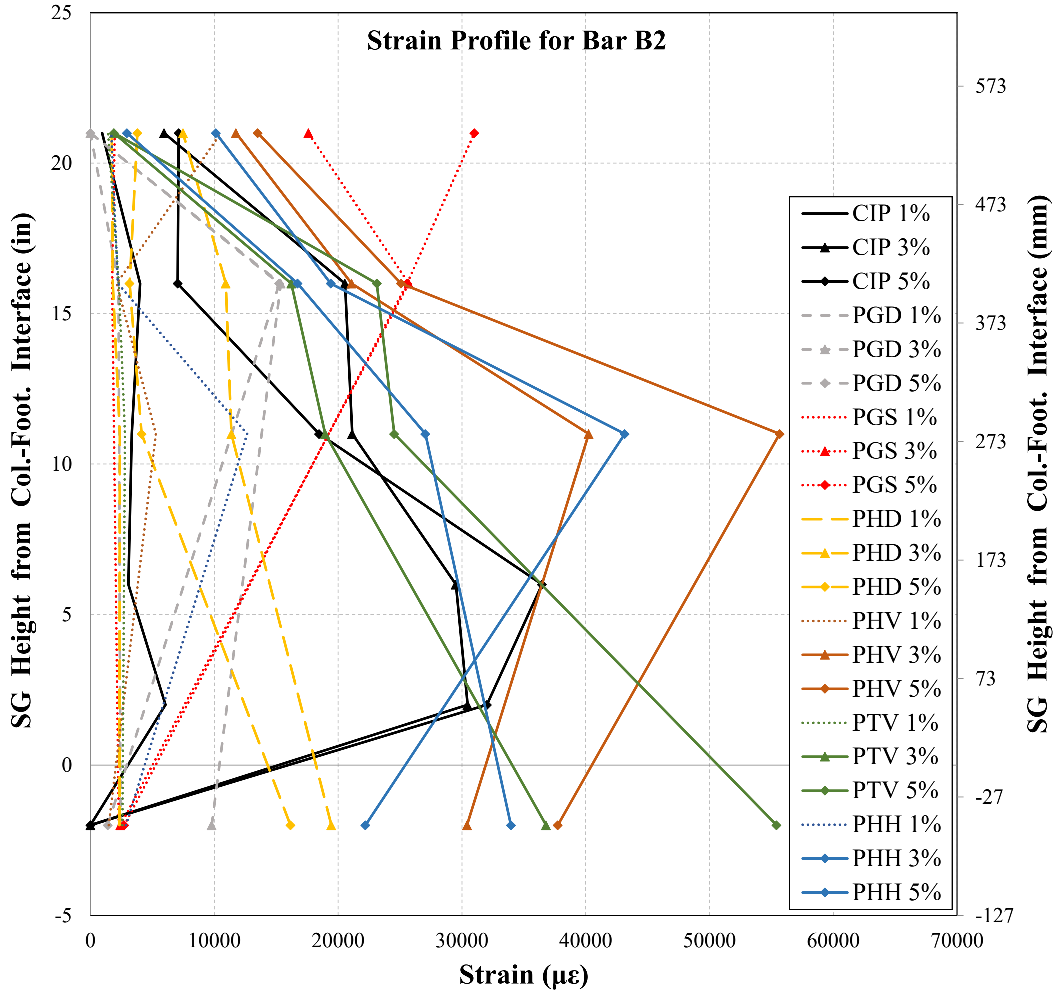

Figure 3.324 Measured CIP, PGD, PGS, PHD, PHV, PTV, and PHH Column Strain Profiles for Bar B2

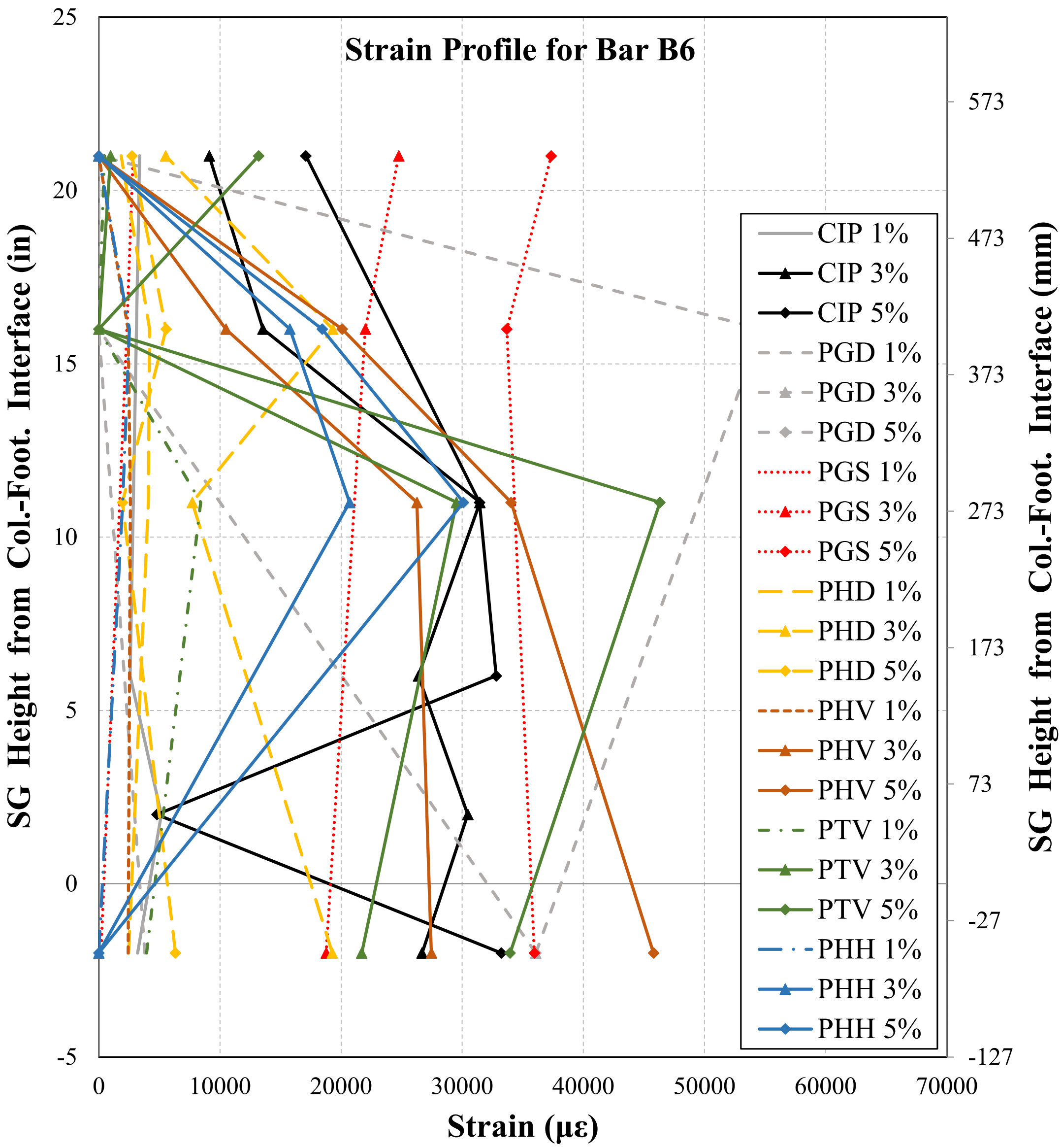

Figure 3.325 Measured CIP, PGD, PGS, PHD, PHV, PTV, and PHH Column Strain Profiles for Bar B6

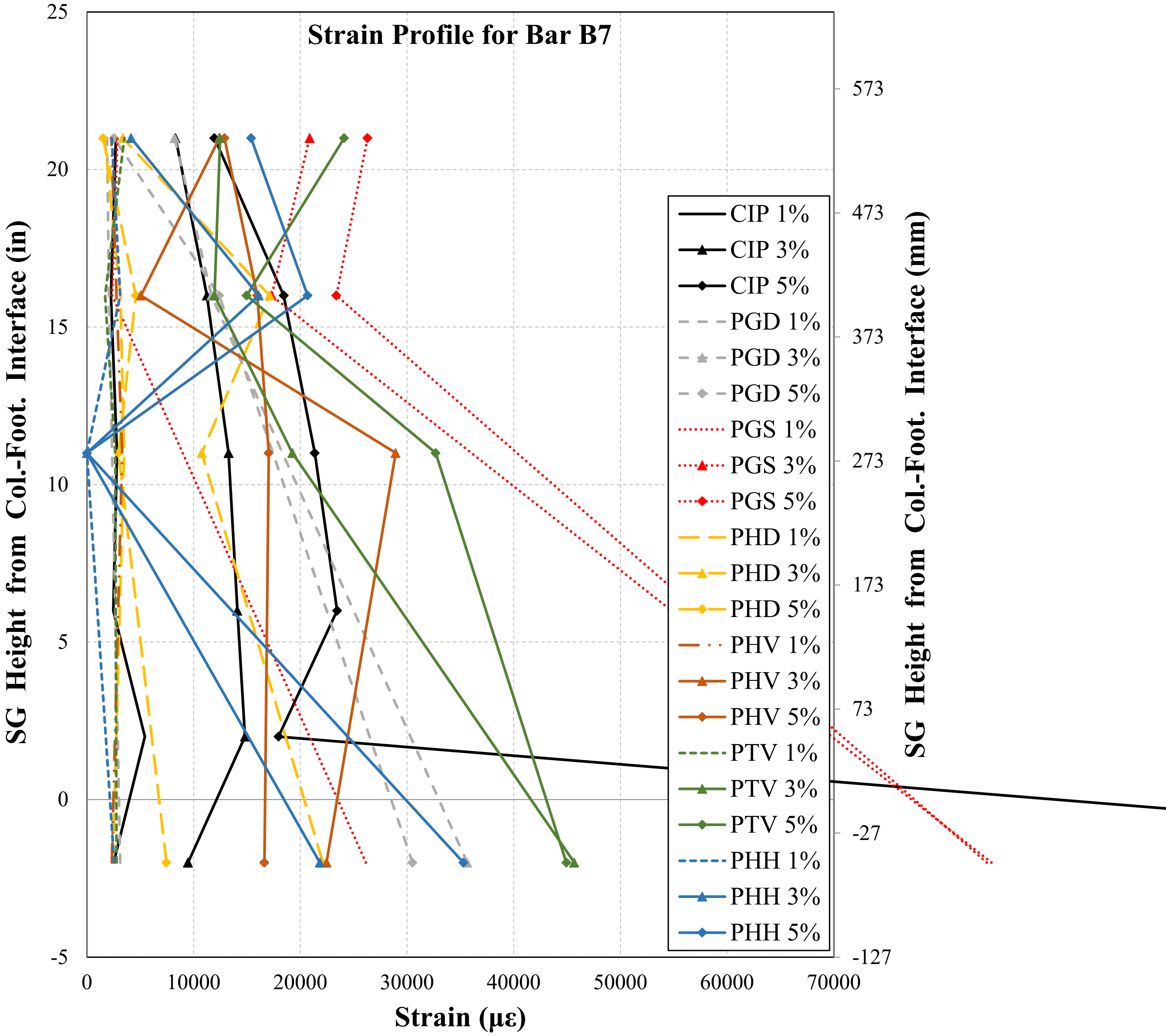

Figure 3.326 Measured CIP, PGD, PGS, PHD, PHV, PTV, and PHH Column Strain Profiles for Bar B7

3.6.4 Energy Dissipation for all Columns

Figure 3.327 shows the cumulative energy dissipation of the CIP and all mechanically spliced columns tested in this project. The precast columns all had a lower energy dissipation than CIP. This is because the longitudinal bars within the couplers do not yield or experience minimal yielding, thus some portion of the mechanically spliced column plastic hinge does not contribute to the column overall displacement. As a result, the dissipated energy, or the strain energy, in mechanically spliced columns is generally smaller than CIP. For small couplers, the dissipated energy of the precast column is expected to be close to that of CIP. For example, a threaded coupler was used in PTV. The energy dissipation of PTV follows well that of CIP.

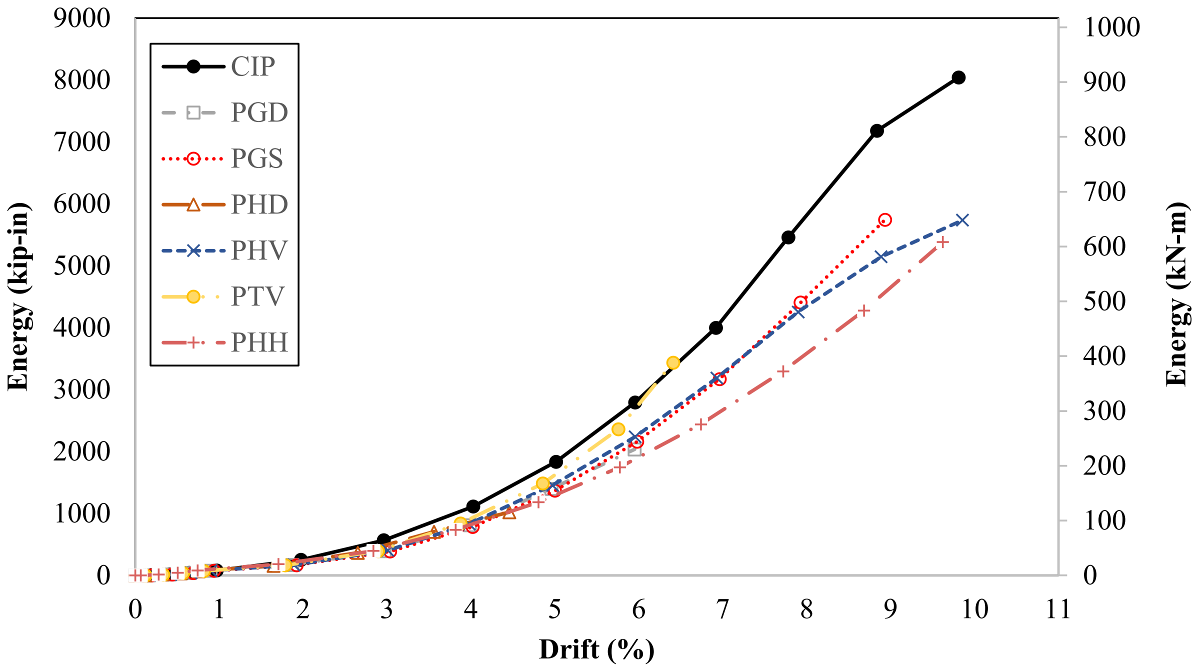

Figure 3.327 Energy Dissipation for CIP, PGD, PGS, PHD, PHV, PTV, and PHH Columns

3.7 Summary and Conclusions of Experimental Study

Seven half-scale precast columns were tested under a slow cyclic loading to failure. One cast-in-place column (CIP) column was also tested to serve as the reference specimen. Six precast columns incorporated a type of mechanical bar splice within the column plastic hinge region, PGS, PGD, PHD, PHV, PTV, and PHH, close to the column-to-footing connection. One column had a new detailing for quick repair by replacement of exposed bars. The summary of the experimental findings is as follows:

- The apparent damages of mechanically spliced bridge columns were generally less than those of CIP due to a higher stiffness of the couplers.
- The mode of failure for CIP and PGS was the longitudinal bar fracture. The mode of failure for PGD and PHD was the longitudinal bar pullout from the base of the mechanical bar splices. The mode of failure for PHV, PTV, PHH, and RPH-R was a loss in strength at the end of testing, typically due to the concrete damages.
- The drift ratio capacity for CIP, PGD, PGS, PHD, PHV, PTV, and PHH was 8.96%, 4.93%, 7.71%, 3.33%, 6.84%, 6.04%, and 8.66%, respectively. Therefore, seismic couplers generally reduce the column displacement capacity due to their size and stiffness. Therefore, mechanically spliced bridge column with seismic couplers may exhibit a displacement capacity that is smaller than a conventional column with a range of insignificant (3%) to major (45%).
- The energy dissipation of all mechanically spliced columns was lower than that in CIP.
- Couplers tend to shift the nonlinearities away. As the result, the strains and curvatures of mechanically spliced columns were higher at the ends of the couplers, and usually the highest at the column base.
- The drift capacity of RPH-R was 9.8, which was higher than the CIP column drift capacity of 8.96%. The stiffness of the repairable column was lower than that for CIP due to the nature of the new connection and the damage of concrete at the rocking face. The repair through replacement of BRR was feasible but difficult at 5% drift ratio due to the Z-shape buckling of exposed bars.
- All columns met the AASHTO seismic requirements, thus they are recommended for use in all 50 states of the nation.

3.8 References

AASHTO SGS (2011) "AASHTO Guide Specifications for Seismic Bridge Design," Washington, D.C., American Association of State Highway and Transportation Officials.

ACI 374.2R-13 (2013). "Guide for Testing Reinforced Concrete Structural Elements Under Slowly Applied Simulated Seismic Loads." American Concrete Institute (ACI) Committee 374, Farmington Hills, MI, 2013.

ASTM A706 (2016). "Standard Specification for Low-Alloy Steel Deformed and Plain Bars for Concrete Reinforcement." West Conshohocken, PA, 6 pp.

ASTM E8 (2012). "Standard Test Methods for Tension Testing of Metallic Materials." ASTM International, West Conshohocken, PA.

ASTM A1034 (Sep. 2016). "Standard Test Methods for Testing Mechanical Splices for Steel Reinforcing Bars." ASTM International, West Conshohocken, PA.

ASTM C109/C109M-11b. (2011). “Standard Test Method for Compressive Strength of Hydraulic Cement Mortars (Using 2-in. or [50-mm] Cube Specimens),” West Conshohocken, PA.

ASTM C39/C39M-12. (2012). “Standard Test Method for Compressive Strength of Cylindrical Concrete Specimens,” West Conshohocken, PA.

ASTM E8 (2012). “Standard Test Methods for Tension Testing of Metallic Materials.” ASTM International, West Conshohocken, PA.

Boudaqa, A., Tazarv, M., and Tuhin, I. (2017). “Ductility without Confinement - A New Design and Construction Approach for RC Bridge Columns,” *International Journal of Bridge Engineering*, Special Issue, pp. 53-77.

Caltrans. (2019). “Caltrans Seismic Design Criteria (SDC), Version 2.0” Sacramento, CA.: California Department of Transportation, 250 pp.

Dahal, P.K., and Tazarv, M. (2020). “Mechanical Bar Splices for Incorporation in Plastic Hinge Regions of RC Members,” *Construction and Building Materials*, Vol. 258, 120308, 17 pp.

Hewes, J.T. (2013). “Analysis of the State of the Art of Precast Concrete Bridge Substructure Systems.” Arizona. Dept. of Transportation, Research Center, Report No. FHWA-AZ-13-687, 124 pp.

Krawinkler, H., and Moncarz, P.D. (1982). “Similitude Requirements for Dynamic Models.” *ACI Special Publication*, Vol. 73, pp. 1-22.

LaVoy, M.R. (2020). “Seismic Performance of Mechanically Spliced Bridge Columns Through Analytical Studies.” MS Thesis, South Dakota State University, 106 pp.

Tazarv, M., and Saiidi, M.S. (2016). “Seismic Design of Bridge Columns Incorporating Mechanical Bar Splices in Plastic Hinge Regions,” *Engineering Structures*, DOI: 10.1016/j.engstruct.2016.06.041, Vol 124, pp. 507-520.

Tazarv, M., Boudaqa, A., and Tuhin, I.A. (2020). “Repairable Precast Moment-Resisting Buildings: Part I – Experimental Investigations,” *ACI Structural Journal*, Vol. 117, No. 6, 147-160 pp.

Zaghi, A.E., and Saiidi, M.S., (2010). “Seismic performance of pipe-pin two-way hinges in concrete bridge columns,” *Journal of Earthquake Engineering*, Vol. 14. No. 8, pp.1253-1302.

4. ANALYTICAL INVESTIGATION OF COLUMN TEST SPECIMENS

4.1 Introduction

The experimental results of eight half-scale bridge columns were presented in the previous chapter. In this chapter, an analytical study is performed to verify current modeling methods for bridge columns, specifically those incorporating mechanical bar splices. A finite element computer program, OpenSees (2016), was used for simulations.

There are several successful studies on how to simulate conventional bridge columns, a few models were developed by the research team (e.g., Tazarv and Saiidi, 2016; LaVoy, 2020). One of those analytical methods will be discussed in the next section for conventional bridge columns. However, there are a few modeling methods developed for mechanically spliced bridge columns. Haber et al. (2015) proposed a multi-element fiber-section finite element method, including a new coupler material model to simulate the response of mechanically spliced bridge columns (Fig. 4.1). Tazarv and Saiidi (2016), and later in NCHRP 935 (2020), proposed three methods to analyze and design mechanically spliced bridge columns, which are summarized in Table 4.1. They also proposed a stress-strain model for couplers (Fig. 4.2), which was discussed in Chapter 2 of this document. Ameli and Pantelides (2017) developed an iterative finite element lumped plasticity model for coupler columns in which the length of the plastic hinge region, which is required in lumped plasticity elements, was iterated. Of different modeling techniques for mechanically spliced bridge columns, the distributed plasticity model developed by Tazarv and Saiidi (2016) (Method 3 in Table 4.1) was selected for further investigation in this chapter.

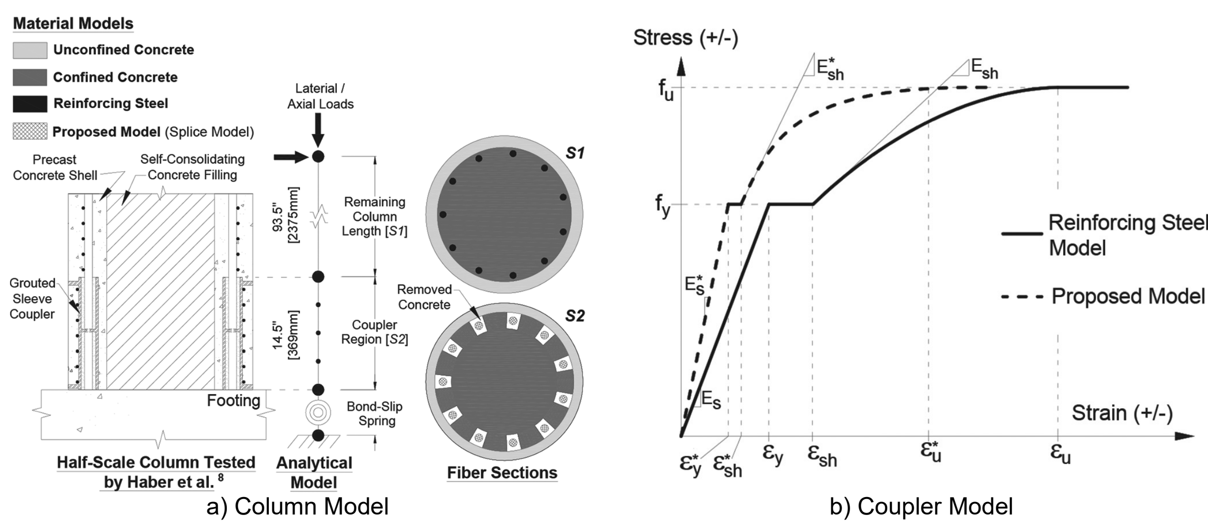

Figure 4.1 Finite Element Modeling Method for Mechanically Spliced Bridge Columns (Haber et al., 2015)

Table 4.1 Modeling Methods for Mechanically Spliced Columns (NCHRP 935)

Design Method	Analysis Type	Column Element in Pushover Analysis	Analysis Requirements
Cast-in-place (CIP) columns	Moment-Curvature or Pushover	Usually conducted using a lumped plasticity model, which requires an analytical plastic hinge length. However, distributed plasticity model can also be utilized	AASHTO Guide Specifications for LRFD Seismic Bridge Design
Method 1. Spliced columns using a displacement ductility equation	Use CIP analysis results	Use CIP analysis results	$\frac{\mu_{sp}}{\mu_{CIP}} = (1 - 0.18\beta)(\frac{H_{sp}}{L_{sp}})^{0.1\beta}$
Method 2. Spliced columns using modified plastic hinge length equation	Moment-Curvature or Pushover	Lumped plasticity model only	Similar to CIP but with $L_p^{sp} = L_p - (1 - \frac{H_{sp}}{L_p})\beta L_{sp} \leq L_p$
Method 3. Spliced columns using proposed stress-strain model for couplers	Pushover only	Distributed plasticity model only	Coupler stress-strain model (Fig. 4.2)

Note: μ_{sp}: The mechanically spliced bent displacement ductility capacity; μ_{CIP}: The corresponding non-spliced cast-in-place bent displacement ductility capacity; β: The coupler rigid length ratio; H_{sp}: The distance from the column end to the nearest face of the coupler embedded either inside the column or inside the column adjoining member (*in.*); L_{sp}: The coupler length (*in.*); L_p^{sp}: The modified plastic hinge length for mechanically spliced bridge columns; L_p: The conventional column analytical plastic hinge length according to the current AASHTO SGS.

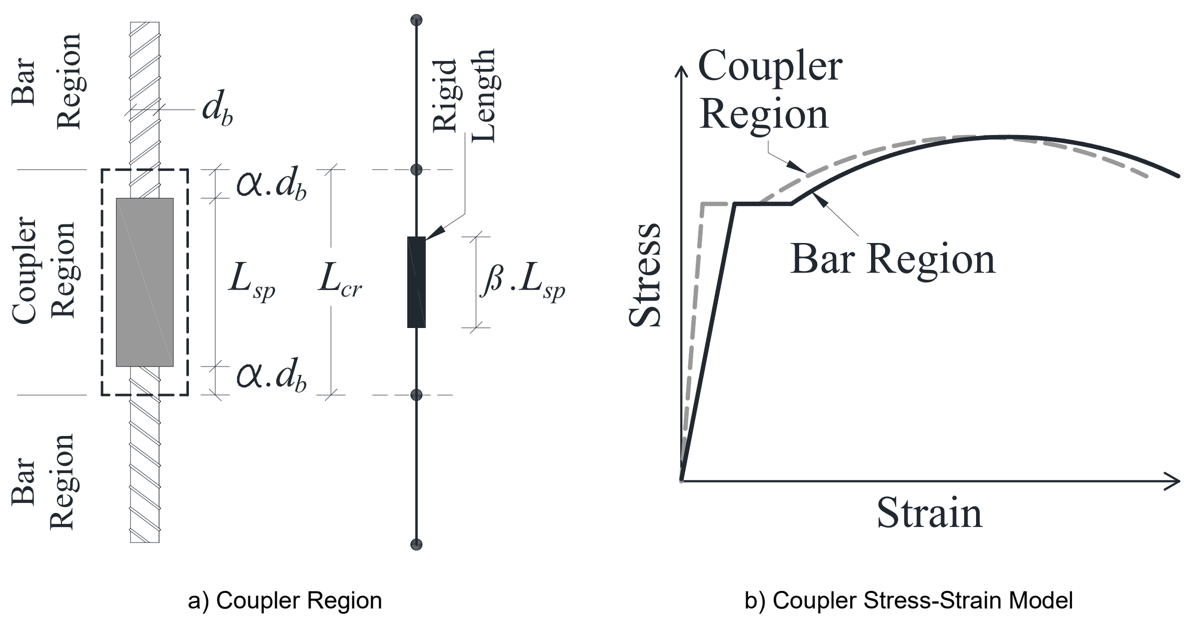

Figure 4.2 Generic Stress-Strain Model for Mechanical Bar Splices (Tazarv and Saiidi, 2016)

4.2 Analysis of Column Test Specimens

This section describes the modeling methods developed for the mechanically spliced bridge column specimens tested in this project. The modeling of the CIP column is also included. Nevertheless, the repairable column, RPH, was not included in this section since it did not follow the detailing of a typical mechanically spliced column.

4.2.1 Modeling Methods

A three-dimensional (3D) fiber-section finite element model with six degrees of freedom (DOFs) was used to simulate all columns in OpenSees (2016). The height for all columns, the distance between the top of footing and the centerline of the actuator, was 8 ft (2.44 m). An octagonal cross-section was used in all columns, which had a medium diagonal of 24 in. (610 mm). Each column was longitudinally reinforced with 10 – No. 8 (25-mm) bars (ρ_l = 1.66%) and transversely with No. 4 (13-mm) hoops at 2 in. (51 mm), resulting is a volumetric transverse steel bar ratio of ρ_s = 2.0%.

Figure 4.3 schematically shows the analytical finite element model developed for CIP, in which a single "forceBeamColumn" element with five integration points was used. The CIP column sectional properties were simulated with the cover, core, and steel bar uniaxial fibers. The core concrete was discretized into 50×50 fibers and modeled with "Concrete01." The cover concrete was discretized into 10×4 fibers and modeled with "Concrete01." The clear cover was defined as the minimum distance between the column surface to the exterior of the confining reinforcement. The fiber properties were based on the measured mechanical properties of each material discussed in Chapter 3. The properties of the confined (or core) concrete were calculated using the model proposed by Mander et al. (1988). Table 4.2 presents a summary of the material models used in the CIP analytical model. The P-D effects and the bond-slip effects (based on a modified stress-strain relationship of steel bars according to Tazarv and Saiidi, (2014) were included.

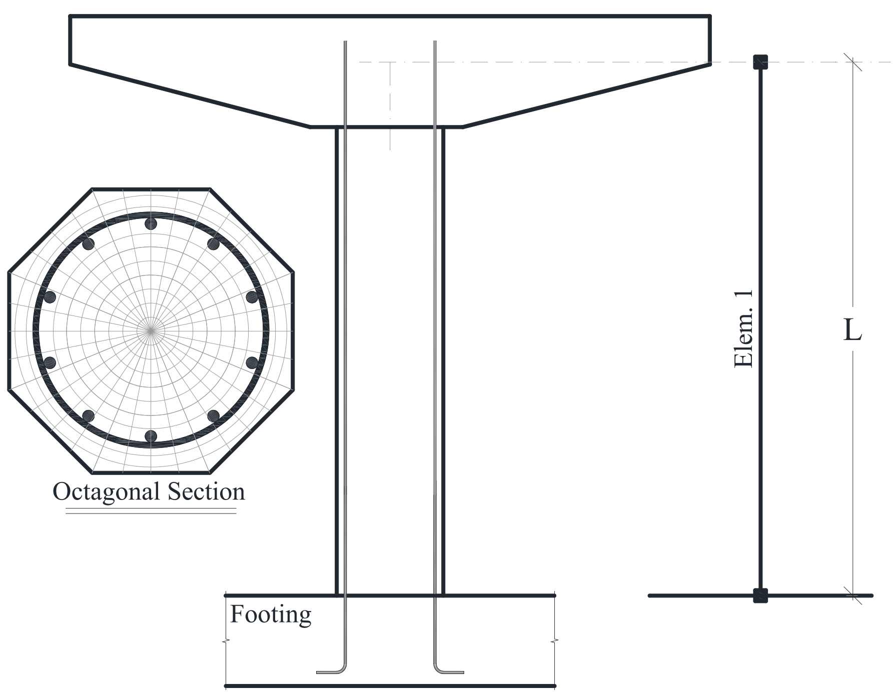

Figure 4.3 Analytical Modeling Method for Cast-in-Place Column

Table 4.2 Sectional Fiber Material Properties Used in CIP

Concrete Fibers	
Application: unconfined concrete Type: Concrete01 f'_{cc} = 4300 psi (29.6MPa) ε_{cc} = 0.002 in/in f'_{cu} = 0.0 psi (0 MPa) ε_{cu} = 0.005 in/in	Application: confined concrete (based on Mander's model) Type: Concrete01 f'_{cc} = 7930 psi (54.7 MPa) ε_{cc} = 0.0104 in/in f'_{cu} = 6950 psi (47.9 MPa) ε_{cu} = 0.0341 in/in
Steel Fibers	
Application: bars at the base section including bond-slip effects Type: ReinforcingSteel f_y = 69.3 ksi (477.8 MPa) f_{su} = 97.4 ksi (671.5 MPa) E_s = 10640 ksi (73360 MPa) E_{sh} = 840 ksi (5800 MPa) ε_{sh} = 0.0091 in/in ε_{su} = 0.126 in/in	Application: reference bars in other sections Type: ReinforcingSteel f_y = 69.3 ksi (477.8 MPa) f_{su} = 97.4 ksi (671.5 MPa) E_s = 29000 ksi (20000 MPa) E_{sh} = 853 ksi (5880 MPa) ε_{sh} = 0.005 in/in ε_{su} = 0.12 in/in

The behavior of the six mechanically spliced precast bridge columns, PGD, PGS, PHD, PHV, PTV, and PHH, were simulated using a consistent modeling method based on Method 3 (Table 4.1) developed by Tazarv and Saiidi (2016). In this method, distributed plasticity elements are used to represent different sections of the column, those without couplers and those with couplers. The effects of couplers are included in the simulation using the coupler stress-strain relationship (Fig. 4.2) at those analytical sections incorporating mechanical bar splices.

Figure 4.4 schematically shows the analytical model for the coupler columns. Similar to CIP, a 3D fiber-section finite element model with six DOFs was used to simulate the precast column behavior in OpenSees (2016). However, three elements were needed to successfully include the sectional changes. Element 1 was a "zeroLength" element to monitor the stress-strain behavior of unspliced reinforcing steel bars (the same as that obtained from the tensile testing) and concrete fibers. In this element, the bond-slip effects can also be included by modifying the longitudinal steel reinforcement properties (e.g., Table 4.3). Elements 2 and 3 were "forceBeamColumn" elements, each with five integration points. Element 2 was used to include the coupler effects by modifying the steel bar properties based on the coupler model (Fig. 4.2). The coupler rigid length factor was based on the measured properties (Table 3.5 of Chapter 3). Figure 4.5 shows the reproduced coupler stress-strain behavior that was used in the analytical study for the six coupler types used in the six precast columns. Note that the curves for the five couplers were approximately the same since the coupler rigid length factor for these couplers were close (0.7, 0.7, 0.79, 0.82, and 0.8 for couplers, respectively, used in PGD, PGS, PHD, PHV, and PHH). Beta was lower for PTV (e.g., Beta was 0.4 for the threaded couplers of PTV). Tables 4.3 to 4.8 provide a summary of the material models/properties used for PGD, PGS, PHD, PHV, PTV, and PHH, respectively.

The stress-strain data was monitored for the extreme concrete and steel fibers at the column base (Element 1 in Fig. 4.3 & 4.4). Furthermore, the column tip displacements and lateral forces were recorded. The column analytical failure point was the displacement at which one of the following limit states first occurred: (1) the extreme steel fiber reached its ultimate tensile strain, (2) the extreme concrete core fiber reached the ultimate compressive strain, and (3) the column lateral load carrying capacity reduced by 15% compared with the peak lateral strength.

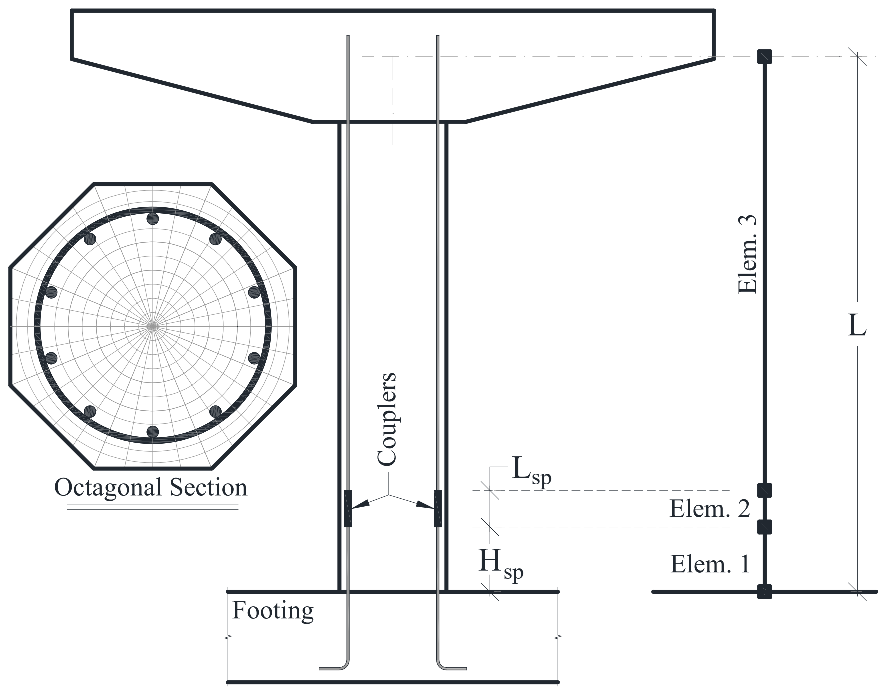

Figure 4.4 Analytical Modeling Method for Mechanically Spliced Columns

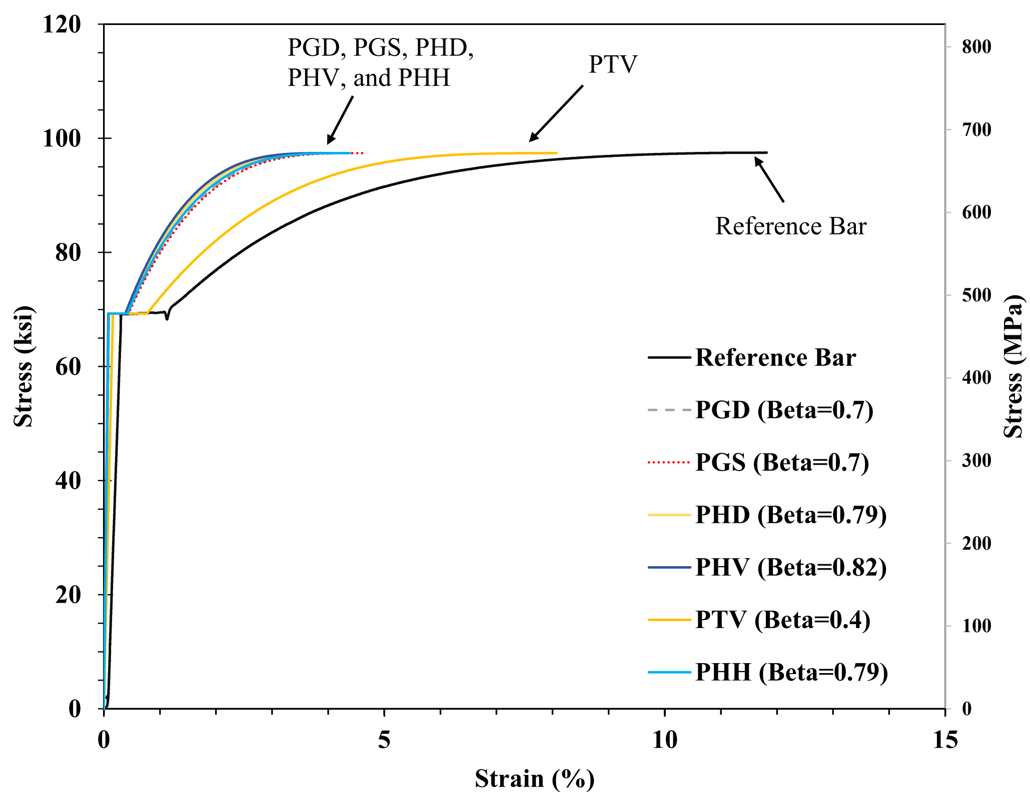

Figure 4.5 Coupler Stress-Strain Relationships Used in Mechanically Spliced Column Analytical Models

Table 4.3 Sectional Fiber Material Properties Used in PGD

Concrete Fibers	
Application: unconfined concrete Type: Concrete01 f'_{cc} = 7950 psi (54.8 MPa) ε_{cc} = 0.002 in/in f'_{cu} = 2540 psi (17.5 MPa) ε_{cu} = 0.005 in/in	Application: confined concrete (based on Mander's model) Type: Concrete01 f'_{cc} = 11730 psi (80.9 MPa) ε_{cc} = 0.0068 in/in f'_{cu} = 8810 psi (60.8 MPa) ε_{cu} = 0.0226 in/in
Steel Fibers	
Application: unspliced (reference) bars (Element 1) including bond-slip effects Type: ReinforcingSteel f_y = 69.3 ksi (477.8 MPa) f_{su} = 97.4 ksi (671.5 MPa) E_s = 10640 ksi (73400 MPa) E_{sh} = 840 ksi (5800 MPa) ε_{sh} = 0.009 in/in ε_{su} = 0.126 in/in	Application: spliced bars (Element 2) with Beta = 0.70; L_{sp} = 16.5 in. (419 mm) Type: ReinforcingSteel f_y = 69.3 ksi (477.8 MPa) f_{su} = 97.4 ksi (671.5 MPa) E_s = 77200 ksi (532000 MPa) E_{sh} = 2270 ksi (15700 MPa) ε_{sh} = 0.0043 in/in ε_{su} = 0.045 in/in
Application: unspliced (reference) bars (Element 3) without bond-slip effects Type: ReinforcingSteel f_y = 69.3 ksi (477.8 MPa) f_{su} = 97.4 ksi (671.5 MPa) E_s = 29000 ksi (200000 MPa) E_{sh} = 853 ksi (5880 MPa) ε_{sh} = 0.0115 in/in ε_{su} = 0.12 in/in	

Table 4.4 Sectional Fiber Material Properties Used in PGS

Concrete Fibers	
Application: unconfined concrete Type: Concrete01 f'_{cc} = 8880 psi (61.2 MPa) ε_{cc} = 0.002 in/in f'_{cu} = 2840 psi (19.6 MPa) ε_{cu} = 0.005 in/in	Application: confined concrete (based on Mander's model) Typeoncrete01 f'_{cc} = 12480 psi (88.5 MPa) ε_{cc} = 0.0065 in/in f'_{cu} = 9090 psi (62.7 MPa) ε_{cu} = 0.0218 in/in
Steel Fibers	
Application: unspliced (reference) bars (Element 1) including bond-slip effects Type: ReinforcingSteel f_y = 69.3 ksi (477.8 MPa) f_{su} = 97.4 ksi (671.5 MPa) E_s = 10000 ksi (69000 MPa) E_{sh} = 840 ksi (5800 MPa) ε_{sh} = 0.016 in/in ε_{su} = 0.126 in/in	Application: spliced bars (Element 2) with Beta = 0.70; L_{sp} = 14.57 in. (370 mm) Type: ReinforcingSteel f_y = 69.3 ksi (477.8 MPa) f_{su} = 97.4 ksi (671.5 MPa) E_s = 75400 ksi (520000 MPa) E_{sh} = 2220 ksi (15300 MPa) ε_{sh} = 0.0044 in/in ε_{su} = 0.0461 in/in
Application: unspliced (reference) bars (Element 3) without bond-slip effects Type: ReinforcingSteel f_y = 69.3 ksi (477.8 MPa) f_{su} = 97.4 ksi (671.5 MPa) E_s = 29000 ksi (200000 MPa) E_{sh} = 853 ksi (5880 MPa) ε_{sh} = 0.0115 in/in ε_{su} = 0.12 in/in	

Table 4.5 Sectional Fiber Material Properties Used in PHD

Concrete Fibers	
Application: unconfined concrete Type: Concrete01 f'_{cc} = 9640 psi (66.5 MPa) ε_{cc} = 0.002 in/in f'_{cu} = 3080 psi (21.2 MPa) ε_{cu} = 0.005 in/in	Application: confined concrete (based on Mander's model) Type: Concrete01 f'_{cc} = 13640 psi (94.0 MPa) ε_{cc} = 0.0062 in/in f'_{cu} = 9410 psi (64.9 MPa) ε_{cu} = 0.0205 in/in
Steel Fibers	
Application: unspliced (reference) bars (Element 1) including bond-slip effects Type: ReinforcingSteel f_y = 69.3 ksi (477.8 MPa) f_{su} = 97.4 ksi (671.5 MPa) E_s = 10640 ksi (73400 MPa) E_{sh} = 840 ksi (5800 MPa) ε_{sh} = 0.0156 in/in ε_{su} = 0.126 in/in	Application: spliced bars (Element 2) with Beta = 0.79; L_{sp} = 9.45 in. (240 mm) Type: ReinforcingSteel f_y = 69.3 ksi (477.8 MPa) f_{su} = 97.4 ksi (671.5 MPa) E_s = 83300 ksi (574000 MPa) E_{sh} = 2450 ksi (16900 MPa) ε_{sh} = 0.0040 in/in ε_{su} = 0.0418 in/in
Application: unspliced (reference) bars (Element 3) without bond-slip effects Type: ReinforcingSteel f_y = 69.3 ksi (477.8 MPa) f_{su} = 97.4 ksi (671.5 MPa) E_s = 29000 ksi (200000 MPa) E_{sh} = 853 ksi (5880 MPa) ε_{sh} = 0.0115 in/in ε_{su} = 0.12 in/in	

Table 4.6 Sectional Fiber Material Properties Used in PHV

Concrete Fibers	
Application: unconfined concrete Type: Concrete01 f'_{cc} = 10120 psi (69.8 MPa) ε_{cc} = 0.0025 in/in f'_{cu} = 4050 psi (27.9 MPa) ε_{cu} = 0.005 in/in	Application: confined concrete (based on Mander's model) Type: Concrete01 f'_{cc} = 14.07 psi (97.0 MPa) ε_{cc} = 0.0059 in/in f'_{cu} = 9380 psi (64.7 MPa) ε_{cu} = 0.0197 in/in
Steel Fibers	
Application: unspliced (reference) bars (Element 1) including bond-slip effects Type: ReinforcingSteel f_y = 69.3 ksi (477.8 MPa) f_{su} = 97.4 ksi (671.5 MPa) E_s = 10250 ksi (70700 MPa) E_{sh} = 840 ksi (5800 MPa) ε_{sh} = 0.016 in/in ε_{su} = 0.126 in/in	Application: spliced bars (Element 2) with Beta = 0.82; L_{sp} = 8.63 in. (219 mm) Type: ReinforcingSteel f_y = 69.3 ksi (477.8 MPa) f_{su} = 97.4 ksi (671.5 MPa) E_s = 86750 ksi (598000 MPa) E_{sh} = 2552 ksi (17600 MPa) ε_{sh} = 0.0038 in/in ε_{su} = 0.04 in/in
Application: unspliced (reference) bars (Element 3) without bond-slip effects Type: ReinforcingSteel f_y = 69.3 ksi (477.8 MPa) f_{su} = 97.4 ksi (671.5 MPa) E_s = 29000 ksi (200000 MPa) E_{sh} = 853 ksi (5880 MPa) ε_{sh} = 0.0115 in/in ε_{su} = 0.12 in/in	

Table 4.7 Sectional Fiber Material Properties Used in PTV

Concrete Fibers	
Application: unconfined concrete Type: Concrete01 f'_{cc} = 10115 psi (69.7 MPa) ε_{cc} = 0.0025 in/in f'_{cu} = 3840 psi (26.5 MPa) ε_{cu} = 0.005 in/in	Application: confined concrete (based on Mander's model) Type: Concrete01 f'_{cc} = 14259 psi (98.3 MPa) ε_{cc} = 0.0061 in/in f'_{cu} = 9636 psi (66.4 MPa) ε_{cu} = 0.0203 in/in
Steel Fibers	
Application: unspliced (reference) bars (Element 1) including bond-slip effects Type: ReinforcingSteel f_y = 69.3 ksi (477.8 MPa) f_{su} = 97.4 ksi (671.5 MPa) E_s = 10900 ksi (75000 MPa) E_{sh} = 840 ksi (5800 MPa) ε_{sh} = 0.0155 in/in ε_{su} = 0.126 in/in	Application: spliced bars (Element 2) with Beta = 0.4; L_{sp} = 9.0 in. (228.6 mm) Type: ReinforcingSteel f_y = 69.3 ksi (477.8 MPa) f_{su} = 97.4 ksi (671.5 MPa) E_s = 43100 ksi (297136 MPa) E_{sh} = 1270 ksi (8700 MPa) ε_{sh} = 0.00774 in/in ε_{su} = 0.08 in/in
Application: unspliced (reference) bars (Element 3) without bond-slip effects Type: ReinforcingSteel f_y = 69.3 ksi (477.8 MPa) f_{su} = 97.4 ksi (671.5 MPa) E_s = 29000 ksi (200000 MPa) E_{sh} = 853 ksi (5880 MPa) ε_{sh} = 0.0115 in/in ε_{su} = 0.12 in/in	

Table 4.8 Sectional Fiber Material Properties Used in PHH

Concrete Fibers	
Application: unconfined concrete Type: Concrete01 f'_{cc} = 9782 psi (67.4 MPa) ε_{cc} = 0.0025 in/in f'_{cu} = 3913 psi (27.0 MPa) ε_{cu} = 0.005 in/in	Application: confined concrete (based on Mander's model) Type: Concrete01 f'_{cc} = 13737 psi (94.7 MPa) ε_{cc} = 0.0060 in/in f'_{cu} = 9363 psi (64.6 MPa) ε_{cu} = 0.0201 in/in
Steel Fibers	
Application: unspliced (reference) bars (Element 1) including bond-slip effects Type: ReinforcingSteel f_y = 69.3 ksi (477.8 MPa) f_{su} = 97.4 ksi (671.5 MPa) E_s = 10400 ksi (71700 MPa) E_{sh} = 840 ksi (5800 MPa) ε_{sh} = 0.00158 in/in ε_{su} = 0.126 in/in	Application: spliced bars (Element 2) with Beta = 0.80; L_{sp} = 7.75 in. (196.9 mm) Type: ReinforcingSteel f_y = 69.3 ksi (477.8 MPa) f_{su} = 97.4 ksi (671.5 MPa) E_s = 79600 ksi (550000 MPa) E_{sh} = 2350 ksi (16200 MPa) ε_{sh} = 0.00419 in/in ε_{su} = 0.0437 in/in
Application: unspliced (reference) bars (Element 3) without bond-slip effects Type: ReinforcingSteel f_y = 69.3 ksi (477.8 MPa) f_{su} = 97.4 ksi (671.5 MPa) E_s = 29000 ksi (200000 MPa) E_{sh} = 853 ksi (5880 MPa) ε_{sh} = 0.0115 in/in ε_{su} = 0.12 in/in	

4.2.2 Force-Displacement Relationships

The calculated pushover response of each column model, which is a global response consisting of the lateral force and lateral displacement (or drift), is compared with its corresponding measured column response. In future studies, the full cyclic response will be included for completeness.

Figure 4.6 shows the calculated and measured force-drift relationships for CIP. The calculated and measured initial stiffness matched well. The calculated forces were lower than those measured in the test between 1% and 3% drifts mainly because the analytical model lost a large portion of the concrete cover fibers in this range (loss of cover fibers means the residual strength of these fibers after reaching 0.005 in./in. strain was minimal). Note that the CIP column concrete cover was higher than a typical conventional column. This was done to include the coupler size and to have the same bar distribution in CIP and precast columns to investigate strength differences caused by the couplers. Furthermore, the calculated forces were slightly lower than the measured forces after 3% drifts, but overall matched well. The CIP calculated peak lateral strength was 61.9 kips (275 kN) while the CIP measured lateral strength was 65.4 kips (291 kN), or a 5.4% difference. The CIP calculated failure drift ratio was 7.64%, whereas the CIP measured failure drift was 8.96% (14.7% error). Furthermore, the model predicts that CIP fails by bar fracture, which was also seen in the actual test. Overall, the analytical model for CIP was able to reproduce the actual behavior with a reasonable accuracy.

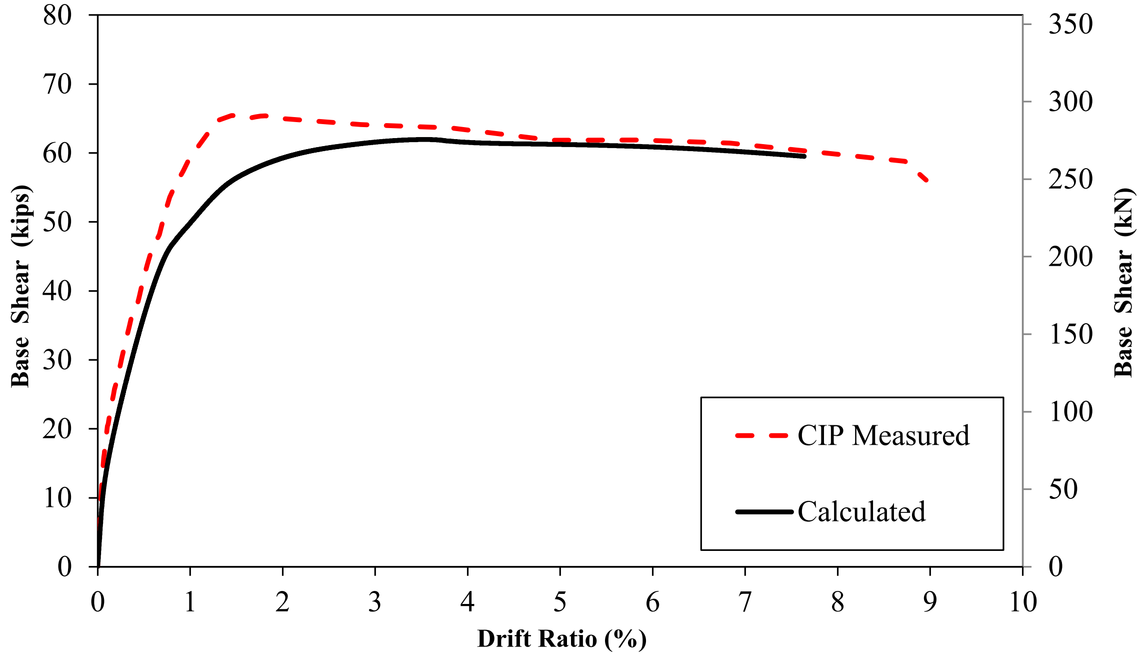

Figure 4.6 Calculated and Measured Force-Drift Relationships for CIP

Figure 4.7 shows the calculated and measured force-drift relationships for PGD. The calculated and measured initial stiffness matched well. The calculated forces were higher at low drift ratios, though the force matched well overall. The PGD calculated peak lateral strength was 72.5 kips (323 kN) while its measured lateral strength was 74.7 kips (332 kN), or a 2.9% difference. The PGD calculated failure drift ratio was 6.24% and its measured failure drift was 4.93% (26.6% error). Overall, the proposed column and coupler modeling methods for PGD were able to reproduce the actual behavior with a reasonable accuracy.

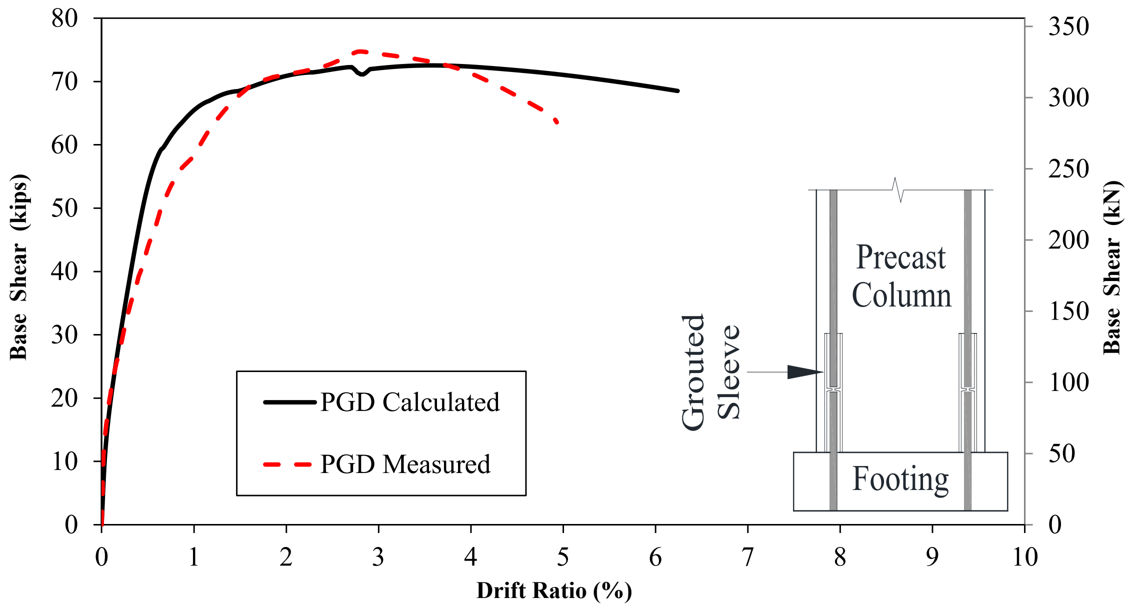

Figure 4.7 Calculated and Measured Force-Drift Relationships for PGD

Figure 4.8 shows the calculated and measured force-drift relationships for PGS. The calculated and measured initial stiffness matched well. The calculated forces were slightly higher, though the calculated forces followed those of the test. The PGS calculated peak lateral strength was 72.2 kips (3022 kN) while its measured lateral strength was 69.6 kips (310 kN), or a 3.3% difference. The PGS calculated drift capacity was 6.03% and its measured failure drift was 7.71% (approximately 21.8% error). Furthermore, the model predicts that PGS fails by bar fracture, which was also seen in the actual test. Overall, the analytical model for PGS was able to reproduce the actual behavior with a good accuracy.

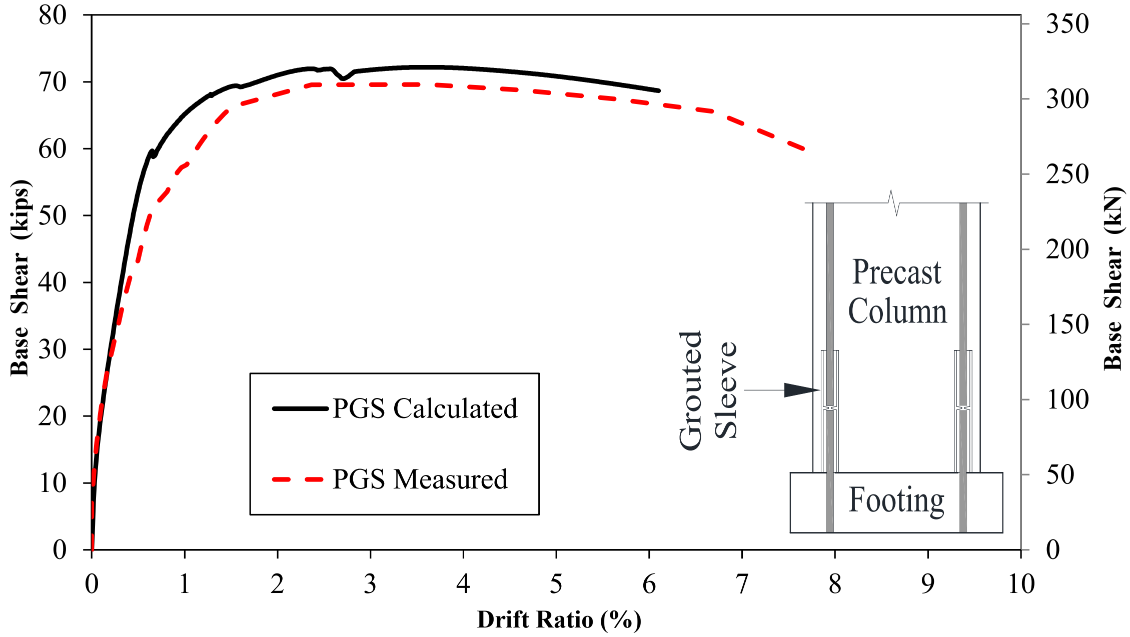

Figure 4.8 Calculated and Measured Force-Drift Relationships for PGS

As discussed in Chapter 3, five grouted-threaded hybrid couplers were prepared and tested, which were the same as those used in the PHD column. Four out of five couplers failed by the bar pullout in the in-air tensile testing. The PHD column with these couplers also failed by the bar pullout at the lowest displacement among all precast columns. Recommendations were made in Chapter 3 for the manufacturer to improve the quality control of this product since some studies reported bar fracture for this coupler type. In summary, only seismic couplers should be used in bridge columns while those used in PHD were not seismic splices based on the tensile testing performed in this project. Furthermore, the coupler model by Tazarv and Saiidi (2016, Fig. 4.2) has only been verified for seismic couplers (those that show bar fracture but not bar pullout or coupler fracture). Nevertheless, a pushover analysis was performed for PHD for completeness. Figure 4.9 shows the calculated and measured force-drift response for PHD. The calculated drift capacity based on the same method used for other precast columns using the average $\beta = 0.79$ was 5.9%, which was significantly higher than that measured in the test.

In an attempt to estimate the failure displacement of the PHD column using the current analytical model, a new technique was explored in which the analysis was stopped where the coupler strain (the first integration point in Element 2 in Fig. 4.4) reached the coupler test strain of 2.36%. Note in all other analyses, the strain of steel bar in Element 1 (base element) was monitored but not the coupler strain because the couplers were assumed to be stronger than their anchoring bars (seismic couplers). A good estimation of the column failure point was observed using this technique. The calculated and measured initial stiffness matched well. The calculated force was slightly higher. The PHD calculated peak lateral strength was 73.65 kips (327.6 kN) while its measured lateral strength was 71.5 kips (318 kN), or a 3.0% error. The PHD calculated drift capacity using the technique discussed above (stopping at the coupler pullout) was 2.71% and the measured failure drift was 3.33%. Overall, the proposed method captured the PHD column performance with a reasonable accuracy.

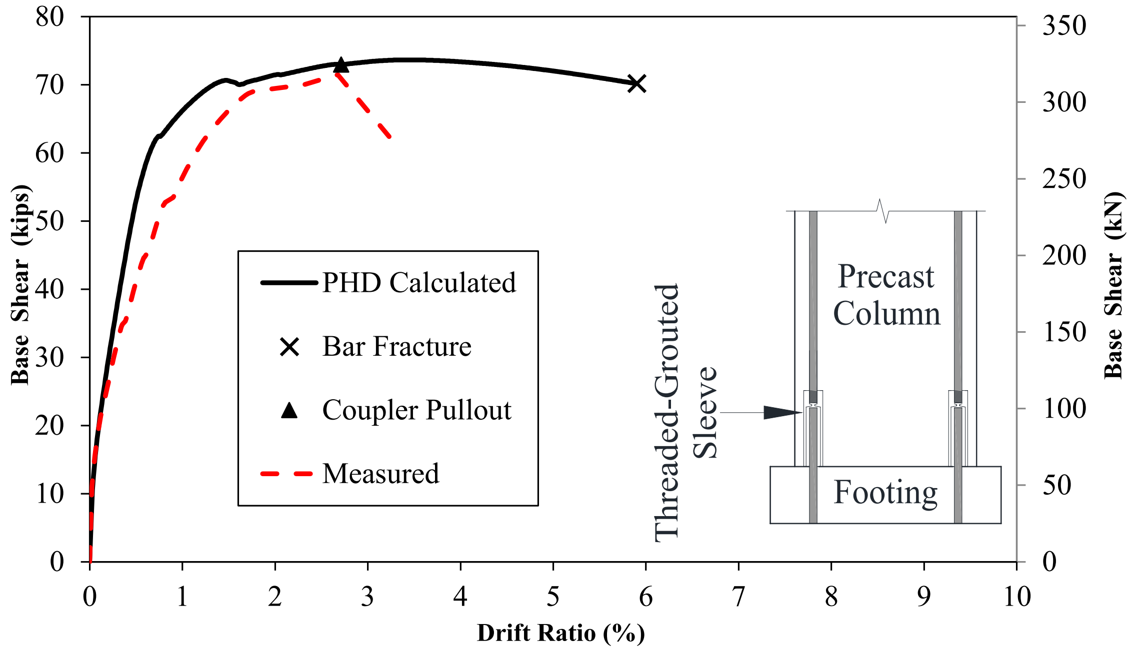

Figure 4.9 Calculated and Measured Force-Drift Relationships for PHD

Figure 4.10 shows the calculated and measured force-drift relationships for PHV. The calculated and measured initial stiffness matched well. The calculated forces were slightly higher, though the force matched well overall. The PHV calculated peak lateral strength was 75.4 kips (335 kN) while its measured lateral strength was 74.2 kips (330 kN), or a 1.6% difference. The PHV calculated failure drift ratio was 5.59% and its measured failure drift was 6.84% (18.3% error). Furthermore, the model predicts that PHV fails by bar fracture, which was also seen in the actual test. Overall, the analytical model for PHV was able to replicate the measured behavior with a good accuracy.

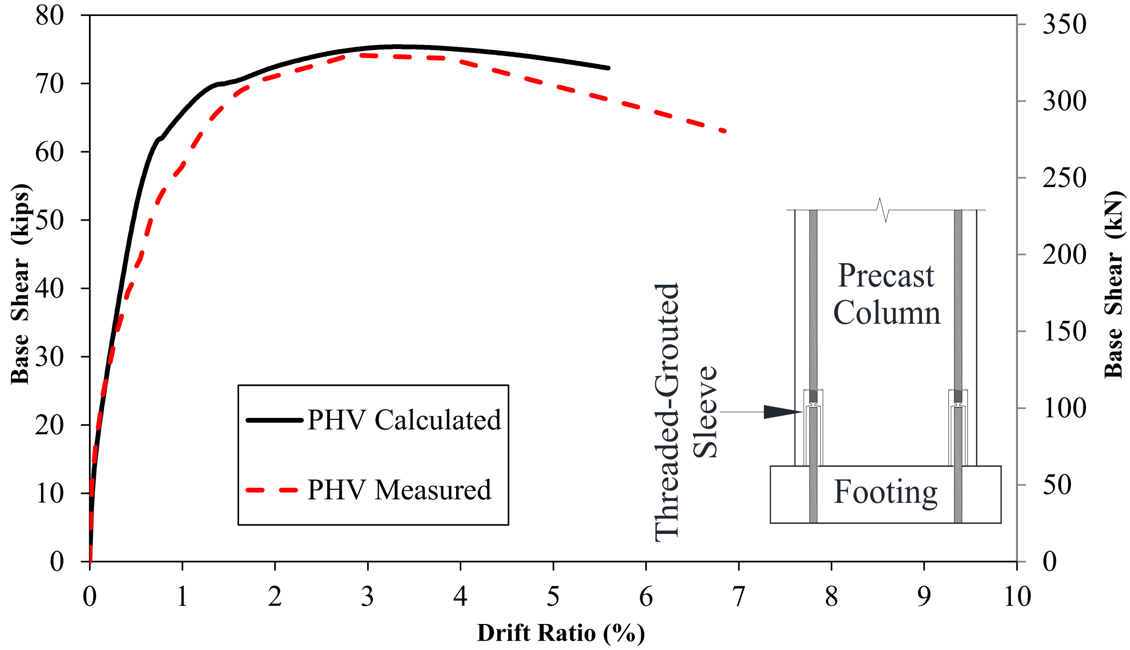

Figure 4.10 Calculated and Measured Force-Drift Relationships for PHV

Figure 4.11 shows the calculated and measured force-drift relationships for PTV. The calculated and measured initial stiffness agreed well. The PTV calculated peak lateral strength was 73.1 kips (325 kN) while its measured lateral strength was 73.7 kips (327.8 kN), or less than 1.0% error. The PTV calculated drift capacity was 6.77% and its measured failure drift was 6.04% (12% error). The model also predicts that PTV fails by bar fracture, which was also seen in the actual test at a similar drift ratio. Overall, the analytical model for PTV was able to reproduce the actual behavior with a good accuracy.

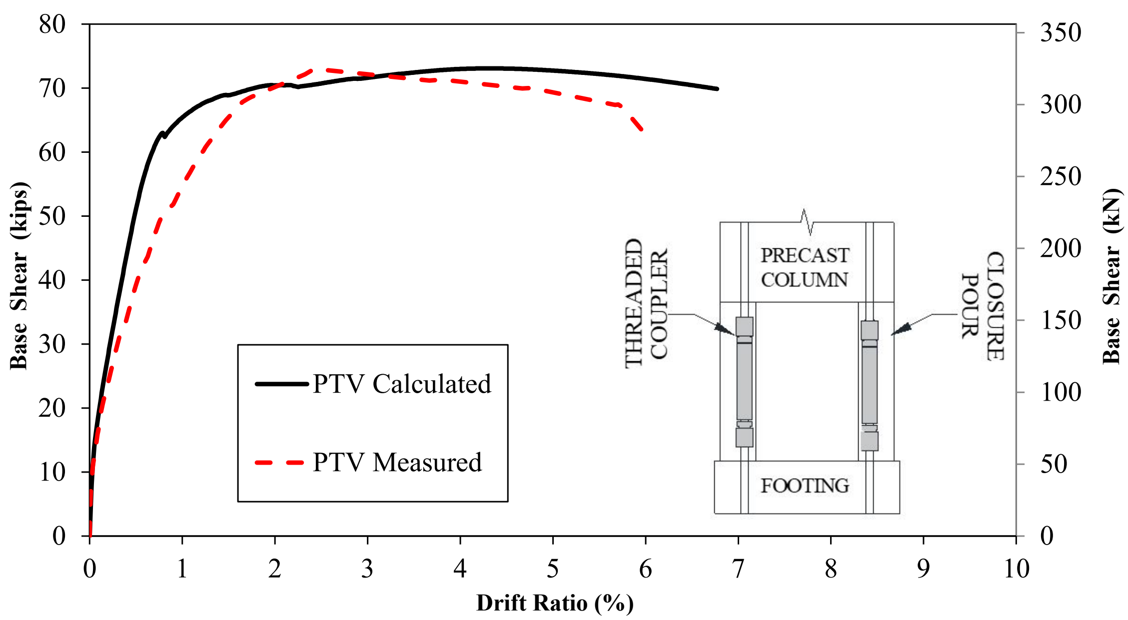

Figure 4.11 Calculated and Measured Force-Drift Relationships for PTV

Figure 4.12. shows the calculated and measured force-drift relationships for PHH. The calculated and measured initial stiffness agreed well. The PHH calculated peak lateral strength was 74.0 kips (329 kN) while its measured lateral strength was 72.3 kips (321 kN), or a 2.3% difference. The PHH calculated failure drift ratio was 6.0% and its measured failure drift ratio was 8.66% (30.7% error). Overall, the analytical model for PHH was able to reproduce the actual behavior with a reasonable accuracy.

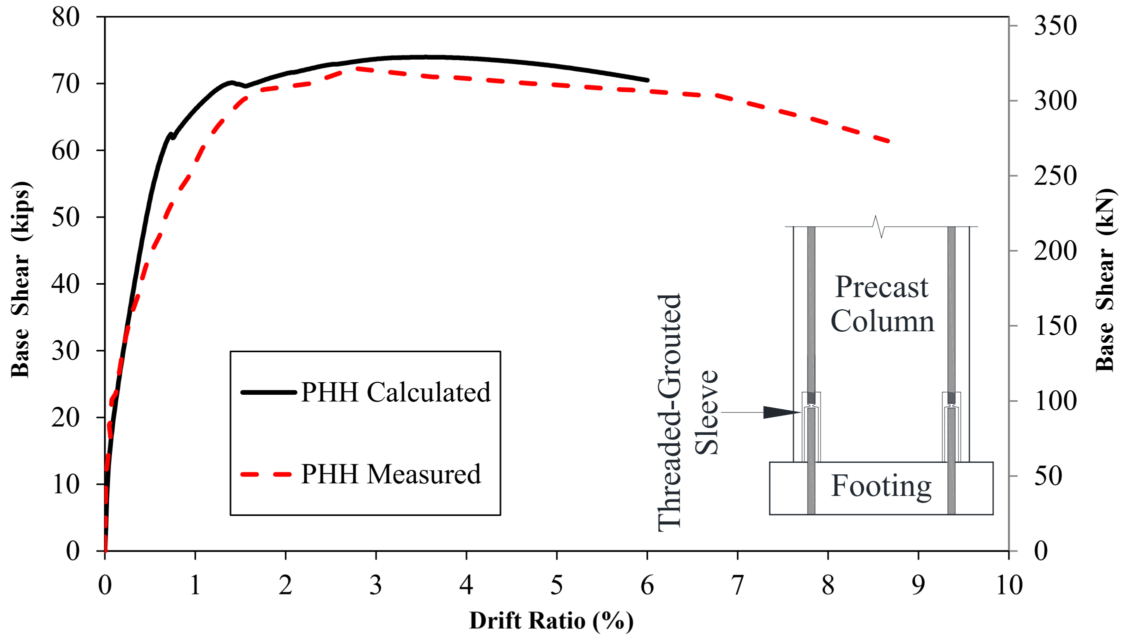

Figure 4.12 Calculated and Measured Force-Drift Relationships for PHH

4.2.3 Summary of Analytical Study

Table 4.6 presents a summary of the analytical study performed on the seven column test specimens. The error between the calculated and measured drifts is also presented in which the positive error means that the calculated displacement is higher than the measured displacement. The proposed analytical modeling method tends to underestimate the failure displacement of the CIP and the mechanically spliced precast columns, which is safe for the design purposes. On average, the proposed model resulted in 8.5% lower displacement capacities for the six mechanically spliced bridge columns.

Table 4.6 Summary of Analytical Study on Column Test Specimens

SP ID	Coupler Type	Manufacturer, Model	Coupler Length, $L_{sp,}$, in. (mm)	Coupler Rigid Length Factor, β	Measured Drift Ratio	Calculated Drift Ratio	Error (%)
CIP	N/A	N/A	N/A	N/A	8.96%	7.64%	-14.7
PGD	Grouted	Dayton Superior Corp., Sleeve Lock	16.5 (419)	0.70	4.93%	6.24%	+26.6
PGS	Grouted	Splice Sleeve North America, Inc., NMB	14.57 (370)	0.70	7.71%	6.03%	-21.8
PHD	Hybrid (Grouted-Threaded)	Dextra America, Inc., Groutec S with Bartec	9.45 (240)	0.79	3.33%	2.71%	-18.6
PHV	Hybrid (Grouted-Threaded)	nVent LENTON Corp., Interlock	8.63 (219)	0..82	6.84%	5.59%	-18.3
PTV	Threaded	nVent LENTON Corp., Ultimate PT15 Position	4.87 (124)	0.40	6.04%	6.77%	+12
PHH	Hybrid (Grouted-Headed)	Headed Reinforcement Corp., HRC560	7 (177.8)	0.80	8.66%	6.0%	-30.7

4.3 Summary and Conclusions

In this chapter, analytical modeling methods were developed, and pushover analyses were performed for the CIP and six mechanically spliced precast bridge columns tested in this project. The CIP and precast models were able to successfully reproduce the force-displacement relationship of each column. Overall, the proposed pushover models were found viable and may be used for the analysis and design of bridge columns incorporating seismic couplers.

4.4 References

AASHTO. (2014). "AASHTO Guide Specifications for LRFD Seismic Bridge Design," Washington, DC: American Association of State Highway and Transportation Officials.

Ameli, M.J., and Pantelides, C.P. (2017). "Seismic Analysis of Precast Concrete Bridge Columns Connected with Grouted Splice Sleeve Connectors." *Journal of Structural Engineering*, 143(2), p.04016176.

Haber, Z.B., Saiidi, M.S. and Sanders, D.H. (2015). "Behavior and Simplified Modeling of Mechanical Reinforcing Bar Splices." *ACI Structural Journal*, 112(2), p.179.

LaVoy, M.R. (2020). "Seismic Performance of Mechanically Spliced Bridge Columns Through Analytical Studies." MS Thesis, South Dakota State University, 106 pp.

Mander, J.B., Priestley, M.J.N., Park, R. (1988). "Theoretical Stress-Strain Model for Confined Concrete," *Journal of Structural Engineering*, ASCE, Vol. 114, No. 8, pp. 1804-1826.

OpenSees. (2016). "Open System for Earthquake Engineering Simulations," Version 2.4.1, Berkeley, CA, Available online: http://opensees.berkeley.edu.

Saiidi, M.S., Mehraein, M., Shrestha, G., Jordan, E., Itani, A., Tazarv, M., Sanders, D., Murphy, T.M., Reno, M.L., and Pohll, M.N. (2020). "Proposed AASHTO Seismic Specifications for ABC Column Connections," National Academies of Sciences, Engineering, and Medicine, NCHRP Report No. 935, Washington, DC: The National Academies Press, 354 pp.

Tazarv, M., and Saiidi, M.S. (2014) "Next Generation of Bridge Columns for Accelerated Bridge Construction in High Seismic Zones," Center For Civil Engineering Earthquake Research, Department of Civil and Environmental Engineering, University of Nevada, Reno, Nevada, Report No. CCEER-14-06, 400 pp.

Tazarv, M., and Saiidi, M.S. (2016). "Seismic Design of Bridge Columns Incorporating Mechanical Bar Splices in Plastic Hinge Regions," *Engineering Structures*, DOI: 10.1016/j.engstruct.2016.06.041, Vol 124, pp. 507-520.

5. ANALYTICAL INVESTIGATION OF MECHANICALLY SPLICED BRIDGE COLUMNS

5.1 Introduction

Mechanical bar splices are not currently allowed to be incorporated in the plastic hinge region of bridge columns located in high seismic areas of the nation. If allowed, precast column connections through bar couplers may gain interest for field applications. The seismic performance of mechanically spliced bridge columns through a systematic and unified experiment was investigated in the present study and discussed in Chapter 3. Furthermore, post-test analyses of the mechanically spliced bridge columns were performed in Chapter 4. Nevertheless, the effects of couplers on the displacement capacities and demands of a wide range of RC bridge columns using validated models are yet to be investigated.

A comprehensive parametric study was conducted in this chapter to determine the effects of nine mechanical bar couplers on the displacement capacity and demand of precast bridge columns. Twenty-two columns were designed with a circular cross section and 23 columns were designed with a square cross section. The column aspect ratio, axial load index, and ductility target were varied in the parametric study. Nonlinear static and dynamic analyses were performed for each mechanically spliced column using the validated models. This chapter presents the details of the parametric study.

5.2 Design and Pushover Modeling Methods for Conventional CIP Columns

Twenty-two CIP columns with a circular section (Table 5.1) and 23 CIP columns with a square section (Table 5.2) were designed to serve as reference models without any couplers. Note that 27 combinations were feasible per section type by varying the column parameters discussed below. However, some of the tall column models with high axial loads could not be analyzed due to convergence issues when P-Δ effects were included. Therefore, those column models were removed from the analysis.

The columns had either 4-ft (1.22-m) diameter (circular cross section) or 4-ft (1.22-m) side dimension (square cross section). Figure 5.1 shows the column detailing and sections. The column aspect ratio (AR), the column axial load index (ALI), and the column displacement ductility (D or μ) were varied to cover a wide range of practical bridge columns. AR is defined as the ratio of the column length to the column height, ALI is the ratio of the column axial load to the product of the column cross-sectional area and the column concrete compressive strength, and D is the ratio of the column ultimate displacement to the column idealized yield displacement as defined in AASHTO SGS (2011). Three ARs of 4, 6, and 8 were chosen corresponding to column heights of 16-ft (4.88-m), 24-ft (7.32-m), and 32-ft (9.75-m), respectively. Furthermore, three ALIs of 5%, 10%, and 15% and three target ductilities of 3, 5, and 7 were included in the design. Tables 5.1 and 5.2 also provide the transverse reinforcement details for each of the combinations that could be designed for the circular and square columns, respectively. The naming convention of each column refers to the specific set of design parameters assigned to each individual column.

All columns were designed with No. 10 (32-mm) bars. This was done since the coupler rigid length factors for No. 10 (32-mm) bars are available for nine coupler products (Dahal and Tazarv, 2020). The circular columns had 18 No.10 (32-mm) longitudinal reinforcing bars ($\rho_l = 1.26\%$) and the square columns had 24 No.10 (32-mm) longitudinal bars evenly spaced around the sections ($\rho_l = 1.32\%$).

Table 5.1 Details of Circular CIP Columns

Circular Column ID	Transverse Reinforcement Details	Ultimate Drift Ratio (%)	Ductility (μ)
CIP-AR4-ALI5-D3	No.3 (10-mm) Hoops @ 11-in. (279-mm)	1.66	2.96
CIP-AR4-ALI5-D5	No.4 (15.mm) Hoops @ 4-in. (102-mm)	3.19	4.91
CIP-AR4-ALI5-D7	No.5 (16-mm) Hoops @ 4.5-in. (114-mm)	4.62	6.90
CIP-AR4-ALI10-D3	No.3 (10-mm) Hoops @ 5-in. (127-mm)	1.66	3.02
CIP-AR4-ALI10-D5	No.5 (16-mm) Hoops @ 4.5-in. (114-mm)	3.01	4.94
CIP-AR4-ALI10-D7	No.7 (22-mm) Hoops @ 5.5-in. (140-mm)	4.45	7.06
CIP-AR4-ALI15-D3	No.4 (15.mm) Hoops @ 6-in. (152-mm)	1.65	3.05
CIP-AR4-ALI15-D5	No.6 (19-mm) Hoops @ 5-in. (127-mm)	3.11	5.10
CIP-AR4-ALI15-D7	No.7 (22-mm) Hoops @ 4.5-in. (114-mm)	4.41	7.00
CIP-AR6-ALI5-D3	No.3 (10-mm) Hoops @ 10-in. (254-mm)	2.53	3.01
CIP-AR6-ALI5-D5	No.4 (15.mm) Hoops @ 4-in. (102-mm)	4.67	5.08
CIP-AR6-ALI5-D7	No.4 (15.mm) Hoops @ 5.in. (76-mm)	6.56	7.05
CIP-AR6-ALI10-D3	No.4 (15.mm) Hoops @ 10-in. (254-mm)	2.35	3.05
CIP-AR6-ALI10-D5	No.5 (16-mm) Hoops @ 5-in. (127-mm)	4.18	4.98
CIP-AR6-ALI10-D7	No.5 (16-mm) Hoops @ 5.in. (76-mm)	5.86	6.81
CIP-AR6-ALI15-D3	No.4 (15.mm) Hoops @ 7.5-in. (191-mm)	2.21	2.95
CIP-AR6-ALI15-D5	No.7 (22-mm) Hoops @ 7-in. (178-mm)	4.16	5.07
CIP-AR8-ALI5-D3	No.3 (10-mm) Hoops @ 12-in. (305-mm)	3.22	3.01
CIP-AR8-ALI5-D5	No.4 (15.mm) Hoops @ 4.5-in. (114-mm)	5.68	4.98
CIP-AR8-ALI5-D7	No.4 (15.mm) Hoops @ 5.in. (76-mm)	7.64	6.64
CIP-AR8-ALI10-D3	No.3 (10-mm) Hoops @ 7.5-in. (191-mm)	2.89	2.98
CIP-AR8-ALI15-D3	No.5 (16-mm) Hoops @ 5-in. (127-mm)	3.06	3.00

Table 5.2 Details of Square CIP Columns

Square Column ID	Transverse Reinforcement Details	Ultimate Drift Ratio (%)	Ductility (μ)
CIP-AR4-ALI5-D3	No.3 (10-mm) Ties @ 12-in. (305-mm)	1.69	3.13
CIP-AR4-ALI5-D5	No.5 (16-mm) Ties @ 12-in. (305-mm)	2.89	4.98
CIP-AR4-ALI5-D7	No.5 (16-mm) Ties @ 7.5-in. (191-mm)	4.27	7.00
CIP-AR4-ALI10-D3	No.3 (10-mm) Ties @ 8-in. (205.mm)	1.51	3.02
CIP-AR4-ALI10-D5	No.4 (15.mm) Ties @ 5-in. (127-mm)	2.81	4.93
CIP-AR4-ALI10-D7	No.7 (22-mm) Ties @ 10-in. (254-mm)	4.03	6.83
CIP-AR4-ALI15-D3	No.4 (15.mm) Ties @ 9.5-in. (241-mm)	1.49	2.98
CIP-AR4-ALI15-D5	No.5 (16-mm) Ties @ 6-in. (152-mm)	2.81	5.02
CIP-AR4-ALI15-D7	No.6 (19-mm) Ties @ 5.5-in. (140-mm)	4.07	6.90
CIP-AR6-ALI5-D3	No.3 (10-mm) Ties @ 12-in. (305-mm)	2.50	3.16
CIP-AR6-ALI5-D5	No.4 (15.mm) Ties @ 8-in. (205.mm)	4.23	5.04
CIP-AR6-ALI5-D7	No.6 (19-mm) Ties @ 11-in. (279-mm)	5.95	6.84
CIP-AR6-ALI10-D3	No.3 (10-mm) Ties @ 8-in. (205.mm)	2.25	3.08
CIP-AR6-ALI10-D5	No.4 (15.mm) Ties @ 5.5-in. (140-mm)	3.92	4.96
CIP-AR6-ALI10-D7	No.5 (16-mm) Ties @ 5.in. (76-mm)	5.55	6.94
CIP-AR6-ALI15-D3	No.4 (15.mm) Ties @ 10-in. (254-mm)	2.17	3.00
CIP-AR6-ALI15-D5	No.7 (22-mm) Ties @ 7-in. (178-mm)	3.84	4.92
CIP-AR8-ALI5-D3	No.3 (10-mm) Ties @ 12-in. (305-mm)	3.24	3.18
CIP-AR8-ALI5-D5	No.4 (15.mm) Ties @ 8.5-in. (216-mm)	5.35	5.05
CIP-AR8-ALI5-D7	No.6 (19-mm) Ties @ 11-in. (279-mm)	7.48	6.99
CIP-AR8-ALI10-D3	No.3 (10-mm) Ties @ 8.5-in. (216-mm)	2.89	3.04
CIP-AR8-ALI10-D5	No.4 (15.mm) Ties @ 6-in. (152-mm)	4.90	5.05
CIP-AR8-ALI15-D3	No.3 (10-mm) Ties @ 5-in. (127-mm)	2.83	3.04

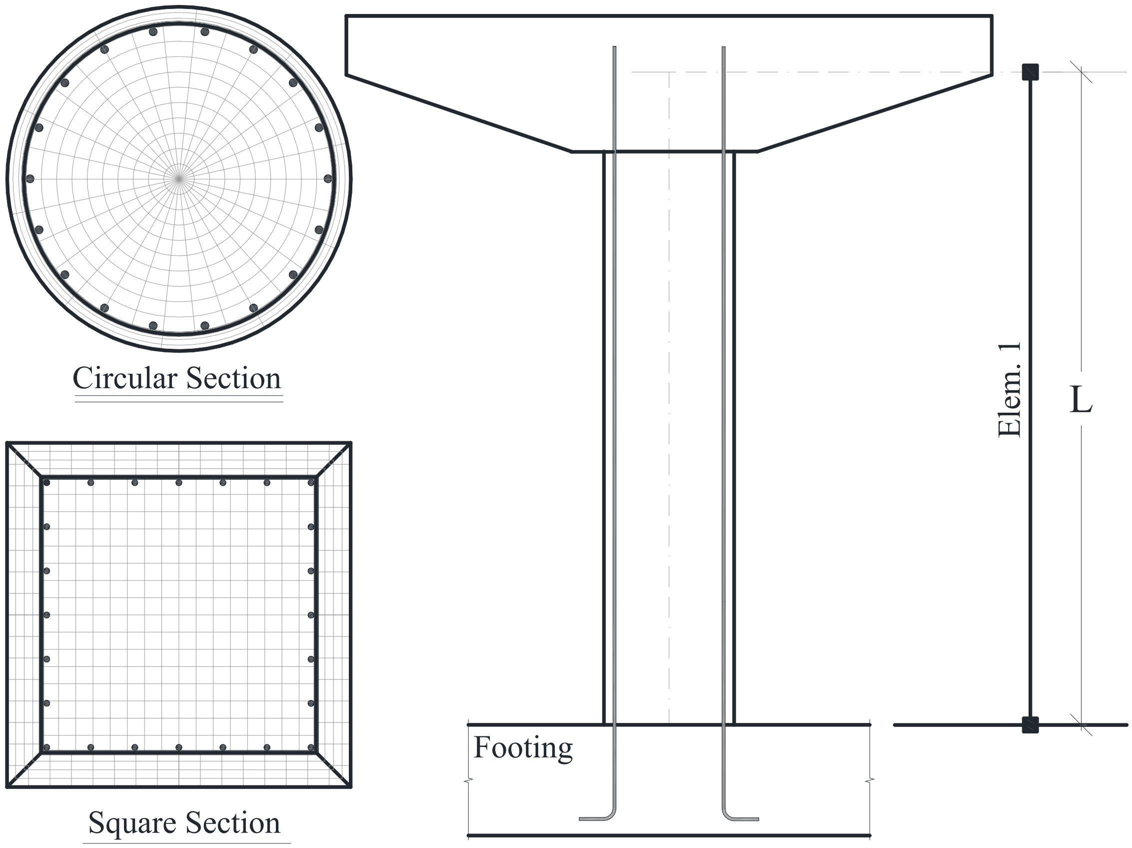

Figure 5.1 Cast-in-Place Reference Column Models in Parametric Study

The modeling of the CIP columns followed the validated model discussed in Sec. 4.2 of Chapter 4. A 3D finite element model with six degrees of freedom (DOFs) was used with the P-Δ effects included. A single "forceBeamColumn" element was used to represent CIP. In circular columns, the core concrete was discretized into 30×10 fibers (as schematically shown in Fig. 5.1) and "Concrete01" material model was used for these fibers. The cover concrete was discretized into 10×10 fibers, which were modeled using the "Concrete01" material model. Clear cover defined as the distance between the column face to the exterior of the confining reinforcement was 2 in. (51 mm). In square columns, the core concrete was discretized into 16×16 rectangular fibers (Fig. 5.1). The core patch began at the center of the column and extended outward ending at the center of the outer ring of the confining reinforcement. The cover concrete at each side of the section was discretized into 16×4 fibers. The inner boundary of the cover patches was set at the center of the outer ring confining reinforcement. "Concrete01" material was used for both the core and cover concrete fibers. The confinement properties of the core concrete were calculated using the model proposed by Mander et al. (1988). The cover concrete compressive strength in all models was set at 5 ksi (34 MPa). All reinforcing bars were modeled following AASHTO SGS (2011) expected mechanical properties for ASTM A706 Gr.60 (414-MPa) steel. All longitudinal bars were modeled using a uniaxial material model named "ReinforcingSteel."

5.3 Design and Pushover Modeling Methods for Mechanically Spliced Columns

Figure 5.2 schematically shows the model detail for circular and square columns. The modeling methods for mechanically spliced bridge columns follow those discussed and validated in the previous chapter for multiple mechanically spliced bridge columns. The result of the same modeling method for another grouted coupler column, GCNP, tested by Haber et al. (2014) is shown in Figure 5.3. The lateral strength of the column was underestimated by 11%. Nevertheless, the column displacement capacity was well estimated using the proposed method. The actual grouted coupler column failed at a drift ratio of 5.95% while the analytical model estimated the column failure to be at a drift ratio of 6.07%, only a 2% difference.

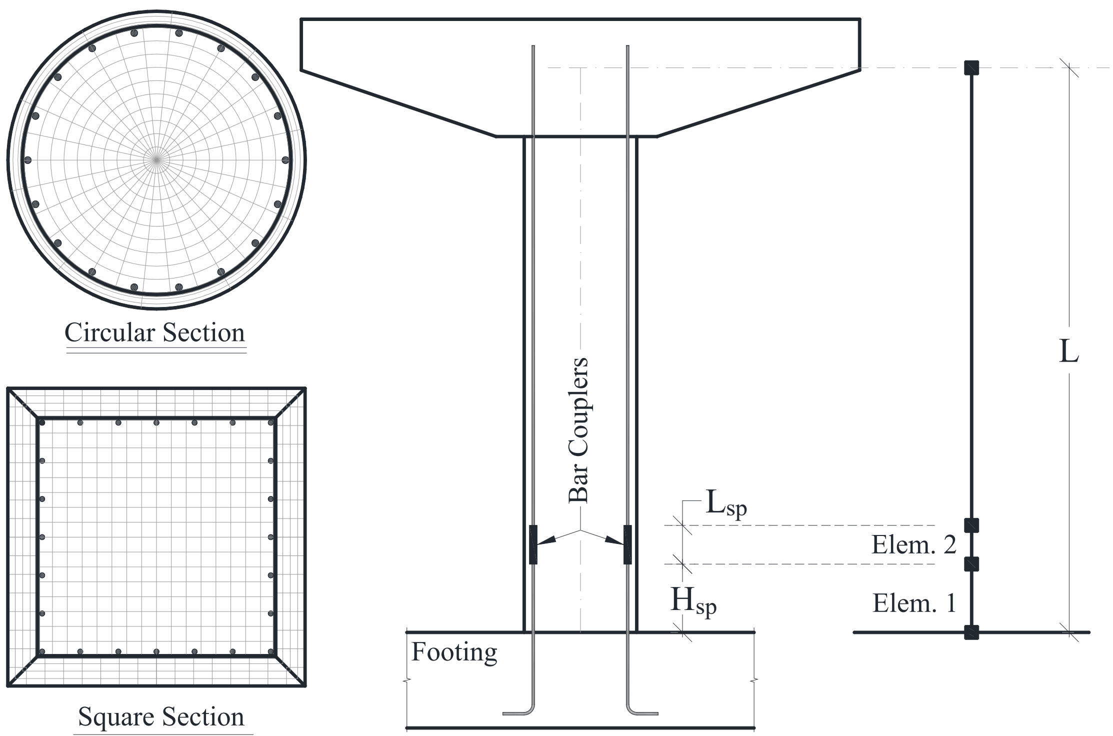

Figure 5.2 Mechanically Spliced Column Analytical Model in Parametric Study

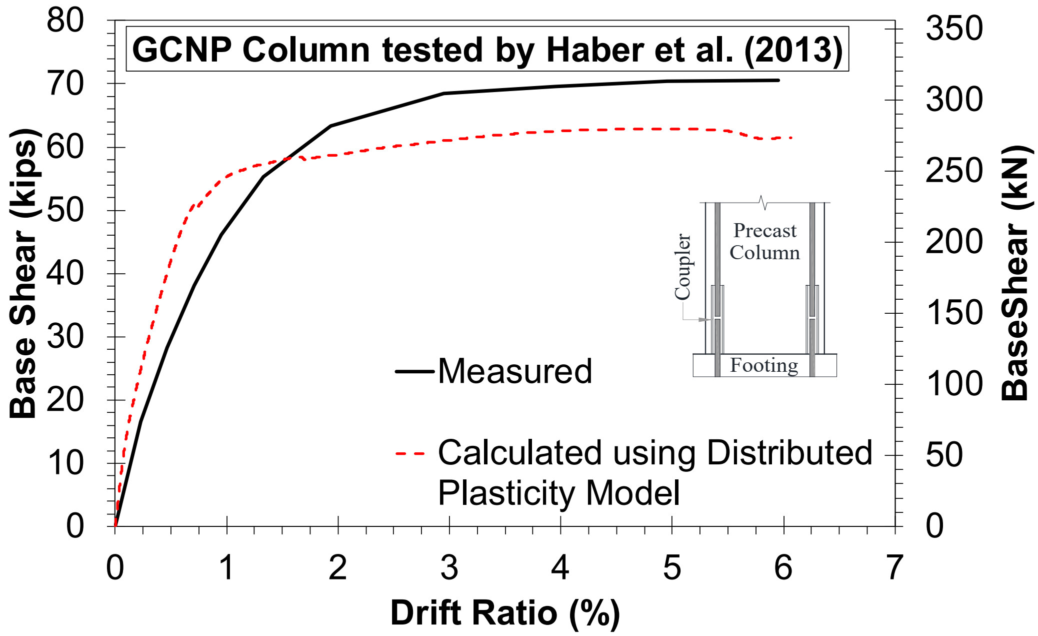

Figure 5.3 Measured and Calculated Force-Drift Relationships for GCNP Column

5.3.1 Reinforcing Steel Bar and Coupler Properties

As was discussed, all longitudinal bars in the present parametric study were assumed to be No. 10 (32-mm) ASTM A706 Grade 60 (414 MPa) steel bars. Table 5.3 presents the AASHTO expected mechanical properties (AASHTO SGS, 2011) for these bars. The steel bar properties (Table 5.3) were used in Element 1 of the CIP models (Fig. 5.1) and Elements 1 and 3 of the spliced models (Fig. 5.2).

Table 5.3 AASTHO Expected Properties for No. 10 (32-mm) ASTM A706 Gr. 60 Reinforcing Bars

Property	Notation	ASTM A706 Grade 60 (414 MPa)
Expected Yield Stress, ksi (MPa)	f_{ye}	68 (469)
Expected Tensile Strength, ksi (MPa)	f_{ue}	95 (655)
Expected Yield Strain	ε_{ye}	0.0023
Onset of Strain Hardening	ε_{sh}	0.0115
Ultimate Tensile Strain	ε_{su}	0.12
Modulus of Elasticity, ksi (MPa)	E_s	29,000 (200,000)

The critical points of the steel material model should be adjusted to include the coupler effect. The properties for each coupler were calculated using the model proposed by Tazarv and Saiidi (2016) as described in Chapter 2. Based on this model, the coupler rigid length factor and the physical length of the coupler have the most influence on the mechanical properties of a splice. Table 5.4 presents the key parameters of the nine bar couplers used in this study, including the coupler length (L_{sp}) and the coupler rigid length factor (β). The length was taken from the manufacturer's product datasheet for each coupler, and the coupler rigid length factors for No. 10 (32-mm) bar splices were those recommended by Dahal and Tazarv (2020). Table 5.5 presents the mechanical properties calculated for each coupler using Tazarv's model. Couplers do not change the strength of the anchored bar(s). Therefore, the splice yield (f_y^{sp}) and ultimate strength (f_u^{sp}) were set equal to those for unspliced steel bars. The two threaded (TH) couplers produced by Dextra America, Inc. were grouped together since there was only a marginal difference between the two products. The properties of the "Bartec Position Splice" were used to represent TH in this study. In summary, eight couplers were used in the parametric study.

The detailing of the CIP columns was modified by incorporating these bar couplers at the column base. Figures 5.4 and 5.5, respectively, show the circular and square column sections spliced with these eight bar couplers. The longitudinal bars of the spliced columns were shifted inward to accommodate the couplers with different geometries. Nevertheless, other design parameters and detailing were kept the same as the reference CIP columns.

Table 5.4 Selected Couplers and Corresponding Properties

Coupler	Manufacturer	Coupler Model	β	L_{sp}, in. (mm)
HR	Headed Reinforcement Corp.	Xtender® 500/510 Standard Coupler	0.55	3.75 (95)
TH	Dextra America, Inc.	Bartec Standard Splice	1.60	2.76 (70)
TH*	Dextra America, Inc.	Bartec Position Splice	1.65	2.76 (70)
THT	nVent LENTON Corp.,	Lenton Plus, Standard Coupler (A12)	1.05	4.23 (107)
SW	Bar Splice Products, Inc.	BarGrip® XL	0.95	8.30 (211)
GSN	Splice Sleeve North America, Inc.	NMB	0.85	17.91 (455)
GSD	Dayton Superior Corp.,	D410 Sleeve-Lock® Grout Sleeve	0.65	17.99 (457)
HYD	Dextra America, Inc.	Griptec®	0.85	11.81 (300)
HYE	nVent LENTON Corp.,	Lenton Interlock	0.80	10.82 (275)

Note: "β" values were for No. 10 (32-mm) bars (Dahal and Tazarv, 2020)
* "Bartec Position Splice" used to represent the behavior of two threaded couplers by Dextra America, Inc.

Table 5.5 Calculated Coupler Mechanical Properties

Coupler	E_s^{sp}, ksi (MPa)	E_{sh}^{sp}, ksi (MPa)	ε_y^{sp}	ε_{sh}^{sp}	ε_u^{sp}
HR	43,148 (297,505)	1,785 (12,308)	0.00158	0.00773	0.08065
TH*	206,032 (1,420,590)	8525 (58,780)	0.00033	0.00162	0.01689
THT	84,316 (581,359)	3489 (24,057)	0.00081	0.00396	0.04127
SW	106,382 (733,504)	4402 (30,352)	0.00064	0.00313	0.03271
GSN	113,470 (782,376)	4695 (32,372)	0.00060	0.00294	0.03067
GSD	67,376 (464,558)	2788 (19,223)	0.00101	0.00495	0.05165
HYD	96,521 (665,512)	3994 (27,539)	0.00070	0.00346	0.03605
HYE	82,364 (567,900)	3408 (23,498)	0.00083	0.00405	0.04225

* "Bartec Position Splice" used to represent the behavior of two threaded couplers by Dextra America, Inc.

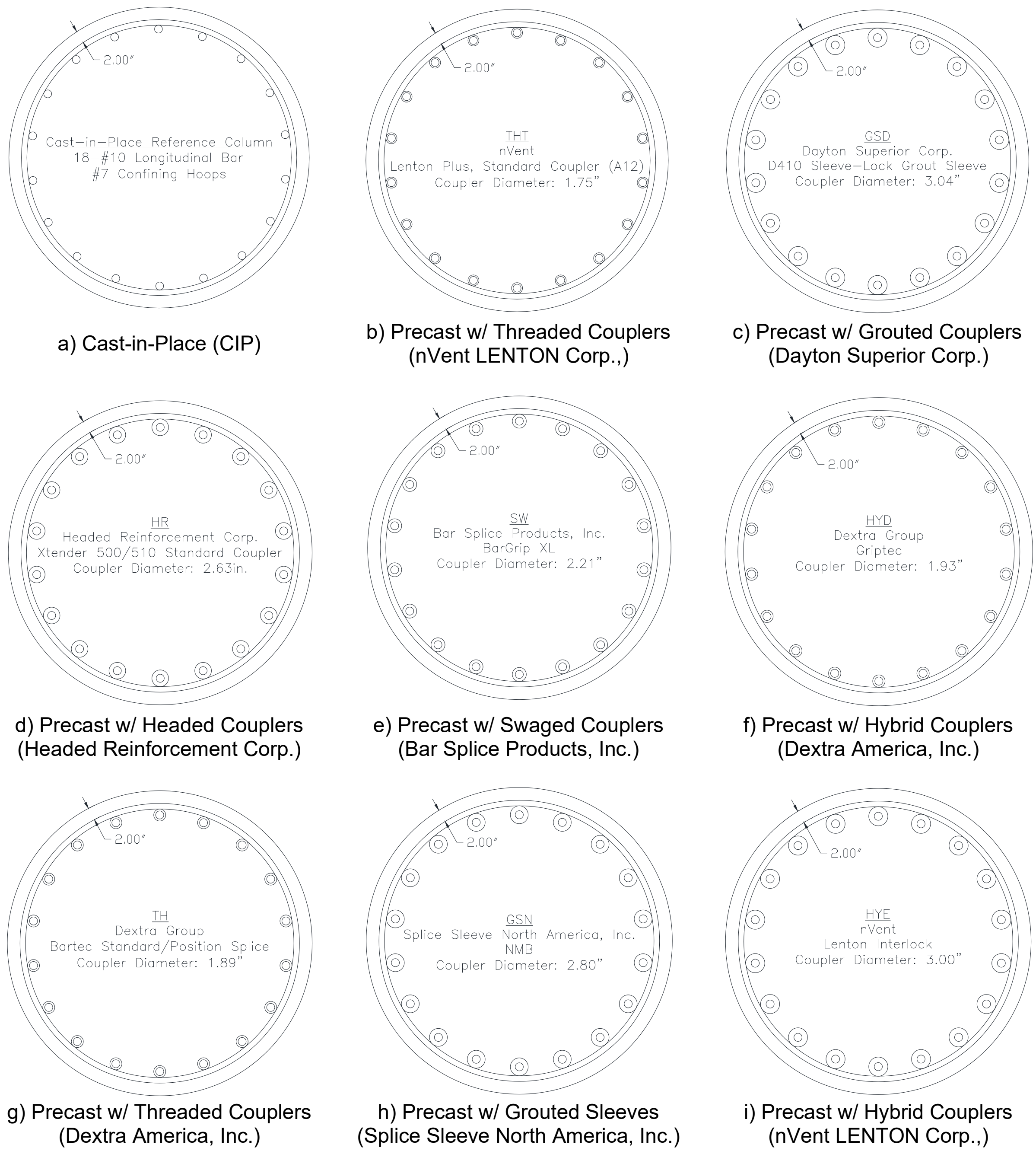

Figure 5.4 Mechanically Spliced Circular Column Sections in Parametric Study

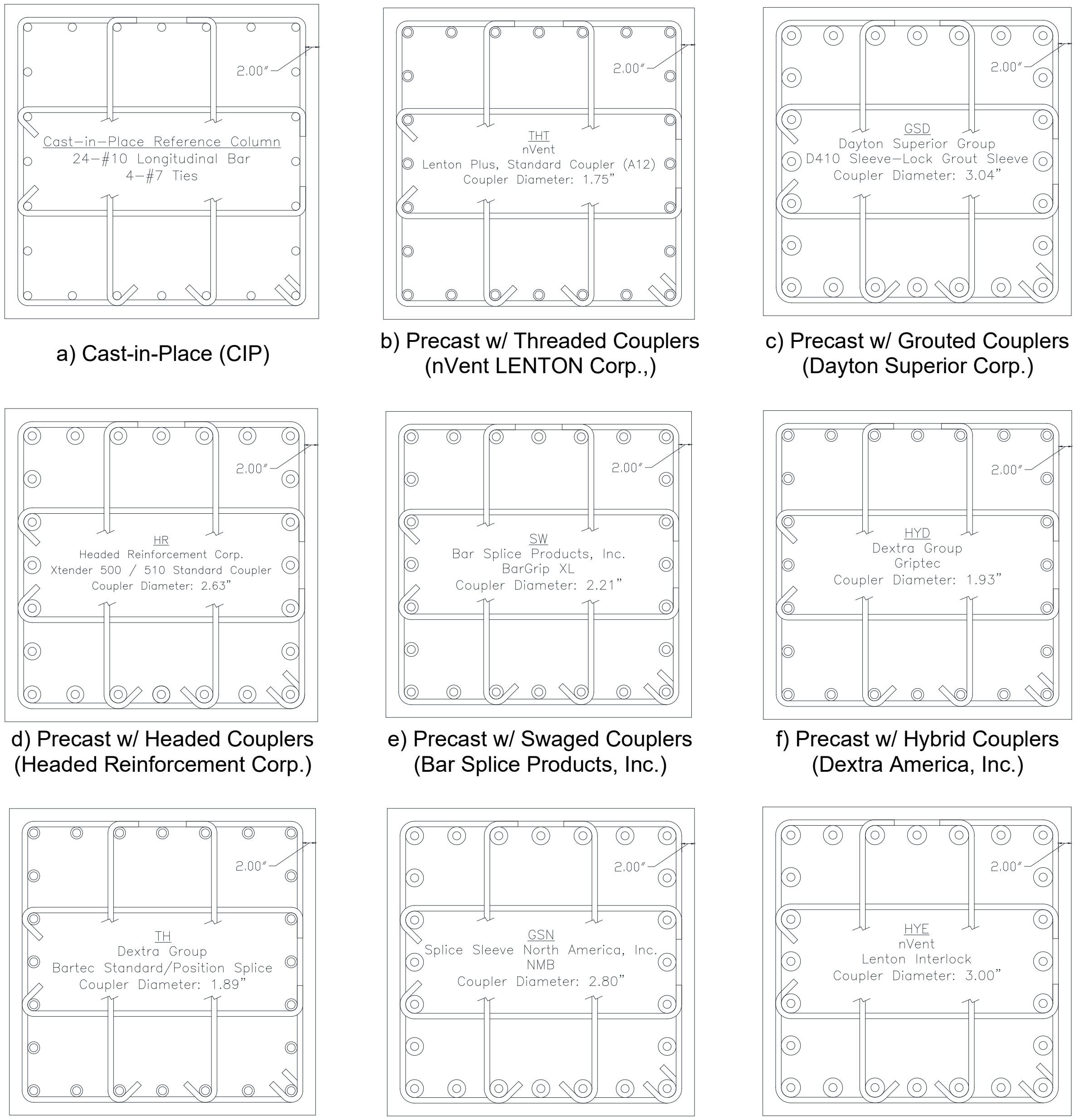

a) Cast-in-Place (CIP)

b) Precast w/ Threaded Couplers (nVent LENTON Corp.,)

c) Precast w/ Grouted Couplers (Dayton Superior Corp.)

d) Precast w/ Headed Couplers (Headed Reinforcement Corp.)

e) Precast w/ Swaged Couplers (Bar Splice Products, Inc.)

f) Precast w/ Hybrid Couplers (Dextra America, Inc.)

g) Precast w/ Threaded Couplers (Dextra America, Inc.)

h) Precast w/ Grouted Sleeves (Splice Sleeve North America, Inc.)

i) Precast w/ Hybrid Couplers (nVent LENTON Corp.,)

Figure 5.5 Mechanically Spliced Square Column Sections in Parametric Study

5.4 Results of Parametric Capacity Analyses

Twenty-two circular and 23 square columns were included in the capacity analyses (or pushover) as the reference CIP columns. Furthermore, eight different coupler products were incorporated at the base of each CIP to investigate the seismic performance of the mechanically spliced columns. A total of 405 bridge columns were analyzed in the present study using a nonlinear static pushover method to determine the column behavior. The results of the pushover analyses are summarized herein.

5.4.1 Pushover Analysis Results

The pushover results for each circular CIP column and its eight corresponding mechanically spliced columns were superimposed in a figure to better comment on the coupler effects (Fig. 5.6 to 5.27). We can see that incorporating mechanical bar splices in the plastic hinge region of precast circular columns generally reduces the column displacement capacity and slightly increases the column lateral strength. The columns with HR couplers exhibited the largest displacement capacities among spliced columns, and columns with GD couplers showed the lowest displacement capacities. For example, the circular "AR4-ALI10-D7" column spliced with HR couplers exhibited 12.3% lower displacement capacity than its corresponding CIP column, and the circular "AR4-ALI10-D7" column spliced with GSN couplers exhibited a 39.6% lower displacement capacity compared with its corresponding CIP. The GSN couplers typically showed the most increase in the base shear. Nevertheless, the lateral strength of the mechanically spliced columns was no more than 7.6% compared with their corresponding CIPs.

Similar to the circular columns, a single pushover plot was generated for each square column to better understand the effect of couplers on the displacement capacity of square columns. Each plot contains the force-drift response of the CIP reference column and the eight spliced columns with the same design parameters as the corresponding CIP column. Figures 5.28 to 5.50 show the pushover (force-drift) plot for each square column. Similar to circular columns, the figures indicate that adding mechanical bar couplers to the plastic hinge region of square columns reduces the displacement capacity. Further, it appears that HR couplers have the least reduction/effects on the square columns and GS couplers have the highest effects. For example, the square "AR4-ALI5-D7" column spliced with HR couplers exhibited 13.9% less displacement capacity than its reference CIP column, and the square "AR4-ALI5-D7" column spliced with GSN couplers exhibited a 40.9% reduction in the displacement capacity.

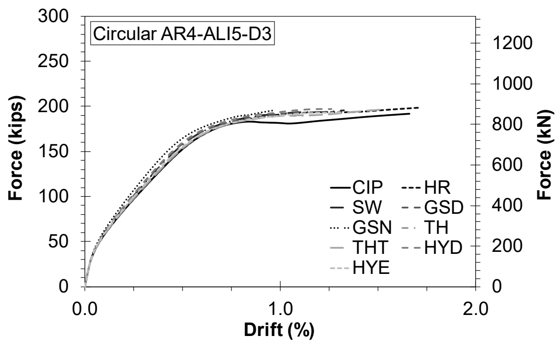

Figure 5.6 Pushover Analysis for Circular AR4-ALI5-D3

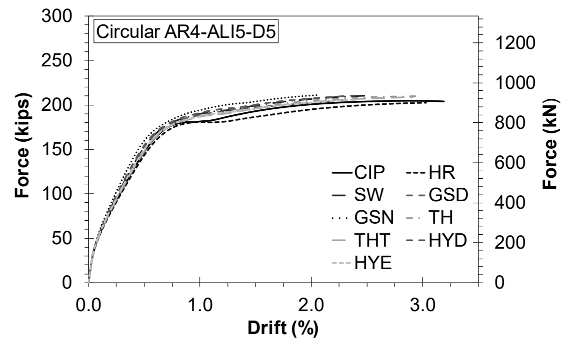

Figure 5.7 Pushover Analysis for Circular AR4-ALI5-D5

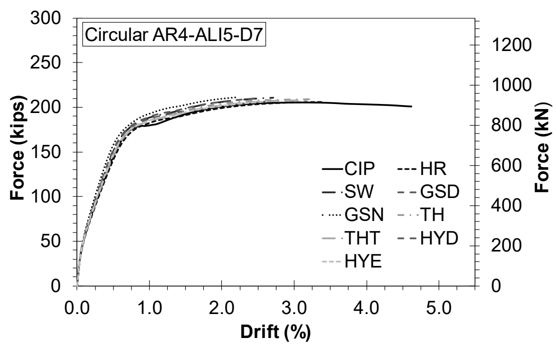

Figure 5.8 Pushover Analysis for Circular AR4-ALI5-D7

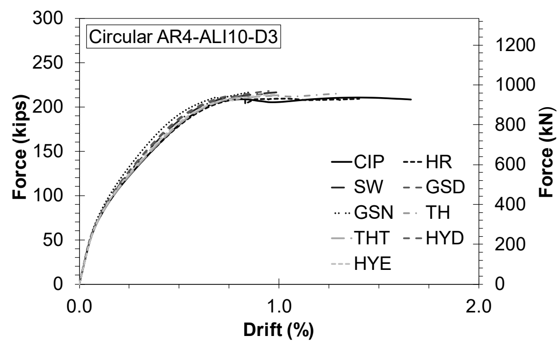

Figure 5.9 Pushover Analysis for Circular AR4-ALI10-D3

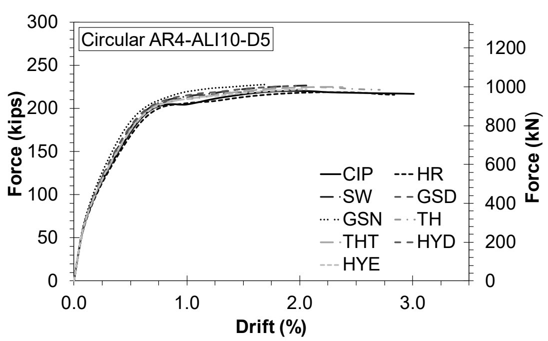

Figure 5.10 Pushover Analysis for Circular AR4-ALI10-D5

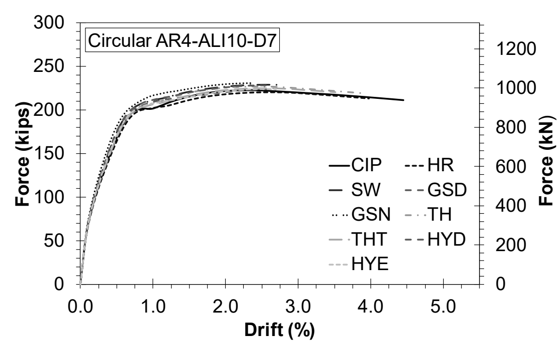

Figure 5.11 Pushover Analysis for Circular AR4-ALI10-D7

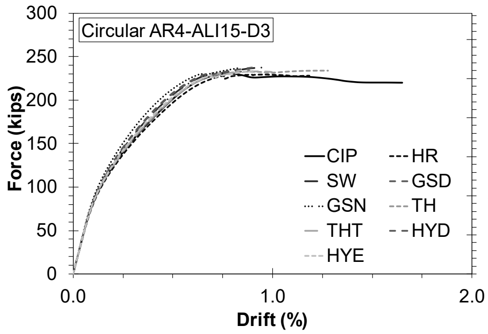

Figure 5.12 Pushover Analysis for Circular AR4-ALI15-D3

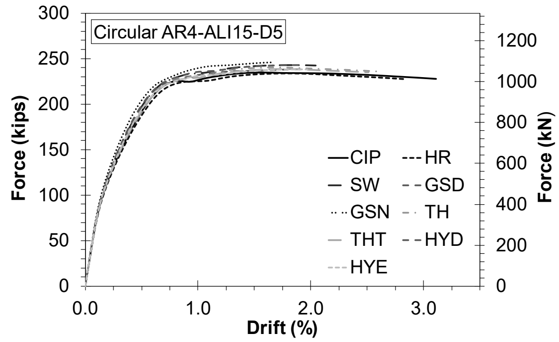

Figure 5.13 Pushover Analysis for Circular AR4-ALI15-D5

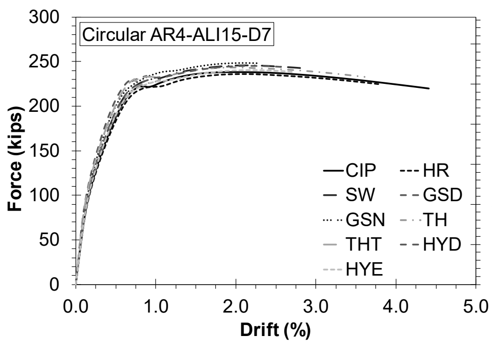

Figure 5.14 Pushover Analysis for Circular AR4-ALI15-D7

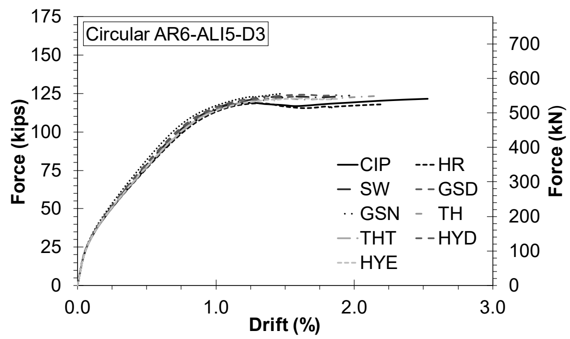

Figure 5.15 Pushover Analysis for Circular AR6-ALI5-D3

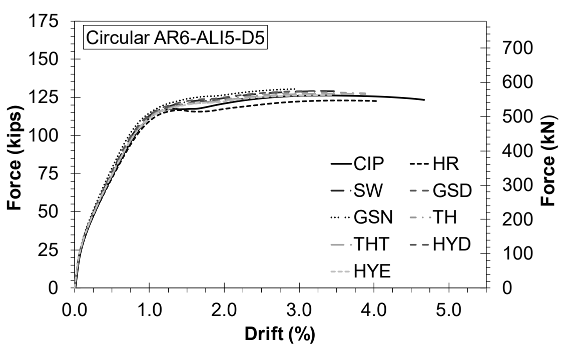

Figure 5.16 Pushover Analysis for Circular AR6-ALI5-D5

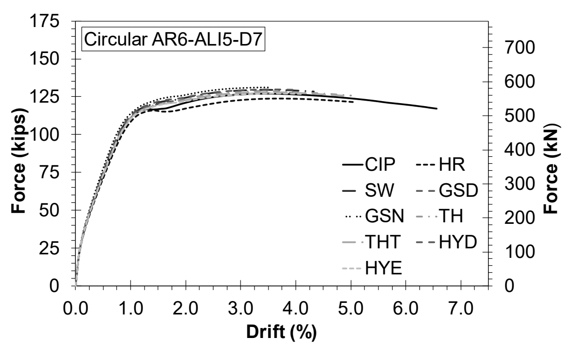

Figure 5.17 Pushover Analysis for Circular AR6-ALI5-D7

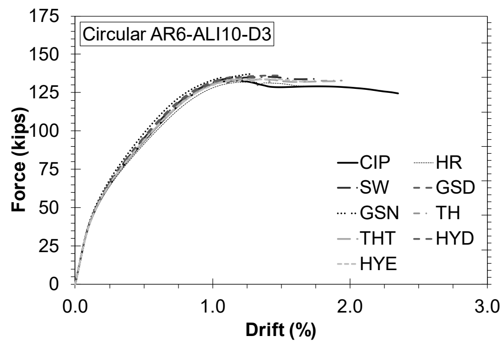

Figure 5.18 Pushover Analysis for Circular AR6-ALI10-D3

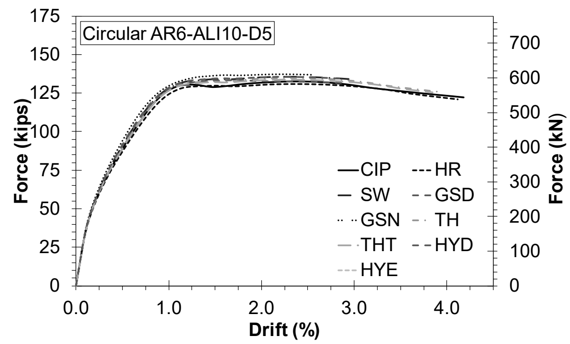

Figure 5.19 Pushover Analysis for Circular AR6-ALI10-D5

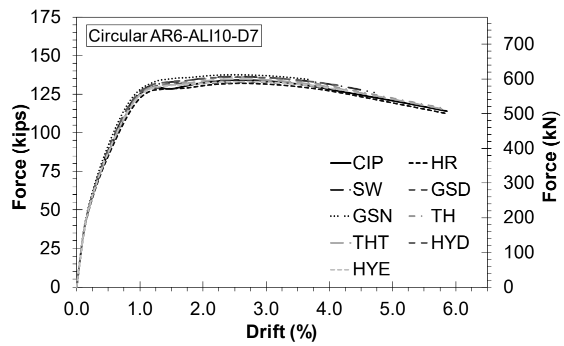

Figure 5.20 Pushover Analysis for Circular AR6-ALI10-D7

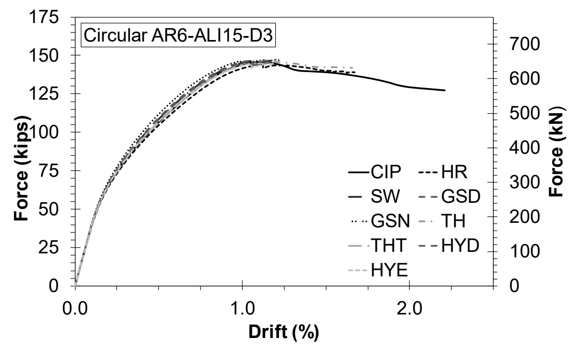

Figure 5.21 Pushover Analysis for Circular AR6-ALI15-D3

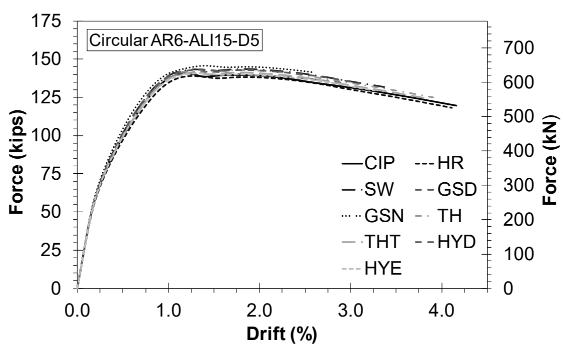

Figure 5.22 Pushover Analysis for Circular AR6-ALI15-D5

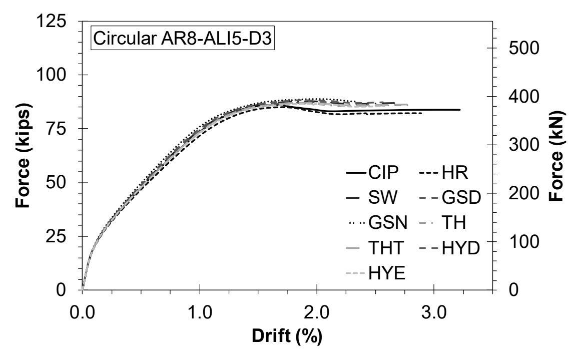

Figure 5.23 Pushover Analysis for Circular AR8-ALI5-D3

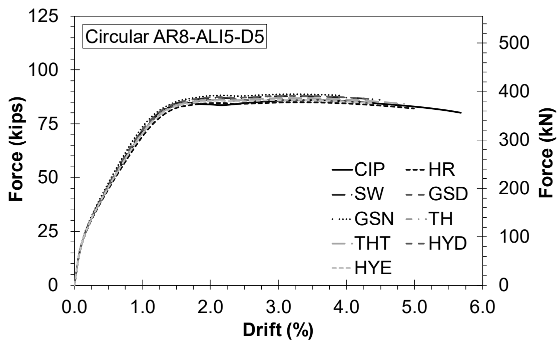

Figure 5.24 Pushover Analysis for Circular AR8-ALI5-D5

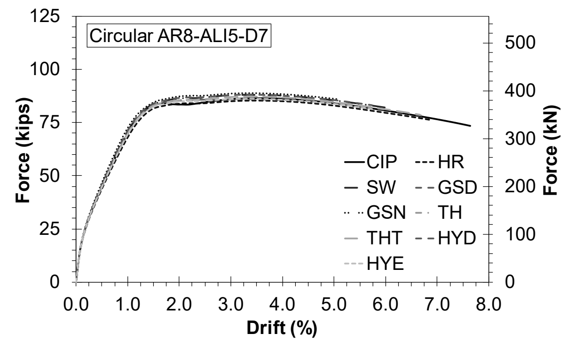

Figure 5.25 Pushover Analysis for Circular AR8-ALI5-D7

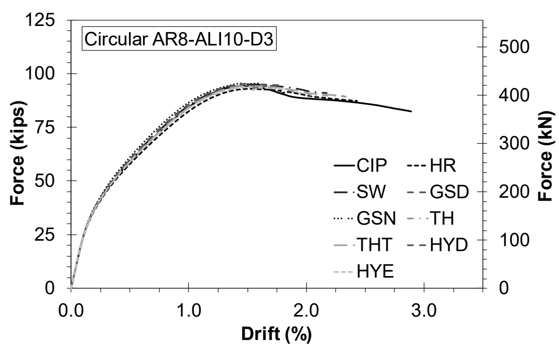

Figure 5.26 Pushover Analysis for Circular AR8-ALI10-D3

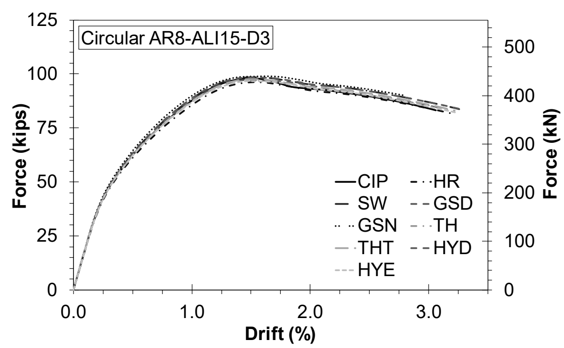

Figure 5.27 Pushover Analysis for Circular AR8-ALI15-D3

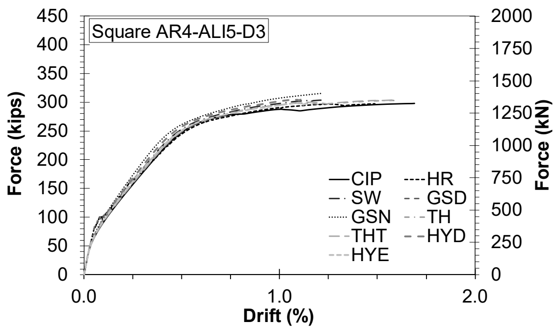

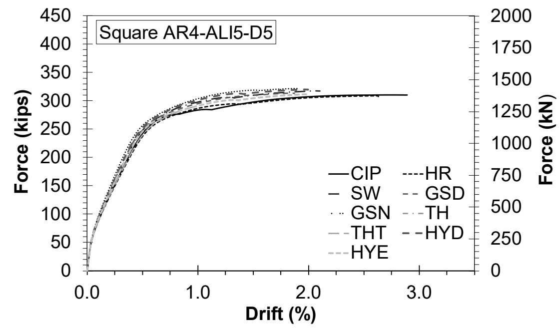

Figure 5.28 Pushover Analysis for Square AR4-ALI5-D3

Figure 5.29 Pushover Analysis for Square AR4-ALI5-D5

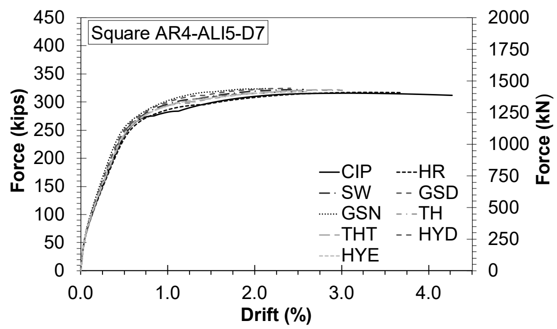

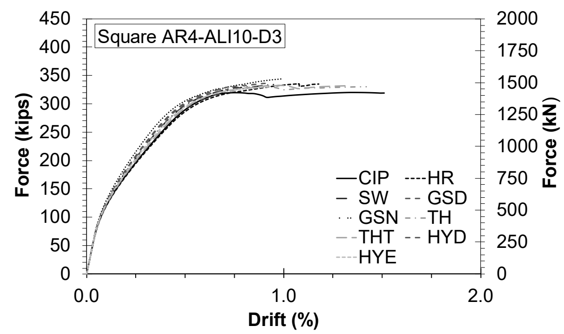

Figure 5.30 Pushover Analysis for Square AR4-ALI5-D7

Figure 5.31 Pushover Analysis for Square AR4-ALI10-D3

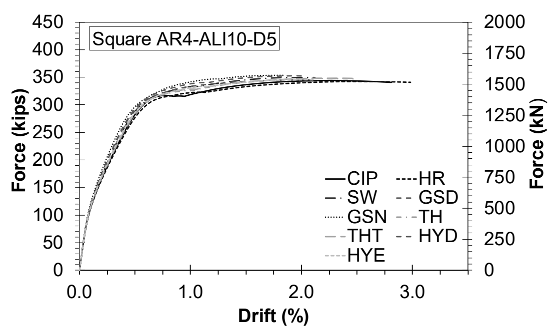

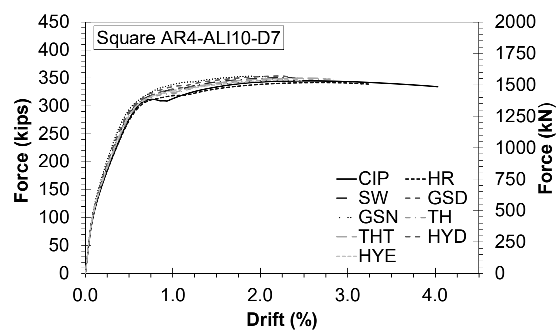

Figure 5.32 Pushover Analysis for Square AR4-ALI10-D5

Figure 5.33 Pushover Analysis for Square AR4-ALI10-D7

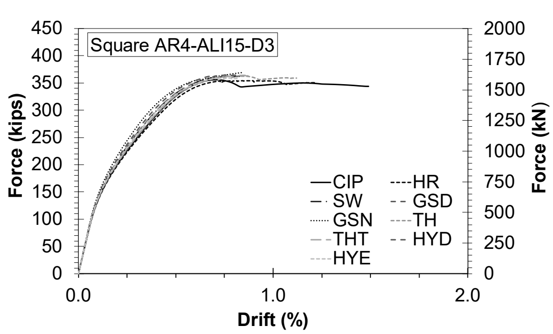

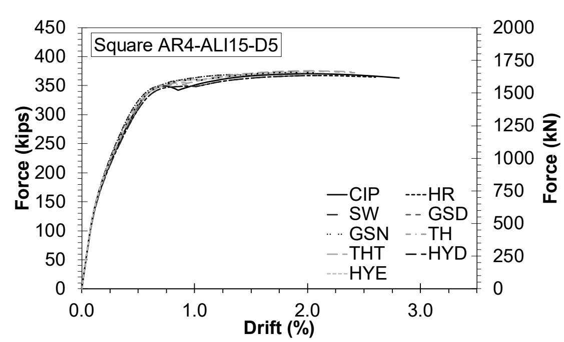

Figure 5.34 Pushover Analysis for Square AR4-ALI15-D3

Figure 5.35 Pushover Analysis for Square AR4-ALI15-D5

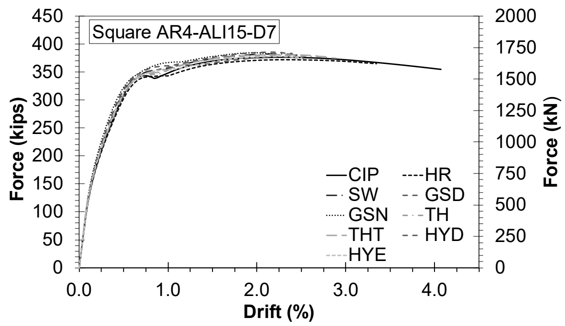

Figure 5.36 Pushover Analysis for Square AR4-ALI15-D7

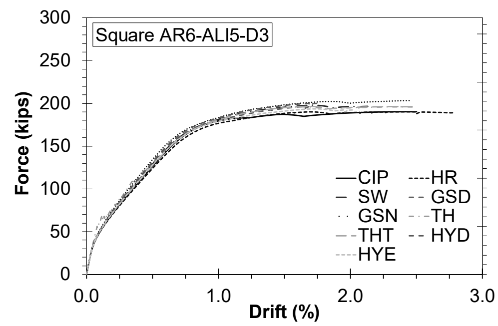

Figure 5.37 Pushover Analysis for Square AR6-ALI5-D3

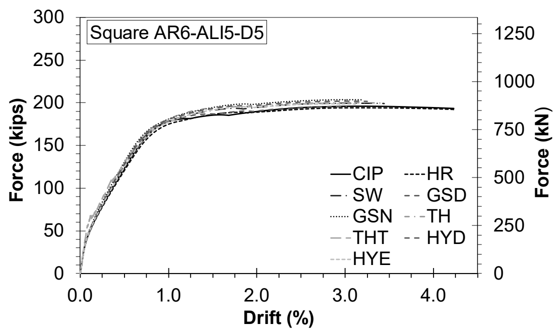

Figure 5.38 Pushover Analysis for Square AR6-ALI5-D5

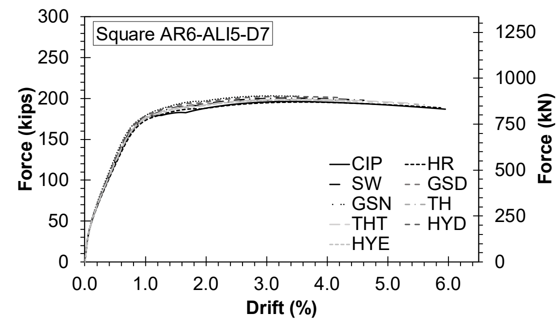

Figure 5.39 Pushover Analysis for Circular AR6-ALI5-D7

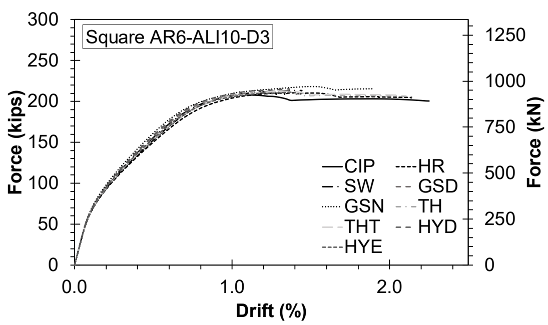

Figure 5.40 Pushover Analysis for Square AR6-ALI10-D3

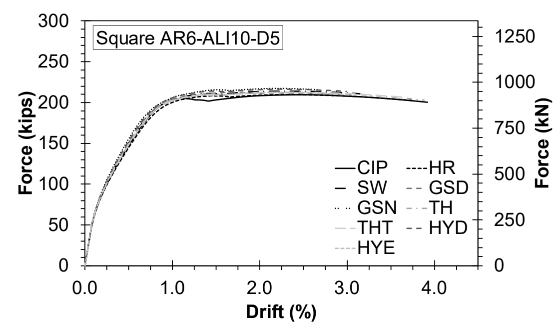

Figure 5.41 Pushover Analysis for Square AR6-ALI10-D5

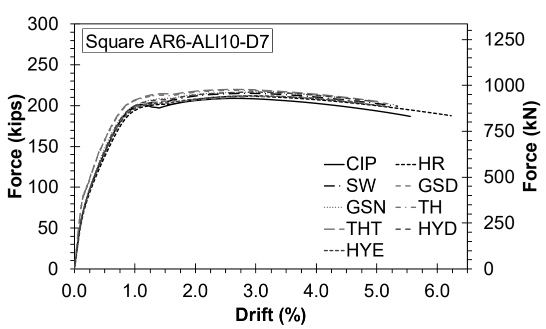

Figure 5.42 Pushover Analysis for Square AR6-ALI10-D7

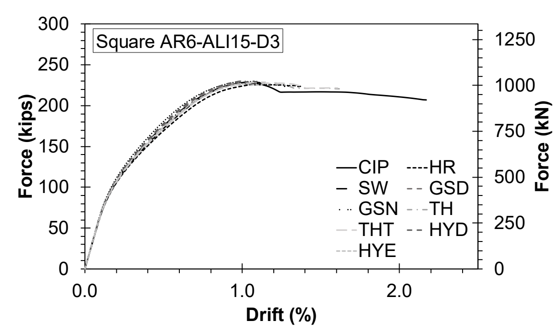

Figure 5.43 Pushover Analysis for Square AR6-ALI15-D3

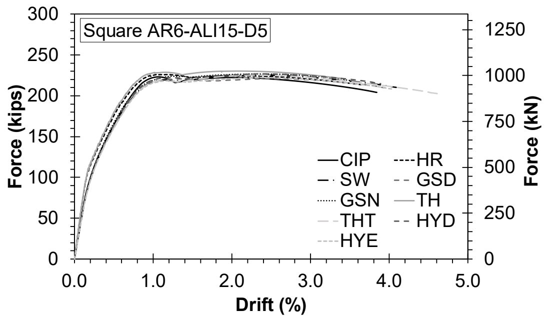

Figure 5.44 Pushover Analysis for Square AR6-ALI15-D5

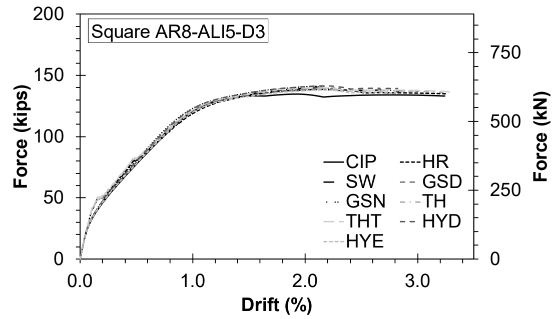

Figure 5.45 Pushover Analysis for Square AR8-ALI5-D3

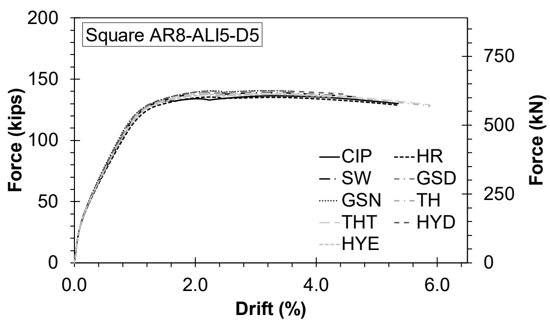

Figure 5.46 Pushover Analysis for Square AR8-ALI5-D5

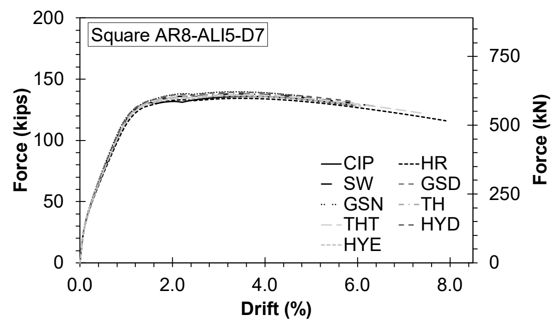

Figure 5.47 Pushover Analysis for Square AR8-ALI5-D7

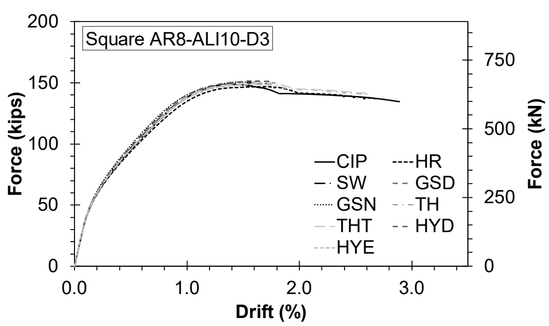

Figure 5.48 Pushover Analysis for Square AR8-ALI10-D3

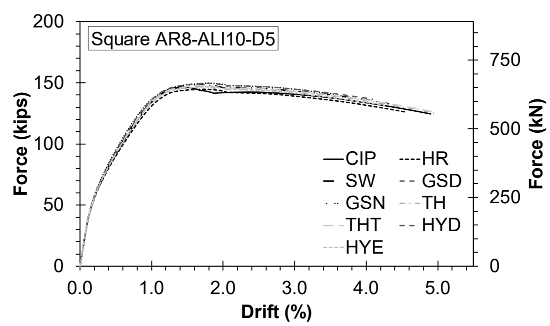

Figure 5.49 Pushover Analysis for Square AR8-ALI10-D5

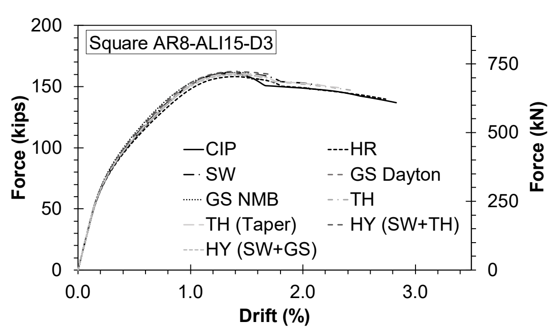

Figure 5.50 Pushover Analysis for Square AR8-ALI15-D3

5.4.2 Summary of Pushover Analyses

Data from each column of the parametric study was compiled in a summary table to better illustrate the effect of using mechanical bar couplers in the plastic hinge region of bridge columns. Tables 5.6 and 5.7 present the displacement ductility of the CIP and spliced columns from all 405 pushover analyses. The difference in the displacement ductility between each spliced column and its corresponding CIP column was also included in the table for comparison. A positive percent difference indicates a reduction in the displacement capacity for the spliced column.

As overall trends, the bar couplers seem to affect the spliced column behavior in the same manner regardless of the section geometry. Columns with high axial load indices and high aspect ratios seem to be less affected by the couplers since those columns tend to fail by geometric nonlinearities rather than the coupler effects.

The data from these tables were presented in graphs (Fig. 5.51 and 5.52) to visualize how varying the coupler properties affect the column displacement ductility capacity. The coupler length was normalized to the column longitudinal bar diameter and was presented as horizontal axis. Furthermore, the spliced column ductilities were normalized to their corresponding CIP ductilities and were presented as the vertical axis. Tazarv and Saiidi (2016) proposed an equation (Eq. 5.1) to predict the ductility loss for mechanically spliced columns. This equation was also included in the graphs using two marginal β factors of 0.65 and 1.0. The lower bound Beta was the lowest measured in all No. 10 (32-mm) bar couplers tested by Dahal and Tazarv (2020), and the upper bound value indicates that the full length of a coupler is rigid, thus the coupler does not contribute to the splice strains. Note that results for spliced columns with a displacement capacity larger than that in CIPs were considered as outlier, thus were removed from the graphs. A linear trendline was also included for each target ductility.

$$\frac{\mu_{sp}}{\mu_{CIP}} = (1 - 0.18\beta)(\frac{H_{sp}}{L_{sp}})^{0.1\beta} \tag{5.1}$$

It can be seen that as the coupler rigid length factor or the coupler length increases, the column displacement ductility generally decreases. Regardless of the column cross section, couplers can reduce the column displacement ductility capacity up to 45%. Most of the data points were above the design lines (based on Eq. 5.1) indicating that this design equation is conservative. Furthermore, the data show that columns utilizing short couplers can exhibit a displacement capacity that is close to that of unspliced columns. For example, the AR6-ALI5-D5 square column spliced with the HR coupler showed 1% lower displacement ductility capacity when compared with its corresponding CIP column.

Table 5.6 Summary of Circular Column Parametric Pushover Study

Circular Column ID	CIP Ductility (μ)	Left Column: Ductility, Right Column: *Ductility Reduction Compard to CIP in %*															
		HR		TH		THT		SW		GSN		GSD		HYD		HYE	
		L_{sp} = 3.75 in.		***L_{sp} = 2.76 in.***		***L_{sp} = 4.23 in.***		***L_{sp} = 8.30 in.***		***L_{sp} = 17.91 in.***		***L_{sp} = 17.99 in.***		***L_{sp} = 11.81 in.***		***L_{sp} = 10.82 in.***	
		β = 0.55		***β = 1.65***		***β = 1.05***		***β = 0.95***		***β = 0.85***		***β = 0.65***		***β = 0.85***		***β = 0.8***	
AR4-ALI5-D3	2.97	2.90	*2.26%*	2.68	*9.75%*	2.69	*9.41%*	2.47	*16.63%*	2.09	*29.61%*	2.19	*26.14%*	2.42	*18.52%*	2.40	*19.12%*
AR4-ALI5-D5	4.91	4.59	*6.44%*	4.60	*6.28%*	4.48	*8.78%*	4.08	*16.83%*	3.66	*25.41%*	4.10	*16.46%*	4.02	*18.01%*	4.02	*18.09%*
AR4-ALI5-D7	6.90	5.01	*27.32%*	4.96	*28.16%*	4.73	*31.40%*	4.30	*37.65%*	3.81	*44.77%*	4.30	*37.71%*	4.19	*39.21%*	4.20	*39.16%*
AR4-ALI10-D3	3.02	2.64	*12.52%*	2.42	*19.72%*	2.43	*19.62%*	2.01	*33.53%*	1.88	*37.77%*	1.94	*35.88%*	1.96	*34.96%*	1.91	*36.65%*
AR4-ALI10-D5	4.94	4.63	*6.22%*	4.51	*8.67%*	4.01	*18.84%*	3.62	*26.75%*	3.32	*32.73%*	3.69	*25.23%*	3.54	*28.27%*	3.55	*28.06%*
AR4-ALI10-D7	7.06	6.19	*12.28%*	6.28	*11.10%*	5.59	*20.79%*	4.63	*34.44%*	4.26	*39.64%*	4.65	*34.17%*	4.47	*36.71%*	4.50	*36.30%*
AR4-ALI15-D3	3.06	2.21	*27.73%*	2.39	*21.64%*	2.27	*25.70%*	1.90	*37.81%*	1.83	*40.10%*	1.85	*39.48%*	1.86	*39.18%*	1.84	*39.80%*
AR4-ALI15-D5	5.10	4.68	*8.16%*	4.35	*14.61%*	4.23	*17.14%*	3.58	*29.81%*	3.07	*39.73%*	3.53	*30.71%*	3.40	*33.36%*	3.46	*32.20%*
AR4-ALI15-D7	7.00	6.07	*13.32%*	5.81	*16.94%*	5.45	*22.11%*	4.72	*32.61%*	4.11	*41.29%*	4.60	*34.26%*	4.39	*37.20%*	4.55	*34.94%*
AR6-ALI5-D3	3.01	2.65	*11.99%*	2.59	*14.11%*	2.55	*15.41%*	2.42	*19.56%*	1.97	*34.56%*	2.01	*33.23%*	2.35	*22.14%*	2.33	*22.81%*
AR6-ALI5-D5	5.08	4.35	*14.38%*	4.31	*15.05%*	4.23	*16.73%*	3.92	*22.78%*	3.45	*31.96%*	3.88	*23.59%*	3.82	*24.71%*	3.83	*24.51%*
AR6-ALI5-D7	7.06	5.28	*25.15%*	5.31	*24.79%*	5.16	*26.85%*	4.70	*33.32%*	4.04	*42.81%*	4.41	*37.56%*	4.45	*36.97%*	4.44	*37.14%*
AR6-ALI10-D3	3.05	2.20	*28.02%*	2.47	*19.11%*	2.42	*20.71%*	2.29	*24.98%*	1.83	*40.18%*	1.84	*39.79%*	1.97	*35.30%*	2.17	*28.97%*
AR6-ALI10-D5	4.98	4.81	*3.26%*	4.65	*6.47%*	4.54	*8.74%*	3.61	*27.36%*	3.23	*35.04%*	3.57	*28.24%*	3.50	*29.67%*	3.53	*29.07%*
AR6-ALI10-D7	6.81	6.75	*0.95%*	6.77	*0.63%*	6.84	*-0.41%*	5.50	*19.26%*	4.50	*33.98%*	4.83	*29.08%*	4.86	*28.67%*	4.95	*27.36%*
AR6-ALI15-D3	2.95	2.15	*27.04%*	2.16	*26.74%*	2.08	*29.39%*	1.69	*42.65%*	1.66	*43.71%*	1.63	*44.83%*	1.67	*43.47%*	1.64	*44.21%*
AR6-ALI15-D5	5.07	4.99	*1.64%*	4.77	*6.01%*	4.68	*7.83%*	4.15	*18.22%*	3.28	*35.35%*	3.59	*29.20%*	3.84	*24.39%*	3.98	*21.45%*
AR8-ALI5-D3	3.01	2.65	*11.90%*	2.60	*13.76%*	2.59	*13.96%*	2.49	*17.15%*	2.27	*24.53%*	2.11	*29.74%*	2.43	*19.24%*	2.40	*20.27%*
AR8-ALI5-D5	4.98	4.23	*15.11%*	4.16	*16.56%*	4.18	*16.06%*	3.94	*21.00%*	3.55	*28.82%*	3.87	*22.32%*	3.84	*22.84%*	3.84	*22.86%*
AR8-ALI5-D7	6.64	5.72	*13.95%*	5.73	*13.83%*	5.68	*14.48%*	5.24	*21.09%*	4.49	*32.41%*	4.76	*28.34%*	4.98	*25.12%*	4.94	*25.72%*
AR8-ALI10-D3	2.98	2.39	*19.84%*	2.31	*22.36%*	2.29	*23.16%*	2.19	*26.59%*	1.72	*42.26%*	1.71	*42.63%*	1.84	*38.17%*	1.82	*38.84%*
AR8-ALI15-D3	3.00	3.07	*-2.43%*	3.10	*-3.27%*	3.14	*-4.57%*	3.23	*-7.60%*	2.81	*6.27%*	3.08	*-2.60%*	3.26	*-8.53%*	3.17	*-5.67%*

Note: "AR" refers to the aspect ratio, "ALI" refers to the column axial load index, "D" refers to the displacement ductility capacity, "CIP" refers to the reference columns, "HR" refers to the headed reinforcement couplers, "L_{sp}" is the coupler length, "β" is the coupler rigid length factor, "TH" refers to the threaded couplers, "SW" refers to the swaged couplers, "GS" refers to the grouted couplers, and "HY" refers to the hybrid couplers; 1 in. = 25.4 mm.

Table 5.7 Summary of Square Column Parametric Pushover Study

Square Column ID	CIP Ductility (μ)	Left Column: Ductility, Right Column: *Ductility Reduction Compard to RC in %*															
		HR		TH		THT		SW		GSN		GSD		HYD		HYE	
		L_{sp} = 3.75 in.		***L_{sp} = 2.76 in.***		***L_{sp} = 4.23 in.***		***L_{sp} = 8.30 in.***		***L_{sp} = 17.91 in.***		***L_{sp} = 17.99 in.***		***L_{sp} = 11.81 in.***		***L_{sp} = 10.82 in.***	
		β = 0.55		***β = 1.65***		***β = 1.05***		***β = 0.95***		***β = 0.85***		***β = 0.65***		***β = 0.85***		***β = 0.8***	
AR4-ALI5-D3	3.13	2.57	*18.02%*	3.05	*2.40%*	3.02	*3.45%*	2.45	*21.76%*	2.65	*15.47%*	2.35	*24.86%*	2.38	*24.00%*	2.35	*24.77%*
AR4-ALI5-D5	4.98	4.53	*9.15%*	4.66	*6.40%*	4.22	*15.28%*	3.83	*23.13%*	3.78	*24.21%*	3.57	*28.37%*	3.74	*24.85%*	3.72	*25.34%*
AR4-ALI5-D7	7.00	6.03	*13.94%*	5.07	*27.65%*	5.01	*28.47%*	4.49	*35.88%*	4.14	*40.92%*	4.66	*33.44%*	4.37	*37.55%*	4.56	*34.84%*
AR4-ALI10-D3	3.02	2.33	*22.78%*	2.84	*5.83%*	2.68	*11.26%*	2.03	*32.78%*	2.31	*23.48%*	1.95	*35.53%*	2.01	*33.48%*	1.99	*34.27%*
AR4-ALI10-D5	4.93	5.25	*-6.41%*	4.50	*8.70%*	4.47	*9.39%*	3.99	*19.02%*	3.77	*23.52%*	4.06	*17.66%*	3.89	*21.15%*	3.99	*19.02%*
AR4-ALI10-D7	6.83	5.62	*17.72%*	5.11	*25.20%*	4.99	*26.93%*	4.60	*32.68%*	4.17	*38.92%*	4.74	*30.53%*	4.51	*33.99%*	4.59	*32.79%*
AR4-ALI15-D3	2.98	2.41	*19.13%*	2.23	*25.13%*	1.82	*39.09%*	1.76	*40.97%*	1.94	*34.80%*	1.75	*41.44%*	1.77	*40.54%*	1.75	*41.41%*
AR4-ALI15-D5	5.02	4.64	*7.61%*	4.41	*12.09%*	4.33	*13.73%*	3.91	*22.12%*	3.70	*26.28%*	4.03	*19.73%*	3.85	*23.31%*	3.90	*22.22%*
AR4-ALI15-D7	6.90	5.71	*17.27%*	5.04	*26.88%*	4.87	*29.38%*	4.50	*34.77%*	4.24	*38.60%*	4.75	*31.16%*	4.44	*35.67%*	4.54	*34.23%*
AR6-ALI5-D3	3.17	3.48	*-9.79%*	3.18	*-0.60%*	3.12	*1.30%*	2.77	*12.58%*	3.27	*-3.32%*	2.30	*27.30%*	2.35	*25.69%*	2.65	*16.15%*
AR6-ALI5-D5	5.04	5.00	*0.75%*	4.28	*15.03%*	4.30	*14.59%*	4.22	*16.12%*	4.08	*18.96%*	3.85	*23.65%*	4.07	*19.22%*	3.80	*24.58%*
AR6-ALI5-D7	6.84	6.71	*1.87%*	6.57	*3.89%*	6.22	*9.01%*	5.46	*20.20%*	4.44	*35.04%*	5.09	*25.52%*	5.08	*25.67%*	5.24	*23.44%*
AR6-ALI10-D3	3.08	2.85	*7.49%*	2.90	*5.87%*	2.78	*9.76%*	2.03	*34.16%*	2.73	*11.45%*	1.95	*36.75%*	1.97	*36.23%*	1.94	*37.04%*
AR6-ALI10-D5	4.96	4.70	*5.30%*	4.91	*0.99%*	4.62	*6.95%*	4.08	*17.88%*	3.61	*27.29%*	4.02	*18.96%*	3.94	*20.64%*	3.92	*20.94%*
AR6-ALI10-D7	6.94	7.32	*-5.46%*	7.04	*-1.48%*	6.73	*3.03%*	6.47	*6.80%*	5.45	*21.43%*	5.99	*13.63%*	6.03	*13.05%*	6.30	*9.19%*
AR6-ALI15-D3	2.71	1.85	*31.72%*	2.25	*17.05%*	2.17	*20.00%*	1.63	*39.83%*	1.58	*41.68%*	1.57	*42.30%*	1.63	*40.06%*	1.60	*40.94%*
AR6-ALI15-D5	4.92	4.99	*-1.26%*	4.73	*3.98%*	5.72	*-16.25%*	5.12	*-4.02%*	4.54	*7.86%*	5.10	*-3.51%*	4.95	*-0.61%*	5.08	*-3.17%*
AR8-ALI5-D3	3.18	3.18	*-0.16%*	3.19	*-0.44%*	3.25	*-2.20%*	2.97	*6.39%*	2.27	*28.46%*	2.35	*26.07%*	2.84	*10.74%*	2.78	*12.56%*
AR8-ALI5-D5	5.05	4.96	*1.84%*	5.56	*-10.04%*	5.56	*-10.14%*	4.49	*11.01%*	3.57	*29.28%*	3.95	*21.73%*	4.78	*5.31%*	4.04	*19.99%*
AR8-ALI5-D7	6.99	7.32	*-4.66%*	6.88	*1.55%*	6.95	*0.54%*	5.97	*14.64%*	4.62	*33.86%*	5.38	*23.10%*	5.51	*21.20%*	5.65	*19.21%*
AR8-ALI10-D3	3.04	2.80	*8.12%*	2.74	*10.09%*	2.75	*9.66%*	1.92	*36.92%*	1.83	*39.84%*	1.86	*38.95%*	1.90	*37.67%*	1.88	*38.23%*
AR8-ALI10-D5	5.05	4.61	*8.81%*	5.12	*-1.27%*	5.05	*0.12%*	4.42	*12.45%*	3.72	*26.27%*	4.26	*15.58%*	4.23	*16.25%*	4.36	*13.74%*
AR8-ALI15-D3	3.04	2.88	*5.29%*	2.57	*15.58%*	2.43	*20.01%*	2.28	*25.04%*	1.67	*45.28%*	1.70	*44.04%*	1.81	*40.52%*	1.77	*41.90%*

Note: "AR" refers to the aspect ratio, "ALI" refers to the column axial load index, "D" refers to the displacement ductility capacity, "CIP" refers to the reference columns, "HR" refers to the headed reinforcement couplers, "L_{sp}" is the coupler length, "β" is the coupler rigid length factor, "TH" refers to the threaded couplers, "SW" refers to the swaged couplers, "GS" refers to the grouted couplers, and "HY" refers to the hybrid couplers; 1 in. = 25.4 mm.

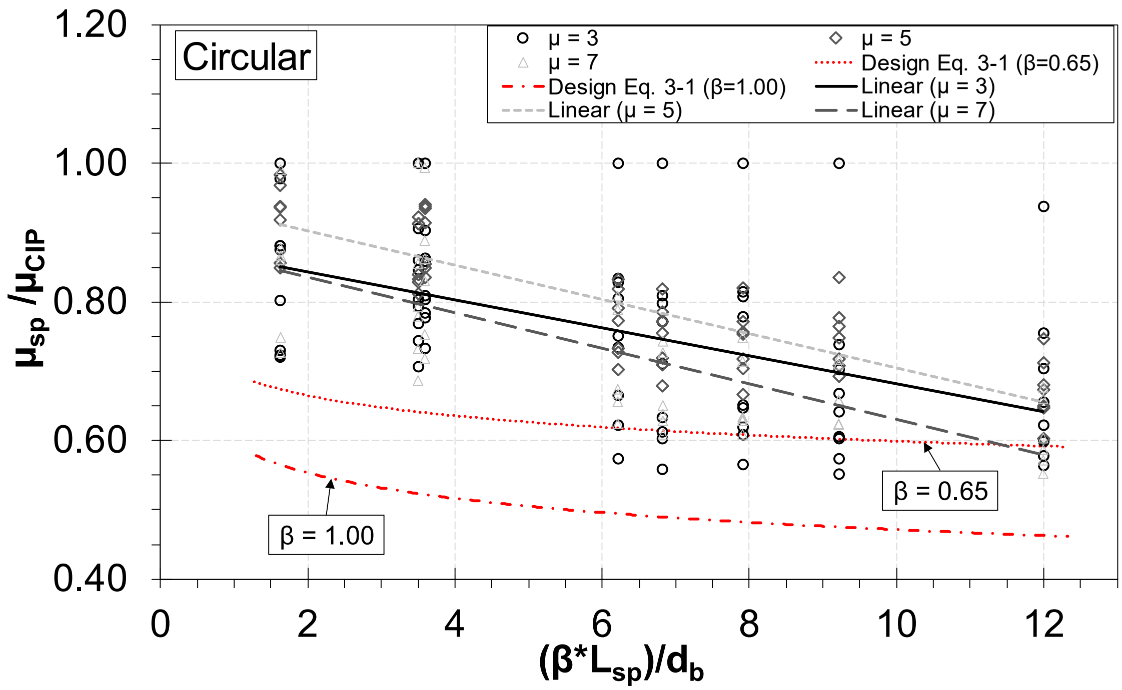

Figure 5.51. Summary Plot of Parametric Pushover Study for Circular Columns

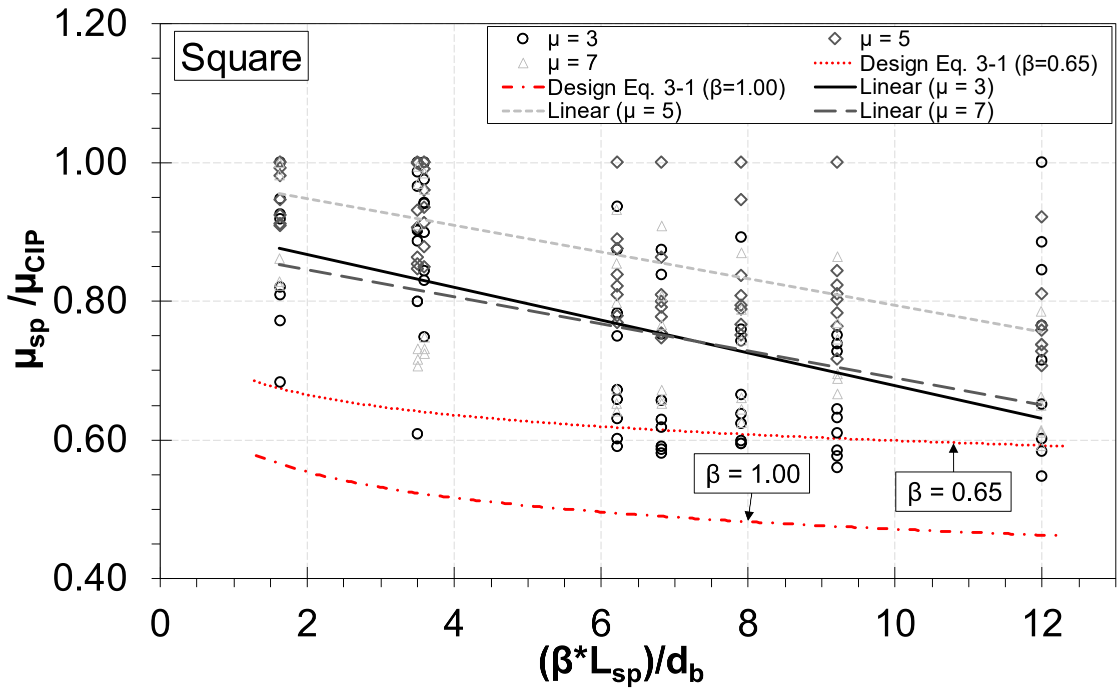

Figure 5.52 Summary Plot of Parametric Pushover Study for Square Columns

5.5 Seismic Demands on Mechanically Spliced Columns

The displacement capacity of bridge columns incorporating mechanical bar couplers in the plastic hinge region was analytically investigated in the previous section. The present work (Chapter 3) and a few other studies (e.g., Haber et al., 2013; Tazarv and Saiidi, 2014; and Ameli and Pantelides, 2016) experimentally investigated the seismic behavior of mechanically spliced bridge columns through cyclic testing. Nevertheless, no study has investigated the dynamic behavior of mechanically spliced bridge columns.

A comprehensive parametric study was conducted in the present analytical work to determine the effect of eight mechanical bar couplers on the displacement demand of bridge columns in high seismic regions. Six columns with a circular cross-section and six columns with a square cross-section were selected from the pushover study discussed in the previous section. All columns selected for the dynamic analysis were designed to exhibit a displacement ductility capacity of 7, which means columns were highly ductile. The aspect ratio and the axial load index of the columns were varied to include a wide range of columns in the analysis. Five synthetic ground motions were produced for a 7.5 magnitude earthquake matching the AASHTO design spectrum. A finite element model was constructed and verified, and dynamic analysis was performed for each column-coupler combination using the validated model. This section discusses the selected columns, modeling methods, and the results of the parametric dynamic study.

5.5.1 Columns Selected for Dynamic Analysis

The goal of the dynamic study is to determine how incorporating mechanical bar couplers in the plastic hinge region of precast bridge columns affects seismic displacement demand. The conventional CIP columns designed in the previous section with a displacement ductility capacity (D or μ) of 7 were selected for the dynamic analysis since these columns are most fit for use in high seismic regions. The aspect ratio (AR) of the columns were varied at 4, 6, and 8, and the axial load index (ALI) was varied at 5%, 10%, and 15%. Note that 12 combinations were feasible per section type by varying the column parameters. However, some of the tall column models with high axial loads could not be analyzed due to convergence issues when P-Δ effects were included as noted in the pushover analysis. Table 5.8 presents the columns selected for the dynamic study. This table also includes the displacement ductility capacity for the conventional CIP columns from the static pushover analysis conducted in the previous section. The properties of the eight coupler products were discussed in the previous section (Table 5.5). Note that these columns were not designed for a specific site or a set of earthquake motions but were designed to achieve a displacement ductility capacity of 7.

Table 5.8 Bridge Columns Selected for Dynamic Analysis

Column ID	Section Geometry	Displacement Ductility Capacity	Drift Ratio Capacity (%)
AR4-ALI5-D7	Circular	6.90	4.62
AR4-ALI10-D7	Circular	7.06	4.45
AR4-ALI15-D7	Circular	7.00	4.41
AR6-ALI5-D7	Circular	7.05	6.56
AR6-ALI10-D7	Circular	6.81	5.86
AR8-ALI5-D7	Circular	6.64	7.64
AR4-ALI5-D7	Square	7.00	4.27
AR4-ALI10-D7	Square	6.83	4.03
AR4-ALI15-D7	Square	6.90	4.07
AR6-ALI5-D7	Square	6.84	5.95
AR6-ALI10-D7	Square	6.94	5.55
AR8-ALI5-D7	Square	6.99	7.48

5.5.2 Dynamic Modeling Methods for Bridge Columns

At the time of this writing, no dynamic test has been carried out on mechanically spliced bridge columns. Nevertheless, previous analytical studies have successfully simulated the dynamic response of large- and full-scale RC columns under shake-table testing. A study by Tazarv and Saiidi (2013) was selected for further investigation since their proposed modeling method can simulate both the peak and residual displacements of the column with good accuracy. First, this verified model is briefly discussed, then modeling details regarding the CIP and mechanically spliced columns are presented.

5.5.2.1 Verified Dynamic Modeling Methods for Conventional RC Columns

Figure 5.53 shows the detail of a full-scale RC bridge column tested at the University of California, San Diego (UCSD) shake table. The full-scale column had an unbraced length of 24 ft (7.32 m) and a circular cross section with a diameter of 4 ft (1.22 m). A concrete block was constructed at the top to simulate seismic masses. The block weighed a total of 501.6 kips (2231.2 kN) resulting in an axial load index of approximately 5%. The column was constructed with 18 No. 11 (36-mm) longitudinal reinforcing bars. The core was confined with No. 5 (16-mm) hoops spaced every 6 in. (152 mm). All steel reinforcement was ASTM A706 Grade 60 (414 MPa). The measured yield strength and ultimate strength of the steel reinforcement was 75.2 ksi (518.5 MPa) and 102.4 ksi (706 MPa), respectively. The concrete compressive strength measured on the test day was 5.95 ksi (40.9 MPa).

The measured response of this column (Fig. 5.54) was used by Tazarv and Saiidi (2013) to develop and validate an analytical model that can be used to predict the nonlinear response of RC bridge columns subjected to seismic loading. They developed a 3D finite element model in OpenSees (2016). The model had four nodes and three elements to model the footing, column, and column head (Fig. 5.53b). The footing and column head were modeled as linear elastic elements. The column was modeled as a "BeamWithHinges" element, which is a lumped plasticity model. This element has a plastic hinge at each end and is linear elastic in between. A fiber section with a core and cover concrete was used. The core was discretized into 10-radial by 10-circumferential fibers of "Concrete02" material. The core was discretized into 10-radial by 10-circumferential fibers of "Concrete01WithSITC" material. The core properties were calculated using the Mander's model (Mander et al., 1988). The longitudinal steel bars were modeled using "ReinforcingSteel" material model. All masses, including 40% of the column mass, were lumped at the top node. The P-Δ effects were included. The Rayleigh damping model was used to include the damping properties of the column.

As shown in Figure 5.54, the model was able to predict the peak and residual displacements of the UCSD column with reasonable accuracy. The model underestimated the peak displacement by 14% and the residual displacement by 7%. Note the residual displacement was defined as the average displacement over the last 10 seconds of the free vibration.

It was determined that the model proposed by Tazarv and Saiidi (2016) were able to predict the peak and residual displacements of RC columns with a reasonable accuracy. Thus, this verified model was adopted for dynamic analyses of both CIP and mechanically spliced columns as detailed in the following sections.

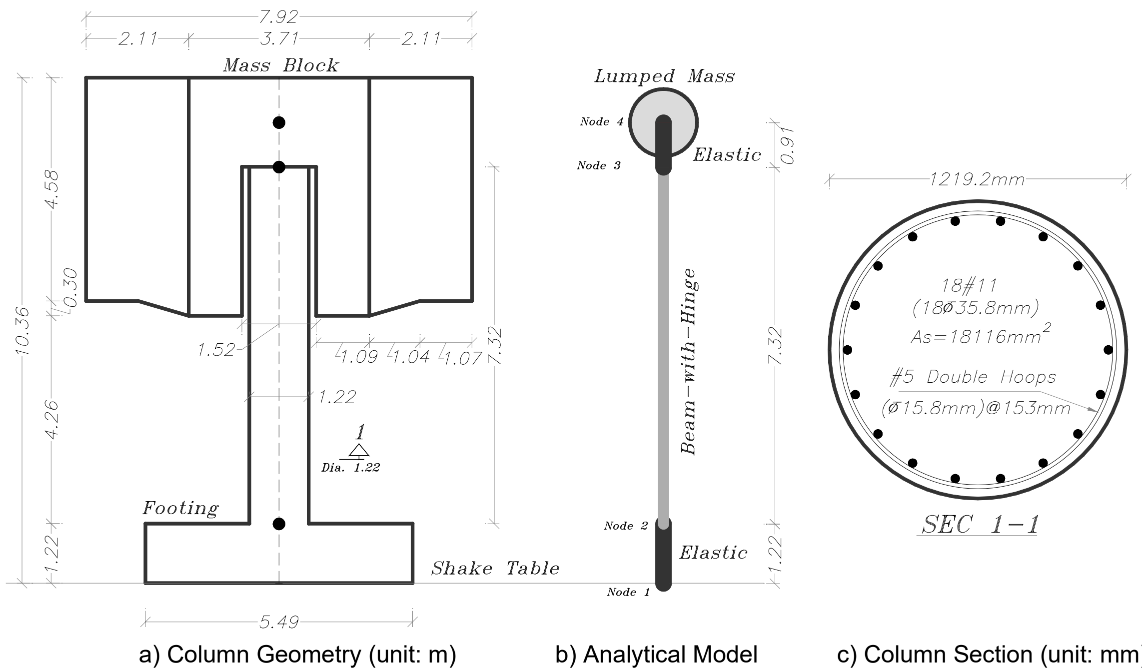

Figure 5.53 Details of Full-Scale RC Column Tested on UCSD Shake-Table (Tazarv and Saiidi, 2013)

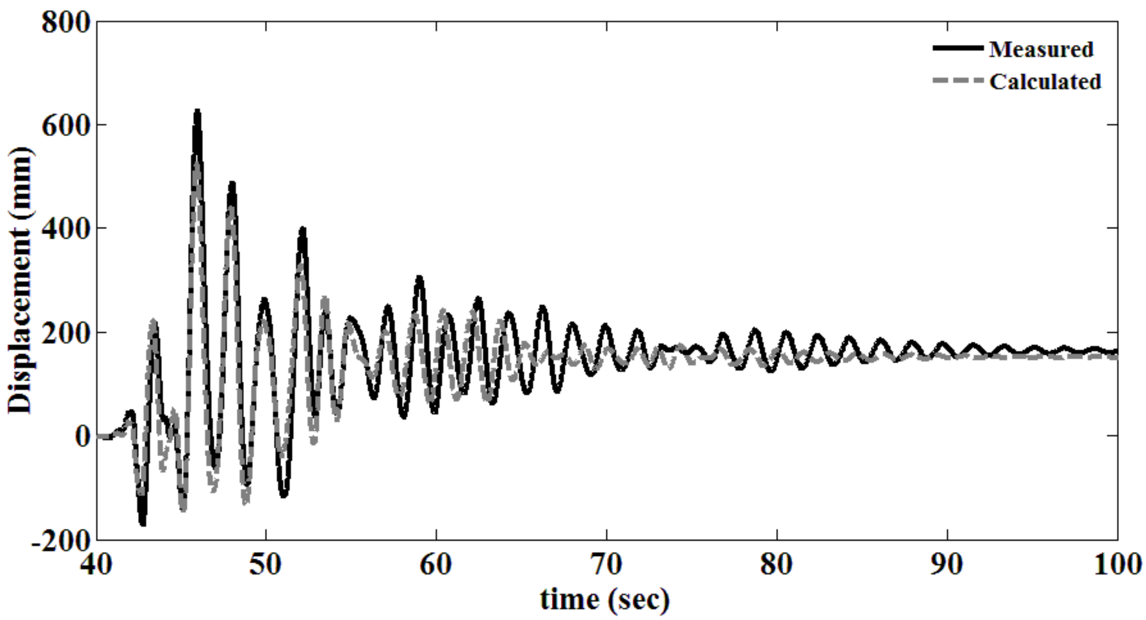

Figure 5.54 Measured and Calculated Displacement Histories of UCSD RC Column Model under EQ5 with EI_{eff}=39% and Damping Ratio 3.0% (Tazarv and Saiidi, 2013)

5.5.2.2 Details of Dynamic Modeling Methods for CIP and Mechanically Spliced Columns

Based on the verified modeling methods proposed by Tazarv and Saiidi (2013) with a few modifications, a 3D fiber-section finite element model with six DOFs was constructed in OpenSees (2016) to simulate the dynamic behavior of unspliced and spliced bridge columns. The columns were subjected to ground motions at the base, and the column nonlinear force and displacement response histories were obtained. This section briefly describes the dynamic models and the modifications that were made.

Figure 5.55 shows a schematic view of the dynamic analytical model for both unspliced and spliced columns. A single "beamWithHinges" element was used to model the entire length of each column in which the effect of couplers can be incorporated into the model by varying the analytical plastic hinge length for each spliced column (refer to Table 4.1). Note this modeling technique is different than what was used in pushover analysis in which the coupler length, location, and properties were directly included in the analysis. In other words, instead of using multiple distributed-plasticity elements, a single lumped-plasticity element is used for mechanically spliced bridge columns. This was done since (1) there is no shake table test data on coupler columns to validate the mechanically spliced column model proposed for pushover analyses, and (2) there is a validated dynamic model for CIP columns incorporating lumped plasticity elements not distributed plasticity elements.

One difference between the UCSD full-scale column model discussed above and the one that was used in dynamic parametric study was that "Concrere01" was used for core and cover concrete. Instead of measured steel bar properties, the AASHTO expected mechanical properties for ASTM A706 Grade 60 (414 MPa) (AASHTO SGS, 2011) was used for all bars in the parametric study. All other modeling methods were the same between the dynamic model, USCD full-scale model, and the pushover model. The plastic hinge length was varied, as discussed next, to include the coupler effects.

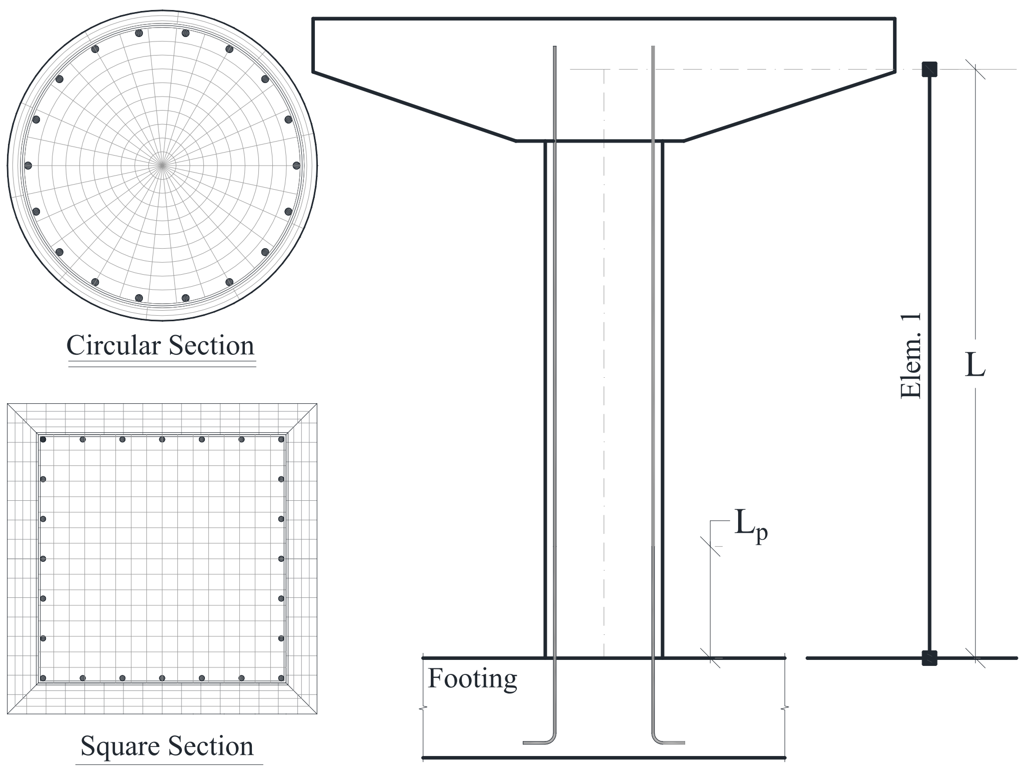

Figure 5.55 Bridge Column Analytical Model for Dynamic Analysis

The analytical plastic hinge length (L_p) is the equivalent length of the column over which the plastic curvature is assumed constant (AASHTO SGS, 2011). The analytical plastic hinge length is used to estimate the plastic rotation and the deformation capacity of bridge columns under excessive loading. Equation 5.2 can be used to estimate the analytical plastic hinge length for conventional unspliced bridge columns as specified by AASHTO SGS (2011) and is adopted in the present study for CIP columns.

$$L_p = 0.08L + 0.15 f_{ye} d_{bl} \geq 0.3 f_{ye} d_{bl} \tag{5.2}$$

where, L_p is the analytical plastic hinge length (in.), L is the unbraced column length (in.), f_{ye} is the expected yield strength of the reinforcement (ksi), and d_{bl} refers to the longitudinal bar diameter (in.).

Tazarv and Saiidi (2016) modified the AASHTO equation to estimate the analytical plastic hinge length for mechanically spliced bridge columns based on the coupler rigid length factor (β), the coupler length (L_{sp}), and the location of the coupler (H_{sp}). The modified analytical plastic hinge length (L_p^{sp}) for mechanically spliced columns based on Tazarv and Saiidi (2016) is:

$$L_p^{sp} = L_p - \left(1 - \frac{H_{sp}}{L_p}\right)\beta L_{sp} \leq L_p \tag{5.3}$$

Eq. 5.3 assumes that the rigid portion of the coupler does not contribute to the plastic lateral deformation, thus can be subtracted from the analytical plastic hinge length (Eq. 5.2). The two equations were used in the present study to investigate the dynamic performance of conventional CIP and mechanically spliced columns using the analytical plastic hinge length as shown in Figure 5.55. Table 5.9 presents the analytical plastic hinge lengths for the unspliced and spliced columns with different coupler products.

Table 5.9 Analytical Plastic Hinge Length for Unspliced and Spliced Columns

Column Aspect Ratio		AR 4	AR 6	AR 8
Column Length, in. (cm)		192 (487.7)	288 (731.5)	384 (975.4)
L_p, in. (cm); used in Unspliced Columns		28.31 (71.91)	35.99 (91.41)	43.67 (110.92)
L_p^{sp}, in. (cm) used in Spliced Columns	HR	26.28 (66.75)	33.96 (86.26)	41.64 (105.77)
	TH	23.84 (60.55)	31.52 (80.06)	39.20 (99.57)
	THT	23.93 (60.78)	31.61 (80.29)	39.29 (99.80)
	SW	20.48 (52.02)	28.16 (71.53)	35.84 (91.03)
	GSN	13.13 (33.35)	20.81 (52.86)	28.49 (72.36)
	GSD	16.65 (42.29)	24.33 (61.80)	32.01 (81.31)
	HYD	18.32 (46.53)	26.00 (66.04)	33.68 (85.55)
	HYE	19.70 (50.04)	27.38 (69.55)	35.06 (89.05)

Note: "AR" refers to the aspect ratio, "HR" refers to the headed reinforcement couplers, "TH" refers to the threaded couplers, "SW" refers to the swaged couplers, "GS" refers to the grouted couplers, and "HY" refers to the hybrid couplers. Refer to Table 5.2 regarding the coupler products.

AASHTO specifies that the flexural stiffness of bridge columns should be reduced based on cracked section properties ($E_c I_{eff}$). The stiffness of the columns in the lumped plasticity element (Fig. 5.55) follows this requirement. Note the reduction of the column lateral stiffness is not needed for distributed plasticity models (like that discussed for pushover analysis) since the nonlinearity is distributed along the length of the member. Figure 5.56 can be used to find the column effective stiffness using the gross flexural stiffness, the column longitudinal reinforcement ratio, and the column axial load. Table 5.10 presents a summary of the effective stiffness ratios used in this study for unspliced and spliced columns.

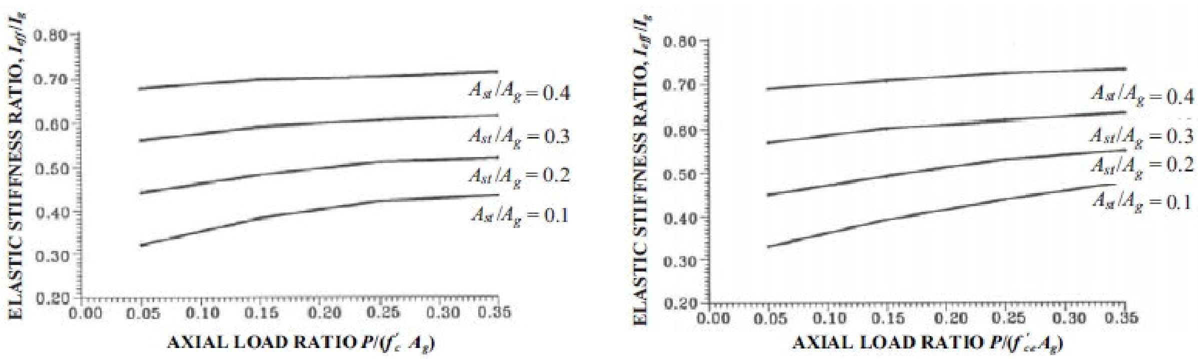

a) Circular Sections b) Square Sections

Figure 5.56 Effective Flexural Stiffness of Cracked Reinforced Concrete Sections (AASHTO SGS, 2011)

Table 5.10 Column Effective Stiffness

Section Geometry	**Elastic Stiffness Ratio (I_{eff}/I_g)**		
	ALI 5%	**ALI 10%**	**ALI 15%**
Circular	0.36	0.38	0.41
Square	0.38	0.40	0.42

Note: "ALI" refers to the Axial Load Index of the column.

5.5.2.3 Mechanically Spliced Column Dynamic Modeling Method Verification

It was discussed that there is currently no shake table test data in the literature on mechanically spliced columns. However, the analytical model discussed in Section 5.5 is versatile and may be used for the dynamic analysis of both unspliced and spliced columns. Tazarv and Saiidi (2013) have shown that this model is valid for nonlinear dynamic analyses of unspliced columns and reported a good match between the measured and calculated responses. As a minimum, it is needed to evaluate the overall accuracy of the proposed dynamic model for mechanically spliced columns tested under slow cyclic loads, the only type of test data that is available.

Haber et al. (2014) tested a half-scale circular precast column that used grouted couplers at the base to connect the column to the footing. The column, which was labeled as "GCNP," test data was used to verify the proposed modeling method discussed above. Table 5.11 presents the key parameters of the analytical model such as the column geometry and the material properties. An analytical model following that discussed in the previous section was developed for GCNP. The measured properties of steel bars and concrete were used in the analysis. The coupler stress-strain behavior was estimated based on a Beta that was calculated using tensile test results for the No. 8 (25 mm) grouted coupler used in GCNP. The coupler effect was incorporated into the model by using the modified analytical plastic hinge length (Eq. 5.3). Figure 5.57a shows the measured and calculated force-drift relationships for GCNP. The initial stiffness was well estimated compared with that from the test, and the lateral strength of the column was underestimated by 14%. Furthermore, the column displacement capacity was estimated with a reasonable accuracy using the proposed method. The actual grouted coupler column failed at a drift ratio of 5.95% while the analytical model estimated the column failure to be at a drift ratio of 5.32%, a 10.6% difference.

This lumped plasticity model was also used for the PGS column tested in the present study. Figure 5.57b shows the results of the analysis. The initial stiffness and the strength were well simulated, and the drift capacity of the column was 22% overestimated (9.4% in the analysis vs. 7.71% in the test). Overall, the proposed modeling method using the modified plastic hinge length to include the coupler effect can represent the behavior of mechanically spliced columns with a reasonable accuracy. Due to the lack of dynamic test data, this model is used herein for the dynamic analysis of mechanically spliced columns.

Table 5.11 Key Parameters of GCNP (Haber et al. 2014) Used in Dynamic Model Verification

General Properties		
Section Geometry	Circular	
Column Height, ft (m)	9 (2.74)	
Column Diameter, ft (m)	2 (0.61)	
Longitudinal Reinforcement	11 - No. 8 (25.4-mm) Bars	
Cover, in. (mm)	1.75 (44.5)	
Axial Load, kips (kN)	208 (925)	
Axial Load Index	10.88%	
Steel Reinforcement Properties		
Measured Yield Strength, ksi (MPa)	f_y =	66.8 (460.6)
Measured Ultimate Strength, ksi (MPa)	f_u =	111.3 (767.4)
Ultimate Strain	ε_u =	0.09
Young's Modulus, ksi (MPa)	E =	29,000 (200,000)
Cover Concrete Properties		
Measured Unconfined Compressive Strength, psi (MPa)	f'_c =	4228.0 (29.2)
Strain at Peak Stress	ε_c =	0.002
Ultimate Concrete Strain	ε_u =	0.005
Core Concrete Properties (Mander et al., 1988)		
Confining Reinforcement, in (mm)	No. 3 bars (10) Spirals @ 2-in (51) Pitch	
Calculated Confined Compressive Strength, psi (MPa)	f'_{cc} =	6384.0 (44.0)
Calculated Strength at Ultimate Strain, psi (MPa)	f'_{cu} =	5945.6 (41.0)
Calculated Strain at Peak Stress	ε_{cc} =	0.0082
Calculated Ultimate Concrete Strain	ε_{cu} =	0.025
Coupler and Plastic Hinge Properties		
Rigid Length Factor	β =	0.7
Coupler Length, in. (mm)	L_{sp} =	14.57 (370)
Spliced Plastic Hinge Length, in. (mm)	L_p^{sp} =	9.87 (251)
Elastic Stiffness Ratio	(I_{eff}/I_g) =	0.46

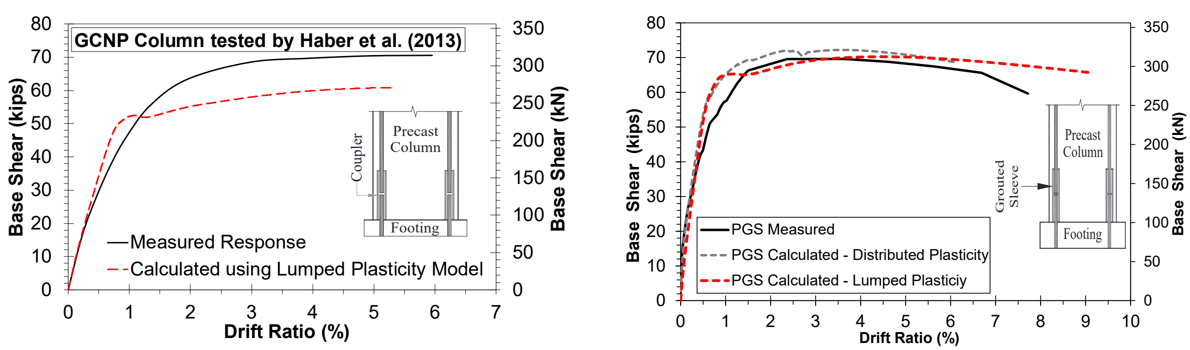

a. GCNP Column (Tested by Haber et al., 2013)

b. PGS Column

Figure 5.57 Validation of Dynamic Modeling Methods for Mechanically Spliced Bridge Columns

5.5.3 Ground Motions for Dynamic Analysis

AASHTO LRFD (2014) allows the use of real or synthetic motions as the input of dynamic analysis. Since the real ground motion spectra exhibit sudden changes in a wide range of frequencies (e.g., Fig. 5.58), it is hard to find a set of motions that does not fail columns with different masses (axial load index from 5% to 15%) under nonlinear dynamic analyses. Therefore, it was decided to use five synthetic motions matching the full design spectrum for a specific site.

Five artificial ground motions were produced based on the AASHTO design spectrum for downtown Los Angeles, which is classified as seismic design category (SDC) D, the highest seismicity in AASHTO. "SeismoArtif" (2019) was used to produce the artificial ground motions in the analysis. The motions were assumed to be near-field with V_{S30} = 310 m/s (1017 ft/s) and an epicenter of 10 km (6.2 miles). The duration of each synthetic ground motion was 28.6 sec with a timestep of 0.01 sec. Figure 5.59 shows the AASHTO design and the synthetic motion spectra, and Figure 5.60 shows the synthetic ground motions.

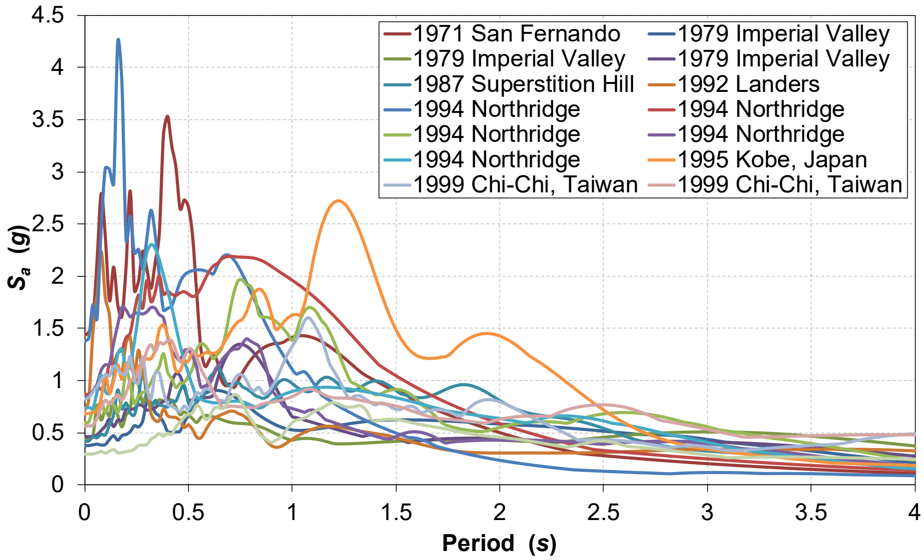

Figure 5.58 Pseudo Acceleration Spectra for 15 Near-Field Earthquakes Recommended by Backer (2007)

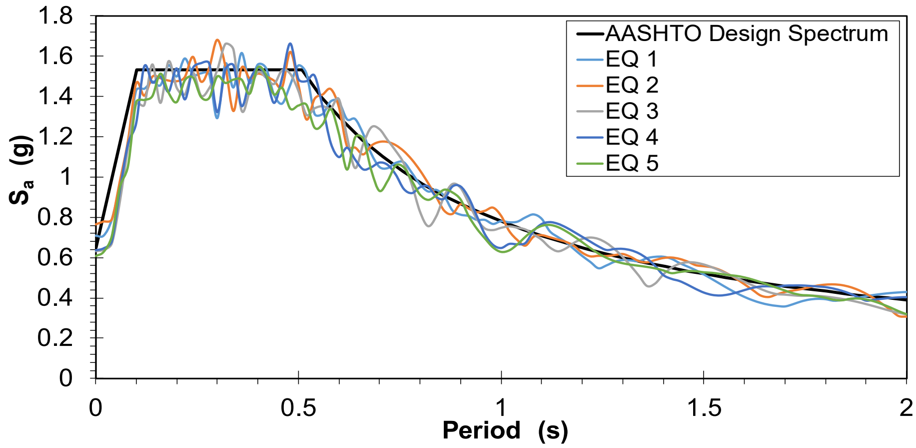

Figure 5.59 AASHTO Design Spectrum for Downtown Los Angeles, CA, and Spectra for Synthetic Motions

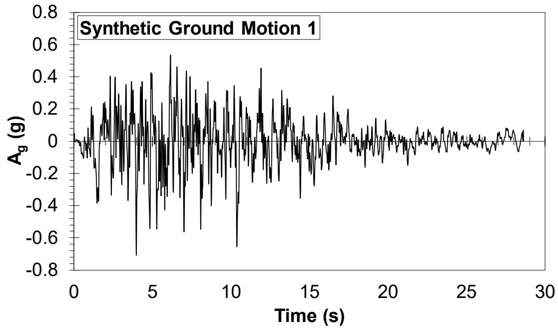

a) Synthetic Ground Motion 1 (EQ1)

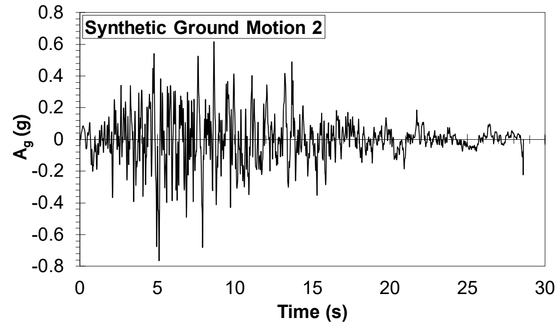

b) Synthetic Ground Motion 2 (EQ2)

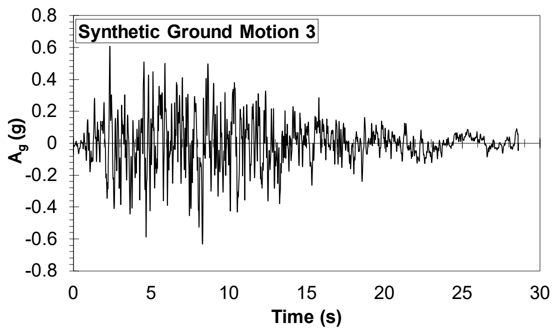

c) Synthetic Ground Motion 3 (EQ3)

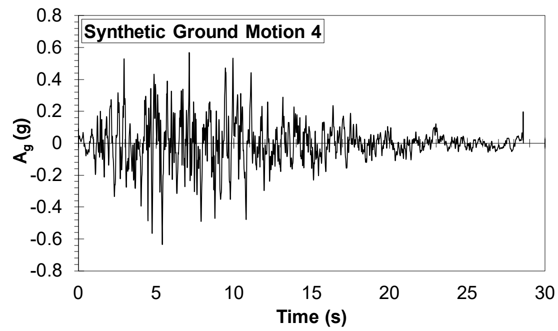

d) Synthetic Ground Motion 4 (EQ4)

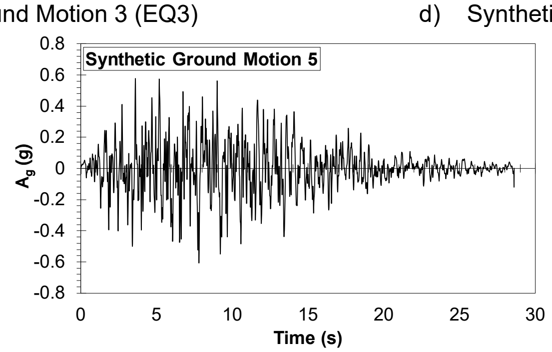

e) Synthetic Ground Motion 5 (EQ5)

Figure 5.60 Synthetic Ground Motions for Dynamic Analyses

5.5.4 Design Drift Demands

The linear-elastic design-level drift demand for each column was calculated using the column natural period and the AASHTO design spectrum (Fig. 5.59). Table 5.12 presents a summary of the design drift demand for circular and square columns. The design level drifts will be used later to compare with nonlinear drift demands. The effective seismic weight (W_{eff}) of each column was the axial load of that column plus 30% of the self-weight of the column. Also included in the table is the natural period (T_n) of each column.

Table 5.12 Column Design Level Drift Demands

Column ID, Section Geometry	Column Length, ft (m)	W_{eff}, kips (kN)	T_n, sec	Design Drift Demand, %
AR4-ALI5-D7, Circular	16 (4.88)	464.45 (2065.9)	0.54	2.13
AR4-ALI10-D7, Circular	16 (4.88)	916.84 (4078.1)	0.74	2.92
AR4-ALI15-D7, Circular	16 (4.88)	1369.23 (6090.3)	0.88	3.43
AR6-ALI5-D7, Circular	24 (7.32)	470.49 (2092.7)	1.01	2.63
AR6-ALI10-D7, Circular	24 (7.32)	922.88 (4105.0)	1.37	3.58
AR8-ALI5-D7, Circular	32 (9.75)	476.51 (2119.5)	1.56	3.05
AR4-ALI5-D7, Square	16 (4.88)	591.36 (2630.4)	0.46	1.62
AR4-ALI10-D7, Square	16 (4.88)	1167.36 (5192.4)	0.63	2.48
AR4-ALI15-D7, Square	16 (4.88)	1743.36 (7754.5)	0.75	2.93
AR6-ALI5-D7, Square	24 (7.32)	599.04 (2664.5)	0.85	2.21
AR6-ALI10-D7, Square	24 (7.32)	1175.04 (5226.6)	1.17	3.05
AR8-ALI5-D7, Square	32 (9.75)	606.72 (2698.7)	1.31	2.57

Note: "AR" refers to the aspect ratio, "ALI" refers to the column axial load index, "D" refers to the displacement ductility capacity, "W_{eff}" refers to the effective seismic weight of the column and includes the axial load and 30% of the column self-weight, and "T_n" refers to the natural period. The density of concrete was assumed to be 150 lb/ft^3 (2403 kg/m^3).

5.6 Results of Parametric Demand Analyses

Six circular and six square columns were included in the dynamic analysis as the reference CIP columns. Furthermore, eight coupler products were utilized at the base of each column to investigate the seismic demands of mechanically spliced columns. Each column was subjected to the five synthetic ground motions discussed in the previous section. Five-hundred-forty (540) nonlinear dynamic analyses were performed in the present study using the verified dynamic model. A summary of the results is presented herein.

5.6.1 Seismic Demand Analysis Results for Circular Columns

Figure 5.61 shows a sample of nonlinear dynamic analysis for the circular AR4-ALI10-D7 column including drift and force histories for the CIP and eight mechanically spliced precast columns. We can see that the drift history for all columns is very close. There are only slight variations between the peak and residual drifts between all columns. Similarly, the force history of the spliced columns follows that of CIP. The graph indicates that the spliced columns with longer couplers have the highest variations in the force response compared with the unspliced columns. In general, the force responses of the spliced columns were higher than those of the unspliced columns, leading to a higher maximum baseshear.

A similar analysis was performed for all other circular columns but only the peak responses were extracted, and the trend was established. The peak drift responses for each circular CIP column and its corresponding eight spliced columns under the five synthetic ground motions were superimposed in a figure to better comment on the seismic effects of couplers (Fig. 5.62 to 5.67). Also included in each figure is the CIP drift capacity and the CIP deign-level drift demand (S_d). The seismic drift demands for the circular columns were less than the drift capacities for all runs except some of the spliced columns under earthquake EQ2.

The graphs show that the drift response of the spliced columns is very close to that for the CIP columns. The maximum displacement deviation between CIP and all spliced circular columns was 7.23%, which was observed in the AR4-ALI5-D7 column spliced with GSD couplers under EQ4. Even though the peak response variations were insignificant, it was observed that the longest and shortest couplers, such as GSN and HR, caused the most variation in column displacement response while the couplers with an intermediate length, such as TH and SW, caused minimal variations. Overall, the displacement demands of circular RC bridge columns are not significantly affected by couplers when they are used in the column plastic hinges.

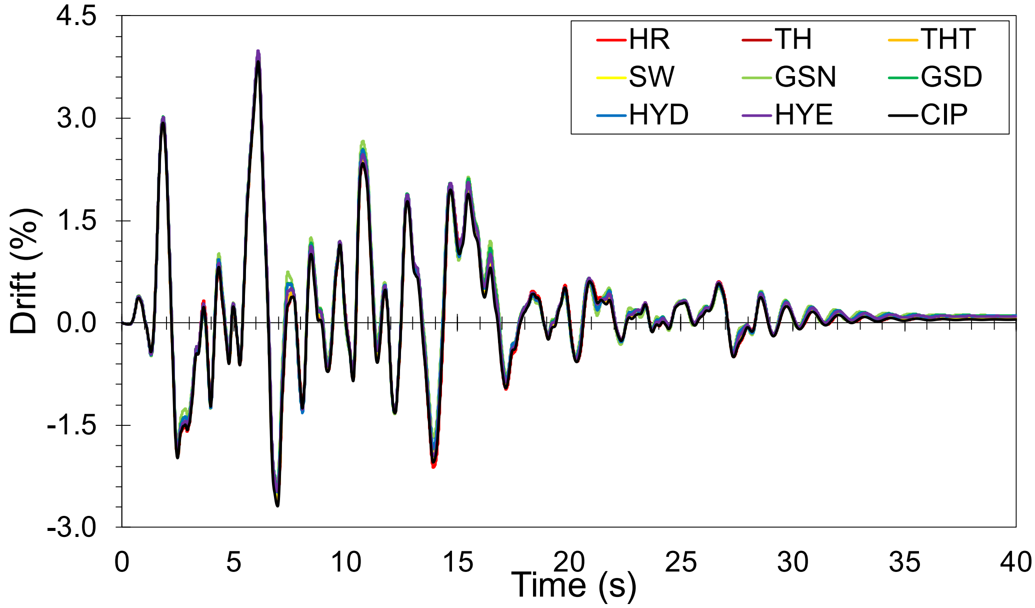

a) Drift Response History under Earthquake EQ2

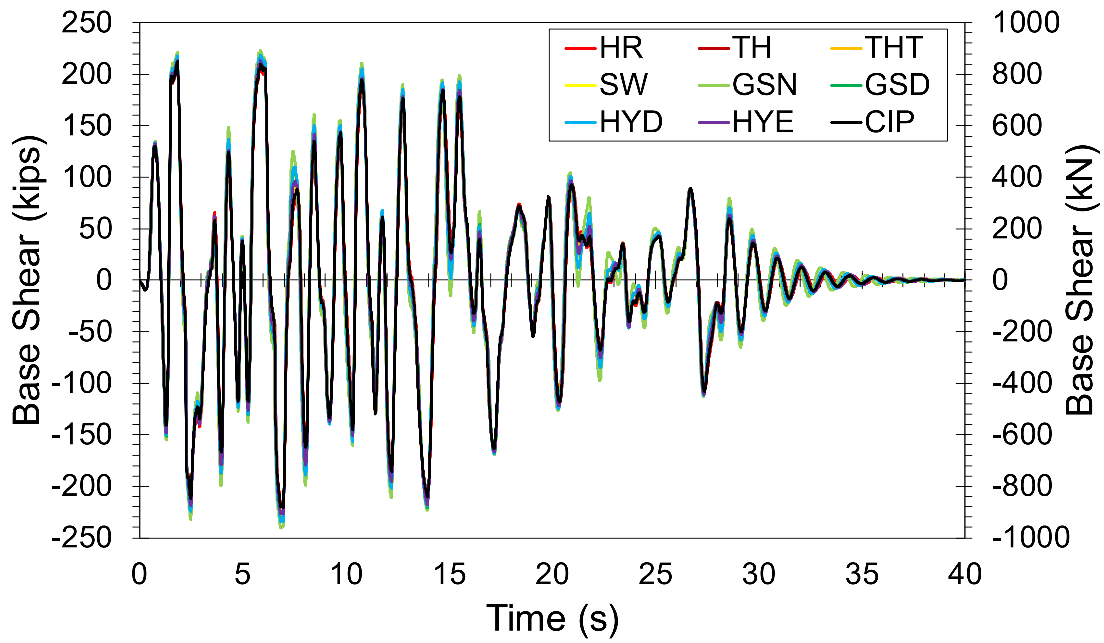

b) Force Response History under Earthquake EQ2

Figure 5.61 Sample Nonlinear Demand Analysis Results for Circular AR4-ALI10-D7 under EQ2

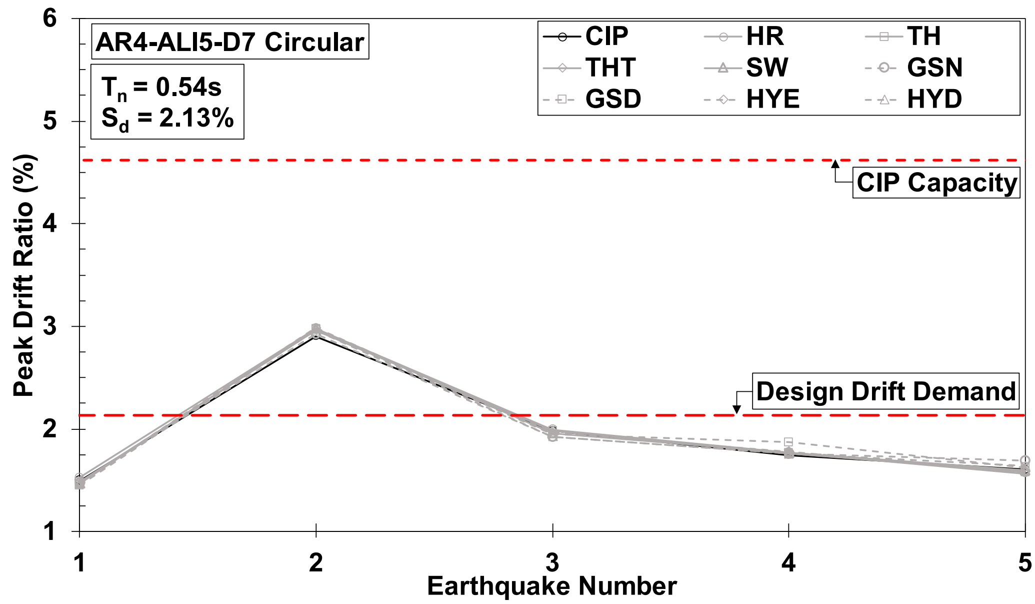

Figure 5.62 Dynamic Drift Response of AR4-ALI5-D7 Circular CIP and Spliced Columns

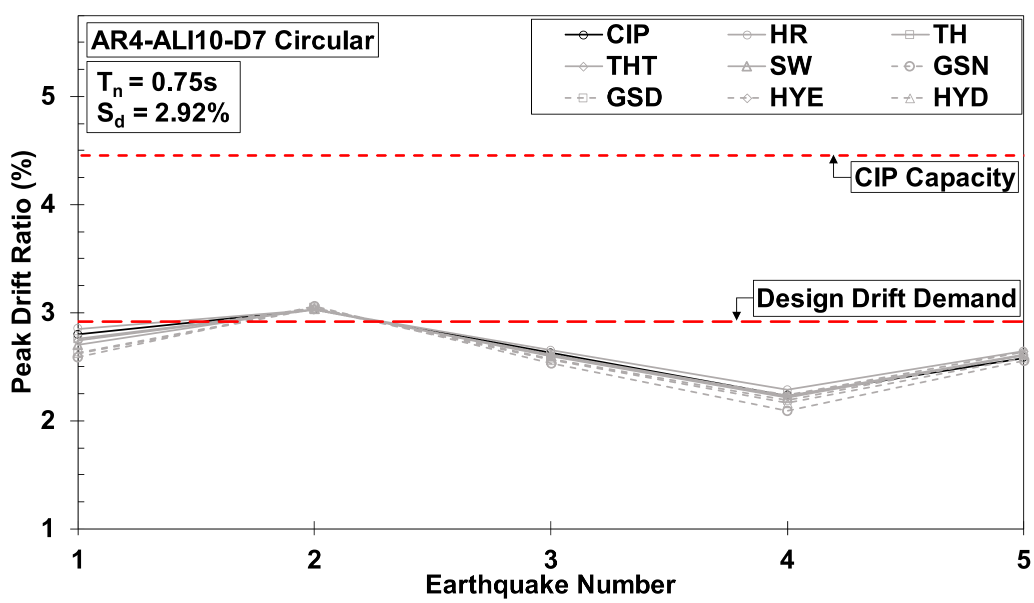

Figure 5.63 Dynamic Drift Response of AR4-ALI10-D7 Circular CIP and Spliced Columns

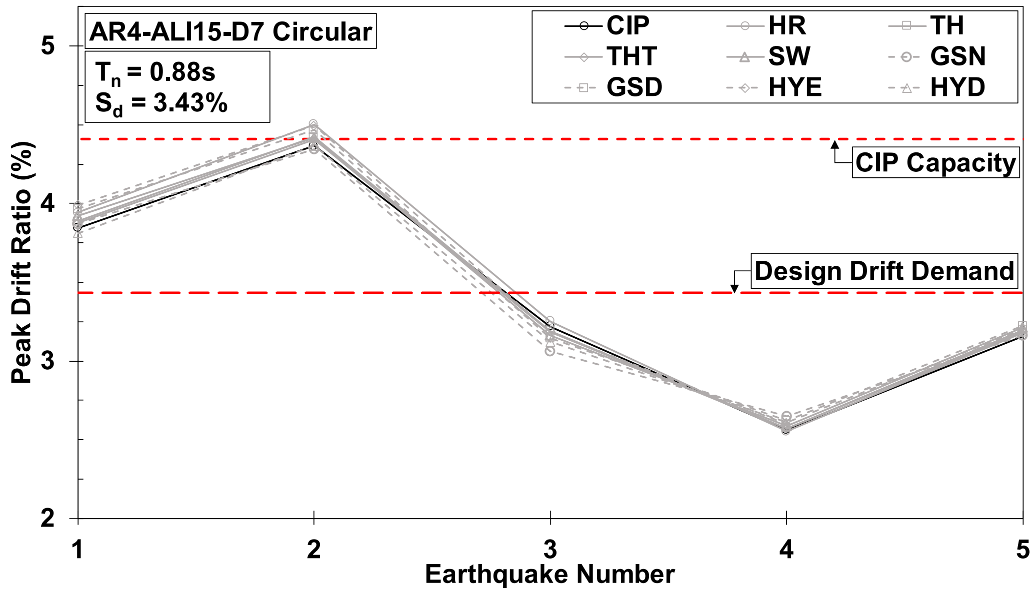

Figure 5.64 Dynamic Drift Response of AR4-ALI15-D7 Circular CIP and Spliced Columns

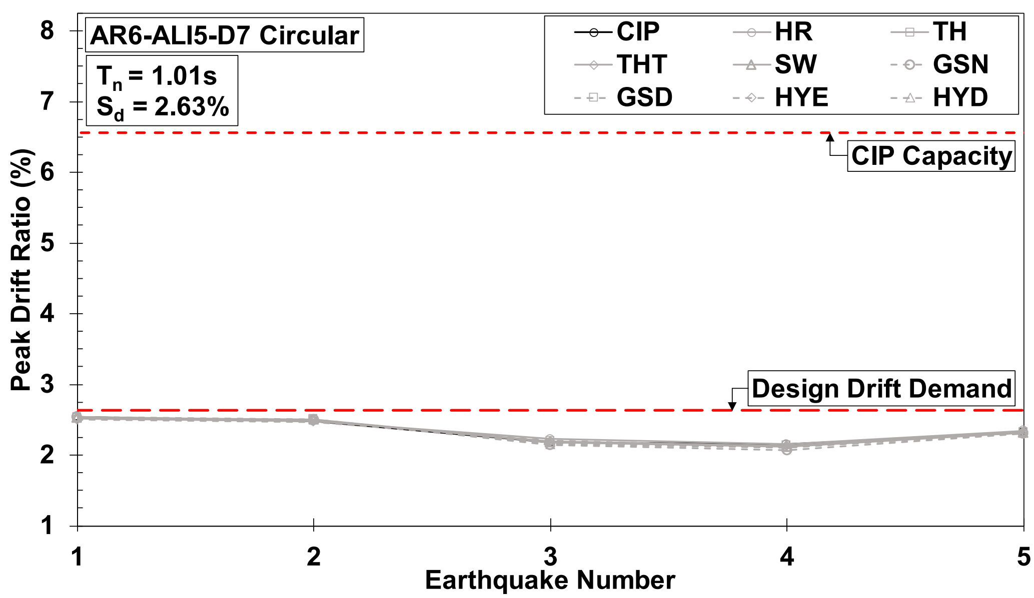

Figure 5.65 Dynamic Drift Response of AR6-ALI5-D7 Circular CIP and Spliced Columns

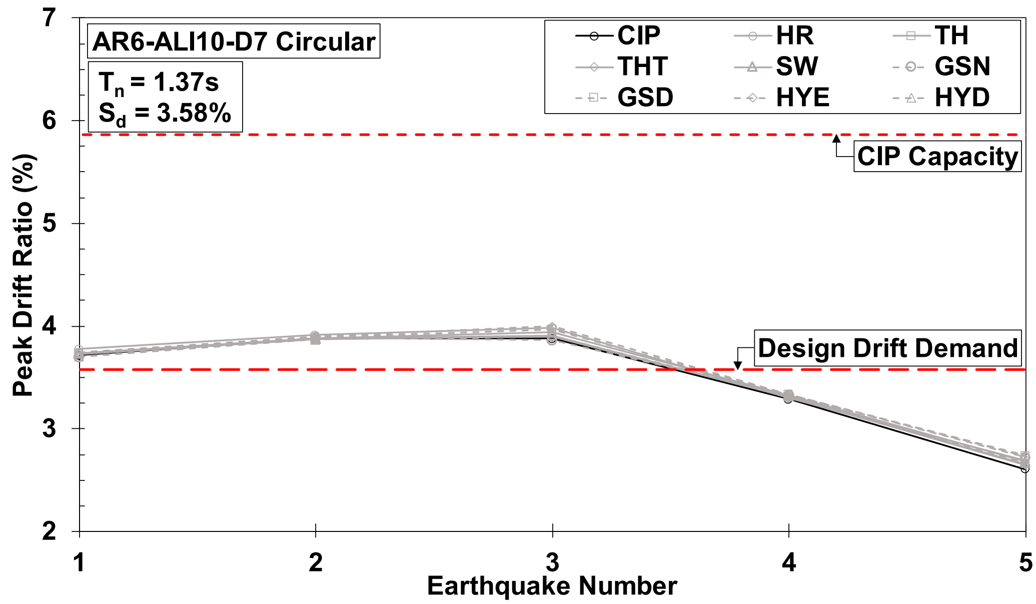

Figure 5.66 Dynamic Drift Response of AR6-ALI10-D7 Circular CIP and Spliced Columns

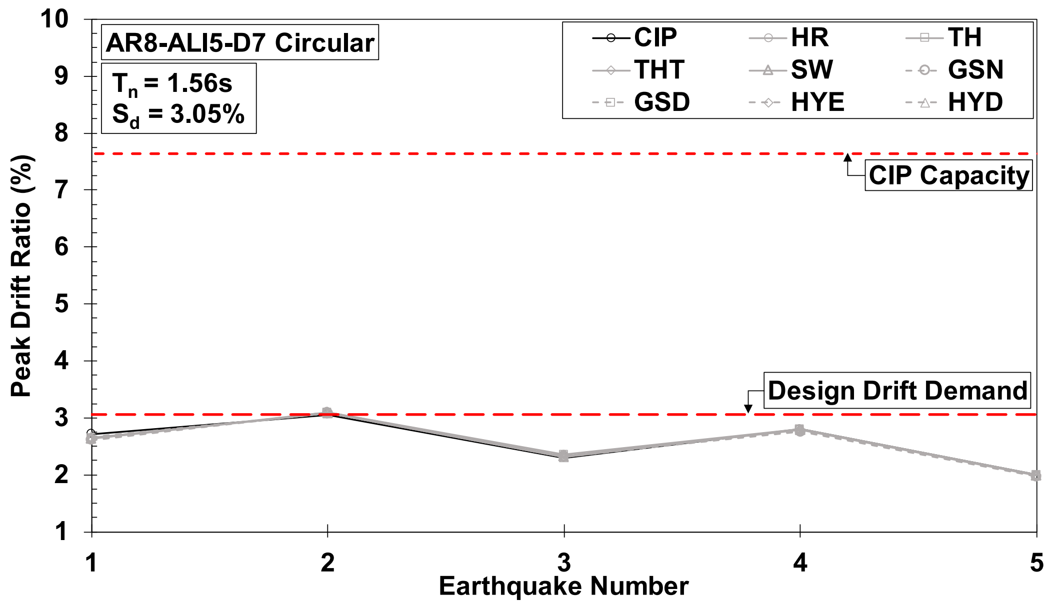

Figure 5.67 Dynamic Drift Response of AR8-ALI5-D7 Circular CIP and Spliced Columns

5.6.2 Seismic Demand Analysis Results for Square Columns

The peak drift responses for each square CIP column and its corresponding eight spliced columns under the five synthetic ground motions were superimposed in a figure to better comment on the seismic effects of couplers (Fig. 5.68 to 5.73). Also included in each figure is the CIP drift capacity and the CIP deign-level drift demand (S_d). The seismic drift demands for the square columns were less than the drift capacities, thus the columns did not fail under the five ground motions and the results could be compared.

The graphs show that the drift demands of the spliced columns are very close to those of CIP. The maximum displacement deviation between CIP and all spliced square columns was 5.51%, which was observed in the AR4-ALI5-D7 column spliced with HYE couplers under EQ2. Even though the peak response variations were insignificant, it was observed that the longest and shortest couplers, such as GSN and HR, can result in the highest effects on the column displacement demands while the couplers with an intermediate length, such as TH and SW, had minimal effects on the displacement demands. Overall, the coupler effects are expected to be minimal on the displacement demands of square bridge columns.

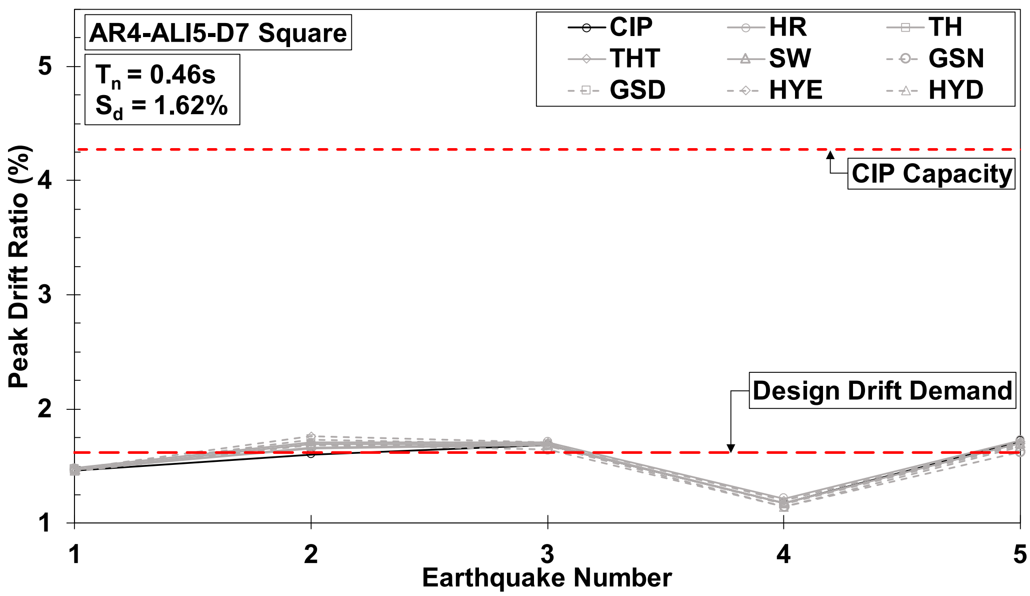

Figure 5.68 Dynamic Drift Response of AR4-ALI5-D7 Square CIP and Spliced Columns

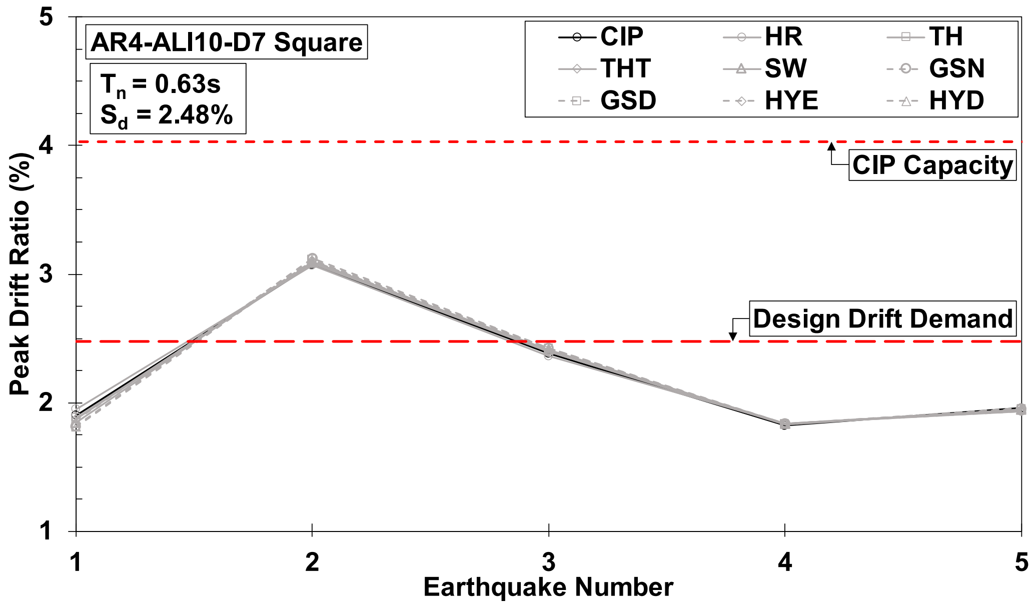

Figure 5.69 Dynamic Drift Response of AR4-ALI10-D7 Square CIP and Spliced Columns

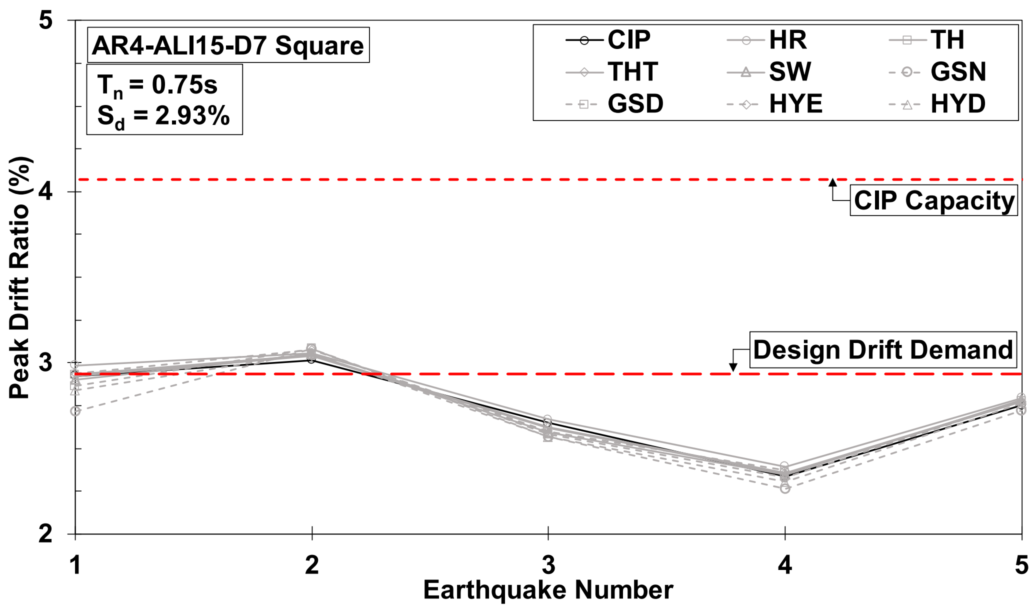

Figure 5.70 Dynamic Drift Response of AR4-ALI15-D7 Square CIP and Spliced Columns

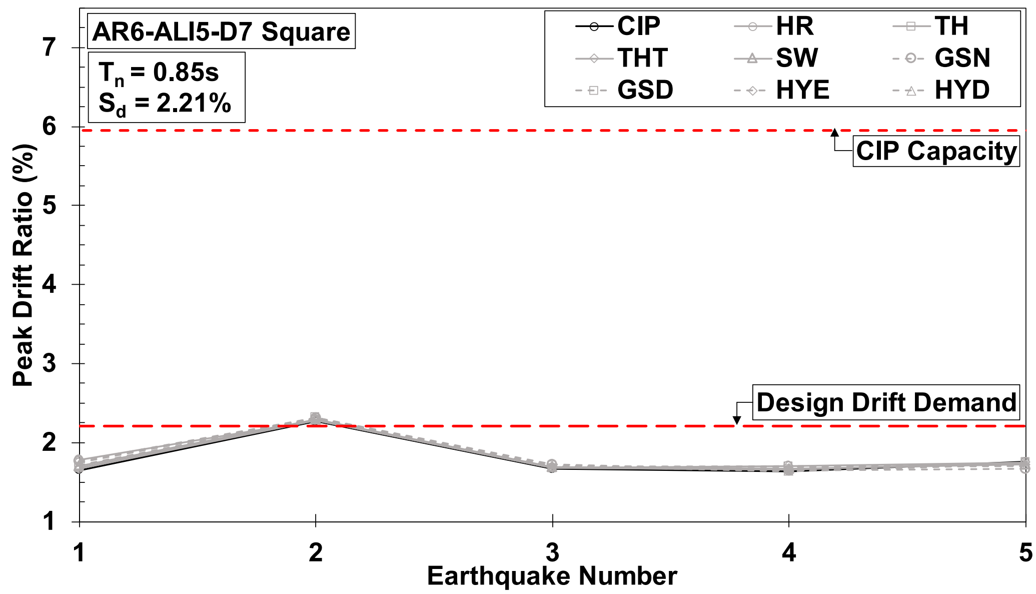

Figure 5.71 Dynamic Drift Response of AR6-ALI5-D7 Square CIP and Spliced Columns

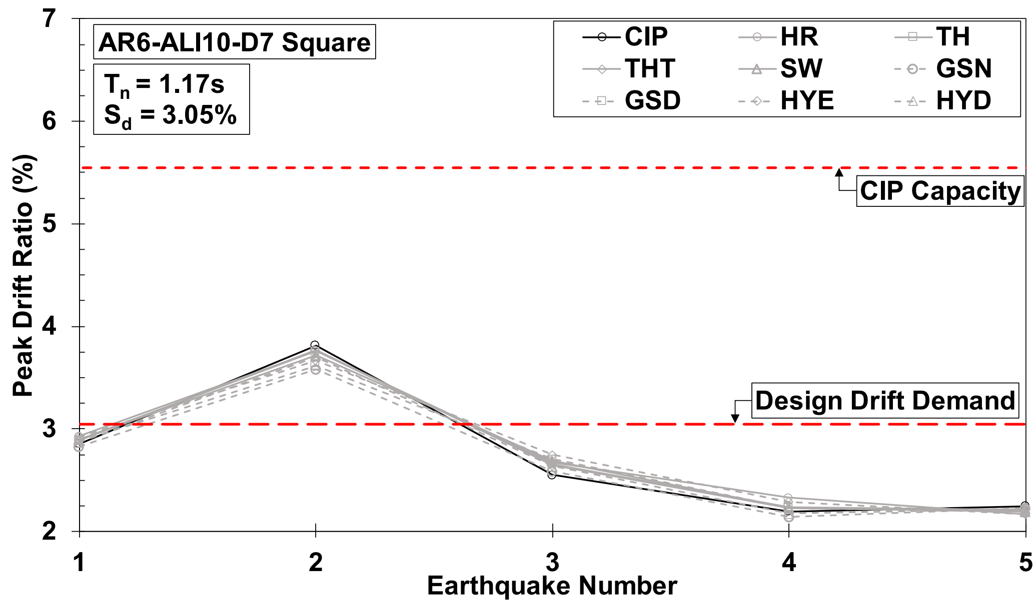

Figure 5.72 Dynamic Drift Response of AR6-ALI10-D7 Square CIP and Spliced Columns

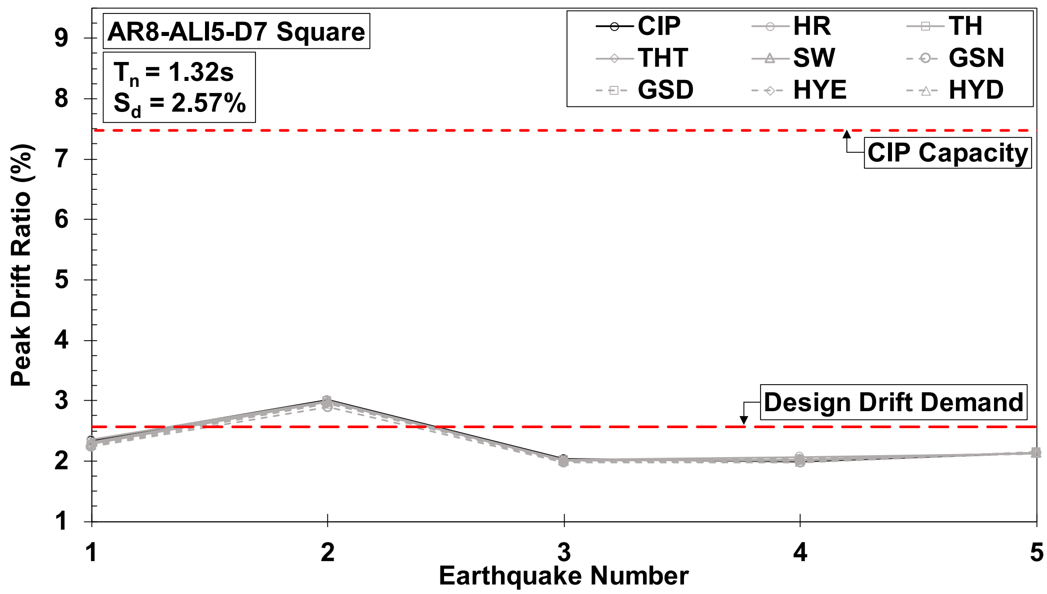

Figure 5.73 Dynamic Drift Response of AR8-ALI5-D7 Square CIP and Spliced Columns

5.6.3 Summary of Seismic Demand Analysis

Data from each run performed on the 12 columns was compiled into two tables to better illustrate the effects of using mechanical bar couplers on the column displacement demands. Tables 5.13 and 5.14 present the results of the seismic demand analyses. The peak drift demands for each unspliced column (CIP) and the corresponding mechanically spliced column were reported for each run in terms of percent difference from the peak drift of CIP. There were several cases where spliced columns did not show any increase in the demand when compared to the unspliced columns. For these cases, the maximum deviation in the demand was reported as a negative value. Figures 5.74 and 5.75 show the summaries of all dynamic analyses for columns with circular and square cross-sections, respectively. The plots show the peak drift demand of each spliced column normalized to the peak drift demand of the CIP column on the vertical axis plotted versus the rigid length factor of the spliced column normalized to the longitudinal bar diameter. These plots show that columns spliced with long and rigid couplers tend to have slightly less peak drift demands than columns spliced with short and less stiff couplers.

From Tables 5.13 and 5.14, it can be inferred that the columns spliced with HR couplers experienced the highest peak drift demands among the eight spliced column types. This was obtained by counting which coupler column experienced the largest drift demand per column type. Followed by HR, columns spliced with GSN, HYE, HYD, GSD, and THT couplers showed the next highest displacement demands. TH and SW did not alter the column displacement demand compared with CIP.

In general, couplers did not have significant effects on the drift demands of bridge columns. Long and rigid couplers tend to make the columns slightly stiffer, thus reducing the displacement demands on columns. The dynamic behavior of columns with low aspect ratios appeared to be affected slightly more by couplers than the columns with higher aspect ratios. This is likely because the force-drift behavior of slender columns is largely controlled by the P-Δ effects and not couplers.

Table 5.13 Summary of Seismic Demand Analysis for Circular Columns

Circular Column ID	Earthquake Motion	Peak CIP Drift (%)	Maximum Increase in Drift Demands	Worst Case Coupler
AR4-ALI5-D7	EQ1	1.50	2.27%	HR
	EQ2	2.90	2.92%	HYE
	EQ3	1.98	0.79%	HR
	EQ4	1.74	7.23%	GSD
	EQ5	1.60	5.63%	GSN
AR4-ALI10-D7	EQ1	2.80	1.89%	HR
	EQ2	3.03	1.05%	GSN
	EQ3	2.62	0.97%	HR
	EQ4	2.23	2.25%	HR
	EQ5	2.58	2.26%	HR
AR4-ALI15-D7	EQ1	3.85	3.75%	HYE
	EQ2	4.36	3.13%	HR
	EQ3	3.22	1.03%	HR
	EQ4	2.56	3.38%	GSN
	EQ5	3.16	2.08%	HYE
AR6-ALI5-D7	EQ1	2.55	-0.24%	GSN
	EQ2	2.48	1.18%	HYD
	EQ3	2.18	2.07%	HR
	EQ4	2.16	-0.09%	HR
	EQ5	2.32	1.08%	HR
AR6-ALI10-D7	EQ1	3.72	1.58%	HR
	EQ2	3.88	0.92%	HR
	EQ3	3.88	3.06%	HYE
	EQ4	3.29	1.47%	GSD
	EQ5	2.61	5.10%	GSD
AR8-ALI5-D7	EQ1	2.72	-1.90%	HYD
	EQ2	3.06	1.44%	HYE
	EQ3	2.30	2.16%	HR
	EQ4	2.80	0.09%	HR
	EQ5	2.00	-0.03%	HR

Note: "AR" refers to the aspect ratio, "ALI" refers to the column axial load index, "D" refers to the displacement ductility capacity, "CIP" refers to the reference columns, "HR" refers to the headed reinforcement couplers, "L_{sp}" is the coupler length, "β" is the coupler rigid length factor, "GS" refers to the grouted couplers, and "HY" refers to the hybrid couplers; 1 in. = 25.4 mm.

Table 5.14 Summary of Seismic Demand Analysis for Square Columns

Square Column ID	Earthquake Motion	Peak CIP Drift (%)	Maximum Increase in Demand (%)	Worst Case Coupler
AR4-ALI5-D7	EQ1	1.46	1.12	HR
	EQ2	1.60	5.51	HYE
	EQ3	1.68	1.38	HR
	EQ4	1.17	2.44	HR
	EQ5	1.72	0.57	HR
AR4-ALI10-D7	EQ1	1.90	1.79	HR
	EQ2	3.07	1.61	GSN
	EQ3	2.38	1.61	GSN
	EQ4	1.82	0.88	HYE
	EQ5	1.96	0.00	HYD
AR4-ALI15-D7	EQ1	2.92	1.58	HR
	EQ2	3.02	1.56	GSN
	EQ3	2.65	0.59	HR
	EQ4	2.33	2.30	HR
	EQ5	2.75	1.36	HR
AR6-ALI5-D7	EQ1	1.65	5.38	HR
	EQ2	2.27	1.87	GSN
	EQ3	1.67	2.39	GSN
	EQ4	1.64	3.14	HR
	EQ5	1.75	-0.07	HR
AR6-ALI10-D7	EQ1	2.86	1.94	HR
	EQ2	3.81	-1.19	THT
	EQ3	2.55	5.08	HYE
	EQ4	2.19	4.10	HR
	EQ5	2.25	-0.60	GSN
AR8-ALI5-D7	EQ1	2.34	0.66	HR
	EQ2	3.00	-0.14	HR
	EQ3	2.03	-0.58	THT
	EQ4	1.99	2.76	HR
	EQ5	2.14	0.35	HYD

Note: "AR" refers to the aspect ratio, "ALI" refers to the column axial load index, "D" refers to the displacement ductility capacity, "CIP" refers to the reference columns, "HR" refers to the headed reinforcement couplers, "L_{sp}" is the coupler length, "β" is the coupler rigid length factor, "GS" refers to the grouted couplers, and "HY" refers to the hybrid couplers; 1 in. = 25.4 mm.

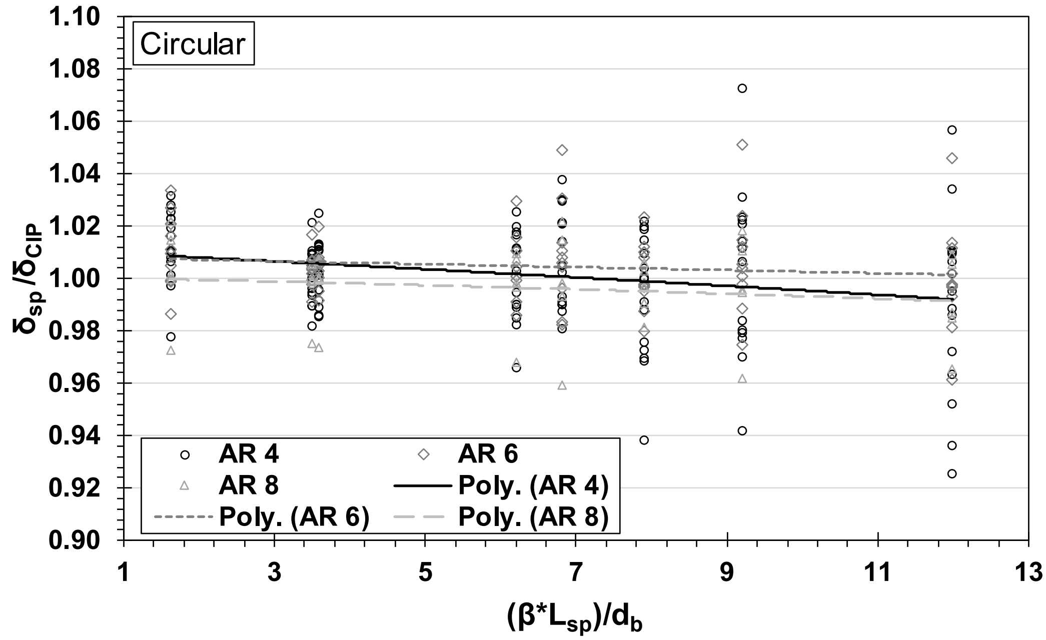

Figure 5.74 Summary Plot of Seismic Demand Analysis for Circular Columns

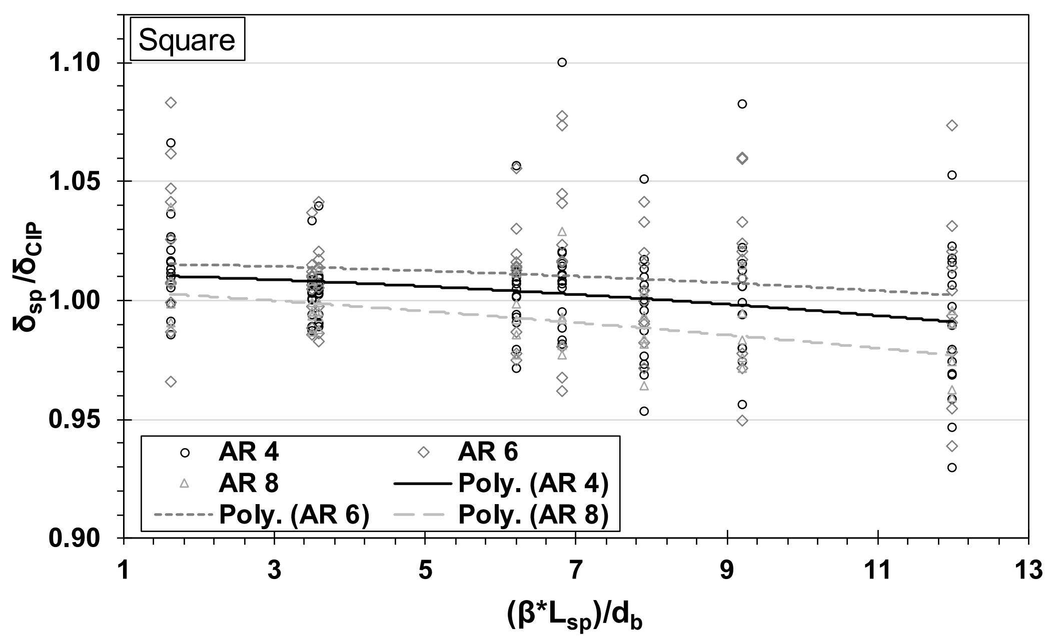

Figure 5.75 Summary Plot of Seismic Demand Analysis for Square Columns

5.7 Summary of Dynamic Analyses

A nonlinear dynamic parametric study was performed to determine the effects of couplers on the seismic demands of bridge columns with circular and square cross sections. A model was constructed and verified using the test data collected from the literature. Six CIP columns with circular cross sections and six CIP columns with square cross sections, all with a displacement ductility capacity of seven, were included. Subsequently, eight coupler types were used at the base of the CIP columns to make them precast. A total of 540 seismic demand analyses were performed on unspliced and spliced columns.

Bridge columns with low aspect ratios and high axial load indices showed slightly higher displacement demands compared with columns with higher aspect ratios and lower axial load indices. Furthermore, the dynamic analyses showed that mechanical bar couplers have minimal effects on the displacement demands of bridge columns. The results showed that couplers with medial lengths had the least effect on seismic demand. Columns spliced with long and stiff couplers tend to show slightly lower displacement demands than columns with shorter and less stiff couplers. This trend was seen for spliced columns with either circular or square cross sections. Overall, couplers might alter the seismic displacement demands of RC bridge columns no more than 7%.

5.8 References

AASHTO SGS. (2011). “AASHTO Guide Specifications for LRFD Seismic Bridge Design,” Washington, DC: American Association of State Highway and Transportation Officials.

ASTM A706/A706M-09b (2009). “Standard Specification for LowAlloy Steel Deformed and Plain Bars for Concrete Reinforcement,” ASTM International, West Conshohocken, PA.

Dahal, P.K., and Tazarv, M. (2020). “Mechanical Bar Splices for Incorporation in Plastic Hinge Regions of RC Members,” *Construction and Building Materials*, Vol. 258, 120308, 17 pp.

Mander, J.B, Priestly, M.J.N. and Park, R. (1988). “Theoretical stress-strain model for confined concrete,” *Journal of Structural Engineering*, ASCE Vol 114, No. 8, pp. 1804 – 1826.

OpenSees. (2016). “Open System for Earthquake Engineering Simulations,” Version 2.4.1, Berkeley, CA, Available online: http://opensees.berkeley.edu.

Seismosoft (2019) “SeismoArtif - A computer program for generation of artificial accelerograms.” Available from URL: www.seismosoft.com

Tazarv, M., and Saiidi, M.S. (2013). “Analytical Studies of the Seismic Performance of a Full-Scale SMA-Reinforced Bridge Column,” (Invited Paper), *International Journal of Bridge Engineering*, Vol. 1, No. 1, pp. 37-50.

Tazarv, M., and Saiidi, M.S. (2014). “Next Generation of Bridge Columns for Accelerated Bridge Construction in High Seismic Zones,” CCEER Report No. 14-06, Center for Civil Engineering Earthquake Research, University of Nevada, Reno, NV.

Tazarv, M., and Saiidi, M.S. (2016). “Seismic Design of Bridge Columns Incorporating Mechanical Bar Splices in Plastic Hinge Regions,” *Engineering Structures*, DOI: 10.1016/j.engstruct.2016.06.041, Vol 124, pp. 507-520.

USGS. (2019) “U.S. Seismic Design Maps Web Services,” United States Geological Survey.

6. EVALUATION OF CURRENT DESIGN METHODS FOR MECHANICALLY SPLICED BRIDGE COLUMNS

6.1 Introduction

A comprehensive experimental database of bridge columns incorporating mechanical bar splices was generated in this project. Furthermore, pushover and dynamic analyses were performed in the previous chapters to better understand the effects of the couplers on the column performance. The post-test pushover analyses of the six precast columns confirmed that such an analytical tool is viable for the design of a new mechanically spliced bridge column. However, the literature offers other analysis/design tools that have not been fully investigated in the present project. In this chapter, current design methods for mechanically spliced bridge columns are briefly reviewed and evaluated using the new column experimental database.

NCHRP 935 (Saiidi et al., 2020) recommends three methods to quantify the effects of bar couplers on the performance of bridge columns as summarized in Table 6.1. The methods are labeled as Method 1, Method 2, and Method 3. Method 1 is based on a simple reduction factor for the displacement ductility capacity using a few coupler properties. In this method, the displacement ductility capacity of CIP is first calculated (using a moment-curvature or pushover analysis), then it is modified based on the coupler properties. Method 2 can be performed using a moment-curvature or pushover analysis, but the plastic hinge length should be modified based on the coupler properties. Method 3 is a pushover analysis using the coupler stress-strain relationship. In this chapter, the accuracy of these three analysis/design methods for mechanically spliced bridge columns is evaluated. Note that Method 3 was fully investigated in Chapter 4 of the present report, and other methods were briefly mentioned in Chapter 5.

Table 6.1 Three Modeling Methods for Mechanically Spliced Bridge Columns (NCHRP 935)

Design Method	Analysis Type	Column Element in Pushover Analysis	Analysis Requirements
Cast-in-place (CIP) columns	Moment-Curvature or Pushover	Usually conducted using a lumped plasticity model, which requires an analytical plastic hinge length. However, distributed plasticity model can also be utilized	AASHTO Guide Specifications for LRFD Seismic Bridge Design
Method 1. Spliced columns using a displacement ductility equation	Use CIP analysis results	Use CIP analysis results	$\frac{\mu_{sp}}{\mu_{CIP}} = (1 - 0.18\beta)(\frac{H_{sp}}{L_{sp}})^{0.1\beta}$
Method 2. Spliced columns using modified plastic hinge length equation	Moment-Curvature or Pushover	Lumped plasticity model only	Similar to CIP but with $L_p^{sp} = L_p - (1 - \frac{H_{sp}}{L_p})\beta L_{sp} \leq L_p$
Method 3. Spliced columns using proposed stress-strain model for couplers	Pushover only	Distributed plasticity model only	Coupler stress-strain model (Fig. 4.2)

Note: μ_{sp}: The mechanically spliced bent displacement ductility capacity; μ_{CIP}: The corresponding non-spliced cast-in-place bent displacement ductility capacity; β: The coupler rigid length ratio; H_{sp}: The distance from the column end to the nearest face of the coupler embedded either inside the column or inside the column adjoining member (*in.*); L_{sp}: The coupler length (*in.*); L_p^{sp}: The modified plastic hinge length for mechanically spliced bridge columns; L_p: The conventional column analytical plastic hinge length according to the current AASHTO SGS.

6.2 Mechanically Spliced Bridge Column Database

NCHRP 935 evaluated the accuracy of the three methods discussed above using data for four mechanically spliced bridge columns. Data for three columns were collected from the literature (GCNP and HCNP from Haber et al., 2014; and GGSS-1 from Pantelides et al., 2014) and the fourth column, GC10, was tested in the NCHRP project. The next section provides more information about these four columns. Furthermore, six mechanically spliced bridge columns, PGS, PGD, PHD, PHV, PTV, and PHH, were tested in the present study. In total, a database of 10 large-scale mechanically spliced bridge columns is compiled herein and is used to evaluate the three design methods for these columns.

6.3 Evaluation of Ductility Reduction Method (Method 1)

For the 10 mechanically spliced bridge columns, the displacement ductility capacity reduction factor accounting for the coupler effects was estimated using Eq. 6.1, and the findings were summarized in Table 6.2. For completeness, the reduction factor ($\frac{\mu_{sp}}{\mu_{CIP}}$) measured in the tests was also reported for each column. Figure 6.1 shows a summary of the evaluation for Method 1.

$$\frac{\mu_{sp}}{\mu_{CIP}} = (1 - 0.18\beta)(\frac{H_{sp}}{L_{sp}})^{0.1\beta} \tag{6.1}$$

The calculated displacement ductility capacities for the mechanically spliced bridge columns had a range of accuracy when compared to the measured values. The estimated displacement ductility capacity of the first four columns (GCNP, HCNP, GGSS-1, and GC10) were almost the same as those measured in the tests with a maximum error of 2.3% (respectively, +1.6%, -2.3%. +1.6%, and -1.5%). Five columns (PGD, PGS, PHV, PTV, and PHH) had a higher range of error from 15% to 35% (respectively, +29.8%, -15%, -28.9%, +23.8%, and -35.5%). A negative sign means that the estimated value was less than the measured one, thus conservative for the design. In one column, PHD, the calculated displacement ductility was not close to that in the test mainly because the couplers were not seismic splices, as discussed in the previous chapters. Excluding PHD, the average error between the calculated and measured displacement ductility capacities for nine precast columns was -2.9%, indicating that Method 1 is overall conservative.

Table 6.2 Evaluation of Ductility Reduction Method for Design of Mechanically Spliced Columns

Reference / Column	**Calculated**	**Measured**
Haber et al. (2014) / GCNP Column with grouted sleeve couplers immediately above the footing surface	$\beta = 0.70$ $H_{sp} = 0.$ use $H_{sp} = 0.1\ in.\ (2.5\ mm)$ $L_{sp} = 14.57\ in.\ (370\ mm)$ thus $\frac{\mu_{sp}}{\mu_{CIP}} = (1 - 0.18\beta)\left(\frac{H_{sp}}{L_{sp}}\right)^{0.1\beta} = \boxed{0.62}$	$\frac{\mu_{sp}}{\mu_{CIP}} = \frac{4.52}{7.36} = \boxed{0.61}$
Haber et al. (2014) / HCNP Column with headed bar couplers 5 *in*. (127 *mm*) above the column-to-footing interface or 4 *in*. (102 *mm*) from the footing surface to the bottom of the coupler	$\beta = 0.85$ $H_{sp} = 4\ in.\ (122\ mm)$ $L_{sp} = 3.13\ in.\ (79\ mm)$ thus $\frac{\mu_{sp}}{\mu_{CIP}} = (1 - 0.18\beta)\left(\frac{H_{sp}}{L_{sp}}\right)^{0.1\beta} = \boxed{0.86}$	$\frac{\mu_{sp}}{\mu_{CIP}} = \frac{6.49}{7.36} = \boxed{0.88}$
Pantelides et al. (2014) / GGSS-1 Column with grouted sleeve couplers immediately above the footing surface	$\beta = 0.70$ $H_{sp} = 0.$ use $H_{sp} = 0.1\ in.\ (2.5\ mm)$ $L_{sp} = 14.57\ in.\ (370\ mm)$ thus $\frac{\mu_{sp}}{\mu_{CIP}} = (1 - 0.18\beta)\left(\frac{H_{sp}}{L_{sp}}\right)^{0.1\beta} = \boxed{0.62}$	$\frac{\mu_{sp}}{\mu_{CIP}} = \frac{5.4}{8.9} = \boxed{0.61}$
NCHRP 935 / GC10 Column with grouted sleeve couplers immediately above the footing surface	$\beta = 0.55$ $H_{sp} = 0.$ use $H_{sp} = 0.1\ in.\ (2.5\ mm)$ $L_{sp} = 18\ in.\ (457\ mm)$ thus $\frac{\mu_{sp}}{\mu_{CIP}} = (1 - 0.18\beta)\left(\frac{H_{sp}}{L_{sp}}\right)^{0.1\beta} = \boxed{0.68}$	$\frac{\mu_{sp}}{\mu_{CIP}} = \frac{5.07}{7.36} = \boxed{0.69}$
Present Study / PGD Column with grouted sleeve couplers immediately above the footing surface	$\beta = 0.70$ $H_{sp} = 0.$ use $H_{sp} = 0.1\ in.\ (2.5\ mm)$ $L_{sp} = 16.5\ in.\ (419.1\ mm)$ thus $\frac{\mu_{sp}}{\mu_{CIP}} = (1 - 0.18\beta)\left(\frac{H_{sp}}{L_{sp}}\right)^{0.1\beta} = \boxed{0.61}$	$\frac{\mu_{sp}}{\mu_{CIP}} = \frac{5.76}{12.37} = \boxed{0.47}$
Present Study / PGS Column with grouted sleeve couplers immediately above the footing surface	$\beta = 0.70$ $H_{sp} = 0.$ use $H_{sp} = 0.1\ in.\ (2.5\ mm)$ $L_{sp} = 14.57\ in.\ (370.1\ mm)$ thus $\frac{\mu_{sp}}{\mu_{CIP}} = (1 - 0.18\beta)\left(\frac{H_{sp}}{L_{sp}}\right)^{0.1\beta} = \boxed{0.62}$	$\frac{\mu_{sp}}{\mu_{CIP}} = \frac{9.08}{12.37} = \boxed{0.73}$
Present Study / PHD* Column with hybrid (grouted-threaded) couplers immediately above the footing surface, NOT seismic coupler	$\beta = 0.79$ (average of five specimens, use 1.01 from the pulled-out specimen) $H_{sp} = 0.$ use $H_{sp} = 0.1\ in.\ (2.5\ mm)$ $L_{sp} = 9.45\ in.\ (240\ mm)$ thus $\frac{\mu_{sp}}{\mu_{CIP}} = (1 - 0.18\beta)\left(\frac{H_{sp}}{L_{sp}}\right)^{0.1\beta} = \boxed{0.52}$	$\frac{\mu_{sp}}{\mu_{CIP}} = \frac{3.60}{12.37} = \boxed{0.29}$

Table 6.2 Continued

Reference / Column	Calculated	Measured
Present Study / PHV Column with hybrid (grouted-threaded) couplers immediately above the footing surface	$\beta = 0.82$ $H_{sp} = 0.$ use $H_{sp} = 0.1\ in.\ (2.5\ mm)$ $L_{sp} = 8.63\ in.\ (219\ mm)$ thus $\frac{\mu_{sp}}{\mu_{CIP}} = (1-0.18\beta)\left(\frac{H_{sp}}{L_{sp}}\right)^{0.1\beta} = \boxed{0.59}$	$\frac{\mu_{sp}}{\mu_{CIP}} = \frac{10.23}{12.37} = \boxed{0.83}$
Present Study / PTV Column with threaded couplers immediately above the footing surface	$\beta = 0.4$ $H_{sp} = 0.$ use $H_{sp} = 0.1\ in.\ (2.5\ mm)$ $L_{sp} = 9.0\ in.\ (228.6\ mm)$ thus $\frac{\mu_{sp}}{\mu_{CIP}} = (1-0.18\beta)\left(\frac{H_{sp}}{L_{sp}}\right)^{0.1\beta} = \boxed{0.78}$	$\frac{\mu_{sp}}{\mu_{CIP}} = \frac{7.77}{12.37} = \boxed{0.63}$
Present Study / PHH Column with hybrid (grouted-headed) couplers immediately above the footing surface	$\beta = 0.80$ $H_{sp} = 0.$ use $H_{sp} = 0.1\ in.\ (2.5\ mm)$ $L_{sp} = 7.75\ in.\ (196.9\ mm)$ thus $\frac{\mu_{sp}}{\mu_{CIP}} = (1-0.18\beta)\left(\frac{H_{sp}}{L_{sp}}\right)^{0.1\beta} = \boxed{0.60}$	$\frac{\mu_{sp}}{\mu_{CIP}} = \frac{11.49}{12.37} = \boxed{0.93}$

* Note that couplers used in PHD were not seismic couplers.

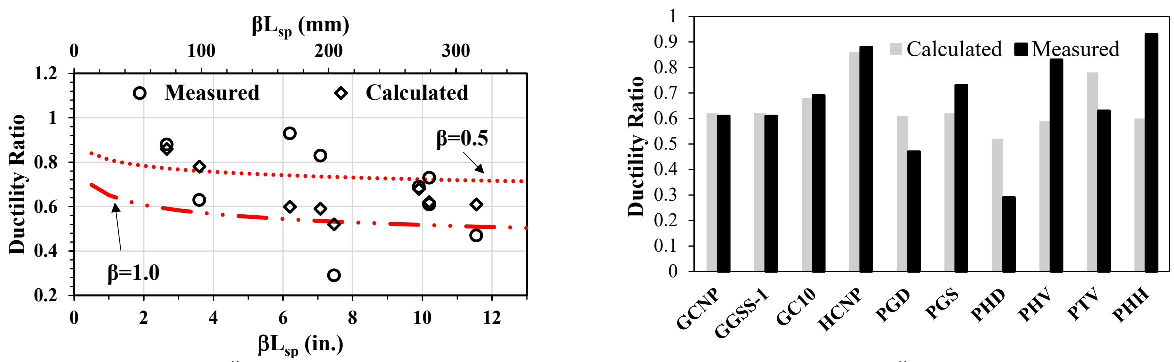

a) Ductility Ratio ($\frac{\mu_{sp}}{\mu_{CIP}}$) vs. Coupler Properties

b) Ductility Ratio ($\frac{\mu_{sp}}{\mu_{CIP}}$) vs. Column ID

Figure 6.1 Evaluation of Ductility Reduction (Method 1) for Design of Mechanically Spliced Columns

6.4 Evaluation of Modified Plastic Hinge Length Method (Method 2)

The 10 mechanically spliced bridge columns discussed in the previous section were reanalyzed but using the proposed modified plastic hinge length:

$$L_p^{sp} = L_p - (1 - \frac{H_{sp}}{L_p})\beta L_{sp} \leq L_p \qquad \text{(Eq. 6.2)}$$

A moment-curvature analysis was performed in accordance with AASHTO SGS (2011), then the results (idealized yield curvature and the ultimate curvature) were used to calculate the displacement ductility capacities.

Table 6.3 presents a summary of the calculations and Figure 6.2 shows the analysis results. Even though it was not needed in Method 2, the displacement ductility capacities for the CIP columns following the current AASHTO method were also included in the table for completeness. The AASHTO moment-curvature method for the displacement ductility capacity estimation showed up to 7.5% error in the reference CIP columns. For spliced columns, the calculated displacement ductility capacity for the four columns from the NCHRP report were close to that measured in the tests with a maximum error of +8%. For other columns, except PHD and PTV, the error had a range from -26.9% to +3.3%. The PHD showed 93% error because it had non-seismic couplers and should not go through such analysis. For PTV, the displacement ductility capacity was overestimated by 26.3% (9.81 in the calculation vs. 7.77 in the test). This is attributed to the low rigid length factor (β = 0.4), which is not common for a threaded coupler with a length of 9 in. (229 mm). Past tests at SDSU showed that threaded couplers exhibit large rigid length factors, sometimes exceeding 1.0. The average error between the calculated and measured displacement ductility capacity for nine columns (excluding PHD) was -3.5%, which is slightly conservative.

It should be noted that Method 2 also allows performing a fiber-section pushover analysis but using the modified plastic hinge length. Nevertheless, this was not performed herein (but in Chapter 5 to validate the dynamic models). Overall, Method 2 based on moment-curvature analysis was found viable in reproducing the test displacement ductility capacity for spliced bridge columns.

Table 6.3 Evaluation of Modified Plastic Hinge Length Method for Design of Mechanically Spliced Columns

Reference / Column	Calculated	Measured
Haber et al. (2014) / GCNP Column with grouted couplers immediately above the footing surface	<u>Non-Spliced Column (CIP):</u> Bar size: No. 8, Column Length=108 in., L_p = 20.4 in. Moment-Curvature Analysis: Idealized Yield Curvature ($\emptyset_{Yi}$): 0.00023 rad/in. Ultimate Curvature ($\emptyset_u$): 0.0032 rad/in. $\mu_{CIP} = 1 + 3\left(\frac{\emptyset_u}{\emptyset_{Yi}} - 1\right)\frac{L_p}{L}\left(1 - 0.5\frac{L_p}{L}\right) = 7.62$ <u>Spliced Column:</u> $\beta = 0.70, \quad H_{sp} = 0., \quad L_{sp} = 14.57\ in.$ $L_p^{sp} = L_p - \left(1 - \frac{H_{sp}}{L_p}\right)\beta L_{sp} \le L_p = 10.2\ in.$ $\mu_{sp} = 1 + 3\left(\frac{\emptyset_u}{\emptyset_{Yi}} - 1\right)\frac{L_p^{sp}}{L}\left(1 - 0.5\frac{L_p^{sp}}{L}\right) = 4.49$	Note: Displacement ductility capacity for a reference column is not needed in this method. It is provided for comparison. $\mu_{CIP} = 7.36$ (+3.4% error) $\mu_{sp} = 4.52$ (-0.7% error)
Haber et al. (2014) / HCNP Column with headed bar couplers 5 *in*. (127 *mm*) above the column-to-footing interface	<u>Non-Spliced Column (CIP):</u> Bar size: No. 8, Column Length=108 in., L_p = 20.4 in. Moment-Curvature Analysis: Idealized Yield Curvature ($\emptyset_{Yi}$): 0.00023 rad/in. Ultimate Curvature ($\emptyset_u$): 0.0032 rad/in. $\mu_{CIP} = 1 + 3\left(\frac{\emptyset_u}{\emptyset_{Yi}} - 1\right)\frac{L_p}{L}\left(1 - 0.5\frac{L_p}{L}\right) = 7.62$ <u>Spliced Column:</u> $\beta = 0.85, \quad H_{sp} = 4, \quad L_{sp} = 3.13\ in.$ $L_p^{sp} = L_p - \left(1 - \frac{H_{sp}}{L_p}\right)\beta L_{sp} \le L_p = 18.26\ in.$ $\mu_{sp} = 1 + 3\left(\frac{\emptyset_u}{\emptyset_{Yi}} - 1\right)\frac{L_p^{sp}}{L}\left(1 - 0.5\frac{L_p^{sp}}{L}\right) = 7.0$	$\mu_{CIP} = 7.36$ (+3.4% error) $\mu_{sp} = 6.48$ (+8% error)
Pantelides et al. (2014) / GGSS-1 Column with grouted couplers immediately above the footing surface	<u>Non-Spliced Column (CIP):</u> Bar size: No. 8, Column Length=93 in., L_p = 20.4 in. Moment-Curvature Analysis: Idealized Yield Curvature ($\emptyset_{Yi}$): 0.00028 rad/in. Ultimate Curvature ($\emptyset_u$): 0.0043 rad/in. $\mu_{CIP} = 1 + 3\left(\frac{\emptyset_u}{\emptyset_{Yi}} - 1\right)\frac{L_p}{L}\left(1 - 0.5\frac{L_p}{L}\right) = 9.41$ <u>Spliced Column:</u> $\beta = 0.70, \quad H_{sp} = 0., \quad L_{sp} = 14.57\ in.$ $L_p^{sp} = L_p - \left(1 - \frac{H_{sp}}{L_p}\right)\beta L_{sp} \le L_p = 10.2\ in.$ $\mu_{sp} = 1 + 3\left(\frac{\emptyset_u}{\emptyset_{Yi}} - 1\right)\frac{L_p^{sp}}{L}\left(1 - 0.5\frac{L_p^{sp}}{L}\right) = 5.46$	$\mu_{CIP} = 8.9$ (+5.4% error) $\mu_{sp} = 5.38$ (+1.5% error)

Table 6.3 Continued

<table>
<tr><th>Reference / Column</th><th>Calculated</th><th>Measured</th></tr>
<tr><td>NCHRP 935 / GC10

Column with grouted couplers immediately above the footing surface</td><td><u>Non-Spliced Column (CIP):</u>
Bar size: No. 10, Column Length=108 in., L_p = 25.91 in.

Moment-Curvature Analysis:
Idealized Yield Curvature ($\emptyset_{Yi}$): 0.00025 rad/in.
Ultimate Curvature ($\emptyset_u$): 0.00278 rad/in.
$\mu_{CIP} = 1 + 3\left(\frac{\emptyset_u}{\emptyset_{Yi}} - 1\right)\frac{L_p}{L}\left(1 - 0.5\frac{L_p}{L}\right) = 7.41$

<u>Spliced Column:</u>
$\beta = 0.55,\ \ H_{sp} = 0.,\ \ L_{sp} = 18.0\ in.$
$L_p^{sp} = L_p - \left(1 - \frac{H_{sp}}{L_p}\right)\beta L_{sp} \leq L_p = 16.01\ in.$
$\mu_{sp} = 1 + 3\left(\frac{\emptyset_u}{\emptyset_{Yi}} - 1\right)\frac{L_p^{sp}}{L}\left(1 - 0.5\frac{L_p^{sp}}{L}\right) = 5.17$</td><td>Note: Displacement ductility capacity for a reference column is not needed in this method. Also, note that no test was done on a reference CIP reinforced with No. 10 bars. However, using the CIP data in Haber et al. (2014):

$\mu_{CIP} = 7.36$
(+0.7% error)

$\mu_{sp} = 5.07$
(+1.9% error)</td></tr>
<tr><td>Present Study / PGD

Column with grouted sleeve couplers immediately above the footing surface</td><td><u>Non-Spliced Column (CIP):</u>
Bar size: No. 8, Column Length=96 in., L_p = 20.79 in.

Moment-Curvature Analysis:
Idealized Yield Curvature ($\emptyset_{Yi}$): 0.000245 rad/in.
Ultimate Curvature ($\emptyset_u$): 0.004659 rad/in.
$\mu_{CIP} = 1 + 3\left(\frac{\emptyset_u}{\emptyset_{Yi}} - 1\right)\frac{L_p}{L}\left(1 - 0.5\frac{L_p}{L}\right) = 11.44$

<u>Spliced Column:</u>
$\beta = 0.7,\ \ H_{sp} = 0.,\ \ L_{sp} = 16.5\ in.$
$L_p^{sp} = L_p - \left(1 - \frac{H_{sp}}{L_p}\right)\beta L_{sp} \leq L_p = 9.24\ in.$
$\mu_{sp} = 1 + 3\left(\frac{\emptyset_u}{\emptyset_{Yi}} - 1\right)\frac{L_p^{sp}}{L}\left(1 - 0.5\frac{L_p^{sp}}{L}\right) = 5.95$</td><td>$\mu_{CIP} = 12.37$
(-7.5% error)

$\mu_{sp} = 5.76$
(+3.3% error)</td></tr>
<tr><td>Present Study / PGS

Column with grouted sleeve couplers immediately above the footing surface</td><td><u>Non-Spliced Column (CIP):</u>
Bar size: No. 8, Column Length=96 in., L_p = 20.79 in.

Moment-Curvature Analysis:
Idealized Yield Curvature ($\emptyset_{Yi}$): 0.000245 rad/in.
Ultimate Curvature ($\emptyset_u$): 0.004659 rad/in.
$\mu_{CIP} = 1 + 3\left(\frac{\emptyset_u}{\emptyset_{Yi}} - 1\right)\frac{L_p}{L}\left(1 - 0.5\frac{L_p}{L}\right) = 11.44$

<u>Spliced Column:</u>
$\beta = 0.7,\ \ H_{sp} = 0.,\ \ L_{sp} = 14.57\ in.$
$L_p^{sp} = L_p - \left(1 - \frac{H_{sp}}{L_p}\right)\beta L_{sp} \leq L_p = 10.59\ in.$
$\mu_{sp} = 1 + 3\left(\frac{\emptyset_u}{\emptyset_{Yi}} - 1\right)\frac{L_p^{sp}}{L}\left(1 - 0.5\frac{L_p^{sp}}{L}\right) = 6.63$</td><td>$\mu_{CIP} = 12.37$
(-7.5% error)

$\mu_{sp} = 9.08$
(-26.9% error)</td></tr>
</table>

Table 6.3 Continued

Reference / Column	Calculated	Measured
Present Study / PHD Column with hybrid (grouted-threaded) couplers immediately above the footing surface, NOT Seismic Couplers	<u>Non-Spliced Column (CIP):</u> Bar size: No. 8, Column Length=96 in., L_p = 20.79 in. Moment-Curvature Analysis: Idealized Yield Curvature ($\emptyset_{Yi}$): 0.000245 rad/in. Ultimate Curvature ($\emptyset_u$): 0.004659 rad/in. $\mu_{CIP} = 1 + 3\left(\frac{\emptyset_u}{\emptyset_{Yi}} - 1\right)\frac{L_p}{L}\left(1 - 0.5\frac{L_p}{L}\right) = 11.44$ <u>Spliced Column:</u> $\beta = 0.79$ (average of five specimens, use 1.01 from the pullout specimen), $H_{sp} = 0.$, $L_{sp} = 9.45\ in.$ $L_p^{sp} = L_p - \left(1 - \frac{H_{sp}}{L_p}\right)\beta L_{sp} \leq L_p = 11.25\ in.$ $\mu_{sp} = 1 + 3\left(\frac{\emptyset_u}{\emptyset_{Yi}} - 1\right)\frac{L_p^{sp}}{L}\left(1 - 0.5\frac{L_p^{sp}}{L}\right) = 6.96$	$\mu_{CIP} = 12.37$ (-7.5% error) μ_{sp} =3.6 (+93.4% error)
Present Study / PHV Column with hybrid (grouted-threaded) couplers immediately above the footing surface	<u>Non-Spliced Column (CIP):</u> Bar size: No. 8, Column Length=96 in., L_p = 20.79 in. Moment-Curvature Analysis: Idealized Yield Curvature ($\emptyset_{Yi}$): 0.000245 rad/in. Ultimate Curvature ($\emptyset_u$): 0.004659 rad/in. $\mu_{CIP} = 1 + 3\left(\frac{\emptyset_u}{\emptyset_{Yi}} - 1\right)\frac{L_p}{L}\left(1 - 0.5\frac{L_p}{L}\right) = 11.44$ <u>Spliced Column:</u> $\beta = 0.82$, $H_{sp} = 0.$, $L_{sp} = 8.63\ in.$ $L_p^{sp} = L_p - \left(1 - \frac{H_{sp}}{L_p}\right)\beta L_{sp} \leq L_p = 13.71\ in.$ $\mu_{sp} = 1 + 3\left(\frac{\emptyset_u}{\emptyset_{Yi}} - 1\right)\frac{L_p^{sp}}{L}\left(1 - 0.5\frac{L_p^{sp}}{L}\right) = 8.17$	$\mu_{CIP} = 12.37$ (-7.5% error) $\mu_{sp} = 10.23$ (-20.1% error)
Present Study / PTV Column with threaded couplers immediately above the footing surface	<u>Non-Spliced Column (CIP):</u> Bar size: No. 8, Column Length=96 in., L_p = 20.79 in. Moment-Curvature Analysis: Idealized Yield Curvature ($\emptyset_{Yi}$): 0.000245 rad/in. Ultimate Curvature ($\emptyset_u$): 0.004659 rad/in. $\mu_{CIP} = 1 + 3\left(\frac{\emptyset_u}{\emptyset_{Yi}} - 1\right)\frac{L_p}{L}\left(1 - 0.5\frac{L_p}{L}\right) = 11.44$ <u>Spliced Column:</u> $\beta = 0.4$, $H_{sp} = 0.$, $L_{sp} = 9.0\ in.$ $L_p^{sp} = L_p - \left(1 - \frac{H_{sp}}{L_p}\right)\beta L_{sp} \leq L_p = 17.19\ in.$ $\mu_{sp} = 1 + 3\left(\frac{\emptyset_u}{\emptyset_{Yi}} - 1\right)\frac{L_p^{sp}}{L}\left(1 - 0.5\frac{L_p^{sp}}{L}\right) = 9.81$	$\mu_{CIP} = 12.37$ (-7.5% error) $\mu_{sp} = 7.77$ (+26.3% error)

Table 6.3 Continued

Reference / Column	**Calculated**	**Measured**
Present Study / PHH Column with hybrid (grouted-headed) couplers immediately above the footing surface	<u>Non-Spliced Column (CIP):</u> Bar size: No. 8, Column Length=96 in., L_p= 20.79 in. Moment-Curvature Analysis: Idealized Yield Curvature ($\emptyset_{Yi}$): 0.000245 rad/in. Ultimate Curvature ($\emptyset_u$): 0.004659 rad/in. $\mu_{CIP} = 1 + 3\left(\frac{\emptyset_u}{\emptyset_{Yi}} - 1\right)\frac{L_p}{L}\left(1 - 0.5\frac{L_p}{L}\right) = 11.44$ <u>Spliced Column:</u> $\beta = 0.8,\ \ H_{sp} = 0.,\ \ L_{sp} = 7.75\ in.$ $L_p^{sp} = L_p - \left(1 - \frac{H_{sp}}{L_p}\right)\beta L_{sp} \leq L_p = 14.59\ in.$ $\mu_{sp} = 1 + 3\left(\frac{\emptyset_u}{\emptyset_{Yi}} - 1\right)\frac{L_p^{sp}}{L}\left(1 - 0.5\frac{L_p^{sp}}{L}\right) = 8.59$	$\mu_{CIP} = 12.37$ (-7.5% error) $\mu_{sp} = 11.49$ (-25.2% error)

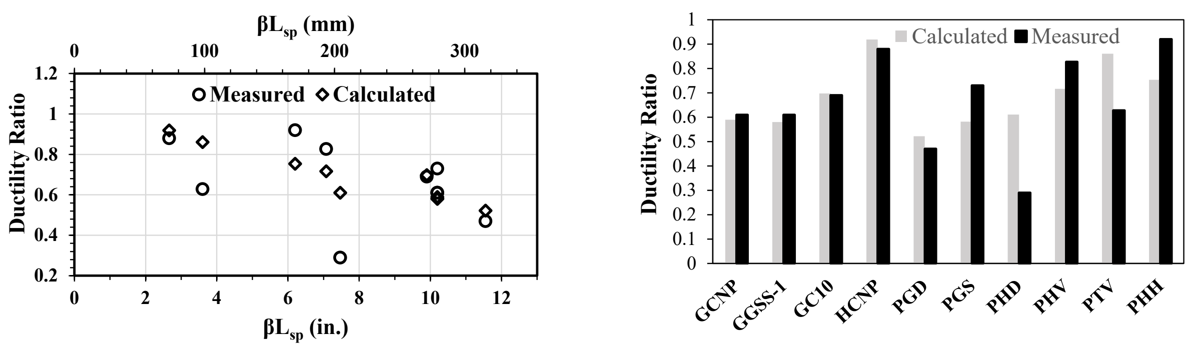

a) Ductility Ratio ($\frac{\mu_{sp}}{\mu_{CIP}}$) vs. Coupler Properties

b) Ductility Ratio ($\frac{\mu_{sp}}{\mu_{CIP}}$) vs. Column ID

Figure 6.2 Evaluation of Modified Plastic Hinge Length (Method 2) for Design of Mechanically Spliced Columns

6.5 Evaluation of Pushover Analysis Method (Method 3)

A distributed plasticity fiber-section pushover analysis is allowed in Method 3. Furthermore, the coupler effects are included at their actual location and using the actual coupler stress-strain relationship within the coupler region. Method 3 was fully investigated in Chapter 4. A summary of the results can be found in Table 4.6. A graphical representation of the table is shown in Figure 6.3. This method was mostly conservative by estimating a smaller displacement (drift) capacity than what was seen in the test. The error between the calculated and measured failure drifts for the CIP column was -14.7% (a drift ratio of 7.64% in the pushover analysis vs. 8.96% in the test). The average error between the calculated and measured failure drifts for six precast columns was -8.5% (+26.6% in PGD, -21.8% in PGS, -18.6% in PHD, -18.3% for PHV, +12% for PTV, and -30.7% for PHH).

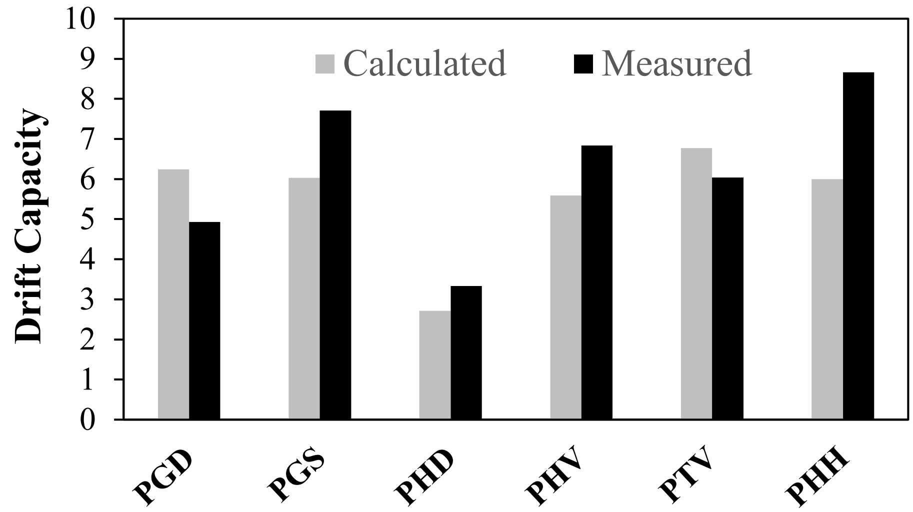

Figure 6.3 Evaluation of Distributed Plasticity Pushover Analysis (Method 3) for Design of Mechanically Spliced Columns

6.6 Comparison of Three Mechanically Spliced Column Design Methods

Table 6.4 presents and Figure 6.4 shows the measured and calculated responses of 10 bridge columns discussed in the previous sections. In the table, the error between the calculated and the measured responses is also presented in parentheses. In Figure 6.4, a red dashed line at 1.0 was included, in which responses above this line indicate that the corresponding method is unconservative and responses below the line indicate a conservative method. All three current design methods of mechanically spliced bridge columns were included. We can see that Method 3 (the pushover analysis with an additional element for couplers including the coupler stress-strain relationship) overall resulted in a better accuracy. Nevertheless, the other two methods, which are simpler and less involved, resulted in a conservative design. The large errors seen in PHD were because this column had couplers that were not seismic graded in the present study. Note that previous tests on the same product showed better performance. Overall, all three methods were found viable for the analysis/design of mechanically spliced bridge columns.

Table 6.4 Evaluation of Current Design Methods for Mechanically Spliced Bridge Columns

Reference	Column ID	Measured Ductility Capacity	Measured Drift Capacity (%)	Method 1 Calculated Ductility Capacity (error)	Method 2* Calculated Ductility Capacity (error)	Method 3 Calculated Drift Capacity (error)
Haber et al. (2014)	GCNP	4.52	5.95	4.56 (+0.9%)	4.49 (-0.7%)	N/A
Haber et al. (2014)	HCNP	6.49	9.85	6.33 (-2.5%)	7.0 (+7.9%)	N/A
Pantelides et al. (2014)	GGSS-1	5.4	8.38	5.52 (+2.2%)	5.46 (+1.5%)	N/A
NCHRP 935	GC10	5.07	7.78	5.00 (-1.3%)	5.17 (+2.0%)	N/A
Present Study	PGD	5.76	4.93	7.55 (+31.1%)	5.95 (+3.3%)	6.24 (+26.6%)
Present Study	PGS	9.08	7.71	7.67 (-15.5%)	6.63 (-27.0%)	6.03 (-21.8%)
Present Study	PHD	3.6	3.33	6.43 (+78.6%)	6.96 (+93.3%)	2.71 (-18.6%)
Present Study	PHV	10.23	6.84	7.30 (-28.6%)	8.17 (-20.1%)	5.59 (-18.3%)
Present Study	PTV	7.77	6.04	9.65 (+24.2%)	9.81 (+26.3%)	6.77 (+12.1%)
Present Study	PHH	11.49	8.66	7.42 (-35.4%)	8.59 (-25.2%)	6.0 (-30.7%)

* Note that moment-curvature was used in Method 2. Alternative in this method is to perform a pushover analysis using a lumped plasticity element with modified plastic hinge length including coupler effects.

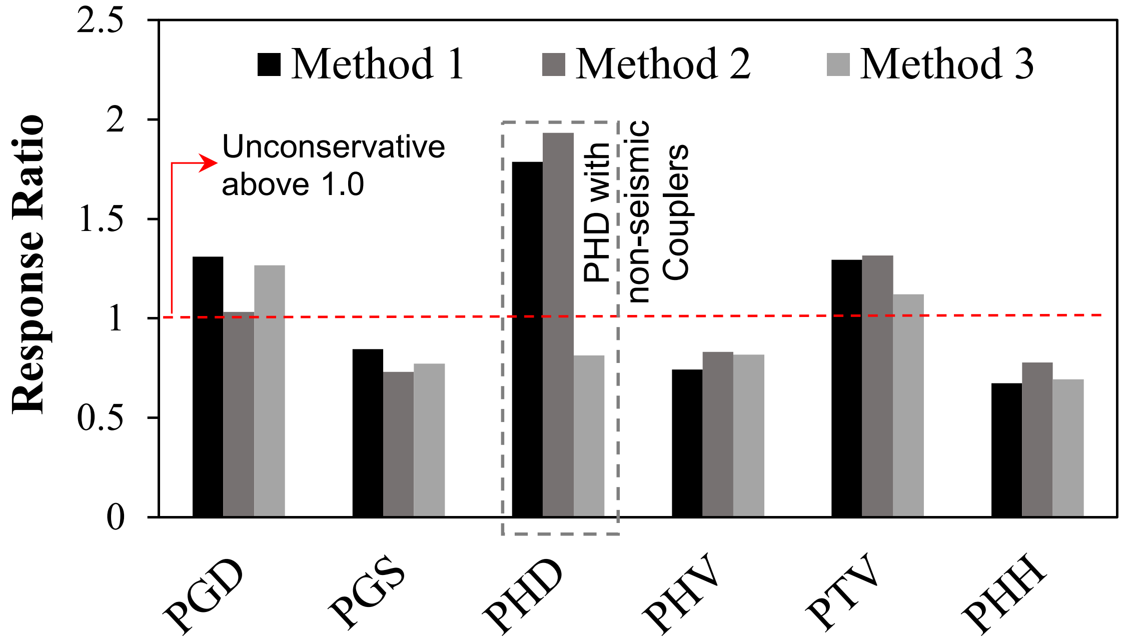

Figure 6.4 Evaluation of Three Design Methods for Mechanically Spliced Bridge Columns

6.7 References

AASHTO. (2011). "AASHTO Guide Specifications for LRFD Seismic Bridge Design," Washington, DC: American Association of State Highway and Transportation Officials.

Haber, Z.B., Saiidi, M.S., and Sanders, D.H. (2014). "Seismic Performance of Precast Columns with Mechanically Spliced Column-footing Connections," *ACI Structural Journal*, Vol. 111, No. 3, pp. 639-650.

Pantelides, C.P., Ameli, M.J., Parks, J.E., and Brown, D.N. (2014). "Seismic Evaluation of Grouted Splice Sleeve Connections for Precast RC Bridge Piers in ABC," Utah Department of Transportation, Report No. UT-14.09, 168 pp.

Saiidi, M.S., Mehraein, M., Shrestha, G., Jordan, E., Itani, A., Tazarv, M., Sanders, D., Murphy, T.M., Reno, M.L., and Pohll, M.N. (2020). "Proposed AASHTO Seismic Specifications for ABC Column Connections," National Academies of Sciences, Engineering, and Medicine, NCHRP Report No. 935, Washington, DC: The National Academies Press, 354 pp.

Tazarv, M. and Saiidi, M.S. (2016) "Seismic Design of Bridge Columns Incorporating Mechanical Bar Splices in Plastic Hinge Regions," *Engineering Structures*, DOI: 10.1016/j.engstruct.2016.06.041, Vol. 124, pp. 507-520

7. SUMMARY AND CONCLUSIONS

7.1 Summary

Bar couplers are currently used in bridge capacity protected members but are prohibited in bridge columns located in high seismic regions. This is mainly because (1) the coupler performance has not been fully established, and (2) the effects of the couplers on the column seismic behavior have not been completely understood. Recent studies have tried to fill these knowledge gaps, but the literature lacks data on how varying the coupler types/products and column properties, such as geometry, aspect ratio, and axial loads, affects the capacity and demand of spliced bridge columns.

The main objectives of the present study were to: (1) establish a comprehensive performance database for mechanically spliced precast bridge columns through large-scale testing, and (2) verify or update current state-of-the-art design methods for mechanically spliced precast bridge columns. To achieve these goals, several tasks were completed. First, the literature was reviewed to synthetize the latest studies on the coupler performance and the spliced column behavior. Second, the coupler products that were suitable for bridge column applications were identified and the manufacturers were contacted for possible collaboration. Subsequently, eight half-scale bridge columns were designed, constructed, and tested using a same lateral loading regime simulating earthquakes. One column followed the conventional cast-in-place (CIP) detailing to serve as the benchmark model and seven utilized a type of coupler product per specimen at the column base. All columns had the same geometry, reinforcement, confinement, aspect ratio, and axial load with only one target variable of the coupler connection. The test data was processed, and a new experimental coupler column performance database was formed. The current analysis/design methods of mechanically spliced bridge columns were evaluated using the new database. Finally, a comprehensive parametric study, including 405 pushover and 540 dynamic analyses, was performed to better understand the displacement capacities and demands of mechanically spliced bridge columns for a wide range of practical parameters.

7.2 Conclusions

Based on the experimental and analytical investigations, the following conclusions were drawn from this study:

- In CIP, flexural and shear cracks developed and extended at low drifts. Spalling began at 2% drift ratio. Major spalling occurred at larger drift ratios, leading to longitudinal bar buckling then bar fracture. The CIP mode of failure was the longitudinal bar fracture. The CIP lateral load capacity was 65.4 kips (291 kN), and the CIP drift capacity was 8.96%.

- In PGD, flexural and shear cracks developed and extended at low drifts. Spalling began at 3% drift ratio. PGD failed due to the longitudinal bar pullout from the coupler base, whereas CIP failed due to the longitudinal bar fracture. The PGD peak lateral force was 74.7 kips (332 kN), and its drift capacity was 4.93%. The lateral load capacity of PGD was 14% higher than that of CIP, and the drift capacity of PGD was 45% less than that of CIP.

- PGS exhibited flexural and shear cracks at low drifts, then concrete spalled at 3% drift ratio. The spalling continued until the end of the test exposing the bars and couplers. Similar to CIP, the failure mode for PGS was the longitudinal bar rupture. The PGS lateral force capacity was 69.6 kips (310 kN), and its drift capacity was 7.71%. The lateral force capacity of PGS was 6.4% higher than that of CIP. The displacement capacity of PGS was 14% lower than that of CIP.

- PHD exhibited flexural and shear cracks throughout the test with some minor spalling occurring during the 3% drift ratio cycles. The mode of failure for PHD was the longitudinal bar pullout from the coupler base. The PHD lateral force capacity was 71.5 kips (318 kN), and its drift capacity was 3.33%. The lateral force capacity of PHD was 9% higher than that of CIP. The drift capacity of PHD was 63% less than CIP. It is recommended that the manufacturer impose higher quality control measures to obtain consistent performance of bar fracture for this coupler type.

- In PHV, flexural and shear cracks developed and extended at low drifts. Spalling began at 3% drift ratio. PHV failed by a gradual loss of strength after the peak lateral force. The measured peak lateral strength was 74.2 kips (330 kN), which was 12.6% higher compared with CIP. The drift capacity of PHV was 6.84%, which was 26.8% lower than CIP.
- PTV experienced flexural cracking around the edges of the closure pour starting at low drifts. Spalling was observed at 1% at the top of the closure pour. PTV failed by the bar fracture, similar to CIP. The peak lateral strength of PTV was 73.0 kips (324.7 kN), an increase of 11.6% compared with CIP. PTV had a drift capacity of 6.04%, which was 32.6% lower than CIP.
- PHH experienced significant flexural and shear cracking. Spalling began at a drift ratio of 4.0% at the column base and continued throughout the test. PHH failed by a gradual loss of strength. PHH reached a peak lateral force of 72.3 kips (321kN), which was 10% higher than the CIP peak lateral force. The measured drift capacity of PHH was 8.66%, which was close to that of CIP with only 3.4% difference.
- RPH exhibited minor flexural cracks throughout the test. Significant spalling at the column base and on the south face above the neck section was initiated at 2.0% and 3.0% drift ratios, respectively. The test was stopped at 5.0% drift ratio to replace the exposed bars (BRR fuses). Limited damage was observed in the second set of testing. However, BRR exhibited a Z-shape buckling starting at 2.0% drift ratio, and this buckling worsened throughout the test. RPH-R (the repaired column) began to fail by strength degradation, but the test was halted after completing the 10% drift cycles since the displacement capacity of the CIP column, the reference column, was reached. RPH showed a peak lateral force of 69.2 kips (308 kN) when the test was stopped at 5.0% drift while RPH-R reached a lateral force of 74.7 kips (332 kN) at a drift ratio of 8.31%. The measured drift capacity of RPH-R was 9.8%, exceeding the 8.9% drift capacity of CIP. Repair and replacement of the BRR was proven to be a viable option with comparable results between the repaired and initial column. However, the initial stiffness of the two sets was not the same and must be improved in future testing. Furthermore, the Z-shape buckling of the longitudinal bars at high displacements was another point of concern, which can be eliminated with the use of tension-only members such as steel tendons.
- The pushover analysis for CIP correctly predicted the mode of failure by longitudinal bar rupture. The calculated peak lateral strength was 61.9 kips (275 kN) while the measured lateral strength was 65.4 kips (291 kN), or a 5.5% difference. The calculated failure drift for CIP was 7.64% while the CIP measured failure drift was 8.96%, or a 15.9% difference.
- The proposed pushover modeling method for the mechanically spliced bridge columns were found reasonably accurate for all spliced columns with seismic couplers. A method was devised to analyze columns with non-seismic couplers, which also successfully reproduced the column (PHD) behavior.
- Three design methods for bridge columns incorporating bar couplers were evaluated using experimental data for 10 precast columns. Method 1, a simple equation to reduce the displacement ductility capacity, resulted in an average error of -2.9 for the columns with seismic couplers. Therefore, this method was overall conservative.

- Method 2, which was based on the modified plastic hinge length, resulted in an average error of -3.5% for the columns incorporating seismic couplers. Therefore, this method was overall conservative.
- Method 3, which was based on the pushover analysis using the coupler stress-strain relationship within the spliced region, resulted in an average error of -6.4% for the columns utilizing seismic couplers. Therefore, this method was overall conservative. This method was the only technique that could reproduce the behavior of the column with non-seismic couplers, PHD, with a reasonable accuracy.

Overall, all mechanically spliced precast bridge columns met the current code seismic requirements, thus they are recommended for use in all 50 U.S. states. Furthermore, the three design methods evaluated herein for mechanically spliced bridge columns were found viable. Some errors were observed, but the general trend was that the three methods usually result in a conservative design for mechanically spliced bridge columns.

REFERENCES

AASHTO SGS (2011) “AASHTO Guide Specifications for Seismic Bridge Design,” Washington, D.C., American Association of State Highway and Transportation Officials.

AASHTO. (2014). “AASHTO Guide Specifications for LRFD Seismic Bridge Design,” Washington, D.C., American Association of State Highway and Transportation Officials.

ACI 374.2R-13 (2013). “Guide for Testing Reinforced Concrete Structural Elements Under Slowly Applied Simulated Seismic Loads.” American Concrete Institute (ACI) Committee 374, Farmington Hills, MI, 2013.

Ameli, M.J., Brown, D.N., Parks, J.E., and Pantelides, C.P. (2014). “Seismic Evaluation of Grouted Splice Sleeve Connections for Precast RC Bridge Piers in ABC.” Utah Department of Transportation, Research Division, Report No. UT-14.09.

Ameli, M.J., Brown, D.N., Parks, J.E., and Pantelides, C.P. (2016). “Seismic Column-to Footing Connections Using Grouted Splice Sleeves.” *ACI Structure Journal*, Vol. 113, No. 5, pp.1021-1030

Ameli, M.J. and. Pantelides, C.P (2017). “Seismic Analysis of Precast Concrete Bridge Columns Connected with Grouted Splice Sleeve Connectors.” *Journal of Structural Engineering*, 10.1061/(ASCE)ST.1943-541X.0001678, ASCE, Vol 143, No. 2.

Ameli, M.J. and Pantelides, C.P. (2017). “Seismic Analysis of Precast Concrete Bridge Columns Connected with Grouted Splice Sleeve Connectors.” *Journal of Structural Engineering*, 143(2), p.04016176.

ASTM A706 (2016). “Standard Specification for Low-Alloy Steel Deformed and Plain Bars for Concrete Reinforcement.” West Conshohocken, PA, 6 pp.

ASTM A706/A706M-09b (2009). “Standard Specification for LowAlloy Steel Deformed and Plain Bars for Concrete Reinforcement,” ASTM International, West Conshohocken, PA.

ASTM A1034 (Sep. 2016). “Standard Test Methods for Testing Mechanical Splices for Steel Reinforcing Bars.” ASTM International, West Conshohocken, PA.

ASTM C39/C39M-12. (2012). “Standard Test Method for Compressive Strength of Cylindrical Concrete Specimens,” West Conshohocken, PA.

ASTM C109/C109M-11b. (2011). “Standard Test Method for Compressive Strength of Hydraulic Cement Mortars (Using 2-in. or [50-mm] Cube Specimens),” West Conshohocken, PA.

ASTM E8 (2012). “Standard Test Methods for Tension Testing of Metallic Materials.” ASTM International, West Conshohocken, PA.

Bompa, D.V., and Elghazouli, A.Y. (2019), “Inelastic Behaviour of RC Members Incorporating Threaded Reinforcement Coupler.” *Engineering Structures*, DOI: 10.1016/j.engstruct.2018.11.053, Vol. 180, pp.468-483.

Boudaqa, A., Tazarv, M., and Tuhin, I. (2017). “Ductility without Confinement - A New Design and Construction Approach for RC Bridge Columns,” *International Journal of Bridge Engineering*, Special Issue, pp. 53-77.

Caltrans. (2019). “Caltrans Seismic Design Criteria (SDC), Version 2.0” Sacramento, CA: California Department of Transportation, 250 pp.

Dahal, P.K., Tazarv, M., and Wehbe, N. (2019). "Mechanical Bar Splices for Accelerated Construction of Bridge Columns," North Dakota State University - Upper Great Plains Transportation Institute, Fargo: Mountain-Plains Consortium (MPC), MPC Report No. 19-372, 142 pp.

Dahal, P.K., and Tazarv, M. (2020). "Mechanical Bar Splices for Incorporation in Plastic Hinge Regions of RC Members," *Construction and Building Materials*, Vol. 258, 120308, 17 pp.

Haber, Z.B., Saiidi, M.S., and Sanders, D.H. (2013). "Precast Column Footing Connections for Accelerated Bridge Construction in Seismic Zones." Rep. No. CCEER 13-08 Center for Civil Engineering Earthquake Research, Dept. of Civil and Environmental Engineering, Univ. of Nevada, Reno. NV.

Haber, Z.B., Saiidi, M.S., and Sanders, D.H. (2014). "Seismic Performance of Precast Columns with Mechanically Spliced Column-footing Connections," *ACI Structural Journal*, Vol. 111, No. 3, pp. 639-650.

Haber, Z.B., Saiidi, M.S. and Sanders, D.H. (2015). "Behavior and Simplified Modeling of Mechanical Reinforcing Bar Splices." *ACI Structural Journal*, 112(2), p.179.

Hewes, J.T. (2013). "Analysis of the State of the Art of Precast Concrete Bridge Substructure Systems." Arizona. Dept. of Transportation, Research Center, Report No. FHWA-AZ-13-687, 124 pp.

Krawinkler, H., and Moncarz, P.D. (1982). "Similitude Requirements for Dynamic Models." ACI Special Publication, Vol. 73, pp. 1-22.

LaVoy, M.R. (2020). "Seismic Performance of Mechanically Spliced Bridge Columns Through Analytical Studies." MS Thesis, South Dakota State University, 106 pp.

Mander, J.B., Priestley, M.J.N., and Park, R. (1988). "Theoretical Stress-Strain Model for Confined Concrete," *Journal of Structural Engineering*, ASCE, Vol. 114, No. 8, pp. 1804-1826.

OpenSees. (2016). "Open System for Earthquake Engineering Simulations," Version 2.4.1, Berkeley, CA, Available online: http://opensees.berkeley.edu.

Pantelides, C.P., Ameli, M.J., Parks, J.E., and Brown, D.N. (2014). "Seismic Evaluation of Grouted Splice Sleeve Connections for Precast RC Bridge Piers in ABC," Utah Department of Transportation, Report No. UT-14.09, 168 pp.

Saiidi, M.S., Mehraein, M., Shrestha, G., Jordan, E., Itani, A., Tazarv, M., Sanders, D., Murphy, T.M., Reno, M.L., and Pohll, M.N. (2020). "Proposed AASHTO Seismic Specifications for ABC Column Connections," National Academies of Sciences, Engineering, and Medicine, NCHRP Report No. 935, Washington, DC: The National Academies Press, 354 pp.

Seismosoft (2019) "SeismoArtif - A computer program for generation of artificial accelerograms." Available from URL: www.seismosoft.com

Tazarv, M., and Saiidi, M.S. (2013). "Analytical Studies of the Seismic Performance of a Full-Scale SMA-Reinforced Bridge Column," (Invited Paper), *International Journal of Bridge Engineering*, Vol. 1, No. 1, pp. 37-50.

Tazarv, M., and Saiidi, M.S. (2014) "Next Generation of Bridge Columns for Accelerated Bridge Construction in High Seismic Zones," Center For Civil Engineering Earthquake Research, Department of Civil and Environmental Engineering, University of Nevada, Reno, Nevada, Report No. CCEER-14-06, 400 pp.

Tazarv, M., and Saiidi, M.S. (2016). "Seismic Design of Bridge Columns Incorporating Mechanical Bar Splices in Plastic Hinge Regions," *Engineering Structures*, DOI: 10.1016/j.engstruct.2016.06.041, Vol 124, pp. 507-520.

Tazarv, M., Boudaqa, A., and Tuhin, I.A. (2020). "Repairable Precast Moment-Resisting Buildings: Part I – Experimental Investigations," *ACI Structural Journal*, Vol. 117, No. 6, 147-160 pp.

USGS. (2019) "U.S. Seismic Design Maps Web Services," United States Geological Survey.

Wang, Z., Qu, H., Li, T., Wei, H., Wang, H., and Duan, H. (2018). "Quasi-Static Cyclic Tests of Precast Bridge Columns with Different Connection Details for High Seismic Zones," *Engineering Structures*, DOI: 10.1016/j.engstruct.2017.12.035, Vol 158, pp. 13-27.